Pharmaceutical and Biomedical Applications of Spectroscopy in the Photon Migration Regime

Tomas Svensson

Doctoral Thesis
2008

Lund University

Pharmaceutical and Biomedical Applications of Spectroscopy in the Photon Migration Regime

Updated version, June 2008

Original version printed in Sweden
by Media-Tryck, Lund, March 2008

Thesis defence took place at Lund University 18 April 2008
Faculty opponent: Prof. Enrico Gratton, University of California

Division of Atomic Physics
Department of Physics
Faculty of Engineering, LTH
Lund University
P.O. Box 118
SE–221 00 Lund
Sweden

http://www.atom.fysik.lth.se
http://www.atom.fysik.lth.se/medweb

ISSN 0281-2762
Lund Reports on Atomic Physics, LRAP-392

ISBN 978-91-628-7469-8

Mere power and mere knowledge exalt human nature, but do not bless it
Francis Bacon (1620)

Abstract

Optical measurement technologies and spectroscopy are of great importance in the modern society. Optical techniques are frequently used in for example quantitative analysis of chemical composition, particle size, velocity and temperature. Near-infrared light is used to determine concentration of active ingredients in pharmaceuticals, laser light is employed in pollution monitoring, the pulse oximeter is used for routine monitoring of arterial oxygenation in patients during surgery, the police utilise pulsed laser light to determine velocities of cars, and so on.

An example of particular importance for industry and science is absorption spectroscopy, i.e. measurements of how materials absorb light of different wavelengths (colours). Since light absorption is intimately linked to atomic and molecular structure, the technique is very important in analytical chemistry for analysis of chemical composition. In clear liquids and gases, where light travels in straight lines, such analysis is well developed, and fairly simple. Quantitative analysis relies on the fact that the optical pathlength is known – simply given by the sample dimensions. Unfortunately, absorption spectroscopy becomes significantly more difficult in materials exhibiting strong light-scattering (turbid materials), such as pharmaceutical solids and biological tissue. Quantitative analysis becomes particularly difficult, partly due to the unknown and optical pathlength, and partly due to that light scattering often has larger impact on the detected light intensity than does absorption.

The present thesis is devoted to two different matters: One part is the development of a novel optical technique for characterisation of solid pharmaceutical materials. The other part being the continued development of photon time-of-flight spectroscopy, as well as exploration of new application areas of this method. These two optical techniques are conceptually and technically very different, but they are both designed for analysis of highly scattering materials (that is, materials in which light frequently changes its direction of propagation). In this thesis, the techniques are applied for chemical analysis and analysis of structural properties of for example pharmaceutical tablets, human prostate tissue, and

female breast tissue. These materials, and many others, scatter light to a much stronger extent than even the densest fog. In a typical pharmaceutical tablet, light is scattered severely enough to completely change its direction each twentieth micrometer. This level of scattering also makes light, on average, travel more than 10 cm when transmitted through a 3 mm thick tablet.

The new optical method for analysis of structure in pharmaceutical solids, presented in this thesis, enables non-destructive measurement of properties such as porosity. Structural properties are measured indirectly through measurements of the very weak, but detectable, light absorption by the oxygen molecules that are dispersed within the sample. The total absorption by oxygen is not only determined by sample porosity, but is also strongly influenced by scattering properties. A moderately compressed tablet of 3 to 4 mm thickness can, due to long optical pathlengths in transmission, give rise to absorptions corresponding to tens of millimetres through ambient air. The sensitivity to sample structure makes this technique highly interesting in, for example, process monitoring. It can also be used in predicting important pharmaceutical parameters such as drug release and dissolution. The technique is based on ultrasensitive, high-resolution diode laser spectroscopy – a technique commonly used for gas analysis in, for example, atmospheric sciences and pollution monitoring. However, the detection of gases within solids and scattering materials is accompanied by several aggravating circumstances, setting special requirements on measurement procedure and instrumentation. While conventional use of the technology involves well defined beamlines and gas cells, this thesis deals with detection of weak intensities of diffuse light and devastating optical interference.

The other part of this thesis is concerned with pharmaceutical and medical applications of ultrashort (picosecond scale, 1×10^{-12} s) laser pulses for analysis of chemical composition and material structure of highly scattering samples. The technique is referred to as time-of-flight spectroscopy or time-resolved spectroscopy. A short pulse of light injected into a scattering material will, upon detection at some distance from the injection location, appear broadened in time due to that different photons (the elementary particle of light) have travelled different distances at the same speed (c_0/n). The measurement of the temporal distribution of the detected light (i.e. the photon time-of-flight distribution) allows circumventing the difficulties encountered in conventional absorption spectroscopy. The time-of-flight distribution is a direct measure of the previously unknown optical pathlength, and the shape of the distribution can be used for quantification of both absorption and scattering. The most important contributions of the present thesis, related to this technique, include the development of sophisticated modelling of light propagation for significant improvements in accuracy, as well as its application to spectroscopy

of pharmaceutical solids and human prostate tissue.

The research concerning pharmaceutical solids is conducted in collaboration with Astra Zeneca R&D, Mölndal. The pharmaceutical industry is continuously looking for new and improved analytical methods. They are currently particularly interested in fast and non-destructive methods for process monitoring and control. Optical techniques are almost often close to ideal in this context.

The interest in prostate spectroscopy is related to the current interest in photodynamic therapy (PDT) of prostate cancer. Clinical trials are currently conducted at several locations worldwide. Our research group in Lund has for a long time explored clinical applications of PDT. These efforts have, for example, resulted in a routine PDT treatment of non-melanoma skin cancer at the Lund University Hospital. In collaboration with SpectraCure AB, our group is currently involved in an ongoing clinical trial that investigates the potential of PDT for primary treatment of prostate cancer. The present thesis shows that time-of-flight spectroscopy is a useful and highly reliable technique for prostate spectroscopy, capable of delivering optical and physiological information of great importance to PDT and its dosimetry. This includes quantification of absorption, scattering, haemoglobin concentration and tissue oxygenation.

In addition, this thesis also combines the two technical components briefly described above. Information on oxygen absorption in combination with direct measurement of photon pathlengths allow what can be called optical porosimetry - that is, a quantitative measure of the amount of gas-filled pores of solid materials. This approach is an interesting alternative to conventional mercury intrusion porosimetry, a technique used for characterisation of very diverse materials, from concrete to pharmaceuticals.

Populärvetenskaplig sammanfattning

Optisk spektroskopi och mätteknik är av enorm betydelse för det moderna samhället. Dessa metoder nyttjar ljus för att exempelvis bestämma kemisk sammansättning, partikelstorlek, hastighet eller temperatur. Laserljus används för att mäta luftföroreningar, pulsoximetern använder ljus för att mäta blodets syresättning hos patienter under operation, och polisen använder ljuspulser för att mäta bilars hastighet, och så vidare.

Ett exempel på en optisk mätteknik av stor vikt för både industri och vetenskap är absorptionsspektroskopin, d.v.s. mätningar av hur mycket ett material absorberar olika ljusvåglängder (färger). Eftersom ljusabsorptionen och dess variation med ljusvåglängd är knuten till atom- och molekyl-struktur kan tekniken användas för bestämning av kemisk sammansättning. I material där ljus färdas rätlinjigt (t.ex. klara vätskor och gaser) är sådan analys mycket välutvecklad, och relativt enkel. Kvantitativ analys möjliggörs av att ljusets väglängd genom materialet är känd. I kraftigt ljusspridande material, såsom farmaceutiska tabletter och pulver eller biologisk vävnad, försvåras analysen avsevärt. Med ljusspridning menas att ljuset byter riktning på grund av att det studsar mot olika partiklar. Kvantitativ analys blir speciellt svår på grund av att väglängden nu är okänd, och att spridningsegenskaperna ofta har större inverkan på mängden detekterat ljus än vad absorptionen har.

Denna avhandling omfattar två saker; dels utvecklandet av en ny optisk mätteknik för analys av farmaceutiska fasta material, och dels vidareutveckling av, samt utforskandet av nya användningsområden för, den så kallade tidsupplösta spektroskopin. Dessa två mättekniker är helt väsensskilda, och dess gemensamma nämnare är endast att de båda är avsedda för analys av material där ljus sprids kraftigt (d.v.s. byter riktning ofta). I denna avhandling används teknikerna till exempel för kemisk analys och analys av struktur hos farmaceutiska tabletter, mänsklig prostatavävnad eller mänsklig bröstvävnad. I dessa, och

många andra material, sprids ljus enormt mycket mer kraftigt än i den tätaste dimma. I en typisk farmaceutisk tablett sprids ljuset så kraftigt att det helt har bytt riktning var tjugonde mikrometer (0.02 mm). Detta resulterar i att medelväglängden för ljus som färdats genom en 3 mm tjock tablett ofta är över 10 cm.

I denna avhandling presenteras en nyutvecklad farmaceutisk mätteknik avsedd för analys av struktur hos farmaceutiska material. Tekniken öppnar för icke-förstörande mätning av egenskaper såsom t.ex. porositet. Egenskaperna mäts indirekt genom mätning av den mycket svaga (men mätbara) ljusabsorptionen hos de syremolekyler som är utspridda i provet. Den totala ljusabsorptionen av syremolekylerna bestäms dock inte bara av provets porositet, utan också av dess ljusspridning. En mindre kompakt tablett med 3-4 mm tjocklek kan på grund av lång optisk väglängd genom provet uppvisa en "syreabsorption" som motsvarar tiotals millimeter genom ren luft. Känsligheten för provets struktur gör att tekniken är högintressant för t.ex. processanalys. Vidare kan den bidra med förutsägelser av viktiga läkemedelsparametrar som frigörelsehastighet och upplösningshastighet. Tekniken är baserad på den ultrakänsliga diodlaser-spektroskopin som används för gasanalys inom t.ex. atmosfärsforskning och luftföroreningsanalys. Att detektera gaser inuti fasta och kraftigt spridande material ställer dock väldigt annorlunda krav på mätförfarande och utrustning.

Den andra beståndsdelen i avhandlingen rör farmaceutiska och medicinska tillämpningar av ultrakorta laserpulser (miljondelar av en miljondels sekund långa) för analys av kemisk sammansättning och materialstruktur hos spridande material. Tekniken kallas ofta tidsupplöst spektroskopi, men dess engelska namn "time-of-flight spectroscopy" är mer beskrivande. En kort ljuspuls som skickats in, och färdats en bit genom ett spridande material kommer vid detektion att upplevas som längre – detta beroende på att ljusets olika delar färdas olika långt (med samma hastighet). Genom att mäta tidsfördelningen hos det detekterade ljuset (d.v.s. ljusets flygtid, time-of-flight) kringgås de problem som traditionell absorptionsspektroskopi drabbas av. Tidsfördelningen ger ett direkt mått på den tidigare okända väglängden, och ljuspulsens intensitetsfördelning kan användas för kvantifiering av både absorption och spridning. Avhandlingens viktigaste bidrag till denna teknologi rör utveckling av sofistikerad modellering av ljusutbredning, resulterande i kraftigt förbättrad mätnoggrannhet, samt teknikens specifika tillämpning för spektroskopi av farmaceutiska material och mänsklig prostatavävnad.

Forskningen kring farmaceutiska tillämpningar sker i nära samarbete med Astra Zeneca R&D Mölndal. Den farmaceutiska industrin är ständigt intresserade av nya och förbättrade mättekniker, och upplever i dagsläget ett kraftigt behov av snabba och icke-förstörande analysmetoder för processkontroll. Optiska

tekniker är i det närmaste ideala i detta sammanhang.

Intresset för prostataspektroskopin hänger samman med det högaktuella intresset för fotodynamisk terapi av prostatacancer. I skrivande stund utförs kliniska prövningar av denna behandlingsform på flera håll i världen. Vår forskargrupp i Lund har länge forskat kring fotodynamisk terapi, vilket bl.a. resulterat i fotodynamisk rutinbehandling av hudcancer (förutom maligna melanom) på Lunds Universitetssjukhus. I samarbete med SpectraCure AB drivs nu kliniska försök (primärbehandling av mänsklig prostatacancer) avsedda att utröna teknikens potential för behandling av prostatacancer. Denna avhandling visar att tidsupplöst spektroskopi är en ypperlig mätteknik, kapabel att pålitligt leverera optisk och fysiologisk information om ljusabsorption, ljusspridning, blodmängd och blodets syresättning i prostatan. Dessa parametrar är av yttersta betydelse för fotodynamisk terapi och dess dosimetri.

De två teknikerna som diskuterats ovan kombineras dessutom i avhandlingen. Informationen om syreabsorption tillsammans med direkt mätning av ljusets väglängd möjliggör vad som kan kallas optisk porosimetri - d.v.s. en kvantiativ mätning av mängden gasfyllda håligheter i fasta material. Tekniken utgör ett intressant alternativ till den konventionella kvicksilver-porosimetrin, som används vid karakterisering av vitt skilda material, alltifrån betong till farmaceutiska tabletter.

List of publications

This thesis is based on the following papers, which will be referred to by their roman numerals in the text.

I **Time and wavelength resolved spectroscopy of turbid media using light continuum generated in a crystal fiber**
A. Abrahamsson, T. Svensson, S. Svanberg
S. Andersson-Engels, J. Johansson and S. Folestad.
Optics Express **12**, 4103-4112 (2004).

II **Scatter correction of transmission near-infrared spectra by photon migration data: Quantitative analysis of solids**
A. Abrahamsson, A. Löwgren, B. Strömdahl, T. Svensson, S. Andersson-Engels, J. Johansson and S. Folestad.
Applied Spectroscopy **59**, 1381-1387 (2005).

III **Characterization of normal breast tissue heterogeneity using time-resolved near-infrared spectroscopy**
T. Svensson, J. Swartling, P. Taroni, A. Torricelli, P. Lindblom, C. Ingvar and S. Andersson-Engels.
Physics in Medicine and Biology **50**, 2559-2271 (2005).

IV **Performance assessment of photon migration instruments: the MEDPHOT protocol**
A. Pifferi, A. Torricelli, A. Bassi, P. Taroni, R. Cubeddu, H. Wabnitz, D. Grosenick, M. Möller, R. Macdonald, J. Swartling, T. Svensson, S. Andersson-Engels, R.L.P. van Veen, H.J.C.M. Sterenborg, J.M Tualle, H.L. Nghiem, S. Avrillier, M. Whelan and H. Stamm.
Applied Optics **44**, 2104-2114 (2005).

V **Least-squares support vector machines modelization for time-resolved spectroscopy**
F. Chauchard, S. Roussel, J.M. Roger, V. Bellon-Maurel, C. Abrahamsson, T. Svensson, S. Andersson-Engels, S. Svanberg.
Applied Optics **44**, 7091-7097 (2005).

VI ***In vivo* optical characterization of human prostate tissue using near-infrared time-resolved spectroscopy**
T. Svensson, S. Andersson-Engels, M. Einarsdóttír and K. Svanberg.
Journal of Biomedical Optics **12**, 014022 (2007).

VII **Noninvasive characterization of pharmaceutical solids by diode laser oxygen spectroscopy**
T. Svensson, L. Persson, M. Andersson, S. Svanberg, S. Andersson-Engels, J. Johansson, and S. Folestad.
Applied Spectroscopy **61**, 784-786 (2007).

VIII **Non-intrusive optical study of gas and its exchange in human maxillary sinuses**
L. Persson, M. Andersson, T. Svensson, M. Cassel-Engquist, K. Svanberg, and S. Svanberg.
Proc. of SPIE: Diagnostic Optical Spectroscopy in Biomedicine IV **6628**, 662804 (2007).

IX **Flexible lock-in detection system based on synchronized computer plug-in boards applied in sensitive gas spectroscopy**
M. Andersson, L. Persson, T. Svensson, S. Svanberg.
Review of Scientific Instruments **78**, 113107 (2007).

X **White Monte Carlo for Time-resolved Photon Migration**
E. Alerstam, S. Andersson-Engels, and T. Svensson.
Journal of Biomedical Optics **13**, 041304 (2008).

XI **High sensitivity gas spectroscopy of porous, highly scattering solids**
T. Svensson, M. Andersson, L. Rippe, J. Johansson, S. Folestad, and S. Andersson-Engels.
Optics Letters **33**, 80-82 (2008).

XII **VCSEL-based oxygen spectroscopy for structural analysis of pharmaceutical solids**
T. Svensson, M. Andersson, L. Rippe, S. Svanberg, S. Andersson-Engels, J. Johansson, and S. Folestad.
Applied Physics B **90**, 345-354 (2008).

XIII **Towards accurate in vivo spectroscopy of the human prostate**
T. Svensson, E. Alerstam, M. Einarsdóttír, K. Svanberg, and S. Andersson-Engels.
Journal of Biophotonics **1**, in press (2008).

XIV **Improved accuracy in time-resolved diffuse reflectance spectroscopy**
E. Alerstam, S. Andersson-Engels and T. Svensson.
Optics Express **16**, 10434-10448 (2008).

Abbreviations

AD	analogue to digital (converter)
DFB	distributed feedback laser
DOSC	direction of optimal shape conservation
dWMS	digital wavelength modulation spectroscopy
HWHM	half width at half maximum
FDPM	frequency domain photon migration
FWHM	full width at half maximum
FSR	free spectral range
GASMAS	gas in scattering media absorption spectroscopy
HITRAN	high-resolution transmission molecular absorption database
IR	infrared
IRF	instrumental response function
LAS	laser absorption spectroscopy
NIR	near infrared
PD	photodiode
PHD	photon hitting density
PDT	photo-dynamic therapy
PMT	photomultiplier tube
ppb	parts per billion ($1/10^9$)
ppm	parts per million ($1/10^6$)
ppt	parts per trillion ($1/10^{12}$)
RAM	residual amplitude modulation
TCSPC	time-correlated single photon counting
TDLAS	tunable diode laser absorption spectroscopy

TOF	time-of-flight
TOFS	time-of-flight spectroscopy
VCSEL	vertical cavity surface emitting laser
WMC	white Monte Carlo
WMS	wavelength modulation spectroscopy

Contents

Papers

Updates and comments

This part lists the updates of this thesis version (the original was printed in March 2008, while this version was created in July 2008).

(i) The formal information on page 2 now contains information on thesis defence. The page also states that this is an updated thesis version.

(ii) Paper **XIII**, marked as *manuscript submitted* in the original thesis version, is now published in Journal of Biophotonics. A new article version replaces the former.

(iii) Paper **XIV**, marked as *manuscript in preparation* in the original thesis version, is now published Optics Express. A new article version replaces the former.

(iv) Michels *et al.* recently published extensive work on the optical properties of fat emulsion (Optics Express **16**, 2008). This important reference is added in Section 3.4.

(v) Kukreti *et al.* have found intrinsic biomarkers of breast cancer (Journal of Biomedical Optics Letters **12**, 2007). This important work is now cited Section 3.6.2.

(vi) The origin of $1f$ baselines in WMS can be due to dull etalons as well as due to non-linear current-to-power tuning characteristics. The last paragraph in Section 4.5 has been updated (originally, the paragraph mentioned only the etalon effect).

(vii) The factor n was unfortunately left out in several expression related to Fourier series expansions in Section 4.4 (*e.g.* $\cos(2\pi f_m t)$ erroneously appeared instead of $\cos(2\pi n f_m t)$). This is now corrected.

(viii) Robichaud *et al.* recently published a comprehensive article on the characteristics of the oxygen A-band. This reference has been added in Section 4.6.

(ix) The is a misprint in Paper XII. In section 3.1 it is unfortunately written that 25 µm corresponds to an absorption fraction of 10^{-7}. The correct absorption fraction is 7×10^{-7}.

Chapter 1

Introduction

This thesis is devoted to spectroscopic analysis of highly scattering (*turbid*) materials, and related applications in pharmaceutical and biomedical sciences. Detailed descriptions of the accomplishments are found in the peer-reviewed scientific papers that are enclosed at the end of the thesis. The five opening chapters describe the scientific and technical context that connects these papers. This first chapter gives a broad introduction to spectroscopy of turbid materials, including applications and some technical aspects. The second chapter provides an introduction to the theory of macroscopic light propagation in turbid media, *i.e. photon migration*. The third chapter describes photon time-of-flight spectroscopy (TOFS), an important technique for monitoring of photon migration and a main component in this thesis. The topic of the fourth chapter is very different, dealing with high-resolution gas spectroscopy (tunable diode laser absorption spectroscopy, TDLAS). A particular focus lies on near-infrared sensing of molecular oxygen. Although the connection with photon migration is far from obvious, the fifth chapter is devoted to the combination of photon migration and high-resolution spectroscopy. This unique merge is most pronounced in Paper **XII**, but is the topic of several of the attached papers.

1.1 Light scattering

Scattering of light is a fundamental factor in our visual perception of the world. Our perception of phenomenons such as the blue sky, red sunsets, clouds, rainbows, snow, fog, milk, and white paint are striking examples of the influence of scattering. Moreover, our every-day experience of colours relies on that directed white sunlight hits objects, that various wavelengths are absorbed when travelling through the material, and that light is scattered in all directions so that we can sense it (*i.e.* see objects).

Process	σ [cm^2]
Resonant absorption	10^{-16}
O_2 abs. at 760 nm	10^{-23}
Mie scattering	10^{-26}-10^{-8}
Rayleigh scattering	10^{-26}
Raman scattering	10^{-29}

Table 1.1. *Typical probabilities for different radiative processes, expressed using the cross-section σ. Values are taken from Ref. [7], with the exception of the NIR absorption of molecular oxygen added for comparison (cf. Section 4.2.1). The resonant absorption refers to a typical cross-section for an electronic dipole transition, but may vary greatly. Note that the Mie cross-section depends strongly on the relation between particle size and wavelength.*

Scattering is an important aspect of the interaction between electromagnetic radiation (light) and matter. Other important radiation processes are absorption, fluorescence and Raman scattering. This thesis is concerned with elastic scattering due to non-uniformities in refractive index. The characteristics of this type of scattering is highly dependent on the relation between the scale of non-uniformities and the light wavelength. J.W.S. Rayleigh described light scattering by small particles in 1871, and became the first scientist to explain the blue colour of the sky [1, 2]. Showing that shorter wavelengths (blue) are scattered more than longer (red), manifested in the famous $1/\lambda^4$ dependence of the scattering cross section, Rayleigh theory explains both blue skies and red sunsets. Scattering by non-uniformities much smaller than the wavelength of light is therefore often referred to as *Rayleigh scattering*. In 1908, G. Mie published a rigorous paper where he employed Maxwells theory of light propagation on the scattering by spherical particles [3, 4]. Although Mie's approach is valid for all (spherical) particle sizes, the term *Mie scattering* is used to describe scattering by particles with sizes comparable to the wavelength of interest. For large-scale non-uniformities, light scattering is well described by geometrical optics (*e.g.* refraction, a fundamental concept that models change in propagation direction). Note that for the general particle shape, scattering must be calculated numerically from Maxwell's equations (*e.g.* using the finite-difference time-domain method or the T-matrix method [5]). For further reading on light scattering, the reader is referred to the book by Bohren and Huffman [6], or that of Mishchenko *et al.* [5] (the latter being freely available electronically). The probability of various absorption and scattering processes are stated in Table 1.1.

The above mentioned aspects of light scattering deals only with the microscopic light scattering of a single particle. In practice, it is common that light is scattered several times before it reaches the observer. Such *multiple scattering* has been studied for several decades within the field of radiative transfer [8, 9], neutron transport [10], diffusion of charged particles [11]. The insight in single particle scattering, as described by Mie, was soon extended to multiple scattering. Laser-based light scattering experiments on polystyrene latex spheres were presented as early as 1963 [12], and multiple scattering was discussed extensively [13, 14]. Today, knowledge on multiple scattering and photon migration is of fundamental importance in for example meteorological sciences, tissue optics and analysis of pharmaceutical solids.

1.2 The optical parameters of scattering media

There is no clear line between a scattering and non-scattering material. All matter consist of particles, and will scatter radi-

ation. Scattering is, however, often negligible in clear materials (*e.g.* gases, water and other clear liquids). In such materials, absorption is the main process that needs to be taken into account. Absorption of light obeys the simple Beer-Lambert-Bouguer law [15]

$$I = I_0 \exp(-\mu_a L) \tag{1.1}$$

where I_0 is the incident light intensity, I is the transmitted intensity, μ_a [cm^{-1}] the absorption coefficient, and L the pathlength. In scattering materials, the description of transmitted and reflected intensity is far more complicated. In the materials investigated in the present thesis, *e.g.* biological tissue and pharmaceutical solids, scattering occur much more frequent than absorption. Spectroscopy of such materials requires sophisticated models of light propagation, as well as specially designed techniques.

A scattering material is normally described using an average *scattering coefficient*, μ_s [cm^{-1}], that states the probability of scattering per unit length, together with an average angular distribution function (the scattering *phase function*). On large spatial scales, (a few millimeters for biological tissue), scattering properties can be summarised by stating the equivalent isotropic scattering process. The so called *reduced scattering coefficient*, μ_s' [cm^{-1}], can here alone describe light scattering, and is related to the scattering coefficient and phase function as stated in Eq. (1.2), where g is the average of the cosine of the scattering angle.

$$\mu_s' = (1 - g)\mu_s \tag{1.2}$$

The reciprocal of μ_s' states how often, on average, light undergoes a complete change in propagation direction (roughly $1/\mu_s'$ is in the order of 1 mm for tissue, and 20 µm or so in pharmaceutical materials, but varies largely). The above mentioned quantities are later formally introduced and discussed in detail (see Section 2.2). Together, they determine the amount of light that is detected for a certain experimental configuration.

The wavelength dependence of the scattering parameters introduced above is mainly related to the sizes of the structures and can, when measured, provide information on material structure [16]. The reduced scattering coefficient approximately exhibits a λ^{-n} dependence, where n is mainly dependent on scatterer size [16, 17]. The scattering coefficient and the angular distribution is more sensitive to variations in size and refractive index, and exhibits a more complex wavelength dependence [16]. Since an increased source-detector separation makes it increasingly difficult to obtain information on μ_s and angular distribution, this suggests that measurements on a microscopic scale have a larger potential for assessment of structural properties of scattering materials.

1.3 Experimental techniques

This section deals with techniques for characterisation of scattering materials, *i.e.* methods that allow extraction of absorption and scattering coefficients and information on the angular scattering distribution. The main focus is on techniques for macroscopic characterisation.

1.3.1 Angle-resolved light scattering

Direct measurements of the angular scattering distribution of turbid media can be made using an angle-resolved setup, *i.e.* a *goniometer* for scattering experiments [18, 19]. Measurements must be made on a small sample, in order to avoid the effects of multiple scattering. It should also be noted that these experiments usually assume that the angular distribution is rotationally symmetric (only dependent on the angle between incident light and scattering direction). For the non-spherical particles, however, the angular distribution depends on particle orientation. For turbid media with randomly oriented scatterers, an average distributions is still sufficient for describing light propagation. In ordered tissues, such as dentin, further investigations of light scattering distributions are of interest [20].

Due to the need for sample preparation (avoiding influence of multiple scattering), the typical goniometric setup for angle-resolved scattering measurements is not suitable for *in situ* applications. There are, however, techniques that allow extraction of single-scattering parameters in the presence of a large diffuse background. The diffuse background can be removed either by means of modelling [21], or by using polarised light and subtraction of the depolarised background [22, 23]. Refinements include the recently introduced technique *angle-resolved low-coherence interferometry*, that allows selective detection of the scattering signals from a localised region (even below the sample surface) [24].

1.3.2 The integrating sphere

Combined measurement of total reflectance, total transmittance, and collimated transmittance is a fairly popular way of extracting optical properties of turbid media. By proper (non-trivial) calibration, this three parameter approach may allow estimation of the absorption coefficient μ_a, the scattering coefficient μ_s, and the average cosine of the scattering angle g. The method utilise an integrating sphere for measurements of total reflectance and total transmittance[25–27], while collimated transmittance is measured separately [28]. In order to succeed in the extraction of the three parameters, the sample must be a thin slab. This requirement lim-

its the applicability of the method. A more detailed introduction to the integrating sphere approach is given in Refs. [29, 30].

1.3.3 Spatially resolved techniques

A commonly used method for characterisation of scattering materials is to investigate the spatial distribution of light due to a localised light source [31–33]. The spatial distribution can be measured in reflectance using optical fibers [31, 32] or cameras [34], or interstitially using fixed or sliding optical fibers [35]. The use of white light allows spectroscopic analysis [36, 37], but the use of a few wavelengths is sufficient in many applications [38]. Technical variants of the spatially resolved spectroscopy include injection of light in an oblique angle and measurement of symmetry shifts in the diffuse reflectance [39, 40], differential pathlength spectroscopy [41], as well as the use of Fourier-transform hyperspectral imaging [42].

In order to be able to extract information on both scattering and absorption, it is necessary to monitor the distribution close to the light source. When the distribution is measured several mean free paths from the light source, the technique normally provides only a value for the effective attenuation. Absolute measurements of the light distribution, although cumbersome, can provide a way of separating scattering and absorption even at longer source-detector separations. Farrell *et al.* and Dam *et al.* provide discussions of this issue [31, 32].

The main disadvantage with spatially resolved techniques is that the short source-detector separations needed for separation of absorption and scattering result in superficial sampling volumes. Furthermore, if larger volumes are to be monitored, the technique can only provide a measure of the effective attenuation (unless absolute measurements are feasible).

1.3.4 Time-of-flight spectroscopy

Injection of short laser pulses into tissue followed by an investigation of pulse shape (photon time-of-flight distribution) at some distance allow determination of absorption and reduced scattering [43–45]. This powerful method, referred to as *time-of-flight spectroscopy* (TOFS), is the topic of Chapter 3, and is thus only briefly introduced here. Qualitatively, the obtained time-of-flight distribution is a product of the simple Beer-Lambert-Bouguer exponential attenuation $\exp(-\mu_a ct)$, and a non-trivial function $S(t)$ that describes the relative probability for photons to appear at different times [46]. The intensity can thus be written as

$$I(t) = \exp(-\mu_a ct) \times S(t) \tag{1.3}$$

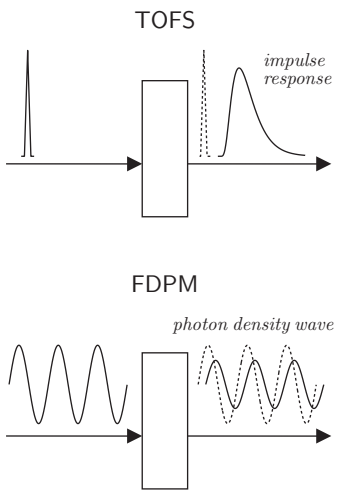

Figure 1.1. *Comparison of TOFS and FDPM. The full impulse response is recorded in TOFS, while FDPM records a delayed and attenuated photon density wave.*

The light propagation term $S(t)$ depends on scattering properties, sample geometry and source/detector locations. It can be simulated or approximated using diffusion theory of light propagation, as described in Chapter 2. Papers **X** and Paper **XIV** are devoted to the development of refined data evaluation and modelling for TOFS.

The advantages with respect to spatially resolved measurements is that one detector position is sufficient, and that no absolute intensity measurements are needed. The disadvantage is the significant increase in system cost and complexity.

1.3.5 Frequency domain photon migration

TOFS involves the full determination of sample impulse response, *i.e.* all modulation frequencies are investigated at the same time. Frequency domain photon migration (FDPM) is the Fourier domain equivalent of TOFS, and is based on monitoring of frequency response. A light source is amplitude modulated, and the amplitude and phase of the generated photon density wave is measured [47–52]. For details on FDPM, the extensive review provided by Chance *et al.* is recommended [51].

The principle of FDPM is illustrated in Fig. 1.1. In theory, sequential examination over all frequencies would reproduce the TOFS impulse response. In practice, FDPM seldom involves frequencies above 1 GHz (although Fishkin *et al.* have utilised frequencies up to 3 GHz [53]). The advantage with respect to TOFS is that it requires less sophisticated instrumentation [51, 54]. However, the bandwidth in FDPM cannot compete with the temporal resolution of TOFS. In addition, TOFS provides direct access to photon pathlengths. Whether this is relevant for practical performance remains an open question, and further comparative investigations are needed.

1.4 Biomedical optics

The great need for efficient diagnostic and therapeutic modalities needs no motivation. Optical methods have been used in medical contexts for many decades, and the field of biomedical optics develops rapidly. The literature on the subject is extensive.

The complex heterogeneity of most biological tissues is a source of strong light scattering. For visible and near-infrared light, scattering is generally considered to fall within the Mie regime. The reason is the abundance of micrometer-sized structures, such as for example cells (10 to 30 µm), cell nuclei (3 to 10 µm), and mitochondria (ellipsoid shape, 1 to 4 µm length and 0.3 to 0.7 µm diameter) [29, 55]. The extreme complexity of even a single cell makes the understanding of light propagation utterly challenging,

and the most successful descriptions include fractal modelling of tissue structure [56–58]. Modelling of light propagation on a more macroscopic scale (mm) typically relies on general theory of radiative transport, where a small set of parameters are used to describe the tissue (*e.g.* average refractive index and average coefficients for absorption and scattering).

The strong dependence on tissue properties, makes optical techniques highly interesting for measurements of medically relevant parameters [59]. Both microscopic and macroscopic parameters are of interest, and have led to the development of a large number of different optical techniques for diagnostics of biological tissues. In addition, the interaction of light with matter is widely used also for therapeutic purposes. Below, Sections 1.4.1 to 1.4.3 give an introduction to the optical properties of tissue. Tissue optics applications are surveyed in Section 1.5. As this thesis deals with macroscopic characterisation of tissues, various techniques for measurements on this scale were discussed in Section 1.3.

1.4.1 Tissue optical properties

In order to exploit the power of spectroscopy, the physiology, biochemistry and morphology of tissue need to be translated into optical parameters. It is important to remember that, depending on which scale measurements are performed, these *tissue optical properties* will represent some kind of tissue average. The two following section discuss the two fundamental optical processes in tissue; scattering and absorption.

1.4.2 Tissue scattering

As implied in Section 1.2, scattering in biological tissue is described using an average scattering coefficient, μ_s, and an average angular distribution function (the scattering *phase function*). On the macroscopically scale (typically a few millimeters), the reduced scattering coefficient, μ_s', can often alone describe light scattering.

It is the microscopic variations in refractive index that is the source of the massive scattering exhibited by biological tissue. Although thus clearly not well defined, the average refractive index is around 1.4. By letting tissue replace the usual cladding of an optical fiber, Bolin *et al.* estimated the average refractive index of various tissues by measuring the angle of the output cone [60]. At 633 nm, they found that the refractive index mainly varies between 1.38 and 1.41, with the exception of adipose (fatty) tissue where the refractive index is about 1.45. The microscopic variations in refractive index have been estimated by Schmitt *et al.* stating that the amplitude of variations in soft tissue is between 0.04 and 0.1 [56]. A detailed overview on how different tissue structures contribute to the overall scattering properties is given by Enejder

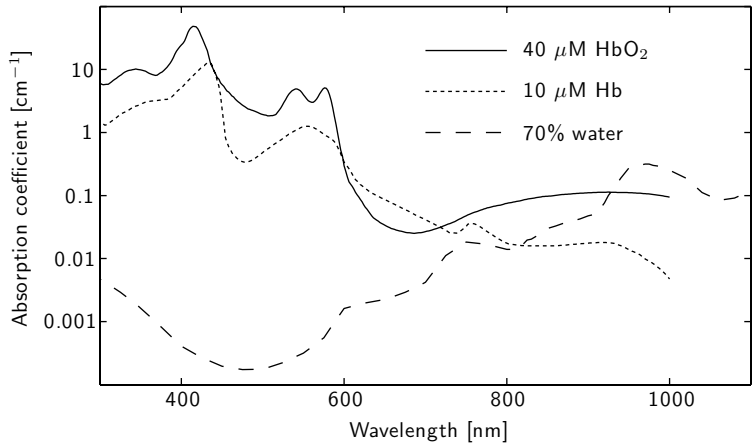

Figure 1.2. *Absorption spectra corresponding to 70% water [63], and a total hemoglobin concentration of 50 μM with 75% oxygen saturation [64]. These values are representative to tissue, but varies largely between tissue types. Blood (hemoglobin) is thus the major absorber in many tissues.*

[29], providing many important references. Advanced modelling of scattering on the microscopic scale is described by for example Schmitt *et al.* [56].

1.4.3 Tissue absorption

The absorption of tissue is built up from a large number of molecules and biomolecules [29, 59, 61]. In the ultra-violet spectral region, high absorption and scattering results in very short optical penetration depths and limits the applicability of tissue spectroscopy. The visible and near-infrared spectral regions offer a much longer penetration depth, and it is in this region that biomedical optics have most applications. Important applications of spectroscopy of biomolecules are, however, also based on the mid-infrared range [62]. Prominent absorbers (*chromophores*) in tissue are water [63], hemoglobin [64], myoglobin [65], lipids [66], cytochromes [61, 67], melanin [68], collagen [69, 70]. Fig. 1.2 shows the absorption spectra of oxy-hemoglobin, deoxy-hemoglobin, and water (the spectra are weighted in order to make the absolute values representative of tissue composition). These chromophores are the major sources of absorption in many important tissues, and is thus of fundamental importance. The region of low absorption, from 650 to 950 nm, is frequently taken advantage of in therapeutic and diagnostic applications (this region is often referred to as the the tissue optical window or therapeutic window [71]).

1.5 Applied tissue optics

It is out of the scope of this thesis to review the numerous biomedical applications that are linked to tissue optics. Nonetheless, in order to motivate the need of tissue spectroscopy, this section briefly introduces some of the therapeutic and diagnostic applications in which tissue optics play an important roll. This is intended as a general motivation for work on tissue optics, as well as a way of putting the publications attached to this thesis in a context. For a more complete introduction to the medical applications of light, the reader is referred to for example the book by Splinter and Hooper [72].

1.5.1 Therapeutics

As discussed in the review by Boulnois, optical therapies relies on photochemical, photothermal, photoablative or photomechanical effects [73]. Important therapeutic applications include photodynamic therapy [74–76], treatment of dermal vascular lesions (*e.g.* port wine stains) [77], laser-assisted eye surgery (*e.g.* reshaping of the cornea) [78, 79], laser cutting and ablation [80, 81], photocoagulation [82, 83], tattoo removal [84], hair removal [85, 86], laser scar revision [87]. A short introduction to some of these topic is given in the thesis of Essenpreis [88]. In the present thesis, photodynamic therapy (PDT) is of particular interest since the prostate spectroscopy developed in Papers **VI**, **X** and **XIII** (see Section 3.6.4) is related to the recent efforts in making PDT a modality for treatment of prostate cancer [89, 90]. PDT is a therapeutic modality in which light is used to activate (excite) a photosensitive drug, which then can produce cytotoxic substances and thus cause tissue destruction [74–76]. The thorough introduction to PDT given in the thesis of Johansson [91] is recommended. Light dosimetry, tissue oxygenation and sensitiser concentrations are important aspects. PDT is used on routine based for treatment of non-melanoma skin cancer, but has been shown effective for various types of small and superficial tumours within the body.

1.5.2 Diagnostics

The overall aim of diagnostic tools is to detect pathology or malfunction. Comprising analytical methods such as absorption, scattering, fluorescence and Raman spectroscopy, biomedical optics has a lot to offer medical diagnostics [59].

The most important contribution from the field is probably blood monitoring. Arterial oxygen saturation has been monitored optically since Millikan introduced the *oximeter* in the 1940s [92]. Today, pulse oximeters are used for routine monitoring in hospitals, and the technique is considered a major breakthrough in

clinical monitoring [93]. Due to the great importance of blood, hemoglobin spectroscopy has numerous other applications. The technique can be used for cancer detection, since tumours are often related to increases in vascularisation (angiogenesis) [94]. This is of particular interest for optical diagnostics of breast tissue and optical mammography, applications further discussed in Section 3.6.2. Furthermore, hemoglobin spectroscopy is used for monitoring of neonatal cerebral oxygenation, being part of the struggle to prevent brain injury in infants (see Section 3.6.3). Papers **III** (breast tissue), **VI** (prostate tissue) and **XIII** (prostate tissue) involve *in vivo* hemoglobin spectroscopy of human tissues.

Diffuse optical imaging and tomography (including fluorescence tomography and molecular imaging), capable of 2 or 3-dimensional mapping physiological or biochemical information, is an emerging technique with many potential applications [95]. This fascinating development is not reviewed here, but a brief introduction with some references is given in Section 3.6.1.

Other kinds of *in vivo* biochemical analysis that are linked to tissue optics is for example, *in vivo* Raman spectroscopy of bone [96] (see also Ref. [97]), fluorescence assessment of tissue metabolism [59], diagnosis of atherosclerosis [59], and non-invasive monitoring of glucose for diabetes management [98].

In recent years, the diagnostic potential of scattering spectroscopy has received increased attention. In a Nature article from 2000, Backman *et al.* showed the potential of microscopic-scale scattering spectroscopy for *in situ* detection of preinvasive cancers [23]. The technique is based on assessment of nuclei size [21]. The important and successful areas of optical coherence tomography (OCT) [99–101] and laser Doppler flowmetry [102] should also be noted. OCT has become a major commercial success, and is today a clinically well accepted technology.

Finally, Paper **VIII** deals with a novel medical application of light. There, high-resolution gas spectroscopy is employed for sensing of gases in the human sinuses (*cf.* Chapter 5). This application may be of diagnostic value, and is discussed in detail in the thesis by Persson [103].

1.6 Spectroscopy of pharmaceutical solids

Many pharmaceutical solids are extremely scattering, surpassing biological tissue by a factor of 10 to 100. In biomedical optics, enormous efforts have been directed to the development of techniques that allow separate measurement of scattering and absorption. The obtained information on absorption is used for chemical analysis, while scattering is used to infer morphology. The approach is often different in pharmaceutical science, where spectroscopic analysis typically is based on calibration and chemometrics.

This is feasible due to the well controlled manufacturing of materials. In contrast, calibration is likely to fail when encountering the severe and unpredictable variations of biological tissue.

As later discussed in Chapters 3 and 5, direct measurements of physical and chemical parameters of solids are of great importance in pharmaceutical science [104–108]. Paper **II** describe how TOFS can be used to improve the robustness of NIR spectroscopy of pharmaceutical tablets (see Section 3.7). Papers **VII**, **XI** and **XII** describes the development of a novel optical method for assessment of structural parameters of pharmaceutical solids (see 5.7).

Chapter 2

Photon migration theory

This chapter deals with the theory of radiative transfer and photon migration. Important topics covered are transport theory, Monte Carlo simulations, and the diffusion approximation of light transport. The theory presented is important in many areas of science, including neutron transport in nuclear physics, meteorological and atmospherical sciences, and biomedical optics. The interested reader can find further details in, for example, the book by Ishimaru [109], the book edited by Welch and van Gemert [110], or the recent book by Wang and Wu [111].

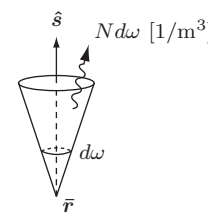

Figure 2.1. *The number of photons per unit volume that travels within $d\omega$ and along $\hat{\boldsymbol{s}}$ equals $Nd\omega$.*

2.1 Radiometric quantities

This section introduces several important quantities, all closely related. The concept of solid angles is of fundamental importance, and a discussion thereof is found in Appendix A.

2.1.1 Photon distribution function

Let $\bar{\boldsymbol{r}}$ denote a position, $\hat{\boldsymbol{s}}$ a direction and t time. The *photon distribution function* is written $N(\bar{\boldsymbol{r}}, \hat{\boldsymbol{s}}, t)$ and is defined as follows:

$$N(\bar{\boldsymbol{r}}, \hat{\boldsymbol{s}}, t) \equiv \text{number of photons per unit of volume and steradian travelling in the direction given by } \hat{\boldsymbol{s}} \text{ [1/m}^3\text{sr]}$$

A geometric interpretation is given in Fig. 2.1. Note that $\hat{\boldsymbol{s}} = \hat{\boldsymbol{s}}(d\omega)$ (holds generally in the following sections).

The photon distribution is of fundamental importance, and as shown below many other important radiometric quantities can be

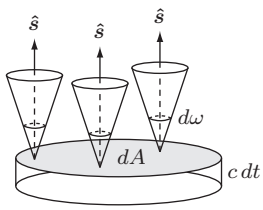

Figure 2.2. *Photons travelling through dA within solid angles $d\omega$ along $\hat{\boldsymbol{s}}$*

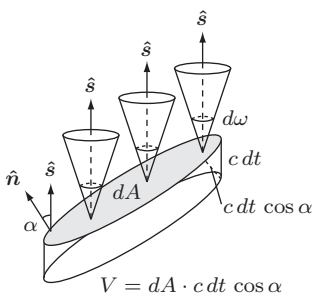

Figure 2.3. *Photons travelling through a leaning dA within solid angles $d\omega$ along $\hat{\boldsymbol{s}}$*

thought of as close relatives. An important class of quantities $\{I_N\}$ are reached by integration over all solid angles:

$$I_N \propto \int_{4\pi} N(\bar{\boldsymbol{r}}, \hat{\boldsymbol{s}}, t)\; d\omega \tag{2.1}$$

In applications where absorption is a main concern (for example in optical dosimetry), such measures are crucial since photons cause absorption no matter in what direction they propagate. When net transfer is the issue one also need to take directionality into account while integrating. This give rise to the class $\{\boldsymbol{I_N}\}$:

$$\boldsymbol{I_N} \propto \int_{4\pi} N(\bar{\boldsymbol{r}}, \hat{\boldsymbol{s}}, t)\hat{\boldsymbol{s}}\; d\omega \tag{2.2}$$

2.1.2 Photon density

The *photon density* is written $\rho(\bar{\boldsymbol{r}}, t)$ and states the number of photons per unit volume in $\bar{\boldsymbol{r}}$ at a certain time t. It may be derived from the photon distribution function by integration over all solid angles.

$$\rho(\bar{\boldsymbol{r}}, t) \equiv \int_{4\pi} N(\bar{\boldsymbol{r}}, \hat{\boldsymbol{s}}, t)\; d\omega \quad [1/\mathrm{m}^3] \tag{2.3}$$

2.1.3 Power and radiance

How much power flows along $\hat{\boldsymbol{s}}$ through a certain small area dA during a time period dt? Let us accept all photons travelling within solid angles $d\omega$. All such photons within a volume dV of thickness $c \cdot dt$ beneath dA will pass dA in the time period dt. Hence, the number of such photons equals $N(\bar{\boldsymbol{r}}, \hat{\boldsymbol{s}}, t) \cdot dA\; c\; dt\; d\omega$ (if we measure per steradian: $N(\bar{\boldsymbol{r}}, \hat{\boldsymbol{s}}, t) \cdot dA\; c\; dt$). Fig. 2.2 presents the situation. The passing energy dE per steradian is given by

$$\frac{dE}{d\omega} = h\nu \cdot N(\bar{\boldsymbol{r}}, \hat{\boldsymbol{s}}, t) \cdot dA\; c\; dt \quad [\mathrm{J/sr}] \tag{2.4}$$

and the power by

$$\frac{dP}{dw} = \frac{dE}{d\omega dt} = h\nu \cdot N(\bar{\boldsymbol{r}}, \hat{\boldsymbol{s}}, t) \cdot dA\; c \quad [\mathrm{W/sr}] \tag{2.5}$$

A related quantity is the *radiance*, $L(\bar{\boldsymbol{r}}, \hat{\boldsymbol{s}}, t)$. It is defined as the power per steradian and per unit area.

$$L(\bar{\boldsymbol{r}}, \hat{\boldsymbol{s}}, t) \equiv \frac{dP}{dAdw} = \frac{dE}{d\omega dt} = h\nu \cdot c \cdot N(\bar{\boldsymbol{r}}, \hat{\boldsymbol{s}}, t) \quad [\mathrm{W/m^2 sr}] \tag{2.6}$$

Note that the derivations above holds only if the area dA is orthogonal to $\hat{\boldsymbol{s}}$. If this is not the case, the area element must be properly projected, as shown in Fig. 2.3. This means that dA must be replaced by $|\hat{\boldsymbol{n}} \cdot \hat{\boldsymbol{s}}|\, dA = dA \cos\alpha$.

2.1.4 Hemispherical flux density

Now, consider a small area element dA with a normal $\hat{\boldsymbol{n}}$. The power per unit area flowing through that surface element in a certain direction is called *hemispherical flux density*[1]. This quantity is given by integrating the radiance over solid angles in the corresponding hemisphere (see Fig. 2.4), and at the same time taking surface orientation into account. Let $F_{\pm}(\bar{\boldsymbol{r}}, t)$ denote the hemispherical flux density in positive (forward) and negative (backward) $\hat{\boldsymbol{n}}$-direction respectively, and $2\pi_{\pm}$ denote the corresponding hemispherical solid angles. If we regard flow along $\hat{\boldsymbol{n}}$ as positive, while the opposite flow is regarded as negative we may calculate the hemispherical flux densities as follows:

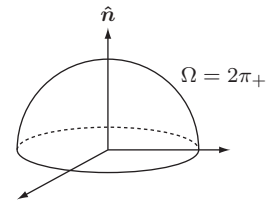

Figure 2.4. *The hemisphere solid angle that defines the hemispherical flux density in $+\hat{\boldsymbol{n}}$-direction.*

$$F_{\pm}(\bar{\boldsymbol{r}}, t, \hat{\boldsymbol{n}}) = \int_{2\pi_{\pm}} L(\bar{\boldsymbol{r}}, \hat{\boldsymbol{s}}, t)(\hat{\boldsymbol{s}} \cdot \pm\hat{\boldsymbol{n}})\, d\omega \quad [\mathrm{W/m^2}] \tag{2.7}$$

The total transfer of power per unit area is then

$$F_{\mathrm{tot}}(\bar{\boldsymbol{r}}, t, \hat{\boldsymbol{n}}) = F_+ + F_- = \int_{4\pi} L(\bar{\boldsymbol{r}}, \hat{\boldsymbol{s}}, t)|\hat{\boldsymbol{s}} \cdot \hat{\boldsymbol{n}}|\, d\omega \tag{2.8}$$

while the net transfer per unit are is

$$F_{\mathrm{net}}(\bar{\boldsymbol{r}}, t, \hat{\boldsymbol{n}}) = F_+ - F_- = \int_{4\pi} L(\bar{\boldsymbol{r}}, \hat{\boldsymbol{s}}, t)(\hat{\boldsymbol{s}} \cdot \hat{\boldsymbol{n}})\, d\omega \tag{2.9}$$

The latter quantity can be used to calculate the net transfer of power P through some surface S. Note that the normal of the surface may vary, that is $\hat{\boldsymbol{n}} = \hat{\boldsymbol{n}}_{\mathrm{s}} = \hat{\boldsymbol{n}}(dS)$.

$$P = \int_S F_{\mathrm{net}}(\bar{\boldsymbol{r}}, t, \hat{\boldsymbol{n}}_{\mathrm{s}})\, dS \quad [\mathrm{W}] \tag{2.10}$$

The concept of *irradiance* is related to hemispherical flux density and should be used when dealing with radiant power incident on surfaces. The corresponding term when dealing with radiant power leaving surfaces is *exitance*.

2.1.5 Fluence

The total amount of power per unit area at a certain point in space, $\bar{\boldsymbol{r}}$, is determined by integrating the radiance over all solid

[1] *Flux* normally refers to a flow in time (energy per second, photons per second etc.). When considering flux through surfaces (energy per second per $\mathrm{m^2}$, $[\mathrm{W/m^2}]$), the term *flux density* is used.

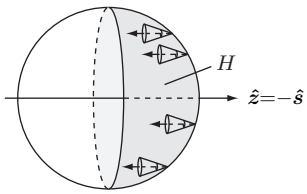

Figure 2.5. *Photons travelling within dw along $\hat{\boldsymbol{s}}$ incident on a small sphere*

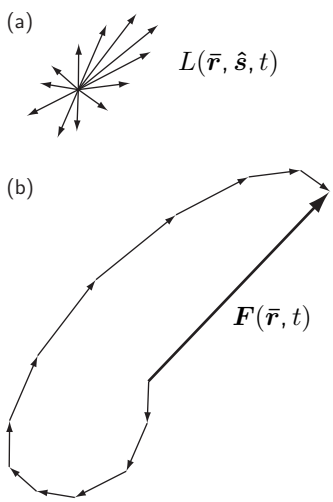

Figure 2.6. *Illustration of how the radiance distribution in (a) is transformed into the net flux density vector shown in (b). Here, the discretisation of the radiance turns the integral of Eq. (2.15) into a simple summation.*

angles. That integral defines a quantity called *fluence* or *fluence rate*, usually written as $\Phi(\bar{\boldsymbol{r}}, t)$.

$$\Phi(\bar{\boldsymbol{r}}, t) \equiv \int_{4\pi} L(\bar{\boldsymbol{r}}, \hat{\boldsymbol{s}}, t)\ d\omega \quad [\mathrm{W/m^2}] \tag{2.11}$$

Note that this power does not pass through any real area since the fluence is built up by photons travelling in different directions. Note the following relations:

$$\Phi(\bar{\boldsymbol{r}}, t) = c \cdot h\nu \cdot \int_{4\pi} N(\bar{\boldsymbol{r}}, \hat{\boldsymbol{s}}, t)\ d\omega = c\, h\nu \cdot \rho(\bar{\boldsymbol{r}}, t) \tag{2.12}$$

The fluence may be interpreted (or defined) as the power incident on a small sphere divided by the cross-sectional area of that sphere. However, that is not obvious looking at Eq. (2.11). Consider a small sphere, and treat each incident direction (within infinitesimal solid angles) separately. Let H denote hemispherical surfaces and use a short format of radiance, $L = L(\bar{\boldsymbol{r}}, \hat{\boldsymbol{s}}, t)$. The power incident along $\hat{\boldsymbol{s}}$ within dw is illustrated in Fig. 2.5 and may according to Section 2.1.3 be calculated as follows:

$$\begin{aligned} P(d\omega) &= \int_H L\, d\omega\, |\hat{\boldsymbol{n}} \cdot \hat{\boldsymbol{s}}|\ dS = L\, d\omega \int_H |\hat{\boldsymbol{n}} \cdot \hat{\boldsymbol{s}}|\ dS = \\ &= L\, d\omega \int_{\varphi=0}^{2\pi} \int_{\theta=0}^{\pi/2} R^2 \cos\theta \sin\theta\ d\varphi d\theta = \pi R^2 L\, d\omega \\ &= H_\perp \cdot L\, d\omega \end{aligned} \tag{2.13}$$

The total incident power is achieved by integration over all directions. Since the cross-section $H_\perp$ is the same in all directions, the total power P is given by

$$P = \pi R^2 \int_{4\pi} L\ d\omega = H_\perp \int_{4\pi} L\ d\omega = H_\perp \cdot \Phi(\bar{\boldsymbol{r}}, t) \tag{2.14}$$

2.1.6 Net flux density and photon current

The *net flux density* of power per unit area, written $\boldsymbol{F}(\bar{\boldsymbol{r}}, t)$, is a vector quantity that may be defined by the following integral:

$$\boldsymbol{F}(\bar{\boldsymbol{r}}, t) \equiv \int_{4\pi} L(\bar{\boldsymbol{r}}, \hat{\boldsymbol{s}}, t)\hat{\boldsymbol{s}}\ d\omega \quad [\mathrm{W/m^2}] \tag{2.15}$$

An interpretation of the net flux density is given in Fig. 2.6. A closely related quantity is the *photon current*, written $\boldsymbol{J}(\bar{\boldsymbol{r}}, t)$ and stating the (net) photon current.

$$\boldsymbol{J}(\bar{\boldsymbol{r}}, t) \equiv \int_{4\pi} c\, N(\bar{\boldsymbol{r}}, \hat{\boldsymbol{s}}, t)\hat{\boldsymbol{s}}\ d\omega = \frac{\boldsymbol{F}(\bar{\boldsymbol{r}}, t)}{h\nu} \quad [1/\mathrm{m^2 s}] \tag{2.16}$$

Net transfer of power P through some surface S, as already discussed in Eq. (2.10), may now be expressed as follows:

$$P = \int_S \boldsymbol{F}(\bar{\boldsymbol{r}}, t) \cdot \hat{\boldsymbol{n}}_{\mathrm{s}} \, dS \quad [\mathrm{W}] \tag{2.17}$$

2.2 Photon transport theory

A common approach when dealing with optical techniques in scattering (turbid) materials is to regard the problem of electromagnetic propagation simply as a problem of particle-like photon propagation (disregarding the wave properties of light). The foundations are given by linear transport theory – a theory originally explored by scientists interested in modelling the propagation of neutrons in nuclear processes. The basic assumption is that the propagation of optical energy may be characterised by modelling two basic interactions (events), namely absorption and scattering. The characteristics of these two interactions in a particular material are often referred to as the optical properties.

2.2.1 Absorption and scattering

Absorption is modelled using a simple interaction probability called the *absorption coefficient*, usually written μ_{a} [1/cm]. The absorption coefficient states the probability of absorption per unit path length. The probability of absorption within an small length ds is thus $\mu_{\mathrm{a}} ds$. The average path length before absorption is given by the reciprocal of μ_{a}, that is, $1/\mu_{\mathrm{a}}$.

The modelling of scattering requires a *scattering coefficient* defined in the same manner as the absorption coefficient. It is written μ_{s} [1/cm], and it can be seen both as the probability of scattering per unit path length and, since scattering does not terminate photon propagation, as the average number of scattering events per unit path length. However, additional modelling is required to account for the direction of propagation after a scattering event. This is done by introducing a *phase function* $p(\hat{\boldsymbol{s}}', \hat{\boldsymbol{s}})$ that states the probability (per steradian) of scattering from $\hat{\boldsymbol{s}}'$ to $\hat{\boldsymbol{s}}$. Considering Fig. 2.7, the probability that the photons scattered from $\hat{\boldsymbol{s}}'$ ends up travelling within $d\omega$ (along $\hat{\boldsymbol{s}}$) equals $p(\hat{\boldsymbol{s}}', \hat{\boldsymbol{s}}) d\omega = p(\hat{\boldsymbol{s}}', \hat{\boldsymbol{s}}) \sin\theta \, d\theta d\varphi$. It should also be mentioned that some authors argue that it may be of interest to take into account the time spent in the scattering process itself, sometimes referred to as a *scattering delay* [112, 113].

The total probability for absorption or scattering is called the *total attenuation coefficient*, written μ_{tot}. Its reciprocal, $1/\mu_{\mathrm{tot}}$, gives the *mean free path* until scattering or absorption occurs. As an example, when collimated laser light irradiates tissue, the

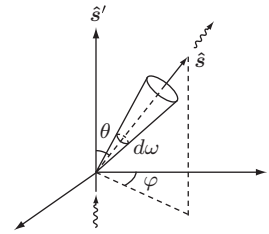

Figure 2.7. *Scattering geometry of phase functions*

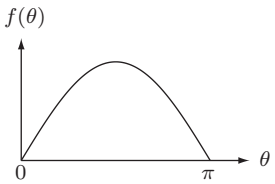

Figure 2.8. *The probability density function of θ in isotropic scattering*

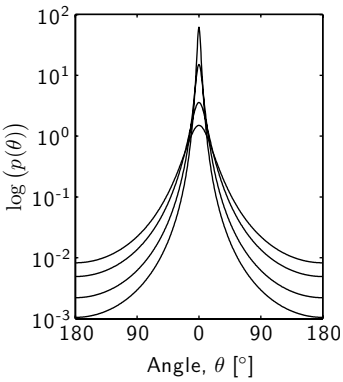

Figure 2.9. *The Henyey-Greenstein phase function for g=0.7, 0.8, 0.9, and 0.95.*

collimated (non-scattered) part will be attenuated according to the Beer-Lambert-Bouguer law of absorption:

$$E(z) = E_0 \exp(-(\mu_a + \mu_s)z) = E_0 \exp(-\mu_{tot} z) \tag{2.18}$$

where E_0 is the irradiance entering the tissue (already compensated for specular reflection) and z is the depth.

Often, it is assumed that the scattering probability depends only on θ, that is $p(\hat{\boldsymbol{s}}', \hat{\boldsymbol{s}}) = p(\theta)$. If the angels θ and φ (see Fig. 2.7) are studied separately as random variables this means that

$$\varphi \in \text{Uniform}(0, 2\pi) \tag{2.19}$$

$$F_\theta(\alpha) = P(\theta \leq \alpha) = 2\pi \int_0^\alpha p(\theta) \sin\theta \; d\theta \tag{2.20}$$

The tendency towards forward scattering may be expressed using a single parameter g called *anisotropy* (or *g-factor*), $g = <\cos\theta>$. Values of g close to 1 imply pronounced forward scattering, and isotropic scattering results in $g = 0$. In accordance to basic probability theory, the anisotropy may be calculated as

$$g = \int p(\hat{\boldsymbol{s}}', \hat{\boldsymbol{s}}) \cos\theta \; d\omega' = \int p(\hat{\boldsymbol{s}}', \hat{\boldsymbol{s}})(\hat{\boldsymbol{s}}' \cdot \hat{\boldsymbol{s}}) \; d\omega' \tag{2.21}$$

For $p(\hat{\boldsymbol{s}}', \hat{\boldsymbol{s}})$ to be a probability density function it is of course required that

$$\int_{4\pi} p(\hat{\boldsymbol{s}}', \hat{\boldsymbol{s}}) \; d\omega' = 2\pi \int_0^\pi p(\theta) \sin\theta \; d\theta = 1 \tag{2.22}$$

In the case of *isotropic scattering*, where $p(\hat{\boldsymbol{s}}', \hat{\boldsymbol{s}})$ is constant $(= k)$ we find

$$1 = \int_0^\pi 2\pi k \sin\theta \; d\theta = 4\pi k \Rightarrow k = \frac{1}{4\pi} \tag{2.23}$$

The probability density function of θ is hence $f(\theta) = \frac{1}{2}\sin\theta$, see Fig. 2.8.

A frequently used phase function is the *Henyey-Greenstein* phase function [114], see Eq. (2.24) and Fig. 2.9.

$$p(\theta) = \frac{1}{4\pi} \frac{1 - g^2}{(1 + g^2 - 2g\cos\theta)^{3/2}} \tag{2.24}$$

It is possible to show that $<\cos\theta> = g$, so the g appearing in Eq. (2.24) is really the anisotropy (see Appendix B). The Henyey-Greenstein phase function is often used without further motivation, despite that it has been shown not capable of reproducing

for example Mie scattering patterns and that better alternatives exist [115, 116]. As pointed out by Kienle *et al.* modelling using an improper phase function can under certain experimental conditions impose significant errors in derived optical properties [33]. Note, however, that there is no simple choice of phase function for materials with unknown particle size distributions and shape variations (*e.g.* biological tissue [58]).

Finally, note that in cases where scattering probability only depend on $\cos\theta$, symmetry yields

$$p(\cos\theta) = p(\hat{\boldsymbol{s}}' \cdot \hat{\boldsymbol{s}}) = p(\hat{\boldsymbol{s}}', \hat{\boldsymbol{s}}) = p(\hat{\boldsymbol{s}}, \hat{\boldsymbol{s}}') \tag{2.25}$$

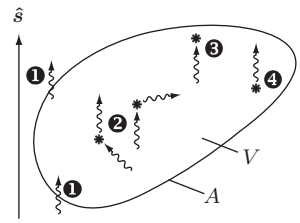

Figure 2.10. *Events covered in photon transport theory:*

1: Boundary transfer
2: Scattering
3: Absorption
4: Source production

2.2.2 The transport equation

Consider a small volume V. Let us examine how the number of photons per steradian travelling along a certain direction $\hat{\boldsymbol{s}}$ within V change in time, that is

$$\int_V \frac{\partial N(\bar{\boldsymbol{r}}, \hat{\boldsymbol{s}}, t)}{\partial t}\, dV = \int_V \frac{\partial N}{\partial t}\, dV \equiv \left(\frac{\partial N}{\partial t}\right)^V \tag{2.26}$$

Contributions involve photons entering/exiting the volume through its boundary surface A, photons lost due to absorption, photons scattered to/from $\hat{\boldsymbol{s}}$ and sources producing new photons. These events are illustrated in Fig. 2.10, and are treated individually below. Note that $N = N(\bar{\boldsymbol{r}}, \hat{\boldsymbol{s}}, t)$ (not explicitly stated below).

The boundary transfer of photons have been discussed in Section 2.1.3 and is given by[2]

$$\left(\frac{\partial N}{\partial t}\right)^V_{\text{transfer}} = -\int_A c\, N \hat{\boldsymbol{s}} \cdot \hat{\boldsymbol{n}}\, dA = -\int_V c\, \nabla N \cdot \hat{\boldsymbol{s}}\, dV \tag{2.27}$$

The losses due to absorption is proportional to the absorption coefficient μ_a. The probability of absorption under a small time period dt is $\mu_\text{a}\, cdt$. The total amount of photons lost is then

$$\left(\frac{\partial N}{\partial t}\right)^V_\text{a} = -\int_V c\, \mu_\text{a}(\bar{\boldsymbol{r}})\, N\, dV \tag{2.28}$$

The same holds for losses due to scattering from $\hat{\boldsymbol{s}}$ to other directions.

$$\left(\frac{\partial N}{\partial t}\right)^V_{\text{s}-} = -\int_V c\, \mu_\text{s}(\bar{\boldsymbol{r}})\, N\, dV \tag{2.29}$$

[2]Here, Gauss' integral theorem is used.
Note that, since $\hat{\boldsymbol{s}}$ is fixed, $\nabla \cdot (cN\hat{\boldsymbol{s}}) = \nabla(cN) \cdot \hat{\boldsymbol{s}} + cN\nabla \cdot \hat{\boldsymbol{s}} = \nabla(cN) \cdot \hat{\boldsymbol{s}}$.

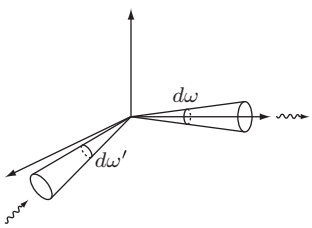

Figure 2.11. *Scattering from $d\omega'$ to $d\omega$*

A different matter is the contribution from photons scattered into the $\hat{\boldsymbol{s}}$ direction from all other directions. The probability per steradian along $\hat{\boldsymbol{s}}$ that a scattered photon incident along $\hat{\boldsymbol{s}}'$ ends up along $\hat{\boldsymbol{s}}$ (see Fig. 2.11) is $p(\hat{\boldsymbol{s}}', \hat{\boldsymbol{s}})$. The number of photons per unit time and steradian scattering from $\hat{\boldsymbol{s}}'$ in the first place is proportional to $c\,\mu_\mathrm{s}$. The density of photons changing direction from $d\omega'$ to $d\omega$ is therefore $N(\hat{\boldsymbol{s}}')d\omega' \cdot c\mu_\mathrm{s} \cdot p(\hat{\boldsymbol{s}}', \hat{\boldsymbol{s}})d\omega$. Integration over all directions $\hat{\boldsymbol{s}}'$ and the complete volume yields the following result:

$$\Big(\frac{\partial N}{\partial t}\Big)^V_{\mathrm{s}_+} = \int_V c\,\mu_\mathrm{s}(\bar{\boldsymbol{r}})\Big(\int_{4\pi} p(\hat{\boldsymbol{s}}', \hat{\boldsymbol{s}})\, N(\hat{\boldsymbol{s}}')\; d\omega'\Big)\; dV \tag{2.30}$$

Sources are taken into account by describing them using a function $q(\bar{\boldsymbol{r}}, \hat{\boldsymbol{s}}, t)$ stating the production of photons per unit volume, steradian and time $[1/\mathrm{m}^3\mathrm{s\,sr}]$. Hence, the contribution from sources may be stated as

$$\Big(\frac{\partial N}{\partial t}\Big)^V_{source} = \int_V q(\bar{\boldsymbol{r}}, \hat{\boldsymbol{s}}, t)\; dV \tag{2.31}$$

We reach the transport equation by summing all contributions and dropping all volume integrations (arbitrary volume).

$$\frac{\partial N}{\partial t} = -c\,\nabla N \cdot \hat{\boldsymbol{s}} - c\,(\mu_\mathrm{a} + \mu_\mathrm{s})N + c\mu_\mathrm{s}\int_{4\pi} p(\hat{\boldsymbol{s}}', \hat{\boldsymbol{s}})\, N(\hat{\boldsymbol{s}}')\; d\omega' + q \tag{2.32}$$

Since radiance L is proportional to photon distribution N, the transport equation is almost identical when expressed in radiance. A very important property of the transport equation is that if $N_0(\bar{\boldsymbol{r}}, \hat{\boldsymbol{s}}, t)$ is a solution for a non-absorbing (μ_a=0) homogenous media with a single light source at $\bar{\boldsymbol{r}} = \bar{0}$, then $\exp(-\mu_\mathrm{a}ct) \times N_0(\bar{\boldsymbol{r}}, \hat{\boldsymbol{s}}, t)$ is a solution when the absorption coefficient is non-zero [117, 118]. This means that a time-resolved impulse response of a homogenous scattering material consists of two separable parts; one factor is related to the scattering properties, and the other factor is an exponential decay that depends on absorption, $\exp(-\mu_\mathrm{a}ct)$ [46]. This fact is more or less expected from the Beer-Lambert-Bouguer law of absorption. In addition, this property is utilised in the scheme for White Monte Carlo simulation introduced in Paper **X** (see Section 2.3 below).

Since the transport equation (or *radiative transport equation*) seldom is analytically solvable, various techniques are used to provide numerical solutions. This includes discretisation of the radiance into angular components [119], the use of photon path integrals [120], and the so called P3 approximation [121]. An overview of such methods is given in the thesis of Swartling [30]. The following sections discuss the important methods of Monte Carlo simulations and diffusion approximation.

2.3 Monte Carlo simulations

Monte Carlo (MC) methods have been used for several decades in order to investigate complex physical processes such as radiative transport [122, 123]. This numerical approach has become the gold standard for modelling of photon migration in biomedical optics [124, 125]. The freely available Monte Carlo implementation for light propagation in layered structures (MCML) has become a standard tool [125], and commercial alternatives are available [126, 127]

The fundamentals of Monte Carlo modelling for light propagation are carefully described in several articles and books [128–131]. Briefly, photons are launched and tracked in an arbitrary geometry with pre-defined optical properties (absorption and scattering), relying on proper generation of random numbers (see for example Paper **X**). The large number of function evaluations renders numerical considerations important [132, 133].

Papers **X** introduce a novel MC method for interstitial and reflectance geometries, specially developed to facilitate routine data evaluation of time-resolved photon migration data. The method is based on White Monte Carlo (WMC) [134–136], *i.e.* a single Monte Carlo simulation is run at zero absorption. The result can be scaled in order to apply for different scattering coefficients, and absorption is added in the final step (*cf.* the discussion of impulse response separability in the previous section). Paper **X** shows that data evaluation using the WMC approach significantly improve the performance of TOFS for during interstitial characterisation of turbid materials. As shown in Paper **XIII**, this achievement is of particular importance in TOFS-based prostate spectroscopy. Paper **XIV** shows that the approach is of great value also in the important case of time-resolved diffuse reflectance.

Fluorescence, Raman scattering, and Doppler-shifts can easily be incorporated in Monte Carlo simulations [137–140].

2.4 Photon diffusion

By using certain assumptions it is possible to reduce the transport equation (2.32) to a diffusion equation. If these simplifying assumptions are utilised, we speak of the diffusion approximation of transport theory. This section provides a derivation of diffusion theory of light propagation (a similar derivation is given in Ref. [46]). The great advantage with this theory (with respect to for example MC) is that it provides analytical solutions that easily can be used in modelling. The disadvantage, however, is its limited validity.

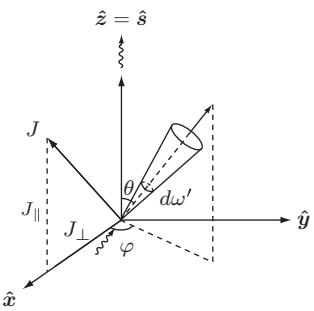

Figure 2.12. *Decomposition of* $\boldsymbol{J}$

2.4.1 Expansion of radiometric quantities

Assume that photon density is built up by a isotropic part and a gradient part, that is

$$N(\bar{\boldsymbol{r}}, \hat{\boldsymbol{s}}, t) = A(\bar{\boldsymbol{r}}, t) + \boldsymbol{B}(\bar{\boldsymbol{r}}, t) \cdot \hat{\boldsymbol{s}} \tag{2.33}$$

Immediate integration over all solid angles concludes that $A(\bar{\boldsymbol{r}}, t) = \frac{1}{4\pi}\rho(\bar{\boldsymbol{r}}, t)$. Moreover, multiplication by $\hat{\boldsymbol{s}}$ followed by integration over all solid angles reveals that $B(\bar{\boldsymbol{r}}, t) = \frac{3}{4\pi c}\boldsymbol{J}(\bar{\boldsymbol{r}}, t)$. Hence,

$$N(\bar{\boldsymbol{r}}, \hat{\boldsymbol{s}}, t) = \frac{1}{4\pi}\rho(\bar{\boldsymbol{r}}, t) + \frac{3}{4\pi c}\boldsymbol{J}(\bar{\boldsymbol{r}}, t) \cdot \hat{\boldsymbol{s}} \quad [1/\mathrm{m}^3\mathrm{sr}] \tag{2.34}$$

We expand the source contribution in a similar manner:

$$q(\bar{\boldsymbol{r}}, \hat{\boldsymbol{s}}, t) = \frac{1}{4\pi}q_0(\bar{\boldsymbol{r}}, t) + \frac{3}{4\pi}\boldsymbol{q_1}(\bar{\boldsymbol{r}}, t) \cdot \hat{\boldsymbol{s}} \quad [1/\mathrm{m}^3\mathrm{s}\,\mathrm{sr}] \tag{2.35}$$

Note that the units of both q_0 and $\boldsymbol{q_1}$ is $[1/\mathrm{m}^3\mathrm{s}]$.

This drastic simplification of the photons density restricts us to materials where scattering dominates over absorption. The expression in Eq. (2.33) is clearly not capable of modelling directed light – no matter how A or $\boldsymbol{B}$ are selected, there will still be photons travelling over a very wide solid angle. Since this in itself implies that the light is diffuse, it is not surprising that this simplification will result in a diffusion equation for light transport.

Note that the simplification presented above is often introduced after having expanded the photon density (or radiance) in a series of spherical harmonics. A truncation of this series that includes only the zero and first order terms yields precisely the expressions given above, and is said to result in the P1-approximation of light transport.

2.4.2 Simplified transport equation

Inserting the truncated expansions from Section 2.4.1 in the transport equation will yield a simplified, but expanded, transport equation. Of special interest is what happens to the term describing the scattering into the direction of interest. The derivation of Eq. (2.36) below utilises (i) the properties of the scattering phase function stated in Eq. (2.25), and (ii) the integral leading to the anisotropy given in Eq. (2.21). It also introduces a Cartesian coordinate system where $\boldsymbol{J}$ lies in the xz-plane and $\hat{\boldsymbol{z}} = \hat{\boldsymbol{s}}$. In these coordinates $\boldsymbol{J}$ may be represented using only two coordinates: $\boldsymbol{J} = J_\parallel\hat{\boldsymbol{s}} + J_\perp\hat{\boldsymbol{x}}$ (see Fig. 2.12). Note that the dependence on $\bar{\boldsymbol{r}}$ and t is not emphasised, *e.g.* $\rho = \rho(\bar{\boldsymbol{r}}, t)$, $\boldsymbol{J} = \boldsymbol{J}(\bar{\boldsymbol{r}}, t)$ and

$\mu = \mu(\bar{\boldsymbol{r}})$.

$$
\begin{aligned}
4\pi \left(\frac{\partial N}{\partial t}\right)_{s_+} &= 4\pi\, c\, \mu_s \int_{4\pi} p(\hat{\boldsymbol{s}}', \hat{\boldsymbol{s}})\, N(\hat{\boldsymbol{s}}')\; d\omega' = \\
&= c\, \mu_s \int_{4\pi} p(\hat{\boldsymbol{s}}', \hat{\boldsymbol{s}}) \left(\rho + \frac{3}{c} \boldsymbol{J} \cdot \hat{\boldsymbol{s}}'\right) d\omega' = \\
&= c\, \mu_s\, \rho \int_{4\pi} p(\hat{\boldsymbol{s}}, \hat{\boldsymbol{s}}')\; d\omega' + 3\mu_s \int_{4\pi} p(\hat{\boldsymbol{s}}' \cdot \hat{\boldsymbol{s}})\, \boldsymbol{J} \cdot \hat{\boldsymbol{s}}'\; d\omega' = \\
&= c\, \mu_s\, \rho + 3|J_{\parallel}|\, \mu_s \int_{4\pi} p(\hat{\boldsymbol{s}}' \cdot \hat{\boldsymbol{s}})\, \hat{\boldsymbol{s}} \cdot \hat{\boldsymbol{s}}'\; d\omega' \\
&\qquad + 3|J_{\perp}|\, \mu_s \int_{4\pi} p(\hat{\boldsymbol{s}}' \cdot \hat{\boldsymbol{s}})\, \hat{\boldsymbol{x}} \cdot \hat{\boldsymbol{s}}'\; d\omega' = \\
&= c\, \mu_s\, \rho + 3|J_{\parallel}|\, \mu_s\, g + 3|J_{\perp}|\, \mu_s \int_{4\pi} p(\hat{\boldsymbol{s}}' \cdot \hat{\boldsymbol{s}})\, \hat{\boldsymbol{x}} \cdot \hat{\boldsymbol{s}}'\; d\omega' \qquad (2.36)
\end{aligned}
$$

The last integral in Eq. (2.36) vanishes, since for any fixed θ, the integrand is anti-symmetric around $\varphi = \pi/2$. Finally, we reach:

$$
4\pi \left(\frac{\partial N}{\partial t}\right)_{s_+} = c\, \mu_s\, \rho + 3\, g\, \mu_s\, (\boldsymbol{J} \cdot \hat{\boldsymbol{s}}) \qquad (2.37)
$$

We are now ready to formulate a simplified transport equation. After inserting the truncated expansions from equations Eq. (2.34) and (2.35) in the transport equation (2.32) and multiplying with 4π, we reach

$$
\frac{\partial \rho}{\partial t} + \frac{3}{c} \frac{\partial (\boldsymbol{J} \cdot \hat{\boldsymbol{s}})}{\partial t} = -c \nabla \rho \cdot \hat{\boldsymbol{s}} - c\mu_a \rho - 3[\hat{\boldsymbol{s}} \cdot \nabla + \mu_{tr}](\boldsymbol{J} \cdot \hat{\boldsymbol{s}}) + 4\pi q \qquad (2.38)
$$

where we have introduced a new coefficient:

$$
\mu_{tr} \equiv \mu_a + (1 - g)\mu_s = \mu_a + \mu_s'. \qquad (2.39)
$$

Integration over all solid angles in Eq. (2.38) yields an equation more appropriate for physical interpretation (once familiar with the integrals presented in Appendix A, derivation is simple).

$$
\frac{\partial \rho}{\partial t} + \nabla \cdot \boldsymbol{J} + c\mu_a \rho - q_0 = 0 \qquad (2.40)
$$

By doing such an integration we disregard directionality and focus on overall (photon) density. The result is a continuity equation in differential form. Similar equations are common in many fields, such as hydrodynamics, electrodynamics and nuclear physics.

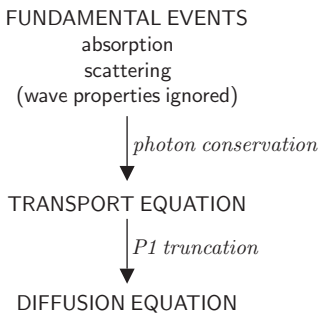

Figure 2.13. *A summary of the steps involved in deriving the diffusion equation.*

A second version of Eq. (2.38) is reached when considering net transport, rather than density. This is accomplished by $\hat{\boldsymbol{s}}$-weighted integration over all solid angles. The outcome is as follows:

$$\frac{\partial \boldsymbol{J}}{\partial t} + \frac{1}{3}c^2 \nabla \rho + c\mu_{\mathrm{tr}} \boldsymbol{J} + c\,\boldsymbol{q_1} = 0 \tag{2.41}$$

2.4.3 The diffusion approximation

Assuming that $\partial \boldsymbol{J}/\partial t$ is negligible[3], and that we are dealing only with isotropic sources[4], Eq. (2.41) reduces to Ficks' first law of diffusion[5].

$$\boldsymbol{J} = -\frac{c}{3\mu_{\mathrm{tr}}} \nabla \rho \tag{2.42}$$

This equation simply states that the net photon current follows the gradient of the photon density. A *diffusion coefficient*[6] $D = 1/3\mu_{\mathrm{tr}}$ [cm] is often introduced. Putting this information into equation Eq. (2.40) yields a slightly modified diffusion relation[7]:

$$\frac{\partial \rho}{\partial t} - cD\nabla^2 \rho + c\mu_{\mathrm{a}} \rho - q_0 = 0 \tag{2.43}$$

The procedures involved in deriving this diffusion equation of light transport are summarised in Fig. 2.13. Remembering Eq. (2.12) we realise that the same relation may be stated in terms of fluence:

$$\frac{1}{c}\frac{\partial \Phi(\bar{\boldsymbol{r}}, t)}{\partial t} - D\nabla^2 \Phi(\bar{\boldsymbol{r}}, t) + \mu_{\mathrm{a}} \Phi(\bar{\boldsymbol{r}}, t) - S(\bar{\boldsymbol{r}}, t) = 0 \tag{2.44}$$

Here, $S(\bar{\boldsymbol{r}}, t) = h\nu\, q_0$ [W/m^3]. A small, isotropic and continuous source of power P_0 corresponds to $S(\bar{\boldsymbol{r}}, t) = \tilde{P}_0 \delta_r$. If the source is pulsed and the pulse energy is E_0, it would correspond to $\tilde{E}_0 \delta_r \delta_t$.

Note that the only imprint of the scattering phase function is the g-dependence of μ_{tr}. The only difference between the cases of isotropic ($g = 0$) and non-isotropic scattering is that μ_{s} is weighted with a factor $(1 - g) \neq 1$ in the latter. Hence, there is no fundamental mathematical difference between these two cases. Non-isotropically scattering materials characterised by g and μ_{s} and

[3] By turning to the frequency domain, considering a light source being modulated at a frequency ω, it can be shown that this approximation hold as longs as $\omega \ll \mu_{\mathrm{s}}' c$ [46]. The issue of neglecting $\partial \boldsymbol{J}/\partial t$ is discussed in detail by Martí-López *et al.* [141]. An extensive investigation of this topic has also been conducted by Fishkin *et al.* [53], utilising modulation frequencies up to 3.2 GHz.

[4] A collimated source can be approximated with an isotropic source displaced one mean free path.

[5] Often written in the form $\boldsymbol{J} = -\chi \nabla c$, where χ is called *diffusivity* [m^2/s], and c is a concentration.

[6] Sometimes called *diffusion length*

[7] Similar to Ficks' second law of diffusion, $\frac{\partial c}{\partial t} = \alpha \nabla^2 c$, where c is a concentration.

can within the diffusion approximation be regarded as isotropically scattering, characterised by $\tilde{g} = 0$ and a scattering coefficient $\tilde{\mu_s} = (1-g)\mu_s$. This equivalent isotropic scattering coefficient is called the *reduced scattering coefficient*, and is defined as $\mu_s' = (1-g)\mu_s$. This also implies that measurements of light propagation on a macroscopic scale cannot be used to extract separate information on g and μ_s – we only achieve knowledge on μ_s'. This inseparability of g and μ_s on the macroscopic scale is often referred to as a *similarity relation* [142]. Absorption, on the other hand, appears on its own in *e.g.* Eq. (2.43) and will therefore not be fully confused with scattering.

Above, it was stated that the diffusion coefficient D depends on absorption:

$$D = \frac{1}{3(\mu_s' + \mu_a)} \tag{2.45}$$

As pointed out by several authors, this is non-physical [46, 117, 143–145]. When using an absorption-dependent diffusion coefficient, the solutions to the diffusion equation are not separable in scattering and absorption – as was the case for the transport equation (see Section 2.2.2). Since the derivation of the diffusion equation relies on that $\mu_s' \gg \mu_a$ [46] (due to the drastic simplifications made in Section 2.4.1), consistency requires that the diffusion coefficient is defined as

$$D = \frac{1}{3\mu_s'} \tag{2.46}$$

This definition is today widely accepted and has been proven, both simulation-wise and experimentally, to better describe light propagation in scattering media [46, 117, 143–145].

2.4.4 Validity of the diffusion approximation

The validity of the diffusion approximation is a complex matter, and should be investigate carefully rather than being taken for granted. Many authors have shown that diffusion theory fails in describing light propagation in many materials of interest [141, 146–150]. In general, breakdown occurs for small source-detector separations (compared to the mean free path of light propagation). Some authors have proposed ways to extend diffusion theory to higher absorptions and smaller source detector separations [151]. As shown in Papers **X**, **XIII**, and **XIV**, the steep slopes in TOFS curves (corresponding to high frequencies) render time-resolved photon migration particularly sensitive to the breakdown of diffusion theory (*cf.* Section 2.4.3, Note (3)). These Papers include careful comparisons between diffusion theory and Monte Carlo simulations, as well as extensive experimental work. Although TOFS for tissue optics often requires the use of refined modelling, diffusion has been found to be a proper model for light propagation in pharmaceutical solids. An example of that is shown in Fig. 2.14.

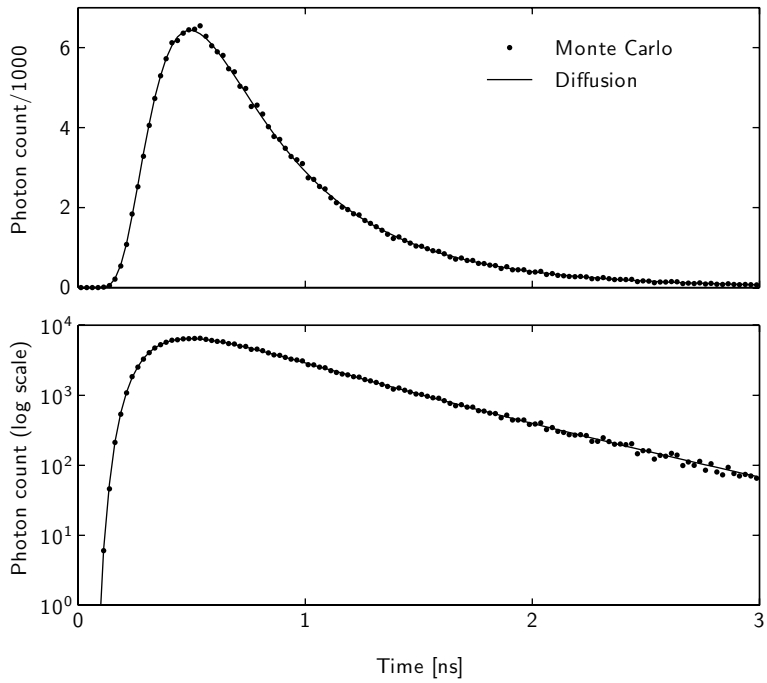

Figure 2.14. *The figure presents previously unpublished results of Monte Carlo simulations of light propagation in a cylindrical object (thickness 3 mm, diameter 10 mm, refractive index 1.5, $g = 0.9$, $\mu_s = 5000\ cm^{-1}$, and $\mu_a = 0$). In order to mimic the experimental conditions of Paper **XII**, photons were injected centrally using a 600 μm diameter top-hat light source. Photons transmitted through the medium, exiting within a central 600 μm diameter area, were used to generate the time-of-flight distribution shown in the figure. The simulation involved the tracking of 5×10^8 photons (terminated after a 3 ns TOF), out of which approximately 2% were transmitted, and 200000 contributing to the TOF distribution. The diffusion response for the utilised optical properties are calculated for an infinite slab of the same thickness (see Section 2.5.3). The excellent agreement justifies the use of diffusion modelling in e.g. Papers **II** and **XII**.*

2.5 Solving the diffusion equation

This section presents approximate solutions of the diffusion equation in geometries of great interest in practical measurement situations. Presented analytical expressions are based on the absorption-independent definition of the diffusion coefficient, $D = 1/3\mu_s'$. Note also that c denotes the speed of light in the material, $c = c_0/n$.

2.5.1 Homogenous infinite medium

A natural starting point when trying to solve the photon diffusion equation is to consider homogenous materials. The simplest case is the so called *infinite medium geometry* where no boundaries need to be taken into account.

Consider a continuous light source $S(\bar{\boldsymbol{r}}, t) = P_0\delta_r$. Assuming that the system is stationary ($d\Phi/dt = 0$) we have (from Eq. (2.44))

$$-\nabla^2\Phi(\bar{\boldsymbol{r}}, t) + 3\mu_s'\mu_a\Phi(\bar{\boldsymbol{r}}, t) = 3\mu_s' S(\bar{\boldsymbol{r}}, t) \tag{2.47}$$

The solution is given by

$$\Phi(\bar{\boldsymbol{r}}, t) = \Phi(r) = P_0 \cdot \frac{3\mu_s'}{4\pi r}\exp(-\mu_{\text{eff}}\, r) \tag{2.48}$$

where μ_{eff} [1/cm] is referred to as the *effective attenuation coefficient*, and is given by

$$\mu_{\text{eff}} = \sqrt{3\mu_s'\mu_a} \tag{2.49}$$

This means that, in the diffuse regime, spatially resolved measurements cannot separate absorption and scattering unless it relies on absolute fluence rate measurements.

Now consider a short isotropic pulse $S(\bar{\boldsymbol{r}}, t) = E_0\delta_r\delta_t$. The resulting fluence (impulse response) is

$$\Phi(r, t) = cE_0\left(\frac{3\mu_s'}{4\pi ct}\right)^{3/2}\exp\left(\frac{-3\mu_s' r^2}{4ct} - \mu_a ct\right) \tag{2.50}$$

where it should be noted that the familiar Beer-Lambertian attenuation is an important feature [45, 152]. The behaviour of this impulse response is illustrated in Fig. 2.15. It should be noted that this expression verifies that TOFS can be used to measure both absorption and scattering without the need for absolute measurements. As shown in Papers **VI**, **X**, and **XIII**, where this solution is used for data evaluation, this is a great advantage compared to spatially resolved measurements of diffuse light.

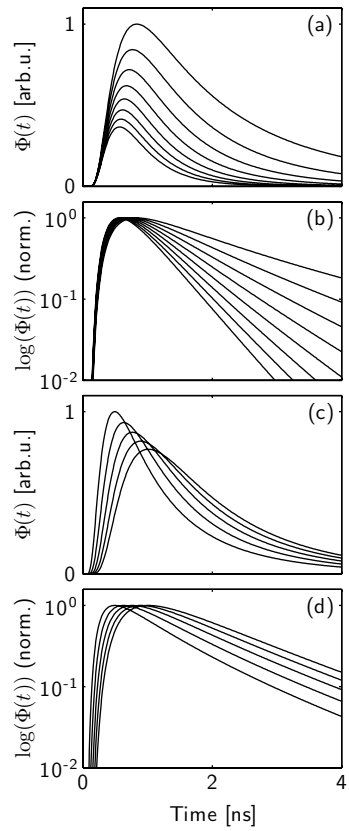

Figure 2.15. *Diffusion impulse response for r=2 cm and n=1.4.*

Parts (a) and (b):
μ_a*=0.01 to 0.08 cm*$^{-1}$
μ_s'*=10 cm*$^{-1}$ *fixed.*

Parts (c) and (d):
μ_a*=0.02 cm*$^{-1}$ *fixed*
μ_s'*=6 to 14 cm*$^{-1}$

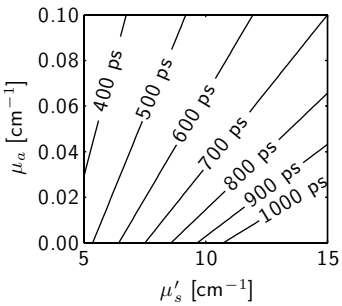

Figure 2.16. *Contour lines of t_p with respect to μ_a and μ_s'. Here, n=1.4 and r=2 cm.*

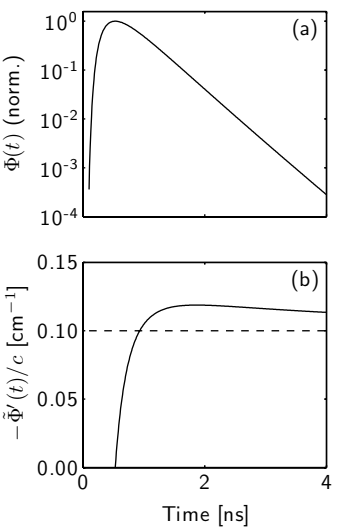

Figure 2.17. *The outcome when estimating μ_a by the slope at different times. Here, the true absorption is 0.1 cm^{-1} (dotted line), and μ_s'=10 cm^{-1}. As shown in (b) the final slope would yield large errors even in system with a large dynamic range (cf. part (a)).*

The time-to-peak, t_p, can easily be derived from Eq. (2.50). We first rewrite this equation by introducing three parameters α, β and γ.

$$\Phi(t) = \alpha t^{-3/2} \exp(\beta t) \exp(\gamma t^{-1}) \tag{2.51}$$

where $\alpha = cE_0\,(3\mu_s'/4\pi c)^{3/2}$, $\beta = -\mu_a c$ and $\gamma = -3\mu_s' r^2/4c$. The time to peak is found by setting the derivative to zero. We arrive at the relation

$$\frac{d\Phi}{dt} = \Phi(t) \cdot \Big[-\gamma t^{-2} - \frac{3}{2} t^{-1} + \beta \Big] = 0 \tag{2.52}$$

which means that the time-to-peak is given by

$$t_p^{-1} = -\frac{3}{4\gamma} + \sqrt{\frac{9}{16\gamma^2} + \frac{\beta}{\gamma}} \tag{2.53}$$

Fig. 2.16 shows how the optical properties influence t_p.

Let us now disregard the amplitude and focus on the shape of our impulse response. We take logarithm of Φ, and calculate its first derivative with respect to t:

$$\tilde{\Phi}'(t) = \frac{d \ln \Phi}{dt} = -\frac{3}{2} \cdot \frac{1}{t} + \frac{3\mu_s' r^2}{4c} \cdot \frac{1}{t^2} - \mu_a c \tag{2.54}$$

We see that as $t \to \infty$, $\tilde{\Phi}' \to -\mu_a c$. This implies that the absorption can be estimated by simply looking at the decay rate of late photons (the *final slope*), that is:

$$\mu_a \simeq -\frac{1}{c} \cdot \tilde{\Phi}'(t)\big|_{\text{late } t} \tag{2.55}$$

In practical cases, however, the signal level is often below the noise level at times where this is a proper approximation. The reason is that the $1/t$ term in Eq. (2.55) does not vanish quickly enough. This is illustrated in Fig. 2.17. Even the improved estimator

$$\Big[-\frac{3}{2ct} - \frac{1}{c} \cdot \tilde{\Phi}'(t) \Big] \Big|_{\text{late } t} \tag{2.56}$$

will produce significant errors. Non-linear curve-fitting is a better alternative (discussed later in Section 3.3).

2.5.2 Homogenous semi-infinite medium

Light propagation in half-space geometries, where only one half-space consists of a scattering material, is an important case. Common ways to refer to this situation is to talk about the *semi-infinite geometry* , or a *semi-infinite medium*. A typical example of a situation where the theory presented here may be useful is when the *diffuse reflectance* is measured (see Fig. 2.18).

An interesting case is when a light source irradiates a small spot on the sample (from the outside). A reasonable way of modelling such a source is to put an isotropic source at a depth z_s (typically, $z_s = 1/\mu_s'$) inside the scattering medium. When considering such a problem, the only difference from Section 2.5.1 is that we need to take boundary effects into account. Physically we know that light leaving the scattering medium will never return. In addition, a mismatch in refractive index will enable internal reflection. Several alternative ways of treating the boundary condition have been investigated during recent years [31, 45, 147, 153–155]. The most commonly used method is to introduce a virtual (extrapolated) boundary at $z = z_b < 0$ where we have zero fluence and a negative mirrored sources[8]. The negative source will reduce the fluence not only so that it is zero at the virtual boundary, but also within the scattering media. This has proven to be a good way of modelling boundary losses. An illustration is given in Fig. 2.19. The source responses from equations Eq. (2.48) and Eq. (2.50) can be recycled. The stationary solution [31, 147] is

$$\Phi(\bar{\boldsymbol{r}}) = \frac{3P_0\mu_s'}{4\pi}\left[\frac{1}{r_+}\exp(-\mu_{\text{eff}}\, r_+) - \frac{1}{r_-}\exp(-\mu_{\text{eff}}\, r_-)\right] \tag{2.57}$$

and the impulse response [45] is given by

$$\begin{aligned}\Phi(\bar{\boldsymbol{r}}, t) =& cE_0\left(\frac{3\mu_s'}{4\pi c}\right)^{3/2} t^{-3/2}\exp(-\mu_a ct) \\ &\times\left[\exp\left(\frac{-3\mu_s' r_+^2}{4ct}\right) - \exp\left(\frac{-3\mu_s' r_-^2}{4ct}\right)\right]\end{aligned} \tag{2.58}$$

where

$$\begin{cases} r_+ = \sqrt{\rho^2 + (z - z_s)^2} \\ r_- = \sqrt{\rho^2 + (z + z_s + 2z_b)^2} \end{cases} \tag{2.59}$$

In practice, it is common to measure the diffuse reflectance $R(\rho)$ [W/m^2], that is: photons leaving the scattering material. Although the reflectance has been calculated in various ways [45, 155], the most proper way is to integrate the radiance over a solid angle corresponding to the numerical aperture of the detecting fibre [147, 154]. It turns out that the detected signal can be expressed as a linear combination of the fluence rate and the net current over the boundary. The expressions are rather lengthy, and are not given here. It should, however, be noted that the impulse responses will exhibit a $\exp(-\mu_a ct)$ decay. Accordingly, several authors have utilised the final decay rate in time-resolved measurements for estimation of absorption [43, 44, 156, 157]. Analogous to the discussion in Section 2.5.1, non-linear curve-fitting is required for more careful modelling. Diffuse reflectance models are

[8] Analytical expressions stating the exact location of the boundary are given by, for example, Haskell [154].

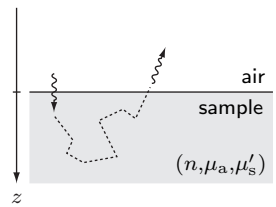

Figure 2.18. *Diffuse reflectance*

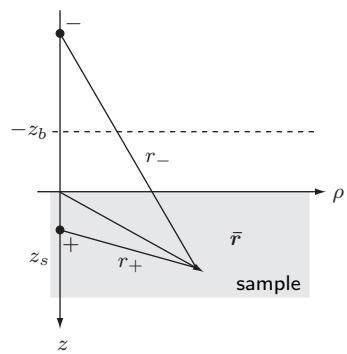

Figure 2.19. *Semi-infinite geometry (cylindrical symmetry, $\bar{\boldsymbol{r}} = (\rho, z)$)*

utilised for phantom experiments in Paper **IV**, and for breast tissue spectroscopy in Paper **III**. In Paper **XIV**, it is shown that time-resolved photon migration (*i.e.* TOFS) benefits strongly from the use of Monte Carlo-based data evaluation. There, the reflectance models discussed here are used for comparison.

2.5.3 Homogenous slab

Analytical expressions for diffusion of light in slab geometries are given in Ref. [158, 159]. Such models are used in Papers **II** and **XII** for modelling of light propagation in pharmaceutical tablets. Fig. 2.14 clearly shows that diffusion modelling for slab geometries is useful in this application.

2.5.4 Advanced geometries

Finite element methods can be used in more advanced geometries [160, 161]. Taroni *et al.* have shown how diffusion approximation can be applied to small samples [162].

In all cases, it should be noted that heterogeneity remains a cumbersome issue [163, 164].

2.6 Sampling Volumes

When detecting photons that have travelled through a highly scattering media, one important question is where detected photons actually have been, *i.e.* the *sampling volume*. The information carried by detected photons can only be used to describe regions in which those photons actually travelled. This may not be a problem when measurements are performed on homogenous materials in simple geometries. However, in many practical situations, one must ensure that photons actually probe desired regions. For example: when measuring interstitially in the human prostate, are the actual paths of detected photons limited to the prostate itself, or is there an impact from surrounding tissue?

In order to describe sampling volumes, Schotland *et al.* introduced the concept of *photon hitting densities* (PHD) [165]. The PHD measures the expected time spent in a certain small region around r by photons originating from a source at r_s and being detected at r_d after a time of flight T. The PHD is denoted $\nu(r, r_\mathrm{s}, r_\mathrm{d}, T)$, and when integrated over space it sums up to the total time of flight T.

$$\iiint \nu(r, r_\mathrm{s}, r_\mathrm{d}, T)\, dV = T \tag{2.60}$$

It can be shown that the PHD can be calculated from the Green's functions, $G(r_1, r_2, t)$, being analytical solutions to the time dependent diffusion equation [158, 165]. The explicit relation is a

convolution like integral, given in Eq. (2.61).

$$\nu(r, r_{\mathrm{s}}, r_{\mathrm{d}}, T) = \frac{1}{G(r_{\mathrm{s}}, r_{\mathrm{d}}, T)} \int_0^T G(r_{\mathrm{s}}, r, t')\, G(r, r_{\mathrm{d}}, T - t')\, dt' \tag{2.61}$$

Intuitively, it is reasonable that the product of the two Green's functions $G(r_{\mathrm{s}}, r, t')$ and $G(r, r_{\mathrm{d}}, T - t')$ measures the probability of travelling first from r_{s} to r in time t', and then from r to r_{d} in time $T - t'$. The situation is illustrated in Fig. 2.20. Integration of all possible combinations of partial time of flights summing up to T yields a measure of the total probability of passing r. That this also is a measure of the expected time spent in r is qualitatively obvious.

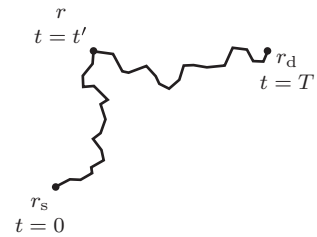

Figure 2.20. *Illustration of a photon path originating from a source at r_s, and via r finally reaching a detector at r_d (with a total time-of-flight T).*

Several authors have discussed the issue of sampling volumes [158, 165, 166]. In simple geometries, such as infinite homogenous media, the PHD can be calculated from Eq. (2.61) in a straight forward manner. This was done in Paper **VI** in order to investigate the sampling volumes during *in vivo* spectroscopy of the human prostate. For any given geometry and given optical properties, Monte Carlo simulations can assist in determining photon paths, and thus sampling volumes.

Chapter 3

Time-of-flight spectroscopy

Absorption spectroscopy plays an important roll in the modern society. Important areas of application include the vast fields of analytical chemistry and process control. Traditionally, it is based on the quantification of intensity loss due to transmission through a sample. A classic example being the investigation of light absorption in clear, but coloured, liquids. The fundamental assumption is that the main loss mechanism is absorption, and that this leads to an exponentially decaying intensity within a sample (Beer-Lambert-Bouguer law of absorption [15]). Furthermore, the analysis relies on that the optical pathlength is known (given by the sample size). However, the analysis of chemical composition is often of great importance also in cases where light scattering is a stronger effect than absorption. The detected signal is then mainly determined by the unknown pathlength distribution and the geometrically determined losses of light due to scattering – thus not only by the absorption coefficient of the sample. Light scattering is prominent in for example applications involving analysis of agricultural products, pharmaceuticals and biological tissues.

Photon time-of-flight spectroscopy (TOFS[1]) allows separation of the effects of absorption and scattering, and measurement of their individual contributions. The technique can therefore improve absorption spectroscopy in applications involving scattering materials. In addition, the obtained scattering data provides information on the structure of the material. This chapter gives an introduction to the use of TOFS for applications in diffuse optics. Although it involves the use of highly sophisticated instrumentation with ultrafast (picosecond) time-resolution, these technical

[1]TOFS is often referred to as time-resolved spectroscopy (TRS). For clarity, since TRS is a much broader term, the term time-of-flight is preferable. Expressions like time-resolved diffuse reflectance, as used in the title of Paper **XIV**, are, however, fairly clear since they state what is actually resolved in time.

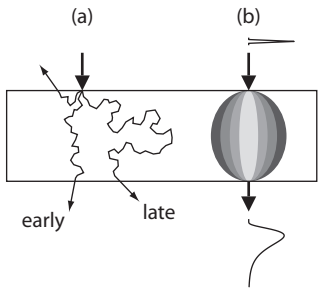

Figure 3.1. *Principles in TOFS. Part (a) illustrates random photon propagation. Many photons are typically "lost" close to the light source (injection location). Transmitted photons can be classified according to their total time-of-flight (early, late etc.). Part (b) shows how a short incident pulse is broadened upon transmission through a scattering sample. It also schematically indicates sample volume for the case of localised detection in transmission. The actual photon TOF distribution is determined by sample optical properties, sample geometry, and detector position (and size).*

tools are well known from the mature field of fluorescence lifetime experiments. The instrumental aspects are therefore only briefly introduced, except for issues of particular importance in photon migration applications. Instead the focus of this chapter is on the need of advanced modelling, practical aspects, as well as on applications. In addition, the aim is to attract the attention to a broad range of aspects of TOFS, and to provide references to to further reading, rather than to give exhaustive coverage of a few selected issues. It should be remembered that the publications enclosed in this thesis provide in-depth coverage of several important issues.

3.1 Introduction

In 1905, Einstein published the first of a few classic articles that revealed that particle nature of light [167]. After stating that certain experiment are better explained if the energy is discontinuously distributed in space, Einstein wrote

> Nach der hier ins Auge zu fassenden Annahme ist bei Ausbreitung eines von einem Punkte ausgehenden Lichstrahles die Energie nicht kontinuerlich auf größer under größser werdene Räume verteil, sondern es besteht dieselbe aus einer endlichen Zahl von in Raumpunkten lokalisiert Energiequanten, welche sich bewegen, ohne sich zu teilen und nur als Ganze absorbiert und erzeugt werden können.

Here, Einstein argues that light consists of a finite number of localised energy quanta, and are absorbed and generated only as a whole. These quanta can be considered as elementary particles, and are called *photons*.

When detecting light that has propagated through a scattering material, the different photons arriving to the detector will have travelled different distances, *i.e.* they exhibit different time-of-flights (TOF). This unknown pathlength distribution prevents the use of the normal procedure for absorption spectrometry. A measurement of the time-of-flight distribution would of course be of great value. But is it doable? Light travels at a speed of about 300 000 000 m/s in air. Astonishingly, time-resolutions on the order of one picosecond (1×10^{-12} s) are since many years obtained on a routine basis with commercial systems. For light applications, this corresponds to a pathlength resolution of 0.3 mm. In fact, resolutions better than 30 µm have been obtained using optical time-of-flight ranging [168]. It so happens that such resolutions are more than sufficient for macroscopical biomedical and pharmaceutical applications in the near-IR. As shown in Paper **III**, near-IR measurements over 10 to 25 mm of breast tissue typically generate distributions spanning over a few nanoseconds. Similarly, as shown in Papers **VI** and **XIII**, measurements in human prostate tissue over similar distances generate TOF distributions ranging from 100 ps

(early light) up to 1 ns. As for example shown in Papers **XII** and by Johansson *et al.* [169], similar time-scales are encountered during measurements on pharmaceutical tablets. Amazingly, propagation through a 3 mm tablet yields average photon pathlengths of more than 100 mm! Other examples of materials exhibiting strong scattering (*i.e.* turbid materials) are pharmaceutical powders, most biological tissues (including also fruit and wood), flour, milk, white plastics, white paint (often due to the additions of titanium dioxide), paper, snow etc. A schematic over light propagation through turbid materials is shown in Fig. 3.1. Experimental time-of-flight distributions from pharmaceutical samples are shown in Fig. 3.2.

As discussed in Chapter 2, the macroscopic properties of highly scattering materials can be described using the absorption coefficient (μ_a) and the reduced scattering coefficient (μ_s'). By revealing the photon pathlength distribution, TOFS can be used for quantitative absorption spectroscopy. In addition, since also the scattering can be quantified, it can also be used for assessment of structural properties. Fig. 3.3 shows how the TOF distribution is influenced by variations in scattering and absorption. There, distributions are calculated from diffusion theory for an interstitial geometry (n=1.5, source-detector separation 2 cm). Scattering is fixed to μ_s'=10 cm^{-1} in (a), and absorption is fixed to μ_s'=0.1 cm^{-1} in (b). Further illustration of why TOFS can separate the effects of scattering and absorption is later given in Fig. 3.11.

For the pharmaceutical tablets investigated in Paper **XII**, μ_s' is in the order of 500 cm^{-1} while $\mu_a = 3 \times 10^{-2}$ cm^{-1}. This means that a photon completely changes its direction each 20 µm, while the average survival range is as large as 50 cm. The survival range corresponds to a time-of-flight of 2.5 ns for a refractive index of 1.5. Since the major fraction of photons are detected within the the first 1 or 2 ns, it is obvious that scattering has a strong influence even on the decay of the time-of-flight distribution. As shown in Papers **VI** and **XIII**, the situation is different in prostate tissue, where μ_s' typically falls within the range 2 to 15 cm^{-1}, and μ_a is about 0.3 to 0.6 cm^{-1} (*i.e.* significantly lower scattering and higher absorption). Nonetheless, scattering is the dominant process. Proper modelling of light propagation is therefore crucial in quantitative analysis of turbid samples. In contrast to conventional absorption spectrometry, modelling in TOFS is a fairly complex issue with many pitfalls. This important issue is a major topic in Papers **X**, **XIII** and **XIV**, and is further discussed in Section 3.3.

The use of photon time-of-flight spectroscopy for characterisation of turbid materials goes back to the 1970s. Multiple scattering is an important topic in atmospherical science, and several authors investigated pulse propagation in clouds [170–173]. Ishimaru developed theories for time-resolved propagation of pulses in turbid materials [174], and Shimizu *et al.* made related experimental work on polystyrene latex spheres [174]. In 1988, Chance *et al.*

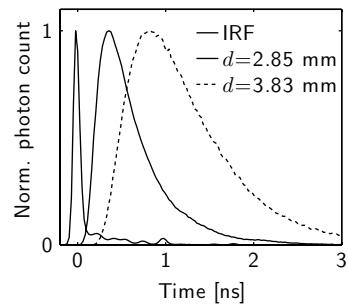

Figure 3.2. *TOF histograms obtained from transmission measurements on two pharmaceutical model tablets (wavelength 786 nm). The tablets were compressed from 300 mg of 150 µm sized granules, and their thicknesses, d are stated in the graph. The narrowest pulse corresponds to the obtained TOF distribution when no sample is present, i.e. the instrumental response function (IRF). A 1 ns TOF corresponds to a pathlength of 20 cm (assuming a refractive index of 1.5).*

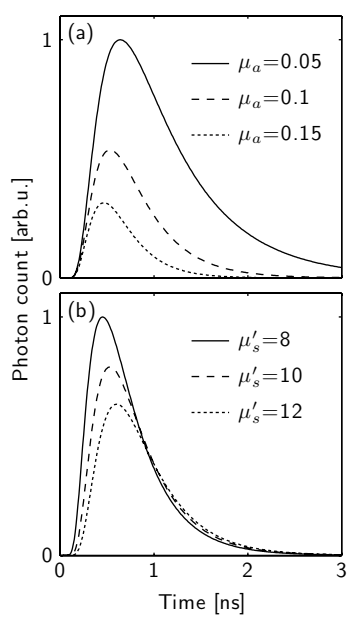

Figure 3.3. *Illustration of influence on variations in optical properties (unit: cm^{-1}).*

presented the use of dual-wavelength time-of-flight spectroscopy for measurements of hemoglobin oxygenation in brain tissue [44], as well as for hemoglobin and myoglobin spectroscopy in muscles [43]. Since then, TOFS and its frequency domain equivalent have become standard tools in the field of biomedical optics. Important biomedical applications are discussed further in Section 3.6, and include optical mammography, brain hemodynamics and diffuse optical tomography. In addition, being interested in PDT of prostate cancer, our research group has introduced TOFS as a powerful tool for *in vivo* spectroscopy of the human prostate (Papers **VI** and **XIII**). This is described in Section 3.6.4. We also employ TOFS for pharmaceutical analysis, as described in Section 3.7. Another application example of TOFS is fruit spectroscopy [175, 176].

3.2 Instrumentation

This section briefly introduces various instrumentations of interest for TOFS, and refers the reader to sources providing more detailed information. Sections 3.2.1 and 3.2.2 introduce two important schemes for optical measurements on the picosecond timescale (or slower). Pulsed narrow-bandwidth light sources such as laser diodes and mode-locked dye or titanium-sapphire lasers are briefly mentioned in Section 3.2.3. Section 3.2.4 discusses the generation of spectral continuum for broadband spectroscopy.

3.2.1 Time-correlated single photon counting

Time-correlated single photon counting (TCSPC) is a mature technique for sensitive detection and high time resolution. Originally mainly used for fluorescence lifetime experiments, it is now widely used in areas such as singe-molecule detection, fluorescence correlation spectroscopy, time-resolved laser scanning microscopy, and diffuse optics and tomography. TCSPC is extensively treated in the book by O'Connor and Phillips [177]. I also strongly recommend the excellent and recent book by Becker, providing a detailed coverage of recent progress, technical aspects, as well as of the most important applications [178]. The development of a TCSPC system for time-resolved diffuse optical tomography is the topic of the thesis by Schmidt [179].

As implied by the name, TCSPC is based on the detection of individual photons. Knowing that the moderate near-infrared light intensity of 1 mW corresponds to millions of billions of photons every second, the sensitivity of single photon counting is striking. A fast detector delivers pulses corresponding to single photon detection events. The time stamp of a photon detection event is measured with respect to a reference pulse from the light source.

TCSPC experiments involve repeated excitation/injection, and detection and timing of zero or one photon each period. The technique is thus not capable of handling the detection of several photons each signal period (it is difficult to perform accurate timing of a stream of closely spaced events). It is the repetitive character of the measurement that allows the build-up of a TCSPC photon histogram (*i.e.* a photon time-of-flight distribution). In fact, TCSPC relies on that the optical signal is very weak – so weak that it is rare to see any photon at all. This is due to that only the first detected photon each period will be noted and analysed. If the probability for detection of two or more photons per period is not negligible, late photons are discriminated. This results in a statistical error is known as *photon pile up*. Instead of acquiring the overall photon distribution, the technique now generates a histogram describing the distribution of the earliest photon. In the limit of low detection rates, these two distributions are equal. In cases with higher light intensities, the optical signal must be attenuated[2] before it reaches the detector. In practice, this means that it is only a small fraction of the excitation/injection pulses that produce a detection event. Using high repetition-rate pulsed lasers still allow fast generation of proper photon histograms (10 to 100 MHz are typical repetition-rates).

A schematic of a typical TCSPC chain is shown in Fig. 3.4. Note that this basic TCSPC setup is not wavelength selective. In order to obtain spectroscopic information, wavelengths must be probed temporally separated, sequentially or in a multichannel configuration. TCSPC instrumentation is used in Papers **III**, **IV**, **VI**, **X**, **XII**, **XIII** and **XIV**. In these, spectroscopy is based on temporally separated pulsing of four different laser diodes (40 MHz repetition rate, 160 million laser pulses per second).

The time resolution in TCSPC can be made as small as 1 ps (1×10^{-12} s). The practical time resolution is, however, to a great extent determined by the pulse shape of the light source, the dispersion in the optical setup, the detector transit time spread, as well as the time jitter in electronics. All these aspects are included in the instrumental response function (IRF). The IRF is readily recordable by performing a recording without any unknown sample. The IRF can be made as short as 25 ps, both with MCP-PMTs and with SP-APDs [178]. Proper deconvolution procedures can yield effective time-resolutions significantly better than the IRF (see for example Sect. 5.1.7 in Ref. [178]).

[2]Time gating can be used to avoid temporal regions with excessive optical signal [180].

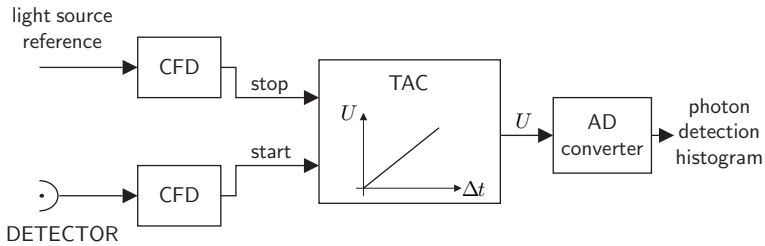

Figure 3.4. *A schematic of a typical TCSPC setup. A fast detector (e.g. a multichannel-plate PMT or a single photon APD) provides an electrical response to a photon detection. The timing is determined relative to a reference pulse. The relative time difference Δt between reference and detected photon is converted to a voltage in a time-to-amplitude converter (TAC). In order to avoid amplitude jitter to induce time jitter, constant fraction discriminators (CFD) are used to process the reference and detector signals.*

3.2.2 Streak cameras

In contrast to TCSPC, a streak camera does not clock photons individually. Instead, the temporal photon distribution is turned into a spatial distribution by letting generated photoelectrons experience a rapidly modulated electric field (a manner similar to that of an oscilloscope). By utilising a spectrometer before this electron deflection process, spectroscopic information can be stored in a second spatial dimension. A schematic illustration of a streak camera is shown Fig. 3.5. The use of streak cameras for broad-band photon time-of-flight spectroscopy is a main topic in the thesis of Abrahamsson [181], and is therefore not discussed further here. A streak camera setup is utilised in Papers **I** and **II**.

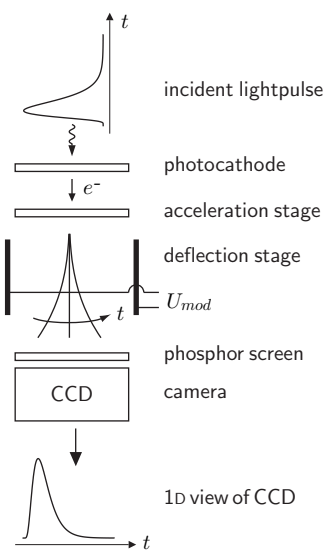

Figure 3.5. *Schematic of a streak camera (the incorporation of a spectroscopic dimension is not shown).*

3.2.3 Light sources

Pulsed diode lasers are popular, compact and reliable light sources in time-resolved spectroscopy, and is commonly used in TOFS. They are available in the range 400 to 1500 nm, offering average powers in the mW range and pulse widths down to 50 ps.

Mode-locking of longitudinal modes in dye and titanium-sapphire lasers is another source of short pulses. Their broad tunability offers a great advantage with respect to laser diodes (the titanium-sapphire can be tuned from 700 to 1000 nm). An example of a versatile TOFS-system based on a combination of dye and titanium-sapphire lasers are presented by Pifferi *et al.* [182]. Commercial systems are also available, see for example the Chameleon lasers offered by *Coherent*.

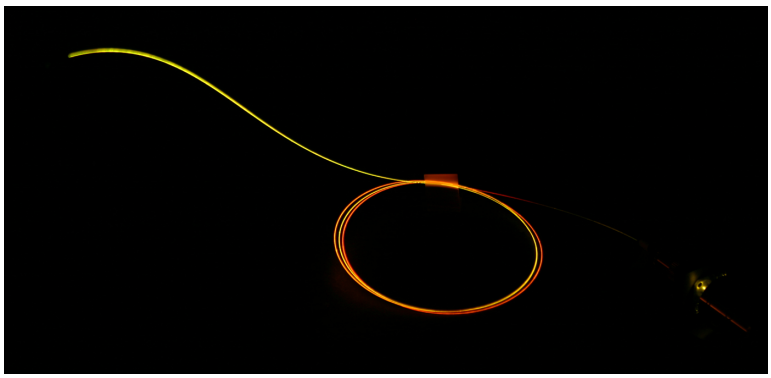

Figure 3.6. *White light (continuum) generation via non-linear optical processes in a photonic crystal fiber (Paper* ***I****). Note that the* 800 nm *invisible laser radiation from the femtosecond pump laser (coming from the right) quickly generates red light, and at longer distances green light. The light captured in this photograph is only the small part that is scattered out of the fiber.*

3.2.4 Continuum generation

As mentioned in the previous section, pulsed monochromatic or narrow-bandwidth light-sources are often utilised in TOFS. For more demanding spectroscopic applications, a spectral continuum is naturally preferable. This is achievable when employing pulsed, high-power lasers in combination with non-linear optical effects. Andersson-Engels *et al.* generated white light by focussing femtosecond high-power laser pulses into water, and used it for *in vivo* TOFS [183]. Non-linear optical effects in special optical fibers can also be used for continuum generation. Paper **I** presents the use of a photonic crystal fiber (PCF) for TOFS in the 500 to 1200 nm range. Fig. 3.6 shows the white-light generation in such a PCF. There, near-infrared detection capability is ensured by the use of an S1 photocathode in a streak camera. Similarly, Bassi *et al.* have developed a system utilising a PCF for TCSPC-based TOFS in the 550 to 1000 nm range [184]. Today, companies, *e.g. Fianium* and *Koheras*, offer commercial systems for supercontinuum generation based on non-linear optical fibers.

3.2.5 Optical Fibers

TOFS requires the use of fairly expensive GRIN (Gradient index) optical fibers. The reason is the mode dispersion (temporal broadening) taking place in standard step index fibers would yield an unacceptably broad IRF.

In applications where sterilisation is required (*e.g. in vivo* applications such as interstitial prostate spectroscopy as presented in

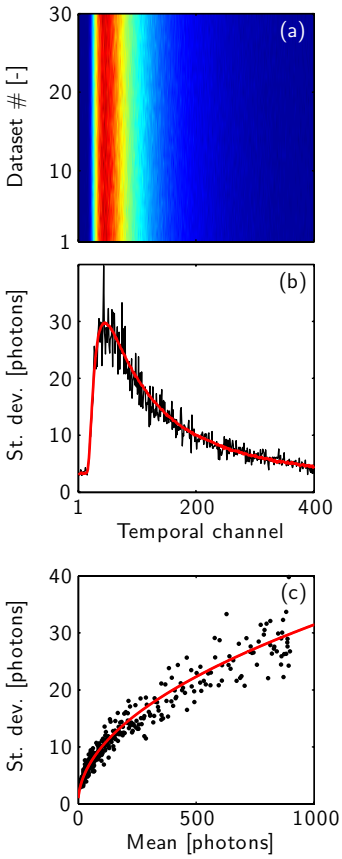

Figure 3.7. *TCSPC noise analysis using 30 time-resolved datasets (from delrin, each with 0.5 s acquisition time, 25 ps channel width). Datasets are viewed in (a), where the photon count is false colour coded. Photon counts are statistically analysed channel by channel in (b). There, the red (smooth) curve states the single dataset standard deviation as calculated from analysis of all 30 datasets. Part (c) illustrates the relation between photon count and standard deviation, see eq. 3.2 (each dot correspond to one channel).*

Papers **VI** and **XIII**), particular care is needed when assembling optical fibers. For biocompability and resistance to sterilisation modalities, polyimide can be considered a suitable jacket for optical fibers. Parts that need additional protection can be covered by an appropriate medical grade polyolefin tubing. For gluing, the use of the epoxy EPO-TEK 353 ND (Epoxy Technology Inc., Massachusetts, USA) is recommended (it is biocompatible and resists several types of sterilisation). Note that blood is easily removed from fibers using cold water. Alcohol can be used in a second step for disinfection.

3.3 Data evaluation

Data evaluation, and modelling in particular, is a major part of TOFS. While the commonly used time-domain diffusion approximation of light propagation appears valid in pharmaceutical applications, it is not appropriate in all biological tissues. The importance of proper modelling is the main topic of Papers **X**, **XIII**, and **XIV**. This section discusses various aspects of data evaluation.

3.3.1 The TOF histogram

At constant intensity, photon detection follow a Poisson process. Although the normal procedure is to consider the number of photons within a certain time as Possion distributed, this section follows another viewpoint. Consider a TCSPC time-of-flight histogram consisting of 1024 channels. When using such a histogram to draw conclusions about the actual photon distribution (for example by employing curve fitting) it is important to consider noise. The number of counts in a channel can be described by a binomially distributed random variable

$$C_i \in \mathrm{Bin}(n, p_i) \qquad i = 1, 2, ..., 1024 \tag{3.1}$$

where n is total counts in the histogram, and p_i is the probability of ending up in channel i at a particular detection. This variable accounts for both real photons, and for PMT dark current. Its mean value is np_i, and its variance $\widehat{\sigma_i}^2 = np_i(1-p_i)$. In most cases (*e.g.* $np_i(1-p_i) > 10$), this binomial distribution can be approximated by a gaussian distribution. Furthermore, if c_i denotes the actual photon count in a certain channel, the corresponding standard deviation σ_i is estimated by

$$\widehat{\sigma_i} = \sqrt{c_i(1 - c_i/n)} \tag{3.2}$$

We see that $\sigma_i \simeq \sqrt{c_i}$, meaning that the square root of the photon count is an estimation of the standard deviation. Note that a noisy dataset may need pre-processing before it is used as a measure of standard deviation.

To estimate the true photon distribution, y_i, we subtract a background level from our histogram. The background level, b, is estimated from the histogram, typically by averaging over a few channels where no signal is present.

$$\widehat{b} = \frac{1}{n_j} \sum_j c_j \tag{3.3}$$

Using hat-notation for estimated parameters (star-notation for corresponding random variables), we have

$$\widehat{y_i} = c_i - \widehat{b} \tag{3.4}$$

The variance of the corresponding estimating random variable Y_i^* equals the variance of $C_i + b^*$. Neglecting the dependence between channels, this variance is

$$\sigma_i^2 = \mathrm{Var}[Y_i] = np_i(1-p_i) + \frac{1}{n_j} np_j(1-p_j) \tag{3.5}$$

By using estimates of p_i and p_j, we can estimate σ_i^2. Using the simple estimations $\widehat{p_i} = c_i/n$ and $\widehat{p_j} = \widehat{b}/n$, we reach

$$\widehat{\sigma_y^2} = c_i(1 - c_i/n) + \frac{1}{n_j} \widehat{b}(1 - \widehat{b}/n) \tag{3.6}$$

This measure of variance may be useful during curve fitting.

3.3.2 Modelling

In order to separate and derive absorption and reduced scattering coefficients (μ_a and μ_s', respectively), TOF histograms must be evaluated using a proper light propagation model. Generally, this is achieved by minimisation of a scalar function χ^2 that measures the goodness of fit between the experimental data and the model. This fit merit function is defined as

$$\chi^2(\boldsymbol{p}) = \sum_{i=1}^{N} \left(\frac{y_i - y(\boldsymbol{p}, t_i)}{\sigma_i} \right)^2 \tag{3.7}$$

where (t_i, y_i) $(i = 1, \ldots, N)$ denotes experimental data (t_i being the time, and y_i the corresponding photon count), $\boldsymbol{p}$ is the set of parameters to be fitted, $y(\boldsymbol{p}, t_i)$ the model prediction, and σ_i are weights (often estimations of standard deviations). This type of minimisation is a curve-fitting problem.

In simple geometries, and when the diffusion approximation of light propagation is valid, evaluation can be performed by fitting analytical models (see Section 2.5) to the TOF histogram. Since photon distributions depend non-linearly on both μ_a and

μ_s', one must employ non-linear optimisation. A frequently used scheme is the so called *Levenberg-Marquardt optimization*, which elegantly combines the methods of *steepest descent* and *inverse Hessian* [185]. The model prediction typically have the form

$$y(\boldsymbol{p}, t_i) = y(\mu_a, \mu_s', k, t_i) = k \cdot \tilde{y}(\mu_a, \mu_s', t_i) \tag{3.8}$$

where k is a scale factor. However, the finite temporal width of the input pulse, and broadening in detection requires us to take the instrumental response function (IRF) into account. Hence, the model prediction is a convolution between a theoretical impulse response (*e.g.* from diffusion theory) and an experimental IRF. The optimal fit is reached iteratively, guided by the parameter derivatives of the merit function. A proper initial guess is of course needed, and can be calculated from (for example) the time-to-peak, and the late photon decay rate. Diffusion modelling based on this procedure is a standard tool for TOFS [155], and is used in several of the publications presented in this thesis. Note that the scale factor k is introduced since it is practically infeasible to perform absolute measurement of light intensities in TOFS. This means that optical properties are derived from the shape of TOF histograms, while amplitude information is disregarded. The ability to extract μ_s' and μ_a without intensity measurements is often a big advantage in clinical applications, as discussed in for example Paper **VI**. Note also that the earliest experimental use of TOFS involved simpler modelling, extracting (only) absorption coefficients from the signal decay rate [43, 44, 156, 157].

Some researchers avoid the use of physical models of light propagation, and instead employ analytical descriptors such as moments and derivatives of the TOF distribution [186, 187].

3.3.3 Uncertainty vs. model errors

As discussed in Section 3.1, the advantage of the time-of-flight approach is the ability to separate absorption from scattering. In particular, it is often of great value that this can be done without the need of absolute intensity measurements (as in spatially resolved measurements, see Section 1.3.3). However, the disregarding of amplitude information allows, to a certain degree, confusion of high scattering with low absorption. With respect to temporal shape, both an increase in scattering, and a decrease in absorption, yield broader pulses with an increasing average TOF. The fact that the opposite is true for their influence on the amount of detected light does not help when performing shape assessment. The limitations in the separation of μ_a and μ_s' due to this aspect is related to signal-to-noise ratios and dynamic range. If noise is properly taken into account, the induced uncertainty in fitted parameters can be estimated with confidence intervals (see for example Press

et al. [188]). Such theoretical considerations can reveal the practical limits in accuracy of derived optical properties (and depend on signal-to-noise ratios and acquisition time). A qualitative discussion of the shapes of TOF distributions encountered is given below.

Consider an impulse response $y_0(t) = k_0 \cdot \tilde{y}(\mu_{a0}, \mu'_{s0}, t)$ taken from Eq. (2.50) discretely sampled at t_i. The difference in shape between this impulse response, and that for a different set of optical properties, (μ_a, μ'_s), can be stated using a least squares measure, as in Eq. (3.9).

$$\Delta_{\text{shape}}(\mu_a, \mu'_s) = \min_k \left\{ \sum_i \left(y_0(t_i) - k \cdot \tilde{y}(\mu_a, \mu'_s, t_i) \right)^2 \right\} \tag{3.9}$$

The minimum in Eq. (3.9) is reached when

$$k = \sum_i y_0(t_i)\tilde{y}(t_i) \Big/ \sum_i \tilde{y}(t_i)^2. \tag{3.10}$$

A related measure is what may be called the *direction of optimal shape conservation* (DOSC). Under influence of noise, this quantity tells us in which direction we are to expect the largest uncertainty. Given a certain change $\delta\mu_a$ in μ_a, there are certain changes $\delta\mu'_s$ and δk that will minimise the induced change in shape. The direction, defined by the ratio $\delta\mu'_s/\delta\mu_a$, may be found from balancing parameter derivatives as indicated in Eq. (3.11).

$$\min_{\delta\mu'_s, \delta k} \sum_i \left\{ \left(\frac{\partial y(t_i)}{\partial \mu_a}\delta\mu_a + \frac{\partial y(t_i)}{\partial \mu'_s}\delta\mu'_s + \frac{\partial y(t_i)}{\partial k}\delta k \right)^2 \right\} \tag{3.11}$$

An example of similarities in temporal shape, and DOSC, in a region of optical properties relevant to biomedical optics, is given in Figs. 3.8, 3.10, and 3.9. An uncertainty not being along the DOSC may be an indication of improper modelling, drifts or other systematic errors.

The issue discussed above should not be confused with model related errors. Papers **X**, **XIII** and **XIV** show that TOFS often suffer greatly from the use of diffusion models for light propagation. This is not a surprise, since it has been long known that the diffusion modelling is very sensitive to the fit range used during curve fitting (*e.g.* the derived optical properties strongly depend on how much of the early light that is disregarded) [147, 148, 155]. This in itself suggests that the model is improper. Already 1990, Yoo *et al.* showed that diffusion models fail to predict the response of short light pulses [146]. In addition, Cubeddu *et al.* pointed out that diffusion modelling often cannot be used for accurate extraction of scattering coefficients [148]. Nonetheless, diffusion modelling has remained the standard for data evaluation. At the same

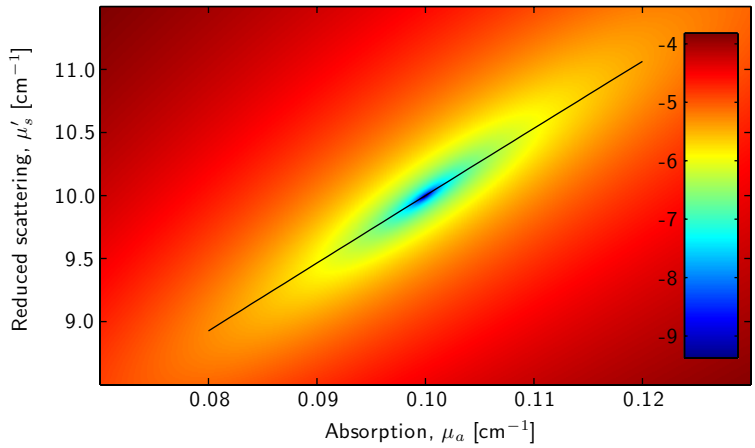

Figure 3.8. *Shape difference in the neighbourhood of* $(\mu_a, \mu_s') = (0.1, 10)$ cm^{-1} *illustrated by plotting* $\log(\Delta_{shape})$. *The solid black line indicates the path of optimal shape conservation, calculated from Eq. (3.11) using steps* $\delta\mu_a = 0.001$ cm^{-1}. *Although* $\delta\mu_s'/\delta\mu_a$ *appears to be constant, it varies slightly, see Fig. 3.9. A visual on the actual shape variation is presented in Fig. 3.10*

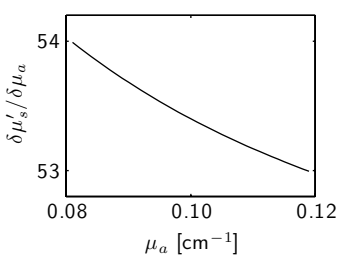

Figure 3.9. *Direction of optimal shape conservation versus* μ_a, *when following the path of optimal shape that passes* $(\mu_a, \mu_s') = (0.1, 10)$ cm^{-1}.

time, TOFS is often accompanied with unexplained artifacts often referred to as μ_a-μ_s' coupling or crosstalk [182] and [Paper **IV**]. Papers **X**, **XIII** and **XIV** explains these artifacts, and avoids them by using a novel scheme for Monte Carlo-based data evaluation. In contrast to slow forward modelling offered by conventional Monte Carlo, the proposed scheme is developed for routine analysis (*i.e.* allows fast inverse modelling). It is important to remember that the artifacts mentioned above should be assigned to the breakdown of diffusion approximation, while the use of terms such as coupling or crosstalk lacks explanatory value. Errors related to the use of diffusion models in inappropriate regions of optical properties is discussed in detail in Papers **X**, **XIII** and Paper **XIV**. It should, however, be remembered that the time-resolved diffusion approximation of light propagation is still useful in important ranges of optical properties. To exemplify, Fig. 2.14 shows previously unpublished evidence that diffusion modelling is valid in applications involving pharmaceutical samples.

3.3.4 Using spectral information

In the typical application of TOFS, derived optical properties are intended for use in spectroscopic evaluation. A few selected wavelengths may be sufficient for monitoring of primary tissue chromophores such as hemoglobin and water [50, 189, 190]. Papers **III**,

VI and **XIII** all involve hemoglobin spectroscopy and estimation of oxygen saturation using four wavelengths. More advanced and robust absorption spectrometry requires properly resolved spectra. Wide spectral coverage in TOFS has been achieved by, for example, Andersson-Engels by means of white-light generation in water (550 to 750 nm) [183]. The setup was used by Johansson *et al.* for the development of a new spectroscopic method for analysis of pharmaceutical solids [169]. Cubeddu *et al.* used mode-locked dye and titanium-sapphire lasers to cover 610 to 1010 nm [191], and more recently extended to the range 550 to 1050 nm [182]. Theses systems have been used primarily for high-performance breast tissue spectroscopy [192], and have allowed extraction of hemoglobin, water, lipid and even collagen content of breast tissue [70].

Paper **I** reports on the use of continuum generation via nonlinear optical phenomena in a photonic crystal fiber for TOFS in the range 500 to 1200 nm. The system is based on streak camera detection and was developed for pharmaceutical applications, as described in Paper **II** and Ref. [193]. Similar broadband TOFS has been performed by Bassi *et al.* who demonstrated fast and simultaneous acquisition of 16 wavelengths using a multianode PMT [184, 194]. Latest developments include the use of compact fibre lasers in combination with supercontinuum generation [195].

Besides using TOFS for absorption spectroscopy (*i.e.* determining of chromophore concentrations), scattering spectroscopy can be used to obtain information of structural properties of turbid samples. Using Mie theory [3], Mourant *et al.* showed that the wavelength-dependence of the reduced scattering coefficient (μ_s') can be described by the expression

$$\mu_s' = a\lambda^{-n} \tag{3.12}$$

where a is related to scatterer concentration, and $n = n(r)$ will be related to the radiuses r of the equivalent Mie scatterers. The dependence on scatterer radius is non-trivial, and has been discussed by Nilsson *et al.* and Mourant *et al.* [17, 55]. Taroni *et al.* provides examples of *in vivo* scattering (and absorption) spectroscopy [196]. Paper **XIII** provides the first scattering spectroscopy of the human prostate.

In contrast to the above mentioned applications of wavelength-resolved absorption and scattering spectroscopy, single wavelength TOFS is capable of providing the auxiliary information necessarily needed for TDLAS-based optical porosimetry (see Chapter 5 and Paper **XII**).

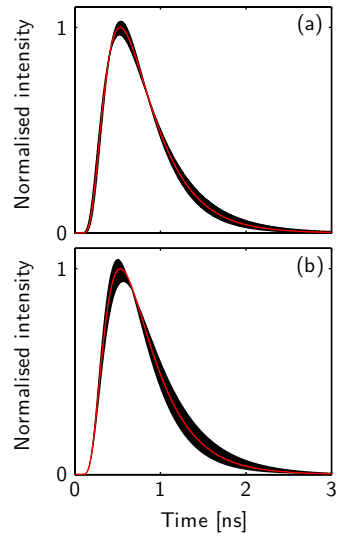

Figure 3.10. *The shape variation, with respect to the reference* $(\mu_a, \mu_s') = (0.1, 10)\ cm^{-1}$*, covered when (a) changing* μ_a *from 0.08-0.12 and keeping* $\mu_s' = 10$ *and minimising shape difference using k only, and (b) walking along the DOSC path shown in Fig. 3.8. The red curve corresponds to the reference optical properties.*

3.4 Phantoms and reference materials

Reference materials are crucial in order to assess performance of methods and instrumentations used for characterisation of tur-

bid materials. The ideal reference material, or *phantom*, has well defined and stable scattering and absorption properties. Unfortunately, it turns out that this is hard to achieve . An excellent review on this topic, focussing on tissue simulating phantoms, was recently provided by Pogue and Patterson [197]. Here, I mention only a few alternatives.

Microspheres is an attractive choice of scatterer, since they can be manufactured in extremely well defined sizes from 30 nm to several micrometers (mono-dispersive), and are available in various size. Although expensive, microspheres are in theory close to the ideal scatterer. However, the possibility of aggregation must be considered [198]. Microspheres have been used for several decades in light scattering experiments. In 1965, Smart *et al.* used 1.3 µm polystyrene latex spheres in experimental studies of multiple light scattering. In 1979, Shimizu *et al.* used microspheres in experimental studies of backscattering of picosecond pulses [174]. Later, Sefkow *et al.* used microspheres in combination with Evans blue dye to control absorption and scattering properties [199]. Similarly, Vishwanath *et al.* used microsphere phantoms for assessing the performance of fluorescence lifetime spectroscopy in turbid media [200]. Although microspheres have been used in many studies involving light scattering, it is not the most common choice of scatterer.

Intralipid, easily available and cheap, is a very popular scatterer used for liquid phantoms. Scattering is there caused by lipid droplets/particles. The optical properties of intralipid has been investigated by for example Driver *et al.* [201], van Staveren *et al.* [202], as well as by Flock *et al.* [203]. According to van Staveren, the following expression estimates the reduced scattering coefficient of phantoms based on a 20% intralipid stock solution:

$$\mu_s'(\lambda) = C \times [0.58(\lambda/\mu\text{m}) - 0.1] \times 0.32(\lambda/\mu\text{m})^{-2.4} \times \frac{\text{cm}^{-1}}{\text{ml/l}} \quad (3.13)$$

Here, C [ml/l] is the concentration of 20%-intralipid in the phantom. For example, a phantom made from 20 ml 20%-intralipid and 480 ml water will exhibit a reduced scattering of about 10 cm^{-1} at 660 nm and about 8 cm^{-1} at 786 nm. While this analysis is appropriate for low concentrations of scatterer, Zaccanti *et al.* reports on the non-linearities encountered in the case of high concentrations of intralipid [204]. Although the typical intralipid phantom is liquid, Cubeddu *et al.* showed how intralipid and ink can be used in solid agar-based phantoms [205]. Note also that a recent article by Michels *et al.* contains an extensive investigation of the optical properties of fat emulsions [206].

In order to control absorption properties, intralipid is often combined with various inks [201, 207, 208]. The optical properties of India ink have been investigated in detail by Madsen *et al.* [209].

They pointed out that the scattering of the ink may not always be negligible (due to a small fraction of larger micrometer-sized particles). Evans blue dye has also been used with intralipid [202]. In Paper **X**, intralipid and ink are used in added scatterer and added absorber series to assess TOFS performance (including comparing the performance of diffusion and Monte Carlo evaluation). Such experiments are excellent for investigation of system performance (especially linearity). Some experimental data from these series are shown in figure Fig. 3.11. The utilised Pelikan Fount India ink, when diluted as 1:10000, was found to exhibit an absorption coefficient of about $0.6\,\mathrm{cm}^{-1}$ at 660 nm and $0.5\,\mathrm{cm}^{-1}$ at 786 nm. Spinelli *et al.* recently discussed calibration of intralipid and ink phantoms, obtaining less than 2% difference in estimated absorption and reduced scattering coefficients between steady-state and TOFS modalities [210].

Another very popular type of phantoms are the epoxy-resin solid phantoms introduced by Firbank *et al.* [211]. Since the base material is clear (non-scattering) and exhibit low absorption in the visible and near-infrared, the optical properties can be controlled by adding appropriate scatterers and absorbers. Firbank *et al.* suggest the use of microspheres in order to create well defined reference phantoms [212]. A common choice is, however, to use titanium dioxide (TiO_2, a common "whitener" used in white paint) as the scatter, while toner ink is added for absorption [211, 213]. Such phantoms form the basis of the international collaboration for performance testing of photon migration instruments (Paper **IV**). This study is also discussed in Section 3.5. In Paper **XIV**, these phantoms are carefully characterised using TOFS in combination with Monte Carlo evaluation. This paper reveals that Monte Carlo modelling of TOFS is needed for proper characterisation of these phantoms. This includes a significant performance improvement by explaining and avoiding artifacts reported for conventional diffusion-modelled TOFS (see for example Paper **IV** and [182]). In contrast, Papers **XI** and **XII** employs TiO_2-based solid phantoms to mimic the properties of pharmaceutical tablets – a case where diffusion modelling is applicable (μ_s' of the order of $500\,\mathrm{cm}^{-1}$, thus dramatically higher than in tissue simulating phantoms).

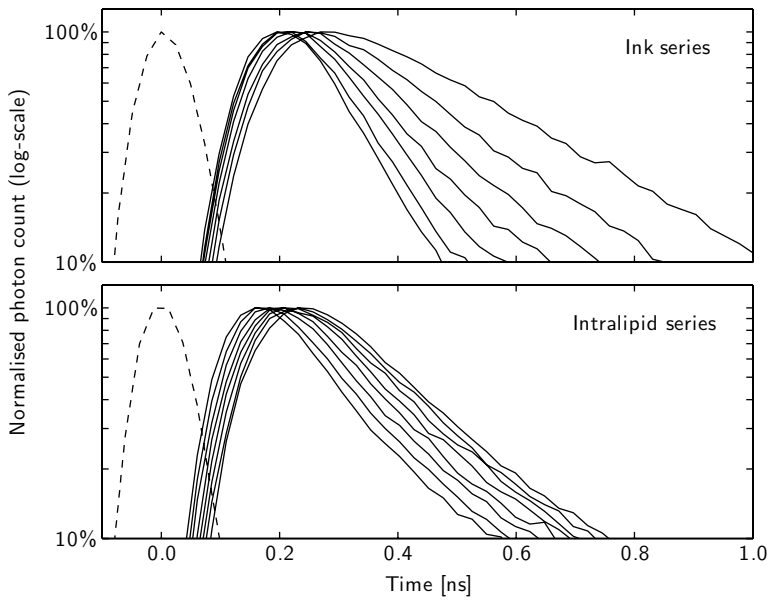

Figure 3.11. *Experimental TOF distributions from (a) added absorber series using ink, and (b) added scatterer series using intralipid. The dashed line shows the system IRF (response without scattering sample). These phantoms were designed to have optical properties in the same range as in vivo prostate tissue (see Paper **VI** and Paper **XIII**). The data corresponds to interstitial measurements at 660 nm, using a 15 mm fiber separation. The optical properties are in (a) μ_s'=9 cm^{-1} and 0.2<μ_a<0.7 cm^{-1}, and in (b) 4<μ_s'<10 cm^{-1} and μ_a=0.4 cm^{-1} (determined by Monte Carlo data evaluation). This figure also illustrates how TOFS can be used to separately determine absorption and scattering. Absorption has a large impact of the photons decay rate, simply from a Beer-Lambert-Bouguer absorption contribution. An increase in absorption $\delta\mu_a$ will be reflected in the TOF histogram by a multiplication of $\exp(-\delta\mu_a ct)$. The major impact of changes in scattering, on the other hand, is on the peak rise and position (as well as on peak width). Compare with Fig. 2.15.*

3.5 Performance

The performance of TOFS depends heavily on the application and is therefore difficult to state in a simple manner. Factors of major importance are

1. Source-detector separation
2. Measurement geometry and physical boundaries
3. Range of optical properties studied
4. Photon counting dynamic range
5. Correctness of IRF recordings
6. Modelling
7. Temporal drifts
8. Practical aspects such as light leakage, uncertainty in source/detector position, heterogeneity, and bleedings
9. Number of wavelengths (spectroscopic performance)

As discussed in Section 3.4, performance assessment is aggravated by the lack of perfectly reliable reference materials.

Source detector separation will determine the characteristics of the obtained TOF histogram. The influence of uncertainties in source-detector separations should therefore be carefully investigated (see for example Paper **III**). In addition, the separation determines fundamentally limiting features such as temporal pulse spread, signal-to-noise, and model appropriateness. Measurement geometry, often un-controllable in practice, and boundaries aggravate modelling. The range of optical properties are of fundamental importance, since it determines how changes in absorption or scattering is reflected in obtained TOF histograms. For example, the possibility of accurate measurements of small absorption coefficients under extreme scattering (*e.g.* pharmaceutical spectroscopy) needs further attention.

In general, a large dynamic range simplifies the separation of absorption and scattering. However, this requires that the IRF is properly measured over a similar dynamic range. IRF recordings must be investigated carefully. Different methods should be tested, and outcome of modelling should be compared. It is recommended that the features observed in the IRF are identified. Changes that are hard to visualise may still yield variations in results. We have experienced significant changes in evaluation outcome between IRF recordings with and without the scattering material in between the light-delivery and detection fibers. In a separate experiment, we found that the fine structure of the IRF (the secondary peaks) depends slightly on the angle in which light is coupled into the detection fiber. Partly due to this IRF uncer-

tainty, the compact four wavelength system used in this thesis have a limited dynamic range. A larger dynamic range can be achieved, see for example the recent work of Pifferi *et al.* [180].

Papers **X**, **XIII** and **XIV** clearly shows the importance of proper modelling. The validity of the selected model should always be verified. Evaluation robustness with respect to fit range should also be checked. These issues were further discussed in Section 3.3.

Since evaluation typically relies on knowledge of the absolute relation between IRF (laser pulse injection) and sample response, temporal drifts may be devastating in TOFS. Light leakage may distort datasets, and may be of particular concern during reflectance measurements on solid phantoms (interstitial or transmittance measurements, if possible, may be preferable). Tissue heterogeneity may aggravate the interpretation of obtained TOF histograms and derived optical properties [163].

The international collaboration presented in Paper **IV** outlines procedures for performance assessment. A common protocol enabling inter-system comparison was described, and included the use of a set of solid tissue phantoms (the MEDPHOT phantoms). The study showed fairly large discrepancies in derived optical properties between the involved photon migration instrumentations – even though measurements were performed under laboratory conditions. At the time of this study, the performance of our TCSPC instrumentation unfortunately reduced by the beginners mistake of inducing temporal drifts by turning lasers on and off (imposing drifts). Since our TCSPC system does not measure IRF continuously, this presumably had a major impact on the results (see Figure 4 in Paper **IV**). The performance of the Lund instrumentation has since then been dramatically improved. This includes significant improvements in IRF recording procedures, and avoiding model-related errors by the development of sophisticated White Monte Carlo (WMC) data evaluation (see Section 3.3). The performance of our TCSPC instrument is investigated in detail in Paper **X**, where our WMC approach is introduced. There, experiments was conducted in an interstitial settings using intralipid-based liquid phantoms. An advantage of performance assessment in interstitial liquid phantoms is that problems related to boundaries and light leakage are minimised, while modelling is kept simple. In Paper **XIV** performance was investigated in diffuse reflectance configuration using TiO_2-based solid phantoms, revealing good reproducibility. Since the WMC approach avoid diffusion artifacts, Paper **XIV** constitutes the most proper characterisation of the MEDPHOT phantoms so far.

In summary, time-of-flight spectroscopy is a powerful tool for characterisation of turbid materials. TOFS systems may be very different in complexity, depending on their area of applications. The four wavelength system used in this thesis (Papers **III**, **X**,

XIII, **XII** and **XIV**) is designed for applications in clinical environments. In contrast, consider the work of for example Pifferi *et al.* who recently published a detailed description of an advanced TOFS system based on tunable titanium-sapphire and dye lasers [182]. It should, however, be remember that frequency domain photon migration is an alternative. If similar performance can be accomplished in the Frequency domain, this will significantly simplify instrumental needs. Careful comparisons between the two approaches would thus be valuable.

3.6 Biomedical applications

The medical and biomedical use of light include numerous therapeutic and diagnostic applications. Photon time-of-flight spectroscopy (TOFS) can assist therapeutic modalities, such photodynamic therapy (PDT), by supplying them with information on the optical properties that govern tissue response. In diagnostics, the reliable absorption and scattering spectroscopy provided by TOFS can be of great value. Brain monitoring, optical mammography, diffuse optical tomography and prostate spectroscopy, being important biomedical applications of TOFS, are discussed separately in the following sections. Hemodynamics (blood monitoring) is an important part of most of these applications [47]. Although TOFS can be used for quantitative hemoglobin spectroscopy, the influence of tissue heterogeneity (*e.g.* presence of blood vessels) complicates interpretation of quantitative values [163]. Other interesting applications involve studies of muscle metabolism [43, 214], fundamental recording of the absorption of collagen [70], studies of light propagation in anisotropic biological materials [215, 216], as well as fluorescence spectroscopy of tissue [217, 218].

3.6.1 Imaging and diffuse optical tomography

Already at an early stage of the development of time-domain photon migration, time-gating and shadowgram imaging was used for detection of heterogeneities in highly scattering materials *in vivo* [219–221]. Imaging capabilities were soon enhanced by the use of full TOF histogram and photon diffusion modelling [222]. The advances in understanding and modelling of light propagation now renders tomographic reconstruction possible. Time-of-flight based instrumentations (or its frequency domain equivalents) are frequently utilised due to their capability for absorption and scattering spectroscopy [179, 223–226]. The advantages of optical tomography include the use of non-ionising radiation, contrast between soft tissues due to variations in scattering and absorption, and the access to functional parameters such as hemoglobin content and oxygenation. A major drawback is the poor spatial resolution.

Several review articles on this topic are available. Hebden *et al.* reviewed experimental techniques [227]. Dunsby and French provides an introduction to techniques for imaging in turbid media [228]. Boas *et al.* have published an introduction to DOT, including a review of related parts of the developments in biomedical optics [229]. Similarly, Gibson *et al.* reviewed the field in 2005, including overviews of the various application areas. In particular, their review include an introduction to the emerging and highly interesting technique of molecular imaging [230] in animal models (*e.g.* fluorescence imaging [231, 232]). The technique has a great potential within the field of drug development. The other major areas of optical tomography, that of brain and breast tissue, are discussed in separate sections below.

3.6.2 Breast diagnostics and optical mammography

Each year, hundreds of thousands women are diagnosed with breast cancer [233]. This unfortunate fact is reflected in the massive effort in development of diagnostic modalities for breast cancer detection, such as X-ray mammography, ultrasound imaging, magnetic resonance imaging (MRI), and positron emission tomography (PET). Already in 1929, Cutler proposed the use of optical transillumination of the female breast for diagnostic purposes [234]. However, a large Swedish clinical study, published 1990, showed that optical diagnostics was inferior to conventional mammography [235]. In contrast to general expectations, their optical method proved less efficient even for dense, young breast where conventional mammography often fails. Although other studies reported on quite different prospects for optical methods, the development of optical mammography halted (see for example the discussion of Cerussi *et al.* [236]).

Later, the improved understanding of light propagation in tissue, and the development of sophisticated techniques such as time-of-flight and frequency domain spectroscopy, revived the interest in optical diagnostics of breast tissue. The *in vivo* optical and physiological properties of breast tissue have since then been extensively studied [70, 192, 237–241] and [Paper **III**], although the contrast between healthy tissue and various lesions is still somewhat unclear [95]. In general, however, optical detection of tumours is typically related to locally increased blood content. In 2005, Physics in Medicine & Biology published a special section on time-domain optical mammography [242]. This special section reports on the findings of the OPTIMAMM project, an international collaboration aimed at assessing the diagnostic potential of time-domain optical mammography (including several clinical trials). Despite contrast and functional information, the poor spatial resolution and difficulties in detecting smaller lesions, optical mammography

is generally considered capable only of complementing, rather than replacing, conventional mammography for routine screening.

Besides these attempts of stand-alone optical mammography, several other uses of optical diagnostics of breast tissue are under investigation. Very promising, by means of careful frequency domain photon migration spectroscopy, Kukreti *et al.* have found intrinsic biomarkers of breast cancer [243]. In contrast, combining the excellent spatial resolution of MRI with the functional information available from DOT shows great potential in breast diagnostics [244, 245]. Furthermore, optical methods may become valuable in breast cancer risk assessment [246]. Finally, optical techniques have the potential of predicting the outcome of cancer treatments. For example, Cerussi *et al.* recently reported that optical spectroscopy can predict the outcome of chemotherapy of breast cancer [247].

3.6.3 Brain monitoring

Near-infrared spectroscopy (NIRS) was introduced for monitoring of hemoglobin in brain by Jöbsis in 1977 [248]. Since then, motivated by the problem of brain injuries, NIRS is commonly used to monitor cerebral oxygenation and metabolism in newborn infants [61, 249–251].

The use of TOFS for brain monitoring goes back to the late 1980s, when Chance *et al.* non-invasively estimated brain tissue oxygenation [44], and Delpy investigated optical pathlengths in rat brain tissue [252]. TOFS-based optical tomography (imaging) is now becoming a powerful tool in studies of hemodynamics and metabolism in the infant brain [95, 251, 253, 254], as well as for brain-activation hemodynamics in the adult head [255, 256]. Note that also the frequency domain equivalent is commonly used for brain monitoring [257].

3.6.4 Prostate spectroscopy

Photodynamic therapy (PDT) has in recent years been considered as a modality for treatment of prostate cancer [89, 90]. Clinical studies are ongoing at several locations worldwide. The reason for this development is that although conventional therapies such as radical prostatectomy, external radiotherapy and brachytherapy can exhibit high cure rates, side-effects are common [258].

The success of PDT relies on (i) proper light dosimetry, (ii) sufficient photosensitiser concentrations, and (iii) sufficient tissue oxygenation. Spectroscopic methods are valuable in the investigation of all these aspect [91]. Knowledge on tissue optical properties are needed to ensure proper dosimetry, sensitiser concentrations can be estimated using spectroscopic techniques, and tissue oxygenation can be measured optically.

A brief review of techniques for *in vivo* measurements of optical and physiological properties of prostate tissue are provided in the Introduction of Paper **VI**. With the exception of the work presented in the present thesis, prostate spectroscopy has relied on spatially resolved stead-state techniques. The steady-state approach relies on relative (μ_{eff} spectroscopy) or absolute measurements (μ_{a} and μ_{s}' spectroscopy). Absolute measurement are extremely difficult to realise *in vivo*. In fact, even relative intensity measurements at different source-detector separation appears difficult in the prostate due to the bleedings induced by needle insertion. In contrast to the steady-state approach, TOFS is insensitive to bleedings and is known to provide reliable absorption and scattering spectroscopy. Paper **VI** introduced TOFS for prostate spectroscopy, and its reliability is verified in clinical measurements on 9 patients. Due to the extreme sensitivity of TCSPC, TOFS exhibited sufficient signal-to-noise for proper spectroscopic evaluation in all measurements. In Paper **XIII**, diffusion modelling is replaced by sophisticated Monte Carlo evaluation, significantly improving measurement accuracy. Fig. 3.12 shows the TOFS instrumentation under operation at the clinic. Besides its use in the PDT context, TOFS-based prostate spectroscopy may have other values. The outcome of radiotherapy is dependent on for example blood perfusion, a parameter which TOFS can assess. Similarly, diffuse optical spectroscopy has for example recently been considered as a tool for prediction of the response of breast cancer chemotherapy.

3.6.5 Practicalities for Clinical Work

Clinical applications require good communication between technicians and medical staff. One should always ensure that everyone involved is aware of what is needed to perform high quality measurements. In the case of time-resolved spectroscopy, crucial issues may be for example background light levels, accuracy in fiber positioning, system startup time, time needed for acclimatisation to operating room temperature etc. Most issues can be solved if everyone is informed of technical presuppositions at an early stage.

3.7 Pharmaceutical applications

Steady-state near-infrared spectroscopy (NIRS) is a very important tool in pharmaceutical analysis, and several review articles and books are devoted to this topic [104, 108, 259–261]. Areas of applications include qualitative and quantitative analysis of tablets, blisters and powders, as well as process monitoring and control. The main advantage of NIRS is that it constitutes a non-destructive and fast method that requires little or no sample preparation. In addition, the development of chemometrics

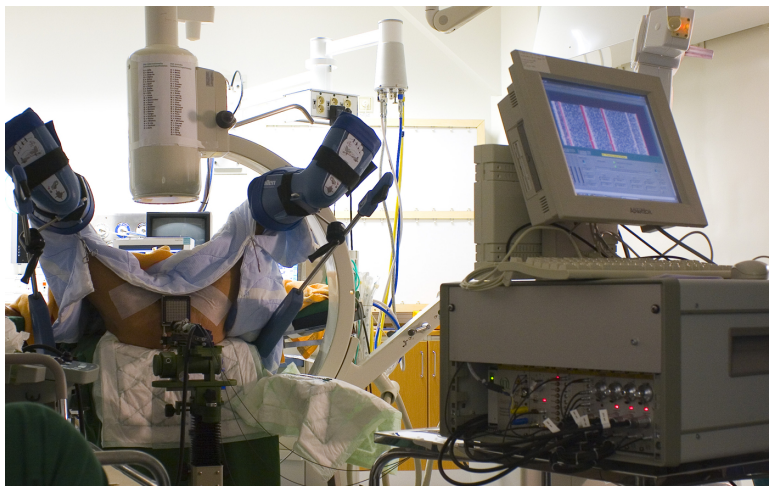

Figure 3.12. *TOFS instrumentation during in vivo prostate spectroscopy. Measurements are performed in connection with primary brachytherapy treatment of prostate cancer. The needles normally used for permanent insertion of radioactive seeds are here used to insert two optical fibers. The TOFS-instrumentation is shown to the right.*

(multivariate analysis) has increased NIRS capability of sensing minor variations in complex datasets. Nonetheless, NIRS is typically based on measurements of diffuse reflectance or transmittance [262–265]. The extremely high scattering exhibited by pharmaceutical samples makes detected light intensities (*e.g.* reflectance and transmittance) highly dependent on the physical (structural) properties. In other words, the physical properties and the chemical content together determine the measurement response. Chemical analysis using steady-state NIRS is therefore limited by small variations in physical properties [169, 266]. This aggravating fact is reflected by the multitude of data pre-treatment procedures aimed at improving spectroscopic performance, *e.g.* first or second order derivatives, standard normal variate, and multiplicative scatter correction.

In contrast to steady-state NIRS, TOFS is inherently capable of separating the effects of scattering and absorption. The technique is therefore considered as a promising tool in pharmaceutical analysis [169]. Burns *et al.* employed TOFS for determination of analyte concentrations and particle size in granular samples [267, 268]. Similarly, Sevick-Muraca *et al.* employed the frequency domain correspondent to TOFS for particle size analysis of pharmaceutical powders [269–271] and suspension of particles [272]. In quantitative analysis of pharmaceutical tablets, Abrahamsson *et al.* verified the strength of TOFS for handling samples with vary-

ing physical properties [193]. Paper **II** describes how TOFS can be used in scatter correction of conventional NIRS data. As discussed in Paper **XII**, TOFS is also of great value in the novel method of optical porosimetry of pharmaceutical tablets (see Chapter 5).

Chapter 4

Tunable diode laser absorption spectroscopy

The isolated existence of atoms and molecules in gas phase brings out the quantum nature of matter. Different species exhibit discrete and unique spectroscopic fingerprints, allowing highly selective sensing. The fundamental vibrational absorption bands in the mid-IR are frequently used for ultra-sensitive detection, while the weaker overtones in the near-IR are used in applications involving higher species concentrations, or when simpler instrumentation is required. Furthermore, the spectroscopic fingerprints are dependent on pressure and temperature, enabling spectroscopic assessment of these important quantities.

This chapter is an introduction to the vast field of *tunable diode laser absorption spectroscopy* (TDLAS). Providing selective, sensitive and reliable sensing of a large number of common species as well as trace gases, the technique has found numerous applications in both industry and science. Since one of the major topics of this thesis is GASMAS, the topic of Chapter 5, the focus in the present chapter is on the TDLAS instrumentation used for this purpose. In particular, this includes an introduction to near-IR sensing of molecular oxygen by means of wavelength modulation spectroscopy (WMS).

4.1 Introduction to TDLAS

High-resolution spectroscopy is of great value due to its capability of careful assessment of the spectrally sharp "fingerprints" exhibited by free gases. The availability of tunable and narrow-linewidth (monochromatic) light sources enables us to perform such experiments without the need of spectrally selective detection. A particulary simple realisation of this spectroscopic scheme is achieved by

the use of diode lasers. By simple adjustments of the diode laser operation current, the laser frequency can be tuned over an absorption line of interest. An absorption spectrum is obtained simply by sending the laser light through the sample of interest, and by measuring the variations in transmitted intensity. The technique is known as tunable diode laser absorption spectroscopy (TDLAS). For introductory reading on this topic, the compact and detailed introduction given by Avetisov is recommended [273].

The spectral fingerprints mentioned above refer mainly to vibrational absorption lines of free gases, and are found in the near- and mid-IR spectral region [274]. Other transition types are also used, for example in work involving oxygen, O_2 [275], and hydrogen, H_2 [276]. Since the fingerprint is of unique character for different gas species, it can be used for selective and quantitative analysis of gas concentrations. Furthermore, the exact appearance of the spectral fingerprint (*i.e.* the *lineshape*) exhibited by a particular gas molecule is highly dependent on parameters such as temperature, pressure and gas mixture. This is reflected by the fact that TDLAS-based lineshape measurements are frequently used in determination of temperature and pressure. Lineshapes are discussed in more detail in Section 4.2

Since the absorption lines of different gases appear at different spectral locations, the availability of tunable light sources at appropriate wavelengths is a major concern. A short up-to-date survey is for example given by Sigrist *et al.* [277]. The semiconductor industry has for several years supplied various lasers operating in the 0.6 to 2.5 µm spectral range. These lasers can be used to probe the fairly weak absorption overtones and combination bands in the near-IR. The fundamental absorption are found in the mid-IR, being about 100 times stronger. Trace gas sensing therefore benefits strongly from the use of tunable mid-IR light-sources for laser absorption spectroscopy (LAS) such as lead salt diode lasers [278, 279], interband cascade diode lasers (ICLs) [280, 281], quantum cascade lasers (QCLs) [282–284], and non-linear DFG- and OPO-systems [285–289]. In this region, however, the multitude of strong absorption lines makes spectral overlaps (sometimes referred to as spectral interference) a real problem. Due to broadening mechanisms (see Section 4.2.1), this is especially prominent at atmospheric pressures. Due to its abundance and its numerous and strong absorption bands, water vapour is often an inconvenient source of spectral interference. In contrast to these infrared light sources, the appearance of blue laser diodes should be noted. These can be used to reach the 200 to 400 nm UV region where many species have strong electronic transitions (often two orders of magnitude stronger than in the mid-IR) [290–293].

The applications of TDLAS are diverse, ranging from air pollution monitoring and atmospheric research [288, 294–297], industrial process control [298–300], combustion [292, 301–307], agri-

culture and forestry [308–311], volcanology [312], security [313], and medical diagnostics [314–317] to temperature measurements [318, 319], isotope analysis [312, 320], plasma science [321–326] and fundamental spectroscopic science [327]. Several review-articles have been published in the past years, for example by Hinkley surveying the field of long-path monitoring as early as 1976 [328], Allen focusing on gas-dynamics and combustion [329], Martin focusing on monitoring of chemical processes, the atmosphere and combustion [330], Röpcke *et al.* focusing on plasma diagnostics [331], Mantz focusing on high-sensitivity applications [332], Zybin *et al.* [333] and Galbacs [334] focusing on atomic absorption spectrometry [335], while Werle [336] as well as for example Song *et al.* [337] provide general overviews. In addition, conferences like TDLS[1] and FLAIR[2] are more or less devoted to tunable laser spectroscopy and its applications. Several companies provide commercial solutions for industrial applications. Thanks to instrumental simplicity and the relatively simple sampling procedures involved, TDLAS is an important complement to techniques like gas-chromatography mass spectrometry (GC-MS). An important disadvantage of TDLAS is the limitations in selectivity and sensitivity when it comes to sensing of larger molecules (*e.g.* broadband absorbers such as hydrocarbon vapours [338]). A small selection of interesting applications are given in Table 4.1.

In contrast to the applications mentioned above, our research group at Lund University (Division of Atomic Physics) has also investigated use of TDLAS for sensing of gases in porous materials. Chapter 5 is devoted to these applications, and a major part of this thesis is the novel application of TDLAS for characterisation of pharmaceutical solids (Papers **VII**, **XI** and **XII**).

[1] Internation Conference on Tunable Diode Laser Spectroscopy, http://tdls.conncoll.edu/

[2] International Conference on Field Laser Applications in Industry and Research, http://www.ino.it/flair/

[3] Robin Warren and Barry Marshall were awarded the Nobel Prize in Medicine for their work on this bacteria. This includes revealing that most stomach ulcers and gastritis were caused by bacterial infection, and not by stress or spicy food as assumed earlier.

[4] A general survey of breath analysis is given by Cao *et al.* [339]

Atmosphere and air pollution		
Monitoring of CO (4.7 µm) emissions from traffic	1975	[294]
Measurements of HCl, HNO_3, N_2O and CH_4 (3.4 to 8 µm) for understanding of the chemistry of ozone depletion	1994	[296]
Simultaneous monitoring of and O_2 (0.76 µm), H_2O (0.98 µm), and CH_4 (3.4 µm via DFG)	2000	[286]
Airborne sensing of formaldehyde (CH_2O, 3.5 µm)	2006	[288]
Industrial applications		
O_2 (0.76 µm) and CO (1.56 µm) monitoring for control of combustion efficiency in waste incinerators. HF monitoring (1.3 µm) in aluminium smelters. NH_3 (1.51 µm) monitoring for abatement diagnostics in coal-fired powerplants.	1998	[298]
On-line sensing of acetylene contaminants (C_2H_2, 1.53 µm) in ethylene gas (C_2H_4) flow in production of plastics.	2006	[299]
Monitoring of water vapour mass flux in pharmaceutical freeze-drying by means of Doppler-shift velocimetry	2007	[300]
Combustion		
Detection of potassium atoms (K, 0.77 µm) that causes turbine corrosion in high-temperature coal power plants	2002	[304]
Analysis of ammonia (NH_3, 10.3 µm), ethylene (C_2H_4, 10.4 µm), nitric oxide (N_2O, 5.3 µm), and carbon dioxide (CO_2, 4.5 µm) in cigarette smoke	2004	[306]
Near-infrared high-pressure and high-temperature measurements of water vapour (H_20, around 1.4 µm)	2007	[307]
Detection of nitric oxide (NO, electronic transition at 226.8 nm) in combustion using a blue GaN external cavity laser and sum-frequency mixing	2007	[292]
Agriculture and forestry		
$^{12}CO_2$ and $^{13}CO_2$ isotope analysis for studies of ecosystem-atmosphere exchange of CO_2 (4.3 µm)	2003	[309]
Measurements of nitrous oxide (N_2O, 4.5 µm) and methane (CH_4, 3.3 µm) from agricultural fields	2006	[310]
Volcanology		
Isotope ratio analysis of carbon in CO_2 (2.0 µm) for volcano surveillance	2004	[312]
Security		
Detection of uranium hexafluoride (UF_6, 7.7 µm)	2007	[313]
Medical diagnostics		
Detection of *Helicobacter Pylori*[3] infection using ^{13}C-urea breath test and CO_2 isotope ratio analysis (2.0 µm)	1999	[314]
Detection of nitric oxide (NO, 5.2 µm) in human breath[4], a marker of disease	2001	[315]
Plasma science		
Spectroscopic diagnostics using methane (CH_4, 8.1 µm), acetylene (C_2H_2, 7.5 µm), and ethane (C_2H_6, 3.3 µm), and modelling of plasmas used for chemical vapour deposition (CVD) of nanocrystalline diamond	2004	[326]
Temperature measurements using fluorocarbons (CF_2 at 9.1 µm), and CF_4 at 7.8 µm) in plasmas used for dry etching in semiconductor industry	1996	[322]

Table 4.1. *A small selection of TDLAS applications, indicating both early and recent work. The wavelength used for gas sensing is stated in parenthesis.*

4.2 Absorption spectroscopy

As all absorption spectroscopy, TDLAS measurements are governed by the Beer-Lambert-Bouguer law – a fundamental relation describing how the light intensity decrease upon interaction with absorbing materials. The law, expressed in a form appropriate in gas spectroscopy, is given in Eq. (4.1)

$$I = I_0\, e^{-\sigma(\nu)NL} \tag{4.1}$$

where ν is the frequency [Hz], I_0 and I [W] are the initial and transmitted intensities respectively, $\sigma(\nu)$ [cm^2/molecule] the frequency-dependent absorption cross section of the gas of interest, N [molecule/cm^3] the number concentration of molecules of that gas, and L [cm] the pathlength. The transmission, $T(\nu)$, is given by the ratio of incident and transmitted intensity

$$T(\nu) = \frac{I}{I_0} = e^{-\sigma(\nu)NL} \tag{4.2}$$

and the *absorption fraction* is $A = 1-T$. The *absorption coefficient* μ_a [cm^{-1}] is defined as

$$\mu_\mathrm{a}(\nu) = \sigma(\nu)N \tag{4.3}$$

The dimensionless *absorbance* α is in this thesis defined as

$$\alpha(\nu) = \sigma(\nu)\, N\, L = \mu_\mathrm{a}\, L = -\ln(T) \tag{4.4}$$

Note that in the field of analytical chemistry, absorbance is defined using the base-10 logarithm.

4.2.1 Spectral lineshapes

The spectroscopic notation involved in expressing the absorption cross-section, $\sigma(\nu)$, *i.e.* descriptions of individual absorption lines, easily becomes confusing. The ambitious reader can consult appendix A in the article describing the 1996 HITRAN database [340]. A more down-to-earth, still highly detailed, introduction can be found in a freely available community text on radiative transfer in the earth system [341].

The magnitude of the absorption cross section is related to the strength of the involved transitions (thus having a quantum mechanical interpretation). Here, we define a linestrength S [cm^2 Hz/molecule] as the integrated cross-section (Eq. (4.5))

$$S = \int_0^\infty \sigma(\nu)d\nu \tag{4.5}$$

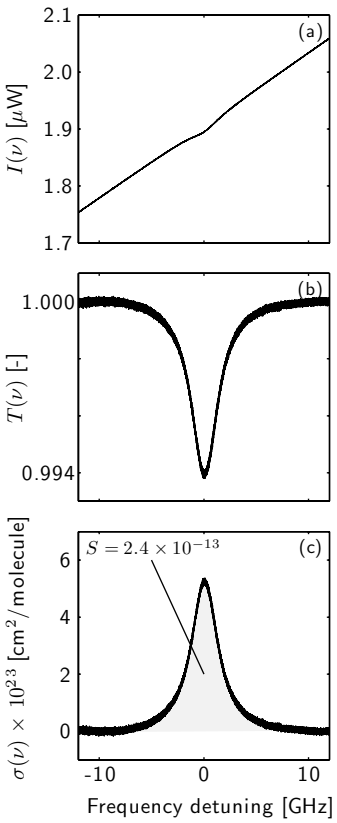

Figure 4.1. *Illustration and calculation of linestrength using experimental data from the R9Q10 line molecular oxygen at atmospheric conditions. See text for details.*

It should be noted that the linestrength is temperature dependent (obeying Boltzmann statistics). Since spectroscopy traditionally has utilised wavenumber, $\bar{\lambda} = 1/\lambda = \nu/c$ [cm^{-1}], linestrength is, however, often stated in the confusing unit [(cm^2/molecule)×cm^{-1}]. This unit can be understood by defining a linestrength in wavenumber, $\bar{S}$ (Eq. (4.6))

$$\bar{S} = \int_0^\infty \sigma(\bar{\lambda}) d\bar{\lambda} \tag{4.6}$$

The relation between S and $\bar{S}$ is simply a unit conversion, and they differ a factor of c as shown in Eq. (4.7).

$$S = \int_0^\infty \sigma(\nu) d\nu = \int_0^\infty \sigma(c\bar{\lambda}) \cdot c\, d\bar{\lambda} = c \int_0^\infty \sigma(\bar{\lambda}) d\bar{\lambda} = c \cdot \bar{S} \tag{4.7}$$

The concept of transmission, absorption cross section and linestrength is illustrated in Fig. 4.1 using experimental data. In the experiment, the divergent output of a VCSEL diode laser was sent $L = 0.225$ m through ambient air. The laser was repetitively scanned[5] over the R9Q10 line of molecular oxygen (760.654 nm vacuum wavelength) at ambient air conditions (25 ℃), and a photodiode detected transmitted light. An etalon was used to determine the frequency scale (in a separate experiment). The frequency scale was assumed linear. Fig. 4.1(a) shows the detected intensity $I(\nu)$ (calculated from the PD responsivity of 0.475 A/W and the amplifier gain of 1.0×10^6 V/A). The weak absorption is barely seen. Fig. 4.1(b) shows the transmission $T(\nu)$, calculated using a second-order baseline estimation of $I_0(\nu)$ (*i.e.* a 2nd order polynomial fitted to the edges of the detected signal). Straightforward calculation shows that the absorption feature has a peak absorption coefficient of approximately $\mu_a = 2.7 \times 10^{-5}$ mm^{-1}. The absorption cross section can be calculated from the transmission together with (i) the known pathlength L, (ii) the Loschmidt number[6] $N_0 = 2.4615 \times 10^{19}$ cm^{-3} stating the number concentration of an ideal gas at $T = 25$ K and standard atmospheric pressure 101.325 kPa , and (iii) the atmospheric oxygen abundance of 20.9 %. The procedure follows readily from Eq. (4.2), and is stated in Eq. (4.8).

$$\sigma(\nu) = -\frac{\ln(I/I_0)}{0.209 \times N_0 L} \tag{4.8}$$

The outcome when applying it to the experimental recording is shown in Fig. 4.1(c). Numerical integration yields a

[5] This approach has been used for many years, and is known as *sweep integration* [342].

[6] Note that the Loschmidt number N_0 is dependent on temperature and pressure as $N_0 = p/(k_B T)$, where $k_B = 1.380\,65 \times 10^{-23}$ J/K is the Boltzmann constant, T [K] temperature, and p [kPa] pressure.

linestrength of $S = 2.4 \times 10^{-13}\,\mathrm{cm^2Hz/molcule}$ translating into $\bar{S} = 8.1 \times 10^{-24}\,\mathrm{cm^2/(molecule\,cm^{-1})}$. Despite the simplicity of this experiment, this is very close to published R9Q10 linestrength of $\bar{S} = 8.35 \times 10^{-24}\,\mathrm{cm^2/(molecule\,cm^{-1})}$ [343][7].

In order to further characterise absorption lines, Eq. (4.9) introduces the normalised *lineshape function* $g(\nu - \nu_0)$ [$\mathrm{Hz^{-1}}$],

$$\sigma(\nu) = S \cdot g(\nu - \nu_0) \tag{4.9}$$

where ν_0 is the absorption line centre (transition frequency). The lineshape is dependent on gas parameters such as temperature and pressure, and this topic has been subject to extensive research for many years. A concise introduction is given by Avetisov [273]. Along with the natural linedwidth (as given by the Heisenberg uncertainty principle), the two most fundamental concepts for understanding the lineshape are *collisional broadening* and *Doppler broadening*.

Collisional broadening (or pressure broadening) is related to the fact that the interaction between a particle and radiation can be disturbed by particle collisions. The results is a broadening of spectral lines (as well as a slight shift in centre frequency), and the effect increases with increasing pressure. In terms of lineshape, pressure broadening is described by the Lorentzian profile

$$g_P(\nu) = \frac{1}{\pi} \frac{\Gamma_P}{(\nu - \nu_0 - \Delta\nu)^2 + \Gamma_P^2} \tag{4.10}$$

where Γ_P is the temperature and pressure dependent Lorentzian HWHM (the *pressure-induced linewidth*), and $\Delta\nu$ is the collision-induced line shift. Zender provides an instructive introduction to the theory of pressure broadening [341]. Since the halfwidth Γ_P is proportional to pressure, it is useful to introduce broadening coefficients, γ [GHz/atm], stating the amount of broadening per unit pressure. The temperature dependence is of the type T^{-n}, where n is gas dependent. It should be noted that the broadening depends on the molecular surrounding. This is reflected by the use of for example air- and self-broadening coefficients, γ_{air} and γ_{self}, respectively). In general, the pressure-induced halfwidth may be written as $\Gamma_P = \Sigma\gamma_i p_i$, where p_i is the partial pressure of the various gas components and γ_i the corresponding broadening-coefficient. For the important case of air-broadening, the width is mainly determined by the nitrogen and oxygen broadening, $\Gamma_P \simeq 0.78\gamma_{\mathrm{N_2}} + 0.21\gamma_{\mathrm{O_2}} + 0.01\gamma_{\mathrm{Ar}}$ (neglecting, for example, water vapour).

Doppler broadening is related to the Doppler effect, *i.e.* the movements of the absorbing molecules will make them experience incoming radiation as red- or blue-shifted. By assuming a

[7] Note that the unit of the linestrength appears to be misprinted in Table 2 of this reference.

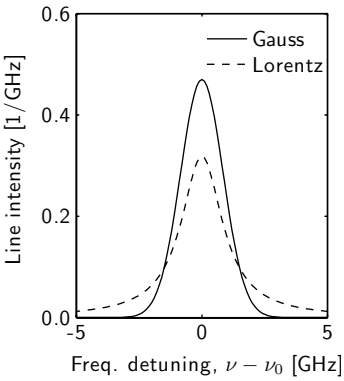

Figure 4.2. *Comparison of a 1 GHz HWHM Lorentzian profile and a 1 GHz HWHM Gaussian profile. Note the persistent wings of the Lorentzian.*

Maxwellian velocity distribution (random thermal motion) it can be shown that the Doppler broadening can be described by a Gaussian profile

$$g_D(\nu) = \frac{1}{\Gamma_D}\sqrt{\frac{\ln 2}{\pi}}\exp\left(-\ln 2\left(\frac{\nu-\nu_0}{\Gamma_D}\right)^2\right) \tag{4.11}$$

where Γ_D is the HWHM given by

$$\Gamma_D = \frac{\nu_0}{c}\sqrt{\frac{2\ln 2\, kT}{m}} \tag{4.12}$$

In gas flows, the net velocity produces a shift in centre frequency, allowing spectroscopic gas velocimetry.

Besides the difference in physical origin, it is customary to note that Doppler broadening is inhomogeneous, *i.e.* the different atoms absorb different wavelengths. In contrast, pressure broadening is homogeneous (all atoms are equally affected by collisions). The difference in shape between a Gaussian (Doppler) and Lorentzian (pressure broadened) profile is illustrated in Fig. 4.2, where $\Gamma_P = \Gamma_D = 1\,\text{GHz}$. At high pressures, lineshapes are best modelled by Lorentzian profiles. Conversely, Gaussian profiles are suitable for describing the low-pressure lineshape. In intermediate regions, the lineshape can be described by the convolution of these two profiles. The resulting profile is referred to as a Voigt profile [344, 345], and the corresponding lineshape is

$$g_V(\nu) = \frac{\ln 2}{\pi\sqrt{\pi}}\frac{\Gamma_P}{\Gamma_D^2}\int_{-\infty}^{\infty}\frac{e^{-t^2}}{\left(\frac{\nu-\nu_0}{\Gamma_D/\ln 2}-t\right)^2+\ln 2\cdot\frac{\Gamma_P^2}{\Gamma_D^2}}\,dt \tag{4.13}$$

There is no analytical expression on how the Voigt HWHM, Γ_V, is related to Γ_P and Γ_D, but the empirical relation in Eq. (4.14) provides a very accurate approximation (within 0.02 %) [346].

$$\Gamma_V \simeq 0.5346\Gamma_P + \sqrt{0.2166\Gamma_P^2 + \Gamma_D^2} \tag{4.14}$$

More advanced lineshape profiles take into account the so called *collisional narrowing* of spectral lineshapes [347, 348]. The effect is related to the fact that collisions restrict the molecular movements, and thus also the Doppler component of the broadening. The Galatry profile takes this into account by assuming a soft collision process [349], while the Rautian-Sobelman profile assumes hard collisions [350].

Let us return to the experimental data used in an estimation of linestrength in relation with Fig. 4.1. We can now use lineshape theory to further analyse the observed absorption imprint. Since no baseline-recording is available, we include an unknown linear baseline in our a model, as stated in Eq. (4.15).

$$I(\nu) = (a_0 + a_1\nu)\times\, e^{-S\,g(\nu-\nu_0)\,NL} \tag{4.15}$$

Modelling requires non-linear curve-fitting, solving for the baseline coefficients a_0 and a_1, as well as the lineshape parameters S, ν_0 and Γ. In Fig. 4.3(a) experimental data are modelled using the Gaussian profile. The bad fit shows that the experimental absorption lineshape is not properly explained by Doppler broadening alone. In contrast, as shown in Fig. 4.3(b), a pure Lorentzian with $\Gamma_P = 1.59\,\text{GHz}$ models the data very well. However, this does not mean that Doppler-broadening necessarily is negligible. In this case, the Doppler component is expected to be $\Gamma_D = 0.43\,\text{GHz}$ (from Eq. (4.12)), while the collisional component is $\Gamma_P = 1.49\,\text{GHz}$ (using the self-broadening coefficient[8] from Table 4, Ref. [343]). Using Eq. (4.14), the resulting Voigt HWHM should be $\Gamma_V = 1.61\,\text{GHz}$. This value is in good agreement with HITRAN simulations, as well as with the fitted Lorentzian profile ($\Gamma_P = 1.59\,\text{GHz}$). The conclusion is that although Doppler broadening is not negligible, the resulting Voigt lineshape is very similar to a Lorentzian profile. In fact, the difference in lineshape between the expected Voigt and the fitted Lorentzian is difficult to visualise. This is illustrated in Fig. 4.3(c), where a 1.59 GHz HWHM Lorentzian profile is compared to a Voigt profile with $\Gamma_D = 0.43\,\text{GHz}$ and $\Gamma_P = 1.49\,\text{GHz}$. This fact renders Voigt-fitting more demanding (more careful characterisation of baseline and frequency scale is required). An often used option is to keep Γ_D fixed to a theoretical value during fitting.

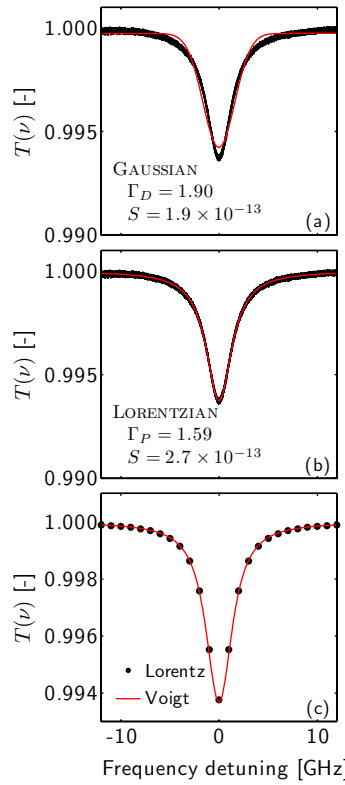

Figure 4.3. *Lineshape analysis (profile curve-fitting) using experimental data from the R9Q10 line molecular oxygen at atmospheric conditions. Part (a) shows the failure of Gaussian modelling, (b) shows that a Lorentzian profile explains the data, and (c) that a Voigt profile may be very similar to a Lorentzian (see text for details).*

[8] The difference between self- and air-broadening is small for oxygen [351].

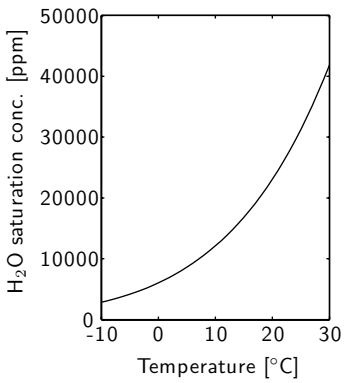

Figure 4.4. *Abundance of water vapour in air at the saturation pressure (100% relative humidity).*

4.3 Experimental techniques

As with most analytical methods, TDLAS can be implemented using a multitude of different technical approaches – all with varying complexity, cost and performance. Although compact and robust setups operating at room temperature are often desired, more demanding applications require the use of advanced light sources and complex detection schemes. In addition, a TDLAS sensor must also be judged with respect to alternative methods for gas analysis, such as non-dispersive infrared sensors (NDIR[9]), Fourier-transform infrared spectroscopy (FTIR), differential optical absorption spectroscopy (DOAS), laser-induced fluorescence (LIF), chemiluminescence, as well as gas chromatography (GC) and mass spectrometry (MS) [352].

4.3.1 Selection of absorption lines

A fundamental question in applied TDLAS is the selection of absorption line. Often, high sensitivity requires the use of strong lines, but during measurements of high concentrations (or over long pathlengths) weaker lines can be the proper choice. In particular, the choice between the weaker lines in near-IR and the fundamental lines in mid-IR have important implications for system complexity (laser diode and detector). For multi-component gas-analysis (the use of multiple absorption lines), a broad tuning range is preferable and can be achieved by the use of external cavity diode lasers. An introduction to the issue of line selection, as well as an overview of detection limits for various molecules at different wavelengths, are given by, for example, Werle [336] and Avetisov [273]. Furthermore, a selected absorption line should be isolated from other absorption lines, especially from those of interfering gas species. A common concern is to avoid interference from water vapour, since this species is fairly abundant in air and exhibits strong absorption lines in many parts of the infrared region. The 3.4 to 5 µm and 8 to 13 µm regions are free from H_2O interference, and are often referred to as the atmospheric windows. The saturation pressure of water vapour can be calculated using empirical relations, such as the Arden Buck equation [353], stated in Eq. (4.16) and illustrated in Fig. 4.4.

$$p = 6.0326 \times 10^{-3} \exp\left(\frac{17.502\,T}{240.97 + T}\right) \tag{4.16}$$

where p [atm] is the pressure, and T [°C] the temperature. The actual concentration of water vapour depends on local conditions

[9] NDIR-systems are typically based on broadband light-sources and optical filtering. The technique is, for example, utilised in commercial solutions for anaesthesia monitoring

(relative humidity). The thousands of ppm water vapour can be compared to the atmospheric levels of important gases such as carbon dioxide (CO_2, 370 ppm) methane (CH_4, 2 ppm) and nitrous oxide (N_2O, 0.3 ppm). The reason why the even more abundant gases oxygen (O_2, 21 %) and nitrogen (N_2, 78 %) are not cumbersome in terms of interference is due to that their lack of electric dipole moment renders them virtually transparent to visible and infrared radiation (electromagnetic radiation does not couple well to their vibrational motions).

4.3.2 Signal enhancement

Many applications of LAS involve measurements of very weak absorptions. Many important trace gases occur at ppb or ppt concentrations, often yielding absorption coefficients on the order of $\mu_a = 1 \times 10^{-8}\,\mathrm{cm}^{-1}$. Thus, short optical pathlengths result in unrealistically small absorption fractions. Since the absorption fraction is, in the case of weak absorptions, proportional to the pathlength

$$A = 1 - T = 1 - \exp(-\mu_a L) \simeq \mu_a L \tag{4.17}$$

the use of long pathlengths is a widely used and very important method for signal enhancement. In some cases, it is possible to achieve long pathlengths simply by separating the light source and the detector, or by using distant retro-reflectors. A common solution is, however, to use White [354, 355] or Herriot [356, 357] type multipass cells, in which the optical path often is 100 m or more. The advantages of this approach includes (i) fast re-sampling and time-resolved monitoring due to small cell volume, (ii) the possibility to perform baseline recordings, and (iii) allowing construction of compact systems. Integrating spheres has recently been considered as an alternative multipass cell for gas absorption applications [358, 359]. It should, however, be noted that in other applications, such as in the GASMAS applications explored in this thesis (Papers **VII**, **VIII**, **XI** and **XII**), the pathlength is uncontrollable and determined by the measurement object (see Chapter 5).

While the use of multi-pass gas cells significantly increase sensitivity, another important aspect is selectivity. By reducing the amount of collisional broadening, measurements at reduced pressures greatly reduce the problem of overlaps between neighbouring absorption lines. The approach and its advantages has been utilised for many years [295, 360, 361], and is considered an important tool in TDLAS. It is used to avoid problems with interfering species or absorption lines, to avoid the need of long laser tuning ranges, as well as for isotope ratio analysis. It should be noted that although a pressure reduction implies decreased absorption fractions, the narrowing of the lineshape keeps the peak absorption fairly constant until the Γ_P approaches Γ_D. This is illustrated

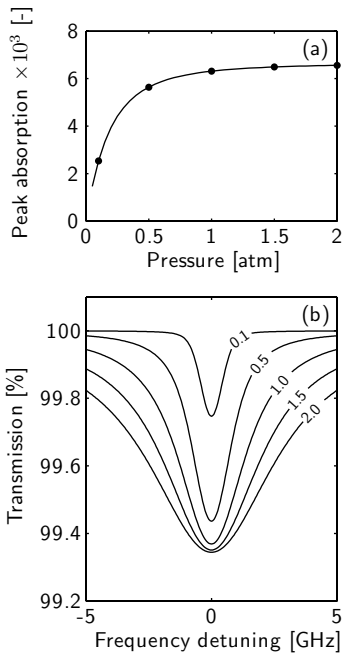

Figure 4.5. *Theoretical simulation of peak absorption versus pressure for the R9Q10 line of molecular oxygen, and a 22.5 cm pathlength. Peak absorption is shown in (a), and Voigt-imprints corresponding to pressures between 0.1 and 2 atm are shown in (b).*

in Fig. 4.5, using the R9Q10 oxygen line where $\Gamma_P = 1.5\,\text{GHz}$ and $\Gamma_D = 0.4\,\text{GHz}$ at atmospheric conditions.

4.3.3 Detection schemes and noise reduction

Quantum noise, often referred to as *shot noise*, constitutes a fundamental limit of optical noise. A 1 mW laser at 760 nm delivers, on average, $N = 3.8 \times 10^{15}$ photons each second. If randomly generated, the actual number of photons delivered during a certain time interval Δt follows a Poisson distribution, having a SNR $\sqrt{N\Delta t}$. This means that the best SNR possible, the *quantum limited* SNR, is proportional to square root of the detected power, $\sqrt{P}$. When using a 1 mW laser, it is thus not possible to detect intensity-losses smaller than $\sqrt{N}/N = 2 \times 10^{-8}$ (within 1 s). In practice, however, measurement performance is degraded by the limited quantum efficiency of detectors, thermal noise in detectors and transimpedance amplifiers, and $1/f$-type laser excess noise. Proper knowledge and account for these issues is crucial for the success of TDLAS. A soft introduction to the topic is given by Kaufmann [362], while a more advanced treatment is given by for example Hobbs [363]. Besides the noise sources mentioned above, a major, problem is the occurrence of optical interference, producing unwanted intensity modulations (*i.e.* baseline variations). In fact, it is this very challenging matter that often limits TDLAS performance. The issue is discussed separately in Section 4.3.4.

Various techniques have been developed to push TDLAS sensitivity towards the quantum limit. Important solutions include (i) double-beam systems with noise cancellation, (ii) modulation techniques and detection at high frequencies, (iii) photoacoustic spectroscopy, (iv) cavity-ringdown spectroscopy. These approaches are briefly described below. Note that the way in which sensitivity and detection limits are stated varies between publications. The smallest detectable absorption fraction is often a natural choice. It is also common to state the smallest detectable absorption coefficient (especially in setups utilising long optical pathlengths).

Measurements of direct absorption, utilised in relation with Fig. 4.1, is the most fundamental experimental approach in TDLAS. The most simple implementation is the single-beam system, in which a single detector is used to detect losses in transmission as the laser is tuned over an absorption line. Double-beam systems for cancellation of noise and systematic spurious signals have been around for a long time. Sophisticated electronic noise cancellation for shot-noise limited performance in simple setups has been presented by Hobbs *et al.* [364, 365]. The technique has been used, for example, in shot-noise limited atomic-absorption spectrometry of chlorine atoms (Cl, 0.84 µm) in low-pressure plasma [366], and for shot-noise limited detection of oxygen at 0.76 µm [367]. Allen

et al. provide several examples of the applicability of the approach [368].

The performance of direct absorption is often degraded by the occurrence of 1/f noise. A common way to avoid such low frequency noise of system components, for example 1/f laser excess noise [369, 370], is to shift the absorption signal to a higher frequency. In TDLAS, this can be achieved by a modulation of the diode laser operation current. Such modulation results in a modulation of the instantaneous laser frequency. Upon interaction with the non-linear transmission-profile of an absorption line, this will result in a periodic modulation of the detected intensity. This allows detection of absorption signal at the fundamental modulation frequency or its overtones. Modulation techniques are discussed in Section 4.4, where the special case of *wavelength modulation spectroscopy* (WMS) is discussed in detail. The extensive overview given by Werle is also recommended [336].

Photoacoustic spectroscopy (PAS) is an interesting alternative to the above mentioned techniques. While the latter are based on the detection of losses in transmitted intensity, PAS utilise the photo-acoustic effect, sensing acoustic waves generated by light absorption [371, 372]. The technique is extremely sensitive, and has been shown detection limit corresponding to absorption coefficients about $1 \times 10^{-9}\,\mathrm{cm}^{-1}$ [373, 374]. Typically, a light source is modulated at the resonance frequency of an acoustically resonant gas-cell (in which absorption occur). Energy is built up in the acoustic mode of the cell, and microphones are used for detection [375]. In contrast to optical detection of transmission variations, the utility signal is in PAS free from a background. Recently, Kosterev *et al.* introduced a simpler and acoustic-noise-immune alternative, in which the acoustic energy is transferred to and built up in high-Q quartz tuning forks that generate piezoelectric signals [374, 376]. The technique is referred to as quartz-enhanced photoacoustic spectroscopy (QEPAS), and has for example been used for QCL-based sensing of ppb-levels of N_2O [377]. Another recent development involves interferometric sensing of cantilever movements [378].

Cavity ring-down spectroscopy (CRDS) is yet another highly sensitive technique used in combination with TDLAS. The technique is based on the trapping of light in an external cavity with high-reflectivity mirrors. After intra-cavity power build-up (and rapid abortion of light injection), the decay in cavity output is mainly related to losses due to mirror reflections and absorption. Sample absorption is obtained by comparing the decay rate (*i.e.* a time constant τ) for an evacuated cavity with that of a filled cavity. Using an external-cavity diode laser and a $\tau = 230\,\mu\mathrm{s}$ cavity, corresponding to an average pathlength of 69 km, the technique has been demonstrated to have a potential of reaching a sensitivity in the $1 \times 10^{-10}\,\mathrm{cm}^{-1}$ range [379]. An extensive review of CRDS is

given by Berden *et al.* [380].

4.3.4 Fighting optical interference

During measurements of the spectrally sharp absorption features of gases, it is of course crucial to avoid artifacts of the same character. As briefly mentioned in the previous section, optical interference and its related artifacts are often the main challenge in TDLAS. The narrow linewidth (MHz) of a typical diode laser translates into coherence lengths of several metres, making TDLAS particularly sensitive to various interference effects. This means that while multi-pass cells can turn minute absorption coefficients into realistic absorption fractions, spectrally sharp fluctuations in intensity due to optical components often remains a limiting factor. These so called *optical interference fringes* creates a cumbersome, unknown background signal from which it may be difficult to separate out absorption imprints. The most simple example of a source of spectrally sharp intensity variations is the etalon and its interference fringes. In terms of laser frequency ν, transmission maximums occur with a separation $\Delta\nu_{\mathrm{FSR}} = c_0/2nL$, called the free spectral range (FSR). In TDLAS, besides creating unwanted background signals, the etalon effect is often used to determine frequency scales during diode laser tuning in TDLAS (later exemplified in Fig. 4.20). Similarly, an $L = 5\,\mathrm{cm}$ air gap between two glass surface may give rise to a 3 GHz FSR interference pattern, and may potentially become an inconvenient artifact. Note also that slow fringes caused by short etalons (surfaces with small separations, optical components) may cause problems. For example, a 1 mm air-gap corresponds to $\Delta\nu_{\mathrm{FSR}} = 150\,\mathrm{GHz}$, and may generate annoying non-linear baselines. These problems, as they appear in modulation spectroscopy, are later illustrated using experimental data in Fig. 4.15. Lenses and optical fibres are another known source of etalon fringes [363, 381]. Interference effects in fiber-optic gas sensors based on micro-optics cells have been described by Stewart *et al.* [382]. Other types of interference fringes include beam overlaps in multi-pass cells [295, 383] as well as optical feedback [384]. The TDLAS user must be prepared to encounter, and suppress, both slowly varying and rapidly modulated baselines (backgrounds) – often at the same time.

The issue of optical interference fringes is heavily discussed in the literature. In general, fringes are reduced if transmissive optics is avoided and anti-reflection coating is utilised [385]. In Paper **XI** and **XII** this is drawn to its extreme by avoiding all optical components, except for the diode laser and the photodiode. Double-beam systems allow elimination of fluctuations that are common to both arms [367, 386–389], and are particularly useful in fiber optic systems [381, 390] and Paper **VII** (see also Fig. 5.3). However, more active methods are often needed in order to reach theoretical sen-

sitivity limits. The methods used can roughly be categorised as specialised optical design [358, 381, 391–394], mechanical dithering [273, 395–400] and [Papers **XI** and **XII**], tailored laser modulation [361, 383, 401–403], signal processing [336, 404–406], baseline recording and subtraction [407, 408], or sample modulation [336, 366, 408–414].

If the fringes and other spurious signals occurring in a system are stable, simple baseline recordings should in principle allow background subtraction. Such background recordings are often performed in trace gas detection by filling the multi-pass cell with a gas sample without the investigated species (sometimes referred to as a zero-air recording) [407]. Unfortunately, fringes are often unstable or non-reproducible, and not all applications allow background recordings. In addition, system instabilities limit the possibility of improving performance by means of averaging [407]. The concept of background subtraction therefore needs to be complemented with other methods. A review of such methods is given below.

Reid *et al.* reported that fringes are efficiently rejected when setting the modulation amplitude in modulation spectroscopy to an integer of the fringe $\Delta\nu_{\mathrm{FSR}}$. To increase stability of the method, they added a low frequent modulation that tuned the laser one free spectral range, while still using the main modulation. A small amplitude of this slower so called *jitter modulation* ensures that the absorption imprint is not distorted. This low-pass method proves efficient for rejection of the uniform and closely spaced fringes occurring in for example White cells [361, 383, 402]. A similar approach was used by Carlisle *et al.* employing low-pass electronic filtering [404, 405]. In order to increase the applicability of such approaches, McManus and Kebabian showed how to adjust the Herriott cell mirrors to achieve fringes with small FSR [392]. Later, Sun and Whittaker presented a generalised variant of the approach, allowing fringe suppression regardless of the fringe-to-absorption linewidth (bandpass rather than low-pass filtering) [403]. Iguchu contributed further to the development of tailored modulations schemes by investigating the performance of non-sinusoidal modulation waveforms [401]. It should, however, be noted that the efficiency of the above mentioned approaches may be greatly reduced in the presence of non-uniform, multiple fringe structures. In general, efficiency is dependent on that the fringe period differs significantly from the absorption linewidth. Unfortunately, this is often not the case. An example is small baselength multipass cells, where fringe spacing often becomes similar to the absorption linewidths exhibited at reduced pressures (0.01 to 0.1 atm) [397]. Furthermore, electronic and digital filtering of TDLAS signals [336, 406] is an alternative to tailored modulation, and can be used to obtain similar fringe rejection. In practice, the use of tailored modulations is limited.

A more generally applicable approach is the use of mechanical dithering. By mechanically changing the effective optical path between elements that generate fringes, the fringe structure can be suppressed by means of averaging. Webster accomplished this by inserting an oscillating Brewster plate between fringe-generating surfaces [395]. Another dithering technique was introduced by Silver *et al.* who used piezoelectric transducers (PZT) for longitudinal modulation of mirrors (in Herriott cells in particular) [396–398]. Wang *et al.* used a common loudspeaker to vibrate a mirror for simple, but still highly efficient, fringe suppression [399]. Similarly, Avetisov *et al.* used a loudspeaker to dither the laser diode itself, efficiently destabilising and averaging out fringes due to etalons and optical feedback [273, 400]. In addition, laser dithering is used in some commercial TDLAS process sensors. Dealing with measurements of gases embedded in scattering solid sample, Papers **XI** and **XII** introduce sample rotation (sample dithering) and tracking coils (beam dithering) as efficient methods for interference suppression by interference-to-noise conversion and averaging. In addition, the Paper **VII** was heavily dependent on vibrations imposed to the setup by means of the vibrators commonly found in *e.g.* mobil phones. Since the interference effects encountered in GASMAS is significantly different from those in conventional TDLAS, they are treated separately in Section 5.3.

A quite different approach was used by Fried *et al.* who employed pressure modulation to induced variations in refractive index, and thus in the optical pathlength between fringe-generating components [397]. Utilising that the refractive index of air changes with pressure as $dn/dp = 2.65 \times 10^{-4}\,\mathrm{atm}^{-1}$ [415], they used a ± 0.01 atm pressure modulation to efficiently suppress fringes originating from their White cell. In their particular case, mirror dithering with a single PZT along the lines of Silver *et al.*, was less efficient (although they suggested the use of multiple PZTs). Interestingly, Werle *et al.* have shown that pressure-induced fluctuations in refractive index in multi-pass cells can limit sensitivity to one order of magnitude above the quantum limit [370].

Tranchart *et al.* has investigated the possibility of avoiding interference fringes by using integrating spheres rather than conventional multi-pass cells [358]. During measurements of water vapour at 0.83 µm and butane at 1.2 µm they showed that the equivalent absorption pathlength was 44 and 20 times the sphere diameter, respectively (for a 10 cm sphere). Baseline modulations due to interference corresponded to an absorption coefficient of less than $5 \times 10^{-7}\,\mathrm{cm}^{-1}$. Masiyano *et al.* have further investigated the use of diffuse surfaces in TDLAS, focussing on implications of laser speckle [394]. Hawe *et al.* have used integrating spheres as multi-pass cells for CO_2 sensing using non-laser light sources [359].

A fundamentally different approach is to modulate the absorption or spectral characteristics of the gas molecules themselves,

and in that way distinguish between absorption and background. This approach is often referred to as *sample modulation* and has been used by several scientists to improve TDLAS performance [336].

To improve sensitivity, Whittaker *et al.* combined dye-laser modulation spectroscopy with photochemical modulation [409, 411]. Jasinski *et al.* performed sensitive detection of silylene radicals (SiH_2) in glow discharges by modulating the discharge voltage [416]. Analogously, Zybin *et al.* used plasma modulation in combination with wavelength modulation spectroscopy, avoiding etalon effects and claiming to obtain detection limits of about 10^{-7} absorption fraction (in atomic-absorption spectrometry) [413]. Such schemes is often referred to as *double modulation*, and employ detection at the sum or difference frequency of the two modulation frequencies. Liger *et al.* later combined the scheme of double modulation with a double-beam configuration, and provide an extensive discussion on noise and detection limits [366].

The above mentioned schemes for sample modulation are based on modulation of the concentration/population of the species under investigation (and thus the absorption). In contrast, the Stark effect can be used to modulate the spectral characteristics of the absorbing species (if the species exhibit sufficient dipole moment and proper symmetry). The Stark effect has been used to tune absorption lines into resonance with the fixed laser lines of for example CO_2 lasers (such powerful lasers are often used in PAS). Stark modulation has been employed used in order to discriminate ammonia absorption (NH_3, at 10.4 µm) from spurious backgrounds and interfering absorption lines (water vapour exhibits a fairly weak Stark effect) [410, 412]. More recently, Werle and Lechner reported on the potential of background suppression in TDLAS by means of Stark modulation [414]. They used a double modulation scheme and a 35 cm single pass Stark-cell for sensing of formaldehyde at 5.7 µm. Dyroff *et al.* extended the formaldehyde experiments by the use of a modified Herriott multi-pass cell and reported on great improvements in system stability, allowing longer time averaging [408]. Besides employing the Stark modulation scheme, they also investigated the use of a scan-by-scan static Stark switching for background subtraction. The Zeeman effect can also be used for sample modulation purposes. Blake *et al.* employed magnetic modulation of a solenoid gas cell for detection of NO, based on magnetic rotation spectroscopy [417]. Using a diode laser operating around 0.76 µm, Brecha *et al.* have investigated the use of this technique for studies of molecular oxygen [418, 419].

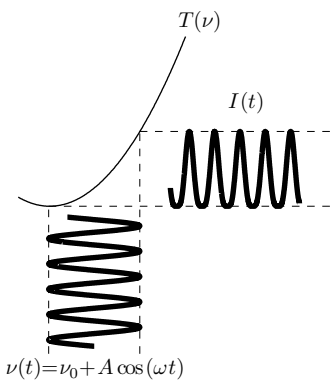

Figure 4.6. *The basic principle of WMS. A non-linear transmission give rise to a periodic but non-sinusoidal response, i.e. harmonic overtone generation occurs. The figure shows a simulation of transmitted intensity during sinusoidal frequency modulation.*

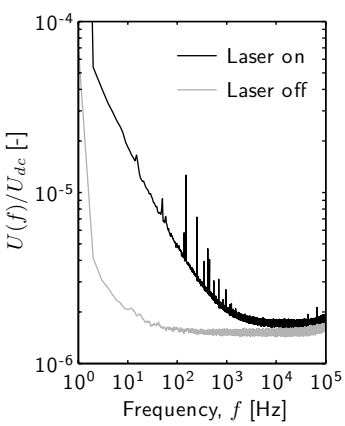

Figure 4.7. *Low frequency noise in the diode laser setup used in Papers* ***XI*** *and* ***XII****. The noise spectra is measured at a 1 Hz bandwidth, and is presented relative to the DC sensor signal (U_{dc}=2.36 V, detected power ∼5 μW, and gain 10^6).*

4.4 Wavelength modulation spectroscopy (WMS)

Techniques for laser modulation are extensively used to improve the performance of TDLAS systems. Simple sinusoidal modulation of the diode laser operation current results in a sinusoidal wavelength (and amplitude) modulation of the laser output. Interaction with a wavelength-dependent and non-linear transmission (*e.g.* absorption lineshape) results in a periodic, but non-sinusoidal, transmission signal that consists of the modulation frequency itself as well as its harmonic overtones. This is illustrated in Fig. 4.6. This can be used to shift the detection frequency to the high frequency region less affected by low frequency noise (*e.g.* 1/f noise), and thus improving system sensitivity. This is typically achieved by letting a lock-in amplifier measure the amplitude of the harmonic components (most commonly, the second) as the laser is tuned over an absorption line of interest. The low frequency noise (1/f type) present in the system used in Papers **XI** and **XII** is shown in Fig. 4.7. Note that utilisation of modulation frequencies around 10 kHz should yield a sensitivity of about 2×10^{-6}. A schematic of a typical WMS setup is given in Fig. 4.8.

Although in principle the same, modulation spectroscopy is divided into wavelength modulation spectroscopy (WMS) [386] and frequency modulation spectroscopy (FMS) [420]. WMS refers to the case where the modulation frequency f_m [Hz] is much smaller than the absorption linewidth Γ_{HWHM} (typically, f_m is the range 10 to 100 kHz). The magnitude of the absorption signal depends heavily on the modulation amplitude ν_a [Hz]. In WMS, optimal (maximised) signals are reached when the the modulation amplitude is slightly larger than the absorption linewidth (*e.g.* a few GHz for measurements at atmospheric pressures). The theory of WMS is based on the concept of instantaneous frequency and intensity, as discussed in Section 4.4.2. FMS, on the other hand, pushes the detection frequency to much higher frequencies, typically employing modulation frequencies of 0.1 to 1 GHz. FMS therefore has the potential of reaching better performance than WMS [387, 405, 421]. Due to the high frequencies involved, the theory of FMS is centered around the electric field and its phase [385]. A disadvantage of FMS with respect to WMS is the accompanying increase in system complexity. In addition, high-frequency WMS is in practice considered capable of reaching performance similar to that of FMS [385].

This section aims at providing an in-depth description of WMS. In particular, the intention is to make a close connection between theory, simulations and experimental work.

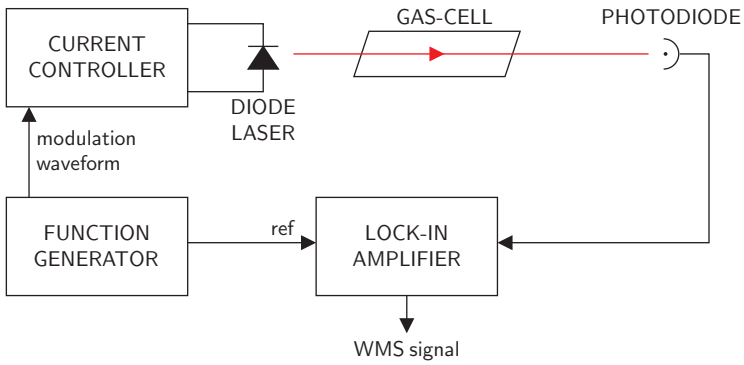

Figure 4.8. *Schematic of the fundamentals of WMS-TDLAS instrumentation.*

4.4.1 Digital wavelength modulation spectroscopy (dWMS)

As mentioned above, the traditional TDLAS system involves some kind of function generator for diode laser modulation. A lock-in amplifier is used for selective detection at harmonics of the modulation frequency. The issue of correct phase setting can be solved by the use of a dual-phase lock-in amplifier. In contrast, Fernholz *et al.* introduced the use of phase-sensitive detection by means of synchronised modulation and data acquisition [422]. Their approach was motivated by a need of fast scanning to circumvent problems with rapidly changing transmission. Avoiding the use of slow standard analog lock-in amplification, they could employ scanning at 1 kHz, while modulating at 300 kHz. They used external function generators which were synchronised with a computer plug-in board. A more compact version of this scheme for data acquisition is presented in Paper **IX**, involving synchronised plug-in boards for both laser modulation and data acquisition. This digital technique is here referred to as digital wavelength modulation spectroscopy (dWMS). The technique inherently supports simultaneous detection of different harmonic overtones. A detailed description of related signal processing and data analysis are given in Paper **XII**.

4.4.2 The Fourier theory of WMS

The theory of WMS is extensively discussed in the literature [385, 386, 423–426]. A review, rich on details, is given by Kluczynski *et al.* [426]. Here, only a brief introduction is given, largely following the notation of Axner *et al.* [426].

Let $T(\nu)$ denote a system-related transmission factor (not related to the monitored absorption), $I_L(\nu)$ the laser intensity, α_0 the peak absorbance and $\bar{\chi}(\nu)$ the peak-normalized lineshape. The signal delivered by a detector, $S(\nu)$, for the case of weak absorption can then be written as

$$\begin{aligned} S(\nu) &= \eta T(\nu) I_L(\nu)\, \exp(-\alpha_0 \bar{\chi}(\nu)) \\ &\simeq \eta T(\nu) I_L(\nu) - \eta \alpha_0 \bar{\chi}(\nu) T(\nu) I_L(\nu) \end{aligned} \tag{4.18}$$

where η is a proportionality constant specific to the detector unit. The two components can be classified as a background signal $S_{bg}(\nu)$, and an absorption signal $S_a(\nu)$, as defined in Eq. (4.19)

$$\begin{aligned} S_{bg}(\nu) &= \eta T(\nu) I_L(\nu) = \eta I_D(\nu) \\ S_a(\nu) &= -\eta \alpha_0 \bar{\chi}(\nu) T(\nu) I_L(\nu) = \eta \alpha_0 \bar{\chi}(\nu) I_D(\nu) \end{aligned} \tag{4.19}$$

where $I_D(\nu)$ is the detected intensity in absence of the absorber.

A sinusoidal modulation (at frequency f_m) of the diode laser operation current results in a sinusoidal modulation of the laser frequency $\nu = \nu(t)$

$$\nu(t) = \nu_c + \nu_a \cos(2\pi f_m t) \tag{4.20}$$

where ν_c is the centre laser frequency and ν_a the modulation amplitude. In diode lasers, this frequency modulation is accompanied with an intensity modulation (often called *residual amplitude modulation*, RAM). Neglecting nonlinearities, the laser output intensity can be written as

$$I_L(t) = I_{L,0}(\nu_c) + \kappa_1 \nu_a \cos(2\pi f_m t + \phi_1) \tag{4.21}$$

where $I_{L,0}$ is the average intensity, and $\kappa_1 = |dI/d\nu|$ the linear intensity-modulation coefficient, and ϕ_1 the phase shift between frequency and amplitude modulation. Since both the laser frequency and the laser intensity now is periodic, the detector signal $S(\nu) = S(\nu(t))$ from Eq. (4.18) will also be periodic. This means that the detector signal, as well as the likewise periodic factors $I_D(\nu)$, $I_L(\nu)$, $T(\nu)$ and $\bar{\chi}(\nu)$, can be expressed using a Fourier series. The Fourier series of a temporally periodic function $F(t)$, with period $1/f_m$, can be written as

$$F(t) = C_0^{even} + \sum_{n=1}^{\infty} C_n^{even} \cos(2\pi n f_m t) + C_n^{odd} \sin(2\pi n f_m t) \tag{4.22}$$

where

$$C_0^{even} = f_m \int_0^{1/f_m} F(t)\, dt$$

$$C_n^{even} = 2f_m \int_0^{1/f_m} F(t)\cos(2\pi n f_m t)\, dt \quad \text{for } (n > 0)$$

$$C_n^{odd} = 2f_m \int_0^{1/f_m} F(t)\sin(2\pi n f_m t)\, dt \tag{4.23}$$

are the so called *even* and *odd* Fourier coefficients. The lineshape term $\bar{\chi}(\nu(t))$ can be expressed using only the even terms (since it is in-phase with the frequency), and its even Fourier components are denoted $\bar{\chi}_n^{even} = \bar{\chi}_n^{even}(\nu_c, \nu_a)$ so that

$$\bar{\chi}(\nu_c, \nu_a, t) = \sum_{n=0}^{\infty} \bar{\chi}_n^{even}(\nu_c, \nu_a)\, \cos(2\pi n f_m t) \tag{4.24}$$

In contrast, due to the out-of-phase component of the laser intensity modulation, both odd and even Fourier components are needed to express the detected intensity.

$$I_D(\nu_c, \nu_a, t) = \sum_{n=0}^{\infty} I_{D,n}^{even}(\nu_c, \nu_a)\, \cos(2\pi n f_m t) \tag{4.25}$$

$$+ \sum_{n=0}^{\infty} I_{D,n}^{odd}(\nu_c, \nu_a)\, \sin(2\pi n f_m t) \tag{4.26}$$

$$\tag{4.27}$$

The non-zero components of the laser intensity output can be calculated from Eq. (4.23), and are stated in Eq. (4.28).

$$I_{L,0}^{even} = I_{L,0}(\nu_c) \tag{4.28}$$

$$I_{L,1}^{even} = \kappa_1 \nu_a \cos\phi_1 \tag{4.29}$$

$$I_{L,1}^{odd} = -\kappa_1 \nu_a \sin\phi_1 \tag{4.30}$$

As for the lineshape term, only even components are needed to describe the transmission factor $T(\nu)$.

$$T(\nu_c, \nu_a, t) = \sum_{n=0}^{\infty} T_n^{even}(\nu_c, \nu_a)\, \cos(2\pi n f_m t) \tag{4.31}$$

Insertion of these Fourier expansions into the expressions for the resulting detector signal, Eq. (4.18) or Eq. (4.19), is a powerful way of understanding how the various harmonics are generated.

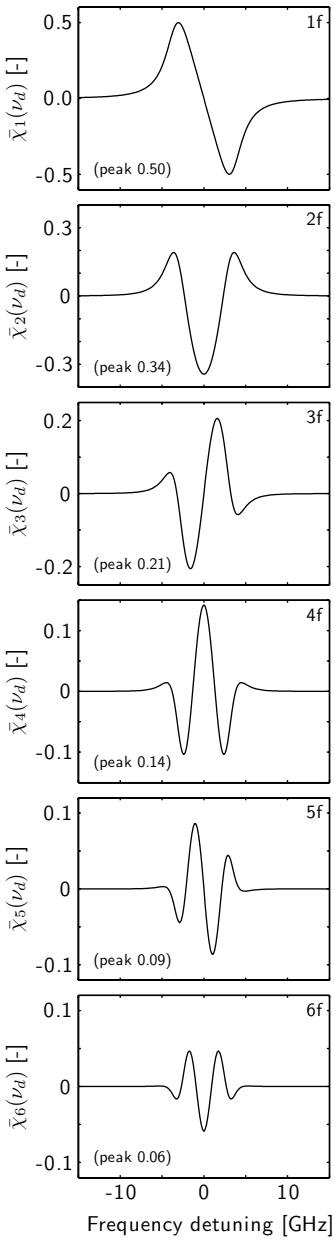

Figure 4.9. *The first 6 Fourier components of a Lorentzian lineshape with $\bar{\nu}_a$=2.2 (see text for details). The frequency scale is calculated for Γ=1.6 GHz. Although seldom experimentally recorded, Paper **XII** investigates the use of 1-6f harmonics.*

As carefully described by Kluczynski and Axner, the various harmonic components of the detector signal (background, absorption or total) will be described by infinite series involving cross terms of detected intensity components and lineshape components [425]. To illustrate the appearance of such sums, the analytic expression for even component of the absorption signal (see Eq. 16 in Ref. [425]) is stated in Eq. (4.32).

$$S_{a,n}^{even}(\nu_c,\nu_c) = -\eta\alpha_0\left[\frac{1+\delta_{n0}}{2}\sum_{m=0}^{n}\bar{\chi}_{n-m}^{even}I_{D,m}^{even} + \frac{2-\delta_{n0}}{4}\sum_{m=0}^{\infty}\bar{\chi}_{n+m}^{even}I_{D,m}^{even} + \frac{2-\delta_{n0}}{4}\sum_{m=0}^{\infty}\bar{\chi}_{m}^{even}I_{D,n+m}^{even}\right] \tag{4.32}$$

Note that the harmonic is proportional to the absorbance. It should also be remembered that in the typical experiment, a lock-in amplifier is used to measure these very harmonics. Depending on the phase settings on the lock-in, it is possible to measure either the even or odd components (or combinations). The even components are in-phase with the frequency modulation, while the odd components are out-of-phase.

4.4.3 Pure wavelength modulation

To simplify, we start by assuming that the system is free from wavelength-dependent transmission effects. This means that the only non-zero Fourier component of $T(\nu(t))$ is T_0^{even} (that is, $T(\nu(t)) = T_0^{even} = T_0$ is constant). We also make the unrealistic assumption that we can tune the diode laser without the accompanying residual amplitude modulation, *i.e.* $\kappa_1 = 0$. Directly from Eq. (4.18), we find that

$$S(t) = \eta T_0 I_{L,0} - \eta T_0 I_{L,0} \times \alpha_0 \bar{\chi}(\nu(t)) \tag{4.33}$$

and that the signal Fourier components are related only to the lineshape components

$$S_n^{even}(\nu_c,\nu_a) = -\eta T_0 I_{L,0} \times \alpha_0 \bar{\chi}_n^{even}(\nu_c,\nu_a) \tag{4.34}$$

$$S_n^{odd}(\nu_c,\nu_a) = 0 \tag{4.35}$$

This means that the in-phase harmonic signal measured by a lock-in amplifier will be proportional to both the detected intensity and the absorbance, and that its shape is given by the Fourier component of the lineshape. For the important case of Lorentzian lineshapes, Arndt has provided analytical expressions for these components [427]. By introducing the HWHM (Γ) normalised frequency

detuning $\bar{\nu}_d$ from the absorption resonance frequency ν_{res}

$$\bar{\nu}_d = (\nu_c - \nu_{res})/\Gamma = \nu_d/\Gamma \tag{4.36}$$

and the linewidth-normalised modulation amplitude

$$\bar{\nu}_a = \nu_a/\Gamma \tag{4.37}$$

the (inconvenient) analytical expression for $n > 0$ can be written as

$$\bar{\chi}_n^{even}(\bar{\nu}_d, \bar{\nu}_a) = 2\,\mathrm{Re}\left\{ \frac{\left[((1-i\bar{\nu}_d)^2 + \bar{\nu}_a^2)^{1/2} - (1-i\bar{\nu}_d)\right]^n}{\bar{\nu}_a^n \times \left[(1-i\nu_d)^2 + \bar{\nu}_a^2\right]^{1/2}} \times i^n \right\} \tag{4.38}$$

The first six components are visualised in Fig. 4.9, using a normalised modulation of $\bar{\nu}_a = 2.2$ (optimised for $2f$ detection, see Section 4.4.4). The peak value states the maximum amplitude (sign disregarded). The non-normalised frequency detuning is based on a HWHM of $\Gamma = 1.6\,\mathrm{GHz}$ (as observed for oxygen under atmospheric conditions, *cf.* Fig. 4.3). The magnitude of the components should be interpreted as the relative amplitude of the harmonic signals with respect to the sample peak absorbance α_0. For example, assume that a lock-in amplifier is used to measure a harmonic component $S_n^{even}(\nu_c, \nu_a)$. If the measured component is normalised using the signal detected in the absence of absorber, that is $\eta T_0 I_{L,0}$, the normalised (or *intensity-corrected*) components are given by

$$\bar{S}_n^{even}(\nu_c, \nu_a) = \frac{S_n^{even}(\nu_c, \nu_a)}{\eta T_0 I_{L,0}} = -\alpha_0 \bar{\chi}_n^{even}(\bar{\nu}_d, \bar{\nu}_a) \tag{4.39}$$

From this equation it is clear that the amplitude of the intensity-corrected harmonic is proportional to the absorbance (and thus species concentration), and proportionality constant is determined by the lineshape Fourier component.

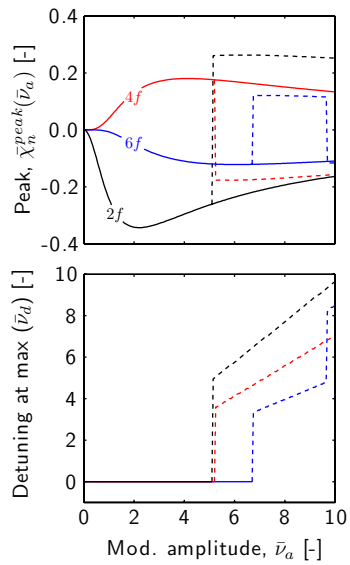

Figure 4.10. *Maximal amplitude of even-ordered harmonics, and corresponding detuning. Dashed lines indicates true maxima and detuning (side-lobes greater than central peak).*

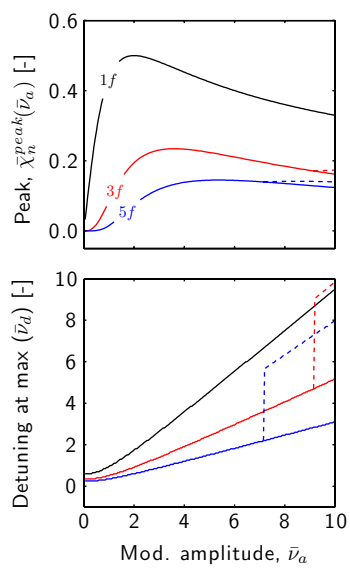

Figure 4.11. *Maximal amplitude of odd-ordered harmonics, and corresponding detuning. Dashed lines reflects that the true maxima jumps to side-lobes for large $\bar{\nu}_a$*

4.4.4 Optimal modulation amplitudes

In order to obtain as large signals as possible, it is interesting to study the selection of the modulation amplitude ν_a. For typical modulation amplitudes, even-order harmonics ($n = 2, 4, 6, \ldots$) are even functions of $\bar{\nu}_d$, and obtain their largest amplitudes at resonance (zero detuning, $\nu_d = 0$). In contrast, odd-order harmonics ($n = 1, 3, 5, \ldots$) are *odd* functions of $\bar{\nu}_d$, and exhibit zero amplitude at resonance, and obtain their maxima at their main peaks. The peak amplitudes are here denoted $\bar{\chi}_n^{peak}(\bar{\nu}_a)$, and depend on the modulation amplitude. The maximum amplitude of even-order harmonics ($\bar{\chi}_n^{opt}$), as well as the corresponding detuning ($\bar{\nu}_a^{opt}$), are shown in Fig. 4.10. The maximal amplitudes for odd-order harmonics are shown in Fig. 4.11. For large modulations, however,

	Lorentzian		Gaussian	
Harmonic	$\bar{\nu}_a^{opt}$	$\bar{\chi}_n^{opt}$	$\bar{\nu}_a^{opt}$	$\bar{\chi}_n^{opt}$
1	2.0	$\pm$0.50		
2	2.2	-0.34	2.1	-0.44
3	3.6	$\pm$0.23		
4	4.1	0.18	3.6	0.24
5	5.3	$\pm$0.15		
6	6.1	-0.12	5.2	-0.15

Table 4.2. *Optimal modulation amplitudes, and corresponding optimal peak amplitudes, for harmonic detection of Lorentzian (from numerical calculations in Figs. 4.10 and 4.11) and Gaussian (from Ref. [426]) lineshapes.*

the maxima of the even-ordered harmonics may be transferred to side-lobes. Similarly, the maxima of odd-ordered harmonics jump from the inner peaks, to their outer side-lobes. Note, however, that the harmonics exhibit maxima at resonance for typical modulation amplitudes ($\bar{\nu} < 5$).

The optimal modulation amplitudes for Lorentzian and Gaussian lineshapes are stated in Table 4.2. Focussed on modulation techniques for nuclear magnetic resonance (NMR) spectroscopy, Arndt provided optimal parameters for the $1f$ and $2f$ Lorentzian case as early as 1965 [427]. Reid and Labrie investigated the influence of modulation amplitude in $2f$ WMS or various lineshapes [423].

An experimental illustration of the importance of the modulation amplitude is given in Fig. 4.12. There, data was acquired for a $L = 50\,\text{mm}$ path, using the system presented later in Section 4.4.1 (carefully described in Paper **XII**). We characterise the R9Q10 oxygen line by using the recent values of $8.35 \times 10^{-24}\,\text{cm}^2/(\text{molecule}\,\text{cm}^{-1})$ for the linestrength, and $\Gamma_L = 0.0495\,\text{cm}^{-1} = 1.49\,\text{GHz}$ for pressure broadening, (from Brecha *et al.* [343]), together with a Doppler width of $\Gamma_D = 0.43\,\text{GHz}$ (from Eq. (4.12)). The peak absorbance, calculated from the resulting Voigt profile, is then 1.3×10^{-3}. Although, as explained in the figure caption, these results are in good agreement with theory, it should be noted that the experiment is performed in the presence of residual amplitude modulation (RAM). The WMS signals obtained under the influence of RAM are discussed in the next section, and are not simply single components of lineshape Fourier components. This is, for example, revealed by a careful look at the $2f$ shapes in Fig. 4.12. A clear, but minor, asymmetry is revealed by comparing the left and right (negative) side-lobes (the right side-lobe has a larger amplitude than the left). These effects are discussed in Section 4.4.5.

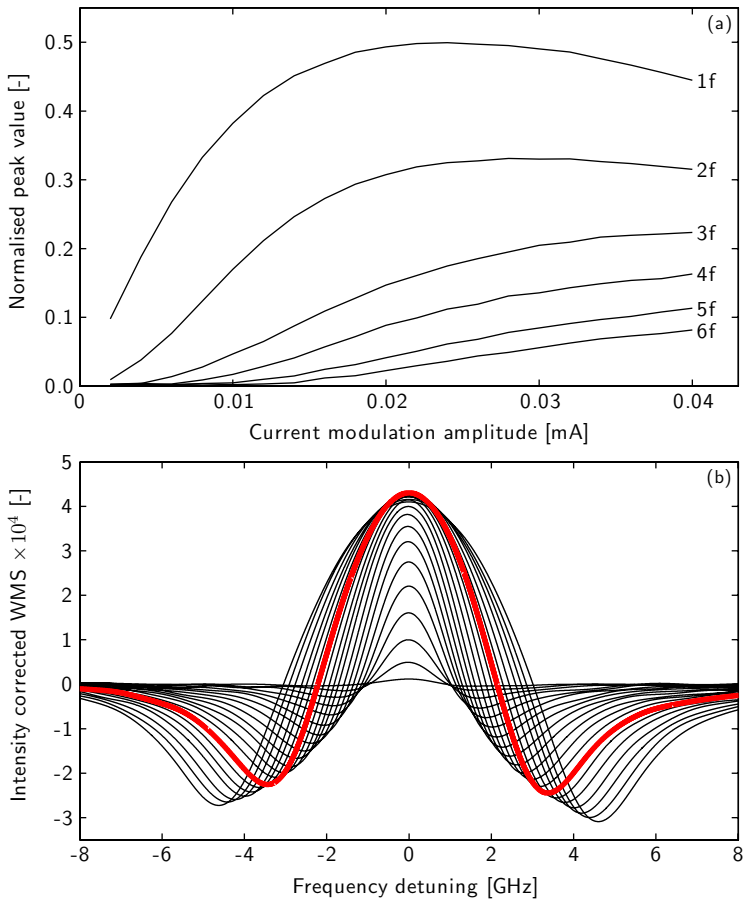

Figure 4.12. *Experimental investigation of the influence of modulation amplitude. Part (a) shows the evolution of the peak value of the first six harmonics. Normalisation is done with respect to the theoretical peak absorbance (1.3×10^{-3} for a 5 cm path), yielding optimal amplitudes of 0.50 ($1f$, 0.024 mA) and 0.33 ($2f$, 0.030 mA). According to the manufacturer, this diode laser has a tuning-rate of -130 GHz/mA (0.25 nm/mA). For the $1f$ and $2f$ optima, this translates into modulation amplitudes of 3.1 GHz and 3.9 GHz. Using a Voigt HWHM of 1.61 GHz, this translates into $\bar{\nu}_a^{opt}$=1.9 ($1f$) and $\bar{\nu}_a^{opt}$=2.4 ($2f$). These results are in good agreement with the expected values presented in Table 4.2. Part (b) shows the $2f$ shapes corresponding to the various modulation amplitudes. The curve corresponding to the largest $2f$ peak is marked by the bold, red line (current amplitude 0.03 mA). Note the broadening of the signal as the modulation amplitude is increased.*

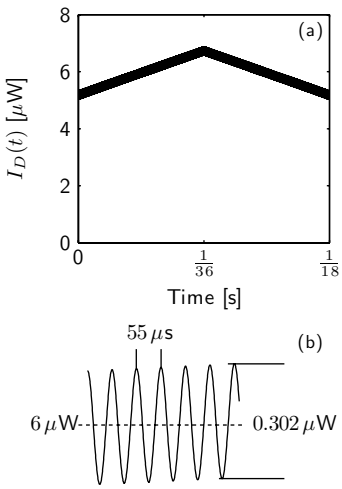

Figure 4.13. *Detected intensity during a WMS scan with optimal modulation amplitude for $2f$ detecion.*

4.4.5 Residual amplitude modulation

The simplifications made in the analysis of Section 4.4.3 do not properly explain the experimental behaviour of diode-laser based WMS. This is because wavelength modulation of diode lasers are accompanied with an intensity modulation, often referred to as *residual amplitude modulation* (RAM). In this section, we do thus not assume that the laser intensity is constant. The laser output is given by

$$I_L(t) = I_{L,0} + \kappa_1 \nu_a \cos(2\pi f_m t + \phi_1) \tag{4.40}$$

We recall the expression for the absorption-related signal from Eq. (4.19), and assume a constant system transmission factor.

$$S_a(t) = \eta T_0 \alpha_0 I_L(t) \bar{\chi}(\nu(t)) \tag{4.41}$$

Inserting the Fourier expansion (see 4.4.2) of the lineshape and the laser intensity we reach

$$\begin{aligned} S_a(t) = \eta T_0 \alpha_0 \times &\Big[I_{L,0} + \kappa_1 \nu_a \cos(2\pi f_m t + \phi_1) \Big] \\ &\times \sum_{n=0}^{\infty} \bar{\chi}_n^{even}(\nu_c, \nu_a) \cos(2\pi n f_m t) \end{aligned} \tag{4.42}$$

As before, we are interested in the signal Fourier components, as this is what we typically measure. Instead of just multiplying together and performing calculations of the resulting Fourier components as shown in Eq. (4.23), a qualitative contemplation over this expression is worthwhile. Without RAM, the n:th signal Fourier component was simply proportional to the n:th lineshape component. Here, the $1f$ modulation of the laser produces a significant change. The multiplication of the $1f$ laser term with the n:th lineshape term will generate components at the $(n-1)$:th and $(n+1)$:th harmonic – simply by means of sum and difference frequency generation! Therefore, we should no longer expect that the second harmonic component of the detected signal has contributions only from $\bar{\chi}^2_{even}$, but also from the $\bar{\chi}^1_{even}$ and $\bar{\chi}^3_{even}$. Since the amplitude modulation is slightly out-of-phase with the frequency modulation, we must also expect that we have an absorption-related contribution to the out-of-phase signal (in practice, however, often negligible). Accordingly, mathematics gives (for $n \geq 2$)

$$S^{even}_{A,n} = -\eta T_0 \alpha_0 \left[\bar{\chi}^{even}_n I_{L,0} + \frac{\bar{\chi}^{even}_{n-1} + \bar{\chi}^{even}_{n+1}}{2} \kappa_1 \nu_a \cos\phi_1 \right] \tag{4.43}$$

$$S^{odd}_{A,n} = -\eta T_0 \alpha_0 \left[\frac{\bar{\chi}^{even}_{n-1} + \bar{\chi}^{even}_{n+1}}{2} \kappa_1 \nu_a \sin\phi_1 \right] \tag{4.44}$$

For the diode laser used in the experiments presented in Fig. 4.12, the experimentally recorded time-dependent signal is shown in Fig. 4.13. The diode laser is scanned using a 18 Hz triangular ramp ($f_m = 18.422\,\text{kHz}$). Both laser power and laser wavelength increase with increasing current, meaning that the right side of the triangular signal generates a signal with an increasing laser frequency to the right. As shown in Paper **XII**, the phase shift between intensity modulation and wavelength modulation is only $0.08\pi\,\text{rad} = 14.4^\circ$ (for this particular VCSEL diode laser and modulation frequency). The wavelength is behind the intensity, so the frequency is 194.4° behind the intensity, hence[10] $\phi_1 = 1.08\pi\,\text{rad} = 194.4^\circ$. For a detected power of 6 µW and an optimal modulation $\nu_a = 2.2\Gamma = 3.52\,\text{GHz}$, the power modulation is 0.302 µW. Since the output intensity at this laser frequency is about 200 µW, we find that the *relative power modulation* is

$$\frac{\kappa_1 \nu_a}{I_{L,0}(\nu_c = \nu_{res})} = \frac{0.151}{6} = 0.025 \Longrightarrow \kappa_1 = 1.43 \times 10^{-15}\,\text{W/Hz} \tag{4.45}$$

which is in good agreement with what the manufacturer states (0.2 mW/mA and 0.25 nm/mA, yielding $\kappa_1 = |dI/d\nu| = 1.5 \times 10^{-15}\,\text{W/Hz}$). Note that the relative power modulation changes over the scan due to changes in the laser intensity. The laser intensity can be approximated as

$$I_{L,0}(\nu_c) \simeq 200\,\mu\text{W} - 1.4\,\mu\text{W/GHz} \times \nu_d \tag{4.46}$$

Analogous to Eq. (4.39), the intensity normalised signal component is ($n \geq 2$)

$$\bar{S}_n^{even}(\nu_c, \nu_a) = -\alpha_0 \left[\bar{\chi}_n^{even} + \frac{\kappa_1 \nu_a \cos\phi_1}{I_{L,0}(\nu_c)} \times \frac{\bar{\chi}_{n-1}^{even} + \bar{\chi}_{n+1}^{even}}{2} \right] \tag{4.47}$$

$$\simeq -\alpha_0 \left[\bar{\chi}_n^{even} - 0.025 \frac{\bar{\chi}_{n-1}^{even} + \bar{\chi}_{n+1}^{even}}{2} \right] \tag{4.48}$$

The expected $2f$ signal is shown in Fig. 4.14, and the small RAM influence is in agreement with experimental data. A stronger RAM distortion is sometimes observed; see for example the $2f$ oxygen WMS recorded using a DFB diode laser shown in Fig. 5.3.

It is important to note that the RAM does not change the fact that the observed signal is proportional to the absorbance. It is not necessary to take all the theoretical WMS signal features into account when using WMS for practical purposes. As explained in Paper **XII**, a calibration WMS spectrum can be acquired and used

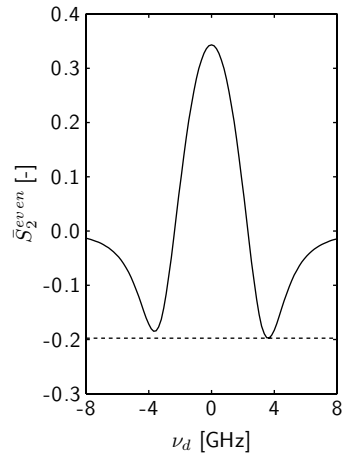

Figure 4.14. *The influence of RAM on normalised $2f$ WMS signals for a relative power modulation of 0.024 (at resonance).*

[10] Kluczynski *et al.* writes (Sect. 3.1 in Ref. [426]) that "ϕ_1 is often close to, but slight smaller than π". This seems to be a mistake; presumably they mean close to but slightly *larger* than π .

as a reference during evaluation of experimental data (solving, in principle, only for absorbance).

RAM of course generate a massive $1f$ modulation in the detected intensity, not being related to the absorption. Formally, the background signal is (from Eq. (4.19))

$$S_{BG}(\nu) = \eta T(\nu) I_L(\nu) = \tag{4.49}$$

$$= \eta T_0 \left(I_{L,0}(\nu_c) + \kappa_1 \nu_a \cos(2\pi f_m t + \phi_1) \right) \tag{4.50}$$

It is, however, clear that the second harmonic ($2f$) is free from such background signals. The $1f$ can, however, be used even though the absorption-related appears on top of a large offset (see for example Paper **XII**). In addition, the $1f$ offset can be used for intensity correction of obtained WMS signals.

4.4.6 Background signals and interference fringes

Until now, we have ignored the fact that most systems are limited by a wavelength-dependent and fluctuating system transmission, *i.e.* $T(\nu)$ not wavelength independent. This issue has been discussed qualitatively in Section 4.3.4. The theory reviewed by Axner *et al.* [425, 426, 428, 429] is a powerful tool for understanding of these phenomenons, but it is out-of-scope to discuss that in detail here. Instead, Section **??** describes a powerful simulation approach for understanding background signals in WMS. Two things are, however, worth mentioning. First, the Fourier analysis of WMS can be used to reliably predict the response to etalon effects. Depending on for example the free spectral range of the occurring etalon-fringe, different harmonic channels may yield different signal-to-background [425, 429]. For example, $4f$ harmonic detection is generally less sensitive to interference fringes than $2f$. Second, a justified question is why the large amplitudes in $1f$ are so seldom utilised. For a Lorentzian lineshape, the $1f$ harmonic yields peaks of ± 0.5 of the peak absorbance, while $2f$ only yields peak amplitudes of -0.34 and +0.19. The most obvious reason is that the RAM-induced offset limits the sensitivity by preventing efficient use of the system dynamic range. Another important reason is the that zero Fourier component of the transmission, T_0^{even}, couples strongly to the average laser intensity, easily generate problematic baselines. All these effects are reflected in the experimental data shown in Fig. 4.15. There, data were acquired over a slightly more than 50 mm pathlength of air. A divergent VCSEL output was directed towards a large-area PD (on-axis configuration). The spacing between the etalon peaks is approximately 2.8 GHz, indicating a surface spacing of about 54 mm. The effect obtained indicates that the laser diode front glass and the PD surface was accidentally well aligned (parallel). Nothing but the gas was present between the laser diode and the

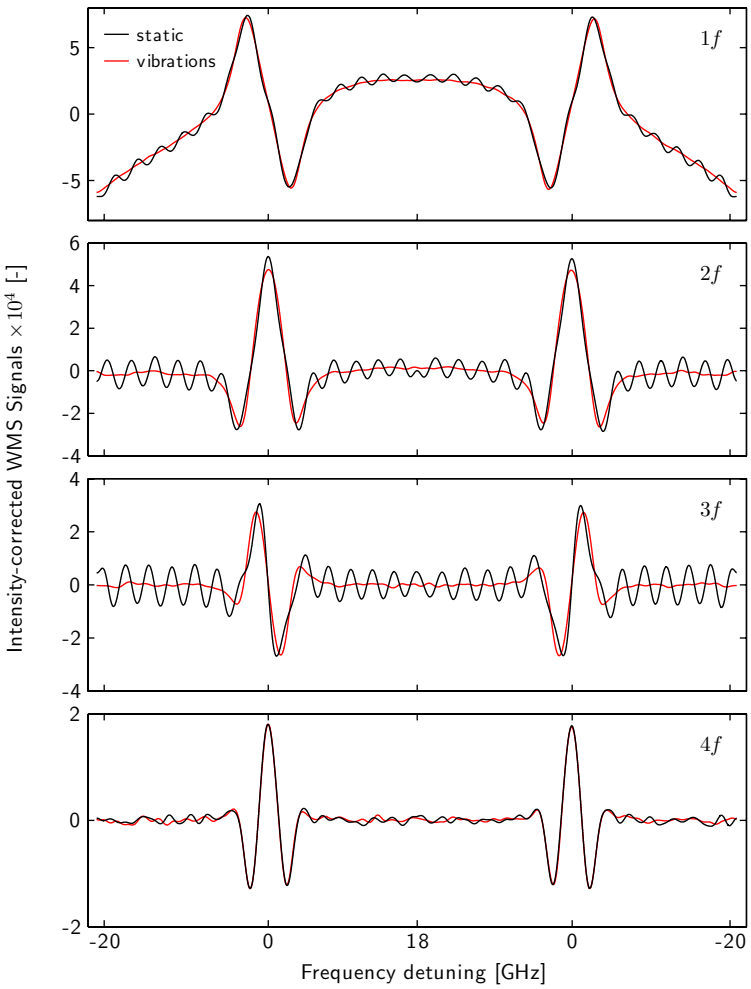

Figure 4.15. *Accidental occurrence of strong etalon-fringes in a WMS experiment ($\Delta\nu_{FSR}$ =2.8 GHz). The outcome of interference suppression by means of mechanical dithering (vibrations) is also shown (red). Both measurements were made in 10 s (180 scan averages). See text for details.*

photodiode surface. When turning on vibrators (*cf.* Section 4.3.4), it is possible to suppress most of these fringes by means of signal averaging. However, and unfortunately, the inconvenient baseline in $1f$ remains.

Besides the theoretical approach for understanding of WMS signals, the WMS simulations that are outlined in Section **??** are recommended. To my knowledge, this approach is not described in the literature. The simulations presented in that section provide

a clear explanation of the distortions observed in Fig. 4.15. The approach is simple and powerful, capable of handling all the interesting aspects of WMS (RAM, etalon-effects, laser non-linearities, large absorption fractions, etc.).

4.5 WMS simulations

WMS simulation is a powerful tool for understanding the generation of WMS signals, including problems like residual amplitude modulation (RAM) and interference fringes (etalons). In fact, since the individual effects like lineshapes, RAM, out-of-phase contributions, and etalons are simple, simulations become significantly simpler than the rather complex Fourier analysis presented in Section 4.4.2. Since this approach, to my knowledge, is not mentioned in the literature, this thesis includes a MatLab script for WMS simulation (Appendix C). The simulation is based on the VCSEL-based oxygen spectroscopy used in Papers **XI** and **XII**, but can easily be modified for other applications.

The basic quantities in these simulations are the operation current and the laser parameters dI/dt [mW/mA] and $d\nu/di$ [GHz/mA]. To mimic the actual measurement procedure, simulations include the linear current ramp, $i_s(t)$, often utilised to scan over the absorption line[11] . The current can thus be expressed as

$$i(t) = i_{dc} + i_s(t) + A_m \sin(2\pi f_m t) \tag{4.51}$$

and the corresponding scan intensity, $I_s(t)$, and instantaneous intensity, $I(t)$, is

$$I_s(t) = I(i = i_{dc}) + i_s(t) \times dI/di \tag{4.52}$$

$$I(t) = I_s(t) + dI/di \times A_m \sin(2\pi f_m t) \tag{4.53}$$

The wavelength follows the intensity with a slight phase shift φ, and the laser frequency is out-of-phase with respect to the wavelength. The instantaneous laser frequency can thus be written

$$\nu(t) = d\nu/di \times \left[i_{scan}(t) - A_m \sin(2\pi f_m t - \varphi - \pi) \right] \tag{4.54}$$

The transmission, $T(\nu(t))$, is a combination of general system transmission (*e.g.* etalon structures) and gas absorption (*e.g.* Lorentzian, Gaussian or Voigt profiles). The time-dependent detected signal is obtained by calculation of the product of intensity and transmission:

$$S(t) = T(\nu(t)) \times I(t) \tag{4.55}$$

[11] The use of rectangular current pulses (µs to ms) can allow non-linear wavelength tuning, while achieving constant output power [400, 430]. The power is determined by the current, while the wavelength is given by the temperature of the active region. During the current pulse, the temperature gradually increase to a new equilibrium.

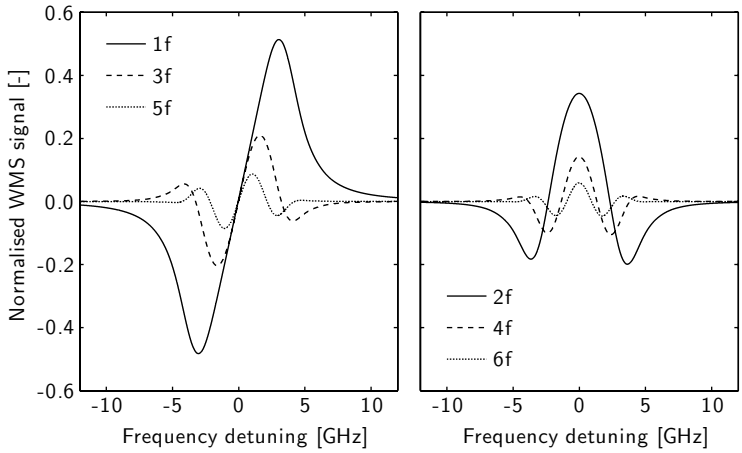

Figure 4.16. *WMS simulations of* $1-6f$ *signals. The peak values very well agree with theoretical expectations.*

A MatLab code for WMS simulations is given in Appendix C. The result of running the simple script is shown in Fig. 4.16. The simulation shows that the troublesome baseline exhibited in $1f$ in Fig. 4.15, as well as in Paper **XII**, is not expected for an ideal WMS system.

Transmission imperfections, such as etalon fringes, are easily incorporated in the simulation. A well aligned etalon gives rise to the frequency dependent transmission $T_E(\nu)$ as stated in Eq. (4.56), where F is the finesse and $\Delta_{FSR} = c/2nL$ is the free spectral range.

$$T_E(\nu) = \frac{1}{1 + F\sin^2(\pi\nu/\Delta_{FSR})} \tag{4.56}$$

For perfectly aligned surface without coating, F is about 0.17[12]. In real cases, using the tilted surfaces and anti-reflection coating, F is significantly smaller.

In order to understand the interference phenomenons encountered in Fig. 4.15, we simulate an etalon effect for $L = 5\,\text{cm}$ and $F = 2 \times 10^{-4}$ (non-perfect alignment and divergent laser beam). The results is shown in Fig. 4.17. Note how a very weak etalon effect still can cause very disturbing background signal. In this case, the situation is extra problematic, since the etalon FSR is close to the absorption linewidth. In contrast, short etalons (large FSR) are a common source of disturbing baselines. A WMS simulation for a 1 mm etalon effect is shown in Fig. 4.18. Note that

[12]The finesse is given by $\frac{4R}{(1-R)^2}$, where $R = 0.04$ is a typical value for the surface reflection.

the slow frequency dependence of the etalon cause an inconvenient baseline in $1f$, while $2f$ is less sensitive (almost a zero baseline). The $1f$ baseline is very similar to that of the experimental data in for example Fig. 4.15 or Paper **XII**. The occurrence of this slow and persistent fringe pattern is presumably related to either a mm surface distance within the diode laser capsule, or non-linear laser power tuning. Since these phenomena may be difficult to avoid, this explains why the $1f$ harmonic is seldom used in TDLAS. Note in particular that the baseline has nothing to do with the triangular variation in average diode laser power during the scan.

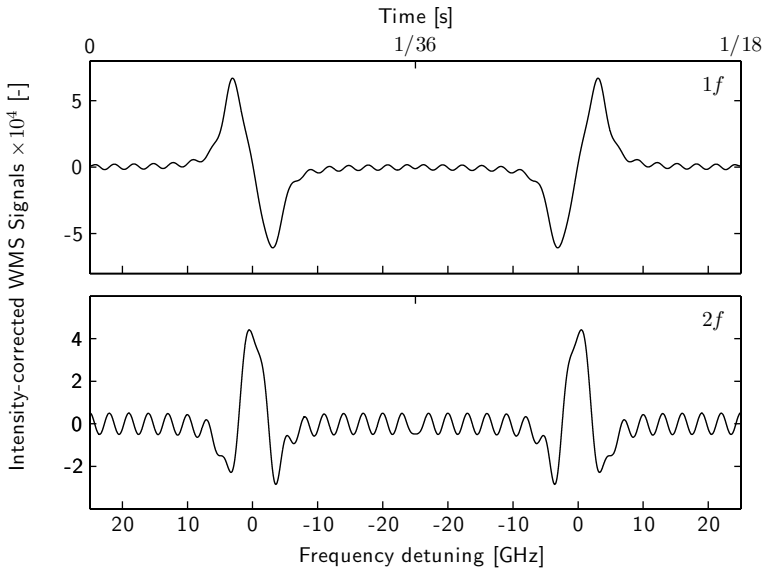

Figure 4.17. *WMS simulations of* $1-2f$ *signals including a 50 mm etalon effect* (Δ_{FSR} *=3 GHz, F=0.0002).*

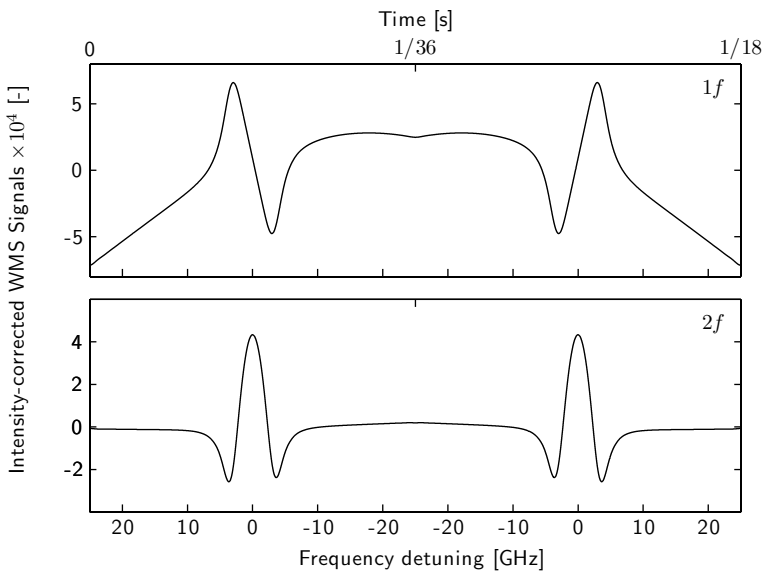

Figure 4.18. *WMS simulations of* $1-2f$ *signals including a 1 mm etalon effect* (Δ_{FSR}*=150 GHz, F=0.01).*

4.6 Oxygen spectroscopy

The near-infrared absorption (from 759 to 770 nm) of molecular oxygen is a marked feature in the atmosphere spectrum, and has been known for more than 200 years. An extensive experimental investigation, together with a detailed theoretical treatment, of this so called *oxygen A-band* was conducted by Babcock and Herzberg in 1948 [275]. More recent work includes high-resolution spectroscopy and lineshape analysis [343, 351, 431]. For this thesis, it is out of scope to provide a proper physical treatment of these fairly complex molecular transitions. Briefly, the A-band refers to the $0 \leftarrow 0$ vibrational transitions of the $b^1\Sigma_g^+ \leftarrow X^3\Sigma_g^-$ electronic transition. These transitions are electric-dipole forbidden and weak. Their importance in atmospherical optics is due to the abundance of oxygen.

Several TDLAS-based oxygen sensors have been constructed and used for various purposes. Nguyen *et al.* employed an external cavity diode laser for WMS-based fundamental investigation of the A-band [432]. With a similar aim, Anderson *et al.* recently employed direct absorption TDLAS for determination of line parameters [343]. Takubo *et al.* investigated the Zeeman effect and its appearance in the magneto-optic spectra of oxygen [433]. Similarly, Brecha *et al.* utilised the magnetic susceptibility of oxygen for TDLAS-based non-invasive sensing of magnetic fields [418, 419]. Gustafsson *et al.* demonstrated simultaneous detection of methane, oxygen and water vapour by means of difference frequency generation [286]. Zappe *et al.* described the use of VCSELs for oxygen detection [434], and Vogel and Ebert demonstrated shot-noise limited oxygen sensing using such lasers [367]. Although the typical VCSEL often is a low-power device, it should be noted that single-mode output of more than 2.5 mW has been demonstrated [435, 436]. Using both a VCSEL and a DFB laser for photoacoustic detection of oxygen, Cattaneo *et al.* shows the potential of PAS as a compact and sensitive technique for oxygen sensing [437]. Scherer *et al.* used a widely tunable (7 nm) VCSEL for measurement of oxygen at high pressures [438]. Arita *et al.* demonstrated the use of multi-mode diode lasers in multi-mode absorption spectrometry (MUMAS) for oxygen sensing [439].

Besides work of more fundamental character, as described in the pervious paragraph, oxygen sensing has many applications. Muta *et al.* performed simultaneous measurements of soot particles and oxygen in a large-scale test furnace [440]. Process control applications are discussed by for example Linnerud [298]. Interested in combustion processed, Wang *et al.* employed VCSELs for sensing of oxygen at high pressures [441]. Sandström *et al.* performed measurements of oxygen in-situ in reheating furnaces (metallurgical applications) [442]. Schlosser *et al.* measured the oxygen concentration in coal-combustion systems [305], as well as during

fire-suppression test [443]. Also in relation to fire-suppression applications, Awtry and Fleming measured oxygen concentrations under conditions of high (above 99%) scattering losses [444]. Lyle *et al.* employed diode lasers for air-mass flow measurements, and used wind tunnels for verification [445]. A rather different application is presented by Templeton *et al.* who monitored oxygen levels in pharmaceutical packages [446].

The use of TDLAS for characterisation of solid, porous materials is referred to as *gas in scattering media absorption spectroscopy* (GASMAS), and is discussed in detail in Chapter 5. In Papers **VII** and **VIII**, a pigtailed DFB laser is used for sensing of oxygen within solids (pharmaceutical tablets and human sinuses, respectively). Papers **XI** and **XII** utilise a low-power VCSEL for the demonstration of high sensitivity GASMAS, as well as pharmaceutical characterisation. Section 4.6.1 gives an introduction to oxygen spectroscopy using VCSELs.

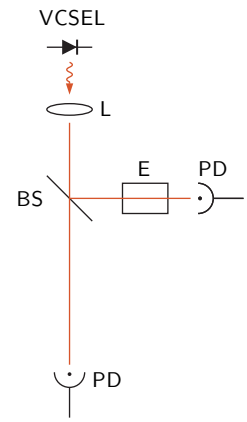

Figure 4.19. *Setup for recording of oxygen spectra. A lens (L) is used for collimation, a beamsplitter (BS) is used to create two beamlines, and an etalon (E) allows frequency calibration.*

4.6.1 VCSEL characterisation

Fig. 4.19 shows a setup used for characterisation of the kind of VCSEL diode lasers used in Papers **XI** and **XII**. Such characterisation examines which absorption lines that a particular laser can interact with. The operating current is then kept fixed, while the laser temperature is scanned (in this case from 10 to 40 °C). A beamsplitter and the use of two photodiodes allows parallel optical recordings of ambient air absorption and the etalon signal needed for frequency scale generation. The etalon used had a free spectral range of 2.41 GHz. A third channel monitors the thermistor resistance, R. All signals were acquired with a NI-4472 National Instruments PCI board. The actual temperature, T is calculated using the Steinhardt-Hart equation, given in Eq. (4.57)

$$T = \left(A + B \cdot \log(R) + C \cdot \log(R)^3\right)^{-1} - 273.15; \qquad (4.57)$$

The coefficients A, B and C are stated by the manufacturer. The resulting signals are shown in Fig. 4.20. The direct signal from the 2 m ambient air beamline is shown in part (a). The etalon fringe signal is shown unresolved in (b), and better resolved in a short time interval in (c), and was used to create a relative frequency scale. Note how the oxygen absorption features are visible also in the etalon signal in part (b). Together with the temperature monitoring (d), the etalon signal allows determination of the temperature tuning coefficient, $d\nu/dT$. As shown in part (e), $d\nu/dT$ is in this case -29 GHz/K (0.055 nm/K at 760 nm). The oxygen absorption spectrum presented in part (f) is reached after baseline correction. This laser reaches 15 absorption lines, and comparison with the HITRAN database reveals that they belong to the R-branch, the range being 761.2-761.8 nm. The measured frequency

separations (between adjacent lines) agree well with data given in HITRAN, see Table 4.3.

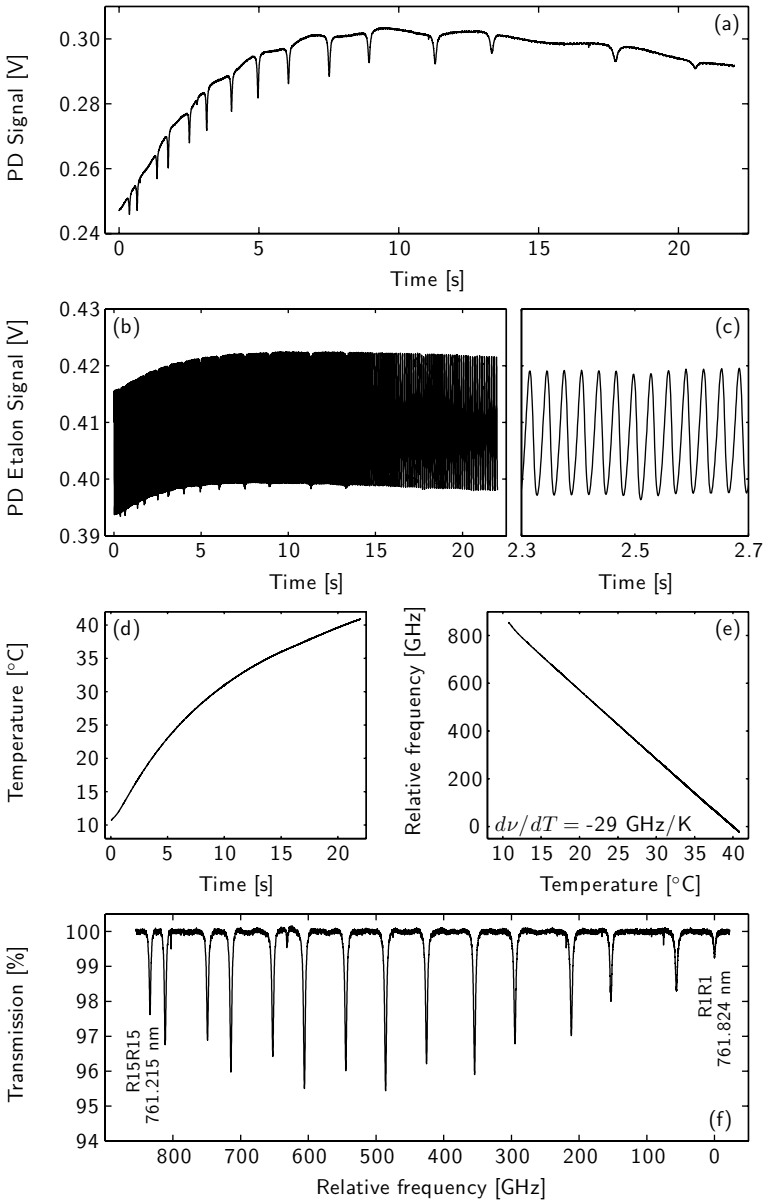

Figure 4.20. *Temperature scan of a VCSEL over the Oxygen R-branch. (temperature increasing with time) (a) Detector signal corresponding to the 2 m ambient air beamline, (b-c) signal from the etalon beamline, (d) thermistor temperature indicating laser temperature, (e) relative frequency, determined from etalon fringes, versus temperature, (f) baseline-corrected transmission. This VCSEL, serial no. E075-279(23-51), is able to reach 15 lines in the oxygen R-branch. See text for details.*

Line	T_{set} [°C]	λ [nm]	$\Delta\nu_H$ [GHz]	$\Delta\nu_m$ [GHz]
R1R1	40.0	761.8241		
			56.4	56.1
R1Q2	38.0	761.7150		
			96.6	96.9
R3R3	34.5	761.5282		
			58.5	58.5
R3Q4	32.5	761.4151		
			83.1	83.2
R5R5	29.6	761.2546		
			59.7	59.7
R5Q6	27.5	761.1393		
			70.8	71.1
R7R7	25.1	761.0026		
			60.6	60.5
R7Q8	23.0	760.8856		
			58.8	58.7
R9R9	20.9	760.7722		
			61.2	61.1
R9Q10	18.8	760.6541		
			46.5	46.7
R11R11	17.2	760.5644		
			61.8	62.0
R11Q12	15.1	760.4453		
			34.5	34.6
R13R13	13.9	760.3788		
			62.7	62.5
R13Q14	11.9	760.2580		
			22.2	22.4
R15R15	11.3	760.2152		

Table 4.3. *Oxygen A-band, the R branch. ν_H are the frequency separation according to HITRAN, while ν_m denote are the measured values corresponding to data in Fig. 4.20.*

The fairly complex baseline of the absorption signal in Fig. 4.20(a) is due to transmissive optical parts. The results of a single beamline experiment (no etalon beamline) is shown in Fig. 4.21. A scale linear in wavelength is achieved by plotting the detector signal versus laser temperature. Identification of the 20 visible absorption features is easily done using HITRAN (the tuning range shown is 759.6 to 761.3 nm, and suggests a temperature tuning coefficient of about 0.049 nm/K). This particular VCSEL was used in Papers **XI** and **XII**, in which the R9Q10 line was utilised.

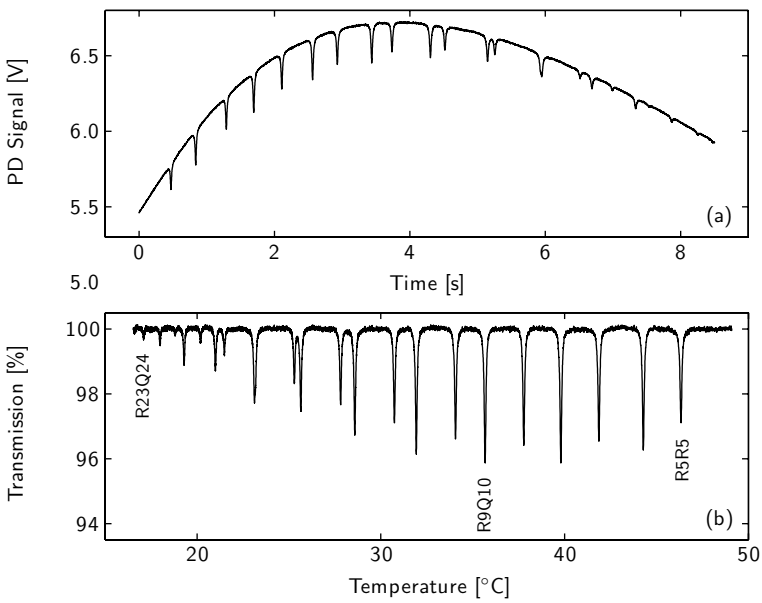

Figure 4.21. *Temperature scan of a VCSEL over the Oxygen R-branch. (a) Detector signal corresponding to a* 2 m *ambient air beamline (temperature decreasing with time) (b) baseline corrected oxygen transmission against laser temperature (scale linear in wavelength). This VCSEL, serial no. E075-342(83-62), is able to reach 21 lines in the oxygen R-branch, and was used in Papers* ***XI*** *and* ***XII****. See text for details.*

4.6.2 Oxygen WMS

The VCSEL-based TDLAS setup for oxygen sensing used in Papers **XI** and **XII** is carefully described in Paper **XII**. Since the instrumentation is dedicated to measurements on high scattering solids and detection of diffuse light, the setup is truly minimalistic. The optical system involves nothing but the VCSEL itself and a large area photodiode. The performance in ambient air free-space measurements is presented, for example, in Figure 4 in Paper **XI** (Allan deviation analysis). There, the sensitivity is better than 1×10^{-5} for a one second acquisition time (further improved for longer acquisition times), and is obtained while having the divergent laser beam directed towards the detector (only a small fraction of the output power ends up at the detector). Another way of performance characterisation is presented in Figure 5 in Paper **XII**, where the pathlength resolution is shown to be in the order of 30 µm (corresponding to an absorption fraction of 8×10^{-7}). Paper **XII** also shows the excellent linearity of the WMS instrumentation and the used procedures for data analysis. In conclusion, the system performance, as verified in these experiments, is considered good in the world of WMS [421].

Experimental recordings are exemplified in Fig. 4.22. The divergent VCSEL output was directed towards a photodiode in a on-axis type experiment (no tilting for reduction of interference fringes). Pathlengths shown are 20 mm, 100 mm and 230 mm. These recordings are intensity-corrected and normalised using the expected peak absorbance $\alpha_{\text{peak}} = \mu_{\text{a}} L$ (calculated using the pathlength L and for a peak absorption coefficient of $\mu_{\text{a}} = 2.7 \times 10^{-5}\,\text{mm}^{-1}$). The obtained peak values can therefore be compared with expected WMS peak values for a modulation amplitude of about $\bar{\nu}_a = 2.2$ (see Section 4.4.4). Although free-space WMS waveforms acquired with this system have not been shown in any publication (for the benefit of figures with actual GASMAS recordings), these particular measurements appear as 3 out of 23 datapoints in Figure 5(c) in Paper **XII**. Note the agreement with expected WMS signals shown in Fig. 4.9 and Fig. 4.16. Note also that the fringe-related $1f$ baseline (see Section **??**) is clearly seen even for the fairly long pathlength of 100 mm. Furthermore, it should be remembered that the 20 mm experiment involves closely separated surfaces (laser to photodiode) and suffers more from interference fringes. The minor disturbances in for example $2f$ and $3f$ (for $\text{l} = 20\,\text{mm}$) should thus be assigned to interference rather than poor signal-to-noise.

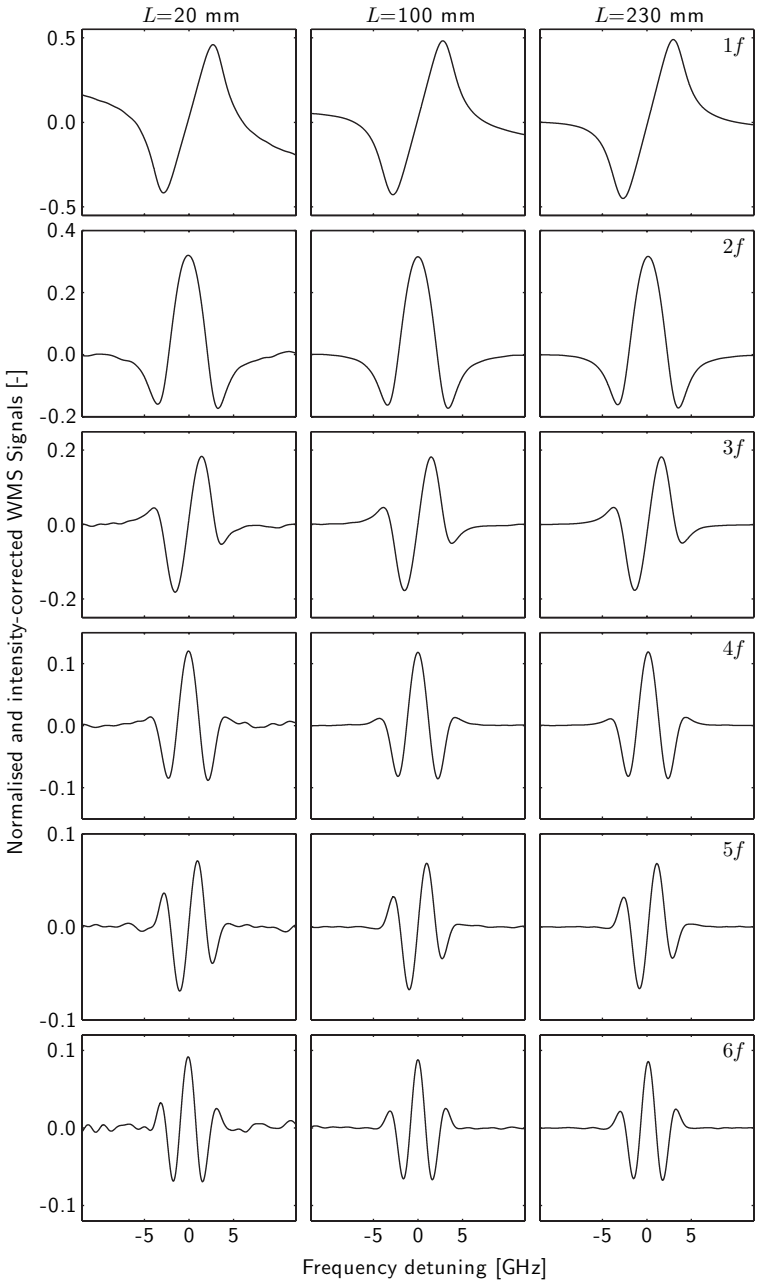

Figure 4.22. *Experimental $1f-6f$ WMS recordings of the R9Q10 line of molecular oxygen using the single-beam, minimalistic system developed and used in Papers* ***XI*** *and* ***XII****. Signals are normalised with respect to the expected peak absorbance. The optical system involves nothing but a VCSEL and a photodiode. See text for details.*

Chapter 5

Gas in scattering media absorption spectroscopy

As discussed in Chapter 4, free gases exhibit sharp and highly structured absorption spectra. Since corresponding spectra of solid materials are typically very dull, high-resolution spectroscopy allows selective detection of gases even when these are dispersed within porous and highly scattering solids such as wood, polystyrene foam and pharmaceutical tablets.

This chapter describes the use of tunable diode laser absorbtion spectroscopy (TDLAS) for sensing of gases dispersed within highly scattering, porous solids. While conventional absorption spectroscopy is carried out with well-defined beamlines and known interaction pathlengths, this task involves dealing with diffuse light, unknown and uncontrollable pathlengths, severe backscattering, and devastating optical interference. These characteristics are further discussed below and motivate that the technique, since its introduction in 2001 [447], is designated as *gas in scattering media absorption spectroscopy* (GASMAS).

5.1 The GASMAS principle

The slow wavelength dependence of absorption and scattering of solids stands in great contrast to the sharp absorption features exhibited by free gases. While sub-nanometer resolution seldom is needed to resolve absorption or scattering spectra of solids, the spectral width of the O_2 absorption lines around 760 nm is about 3 GHz FWHM (atmospheric conditions), corresponding to about 0.006 nm. It is this contrast that allows detection of gases contained within porous materials, even when bulk scattering and/or absorption are much stronger processes.

Material	Thickness [mm]	L_{eq} [mm]
Wood	10	123
Apple	26	33
Lump sugar	12	20
Granulated salt	18	170
Wheat flour	18	380
Polystyrene foam	19	600

Table 5.1. *Results from GASMAS transmission experiments as presented by Sjöholm et al. Reproduced from [447].*

An illustration of the GASMAS principle is given in for example Figure 1 in Paper **VII**. After having injected light into a highly scattering and porous material, a gas absorption imprint is generated as the light passes through gas-filled pores. Thus, a spectrum carrying high-resolution gas absorption imprints may be detected at in principle any point. Since GASMAS is based on TDLAS, this spectra is acquired sequentially by scanning a narrow-band light-source across an absorption feature. The obtained signal (often a $2f$ WMS signal) is from now on referred to as a GASMAS signal. The pores may be anything from a single large cavity (as in the sinus measurements in Paper **VIII**), to the innumerable microscopic cavities of a compressed powder (as in Paper **XI**). In the case of a more or less homogenous porosity, the magnitude of absorption imprint will increase with an increasing source-detector separation. In fact, high scattering and the accompanying elongation of pathlengths may result in surprisingly large gas absorption imprints. For example, as shown in Papers **VII** and **XII**, a 4 mm thick pharmaceutical tablet may in a transmission experiment exhibit an imprint equal to that of a 40 mm pathlength through pure ambient air, *i.e.* the *equivalent pathlength* is 40 mm (40 mm L_{eq}). However, at the same time as scattering may enhance the signal in the above described manner, Paper **XI** revealed that GASMAS is inherently limited by optical interference originating from the highly scattering samples themselves. This is an important aspect, and is described in detail in Section 5.3.

Finally, it should be noted that many of the sophisticated methods for improving performance of TDLAS, as discussed in Chapter 4, are not applicable in GASMAS. This includes, for example, the use of multi-pass gas cells, photoacoustic detection and cavity ring-down spectroscopy.

5.2 A small review

GASMAS is a niche technique within the field of high-resolution laser absorption spectroscopy, and has so far only been explored here at the Department of Physics, Lund University. The technique was introduced by Sjöholm *et al.* in 2001 [447], who showed

the possibility of detecting molecular oxygen within materials such as polystyrene foam, wood, fruit, sugar, wheat flour and granulated salt (see Table 5.1). Their optical setup is schematically illustrated in Fig. 5.1(a), and involved a 760 nm Fabry-Pérot diode laser as a narrow-band light source, and a photomultiplier tube (PMT) for detection. Actual oxygen absorption signals were acquired by employing WMS and conventional analog lock-in amplification (see Section 4.4), and they stated a system sensitivity of 1.25 mm L_{eq}. Light was guided to the sample using a multi-mode optical fiber. In order to be able to add well-defined pathlengths through ambient air to add known oxygen absorption offsets (by moving the fiber away from the sample), a collimating lens was used to collimate the divergent fiber output. At the same time, the regions of collimation and fiber coupling was flushed with nitrogen in order to avoid unwanted oxygen absorption offset. This configuration was adopted to allow quantitative analysis of GASMAS absorption signals by means of a standard addition procedure (as depicted in Fig. 5.2). Besides using this setup for static studies of the above mentioned materials, they also presented dynamic measurements of oxygen reinvasion into polystyrene foam (the foam was stored in a pure nitrogen environment prior to measurements).

Since the optical pathlength (*e.g.* pathlength distribution) is unknown in a turbid material, it is difficult to interpret the GASMAS in terms of oxygen concentration and porosity. By employing photon time-of-flight spectroscopy (TOFS), the pathlength distribution can be measured. In a feasibility study, Somesfalean *et al.* used TOFS in combination with GASMAS to estimate the porosity of polystyrene foam [448]. In Paper **XII**, this approach is explored in detail (with the purpose of determining porosity of pharmaceutical tablets).

The approach presented by Sjöholm *et al.* was later used in detailed GASMAS studies of wood [449] and fruit [450]. During studies of wood drying, Andersson *et al.* later extended the approach by measuring both molecular oxygen and water vapour (at 980 nm) [451]. While the above mentioned experiments were performed in a transmission configuration, Persson *et al.* developed a reflectance probe for GASMAS [390, 454]. In Ref. [390], the reflectance probe was used to detect oxygen in the sinus cavities of human subjects. Although obtained signals were very weak, this study indicated that continued efforts might be worthwhile. Partly for this purpose, a fibre-based dual-beam system was developed by Persson *et al.* [452]. This optical setup is illustrated in Fig. 5.1(b). Involving a pigtailed DFB together with a 90/10 fibre-optic beam-splitter, the system allows balanced detection between measurement and reference arms. One of the single-mode output fibres are directly directed to a reference detector, while the other injects light into the sample. The two signals were separately processed by two analog lock-in amplifiers, and the signal

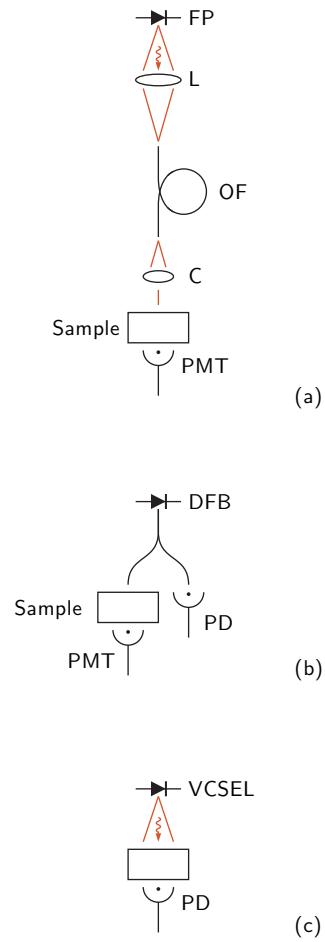

Figure 5.1. *Summary of optical setups used for GASMAS. The original optical approach from [447] is illustrated in (a), and was employed also in [390, 448–451]. The dual-beam fiber-based system was introduced in [452], and used in [453] as well as in Papers **VII**, **VIII** and **IX**. The minimalistic approach illustrated in (c) was used with great success in Papers **IX**, **XI** and **XII**. [OF=Optical Fiber, L=Lens, C=Collimation]*

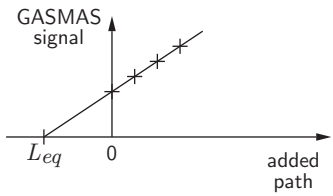

Figure 5.2. *Standard addition for determination of GASMAS L_{eq}*

balancing was performed at a post-processing software level. The sensitivity of this system is not better than the original setup presented by Sjöholm *et al.*, but it required less efforts for suppression of optical interference fringes (fringes are discussed in Section 4.3.4 and Section 5.3). Using this system, Paper **VIII** shows that fairly large signals are encountered when studying the human maxillary sinuses in transmission-like geometry (significantly larger than in the reflectance geometry used in [390]). By injecting light inside the mouth and detecting it on the outside (at the cheekbone), the GASMAS signal reached up to 30 mm L_{eq}. By flushing the nasal cavity with nitrogen, this work also revealed the possibility of studying gas exchange between the nasal cavity and the maxillary sinuses. Persson *et al.* have since continued to investigate of GASMAS-based examination of human sinuses, both theoretically [127], and experimentally [453]. This includes measurements of oxygen and water vapour in both frontal and maxillary sinuses.

Soon after its introduction, GASMAS was considered as a potential tool for characterisation of pharmaceutical materials [455]. In Paper **VII**, we successfully employed the dual-beam fiber-optic system to investigate a set of pharmaceutical tablets. The tablets were compressed manually at different forces (thicknesses 3-4 mm), and obtained GASMAS signals ranged from 5 to 40 mm L_{eq}. This success led to the development of a setup dedicated to pharmaceutical characterisation. In order to improve performance, components known to add unwanted optical interference fringes (*e.g.* optical fibres and lenses) was removed . Papers **XI** and **XII** present a minimalistic and cost-efficient instrumentation, demonstrating significantly improved GASMAS performance. The optical setup is shown in Fig. 5.1(c), and involves nothing but a diode laser source and a photodiode (the divergent laser output is directly injected into the sample). Measurements on pharmaceutical tablets verify an excellent day-to-day reproducibility (0.3 mm L_{eq}, presumably limited by mechanical positioning). The system was also used to demonstrate increased speed for dynamic gas exchange measurements. The first step towards optical porosimetry of pharmaceutical solids is presented in Paper **XII**, in which TOFS is employed as an auxiliary technique to estimate tablet porosity. This also includes a carefully comparison between GASMAS and photon migration, revealing a good covariation between GASMAS L_{eq} and average photon time-of-flight. Part of the success in these experiments is related to an improved understanding of what limits GASMAS experiments. Paper **XI** reveals that severe optical interference fringes originates from the sample, and introduces methods for efficient suppression. This issue is further discussed in Section 5.3. In addition, it is worth noting that the data acquisition in Papers **IX**, **XI** and **XII** is based on digital phase-sensitive WMS detection (further discussed in Section 4.4.1) instead of analog lock-in amplification. While lock-in based detection requires

Author	Year	Focus	Ref.
Sjöholm *et al.*	2001	Concept introduction	[447]
Somesfalean *et al.*	2002	Concentration measurements by combining GASMAS and TOFS	[448]
Alnis *et al.*	2003	GASMAS on wood samples	[449]
Persson *et al.*	2005	Gas exchange in fruits	[454]
Persson *et al.*	2006	Gas exchange in fruits	[450]
Andersson *et al.*	2006	Wood drying (oxygen and water vapour)	[451]
Persson *et al.*	2006	Introducing *in vivo* GASMAS monitoring of the human sinuses	[390]
Persson *et al.*	2007	Development of a dual-beam setup for GASMAS	[452]
Svensson *et al.*	2007	Characterisation of pharmaceutical tablets	**VII**
Persson *et al.*	2007	*In vivo* detection of oxygen in human maxillary sinuses	**VIII**
Persson *et al.*	2007	Monte Carlo simulations for GASMAS of human maxillary sinuses	[127]
Persson *et al.*	2007	*In vivo* detection of oxygen and water vapour in human sinuses	[453]
Andersson *et al.*	2007	Instrumentation, digital GASMAS	**IX**
Svensson *et al.*	2008	Instrumentation, high performance and interference	**XI**
Svensson *et al.*	2008	Pharmaceutical characterisation, signal processing, performance, TOFS, and porosimetry	**XII**

Table 5.2. *A review of GASMAS publications*

one lock-in amplifier for each detector and detection frequency, this phase-sensitive approach allows simultaneous multi-harmonic WMS detection. Paper **XII** exemplifies $1f$-$6f$ WMS signals obtained in GASMAS measurements. This scheme for data acquisition in TDLAS was described by Fernholz *et al.* [422], and introduced for use in GASMAS in Paper **IX**.

An overview of GASMAS publications is given in Table 5.2.

5.3 Interference

Since TDLAS is devoted to measurements of spectrally sharp absorption features, it is crucial to avoid artifacts of such character. The spectrally dull absorption and scattering spectra of solids can be considered as a spectrally constant background level of signal attenuation, and does not constitute a problem in this respect. Nonetheless, spectrally sharp artifacts are known to be a major limitation in TDLAS. The most simple example of a source of spectrally sharp intensity variations is the etalon and its interference fringes. The issue is discussed in detail in Section 4.3.4.

Often, however, one do not only encounter simple and clean etalon fringes like these shown in Fig. 4.15. Instead, one often face highly structured and complex optical fingerprints – sometimes stable and sometimes changing in time. Whether they can be understood only in terms of multiple etalon effects remains an open question. Fig. 5.3 shows an example of the fingerprint exhibited

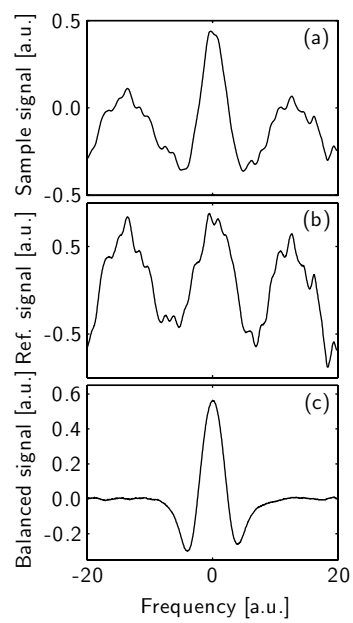

Figure 5.3. *Interference fringes in a dual-beam fiber-optic setup: (a) sample signal, (b) reference signal, and (c) balanced signal. See text for details.*

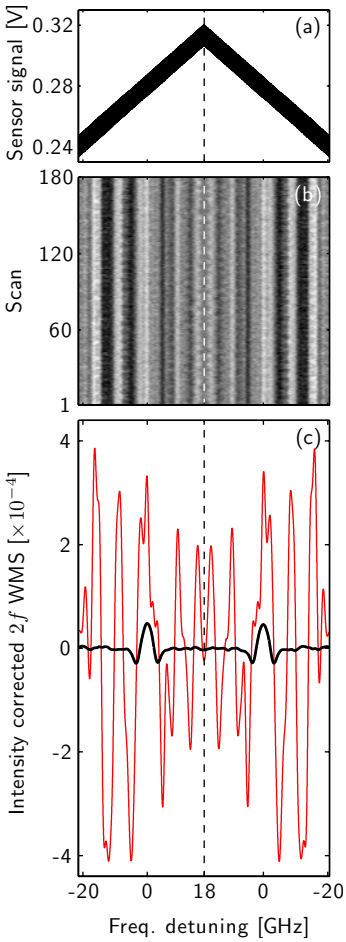

Figure 5.4. *Static GASMAS measurements on an epoxy tablet. Direct sensor signal is shown in (a). Part (b) shows the scan by scan evolution of the intensity corrected WMS signal measured under static conditions (*180 scans, 10 s*). Part (c) shows the static signal corresponding to raw data averaging over the 180 scans (red), together with the oxygen WMS imprint revealed by means of sample rotation (black). The oxygen imprint corresponds to about* 5 mm L_{eq} *(*1.4×10^{-4} *absorption fraction). Note the symmetry around the triangular ramp top (dashed line).*

by a dual-beam fibre-optic TDLAS system of the type illustrated in Fig. 5.1(b). Data originates from an oxygen measurement over a 30 mm air path (no scattering material involved). Note that the fringe structures are common to both sample and reference arms.

Turning from TDLAS in general to the particular case of GASMAS, the situation proves to be even worse. During efforts to understand the limiting factors in GASMAS, it became clear that severe optical interference originate from the highly scattering samples themselves. These important findings are reported and discussed in Paper **XI**. Since this means that both our utility signal (gas absorption) and a strong disturbance are generated in the sample under examination, the issue cannot be resolved by a dual-beam approach. This is in good agreement with experiences from Paper **VII**, where we found it crucial to impose vibrations to both sample and setup in order to obtain useful signals. The vibrations allow us to convert unwanted interference to noise, and suppress it by means of averaging. Although scarcely discussed, adding vibrations (mechanical dithering) has been an important trick in most GASMAS work.[1] An exception are measurements involving biological tissue, where it appears as if the non-static nature of tissue provides a sufficient interference-to-noise conversion. In Paper **XI**, sample rotation and beam dithering were introduced as systematic and efficient methods for interference-to-noise conversion. A more demanding, but interesting, solution would be to modulate the resonance frequency of the gas molecules. This approach, sometimes referred to as sample modulation, has been used for background suppression in sensitive TDLAS of formaldehyde [408, 414]. In GASMAS, if applicable, the technique may enable us to avoid the conversion of a stable interference pattern to noise, potentially increasing both speed and sensitivity.

To further highlight the importance of interference in GASMAS, I turn the attention to experiences from measurements on non-porous epoxy phantoms and pharmaceutical solids. Data originates from the setup illustrated in Fig. 5.1 and used in Papers **XI** and **XII**. Measurements are performed on the R9Q10 absorption line of molecular oxygen, here assumed to have a peak absorption coefficient of 2.83×10^{-5} at atmospheric conditions (this value is taken from HITRAN, but as shown by Anderson *et al.* the true value may be smaller [343]). The epoxy phantoms were manufactured to mimic the optical properties of pharmaceutical solids (*cf.* Figure 10 in Paper **XII**), but at the same time ensure zero porosity. They are characterised and used in Papers **XI** and **XII**. During measurements on these tablet-like samples, an oxygen signal is expected to appear only to the extent that an ambient air path is added. Under static conditions, however, the WMS signal is completely dominated by random interference. This is illustrated

[1] Personal communication: Gabriel Somesfalean (January 2008).

in Fig. 5.4, presenting measurements performed on a non-porous epoxy phantom with few millimetres of added path. The symmetry with respect to the scan (top of the triangular ramp) ensures that it is an interference pattern (and not any other kind of noise). Furthermore, this pattern is stable over tens of minutes, but changes drastically upon movement of the sample.

By studying the influence of the laser-sample distance L (ambient air pathlength offset, *cf.* Figure 2 in Paper **XII**), the origin of the interference was investigated further. Such an investigation is shown in Fig. 5.5, where the oxygen absorption has been moved to the edge of the scan in order to allow examination of the interference pattern itself. A quantitative measure of the interference level is introduced by calculating the standard deviation of the signal in the range free from oxygen imprint (denoted I_σ, *cf.* Figure 2 in Paper **XI**). An oxygen imprint corresponding to about 25 mm in ambient air is shown in part (a). The random interference exhibited by the $2f$ WMS signal under static operation, and its dependence on the laser to sample distance is shown in part (b). Part (c) provides a quantitative measure of the interference level, together with a line giving the expected peak value of the $2f$ WMS oxygen imprint. The expected is given by $0.3L \cdot 2.83 \times 10^{-5}$, as motivated in Paper **XII**. Note that in the region where the interference level is lower than the expected oxygen imprint, the oxygen imprint is visible in (b). However, as shown in part (d), even in such cases, the interference is still severe (data from the final 25 mm distance is shown). An extension of this experiment to distances up to 75 mm is presented in Paper **XI**[2], and shows that the interference level remains virtually constant after 25 mm. These experiments constitute a convincing evidence that the interference originates from the sample (a transmission effect). The slight decrease in interference for short distances is presumably related to the increase in light injection spot size (extending the optical path-distribution and cancelling out interference). The issue, however, deserves future attention since the influence of diffuse optical feedback into the VCSEL has not been investigated.

In GASMAS characterisation of pharmaceutical tablets, the signals of interest may correspond to only a few millimetres of ambient air pathlength (see Paper **XII**). In such cases, interference levels of the magnitude shown in Figs. 5.4 and 5.5 are, of course, intolerable. Unfortunately, the interference encountered for pharmaceutical tablets is similar to that of the epoxy phantoms. This should come as no surprise, as the epoxy tablets were

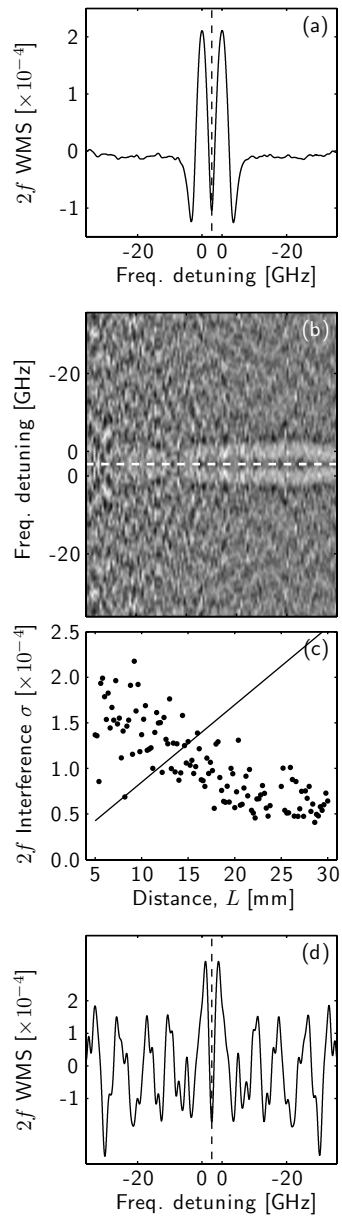

Figure 5.5. *Random interference and its dependence on laser-sample distance L. Measurements on a 3 mm highly scattering, non-porous epoxy tablet. See text for details.*

[2]If one looks closely at Figure 2(b) in Paper **XI**, it can be seen that each and every marker actually consist of two almost perfectly overlaying dots. Every measurement was repeated twice, and the interference was highly reproducible. Unfortunately not mentioned in the article, both these measurements are included in the figure. The stability was, however, reported by stating the fact that the interference was found stable over several minutes.

designed to exhibit scattering properties similar to that of pharmaceutical solids. The development of systematic tools for interference suppression (Paper **XI**) was therefore essential for the success of GASMAS in pharmaceutical applications. An example of interference in a measurement of a pharmaceutical tablet is given in Fig. 5.6. Although the oxygen imprint in the presented measurement is almost as high as 40 mm L_{eq} (1×10^{-3} absorption fraction), it is hidden in interference. For $2f$, the interference level is $I_{\sigma}^{stat} = 1.3 \times 10^{-4}$ in the static measurement and $I_{\sigma}^{rot} = 5.0 \times 10^{-6}$ when sample rotation was employed. Since the interference now has been converted into noise, this can also be referred to as a noise level. This reduction can be understood by considering the $2f$ signal as a random variable with standard deviation I_{σ}^{stat}. Under static conditions, the signal does not change from scan to scan. When employing mechanical dithering, however, signal averaging over 1080 scans should yield an interference level of about $I_{\sigma}^{stat}/\sqrt{1080} = 4 \times 10^{-6}$. Considering that (i) the static measurement is performed over 60 s, averaging out other sources of noise than stable optical interference, (ii) some minor movements may have occurred during the static measurement, (iii) sample rotation may add noise, and (iv) that the static interference pattern may not be typical, this is in good agreement with the observed $I_{\sigma}^{rot} = 5.0 \times 10^{-6}$. Furthermore, this suggests that increasing the scan rate may be advantageous.

In conclusion, GASMAS is typically limited by optical interference originating from the highly scattering sample. This kind of interference should be distinguished from effects related to the optical setup itself (*e.g.* etalon fringes from aligned surfaces). Thus, GASMAS does not only suffer from the background signals familiar from conventional TDLAS. To address this aggravating circumstance, efforts should be directed towards development of efficient methods for interference suppression. Papers **XI** and Paper **XII** introduced sample rotation and tracking coils as efficient dithering-methods for interference-to-noise conversion. Further improvements may, for example, include increasing scan frequencies.

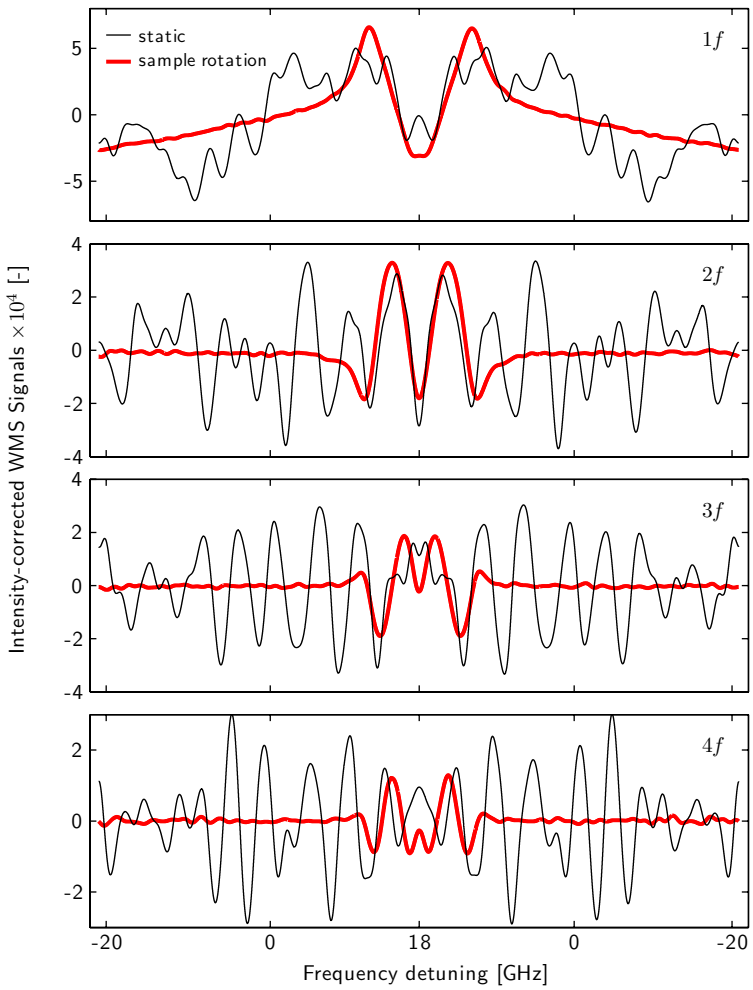

Figure 5.6. *Interference during measurements on a pharmaceutical tablet (tablet $A_{3.53}$, cf. Paper **XII**). Interference dominates in static measurements (black). The oxygen absorption is revealed by employing sample rotation (red). The oxygen imprint was placed at the edge of the scan, and the acquisition time was in both cases 60 s (1080 scan averages). Referring to Figure 1 in Paper **XII**, WMS signals are calculated from the sensor signal $s_D(t)$. See text for details.*

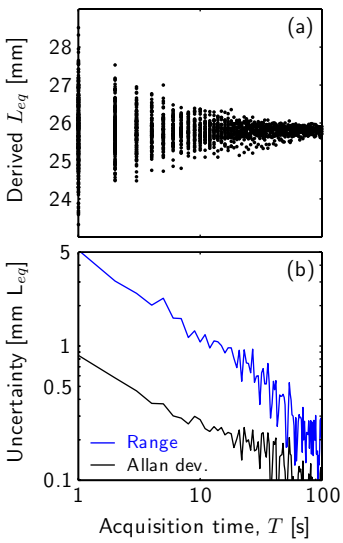

Figure 5.7. *Uncertainty in GASMAS during measurements on a pharmaceutical sample (sample rotation employed). Derived L_{eq} from repeated measurements are shown in (a). Comparison between Allan deviation and range as measures of uncertainty is presented in (b).*

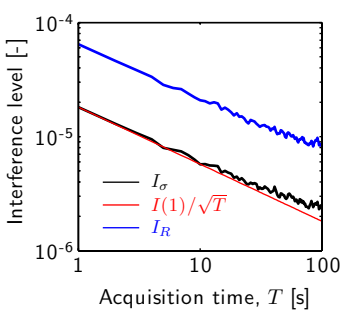

Figure 5.8. *Uncertainty in GASMAS L_{eq} versus the $2f$ WMS interference level (sample rotation employed). The interference level is given both in terms of standard deviation (I_σ, black) and range (I_R, blue). The expected decrease in I_σ is indicated.*

5.4 Performance

Papers **XI** and **XII** provide the first detailed investigations of GASMAS performance. There, two independent experimental procedures are used to show that the sensitivity of the utilised GASMAS instrumentation is about 0.1 mm L_{eq} (3×10^{-6} absorption fraction). Here, sensitivity is used in a broad sense, and should be interpreted as the capability of sensing signal changes or variations between samples. The first procedure is a standard addition type measurement, investigating how well the system can detect small changes in added optical pathlength (*cf.* Figure 3 in Paper **XI**). The outcome is a measure of pathlength resolution, and can be translated into absorption fraction resolution. The second procedure involves measurement repetition and calculation of Allan deviation (*cf.* Figure 4 in Paper **XI**), revealing the efficiency of averaging and providing a measure of reproducibility (precision). This experiment is of limited interest if carried out under static conditions, since stable interference may result in an excellent repeatability, but poor accuracy.

It should be noted that the statement of a 0.1 mm L_{eq} sensitivity is based on a 1σ-measure (one standard deviation). The level of uncertainty can of course be measured in other ways. The thoughest measure is simply to state the range of values obtained when a measurement is repeated. A comparison between Allan deviation and range as measures of uncertainty is presented in Fig. 5.7. There, the 400 consecutive single second measurements from Figure 4 in Paper **XI** are used to investigate uncertainty and averaging efficiency (400 obtained L_{eq}-values for 1 s measurements, 200 for 2 s, etc.). For acquisition times above 60 s, the range of derived L_{eq} is less than 0.3 mm L_{eq}, confirming that Paper **XI** indeed presents the first sub-millimetre GASMAS performance.

Neither of the two mentioned procedures give direct information on the limit of detection, or noise equivalent signal levels. Such characterisation would require that the setup and sample is kept in a controlled atmosphere, allowing controlled reduction in gas concentration (and, thus, absorption fraction). Although interesting, such experiments have not yet been performed in GASMAS. An estimation of the limit of detection is, however, available from the interference (noise) level in obtained WMS signals. The interference level and its dependence on averaging time is shown in Fig. 5.8. Here I_σ denotes the interference level standard deviation, and I_R the interference level range. The expected decay in interference level is indicated, and is given by $I_\sigma(T=1)/\sqrt{(T)}$ (note that since the scan frequency is 18 Hz, a one second measurement is based on 18 raw data averages). The good agreement between observed and expected decrease confirms that sample rotation converts stable interference into noise (*cf.* Section 5.3). Let us define *noise equivalent absorption* (NEA) as the absorption fraction that

give rise to a $2f$ WMS peak that equals the interference level I_σ. Since the $2f$ WMS peak is given by $0.3 L_{eq} \cdot 2.7 \times 10^{-5} = 0.3 \cdot \text{NEA}$, the NEA is given by

$$\text{NEA} = I_\sigma / 0.3 \tag{5.1}$$

At a 60 s acquisition time, the interference is slightly below $I_\sigma = 3 \times 10^{-6}$. The corresponding NEA is then 1×10^{-5}, and corresponds to a 0.35 mm pathlength through ambient air. This number can be used as an estimation of the limit of detection.

Finally, since the L_{eq} depends not only on the sample, but also at source and detector geometry, there is nothing as a true value of L_{eq} for a particular sample (*i.e.* the GASMAS L_{eq} is not a material constant). Therefore, it is somewhat difficult to ask for a measure of GASMAS accuracy. In addition, it should be noted that one limiting factor in assigning L_{eq} values to samples is the uncertainty in optical pathlength offsets (*cf.* Figure 2 in Paper **XII**).

5.5 Optical Porosimetry

Porous materials are important in many areas of science and engineering, spanning from the understanding of construction materials to cutting edge applications [456]. To exemplify, the degradation of construction materials such as cement and concrete is related to permeability and capillary flow – and thus porosity. The pore characteristics of adsorbents, catalysts and filters determine to a great extent their performance. In pharmaceutical science, porosity affect tablet dissolution and drug release. In electronics, porosity is a key to create materials with low dielectric constants, allowing smaller and smaller microelectronic devices [457]. Hopefully, this limited and selective list of applications illustrates the importance of methods for characterisation of porous materials. Important techniques for this purpose include mercury intrusion porosimetry [458, 459] and gas adsorption [460] (see also Ref. [461]). By employing certain theoretical models, these techniques claim to provide very specific data, such as pore size distribution and surface area. On the other hand, they are known to have their limitations and flaws (see for example the work by Diamond [462], and that of Farber *et al.* [463]).

GASMAS, being sensitive to variations in both scattering properties and pore volume, may serve a non-destructive analytical tool or as a process sensor in some applications involving porous materials. In addition, as shown by Somesfalean *et al.* [448], GASMAS in combination with time-of-flight spectroscopy allows estimation of porosity. The technique is explored in detail in Paper **XII**, in which the term *optical porosimetry* is introduced. Since GASMAS is a fairly recent method, it still awaits the right applications. Non-intrusive sinus monitoring, briefly discussed in Section 5.6, to-

gether with characterisation of pharmaceutical solids, described in Section 5.7, are two promising fields of applications.

5.6 Biomedical applications

Infections and inflammations in the air filled cavities of the human skull, *i.e. sinusitis*, affects a large number of people. By assessing the gas content of these cavities, as in Paper **VIII**, GASMAS may be of diagnostic value. This application is discussed in detail by Persson [103].

5.7 Pharmaceutical applications

Pharmaceutical sciences employ a large number of different methods in order to measure, characterise and understand properties of solid pharmaceutical materials [104, 107]. Both chemical and physical analysis are important aspects [105]. Physical properties (or *bulk* properties), such as surface area and porosity, impact important pharmaceutical parameters such as disintegration and dissolution (drug delivery).

Mercury intrusion porosimetry [458, 461] is an important method used for assessment of structural properties of pharmaceutical solids [464–466]. Although the technique is believed to provide accurate estimations of porosity, its capability to measure pore size distribution is debated. Recent work on pharmaceutical characterisation using X-ray tomography indicates that mercury porosimetry really measure pore neck-size rather than pore size, and that errors are as large as two orders of magnitude [463].

In recent years, the introduction of new tools for fast and non-destructive pharmaceutical analysis has received increased attention, especially in relation to quality control and process analytical technology (PAT). In this context, spectroscopic techniques typically offer advantages in terms speed, compactness, versatility, and ability to perform noninvasive analysis.

GASMAS can measure the content of free gas in solid samples, and is an interesting complementary approach to the above mentioned techniques. Its instrumental simplicity and low cost is a great advantage. As shown in Paper **XII**, GASMAS can detect small variations in physical properties between individual tablets. This suggest that the technique can be highly valuable in on-line process monitoring and during manufacturing. In addition, GASMAS in combination with an implementation of frequency domain photon migration (*i.e.* unravelling of photon pathlengths), can form a very compact instrumentation for optical porosimetry. Potential applications are further discussed in an international patent [455], as well as in Papers **VII** and **XII**.

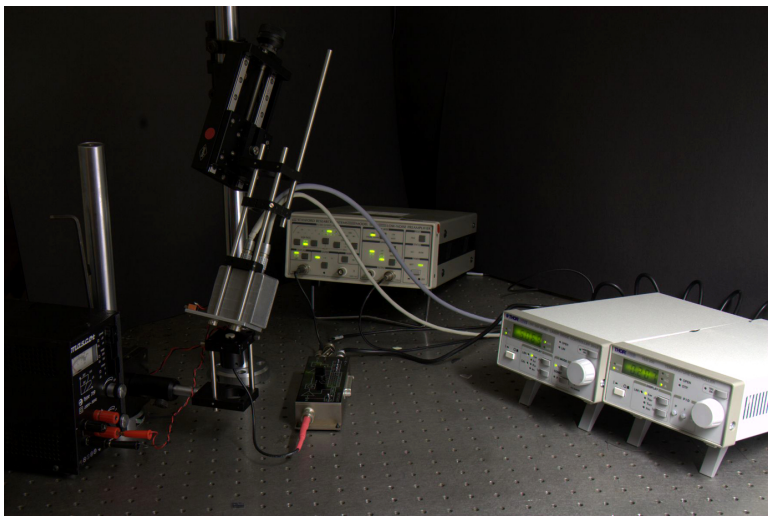

Figure 5.9. *The WMS setup used in Papers **XI** and **XII**. The configuration shown is used for pharmaceutical applications. The two white boxes to the right are the diode laser current and temperature controllers. The black box to the left is a low voltage power supply, and feeds the vibrators used for sample rotation and laser diode dithering. The diode laser (VCSEL) is mounted on a translation stage, and its divergent output beam is directed towards a pharmaceutical tablet. The tablet rests on top of a large area photodiode. The small box in the centre is a low-noise transimpedance amplifier. The pre-amplifier in the background is used for high-pass filtering. Both the high-pass filter signal and a direct detector signal is sampled. The computer generating modulation signals and acquiring detector signals is not shown.*

The GASMAS instrumentation used in the pharmaceutical applications is shown in Fig. 5.9.

Appendix A

Solid angles

A *solid angle* [1] originating from a point P is defined and measured by its cross section with the unity sphere centered at P. Fig. A.1 illustrates this by stating that the solid angle $d\omega$ equals the cross section between that solid angle and the unity sphere (the shaded area dA). It is a expansion of the concept of radians, aimed to cover three dimensional angles. Since the area of a unity sphere is 4π, a solid angle is within the range $[0, \pi]$. Solid angles are usually denoted ω or Ω, and their unit is *steradians* [sr]. In spherical coordinates, $d\varphi$ and $d\theta$ define a solid angle $d\omega = \sin\theta \; d\varphi d\theta$. Note that $d\omega$ is the area on the unity sphere spanned by $d\varphi$ and $d\theta$. As an example, consider the conical solid angle Ω defined by a certain polar angle φ_0 as shown in Fig. A.2. The magnitude of that solid angle may be determined as follows:

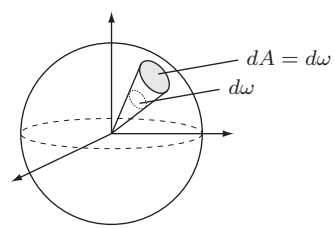

Figure A.1. *A solid angle $d\omega$.*

$$\Omega = A = \iint_A dA = \int_{\theta=0}^{\theta_0} \int_{\varphi=0}^{2\pi} \sin\theta \; d\varphi d\theta$$
$$= 2\pi \int_0^{\theta_0} \sin\theta \; d\theta = 2\pi(1 - \cos\theta_0) \tag{A.1}$$

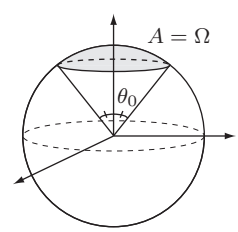

Figure A.2. *A conical angle.*

Some radiometric quantities are based on the concept of solid angles. Radiance, [W/m^{2}sr], is a good example. Let $\hat{\boldsymbol{s}} = \hat{\boldsymbol{s}}(d\omega)$ denote the directionality of a small solid angle. Integrals such as

$$\int_{4\pi} f(\bar{\boldsymbol{r}}, \hat{\boldsymbol{s}}) \; d\omega \tag{A.2}$$

deals with the total flux density of a scalar quantity f [some unit/m^{2}sr] at a certain point $\bar{\boldsymbol{r}}$. Integrals such as

$$\int_{4\pi} f(\bar{\boldsymbol{r}}, \hat{\boldsymbol{s}}) \hat{\boldsymbol{s}} \; d\omega \tag{A.3}$$

[1] Swedish: rymdvinkel

returns the net flux density. Others solid angle integrals of interest include ($\boldsymbol{A}, \boldsymbol{B}$ being constant vectors not dependent on $\hat{\boldsymbol{s}}$)

$$\int_{4\pi} \hat{\boldsymbol{s}}\, d\omega \tag{A.4}$$

$$\int_{4\pi} \boldsymbol{A}\cdot\hat{\boldsymbol{s}}\, d\omega \tag{A.5}$$

$$\int_{4\pi} (\boldsymbol{A}\cdot\hat{\boldsymbol{s}})\hat{\boldsymbol{s}}\, d\omega \tag{A.6}$$

$$\int_{4\pi} (\boldsymbol{A}\cdot\hat{\boldsymbol{s}})(\boldsymbol{B}\cdot\hat{\boldsymbol{s}})\, d\omega \tag{A.7}$$

$$\int_{4\pi} (\boldsymbol{A}\cdot\hat{\boldsymbol{s}})(\boldsymbol{B}\cdot\hat{\boldsymbol{s}})\hat{\boldsymbol{s}}\, d\omega \tag{A.8}$$

All these integrals may be transformed into surface integrals in spherical coordinates.

Anti-symmetry in $\hat{\boldsymbol{s}}$ forces integrals A.4, A.5 and A.8 to zero. If $I = I(\hat{\boldsymbol{s}})$ denotes the integrand, anti-symmetry requires that $I(-\hat{\boldsymbol{s}}) = -I(\hat{\boldsymbol{s}})$ is satisfied. For pedagogic reasons, mathematical proofs of A.4 and A.5 is given here.

$$\begin{aligned}
&\int_{4\pi} \hat{\boldsymbol{s}}\, d\omega = \iint \hat{\boldsymbol{r}}\sin\theta\, d\varphi d\theta = \\
&= \iint (\cos\varphi\sin\theta\ \hat{\boldsymbol{x}} + \sin\varphi\sin\theta\ \hat{\boldsymbol{y}} + \cos\theta\ \hat{\boldsymbol{z}})\sin\theta\, d\varphi d\theta = \\
&= \int_0^{2\pi} \cos\varphi\, d\varphi \int_0^{\pi} \sin^2\theta\, d\theta\ \hat{\boldsymbol{x}} + \ldots = \bar{\boldsymbol{0}}
\end{aligned} \tag{A.9}$$

Integral A.5 is easily calculated if the cartesian coordinate system are chosen so that $\boldsymbol{A}$ is parallel to $\hat{\boldsymbol{z}}$ ($\boldsymbol{A} = |\boldsymbol{A}|\hat{\boldsymbol{z}}$).

$$\begin{aligned}
&\int_{4\pi} \boldsymbol{A}\cdot\hat{\boldsymbol{s}}\, d\omega = \left\{\boldsymbol{A}\cdot\hat{\boldsymbol{s}} = \boldsymbol{A}\cdot\hat{\boldsymbol{r}} = |\boldsymbol{A}|\cos\theta\right\} = \\
&= \iint |\boldsymbol{A}|\cos\theta\sin\theta\, d\varphi d\theta = 2\pi|\boldsymbol{A}|\int_0^{\pi} \frac{\sin 2\theta}{2} = 0
\end{aligned} \tag{A.10}$$

The same approach is also helpful in calculating A.6, but the out-

come is different.

$$\begin{aligned}
&\int_{4\pi} (\boldsymbol{A}\cdot\hat{\boldsymbol{s}})\hat{\boldsymbol{s}}\ d\omega = \iint |\boldsymbol{A}|\cos\theta\sin\theta\ \hat{\boldsymbol{r}}\ d\varphi d\theta = \\
&= |\boldsymbol{A}| \iint \cos\theta\sin^2\theta\cos\varphi\ d\varphi d\theta\ \hat{\boldsymbol{x}} + \\
&+ |\boldsymbol{A}| \iint \cos\theta\sin^2\theta\sin\varphi\ d\varphi d\theta\ \hat{\boldsymbol{y}} + \\
&+ |\boldsymbol{A}| \iint \cos\theta\sin^2\theta\ d\varphi d\theta\ \hat{\boldsymbol{z}} = \\
&= |\boldsymbol{A}| \iint \cos\theta\sin^2\theta\ d\varphi d\theta\ \hat{\boldsymbol{z}} = 2\pi|\boldsymbol{A}| \int \cos\theta\sin^2\theta\ d\theta\ \hat{\boldsymbol{z}} = \\
&= 2\pi|\boldsymbol{A}|\Big[-\frac{\cos^3\theta}{3}\Big]_0^{\pi}\ \hat{\boldsymbol{z}} = \frac{4\pi}{3}|\boldsymbol{A}|\hat{\boldsymbol{z}} = \frac{4\pi\boldsymbol{A}}{3}
\end{aligned} \tag{A.11}$$

Since the scalar product is linear ($\boldsymbol{a}\cdot(\boldsymbol{b}+\boldsymbol{c}) = \boldsymbol{a}\cdot\boldsymbol{b} + \boldsymbol{a}\cdot\boldsymbol{c}$)) and integrals may be seen as generalised sums, the value of A.7 may not come as a surprise.

$$\int_{4\pi} (\boldsymbol{A}\cdot\hat{\boldsymbol{s}})(\boldsymbol{B}\cdot\hat{\boldsymbol{s}})\ d\omega = \frac{4\pi}{3}(\boldsymbol{A}\cdot\boldsymbol{B}) \tag{A.12}$$

Appendix B

The Henyey-Greenstein phase function

That the Henyey-Greenstein phase function (single scattering function) really is a probability density function is shown below:

$$
\begin{aligned}
&P(0 < \theta < \pi) = \int_0^{\pi} 2\pi p(\theta) \sin\theta \; d\theta = \{x = \cos\theta\} = \\
&= \int_{-1}^{1} \frac{1}{2} \frac{1 - g^2}{(1 + g^2 - 2gx)^{3/2}} \; dx = \\
&= \frac{1 - g^2}{g} \Big[(1 + g^2 - 2gx)^{-1/2} \Big]_{-1}^{1} = 1
\end{aligned}
\tag{B.1}
$$

The anisotropy is determined after partial integration (using the same substitution).

$$
\begin{aligned}
&< \cos\theta > = \int_0^{\pi} 2\pi p(\theta) \cos\theta \sin\theta \; d\theta = \{x = \cos\theta\} = \\
&= \int_{-1}^{1} \frac{1 - g^2}{2} \frac{x}{(1 + g^2 - 2gx)^{3/2}} \; dx = \ldots = g
\end{aligned}
\tag{B.2}
$$

Appendix C

WMS Simulations

This appendix outlines how WMS can be simulated. For simple comparison with the oxygen spectroscopy carried out in this thesis, the MatLab code for WMS simulations presented here mimic the system used in Paper **XII**. The Fourier evaluation is described in detail in Paper **XII**. The code is surprisingly simple, and it constitute a very attractive and powerful alternative to theoretical approaches. Note that the addition of etalon fringes is deactivated below (remove commenting for activation).

```
% Acquisition parameters
fm=18432;   % Hz
N=134400;   % samples (fs=18 Hz)
fs=2419200; % samples/s
dt=1/fs;    % Sample period [s]
t=(0:(N-1))*dt; % Time scale

% Laser parameters
dv_di=-130        % GHz/mA;
dI_di=0.2        % mW/mA;
phi=14.4/180*pi; % Phase-lag of wavelength

% Modulation parameters
HWHM=1.6;          % Absorption linewith [GHz]
As=50/130;         % Scan amplitude to get a 50 GHz scan
Am=(2.2*HWHM/130); % Modulation amplitude (optimal for 2f)

% Diode laser operation
i_dc=4;   % DC current [mA]
I_dc=0.2; % Laser output at i_dc [mW]

% Current scan, i_s(t)
i_s=(0:(N/2-1))/(N/2-1);
i_s=[i_s,fliplr(i_s)+1/(N/2-1)]*As;
```

```
% Operation current, i(t)
i=i_dc+i_s+Am*sin(2*pi*fm*t);

% Intensity for pure scan, I_s(t)
I_s=I_dc+i_s*dI_di;

% Intensity, I(t)
I=I_s+dI_di*Am*sin(2*pi*fm*t);

% Frequency for pure scan
v_s=dv_di*i_s;

% Laser frequency, v(t)
v=dv_di*i_s-dv_di*Am*sin(2*pi*fm*t-phi-pi);

% Absorption line
L=100;      % Pathlength [cm]
v0=-25;     % Resonance position [GHz]
S=2.5e-13; % Linestrength [cm^2 Hz]

% Oxygen number concentration [cm^{-3}]
N_O2=0.209*2.4615e19

% Lorentzian transmission, T(v)
T=1 - S/pi*1e-9*HWHM./((v-v0).^2+HWHM^2)*N_O2*L;

% % Add etalon fringes
% FSR=(300e8/(2*5))/1e9; % [GHz] (FSR=c/2nL)
% F=0.0002;
% T_E=1./(1+F*(sin(pi*v/FSR)).^2);
% T=T.*T_E;

% Detected signal
S=(T.*I)';

% Fourier WMS evaluation
n_shift=fm/(fs/N);        % Downshifting one fm-unit
f = (-N/2:(N/2-1))'*fs/N; % Frequency scale
df=1000;                  % Filter width [Hz]

figure
hold on

for nf=1:6

    spec=fftshift(fft(S)).*exp(-((f-nf*fm)/df).^8);
    S_c = ifft(fftshift(circshift(spec,-nf*n_shift)));
    a=angle(max(S_c-mean(S_c)));
    WMS=2*real((S_c-mean(S_c))*exp(-j*a));

    % Intensity-corrected WMS signal
```

```
    IC_WMS{nf}=WMS./I_s';

    % % Frequency scale plot
    % plot(v_s-v0,IC_WMS{nf}/(1-min(T)),'k')

    % Time evolution plot
    plot(t,IC_WMS{nf}/(1-min(T)),'k')

end
```

Comments on the papers

I **Time and wavelength resolved spectroscopy of turbid media using light continuum generated in a crystal fiber**
A. Abrahamsson, T. Svensson, S. Svanberg
S. Andersson-Engels, J. Johansson and S. Folestad.
Optics Express **12**, 4103-4112 (2004).

This paper reports on a novel system for time-of-flight spectroscopy. Using an S1 photocathode-based streak camera, and supercontinuum generation in a photonic crystal fibre, TOFS is realised in the 550 to 1150 nm range.

I developed tools for diffusion modelling of TOFS, and performed data evaluation. I took minor part in experimental work, and made substantial contributions to the manuscript.

II **Scatter correction of transmission near-infrared spectra by photon migration data: Quantitative analysis of solids**
A. Abrahamsson, A. Löwgren, B. Strömdahl, T. Svensson,
S. Andersson-Engels, J. Johansson and S. Folestad.
Applied Spectroscopy **59**, 1381-1387 (2005).

By combining conventional NIR spectroscopy with TOFS at a few wavelengths, this paper improved the robustness of the prediction of analyte concentrations in pharmaceutical tablets with varying scattering properties.

I contributed to data analysis and manuscript preparation.

III **Characterization of normal breast tissue heterogeneity using time-resolved near-infrared spectroscopy**
T. Svensson, J. Swartling, P. Taroni, A. Torricelli, P. Lindblom, C. Ingvar and S. Andersson-Engels.
Physics in Medicine and Biology **50**, 2559-2271 (2005).

This paper investigates the degree of heterogeneity encountered in time-resolved reflectance spectroscopy of healthy breast tissue in vivo. Such heterogeneity provides an indication of the contrast needed in detection of breast tumours.

I performed a major part of the experimental work, developed MATLAB software for data evaluation, and was responsible for data analysis. I prepared most parts of the manuscript.

IV **Performance assessment of photon migration instruments: the MEDPHOT protocol**
A. Pifferi, A. Torricelli, A. Bassi, P. Taroni, R. Cubeddu, H. Wabnitz, D. Grosenick, M. Möller, R. Macdonald, J. Swartling, T. Svensson, S. Andersson-Engels, R.L.P. van Veen, H.J.C.M. Sterenborg, J.M Tualle, H.L. Nghiem, S. Avrillier, M. Whelan and H. Stamm.
Applied Optics **44**, 2104-2114 (2005).

This paper presents an international collaboration involving several European academic institutions, aimed at comparing and elucidating the performance of methods and instrumentation for characterisation of turbid materials. It includes measurements of a large set of reference sample, and showed a fairly large discrepancy between instruments.

I took part in all experimental work performed by the Lund research group. I performed data evaluation and delivered our results to Antonio Pifferi, who had the main responsibility in manuscript preparation.

V **Least-squares support vector machines modelization for time-resolved spectroscopy**
F. Chauchard, S. Roussel, J.M. Roger, V. Bellon-Maurel, C. Abrahamsson, T. Svensson, S. Andersson-Engels, S. Svanberg.
Applied Optics **44**, 7091-7097 (2005).

This paper reports on a new approach for modelling of time-of-flight data, in which a theoretical calibration procedures is used to extract optical properties. Calibration based on, for example, Monte Carlo may be of value in situation where direct forward modelling is difficult.

I was responsible for the conventional diffusion modelling of light propagation, and took minor part in experimental work and manuscript preparation.

VI ***In vivo* optical characterization of human prostate tissue using near-infrared time-resolved spectroscopy**
T. Svensson, S. Andersson-Engels, M. Einarsdóttír and K. Svanberg.
Journal of Biomedical Optics **12**, 014022 (2007).

This paper reports on the novel application of time-of-flight spectroscopy (TOFS) to in vivo characterisation of human prostate tissue. Data was recorded in the operating theatre in connection with primary brachytherapy treatment of prostate cancer, and involved 9 patients. All measurements were conducted at the Lund University Hospital. TOFS was found highly reliable, capable of performing both absorption and scattering spectroscopy in all measurements.

I was technically responsible, and performed all experiments in cooperation with medical staff. I performed instrumental improvements, and was responsible for assembly of optical fibers resisting sterilisation. I was responsible for data evaluation, and wrote the major part of the manuscript.

VII **Noninvasive characterization of pharmaceutical solids by diode laser oxygen spectroscopy**
T. Svensson, L. Persson, M. Andersson, S. Svanberg, S. Andersson-Engels, J. Johansson, and S. Folestad.
Applied Spectroscopy **61**, 784-786 (2007).

This short paper is the first publication on gas in scattering media absorption spectroscopy (GASMAS) for characterisation of pharmaceutical tablets.

I was responsible for experimental work, data evaluation and prepared the manuscript.

VIII **Non-intrusive optical study of gas and its exchange in human maxillary sinuses**
L. Persson, M. Andersson, T. Svensson, M. Cassel-Engquist, K. Svanberg, and S. Svanberg.
Proc. of SPIE: Diagnostic Optical Spectroscopy in Biomedicine IV **6628**, 662804 (2007).

This paper reports on the novel use of GASMAS for detection of oxygen located in human maxillary sinuses. The technique is still under exploration, and may be useful in sinusitis diagnostics.

I took a minor part in experimental work, and made substantial contributions to manuscript preparation.

IX **Flexible lock-in detection system based on synchronized computer plug-in boards applied in sensitive gas spectroscopy**
M. Andersson, L. Persson, T. Svensson, S. Svanberg.
Review of Scientific Instruments **78**, 113107 (2007).

This paper reports on the development of compact, flexible and fully digital TDLAS instrumentation.

I took part in the development of the data acquisition system, and was involved in experimental work. I made substantial contributions to the manuscript.

X **White Monte Carlo for Time-resolved Photon Migration**
E. Alerstam, S. Andersson-Engels, and T. Svensson.
Journal of Biomedical Optics **13**, 041304 (2008).

This paper reports on the development of a powerful scheme for Monte Carlo (MC) simulation of light propagation. While conventional MC is suitable mainly for forward modelling, the proposed scheme allows fast routine analysis of experimental data (i.e. solving the inverse problem of light propagation). The paper shows that this White Monte Carlo (WMC) approach significantly improves the performance of TOFS. This includes careful theoretical comparison of MC and conventional diffusion modelling over a range of optical properties of great importance for tissue optics. Thorough experimental investigations using intralipid phantoms and an interstitial configuration verifies the improved performance.

I took initiative to and supervised the diploma project that resulted in this important achievement. I was responsible for the experimental design and took part in the experimental work. I supported and took part in the development of the WMC approach. I wrote major part of the manuscript.

XI **High sensitivity gas spectroscopy of porous, highly scattering solids**
T. Svensson, M. Andersson, L. Rippe, J. Johansson, S. Folestad, and S. Andersson-Engels.
Optics Letters **33**, 80-82 (2008).

This letter reports on significant improvements in GASMAS performance, and presents completely new and important insights in the unique interference effects that limits sensitivity in GASMAS experiments. It also demonstrates dithering methods for efficient interference suppression. The performance improvements are achieved using an optical setup which is significantly simpler than in earlier systems. The setup employs digital data acquisition, as introduced in Paper **IX**.

I was responsible system design and construction. I also performed all experiments, developed Fourier based methods for data evaluation, and wrote the manuscript.

XII **VCSEL-based oxygen spectroscopy for structural analysis of pharmaceutical solids**
T. Svensson, M. Andersson, L. Rippe, S. Svanberg, S. Andersson-Engels, J. Johansson, and S. Folestad.
Applied Physics B **90**, 345-354 (2008).

This article reports on the use of a novel system for GASMAS, also used in Paper **XI**, for characterisation of pharmaceutical solids. This includes extensive investigations of system performance, both in GASMAS and in free space oxygen measurements. The paper also contains the first in depth comparison of GASMAS with photon migration. The excellent covariation between TOFS and GASMAS shows that both techniques are capable of sensing small individual variations between different samples. In addition, the procedures developed for data evaluation are carefully described.

I was responsible for system development, and performed all GASMAS and TOFS experiments. In addition, I developed methods for data evaluation, performed data analysis, and prepared the manuscript. I also took part in the manual manufacturing of the pharmaceutical tablets.

XIII **Towards accurate in vivo spectroscopy of the human prostate**
T. Svensson, E. Alerstam, M. Einarsdóttír, K. Svanberg, and S. Andersson-Engels.
Journal of Biophotonics **1**, in press (2008).

This letter reports on the use of the sophisticated modelling developed in Paper **X** for evaluation of TOFS-based prostate spectroscopy. Due to the relatively high absorption and low scattering of the prostate, this paper shows that diffusion modelling, as used in Paper **VI**, will induce significant errors in derived optical properties. The paper is based on previously unpublished clinical data.

I was responsible for the experimental work, took part in data evaluation, and was responsible for manuscript preparation.

XIV **Improved accuracy in time-resolved diffuse reflectance spectroscopy**
E. Alerstam, S. Andersson-Engels and T. Svensson.
Optics Express **16**, 10434-10448 (2008).

This paper employs the WMC modelling from Paper **X** to enhance the performance of time-resolved diffuse reflectance. Although it was stated in Paper **X** that the WMC approach is applicable to reflectance configurations, that paper only investigated its use in interstitial settings. Careful theoretical analysis shows that time-domain diffusion modelling is inappropriate for certain ranges of optical properties of importance in tissue optics. These findings are verified in careful experiments on the internationally used reference materials utilised in Paper **IV**. Previously experienced artifacts of TOFS is explained and avoided. The presented characterisation of the reference samples is thus an important contribution to the MEDPHOT initiative for performance assessment of photon migration instruments.

I took part in all experimental work, was involved in data evaluation, and made substantial contributions to manuscript preparation.

Acknowledgements

The successful completion of this thesis would not have been possible without professional and personal support from colleagues, friends and family.

First of all, I would like to express my deepest gratitude to my supervisor Prof. Stefan Andersson-Engels. We have done a lot of interesting science together, and your constant encouragement and support of my work have been very important. I also hold the largest respect for all the very hard work you humbly put into our research group. Your efforts have created a truly international and collaborative atmosphere, and have given me the very fortunate opportunity of attending many international conferences throughout Europe and America. In particular, I admire the success you and Prof. Peter Andersen have had in organising the biannual summer school at the Island of Ven here in Sweden. It is a great achievement of yours to have attracted international top scientists to come and closely interact with attending PhD students from all over the world during a full week. Attending was very inspiring.

My strong admiration also goes to my co-supervisor Prof. Sune Svanberg, being an important part in keeping our division an internationally competitive environment in a broad range of physical sciences, forming a very good place for young researchers to develop. Your broad knowledge in physics, combined with a never ending enthusiasm for everything from language to ornithology, is truly appreciated. Warmest of thanks also to my supervisors at Astra Zeneca – Prof. Jonas Johansson and Prof. Staffan Folestad. You have allowed the pharmaceutical projects to evolve in a true scientific spirit, showing your interest in both theoretical, technical and practical aspects. I am also very grateful for continuously support for my way of working. And Jonas, I have truly appreciated your company on our mutual trips to the FACSS conferences in Oregon, Tennessee and Florida. I am also indebted to Prof. Katarina Svanberg. Our collaboration at the clinic concerning prostate spectroscopy has been very rewarding. Besides your professional skills as a medical doctor, oncologist and scientist, I have throughout my time as a PhD student also benefited from your personal

support and caring attitude. I also want to thank Dr. Margrét Einarsdóttír, Jonas Nilsson, Dr. Inger-Lena Lamm and all other members of the brachytherapy team at the Lund University Hospital – both for professional cooperation in our prostate research and for very interesting moments in the operating theatre. I would also like to thank Ass. Prof. Eva Enqvist for giving me the opportunity to teach mathematical statistics at Linköping University before I started my PhD in Lund.

I am overwhelmingly grateful to my technical and scientific mentors Lars Rippe and Mats Andersson, good friends and former colleagues. Thank you for daily interesting discussions and for taking the time to transfer invaluable know-how to a younger PhD student. You have contributed with many ideas of great importance for the work on diode laser spectroscopy presented in this thesis. During the last year, I have also been very fortunate to have worked tightly with my younger and brilliant colleague Erik Alerstam. Your curiosity and creativity, in combination with hard work, have been very important for our recent achievements in time-of-flight spectroscopy. It has been great fun working with you, and you are a good friend.

Special thanks to my former office-mate Ann Johansson. I admire your work, and have appreciated having your laughter around. Christoffer Abrahamsson is acknowledged for collaboration on time-of-flight spectroscopy, as well as for being a good travel companion. Thanks also to Johan Axelsson, Niels Bendsoe, Florian Forster, Thomas Johansson, Jenny Skans, Marcelo Soto-Thompson, Pontus Svenmarker, Johannes Swartling and Nazila Yavari - current and former colleagues - being a part of the scientific and friendly atmosphere of the biomedical optics group. I also wish to acknowledge our Italian colleagues at Polytecnico di Milano, especially Antonio Pifferi and Alessandro Torricelli, for joint experimental collaborations and for sharing their experiences in time-of-flight spectroscopy. Your hospitality during mine and Johannes Swartling's stay in Milan is very much appreciated. Additional thanks goes to the members of the applied molecular spectroscopy group, in which I have been a part time member; Linda Persson for fruitful collaboration and for being a good friend, Rasmus Grönlund for many laughters and nice lunches, and Märta Lewander for friendship and for giving feedback to this thesis. Thanks also to all other personnel of the Division of Atomic Physics, especially Stefan Kröll for nice lunches and interesting discussions, Minna Ramkull and Henrik Steen for helping me with administrative issues, Per Johnsson and his predecessors for developing a nice LaTeXstructure for thesis writing, and Johan Mauritsson for pleasant wine tastings and many nice chats.

It would have been very tough for me to complete this work without the joy spread by good friends. When moving to Malmö, my found new friends and roommates in Anders & Sanna Jälevik,

Anna & Björn Rixman and Kristina Geisler – an important thing for someone who left many good friends in Linköping. My friends from the student time in Linköping remains dear, and their support and encouragement have been invaluable. My oldest university mates Johannes Rytzler, Daniel Tenselius, Martin Svalander and Mikael Sundberg are close to my heart, as are Anders & Darya, Elin & Robert, Erika Nordström, Hanna Mattsson, Lina Vallin, Per Eneqvist, Zara Öberg, ÄjKäj & Micke and many others. Warm thanks also to the brilliant field ornithologist Jesper Segergren and many other birdwatchers who welcomed me into the twitcher community of Skåne. Having ornithology besides my daily work in dark labs and in front of the computer has been important. The trip to Faeroe Islands in October 2006 is a highlight! My generous friends from Åland have also done an important job in helping me keeping one foot outside the Department of Physics. Midsummer celebrations in the beautiful archipelago of Åland, or sailing with wooden tallships like Albanus are always welcome energy injections. Similarly, the many glad moments with Anna Nilsson, Jensa and the other SPREK-girls have been continuous vitamin injections.

I am also infinitely fortunate to have a loyal and warm family. I deeply appreciate the strong encouragement and support offered by my beloved mother and my missed, late father, and my loved siblings Petra, Stefan, Lajla, Martin, Sara and Julia. Likewise, Hanna's family, Tomas & Ann-Sofie Leidstedt, Elin & Gustav, and Gustav, makes life pleasant with their kindness and overwhelming generosity. Tomas & Ann-Sofie's extreme talents in serving great dinners to a tired PhD student is deeply appreciated ...

And finally, my beloved Hanna. You are there even in the hardest of times. If this thesis is some kind of achievement, it is half yours. Thank you for your enormous support.

References

1. J.W.S. Rayleigh. *On the light from the sky, its polarization and colour.* Phil. Mag. **41**, 107–120, 274–279 (1871).

2. J.W.S. Rayleigh. *On the scattering of light by small particles.* Phil. Mag. **41**, 447 (1871).

3. G. Mie. *Beiträge zur Optik trüber Medien, speziell kolloidaler Metallösungen.* Ann. Phys. **330**, 377–445 (1908).

4. P. Lilienfeld. *Gustav Mie: the person.* Appl. Opt. **30**, 4696–4698 (1991).

5. M.I. Mishchenko, L.D. Travis and A.A. Lacis. *Scattering, absorption, and emission of light by small particles.* Cambridge University Press (2002). URL http://www.giss.nasa.gov/~crmim/books.html.

6. C.F. Bohren and D.R. Huffman. *Absorption and scattering of light by small particles.* Wiley (1983).

7. S. Svanberg. *Atomic and molecular spectroscopy.* Springer (2001).

8. A. Schuster. *Radiation through a foggy atmosphere.* Astrophys. J. **21**, 1–22 (1905).

9. W.M. Irvine. *Diffuse reflection and transmission by cloud and dust layers.* J. Quant. Spectrosc. Radiat. Transfer **8**, 471–485 (1968).

10. O. Halpern and R.K. Luneburg. *Multiple scattering of neutrons .2. diffusion in a plate of finite thickness.* Phys. Rev. **76**, 1811–1819 (1949).

11. M.C. Wang and E. Guth. *On the theory of multiple scattering, particularly of charged particles.* Phys. Rev. **84**, 1092–1111 (1951).

12. D.H. Woodward. *He-Ne laser as source for light scattering measurements.* Appl. Opt. **2**, 1205–1207 (1963).

13. D.H. Woodward. *Multiple light scattering by spherical dielectric particles.* J. Opt. Soc. Am. **54**, 1325–1331 (1964).

14. C. Smart, R. Jacobsen, M. Kerker, J.P. Kratohvi and E. Matijevi. *Experimental study of multiple light scattering.* J. Opt. Soc. Am. **55**, 947–955 (1965).

15. A. Beer. *Bestimmung der Absorption des rothen Lichts in farbigen Flüssigkeiten.* Ann. Phys. **162**, 78–88 (1852).

16. J.R. Mourant, T. Fuselier, J. Boyer, T.M. Johnson and I.J. Bigio. *Predictions and measurements of scattering and absorption over broad wavelength ranges in tissue phantoms.* Appl. Opt. **36**, 949–957 (1997).

17. A.M.K. Nilsson, C. Sturesson, D.L. Liu and S. Andersson-Engels. *Changes in spectral shape of tissue optical properties in conjunction with laser-induced thermotherapy.* Appl. Opt. **37**, 1256–1267 (1998).

18. S.T. Flock, B.C. Wilson and M.S. Patterson. *Total attenuation coefficients and scattering phase functions of tissues and phantom materials at 633 nm.* Med. Phys. **14**, 835–841 (1987).

19. R. Drezek, A. Dunn and R. Richards-Kortum. *Light scattering from cells: finite-difference time-domain simulations and goniometric measurements.* Appl. Opt. **38**, 3651–3661 (1999).

20. F.K. Forster, A. Kienle, R. Michels and R. Hibst. *Phase function measurements on nonspherical scatterers using a two-axis goniometer.* J. Biomed. Opt. **11**, 024018 (2006).

21. L.T. Perelman, V. Backman, M. Wallace, G. Zonios, R. Manoharan, A. Nusrat, S. Shields, M. Seiler, C. Lima, T. Hamano, I. Itzkan, J. Van Dam, J.M. Crawford and M.S. Feld. *Observation of periodic fine structure in reflectance from biological tissue: A new technique for measuring nuclear size distribution.* Phys. Rev. Lett. **80**, 627–630 (1998).

22. V. Backman, R. Gurjar, K. Badizadegan, L. Itzkan, R.R. Dasari, L.T. Perelman and M.S. Feld. *Polarized light scattering spectroscopy for quantitative measurement of epithelial cellular structures in situ.* IEEE J. Sel. Top. Quant. **5**, 1019–1026 (1999).

23. V. Backman, M.B. Wallace, L.T. Perelman, J.T. Arendt, R. Gurjar, M.G. Muller, Q. Zhang, G. Zonios, E. Kline, T. McGillican, S. Shapshay, T. Valdez, K. Badizadegan, J.M. Crawford, M. Fitzmaurice, S. Kabani, H.S. Levin, M. Seiler, R.R. Dasari, I. Itzkan, J. Van Dam and M.S. Feld. *Detection of preinvasive cancer cells.* Nature **406**, 35–36 (2000).

24. A. Wax, C.H. Yang, V. Backman, K. Badizadegan, C.W. Boone, R.R. Dasari and M.S. Feld. *Cellular organization and substructure measured using angle-resolved low-coherence interferometry.* Biophys. J. **82**, 2256–2264 (2002).

25. A.H. Taylor. *The measurement of diffuse reflection factors and a new absolute reflectometer.* J. Opt. Soc. Am. **4**, 9 (1920).

26. J.W. Pickering, S.A. Prahl, N. van Wieringen, J.F. Beek, H.J.C.M. Sterenborg and M.J.C. van Gemert. *Double-integrating-sphere system for measuring the optical-properties of tissue.* Appl. Opt. **32**, 399–410 (1993).

27. S.A. Prahl, M.J.C. van Gemert and A.J. Welch. *Determining the optical properties of turbid media by using the adding-doubling method.* Appl. Opt. **32**, 559 (1993).

28. L.H. Wang and S.L. Jacques. *Error estimation of measuring total interaction coefficients of turbid media using collimated light transmission.* Phys. Med. Biol. **39**, 2349–2354 (1994).

29. A.M.K. Enejder. *Light scattering and absorption in tissue - models and measurements.* PhD thesis, Lund University Lund Reports on Atomic Physics, LRAP 219 (1997). URL http://www.atom.fysik.lth.se/medweb/.

30. J. Swartling. *Biomedical and atmospheric applications of optical spectroscopy in scattering media.* PhD thesis, Lund University Lund Reports on Atomic Physics, LRAP 290 (2002). URL http://www.atom.fysik.lth.se/medweb/.

31. T.J. Farrell, M.S. Patterson and B. Wilson. *A diffusion-theory model of spatially resolved, steady-state diffuse reflectance for the noninvasive determination of tissue optical-properties invivo.* Med. Phys. **19**, 879–888 (1992).

32. J.S. Dam, C.B. Pedersen, T. Dalgaard, P.E. Fabricius, P. Aruna and S. Andersson-Engels. *Fiber-optic probe for noninvasive real-time determination of tissue optical properties at multiple wavelengths.* Appl. Opt. **40**, 1155–1164 (2001).

33. A. Kienle, F.K. Forster and R. Hibst. *Influence of the phase function on determination of the optical properties of biological tissue by spatially resolved reflectance.* Opt. Lett. **26**, 1571–1573 (2001).

34. A. Kienle, L. Lilge, M.S. Patterson, R. Hibst, R. Steiner and B.C. Wilson. *Spatially resolved absolute diffuse reflectance measurements for noninvasive determination of the optical scattering and absorption coefficients of biological tissue.* Appl. Opt. **35**, 2304–2314 (1996).

35. A. Dimofte, J.C. Finlay and T.C. Zhu. *A method for determination of the absorption and scattering properties interstitially in turbid media.* Phys. Med. Biol. **50**, 2291–2311 (2005).

36. M.G. Nichols, E.L. Hull and T.H. Foster. *Design and testing of a white-light, steady-state diffuse reflectance spectrometer for determination of optical properties of highly scattering systems.* Appl. Opt. **36**, 93–104 (1997).

37. R.M.P. Doornbos, R. Lang, M.C. Aalders, F.W. Cross and H.J.C.M. Sterenborg. *The determination of in vivo human tissue optical properties and absolute chromophore concentrations using spatially resolved steady-state diffuse reflectance spectroscopy.* Phys. Med. Biol. **44**, 967–981 (1999).

38. F. Bevilacqua, D. Piguet, P. Marquet, J.D. Gross, B.J. Tromberg and C. Depeursinge. *In vivo local determination of tissue optical properties: applications to human brain.* Appl. Opt. **38**, 4939–4950 (1999).

39. L.H. Wang and S.L. Jacques. *Use of a laser-beam with an oblique angle of incidence to measure the reduced scattering coefficient of a turbid medium.* Appl. Opt. **34**, 2362–2366 (1995).

40. S.P. Lin, L.H. Wang, S.L. Jacques and F.K. Tittel. *Measurement of tissue optical properties by the use of oblique-incidence optical fiber reflectometry.* Appl. Opt. **36**, 136–143 (1997).

41. J.R. Mourant, I.J. Bigio, D.A. Jack, T.M. Johnson and H.D. Miller. *Measuring absorption coefficients in small volumes of highly scattering media: source-detector separations for which path lengths do not depend on scattering properties.* Appl. Opt. **36**, 5655–5661 (1997).

42. T.H. Pham, F. Bevilacqua, T. Spott, J.S. Dam, B.J. Tromberg and S. Andersson-Engels. *Quantifying the absorption and reduced scattering coefficients of tissuelike turbid media over a broad spectral range with noncontact Fourier-transform hyperspectral imaging.* Appl. Opt. **39**, 6487–6497 (2000).

43. B. Chance, S. Nioka, J. Kent, K. Mccully, M. Fountain, R. Greenfeld and G. Holtom. *Time-resolved spectroscopy of hemoglobin and myoglobin in resting and ischemic muscle.* Anal. Biochem. **174**, 698–707 (1988).

44. B. Chance, J.S. Leigh, H. Miyake, D.S. Smith, S. Nioka, R. Greenfeld, M. Finander, K. Kaufmann, W. Levy, M. Young, P. Cohen, H. Yoshioka and R. Boretsky. *Comparison of time-resolved and time-unresolved measurements of deoxyhemoglobin in brain.* P. Natl. Acad. Sci. USA **85**, 4971–4975 (1988).

45. M.S. Patterson, B. Chance and B.C. Wilson. *Time resolved reflectance and transmittance for the noninvasive measurement of tissue optical-properties.* Appl. Opt. **28**, 2331–2336 (1989).

46. T. Durduran, A.G. Yodh, B. Chance and D.A. Boas. *Does the photon-diffusion coefficient depend on absorption?* J. Opt. Soc. Am. A **14**, 3358–3365 (1997).

47. E.M. Sevick, B. Chance, J. Leigh, S. Nioka and M. Maris. *Quantitation of time-resolved and frequency-resolved optical-spectra for the determination of tissue oxygenation.* Anal. Biochem. **195**, 330–351 (1991).

48. J.B. Fishkin and E. Gratton. *Propagation of photon-density waves in strongly scattering media containing an absorbing semiinfinite plane bounded by a straight edge.* J. Opt. Soc. Am. A **10**, 127–140 (1993).

49. B.J. Tromberg, L.O. Svaasand, T.T. Tsay and R.C. Haskell. *Properties of photon density waves in multiple-scattering media.* Appl. Opt. **32**, 607–616 (1993).

50. J.B. Fishkin, O. Coquoz, E.R. Anderson, M. Brenner and B.J. Tromberg. *Frequency-domain photon migration measurements of normal and malignant tissue optical properties in a human subject.* Appl. Opt. **36**, 10–20 (1997).

51. B. Chance, M. Cope, E. Gratton, N. Ramanujam and B. Tromberg. *Phase measurement of light absorption and scatter in human tissue.* Rev. Sci. Instr. **69**, 3457–3481 (1998).

52. T.H. Pham, O. Coquoz, J.B. Fishkin, E. Anderson and B.J. Tromberg. *Broad bandwidth frequency domain instrument for quantitative tissue optical spectroscopy.* Rev. Sci. Instr. **71**, 2500–2513 (2000).

53. J.B. Fishkin, S. Fantini, M.J. VandeVen and E. Gratton. *Gigahertz photon density waves in a turbid medium: theory and experiments.* Phys. Rev. E **53**, 2307–2319 (1996).

54. S. Fantini, M.A. Franceschini, J.B. Fishkin, B. Barbieri and E. Gratton. *Quantitative-determination of the absorption-spectra of chromophores in strongly scattering media - a light-emitting-diode based technique.* Appl. Opt. **33**, 5204–5213 (1994).

55. J.R. Mourant, J.P. Freyer, A.H. Hielscher, A.A. Eick, D. Shen and T.M. Johnson. *Mechanisms of light scattering from biological cells relevant to noninvasive optical-tissue diagnostics.* Appl. Opt. **37**, 3586–3593 (1998).

56. J.M. Schmitt and G. Kumar. *Optical scattering properties of soft tissue: a discrete particle model.* Appl. Opt. **37**, 2788–2797 (1998).

57. M. Xu and R.R. Alfano. *Fractal mechanisms of light scattering in biological tissue and cells.* Opt. Lett. **30**, 3051–3053 (2005).

58. T.T. Wu, J.Y. Qu and M. Xu. *Unified Mie and fractal scattering by biological cells and subcellular structures.* Opt. Lett. **32**, 2324–2326 (2007).

59. R. Richards-Kortum and E. Sevick-Muraca. *Quantitative optical spectroscopy for tissue diagnosis.* Annu. Rev. Phys. Chem. **47**, 555–606 (1996).

60. F.P. Bolin, L.E. Preuss, R.C. Taylor and R.J. Ference. *Refractive-index of some mammalian-tissues using a fiber optic cladding method.* Appl. Opt. **28**, 2297–2303 (1989).

61. M. Cope. *The application of near infrared spectroscopy to non invasive monitoring of cerebral oxygenation in the newborn infant.* PhD thesis, University College London (1991). URL http://www.medphys.ucl.ac.uk/research/borl/homepages/mcope/index.htm.

62. H. Mantsch and M. Jackson. *Molecular-spectroscopy in biodiagnostics (from Hippocrates to Herschel and beyond).* J. Mol. Struct. **347**, 187–206 (1995).

63. G.M. Hale and M.R. Querry. *Optical constants of water in 200-nm to 200-μm wavelength region.* Appl. Opt. **12**, 555–563 (1973).

64. S.A. Prahl. Optical absorption of hemoglobin (2006). URL http://omlc.ogi.edu/spectra/hemoglobin/index.html.

65. E. Antonini and M. Brunori. *Hemoglobin and myoglobin in their reactions with ligands.* North-Holland Publishing Company (1971).

66. R.L.P. van Veen, H.J.C.M. Sterenborg, A. Pifferi, A. Torricelli, E. Chikoidze and R. Cubeddu. *Determination of visible near-IR absorption coefficients of mammalian fat using time- and spatially resolved diffuse reflectance and transmission spectroscopy.* J. Biomed. Opt. **10**, 054004 (2005).

67. E.L. Hull and T.H. Foster. *Cytochrome spectroscopy in scattering suspensions containing mitochondria and red blood cells.* Appl. Spectrosc. **55**, 149–154 (2001).

68. S.L. Jacques. Optical absorption of melanin (2008). URL http://omlc.ogi.edu/spectra/melanin/index.html.

69. A.M.K. Nilsson, D. Heinrich, J. Olajos and S. AnderssonEngels. *Near infrared diffuse reflection and laser-induced fluorescence spectroscopy for myocardial tissue characterisation.* Spectrochim. Acta A **53**, 1901–1912 (1997).

70. P. Taroni, D. Comelli, A. Pifferi, A. Torricelli and R. Cubeddu. *Absorption of collagen: effects on the estimate of breast composition and related diagnostic implications.* J. Biomed. Opt. **12**, 014021 (2007).

71. J.A. Parrish. *New concepts in therapeutic photomedicine - photochemistry, optical targeting and the therapeutic window.* J. Invest. Dermatol. **77**, 45–50 (1981).

72. R. Splinter and B.A. Hooper. *An introduction to biomedical optics.* Taylor & Francis (2007).

73. J.L. Boulnois. *Photophysical processes in recent medical laser developments - a review.* Laser Med. Sci. **1**, 47–66 (1986).

74. B.C. Wilson and M.S. Patterson. *The physics of photodynamic therapy.* Phys. Med. Biol. **31**, 327–360 (1986).

75. B.W. Henderson and T.J. Dougherty. *How does photodynamic therapy work.* Photochem. Photobiol. **55**, 145–157 (1992).

76. M. Ochsner. *Photophysical and photobiological processes in the photodynamic therapy of tumours.* J. Photoch. Photobio. B **39**, 1–18 (1997).

77. R.R. Anderson and J.A. Parrish. *Microvasculature can be selectively damaged using dye lasers: a basic theory and experimental evidence in human skin.* Laser Surg. Med. **1**, 263–276 (1981).

78. S.L. Trokel, R. Srinivasan and B. Braren. *Excimer laser-surgery of the cornea.* Am. J. Ophthalmol. **96**, 710–715 (1983).

79. M. S. Kitai, V. L. Popkov, V.A. Semchishen and A.A. Kharizov. *The physics of UV laser cornea ablation.* IEEE J. Quantum Elect. **27**, 302–307 (1991).

80. M.L. Wolbarsht. *Laser surgery - CO_2 or HG.* IEEE J. Quantum Elect. **20**, 1427–1432 (1984).

81. J.T. Walsh, T.J. Flotte, R.R. Anderson and T.F. Deutsch. *Pulsed CO_2-laser tissue ablation - effect of tissue-type and pulse duration on thermal-damage.* Laser Surg. Med. **8**, 108–118 (1988).

82. C.P. Swain, D.W. Storey, T.C. Northfield, S.G. Bown, J.S. Kirkham and P.R. Salmon. *Controlled trial of argon-laser photo-coagulation in bleeding peptic-ulcers.* Lancet **2**, 1313–1316 (1981).

83. A.C. Steger, W.R. Lees, K. Walmsley and S.G. Bown. *Interstitial laser hyperthermia - a new approach to local destruction of tumors.* Brit. Med. J. **299**, 362–365 (1989).

84. E.F. Bernstein. *Laser treatment of tattoos.* Clin. Dermatol. **24**, 43–55 (2006).

85. M.C. Grossman, C. Dierickx, W. Farinelli, T. Flotte and R.R. Anderson. *Damage to hair follicles by normal-mode ruby laser pulses.* J. Am. Acad. Dermatol. **35**, 889–894 (1996).

86. E.V. Ross, Z. Ladin, M. Kreindel and C. Dierickx. *Theoretical considerations in laser hair removal.* Dermatol. Clin. **17**, 333–355 (1999).

87. T. Alster and L. Zaulyanov-Scanlon. *Laser scar revision: A review.* Dermatol. Surg. **33**, 131–140 (2007).

88. M. Essenpreis. *Thermally induced changes in optical properties of biological tissues.* PhD thesis, University College London (1992). URL http://www.medphys.ucl.ac.uk/research/borg/theses.htm.

89. C.M. Moore, I.M. Hoh, S.G. Bown and M. Emberton. *Does photodynamic therapy have the necessary attributes to become a future treatment for organ-confined prostate cancer?* BJU Int. **96**, 754–758 (2005).

90. J.H. Pinthus, A. Bogaards, R. Weersink, B.C. Wilson and J. Trachtenberg. *Photodynamic therapy for urological malignancies: Past to current approaches.* J. Urol. **175**, 1201–1207 (2006).

91. A. Johansson. *Spectroscopic techniques for photodynamic therapy.* PhD thesis, Lund University Lund Reports on Atomic Physics, LRAP 387 (2007). URL http://www.atom.fysik.lth.se/medweb/.

92. G.A. Millikan. *The oximeter, an instrument for measuring continuously the oxygen saturation of arterial blood in man.* Rev. Sci. Instr. **13**, 434–444 (1942).

93. J.F. Kelleher. *Pulse Oximetry.* J. Clin. Monitor. **5**, 37–62 (1989).

94. A. Rice and C.M. Quinn. *Angiogenesis, thrombospondin, and ductal carcinoma in situ of the breast.* J. Clin. athol. **55**, 569–574 (2002).

95. A.P. Gibson, J.C. Hebden and S.R. Arridge. *Recent advances in diffuse optical imaging.* Phys. Med. Biol. **50**, R1–R43 (2005).

96. P. Matousek, E.R.C. Draper, A.E. Goodship, I.P. Clark, K.L. Ronayne and A.W. Parker. *Noninvasive raman spectroscopy of human tissue in vivo.* Appl. Spectrosc. **60**, 758–763 (2006).

97. J. Wu, Y. Wang, L. Perelman, I. Itzkan, R.R. Dasari and M.S. Feld. *3-dimensional imaging of objects embedded in turbid media with fluorescence and raman-spectroscopy.* Appl. Opt. **34**, 3425–3430 (1995).

98. O.S. Khalil. *Spectroscopic and clinical aspects of noninvasive glucose measurements.* Clin. Chem. **45**, 165–177 (1999).

99. D. Huang, E.A. Swanson, C.P. Lin, J.S. Schuman, W.G. Stinson, W. Chang, M.R. Hee, T. Flotte, K. Gregory, C.A. Puliafito and J.G. Fujimoto. *Optical coherence tomography.* Science **254**, 1178–1181 (1991).

100. A.F. Fercher, W. Drexler, C.K. Hitzenberger and T. Lasser. *Optical coherence tomography - principles and applications.* Rep. Prog. Phys. **66**, 239–303 (2003).

101. C.Y. Xu, P.S. Carney and S.A. Boppart. *Wavelength-dependent scattering in spectroscopic optical coherence tomography.* Opt. Express **13**, 5450–5462 (2005).

102. A. Humeau, W. Steenbergen, H. Nilsson and T. Strömberg. *Laser Doppler perfusion monitoring and imaging: novel approaches.* Med. Biol. Eng. Comput. **45**, 421–435 (2007).

103. L. Persson. *Laser Spectroscopy in Scattering Media for Biological and Medical Applications.* PhD thesis, Lund University Lund Reports on Atomic Physics, LRAP 385 (2007).

104. H.G. Brittain, S.J. Bogdanowich, D.E. Bugay, J. Devincentis, G. Lewen and A.W. Newman. *Physical characterization of pharmaceutical solids.* Pharmaceut. Res. **8**, 963–973 (1991).

105. H.G. Brittain, editor. *Physical characterisation of pharmaceutical solids.* volume 70 of *Drugs and the pharmaceutical sciences.* CRC Press (1995).

106. P. Frake, I. Gill, C.N. Luscombe, D.R. Rudd, J. Waterhouse and U.A. Jayasorriya. *Near-infrared mass median particle size determination of lactose monohydrate, evaluating several chemometric approaches.* Analyst **123**, 2043–2046 (1998).

107. D.E. Bugay. *Characterization of the solid-state: spectroscopic techniques.* Adv. Drug Deliver. Rev. **48**, 43–65 (2001).

108. J. Workman, M. Koch and D.J. Veltcamp. *Process analytical chemistry.* Anal. Chem. **75**, 2859–2876 (2003).

109. A. Ishimaru. *Wave propagation and scattering in random media.* Academic Press (1978).

110. A.J. Welch and M.J.C. van Gemert, editors. *Optical-thermal response of laser-irradiated tissue.* Plenum Press (1995).

111. L. Wang and H. Wu. *Biomedical Optics: Principles and Imaging.* Wiley (2007).

112. I.V. Yaroslavsky, A.N. Yaroslavsky, V.V. Tuchin and H.J. Schwarzmaier. *Effect of the scattering delay on time-dependent photon migration in turbid media.* Appl. Opt. **36**, 6529–6538 (1997).

113. S. Willmann, A. Terenji, H. Busse, I.V. Yaroslavsky, A.N. Yaroslavsky, H.J. Schwarzmaier and P. Hering. *Scattering delay time of Mie scatterers determined from steady-state and time-resolved optical spectroscopy.* J. Opt. Soc. Am. A **17**, 745–749 (2000).

114. L.G. Henyey and J.L. Greenstein. *Diffuse radiation in the galaxy.* Astrophys. J. **93**, 70–83 (1941).

115. P.Y. Liu. *A new phase function approximating to Mie scattering for radiative transport-equations.* Phys. Med. Biol. **39**, 1025–1036 (1994).

116. L. Reynolds, C. Johnson and A. Ishimaru. *Diffuse reflectance from a finite blood medium - applications to modeling of fiber optic catheters.* Appl. Opt. **15**, 2059–2067 (1976).

117. K. Furutsu and Y. Yamada. *Diffusion-approximation for a dissipative random medium and the applications.* Phys. Rev. E **50**, 3634–3640 (1994).

118. K. Furutsu. *Pulse wave scattering by an absorber and integrated attenuation in the diffusion approximation.* J. Opt. Soc. Am. A **14**, 267–274 (1997).

119. G. Yoon, A.J. Welch, M. Motamedi and M.C.J. van Gemert. *Development and application of 3-dimensional light-distribution model for laser irradiated tissue.* IEEE J. Quantum Elect. **23**, 1721–1733 (1987).

120. L.T. Perelman, J. Wu, Y. Wang, I. Itzkan, R.R. Dasari and M.S. Feld. *Time-dependent photon migration using path-integrals.* Phys. Rev. E **51**, 6134–6141 (1995).

121. L.C.L. Chin, W.M. Whelan and I.A. Vitkin. *Information content of point radiance measurements in turbid media: implications for interstitial optical property quantification.* Appl. Opt. **45**, 2101–2114 (2006).

122. J.M. Hammersley and D.C. Handscomb. *Monte Carlo methods.* John Wiley & Sons (1964).

123. E.A. Bucher. *Computer-simulation of light pulse propagation for communication through thick clouds.* Appl. Opt. **12**, 2391–2400 (1973).

124. B.C. Wilson and G. Adam. *A Monte Carlo model for the absorption and flux distributions of light in tissue.* Med. Phys. **10**, 824–830 (1983).

125. L.H. Wang, S.L. Jacques and L.Q. Zheng. *MCML Monte Carlo modeling of light transport in multilayered tissues.* Comput. Meth. Prog. Bio. **47**, 131–146 (1995).

126. Using VOXELS in ASAP: modeling fluorescence and volume scatter. Technical report Breault Research Organization (2006).

127. L. Persson, E. Kristensson, L. Simonsson and S. Svanberg. *Monte Carlo simulations related to gas-based optical diagnosis of human sinusitis.* J. Biomed. Opt. **12**, 054002 (2007).

128. S.A. Prahl. *Light Transport in Tissue.* PhD thesis, University of Texas at Austin (1988).

129. S. A. Prahl, M. Keijzer, S. L. Jacques and A. J. Welch. *A Monte Carlo Model of Light Propagation in Tissue.* In G.J. Müller and D.H. Sliney, editors, *SPIE Proceedings of Dosimetry of Laser Radiation in Medicine and Biology* volume IS 5, pages 102–111 (1989).

130. Steven L. Jaques and Lihong Wang. *Monte Carlo modeling of light transport in tissues, optical-thermal response of laser-irradiated tissue* chapter 4, pages 73–100. Plenum Press, New York, USA New York (1995).

131. L. Wang and S.L. Jacques. *Monte Carlo modeling of light transport in multi-layered tissues in standard C* (1998).

132. T. Binzoni, T.S. Leung, A.H. Gandjbakhche, D. Ruefenacht and D.T. Delpy. *The use of the Henyey-Greenstein phase function in Monte Carlo simulations in biomedical optics*. Phys. Med. Biol. **51**, N313–N322 (2006).

133. N.S. Zolek, A. Liebert and R. Maniewski. *Optimization of the Monte Carlo code for modeling of photon migration in tissue*. Comput. Meth. Prog. Bio. **84**, 50–57 (2006).

134. A. Kienle and M.S. Patterson. *Determination of the optical properties of turbid media from a single Monte Carlo simulation*. Phys. Med. Biol. **41**, 2221–2227 (1996).

135. A. Pifferi, R. Berg, P. Taroni and S. Andersson-Engels. *Fitting of Time-resolved reflectance curves with a Monte Carlo model*. In *Trends in optics and Photonics: Advances in Optical Imaging and Photon Migration* volume 2 pages 311–314. Optical Society of America (1996).

136. A. Pifferi, P. Taroni, G. Valentini and S. Andersson-Engels. *Real-time method for fitting time-resolved reflectance and transmittance measurements with a Monte Carlo model*. Appl. Opt. **37**, 2774–2780 (1998).

137. H.W. Jentink, F.F.M. de Mul, R.G.A.M. Hermsen, R. Graaff and J. Greve. *Monte Carlo simulations of laser Doppler blood flow measurements in tissue*. Appl. Opt. **29**, 2371 (1990).

138. J. Swartling, A. Pifferi, A.M.K. Enejder and S. Andersson-Engels. *Accelerated Monte Carlo models to simulate fluorescence spectra from layered tissues*. J. Opt. Soc. Am. A **20**, 714–727 (2003).

139. N. Everall, T. Hahn, P. Matousek, A.W. Parker and M. Towrie. *Photon migration in Raman spectroscopy*. Appl. Spectrosc. **58**, 591–597 (2004).

140. K. Vishwanath and M.A. Mycek. *Time-resolved photon migration in bi-layered tissue models*. Opt. Express **13**, 7466–7482 (2005).

141. L. Marti-Lopez, J.C. Hebden and J.Marti-Lopez Bouza-Dominguez. *Estimates of minimum pulse width and maximum modulation frequency for diffusion optical tomography*. Opt. Laser Eng. **44**, 1172–1184 (2006).

142. R. Graaff, J.G. Aarnoudse, F.F.M. Demul and H.W. Jentink. *Similarity relations for anisotropic scattering in absorbing media*. Opt. Eng. **32**, 244–252 (1993).

143. M. Bassani, F. Martelli, G. Zaccanti and D. Contini. *Independence of the diffusion coefficient from absorption: Experimental and numerical evidence*. Opt. Lett. **22**, 853–855 (1997).

144. T. Nakai, G. Nishimura, K. Yamamoto and M. Tamura. *Expression of optical diffusion coefficient in high-absorption turbid media*. Phys. Med. Biol. **42**, 2541–2549 (1997).

145. R. Graaff and J.J. Ten Bosch. *Diffusion coefficient in photon diffusion theory*. Opt. Lett. **25**, 43–45 (2000).

146. K.M. Yoo, F. Liu and R.R. Alfano. *When does the diffusion-approximation fail to describe photon transport in random-media.* Phys. Rev. Lett. **64**, 2647–2650 (1990).

147. A. Kienle and M.S. Patterson. *Improved solutions of the steady-state and the time-resolved diffusion equations for reflectance from a semi-infinite turbid medium.* J. Opt. Soc. Am. A **14**, 246–254 (1997).

148. R. Cubeddu, A. Pifferi, P. Taroni, A. Torricelli and G. Valentini. *Experimental test of theoretical models for time-resolved reflectance.* Med. Phys. **23**, 1625–1633 (1996).

149. F. Martelli, M. Bassani, L. Alianelli, L. Zangheri and G. Zaccanti. *Accuracy of the diffusion equation to describe photon migration through an infinite medium: numerical and experimental investigation.* Phys. Med. Biol. **45**, 1359–1373 (2000).

150. H. P. Xu, T. J. Farrell and M. S. Patterson. *Investigation of light propagation models to determine the optical properties of tissue from interstitial frequency domain fluence measurements.* J. Biomed. Opt. **11** (2006).

151. V. Venugopalan, J.S. You and B.J. Tromberg. *Radiative transport in the diffusion approximation: An extension for highly absorbing media and small source-detector separations.* Phys. Rev. E **58**, 2395–2407 (1998).

152. S. Chandrasekhar. *Stochastic problems in physics and astronomy.* Rev. Mod. Phys. **15**, 1–89 (1943).

153. G. Eason, A.R. Veitch, R.M. Nisbet and F.W. Turnbull. *Theory of backscattering of light by blood.* J Phys. D Appl. Phys. **11**, 1463–1479 (1978).

154. R.C. Haskell, L.O. Svaasand, T.T. Tsay, T.C. Feng and M.S. Mcadams. *Boundary-conditions for the diffusion equation in radiative-transfer.* J. Opt. Soc. Am. A **11**, 2727–2741 (1994).

155. A.H. Hielscher, S.L. Jacques, L.H. Wang and F.K. Tittel. *The influence of boundary-conditions on the accuracy of diffusion-theory in time-resolved reflectance spectroscopy of biological tissues.* Phys. Med. Biol. **40**, 1957–1975 (1995).

156. S.L. Jacques. *Time-resolved reflectance spectroscopy in turbid tissues.* IEEE T. Biomed. Eng. **36**, 1155–1161 (1989).

157. B.C. Wilson and S.L. Jacques. *Optical reflectance and transmittance of tissues - principles and applications.* IEEE J. Quantum Elect. **26**, 2186–2199 (1990).

158. M.S. Patterson, S. Andersson-Engels, B.C. Wilson and E.K. Osei. *Absorption-spectroscopy in tissue-simulating materials - a theoretical and experimental-study of photon paths.* Appl. Opt. **34**, 22–30 (1995).

159. D. Contini, F. Martelli and G. Zaccanti. *Photon migration through a turbid slab described by a model based on diffusion approximation: I. Theory.* Appl. Opt. **36**, 4587–4599 (1997).

160. S.R. Arridge, M. Schweiger, M. Hiraoka and D.T. Delpy. *A finite-element approach for modeling photon transport in tissue.* Med. Phys. **20**, 299–309 (1993).

161. B.W. Pogue, S. Geimer, T.O. McBride, S.D. Jiang, U.L. Osterberg and K.D. Paulsen. *Three-dimensional simulation of near-infrared diffusion in tissue: boundary condition and geometry analysis for finite-element image reconstruction.* Appl. Opt. **40**, 588–600 (2001).

162. P. Taroni, D. Comelli, A. Farina, A. Pifferi and A. Kienle. *Time-resolved diffuse optical spectroscopy of small tissue samples.* Opt. Express **15**, 3301–3311 (2007).

163. H. Liu, B. Chance, A.H. Hielscher, S.L. Jacques and F.K. Tittel. *Influence of blood-vessels on the measurement of hemoglobin oxygenation as determined by time-resolved reflectance spectroscopy.* Med. Phys. **22**, 1209–1217 (1995).

164. S. Carraresi, S. Tahani, F. Martelli and G. Zaccanti. *Accuracy of a perturbation model to predict the effect of scattering and absorbing inhomogeneities on photon migration.* Appl. Opt. **40**, 4622–4632 (2001).

165. J.C. Schotland, J.C. Haselgrove and J.S. Leigh. *Photon hitting density.* Appl. Opt. **32**, 448–453 (1993).

166. S.R. Arridge. *Photon-measurement density-functions, part 1: analytical forms.* Appl. Spectrosc. **34**, 7395–7409 (1995).

167. A. Einstein. *Über einen die Erzeugung und Verwandlung des Lichtes betreffenden heuristischen Gesichtspunkt.* Ann. Phys. **322**, 132–148 (1905).

168. J.S. Massa, G.S. Gerald Buller, A.C. Walker, S. Cova, M. Umasuthan and A.M. Wallacea. *Time-of-flight optical ranging system based on time-correlated single-photon counting.* Appl. Opt. **37**, 7298–7304 (1998).

169. J. Johansson, S. Folestad, M. Josefson, A. Sparen, C. Abrahamsson, S. Andersson-Engels and S. Svanberg. *Time-resolved NIR/Vis spectroscopy for analysis of solids: Pharmaceutical tablets.* Appl. Spectrosc. **56**, 725–731 (2002).

170. J.A. Weinman and S.T. Shipley. *Effects of multiple-scattering on laser pulses transmitted through clouds.* J. Geophys. Res. **77**, 7123–7128 (1972).

171. E.A. Bucher and R.M. Lerner. *Experiments on light pulse communication and propagation through atmospheric clouds.* Appl. Opt. **12**, 2401–2414 (1973).

172. B.J. Brinkworth. *Pulsed-lidar reflectance of clouds.* Appl. Opt. **12**, 427–428 (1973).

173. J.A. Weinman. *Effects of multiple-scattering on light-pulses reflected by turbid atmospheres.* J. Atmos. Sci. **33**, 1763–1771 (1976).

174. K. Shimizu, A. Ishimaru, L. Reynolds and A.P. Bruckner. *Backscattering of a picosecond pulse from densely distributed scatterers.* Appl. Opt. **18**, 3484–3488 (1979).

175. R. Cubeddu, C. D'Andrea, A. Pifferi, P. Taroni, A. Torricelli, G. Valentini, M. Ruiz-Altisent, C. Valero, C. Ortiz, C. Dover and D. Johnson. *Time-resolved reflectance spectroscopy applied to the nondestructive monitoring of the internal optical properties in apples.* Appl. Spectrosc. **55**, 1368–1374 (2001).

176. F. Chauchard, J.M. Roger, V. Bellon-Maurel, C. Abrahamsson, S. Andersson-Engels and S. Svanberg. *MADSTRESS: A linear approach for evaluating scattering and absorption coefficients of samples measured using time-resolved spectroscopy in reflection.* Appl. Spectrosc. **59**, 1229–1235 (2005).

177. D.V. O'Connor and D. Phillips. *Time-correlated single photon counting.* Academic Press (1984).

178. W. Becker. *Time-correlated single photon counting techniques.* Spinger (2005).

179. F. Schmidt. *Development of a time-resolved optical tomography system for neonatal brain imaging.* PhD thesis, University College London (1999). URL http://www.medphys.ucl.ac.uk/research/borg/theses.htm.

180. A. Pifferi, A. Torricelli, L. Spinelli, D. Contini, R. Cubeddu, F. Martelli, G. Zaccanti, A. Tosi, A.D. Mora, F. Zappa and S. Cova. *Time-resolved diffuse reflectance at small source-detector separation using a time-gated single-photon avalanche diode.* Novel optical instrumentation for biomedical applications III **6631**, B66310 (2007).

181. C. Abrahamsson. *Time-resolved spectroscopy for pharmaceutical applications.* PhD thesis, Lund Unviersity, Lund Reports on Atomic Physics, LRAP 348 (2005). URL http://www.atom.fysik.lth.se/medweb/.

182. A. Pifferi, A. Torricelli, P. Taroni, D. Comelli, A. Bassi and R. Cubeddu. *Fully automated time domain spectrometer for the absorption and scattering characterization of diffusive media.* Rev. Sci. Instr. **78**, 053103 (2007).

183. S. Andersson-Engels, R. Berg, A. Persson and S. Svanberg. *Multispectral tissue characterization with time-resolved detection of diffusely scattered white-light.* Opt. Lett. **18**, 1697–1699 (1993).

184. A. Bassi, J. Swartling, C. D'Andrea, A. Pifferi, A. Torricelli and R. Cubeddu. *Time-resolved spectrophotometer for turbid media based on supercontinuumgeneration in a photonic crystal fiber.* Opt. Lett. **29**, 2405–2407 (2004).

185. D.W. Marquardt. *An algorithm for least-squares estimation of nonlinear parameters.* J. Soc. Indust. Appl. Math. **11**, 431–441 (1963).

186. L. Leonardi and D.H. Burns. *Quantitative constituent measurements in scattering media from statistical analysis of photon time-of-flight distributions.* Anal. Chim. Acta **348**, 543–551 (1997).

187. L. Leonardi and D.H. Burns. *Quantitative measurements in scattering media: Photon time-of-flight analysis with analytical descriptors.* Appl. Spectrosc. **53**, 628–636 (1999).

188. W. Press, S. Teukolsky, W. Vetterling and B. Flannery. *Numerical recipes in C: the art of scientific computing (2nd edition).* Cambridge University Press (1992).

189. N. Shah, A. Cerussi, C. Eker, J. Espinoza, J. Butler, J. Fishkin, R. Hornung and B. Tromberg. *Noninvasive functional optical spectroscopy of human breast tissue.* P. Natl. Acad. Sci. USA **98**, 4420–4425 (2001).

190. A. Pifferi, P. Taroni, A. Torricelli, F. Messina, R. Cubeddu and G. Danesini. *Four-wavelength time-resolved optical mammography in the 680-980-nm range.* Opt. Lett. **28**, 1138–1140 (2003).

191. R. Cubeddu, A. Pifferi, P. Taroni, A. Torricelli and G. Valentini. *Non-invasive absorption and scattering spectroscopy of bulk diffusive media: An application to the optical characterization of human breast.* Appl. Phys. Lett. **74**, 874–876 (1999).

192. A. Pifferi, J. Swartling, E. Chikoidze, A. Torricelli, P. Taroni, A. Bassi, S. Andersson-Engels and R. Cubeddu. *Spectroscopic time-resolved diffuse reflectance and transmittance measurements of the female breast at different interfiber distances.* J. Biomed. Opt. **9**, 1143–1151 (2004).

193. C. Abrahamsson, J. Johansson, S. Andersson-Engels, S. Svanberg and S. Folestad. *Time-resolved NIR spectroscopy for quantitative analysis of intact pharmaceutical tablets.* Anal. Chem. **77**, 1055–1059 (2005).

194. J. Swartling, A. Bassi, C. D'Andrea, A. Pifferi, A. Torricelli and R. Cubeddu. *Dynamic time-resolved diffuse spectroscopy based on supercontinuum light pulses.* Appl. Opt. **44**, 4684–4692 (2005).

195. A. Bassi, A. Farina, C. D'Andrea, A. Pifferi, G. Valentini and R. Cubeddu. *Portable, large-bandwidth time-resolved system for diffuse optical spectroscopy.* Opt. Express **15**, 14482–14487 (2007).

196. P. Taroni, A. Pifferi, A. Torricelli, D. Comelli and R. Cubeddu. *In vivo absorption and scattering spectroscopy of biological tissues.* Photochem. Photobiol. Sci. **2**, 124–129 (2003).

197. B.W. Pogue and M.S. Patterson. *Review of tissue simulating phantoms for optical spectroscopy, imaging and dosimetry.* J. Biomed. Opt. **11**, 041102 (2006).

198. TechNote #202 - Microsphere Aggregation. Technical Report Rev. #002 Active: 8/27/99 Bangs Laboratories (1999).

199. A. Sefkow, M. Bree and M.A. Mycek. *Method for measuring cellular optical absorption and scattering evaluated using dilute cell suspension phantoms.* Appl. Spectrosc. **55**, 1495–1501 (2001).

200. K. Vishwanath, B. Pogue and M.A. Mycek. *Quantitative fluorescence lifetime spectroscopy in turbid media: comparison of theoretical, experimental and computational methods.* Phys. Med. Biol. **47**, 3387–3405 (2002).

201. I. Driver, J.W. Feather, P.R. King and J.B. Dawson. *The optical-properties of aqueous suspensions of intralipid, a fat emulsion.* Phys. Med. Biol. **34**, 1927–1930 (1989).

202. H.J. van Staveren, C.J.M. Moes, J. van Marle, S.A. Prahl and M.J.C. van Gemert. *Light-scattering in intralipid-10-percent in the wavelength range of 400-1100 nm.* Appl. Opt. **30**, 4507–4514 (1991).

203. S.T. Flock, S.L. Jacques, B.C. Wilson, W.M. Star and M.J.C. van Gemert. *Optical-properties of intralipida phantom medium for light-propagation studies.* Laser Surg. Med. **12**, 510–519 (1992).

204. G. Zaccanti, S. Del Bianco and F. Martelli. *Measurements of optical properties of high-density media.* Appl. Opt. **42**, 4023–4030 (2003).

205. R. Cubeddu, A. Pifferi, P. Taroni, A. Torricelli and G. Valentini. *A solid tissue phantom for photon migration studies.* Phys. Med. Biol. **42**, 1971–1979 (1997).

206. R. Michels, F. Foschum and A. Kienle. *Optical properties of fat emulsions.* Opt. Express **16**, 5907–5925 (2008).

207. B.C. Wilson, M.S. Patterson and D.M. Burns. *Effect of photosensitizer concentration in tissue on the penetration depth of photoactivating light.* Laser Med. Sci. **1**, 235–244 (1986).

208. S.T. Flock, B.C. Wilson and M.S. Patterson. *Monte Carlo modeling of light-propagation in highly scattering tissues: II. Comparison with measurements in phantoms.* IEEE T. Biomed. Eng. **36**, 1169–1173 (1989).

209. S.J. Madsen, M.S. Patterson and B.C. Wilson. *The use of india ink as an optical absorber in tissue-simulating phantoms.* Phys. Med. Biol. **37**, 985–993 (1992).

210. L. Spinelli, F. Martelli, A. Farina, A. Pifferi, A. Torricelli, R. Cubeddu and G. Zaccanti. *Calibration of scattering and absorption properties of a liquid diffusive medium at NIR wavelengths. Time-resolved method.* Opt. Express **15**, 6589–6604 (2007).

211. M. Firbank and D.T. Delpy. *A design for a stable and reproducible phantom for use in near-infrared imaging and spectroscopy.* Phys. Med. Biol. **38**, 847–853 (1993).

212. M. Firbank, M. Oda and D.T. Delpy. *An improved design for a stable and reproducible phantom material for use in near-infrared spectroscopy and imaging.* Phys. Med. Biol. **40**, 955–961 (1995).

213. J. Swartling, J. S. Dam and S. Andersson-Engels. *Comparison of spatially and temporally resolved diffuse-reflectance measurement systems for determination of biomedical optical properties.* Appl. Opt. **42**, 4612–4620 (2003).

214. A. Torricelli, D. Contini, L. Spinelli, R. Cubeddu, F. Molteni, S. Ferrante, A. Pedrocchi and G. Ferrigno. *Monitoring muscle metabolic indexes by time-domain near infrared spectroscopy during knee flex-extension induced by functional electrical stimulation.* Diffuse Optical Imaging of Tissue **6629**, 66291L (2007).

215. A. Kienle and R. Hibst. *Light guiding in biological tissue due to scattering.* Phys. Rev. Lett. **97** (2006).

216. A. Kienle, C. Wetzel, A. Bassi, D. Comelli, P. Taroni and A. Pifferi. *Determination of the optical properties of anisotropic biological media using an isotropic diffusion model.* J. Biomed. Opt. **12**, 014026 (2007).

217. M.S. Patterson and B.W. Pogue. *Mathematical-model for time-resolved and frequency-domain fluorescence spectroscopy in biological tissue.* Appl. Opt. **33**, 1963–1974 (1994).

218. B.B. Das, F. Liu and R.R. Alfano. *Time-resolved fluorescence and photon migration studies in biomedical and model random media.* Rep. Prog. Phys. **60**, 227–292 (1997).

219. S. Andersson-Engels, R. Berg, S. Svanberg and O. Jarlman. *Time-resolved transillumination for medical diagnostics.* Opt. Lett. **15**, 1179–1181 (1990).

220. R. Berg, S. Andersson-Engels, O. Jarlman and S. Svanberg. *Time-gated viewing studies on tissuelike phantoms.* Appl. Opt. **35**, 3432–3440 (1996).

221. R. Cubeddu, A. Pifferi, P. Taroni, A. Torricelli and G. Valentini. *Time-resolved imaging on a realistic tissue phantom: mu(s)' and mu(a) images versus time-integrated images.* Appl. Opt. **35**, 4533–4540 (1996).

222. J.C. Hebden and D.T. Delpy. *Enhanced time-resolved imaging with a diffusion model of photon transport.* Opt. Lett. **19**, 311 (1994).

223. F.E.W. Schmidt, M.E. Fry, E.M.C. Hillman, J.C. Hebden and D.T. Delpy. *A 32-channel time-resolved instrument for medical optical tomography.* Rev. Sci. Instr. **71**, 256–265 (2000).

224. E. Hillman. *Experimental and theoretical investigations of near infrared tomographic imaging methods and clinical applications.* PhD thesis, University College London (2002). URL http://www.medphys.ucl.ac.uk/research/borg/theses.htm.

225. F. Gao, H.J. Zhao and Y. Yamada. *Improvement of image quality in diffuse optical tomography by use of full time-resolved data.* Appl. Opt. **41**, 778–791 (2002).

226. A.H. Barnett, J.P. Culver, A.G. Sorensen, A. Dale and D.A. Boas. *Robust inference of baseline optical properties of the human head with three-dimensional segmentation from magnetic resonance imaging.* Appl. Opt. **42**, 3095–3108 (2003).

227. J.C. Hebden, S.R. Arridge and D.T. Delpy. *Optical imaging in medicine: I. Experimental techniques.* Phys. Med. Biol. **42**, 825–840 (1997).

228. C. Dunsby and P.M.W. French. *Techniques for depth-resolved imaging through turbid media including coherence-gated imaging.* J Phys. D Appl. Phys. **36**, R207–R227 (2003).

229. D.A. Boas, D.H. Brooks, E.L. Miller, C.A. DiMarzio, M. Kilmer, R.J. Gaudette and Q. Zhang. *Imaging the body with diffuse optical tomography.* IEEE Signal Proc. Mag. **18**, 57–75 (2001).

230. C. Bremer, V. Ntziachristos and R. Weissleder. *Optical-based molecular imaging: contrast agents and potential medical applications.* Eur. Radiol. **13**, 231–243 (2003).

231. V. Ntziachristos, C. Bremer and R. Weissleder. *Fluorescence imaging with near-infrared light: new technological advances that enable in vivo molecular imaging.* Eur. Radiol. **13**, 195–208 (2003).

232. E.E. Graves, J. Ripoll, R. Weissleder and V. Ntziachristos. *A submillimeter resolution fluorescence molecular imaging system for small animal imaging.* Med. Phys. **30**, 901–911 (2003).

233. D.M. Parkin, F. Bray, J. Ferlay and P. Pisani. *Estimating the world cancer burden: GLOBOCAN 2000.* Int. J. Cancer **94**, 153–156 (2001).

234. M. Cutler. *Transillumination of the breast.* Ann. Surg. **93**, 223–234 (1931).

235. A. Alveryd, I. Andersson, K. Aspegren, G. Balldin, N. Bjurstam, G. Edström, G. Fagerberg, U. Glas, O. Jarlman, S.A. Larsson, E. Lidbrink, H. Lingaas, M. Löfgren, C. M. Rudenstam, L. Strender, L. Samuelsson, L. Tabar, A. Taube, H. Wallberg, P. Åkesson and D. Hallberg. *Lightscanning versus mammography for the detection of breast-cancer in screening and clinical-practice - a swedish multicenter study.* Cancer **65**, 1671–1677 (1990).

236. A.E. Cerussi, D. Jakubowski, N. Shah, F. Bevilacqua, R. Lanning, A.J. Berger, D. Hsiang, J. Butler, R.F. Holcombe and B.J. Tromberg. *Spectroscopy enhances the information content of optical mammography.* J. Biomed. Opt. **7**, 60–71 (2002).

237. A. Torricelli, A. Pifferi, P. Taroni, E. Giambattistelli and R. Cubeddu. *In vivo optical characterization of human tissues from 610 to 1010 nm by time-resolved reflectance spectroscopy.* Phys. Med. Biol. **46**, 2227–2237 (2001).

238. T. Durduran, R. Choe, J.P. Culver, L. Zubkov, M.J. Holboke, J. Giammarco, B. Chance and A.G. Yodh. *Bulk optical properties of healthy female breast tissue.* Phys. Med. Biol. **47**, 2847–2861 (2002).

239. L. Spinelli, A. Torricelli, A. Pifferi, P. Taroni, G. M. Danesini and R. Cubeddu. *Bulk optical properties and tissue components in the female breast from multiwavelength time-resolved optical mammography.* J. Biomed. Opt. **9**, 1137–1142 (2004).

240. N. Shah, A. E. Cerussi, D. Jakubowski, D. Hsiang, J. Butler and B.J. Tromberg. *Spatial variations in optical and, physiological properties of healthy breast tissue.* J. Biomed. Opt. **9**, 534–540 (2004).

241. B.W. Pogue, S.D. Jiang, H. Dehghani, C. Kogel, S. Soho, S. Srinivasan, X.M. Song, T.D. Tosteson, S.P. Poplack and K.D. Paulsen. *Characterization of hemoglobin, water, and NIR scattering in breast tissue: Analysis of intersubject variability and menstrual cycle changes.* J. Biomed. Opt. **9**, 541–552 (2004).

242. J.C. Hebden and H. Rinneberg, editors. *Time-domain optical mammography.* Special issue in Phys. Med. Biol., Institute of Physics Publishing (2005).

243. S. Kukreti, A. Cerussi, B. Tromberg and E. Gratton. *Intrinsic tumor biomarkers revealed by novel double-differential spectroscopic analysis of near-infrared spectra.* J. Biomed. Opt. **12** (2007).

244. V. Ntziachristos, A.G. Yodh, M. Schnall and B. Chance. *Concurrent MRI and diffuse optical tomography of breast after indocyanine green enhancement.* P. Natl. Acad. Sci. USA **97**, 2767–2772 (2000).

245. C.M. Carpenter, B.W. Pogue, S.D. Jiang, H. Dehghani, X. Wang, K.D. Paulsen, W.A. Wells, J. Forero, C. Kogel, J.B. Weaver and S.P. Poplack. *Image-guided optical spectroscopy provides molecular-specific information in vivo: MRI-guided spectroscopy of breast cancer hemoglobin, water, and scatterer size.* Opt. Lett. **32**, 933–935 (2007).

246. K.M. Blackmore, J.A. Knight, R. Jong and L. Lilge. *Assessing breast tissue density by transillumination breast spectroscopy (TIBS): an intermediate indicator of cancer risk.* Brit. J. Radiol. **80**, 545–556 (2007).

247. A. Cerussi, D. Hsiang, N. Shah, R. Mehta, A. Durkin, J. Butler and B.J. Tromberg. *Predicting response to breast cancer neoadjuvant chemotherapy using diffuse optical spectroscopy.* P. Natl. Acad. Sci. USA **104**, 4014–4019 (2007).

248. F.F. Jöbsis. *Noninvasive, infrared monitoring of cerebral and myocardial oxygen sufficiency and circulatory parameters.* Science **198**, 1264–1267 (1977).

249. A.D. Edwards, C. Richardson, M. Cope, J.S. Wyatt, D.T. Delpy and E.O.R. Reynolds. *Cotside measurement of cerebral blood-flow in ill newborn-infants by near-infrared spectroscopy.* Lancet **2**, 770–771 (1988).

250. B. Chance, E. Anday, S. Nioka, S. Zhou, L. Hong, K. Worden, C. Li, T. Murray, Y. Ovetsky, D. Pidikiti and R. Thomas. *A novel method for fast imaging of brain function, non-invasively, with light.* Opt. Express **2**, 411–423 (1998).

251. J.C. Hebden, A. Gibson, R.M. Yusof, N. Everdell, E.M.C. Hillman, D.T. Delpy, S.R. Arridge, T. Austin, J.H. Meek and J.S. Wyatt. *Three-dimensional optical tomography of the premature infant brain.* Phys. Med. Biol. **47**, 4155–4166 (2002).

252. D.T. Delpy, M. Cope, P. Vanderzee, S. Arridge, S. Wray and J. Wyatt. *Estimation of optical pathlength through tissue from direct time of flight measurement.* Phys. Med. Biol. **33**, 1433–1442 (1988).

253. D.A. Benaron, S.R. Hintz, A. Villringer, D. Boas, A. Kleinschmidt, J. Frahm, C. Hirth, H. Obrig, J.C. van Houten, E.L. Kermit, W.F. Cheong and D.K. Stevenson. *Noninvasive functional imaging of human brain using light.* J. Cerebr. Blood F. Met. **20**, 469–477 (2000).

254. J.C. Hebden and T. Austin. *Optical tomography of the neonatal brain.* Eur. Radiol. **17**, 2926–2933 (2007).

255. J. Selb, J.J. Stott, M.A. Franceschini, A.G. Sorensen and D.A. Boas. *Improved sensitivity to cerebral hemodynamics during brain activation with a time-gated optical system: analytical model and experimental validation.* J. Biomed. Opt. **10**, 011013 (2005).

256. D. Comelli, A. Bassi, A. Pifferi, P. Taroni, A. Torricelli, R. Cubeddu, F. Martelli and G. Zaccanti. *In vivo time-resolved reflectance spectroscopy of the human forehead.* Appl. Opt. **46**, 1717–1725 (2007).

257. E. Gratton, V. Toronov, U. Wolf, M. Wolf and A. Webb. *Measurement of brain activity by near-infrared light.* J. Biomed. Opt. **10** (2005).

258. R. Kirby. *Treatment options for early prostate cancer - initial experience with radiofrequency interstitial tumor ablation (RITA) through a transperineal ultrasound-guided approach.* Urology **52**, 948–962 (1998).

259. M. Blanco, J. Coello, H. Iturriaga, S. Maspoch and C. de la Pezuela. *Near-infrared spectroscopy in the pharmaceutical industry.* Analyst **123**, 135R–150R (1998).

260. G. Reich. *Near-infrared spectroscopy and imaging: Basic principles and pharmaceutical applications.* Adv. Drug Deliver. Rev. **57**, 1109–1143 (2005).

261. J. Luypaert, D.L. Massart and Y.V. Heyden. *Near-infrared spectroscopy applications in pharmaceutical analysis.* Talanta **72**, 865–883 (2007).

262. B.F. MacDonald and K.A. Prebble. *Some applications of near-infrared reflectance analysis in the pharmaceutical-industry.* J. Pharmaceut. Biomed. **11**, 1077–1085 (1993).

263. J. Gottfries, H. Depui, M. Fransson, M. Jongeneelen, M. Josefson, F.W. Langkilde and D.T. Witte. *Vibrational spectrometry for the assessment of active substance in metoprolol tablets: A comparison between transmission and diffuse reflectance near-infrared spectrometry.* J. Pharmaceut. Biomed. **14**, 1495–1503 (1996).

264. P. Corti, G. Ceramelli, E. Dreassi and S. Mattii. *Near infrared transmittance analysis for the assay of solid pharmaceutical dosage forms.* Analyst **124**, 755–758 (1999).

265. A. Sparén, M. Malm, M. Josefson, S. Folestad and J. Johansson. *Light leakage effects with different sample holder geometries in quantitative near-infrared transmission spectroscopy of pharmaceutical tablets.* Appl. Spectrosc. **56**, 586–592 (2002).

266. M. Blanco, J. Coello, H. Iturriaga, S. Maspoch and N. Pou. *Influence of the procedure used to prepare the calibration sample set on the performance of near infrared spectroscopy in quantitative pharmaceutical analyses.* Analyst **126**, 1129–1134 (2001).

267. W.F. Long and D.H. Burns. *Particle sizing and optical constant measurement in granular samples using statistical descriptors of photon time-of-flight distributions.* Anal. Chim. Acta **434**, 113–123 (2001).

268. F. Pandozzi and D.H. Burns. *Power law analysis estimates of analyte concentration and particle size in highly scattering granular samples from photon time-of-flight measurements.* Anal. Chem. **79**, 6792–6798 (2007).

269. T.S. Pan and E.M. Sevick-Muraca. *Volume of pharmaceutical powders probed by frequency-domain photon migration measurements of multiply scattered light.* Anal. Chem. **74**, 4228–4234 (2002).

270. Z.G. Sun, S. Torrance, F.K. McNeil-Watson and E.M. Sevick-Muraca. *Application of frequency domain photon migration to particle size analysis and monitoring of pharmaceutical powders.* Anal. Chem. **75**, 1720–1725 (2003).

271. T.S. Pan, S.S. Dali and E.M. Sevick-Muraca. *Evaluation of photon migration using a two speed model for characterization of packed powder beds and dense particulate suspensions.* Opt. Express **13**, 3600–3618 (2005).

272. S.M. Richter and E.M. Sevick-Muraca. *Characterization of concentrated colloidal suspensions using time-dependent photon migration measurements.* Colloid. Surface. A **172**, 163–173 (2000).

273. V. Avetisov. *High-sensitivity high-resolution diode laser spectroscopy in the near-infrared region.* PhD thesis, Lund University, Lund Reports on Atomic Physics, LRAP 189 (1996).

274. C. Banwell and E. McCash. *Fundamentals of molecular spectroscopy.* McGraw-Hill 4th edition (1994).

275. H.D. Babcock and L. Herzberg. *Fine structure of the red system of atmospheric oxygen bands.* Astrophys. J. **108**, 167–190 (1948).

276. J. Reid and A.R.W. Mckellar. *Observation of $S_0(3)$ pure rotational quadrupole transition of H_2 with a tunable diode-laser.* Phys. Rev. A **18**, 224–228 (1978).

277. M.W. Sigrist, R. Bartlome, D. Marinov, J.M. Rey, D.E. Vogler and H. Wächter. *Trace gas monitoring with infrared laser-based detection schemes.* Appl. Phys. B **90**, 289–300 (2008).

278. J.N. Walpole. *Advances in lead salt tunable diode laser performance.* IEEE J. Quantum Elect. **9**, 652–653 (1973).

279. P. Werle, F. Slemr, K. Maurer, R. Kormann, R. Mucke and B. Janker. *Near- and mid-infrared laser-optical sensors for gas analysis.* Opt. Laser Eng. **37**, 101–114 (2002).

280. J.R. Meyer, I. Vurgaftman, R.Q. Yang and L.R. Ram-Mohan. *Type-II and type-I interband cascade lasers.* Electron. Lett. **32**, 45–46 (1996).

281. R.Q. Yang, B.H. Yang, D. Zhang, C.H. Lin, S.J. Murry, H. Wu and S.S. Pei. *High power mid-infrared interband cascade lasers based on type-II quantum wells.* Appl. Phys. Lett. **71**, 2409–2411 (1997).

282. J. Faist, F. Capasso, D.L. Sivco, C. Sirtori, A.L. Hutchinson and A.Y. Cho. *Quantum Cascade Laser*. Science **264**, 553–556 (1994).

283. G. Duxbury, N. Langford, M.T. McCulloch and S. Wright. *Quantum cascade semiconductor infrared and far-infrared lasers: from trace gas sensing to non-linear optics*. Chem. Soc. Rev. **34**, 921–934 (2005).

284. A. Kosterev, G. Wysocki, Y. Bakhirkin, S. So, R. Lewicki, M. Fraser, F. Tittel and R.F. Curl. *Application of quantum cascade lasers to trace gas analysis*. Appl. Phys. B **90**, 165–176 (2008).

285. W.C. Eckhoff, R.S. Putnam, S.X. Wang, R.F. Curl and F.K. Tittel. *A continuously tunable long-wavelength cw IR source for high-resolution spectroscopy and trace-gas detection*. Appl. Phys. B **63**, 437–441 (1996).

286. U. Gustafsson, J. Sandsten and S. Svanberg. *Simultaneous detection of methane, oxygen and water vapour utilising near-infrared diode lasers in conjunction with difference-frequency generation*. Appl. Phys. B **71**, 853–857 (2000).

287. D. Richter and P. Weibring. *Ultra-high precision mid-IR spectrometer I: Design and analysis of an optical fiber pumped difference-frequency generation source*. Appl. Phys. B **82**, 479–486 (2006).

288. P. Weibring, D. Richter, A. Fried, J.G. Walega and C. Dyroff. *Ultra-high-precision mid-IR spectrometer II: system description and spectroscopic performance*. Appl. Phys. B **85**, 207–218 (2006).

289. A.K.Y. Ngai, S.T. Persijn, G. Von Basum and F.J.M. Harren. *Automatically tunable continuous-wave optical parametric oscillator for high-resolution spectroscopy and sensitive trace-gas detection*. Appl. Phys. B **85**, 173–180 (2006).

290. H. Leinen, D. Glassner, H. Metcalf, R. Wynands, D. Haubrich and D. Meschede. *GaN blue diode lasers: a spectroscopist's view*. Appl. Phys. B **70**, 567–571 (2000).

291. J. Alnis, U. Gustafsson, G. Somesfalean and S. Svanberg. *Sum-frequency generation with a blue diode laser for mercury spectroscopy at 254 nm*. Appl. Phys. Lett. **76**, 1234–1236 (2000).

292. T.N. Anderson, R.P. Lucht, S. Priyadarsan, K. Annamalai and J.A. Caton. *In situ measurements of nitric oxide in coal-combustion exhaust using a sensor based on a widely tunable external-cavity GaN diode laser*. Appl. Opt. **46**, 3946–3957 (2007).

293. J. Shao, L. Lathdavong, P. Thavixay and O. Axner. *Detection of nitric oxide at low ppb·m concentrations by differential absorption spectrometry using a fully diode-laser-based ultraviolet laser system*. J. Opt. Soc. Am. B **24**, 2294–2306 (2007).

294. R.T. Ku, E.D. Hinkley and J.O. Sample. *Long-path monitoring of atmospheric carbon-monoxide with a tunable diode laser system*. Appl. Opt. **14**, 854–861 (1975).

295. J. Reid, J. Shewchun, B.K. Garside and E.A. Ballik. *High sensitivity pollution detection employing tunable diode-lasers*. Appl. Opt. **17**, 300–307 (1978).

296. C.R. Webster, R.D. May, C.A. Trimble, R.G. Chave and J. Kendall. *Aircraft (ER-2) laser infrared-absorption spectrometer (ALIAS) for in-situ stratospheric measurements of HCl, N_2O, CH_4, NO_2, and HNO_3*. Appl. Opt. **33**, 454–472 (1994).

297. G.W. Sachse, G.F. Hill, L.O. Wade and M.G. Perry. *Fast-response, high-precision carbon-monoxide sensor using a tunable diode-laser absorption technique.* J. Geophys. Res. Atmos. **92**, 2071–2081 (1987).

298. I. Linnerud, P. Kaspersen and T. Jæger. *Gas monitoring in the process industry using diode laser spectroscopy.* Appl. Phys. B **67**, 297–305 (1998).

299. D.E. Vogler and M.W. Sigrist. *Near-infrared laser based cavity ringdown spectroscopy for applications in petrochemical industry.* Appl. Phys. B **85**, 349–354 (2006).

300. H. Gieseler, W.J. Kessler, M. Finson, S.J. Davis, P.A. Mulhall, V. Bons, D.J. Debo and M.J. Pikal. *Pharmaceutical technology - Evaluation of tunable diode laser absorption spectroscopy for in-process water vapor mass flux measurements during freeze drying.* J. Pharm. Sci. **96**, 1776–1793 (2007).

301. K.G. Sulzmann, J.E.L. Lowder and S.S. Penner. *Estimates of possible detection limits for combustion intermediates and products with line-center absorption and derivative spectroscopy using tunable lasers.* Combust. Flame **20**, 177–191 (1973).

302. R.K. Hanson, P.A. Kuntz and C.H. Kruger. *High-resolution spectroscopy of combustion gases using a tunable ir diode-laser.* Appl. Opt. **16**, 2045–2048 (1977).

303. J. Wang, M. Maiorov, D.S. Baer, D.Z. Garbuzov, J.C. Connolly and R.K. Hanson. *In situ combustion measurements of CO with diode-laser absorption near 2.3 mu m.* Appl. Opt. **39**, 5579–5589 (2000).

304. E. Schlosser, T. Fernholz, H. Teichert and V. Ebert. *In situ detection of potassium atoms in high-temperature coal-combustion systems using near-infrared-diode lasers.* Spectrochim. Acta A **58**, 2347–2359 (2002).

305. E. Schlosser, J. Wolfrum, L. Hildebrandt, H. Seifert, B. Oser and V. Ebert. *Diode laser based in situ detection of alkali atoms: development of a new method for determination of residence-time distribution in combustion plants.* Appl. Phys. B **75**, 237–247 (2002).

306. R.E. Baren, M.E. Parrish, K.H. Shafer, C.N. Harward, S. Quan, D.D. Nelson, J.B. McManus and M.S. Zahniser. *Quad quantum cascade laser spectrometer with dual gas cells for the simultaneous analysis of mainstream and sidestream cigarette smoke.* Spectrochim. Acta A **60**, 3437–3447 (2004).

307. G.B. Rieker, X. Liu, H. Li, J.B. Jeffries and R.K. Hanson. *Measurements of near-IR water vapor absorption at high pressure and temperature.* Appl. Phys. B **87**, 169–178 (2007).

308. I.J. Simpson, G.W. Thurtell, G.E. Kidd, M. Lin, T.H. Demetriadesshah, I.D. Flitcroft, E.T. Kanemasu, D. Nie, K.F. Bronson and H.U. Neue. *Tunable diode-laser measurements of methane fluxes from an irrigated rice paddy field in the philippines.* J. Geophys. Res. Atmos. **100**, 7283–7290 (1995).

309. D.R. Bowling, S.D. Sargent, B.D. Tanner and J.R. Ehleringer. *Tunable diode laser absorption spectroscopy for stable isotope studies of ecosystem-atmosphere CO_2 exchange.* Agr. Forest Meteorol. **118**, 1–19 (2003).

310. E. Pattey, I. B. Strachan, R.L. Desjardins, G.C. Edwards, D. Dow and J.I. MacPherson. *Application of a tunable diode laser to the measurement of CH_4 and N_2O fluxes from field to landscape scale using several micrometeorological techniques.* Agr. Forest Meteorol. **136**, 222–236 (2006).

311. J. Zhang, T.J. Griffis and J.M. Baker. *Using continuous stable isotope measurements to partition net ecosystem CO_2 exchange.* Plant Cell Environ. **29**, 483–496 (2006).

312. A. Castrillo, G. Casa, M. van Burgel, D. Tedesco and L. Gianfrani. *First field determination of the C-13/C-12 isotope ratio in volcanic CO2 by diode-laser spectrometry.* Opt. Express **12**, 6515–6523 (2004).

313. A.G. Berezin, S.L. Malyugin, A.I. Nadezhdinskii, D.Y. Namestnikov, Y.Y. Ponurovskii, D.B. Stavrovskii, Y.P. Shapovalov, I.E. Vyazov, V.Y. Zaslavskii, Y.G. Selivanov, N.M. Gorshunov, G.Y. Grigoriev and S.S. Nabiev. *UF6 enrichment measurements using TDLS techniques.* Spectrochim. Acta A **66**, 796–802 (2007).

314. L.G. Sandström, S.H. Lundqvist, A.B. Petterson and M.S. Shumate. *Tunable diode laser spectroscopy at 1.6 and 2 μm for detection of Helicobacter pylori infection using C-13-urea breath test.* IEEE J. Sel. Top. Quant. **5**, 1040–1048 (1999).

315. L. Menzel, A.A. Kosterev, R.F. Curl, F.K. Tittel, C. Gmachl, F. Capasso, D.L. Sivco, J.N. Baillargeon, A.L. Hutchinson, A.Y. Cho and W. Urban. *Spectroscopic detection of biological NO with a quantum cascade laser.* Appl. Phys. B **72**, 859–863 (2001).

316. M.R. McCurdy, Y.A. Bakhirkin and F.K. Tittel. *Quantum cascade laser-based integrated cavity output spectroscopy of exhaled nitric oxide.* Appl. Phys. B **85**, 445–452 (2006).

317. D. Marinov, J.M. Rey, M.G. Muller and M.W. Sigrist. *Spectroscopic investigation of methylated amines by a cavity-ringdown-based spectrometer.* Appl. Opt. **46**, 3981–3986 (2007).

318. G.B. Rieker, H. Li, X. Liu, J.B. Jeffries, R.K. Hanson, M.G. Allen, S.D. Wehe, P.A. Mulhall and H.S. Kindle. *A diode laser sensor for rapid, sensitive measurements of gas temperature and water vapour concentration at high temperatures and pressures.* Meas. Sci. Technol. **18**, 1195–1204 (2007).

319. A. Lytkine, A. Lim, W. Jäger and J. Tulip. *Gas temperature measurements using widely tunable long-wavelength VCSEL.* Appl. Phys. B **90**, 323–327 (2008).

320. J.F. Becker, T.B. Sauke and M. Loewenstein. *Stable isotope analysis using tunable diode-laser spectroscopy.* Appl. Opt. **31**, 1921–1927 (1992).

321. S.K. Loh and J.M. Jasinski. *Direct kinetic-studies of SiH_3+SiH_3, H, CCl_4, SiD_4, Si_2H_6, and C_3H_6 by tunable infrared diode-laser spectroscopy.* J. Chem. Phys. **95**, 4914–4926 (1991).

322. M. Haverlag, E. Stoffels, W.W. Stoffels, G.M.W. Kroesen and F.J. deHoog. *Measurement of the gas temperature in fluorocarbon radio frequency discharges using infrared absorption spectroscopy.* J. Vac. Sci. Technol. A **14**, 380–383 (1996).

323. J. Ropcke, L. Mechold, M. Kaning, J. Anders, F.G. Wienhold, D. Nelson and M. Zahniser. *IRMA: A tunable infrared multicomponent acquisition system for plasma diagnostics.* Rev. Sci. Instr. **71**, 3706–3710 (2000).

324. F. Hempel, P.B. Davies, D. Loffhagen, L. Mechold and J. Röpcke. *Diagnostic studies of H_2-Ar-N_2 microwave plasmas containing methane or methanol using tunable infrared diode laser absorption spectroscopy.* Plasma Sources Sci. T. **12**, S98–S110 (2003).

325. S. Kim, P. Klimecky, J.B. Jeffries, F.L. Terry and R.K. Hanson. *In situ measurements of HCl during plasma etching of poly-silicon using a diode laser absorption sensor.* Meas. Sci. Technol. **14**, 1662–1670 (2003).

326. G. Lombardi, K. Hassouni, F. Benedic, F. Mohasseb, J. Röpcke and A. Gicquel. *Spectroscopic diagnostics and modeling of Ar/H-2/CH4 microwave discharges used for nanocrystalline diamond deposition.* J. Appl. Phys. **96**, 6739–6751 (2004).

327. R.S. Eng, J.F. Butler and K.J. Linden. *Tunable diode-laser spectroscopy - an invited review.* Opt. Eng. **19**, 945–960 (1980).

328. E.D. Hinkley. *Laser spectroscopic instrumentation and techniques - long-path monitoring by resonance-absorption.* Opt. Quant. Electron. **8**, 155–167 (1976).

329. M.G. Allen. *Diode laser absorption sensors for gas-dynamic and combustion flows.* Meas. Sci. Technol. **9**, 545–562 (1998).

330. P.A. Martin. *Near-infrared diode laser spectroscopy in chemical process and environmental air monitoring.* Chem. Soc. Rev. **31**, 201–210 (2002).

331. J. Röpcke, G. Lombardi, A. Rousseau and P.B. Davies. *Application of mid-infrared tuneable diode laser absorption spectroscopy to plasma diagnostics: a review.* Plasma Sources Sci. T. **15**, S148–S168 (2006).

332. A.W. Mantz. *A review of the applications of tunable diode-laser spectroscopy at high-sensitivity.* Microchem. J. **50**, 351–364 (1994).

333. A. Zybin, J. Koch, H.D. Wizemann, J. Franzke and K. Niemax. *Diode laser atomic absorption spectrometry.* Spectrochim. Acta B **60**, 1–11 (2005).

334. G. Galbacs. *A review of applications and experimental improvements related to diode laser atomic spectroscopy.* Appl. Spectrosc. Rev. **41**, 259–303 (2006).

335. A.A. Bol'shakov, A.A. Ganeev and V.M. Nemets. *Prospects in analytical atomic spectrometry.* Uspekhi Khimii **75**, 322–338 (2006).

336. P. Werle. *A review of recent advances in semiconductor laser based gas monitors.* Spectrochim. Acta A **54**, 197–236 (1998).

337. K. Song and E. C. Jung. *Recent Developments in Modulation Spectroscopy for Trace Gas Detection Using Tunable Diode Lasers.* Appl. Spectrosc. Rev. **38**, 395–432 (2003).

338. K.L. McNesby, R.T. Wainner, R.G. Daniel, A.W. Miziolek, W.M. Jackson and I.A. McLaren. *High-sensitivity laser absorption measurements of broadband absorbers in the near-infrared spectral region.* Appl. Opt. **39**, 5006–5011 (2000).

339. W.Q. Cao and Y.X. Duan. *Current status of methods and techniques for breath analysis.* Crit. Rev. Anal. Chem. **37**, 3–13 (2007).

340. L.S. Rothman, C.P. Rinsland, A. Goldman, S.T. Massie, D.P. Edwards, J.M. Flaud, A. Perrin, C. Camy-Peyret, V. Dana, J.Y. Mandin, J. Schroeder, A. McCann, R.R. Gamache, R.B. Wattson, K. Yoshino, K.V. Chance, K.W. Jucks, L.R. Brown, V. Nemtchinov and P. Varanasi. *The HITRAN molecular spectroscopic database and HAWKS (HITRAN Atmospheric Workstation): 1996 edition.* J. Quant. Spectrosc. Radiat. Transfer **60**, 665–710 (1998).

341. C. Zender. Radiative transfer in the earth system (2008). URL http://dust.ess.uci.edu/facts.

342. D.E. Jennings. *Absolute line strengths in ν_4, $^{12}CH_4$: a dual-beam diode-laser spectrometer with sweep integration.* Appl. Opt. **19**, 2695–2700 (1980).

343. B. Anderson and R.J. Brecha. *Tunable diode laser absorption measurement of oxygen A-band line strengths.* Appl. Phys. B **87**, 379–385 (2007).

344. W. Voigt. Sitzungsber. K. Bayerische Akad. Wiss. **42**, 603–620 (1912).

345. J. Humlicek. *Optimized computation of the Voigt and complex probability functions.* J. Quant. Spectrosc. Radiat. Transfer **27**, 437–444 (1982).

346. J.J. Olivero and R.L. Longbothum. *Empirical fits to Voigt line-width - brief review.* J. Quant. Spectrosc. Radiat. Transfer **17**, 233–236 (1977).

347. R.H. Dicke. *The effect of collisions upon the Doppler width of spectral lines.* Phys. Rev. **89**, 472–473 (1953).

348. F. Herbert. *Spectrum line-profiles - generalized Voigt function including collisional narrowing.* J. Quant. Spectrosc. Radiat. Transfer **14**, 943–951 (1974).

349. L. Galatry. *Simultaneous effect of Doppler and foreign gas broadening on spectral lines.* Phys. Rev. **122**, 1218–1223 (1961).

350. S.G. Rautian and I.I. Sobelman. *Effect of collisions on Doppler broadening of spectral lines.* Sov. Phys. Usp. **9**, 701– (1967).

351. K.J. Ritter and T.D. Wilkerson. *High-resolution spectroscopy of the oxygen A-band.* J. Mol. Spectrosc. **121**, 1–19 (1987).

352. M.W. Sigrist, editor. *Air monitoring by spectroscopic techniques.* Wiley (1994).

353. A.L. Buck. *New equations for computing vapor-pressure and enhancement factor.* J. Appl. Meteorol. **20**, 1527–1532 (1981).

354. J.U. White. *Long optical paths of large aperture.* J. Opt. Soc. Am. **32**, 285–288 (1942).

355. J.U. White. *Very long optical paths in air.* J. Opt. Soc. Am. **66**, 411–416 (1976).

356. D. Herriott, R. Kompfner and H. Kogelnik. *Off-axis paths in spherical mirror interferometers.* Appl. Opt. **3**, 523–526 (1964).

357. D.R. Herriott and H.J. Schulte. *Folded optical delay lines.* Appl. Opt. **4**, 883–889 (1965).

358. S. Tranchart, I.H. Bachir and J.L. Destombes. *Sensitive trace gas detection with near-infrared laser diodes and an integrating sphere.* Appl. Opt. **35**, 7070–7074 (1996).

359. E. Hawe, P. Chambers, C. Fitzpatrick and E. Lewis. *CO_2 monitoring and detection using an integrating sphere as a multipass absorption cell.* Meas. Sci. Technol. **18**, 3187–3194 (2007).

360. E.D. Hinkley. *High-resolution infrared spectroscopy with a tunable diode laser.* Appl. Phys. Lett. **16**, 351–354 (1970).

361. D.T. Cassidy and J. Reid. *Harmonic detection with tunable diode-lasers - 2-tone modulation.* Appl. Phys. B **29**, 279–285 (1982).

362. K. Kaufmann. *Choosing your detector.* SPIE's oemagazine pages 25–27 (2005).

363. P.C.D. Hobbs. *Building electro-optical systems - making it all work.* John Wiley & Sons (2000).

364. K. Haller and P. Hobbs. *Double beam laser absorption spectroscopy: shot-noise limited performance at baseband with a novel electronic noise canceller.* Proc. SPIE **1435**, 298–309 (1991).

365. P. Hobbs. *Ultrasensitive laser measurements without tears.* Appl. Opt. **36**, 903–920 (1997).

366. V. Liger, A. Zybin, Y. Kuritsyn and K. Niemax. *Diode-laser atomic-absorption spectrometry by the double-beam-double-modulation technique.* Spectrochim. Acta B **52**, 1125–1138 (1997).

367. P. Vogel and V. Ebert. *Near shot noise detection of oxygen in the A-band with vertical-cavity surface-emitting lasers.* Appl. Phys. B **72**, 127–135 (2001).

368. M.G. Allen, K.L. Carleton, S.J. Davis, W.J. Kessler, C.E. Otis, D.A. Palombo and D.M. Sonnenfroh. *Ultrasensitive dual-beam absorption and gain spectroscopy - applications for near-infrared and visible diode-laser sensors.* Appl. Opt. **34**, 3240–3249 (1995).

369. P. Werle, F. Slemr, M. Gehrtz and C. Brauchle. *Wideband noise characteristics of a lead-salt diode-laser - possibility of quantum noise limited tdlas performance.* Appl. Opt. **28**, 1638–1642 (1989).

370. P. Werle. *Laser excess noise and interferometric effects in frequency-modulated diode-laser spectrometers.* Appl. Phys. B **60**, 499–506 (1995).

371. A.G. Bell. *On the production and reproduction of sound by light.* Am. J. Sci. **20**, 305–324 (1880).

372. G.A. West, J.J. Barrett, D.R. Siebert and K.V. Reddy. *Photo-acoustic spectroscopy.* Rev. Sci. Instr. **54**, 797–817 (1983).

373. M.E. Webber, M. Pushkarsky and C.K.N. Patel. *Fiber-amplifier-enhanced photoacoustic spectroscopy with near-infrared tunable diode lasers.* Appl. Opt. **42**, 2119–2126 (2003).

374. A. A. Kosterev, F. K. Tittel, D. V. Serebryakov, A. L. Malinovsky and I. V. Morozov. *Applications of quartz tuning forks in spectroscopic gas sensing.* Rev. Sci. Instr. **76**, 043105 (2005).

375. A. Miklos, P. Hess and Z. Bozoki. *Application of acoustic resonators in photoacoustic trace gas analysis and metrology.* Rev. Sci. Instr. **72**, 1937–1955 (2001).

376. A.A. Kosterev, Y.A. Bakhirkin, R.F. Curl and F.K. Tittel. *Quartz-enhanced photoacoustic spectroscopy.* Opt. Lett. **27**, 1902–1904 (2002).

377. A. A. Kosterev, Y. A. Bakhirkin and F. K. Tittel. *Ultrasensitive gas detection by quartz-enhanced photoacoustic spectroscopy in the fundamental molecular absorption bands region*. Appl. Phys. B **80**, 133–138 (2005).

378. T. Laurila, H. Cattaneo, V. Koskinen, J. Kauppinen and R. Hernberg. *Diode laser-based photoacoustic spectroscopy with interferometrically-enhanced cantilever detection*. Opt. Express **13**, 2453–2458 (2005).

379. D. Romanini, A.A. Kachanov and F. Stoeckel. *Diode laser cavity ring down spectroscopy*. Chem. Phys. Lett. **270**, 538–545 (1997).

380. G. Berden, R. Peeters and G. Meijer. *Cavity ring-down spectroscopy: Experimental schemes and applications*. Int. Rev. Phys. Chem. **19**, 565–607 (2000).

381. R. Engelbrecht. *A compact NIR fiber-optic diode laser spectrometer for CO and CO_2: analysis of observed 2f wavelength modulation spectroscopy line shapes*. Spectrochim. Acta A **60**, 3291–3298 (2004).

382. G. Stewart, A. Mencaglia, W. Philp and W. Jin. *Interferometric signals in fiber optic methane sensors with wavelength modulation of the DFB laser source*. J. Lightwave Technol. **16**, 43–53 (1998).

383. J. Reid, M. Elsherbiny, B.K. Garside and E.A. Ballik. *Sensitivity limits of a tunable diode-laser spectrometer, with application to the detection of NO_2 at the 100-ppt level*. Appl. Opt. **19**, 3349–3354 (1980).

384. M. Fukuda, S. Ooyama, A. Utsumi, Y. Kondo, T. Kurosaki and T. Masuda. *Effect of optical feedback noise on tunable diode laser spectroscopy*. Appl. Phys. B **90**, 269–272 (2008).

385. J. A. Silver. *Frequency-modulation spectroscopy for trace species detection: theory and comparison among experimental methods*. Appl. Opt. **31**, 707–717 (1992).

386. E.I. Moses and C.L. Tang. *High-sensitivity laser wavelength-modulation spectroscopy*. Opt. Lett. **1**, 115– (1977).

387. M. Gehrtz, G.C. Bjorklund and E.A. Whittaker. *Quantum-limited laser frequency-modulation spectroscopy*. J. Opt. Soc. Am. B **2**, 1510–1526 (1985).

388. C.B. Carlisle and D.E. Cooper. *Tunable-diode-laser frequency-modulation spectroscopy using balanced homodyne detection*. Opt. Lett. **14**, 1306– (1989).

389. P. Hobbs. *Shot noise limited optical measurements at baseband with noisy lasers*. Proc. SPIE **1376**, 216–221 (1990).

390. L. Persson, K. Svanberg and S. Svanberg. *On the potential of human sinus cavity diagnostics using diode laser gas spectroscopy*. Appl. Phys. B **82**, 313–317 (2006).

391. D.T. Cassidy and J. Reid. *Atmospheric-pressure monitoring of trace gases using tunable diode-lasers*. Appl. Opt. **21**, 1185–1190 (1982).

392. J.B. McManus and P.L. Kebabian. *Narrow optical interference-fringes for certain setup conditions in multipass absorption cells of the herriott type*. Appl. Opt. **29**, 898–900 (1990).

393. C.D. Mansfield and H.N. Rutt. *Evaluation of multiple beam interference effects in infrared gas spectroscopy*. Meas. Sci. Technol. **10**, 206–210 (1999).

394. D. Masiyano, J. Hodgkinson and R.P. Tatam. *Use of diffuse reflections in tunable diode laser absorption spectroscopy: implications of laser speckle for gas absorption measurements.* Appl. Phys. B pages – (2008).

395. C.R. Webster. *Brewster-plate spoiler - a novel method for reducing the amplitude of interference-fringes that limit tunable-laser absorption sensitivities.* J. Opt. Soc. Am. B **2**, 1464–1470 (1985).

396. J.A. Silver and A.C. Stanton. *Optical interference fringe reduction in laser-absorption experiments.* Appl. Opt. **27**, 1914–1916 (1988).

397. A. Fried, J.R. Drummond, B. Henry and J. Fox. *Reduction of interference-fringes in small multipass absorption cells by pressure modulation.* Appl. Opt. **29**, 900–902 (1990).

398. D.S. Bomse, Stanton A.C. and J.A. Silver. *Frequency modulation and wavelength modulation spectroscopies: comparison experimental methods using a lead-salt diode laser.* Appl. Opt. **31**, 718–731 (1992).

399. L.G. Wang, D.A. Tate, H. Riris and T.F. Gallagher. *High-sensitivity frequency-modulation spectroscopy with a GaAlAs diode laser.* J. Opt. Soc. Am. B **6**, 871–876 (1989).

400. V.G. Avetisov and P. Kauranen. *High-resolution absorption measurements by use of two-tone frequency-modulation spectroscopy with diode lasers.* Appl. Opt. **36**, 4043–4054 (1997).

401. T. Iguchi. *Modulation wave-forms for 2nd-harmonic detection with tunable diode-lasers.* J. Opt. Soc. Am. B **3**, 419–423 (1986).

402. N.Y. Chou, G.W. Sachse, L.G. Wang and T.F. Gallagher. *Optical fringe reduction technique for FM spectroscopy laser spectroscopy.* Appl. Opt. **28**, 4973–4975 (1989).

403. H.C. Sun and E.A. Whittaker. *Novel etalon fringe rejection technique for laser-absorption spectroscopy.* Appl. Opt. **31**, 4998–5002 (1992).

404. D.E. Cooper and C.B. Carlisle. *High-sensitivity FM spectroscopy spectroscopy with a lead-salt diode-laser.* Opt. Lett. **13**, 719–721 (1988).

405. C.B. Carlisle, D.E. Cooper and H. Preier. *Quantum noise-limited FM spectroscopy spectroscopy with a lead-salt diode-laser.* Appl. Opt. **28**, 2567–2576 (1989).

406. H. Riris, C.B. Carlisle, R.E. Warren and D.E. Cooper. *Signal-to-noise ratio enhancement in frequency-modulation spectrometers by digital signal-processing.* Opt. Lett. **19**, 144–146 (1994).

407. P. Werle, R. Miicke and F. Slemr. *The limits of signal averaging in atmospheric trace-gas monitoring by tunable diode-laser absorption spectroscopy (TDLAS).* Appl. Phys. B **57**, 131–139 (1993).

408. C. Dyroff, P. Weibring, A. Fried, D. Richter, J. G. Walega, A. Zahn, W. Freude and P. Werle. *Stark-enhanced diode-laser spectroscopy of formaldehyde using a modified Herriott-type multipass cell.* Appl. Phys. B **88**, 117–123 (2007).

409. H.E. Hunziker. *New technique for gas-phase kinetic spectroscopy of molecules in triplet state.* IBM J. Res. Dev. **15**, 10–& (1971).

410. M.J. Kavaya, J.S. Margolis and M.S. Shumate. *Optoacoustic detection using Stark modulation.* Appl. Opt. **18**, 2602– (1979).

411. E. A. Whittaker, H. R. Wendt, H. E. Hunziker and G. C. Bjorklund. *Laser FM spectroscopy spectroscopy with photochemical modulation - a sensitive, high-resolution technique for chemical intermediates.* Appl. Phys. B **35**, 105–111 (1984).

412. H. Sauren, D. Bicanic, W. Hillen, H. Jalink, K. van Asselt, J. Quist and J. Reuss. *Resonant Stark spectrophone as an enhanced trace level ammonia concentration detector: design and performance at CO2 laser frequencies.* Appl. Opt. **29**, 2679– (1990).

413. A. Zybin, C. Schnürer-Patschan and K. Niemax. *Wavelength modulation diode-laser atomic-absorption spectrometry in modulated low-pressure helium plasmas for element-selective detection in gas-chromatography.* J. Anal. At. Spectrom. **10**, 563–567 (1995).

414. P. Werle and S. Lechner. *Stark-modulation-enhanced FM-spectroscopy.* Spectrochim. Acta A **55**, 1941–1955 (1999).

415. S. Paddi Reddy, W. Ivancic, V. Malathy Devi, A. Baldacci, K. Narahari Rao, A.W. Mantz and R.S. Eng. *Tunable diode laser spectroscopy in the infrared: some practical considerations of techniques and calibration with ν_2 lines of HCN.* Appl. Opt. **18**, 1350– (1979).

416. J.M. Jasinski, E.A. Whittaker, G.C. Bjorklund, R.W. Dreyfus, R.D. Estes and R.E. Walkup. *Detection of SiH_2 in silane and disilane glow-discharges by frequency-modulation absorption-spectroscopy.* Appl. Phys. Lett. **44**, 1155–1157 (1984).

417. T.A. Blake, C. Chackerian and J.R. Podolske. *Prognosis for a mid-infrared magnetic rotation spectrometer for the in situ detection of atmospheric free radicals.* Appl. Opt. **35**, 973– (1996).

418. R.J. Brecha, L.M. Pedrotti and D. Krause. *Magnetic rotation spectroscopy of molecular oxygen with a diode laser.* J. Opt. Soc. Am. B **14**, 1921–1930 (1997).

419. R.J. Brecha. *Noninvasive magnetometry based on magnetic rotation spectroscopy of oxygen.* Appl. Opt. **37**, 4834–4839 (1998).

420. G.C. Bjorklund. *Frequency-modulation spectroscopy: a new method for measuring weak absorptions and dispersions.* Opt. Lett. **5**, 15–17 (1980).

421. P. Werle, F. Slemr, M. Gehrtz and C. Brauchle. *Quantum-limited FM spectroscopy spectroscopy with a lead-salt diode-laser - a comparison of theoretical and experimental-data.* Appl. Phys. B **49**, 99–108 (1989).

422. T. Fernholz, H. Teichert and V. Ebert. *Digital, phase-sensitive detection for in situ diode-laser spectroscopy under rapidly changing transmission conditions.* Appl. Phys. B **75**, 229–236 (2002).

423. J. Reid and D. Labrie. *2nd-harmonic detection with tunable diode-lasers - comparison of experiment and theory.* Appl. Phys. B **26**, 203–210 (1981).

424. J.M. Supplee, E.A. Whittaker and W. Lenth. *Theoretical description of frequency-modulation and wavelength modulation spectroscopy.* Appl. Opt. **33**, 6294–6302 (1994).

425. P. Kluczynski and O. Axner. *Theoretical description based on Fourier analysis of wavelength-modulation spectrometry in terms of analytical and background signals.* Appl. Opt. **38**, 5803–5815 (1999).

426. P. Kluczynski, J. Gustafsson, Å. Lindberg and O. Axner. *Wavelength modulation absorption spectrometry - an extensive scrutiny of the generation of signals.* Spectrochim. Acta B **56**, 1277–1354 (2001).

427. R. Arndt. *Analytical line shapes for lorentzian signals broadened by modulation.* J. Appl. Phys. **36**, 2522–2524 (1965).

428. P. Kluczynski, A.M. Lindberg and O. Axner. *Characterization of background signals in wavelength-modulation spectrometry in terms of a Fourier based theoretical formalism.* Appl. Opt. **40**, 770–782 (2001).

429. J. Gustafsson, N. Chekalin and O. Axner. *Improved detectability of wavelength modulation diode laser absorption spectrometry applied to window-equipped graphite furnaces by 4th and 6th harmonic detection.* Spectrochim. Acta B **58**, 111–122 (2003).

430. H. Preier and W. Riedel. *NO spectroscopy by pulsed $PbS_{1-x}Se_x$ diode lasers.* J. Appl. Phys. **45**, 3955–3958 (1974).

431. D. J. Robichaud, J. T. Hodges, L. R. Brown, D. Lisak, P. Maslowski, L. Y. Yeung, M. Okumura and C. E. Miller. *Experimental intensity and lineshape parameters of the oxygen A-band using frequency-stabilized cavity ring-down spectroscopy.* J. Mol. Spectrosc. **248**, 1–13 (2008).

432. Q.V. Nguyen, R.W. Dibble and T. Day. *High-resolution oxygen absorption-spectrum obtained with an external-cavity continuously tunable diode-laser.* Opt. Lett. **19**, 2134–2136 (1994).

433. Y. Takubo, K. Muroo, S. Miwa, K. Yamamoto, K. Suzuki and M. Yamamoto. *Resonant magneto-optic spectra of the $b^1\Sigma_g^+ - X^3\Sigma_g^-$ transition of oxygen molecules.* J. Mol. Spectrosc. **178**, 31–39 (1996).

434. H.P. Zappe, M. Hess, M. Moser, R. Hovel, K. Gulden, H.P. Gauggel and F.M. di Sopra. *Narrow-linewidth vertical-cavity surface-emitting lasers for oxygen detection.* Appl. Opt. **39**, 2475–2479 (2000).

435. J.M. Ostermann, F. Rinaldi, P. Debernardi and R. Michalzik. *VCSELs with enhanced single-mode power and stabilized polarization for oxygen sensing.* IEEE Photonic. Tech. L. **17**, 2256–2258 (2005).

436. F. Rinaldi, J.M. Ostermann, A. Kroner and R. Michalzik. *High-performance AlGaAs-based VCSELs emitting in the 760 mn wavelength range.* Opt. Commun. **270**, 310–313 (2007).

437. H. Cattaneo, T. Laurila and R. Hernberg. *Photoacoustic detection of oxygen using cantilever enhanced technique.* Appl. Phys. B **85**, 337–341 (2006).

438. B. Scherer, J. Woellenstein, M. Weidemueller, W. Salzmann, J.M. Ostermann, F. Rinaldi and R. Michalzik. *Oxygen measurements at high pressures using a low cost, polarization stabilized, widely tunable vertical-cavity surface-emitting laser.* In *Smart Sensors, Actuators, and MEMS III* volume 6589 (2007).

439. Y. Arita, R. Stevens and P. Ewart. *Multi-mode absorption spectroscopy of oxygen for measurement of concentration, temperature and pressure.* Appl. Phys. B **90**, 205–211 (2008).

440. K. Muta, M. Tanoura, K. Fujimura and K. Tokuda. *Simultaneous detection of oxygen and soot particle by visible diode laser absorption spectroscopy.* In *Combustion Diagnostics* volume 3108 (1997).

441. J. Wang, S.T. Sanders, J.B. Jeffries and R.K. Hanson. *Oxygen measurements at high pressures with vertical cavity surface-emitting lasers.* Appl. Phys. B **72**, 865–872 (2001).

442. L. Sandström and D. Malmberg. *On-line and in situ monitoring of oxygen concentration and gas temperature in a reheating furnace utilizing tunable diode-laser spectroscopy.* Spectrochim. Acta A **58**, 2449–2455 (2002).

443. H.E. Schlosser, J. Wolfrum, V. Ebert, B.A. Williams, R.S. Sheinson and J.W. Fleming. *In situ determination of molecular oxygen concentrations in full-scale fire-suppression tests using tunable diode laser absorption spectroscopy.* Proceedings of the Combustion Institute **29**, 353–360 (2002).

444. A.R. Awtry and J.W. Fleming. *Simultaneous diode-laser-based in situ measurement of liquid water content and oxygen mole fraction in dense water mist environments.* Opt. Lett. **31**, 900–902 (2006).

445. K.H. Lyle, J.B. Jeffries and R.K. Hanson. *Diode-laser sensor for airmass flux 1: Design and wind-tunnel validation.* AIAA Journal Journal **45**, 2204–2212 (2007).

446. A.C. Templeton, Y.R. Han, R. Mahajan, R.T. Chern and A.R. Reed. *Rapid headspace oxygen analysis for pharmaceutical packaging applications.* Pharm. Technol. **26**, 44–61 (2002).

447. M. Sjöholm, G. Somesfalean, J. Alnis, S. Andersson-Engels and S. Svanberg. *Analysis of gas dispersed in scattering media.* Opt. Lett. **26**, 16–18 (2001).

448. G. Somesfalean, M. Sjöholm, J. Alnis, C. af Klinteberg, S. Andersson-Engels and S. Svanberg. *Concentration measurement of gas embedded in scattering media by employing absorption and time-resolved laser spectroscopy.* Appl. Opt. **41**, 3538–3544 (2002).

449. J. Alnis, B. Anderson, M. Sjöholm, G. Somesfalean and S. Svanberg. *Laser spectroscopy of free molecular oxygen dispersed in wood materials.* Appl. Phys. B **77**, 691–695 (2003).

450. L. Persson, H. Gao, M. Sjöholm and S. Svanberg. *Diode laser absorption spectroscopy for studies of gas exchange in fruits.* Opt. Laser Eng. **44**, 687–698 (2006).

451. M. Andersson, L. Persson, M. Sjöholm and S. Svanberg. *Spectroscopic studies of wood-drying processes.* Opt. Express **14**, 3641–3653 (2006).

452. L. Persson, F. Andersson, M. Andersson and S. Svanberg. *Approach to optical interference fringes reduction in diode laser absorption spectroscopy.* Appl. Phys. B **87**, 523–530 (2007).

453. L. Persson, M. Andersson, M. Cassel-Engquist, K. Svanberg and S. Svanberg. *Gas monitoring in human sinuses using tunable diode laser spectroscopy.* J. Biomed. Opt. **12**, 054001 (2007).

454. L. Persson, B. Anderson, M. Andersson, M. Sjöholm and S. Svanberg. *Studies of gas exchange in fruits using laser spectroscopic techniques.* In *Proceedings of FRUTIC 05: Information and technology for sustainable fruit and vegetable production* (2005).

455. J. Johansson, S. Folestad, S. Svanberg, M. Sjöholm, G. Somesfalean, C. Abrahamsson and S. Andersson-Engels. Method for analysing a pharmaceutical sample. International patent PCT no. WO 03/078983, EP-1488213 (2003).

456. M.E. Davis. *Ordered porous materials for emerging applications.* Nature **417**, 813–821 (2002).

457. K. Maex, M.R. Baklanov, D. Shamiryan, F. Iacopi, S.H. Brongersma and Z.S. Yanovitskaya. *Low dielectric constant materials for microelectronics.* J. Appl. Phys. **93**, 8793–8841 (2003).

458. H.L. Ritter and L.C. Drake. *Pore-size distribution in porous materials: pressure porosimeter and determination of complete macropore-size distributions.* Ind. Eng. Chem. **17**, 782–786 (1945).

459. P.A. Webb. An introduction to the physical characterization of materials by mercury intrusion porosimetry with emphasis on reduction and presentation of experimental data. Technical report Micromeritics (2001).

460. E.P. Barrett, L.G. Joyner and P.P. Halenda. *The determination of pore volume and area distributions in porous substances: computations from nitrogen isotherms.* J. Am. Chem. Soc. **73**, 373–380 (1951).

461. J.M. Haynes and P. Rossi-Doria, editors. *Principles and applications of pore structural characterization.* Arrowsmith (1985).

462. S. Diamond. *Mercury porosimetry - An inappropriate method for the measurement of pore size distributions in cement-based materials.* Cement Concrete Res. **30**, 1517–1525 (2000).

463. L. Farber, G. Tardos and J.N. Michaels. *Use of X-ray tomography to study the porosity and morphology of granules.* Powder Technol. **132**, 57–63 (2003).

464. P.J. Dees and J. Polderman. *Mercury porosimetry in pharmaceutical technology.* Powder Technol. **29**, 187–197 (1981).

465. S. Westermarck, A.M. Juppo, K. Koiranen and J. Yliruusi. *Mercury porosimetry of pharmaceutical powders and granules.* J. Porous Mat. **5**, 77–86 (1998).

466. S. Westermarck. *Use of mercury porosimetry and nitrogen adsorption in characterisation of the pore structure of mannitol and microcrystalline cellulose powders, granules and tablets.* PhD thesis, University of Helsinki (2000).

Papers

Paper I

Time and wavelength resolved spectroscopy of turbid media using light continuum generated in a crystal fiber

A. Abrahamsson, T. Svensson, S. Svanberg S. Andersson-Engels, J. Johansson and S. Folestad.

Optics Express **12**, 4103-4112 (2004).

Time and wavelength resolved spectroscopy of turbid media using light continuum generated in a crystal fiber

Christoffer Abrahamsson, Tomas Svensson, Sune Svanberg, and Stefan Andersson-Engels

Department of Physics, Lund Institute of Technology, P.O. Box 118, SE-221 00 Lund, Sweden
christoffer.abrahamsson@fysik.lth.se, tomas.svensson@fysik.lth.se, sune.svanberg@fysik.lth.se, stefan.andersson-engels@fysik.lth.se

Jonas Johansson, Staffan Folestad

AstraZeneca R&D Mölndal, Analytical Development, S-431 83 Mölndal, Sweden
jonas.johansson@astrazeneca.com, staffan.folestad@astrazeneca.com

Abstract: We report a novel system for time-resolved diffuse remission spectral measurements, based on short light continuum pulses generated in an index-guided crystal fiber, and a spectrometer-equipped streak camera. The system enables spectral recordings of absorption and reduced scattering coefficients of turbid media in the wavelength range 500 - 1200 nm with a spectral resolution of 5 nm and a temporal resolution of 30 ps. The optical properties are calculated by fitting the solution of the diffusion equation to the time-dispersion curve at each wavelength. Example measurements are presented from an apple, a finger and a pharmaceutical tablet.

OCIS codes: (300.6500) spectroscopy, time-resolved, (290.7050) turbid media, (170.1470) blood/tissue constituent monitoring, (170.3660) light propagation in tissues, (060.5060) phase modulation

References and links

1. P. Geladi, D. MacDougall, and H. Martens, "Linearization and scatter correction for near-infrared reflectance spectra of meat," Appl. Spectrosc. **39,** 491-500 (1985).
2. S. Wold, H. Antii, F. Lindgren, and J. Ohman, "Orthogonal signal correction of near-infrared spectra," Chemom. Intell. Lab. Syst. **44,** 175-185 (1998).
3. V. Centner, J. Verdú-Andrés, B. Walczak, D. Jouan-Rimbaud, F. Despagne, L. Pasti, R. Poppi, D-L. Massart, and O. E. de Noord, "Comparison of multivariate calibration techniques applied to experimental NIR data sets," Appl. Spectrosc. **54,** 608-629 (2000).
4. I. Georgakoudi, B. C. Jacobson, J. van Dam, V. Backman, M. B. Wallace, M. G. Muller, Q. Zhang, K. Badizadegan, D. Sun, G. A. Thomas, L. T. Perelman, and M. S. Feld, "Fluorescence, reflectance, and light-scattering spectroscopy for evaluating dysplasia in patients with Barrett's esophagus," Gastroenterology. **120,** 1620-1629 (2001).
5. T. Burger, J. Kuhn, R. Caps, and J. Fricke, "Quantitative determination of the scattering and absorption coefficients from diffuse reflectance and transmittance measurements," J. Appl. Spectrosc. **51,** 309-317 (1997).
6. O. Berntsson, T. Burger, S. Folestad, L. G. Danielsson, J. Kuhn, and J. Fricke, "Effective sample size in diffuse reflectance near-IR spectrometry," Anal. Chem. **71,** 617-623 (1999).
7. M. S. Patterson, B. Chance, and B. C. Wilson, "Time resolved reflectance and transmittance for the non-invasive measurement of optical properties," Appl. Opt. **28,** 2331-2336 (1989).
8. M. S. Patterson, J. D. Moulton, B. C. Wilson, and B. Chance, "Applications of time-resolved light scattering measurements to photodynamic therapy dosimetry," in *Photodynamic Therapy: Mechanisms II*, Proc. SPIE **1205**, 62-75 (1990).
9. S. J. Madsen, M. S. Patterson, B. C. Wilson, Y. D. Park, J. D. Moulton, S. L. Jacques, and Y. Hefetz, "Time resolved diffuse reflectance and transmittance studies in tissue simulating phantoms: a comparison between theory and experiment," in *Time-Resolved Spectroscopy and Imaging of Tissue* B. Chance, ed. Proc. SPIE **1431**, 42-51 (1991).

#4822 - $15.00 US Received 16 July 2004; revised 16 August 2004; accepted 16 August 2004

10. S. Andersson-Engels, R. Berg, and S. Svanberg, "Effects of optical constants on time-gated transillumination of tissue and tissue-like media," J. Photochem. Photobiol. B. **16,** 155-167 (1992).
11. S. Andersson-Engels, R. Berg, A. Persson, and S. Svanberg, "Multispectral tissue characterization with time-resolved detection of diffusely scattered white light," Opt. Lett. **18,** 1697-1699 (1993).
12. R. Cubeddu, C. D'Andrea, A. Pifferi, P. Taroni, A. Torricelli, G. Valentini, M. Ruiz-Altisent, C. Valero, C. Ortiz, C. Dover, and D. Johnson, "Time-resolved reflectance spectroscopy applied to the nondestructive monitoring of the internal optical properties in apples," Appl. Spectrosc. **55,** 1368-1374 (2001).
13. J. R. Lakowicz and K. Berndt, "Frequency-domain measurements of photon migration in tissues," Chem. Phys. Lett. **166,** 246 (1990).
14. J. Fishkin, E. Gratton, M. J. vandeVen, and W. W. Mantulin, "Diffusion of intensity modulated near-infrared light in turbid media," in *Time-Resolved Spectroscopy and Imaging of Tissue* B. Chance, ed. Proc. SPIE **1431**, 122-135 (1991).
15. M. Patterson, J. D. Moulton, B. C. Wilson, K. W. Berndt, and J. R. Lakowicz, "Frequency-domain reflectance for the detemination of the scanttering and absorption properties of tissue," Appl. Opt. **30,** 4474-4476 (1991).
16. S. J. Madsen, E. R. Anderson, R. C. Haskell, and B. J. Tromberg, "Portable, high-bandwidth frequency-domain photon migration instrument for tissue spectroscopy," Opt. Lett. **19,** 1934-1936 (1994).
17. E. Gratton and J. Maier, "Frequency-domain measurements of photon migration in highly scattering media," Medical Optical Tomography. 534-544 (1996).
18. M. A. Franceschini, V. Toronov, M. E. Filiaci, E. Gratton, and S. Fantini, "On-line optical imaging of the human brain with 160-ms temporal resolution," Opt. Express. **6,** 49-57 (2000), http://www.opticsexpress.org/abstract.cfm?URI=OPEX-6-3-49.
19. F. Bevilacqua, A. J. Berger, A. E. Cerussi, D. Jakubowski, and B. J. Tromberg, "Broadband absorption spectroscopy in turbid media by combined frequency-domain and steady-state methods," Appl. Opt. **39,** 6498-6507 (2000).
20. T. J. Farrell, B. C. Wilson, and M. S. Patterson, "The use of a neural network to determine tissue optical properties from spatially resolved diffuse reflectance measurements," Phys. Med. Biol. **37,** 2281-2286 (1992).
21. J. S. Dam, C. B. Pedersen, T. Dalgaard, P. E. Fabricius, P. Aruna, and S. Andersson-Engels, "Fiber optic probe for non-invasive real-time determination of tissue optical properties at multiple wavelengths," Appl. Opt. **40,** 1155-1164 (2001).
22. R. L. P. van Veen, W. Verkruysse, and H. J. C. M. Sterenborg, "Diffuse-reflectance spectroscopy from 500 to 1060 nm by correction for inhomogeneously distributed absorbers," Opt. Lett. **27,** 246-248 (2002).
23. R. Cubeddu, A. Pifferi, P. Taroni, A. Torricelli, and G. Valentini, "Noninvasive absorption and scattering spectroscopy of bulk diffusive media: An application to the optical characterization of human breast," Appl. Phys. Lett. **74,** 874-876 (1999).
24. A. Pifferi, J. Swartling, E. Chikoidze, A. Torricelli, P. Taroni, S. Andersson-Engels, and R. Cubeddu, "Spectroscopic time-resolved diffuse reflectance and transmittance measurements of the female breast at different interfiber distances," J. Biomedical Optics. (to be published).
25. R. R. Alfano and S. L. Shapiro, "Observation of self-phase modulation and small-scale filaments in crystals and glasses," Phys. Rev. Lett. **24,** 592-594 (1970).
26. R. L. Fork, C. V. Shank, C. Hirlimann, R. Yen, and W. J. Tomlinson, "Femotsecond white-light continuum pulses," Opt. Lett. **8,** 1-3 (1983).
27. O. Jarlman, R. Berg, S. Andersson-Engels, S. Svanberg, and H. Pettersson, "Time-resolved white light transillumination for optical imaging," Acta Radiol. **38,** 185-189 (1997).
28. J. Johansson, S. Folestad, M. Josefson, A. Sparen, C. Abrahamsson, S. Andersson-Engels, and S. Svanberg, "Time-resolved NIR/Vis spectroscopy for analysis of solids: Pharmaceutical tablets," Appl. Spectrosc. **56,** 725-731 (2002).
29. J. K. Ranka, R. S. Windeler, and A. J. Stentz, "Visible continuum generation in air-silica microstructure optical fibers with anomalous dispersion at 800 nm," Opt. Lett. **25,** 25-27 (2000).
30. J. C. Knight, T. A. Birks, R. F. Cregan, P. S. J. Russell, and J. P. de Sandro, "Photonic crystals as optical fibres - physics and applications," Optical Materials. **11,** 143-151 (1999).
31. C. Abrahamsson, S. Andersson-Engels, S. Folestad, J. Johansson, and S. Svanberg. "New measuring technique", Patent Application PCT WO 2002075286 (2002)
32. G. Genty, M. Lehtonen, H. Ludvigsen, J. Broeng, and M. Kaivola, "Spectral broadening of femtosecond pulses into continuum radiation in microstructured fibers," Opt. Express. **10,** 1083-1098 (2002), http://www.opticsexpress.org/abstract.cfm?URI=OPEX-10-20-1083.
33. J. Swartling, J. S. Dam, and S. Andersson-Engels, "Comparison of spatially and temporally resolved diffuse-reflectance measurement systems for determination of biomedical optical properties," Appl. Opt. **42,** 4612-4620 (2003).
34. R. C. Haskell, L. O. Svaasand, T.-T. Tsay, T.-C. Feng, M. S. McAdams, and B. J. Tromberg, "Boundary conditions for the diffusion equation in radiative transfer," J. Opt. Soc. Am. A. **11,** 2727-2741 (1994).
35. R. Cubeddu, A. Pifferi, P. Taroni, A. Torricelli, and G. Valentini, "Experimental test of theoretical models for time-resolved reflectance," Med. Phys. **23,** 1625-1633 (1996).

#4822 - $15.00 US Received 16 July 2004; revised 16 August 2004; accepted 16 August 2004

36. C. Abrahamsson, J. Johansson, A. Sparén, and F. Lindgren, "Comparison of different variable selection methods conducted on NIR transmission measurements on intact tablets," Chemom. Intell. Lab. Syst. **69,** 3-12 (2003).

1. Introduction

Over the last decade there has been a lot of effort to develop techniques to extract the absorption and sometimes scattering properties of turbid media. Several areas of research need a tool for such measurements - biomedical applications including tissue diagnostics and physiological measurements, the pharmaceutical industry for on-line measurements of active substance concentration in pharmaceutical preparations, and the food industry for non-destructive measurements of the quality of products. Two, generally different approaches, have been employed to do this. The first one is based on measurements from which it is possible to extract the absorption and scattering properties more or less independently. The measurements can be time-resolved, spatially-resolved or be made in the frequency domain with a modulated light source. The other approach uses spectrally-resolved measurements and utilizes multivariate analysis following training on a large set of known samples. The latter method has been developed mainly within NIR spectroscopy, where scattering has been seen as a complication, yielding uncertainties in the evaluation of the recorded data [1,2]. Large training sets and complex calibration models have often been necessary to span the entire region of the important parameters of the samples under investigation [3]. This approach has two major limitations - it needs frequent calibrations and it is not very robust.

In many respects it is more appealing to use the model-based approach to obtain the absorption and/or scattering properties [4-6]. Frequently time-resolved techniques have been employed (see, for example [7-12]), but also frequency domain [13-19] and spatially resolved [20-22] techniques have been utilized. Such measurements are most often performed at multiple wavelengths in order to enable the desired information to be obtained. This can be achieved with diode lasers at fixed wavelengths or by scanning a tunable laser over the wavelength region of interest [23,24]. Parallel detection of all wavelengths of interest is possible with a short-pulsed broad light source. Such a suitable source is continuum generation employing non-linear interaction in a special optical medium as a result of high peak-power illumination [25,26]. A system based on this technology has been developed in our laboratory. It relies on focusing a high-power laser beam in a sapphire crystal or a cuvette of water [11,27,28]. The laser system in that work runs at 10 Hz, and some averaging is required to achieve a sufficient signal-to-noise ratio to extract the absorption properties with reasonable accuracy. This results in a substantial acquisition time and the time-jitter between the pulses also reduces the time resolution of the system.

Light continuum generation has been utilized for many spectroscopy applications. Recently, non-linear effects in microstructured fibers, designed to have a very low dispersion and thus retain a high pulse peak power throughout the full length of the fiber, have been employed for this purpose [29,30]. Since the non-linear efficiency is very high for these fibers, it is sufficient to use it the with moderate peak powers, obtained by mode-locked lasers. Thus a relatively compact new light source is available for spectroscopy of turbid media [31].

The objectives of this study were twofold: first to demonstrate the function of a complete time-resolved spectroscopy system based on continuum generation in an index-guiding crystal fiber in the entire wavelength range 500 - 1200 nm, covering most of the wavelengths of interest for the applications mentioned above. Next, we show measurements conducted on three types of samples to demonstrate the capability of the system.

#4822 - $15.00 US Received 16 July 2004; revised 16 August 2004; accepted 16 August 2004

2. Material and methods

2.1 System description

The arrangement of the system is depicted in Fig. 1. The Ar-ion laser pumped mode-locked Ti:Sapphire laser produced pulses shorter than 100 fs at a repetition rate of 80 MHz. The wavelength of the laser light was centered around 800 nm, and the energy of each pulse was 4 nJ. An optical isolator was used after the laser, to prevent optical reflections that provide unwanted feedback to the laser causing unstable output conditions. A prism compressor was used in the set-up to compensate for the time dispersion caused by the different optical components. The light output from the compressor was focused into a 100 cm long index-guiding crystal fiber (ICF) (Crystal Fiber A/S, Copenhagen, Denmark) using a conventional x40 microscope objective lens with a numeric aperture of 0.65. The ICF had a core diameter of 2 µm and was manufactured to have minimum dispersion at 760 nm. A light continuum was generated by employing non-linear optical effects in the fiber, mainly self-phase modulation and stimulated Raman scattering [32]. A low dispersion of the light inside the fiber combined with small core diameter results in a high peak power of the light in the entire length of the fiber, yielding a high non-linear efficacy resulting in widely spectrally broadened light emission. As a result of this, light pulses with a spectral width spanning from 500 nm to at least 1200 nm were accessible. The light distribution was, however, not perfectly flat throughout the entire wavelength region, but relatively modulated. An advantage of this technique is that it is totally independent of such modulations as long as sufficient light intensity was obtained for all wavelengths of interest, since the optical properties are derived from the time dispersion curves in the sample.

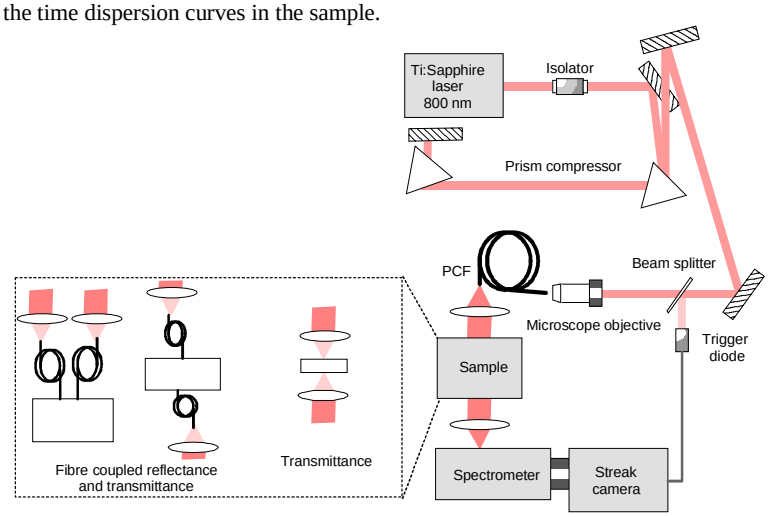

Fig. 1. Optical arrangement of the system. Three types of sample geometry were employed, a fiber-based probe in diffuse transmission or reflection, as well as a direct transmission of a slightly focused beam from the crystal fiber.

For the sample measurements, either of three geometries was employed as indicated in Fig. 1. Most samples have been measured with a fiber-based probe. The light from the distal end of the ICF is coupled into a 600 µm diameter gradient index fiber that is held in contact with the sample to be measured. Another fiber was used to pick up the remitted light at a certain position of the sample. This was performed either in reflectance or in transmission mode. A third probe geometry, employed mainly for measurements of pharmaceutical tablets, utilized a non-contact beam arrangement. Here, light from the distal end of the ICF was

#4822 - $15.00 US Received 16 July 2004; revised 16 August 2004; accepted 16 August 2004

slightly focused onto the tablet surface using a lens. The spot size on the tablet was approximately 2 mm. The tablet was held into place by a circular iris holder, suppressing any light scattered away outside the tablet. Another lens system was used to image the transmitted light onto the entrance slit of the detection system. The detection comprised an imaging spectrometer and a streak camera, yielding spectrally and temporally resolved data in the wavelength region from 500 to 1200 nm. A 25 cm imaging spectrometer (Chromex, Model 250 IS) was equipped with an adjustable entrance slit and three gratings with 30 to 150 grooves/mm. If the entire wavelength range was to be measured, it was necessary to take more than one recording, with different positions of the grating. The spectrally dispersed light at the output of the spectrometer was captured by the streak camera (Hamamatsu, Model C5680). The streak tube utilized an S1 photocathode in order to cover the entire wavelength range of interest. The streak camera operated in synchro-scan mode, allowing all light pulses to be collected. A small portion of the laser light was redirected by a beam splitter onto a photodiode that triggered the streak camera sweep. The system had a total temporal range of 2.1 ns with resolution of 4.5 ps. The instrumental response function was in the range of 30 ps when averaging over 50 s.

2.2 Measurement procedure

In preparation of each measurement session, the source optics needed alignment. This is due to the small diameter of the ICF and a long distance between the pump laser and the source in our arrangement. Misalignment resulted in reduced output power with a less broad spectral profile. Firstly, the optical coupling into the ICF was optimized by adjusting the position of the input end of the fiber with the use of an XYZ translation mount. A routine for this adjustment emerged, where the visually observed intensity of the green light generated in the fiber was used in the adjustments [32]. A better optical coupling resulted in higher light intensity within the fiber and thus higher peak power and better non-linear efficiency. The next step was to adjust the dispersion of the pulse by the prism compressor. This was again adjusted by observing the green light generated in the fiber. After an iterative procedure, a measured spectral profile as illustrated in Fig. 2 was obtained. Small adjustments resulted in significant changes in both intensity and spectral profile of the light continuum.

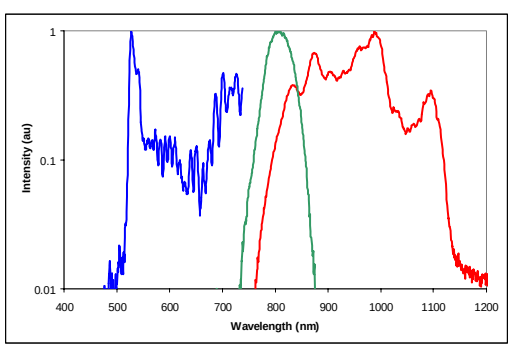

Fig. 2. Detected light intensity without any sample as a function of wavelength Three settings of the spectrometer was employed to cover the entire range. The middle region was measured using the Ti:Sapphire laser only, without any crystal fiber.

Prior to each sample measurement, an instrumental response function was recorded. This was either done by connecting two fibers to each end of a thin metal tube indented at the middle to decrease the light measured, or by inserting a pin-hole in the light path. The light intensity was further reduced by inserting absorbing glass filters. The instrumental response function was important in the subsequent analysis to determine the time of the laser pulse in the

#4822 - $15.00 US Received 16 July 2004; revised 16 August 2004; accepted 16 August 2004

camera streak without the dispersion caused by the sample and to measure the dispersion of the measured pulse due to the system characteristics.

The next step was to insert the sample to be examined and adjust the recorded signal level. The main adjustments were made by setting the integration time of the CCD camera. The time was normally set between one and five seconds, while typically 50 - 100 readouts were accumulated in the computer before analysis. This resulted in an acquisition time of approximately one to five minutes. For very high light levels, an optical neutral density filter was employed to reduce the recorded light intensity. Other parameters influencing the recorded signal level was kept constant between measurements, not to alter the characteristics of the detection. The gain of the multi channel plate (MCP) in the streak camera was thus kept fixed, so that the dark current level in the camera system would remain the same for all measured samples. The slit widths of the streak camera and spectrometer were also kept at fixed widths, 50 and 100 μm, respectively.

2.3 Sample measurements

Before the system was utilized for measurements on various samples, its potential to extract optical properties from a homogenous turbid medium was evaluated. For this check, four tissue phantoms as prepared according to Ref. [33] were employed. The 6.5 cm diameter and 5.5 cm thick epoxy phantoms contained TiO_2 particles as scattering centers and toner powder as absorber. The phantoms were measured in a diffuse reflectance geometry using a 1.0 meter long 600 μm core diameter gradient index fiber as a source and collection fiber, respectively. The inter-fiber distance during the recordings was 8 mm. As a gold standard for the determination of expected optical properties, integrating sphere measurements of 1.00 mm thick samples, prepared simultaneously as the phantoms were used [33].

Following these initial measurements, a number of samples were studied, to illustrate the potential of this system in determining absorption and scattering spectra of turbid samples. Firstly, apples were analysed. A small piece of a fresh Golden Delicious apple obtained from a nearby grocery store was removed, creating a flat skinless surface with a diameter of approximately 30 mm. The apple was measured immediately after the cut with the same diffuse reflection geometry as used for the phantoms.

Next, the tip of the index finger of a volunteer was measured. The finger was measured in transillumination using the same fibers as above for light delivery and collection. The measurement was conducted through the nail. The thickness of the finger was 7 mm. The evaluation was conducted assuming transmission through a infinite slab of thickness 7 mm. Finally, a pharmaceutical tablet (typical immediate release tablet, AstraZeneca R&D Mölndal, Sweden) especially prepared for optical measurements was examined. The tablet was produced in a cylindrical shape with flat end surfaces and a diameter of 13 mm and a thickness of 2 mm. For this measurement, the light continuum from the crystal fiber was slightly focused with a microlens to form a convergent beam with a diameter of 2 mm at the surface of the tablet. The diffuse light transmitted through the tablet was collected and focused onto the entrance slit of the spectrometer using two achromatic lenses.

2.4 Evaluation of absorption and scattering spectra

The recorded data images were evaluated as indicated in Fig. 3. A recorded image contained temporally (x-axis) and spectrally (y-axis) resolved information of the remitted light, accumulated from a sample during typically one minute. The optical properties were then analyzed at each wavelength independently by fitting the experimental data to an analytical solution of the diffusion approximation of the transport equation for a homogeneous semi-infinite medium or an infinite slab [7]. In the evaluation procedure, boundaries are accounted for by employing an extrapolated boundary condition [34]. The best fit was reached iteratively with a Levenberg-Marquardt algorithm, where μ_s', μ_a and an overall amplitude

#4822 - $15.00 US Received 16 July 2004; revised 16 August 2004; accepted 16 August 2004

factor are varied in order to minimize a χ^2 merit norm. The temporal shift between the IRF and experimental data is known and is thus not regarded as a free fit parameter. Each iteration involves a convolution between the theoretical time-dispersion curve and the IRF. The fitting range included all points with a number of counts higher than 80% of the peak value on the rising edge of the curve and 1% on the tail [35]. A typical outcome is presented in Fig. 3, and an example of the proceedings of the algorithm is given in Fig. 4.

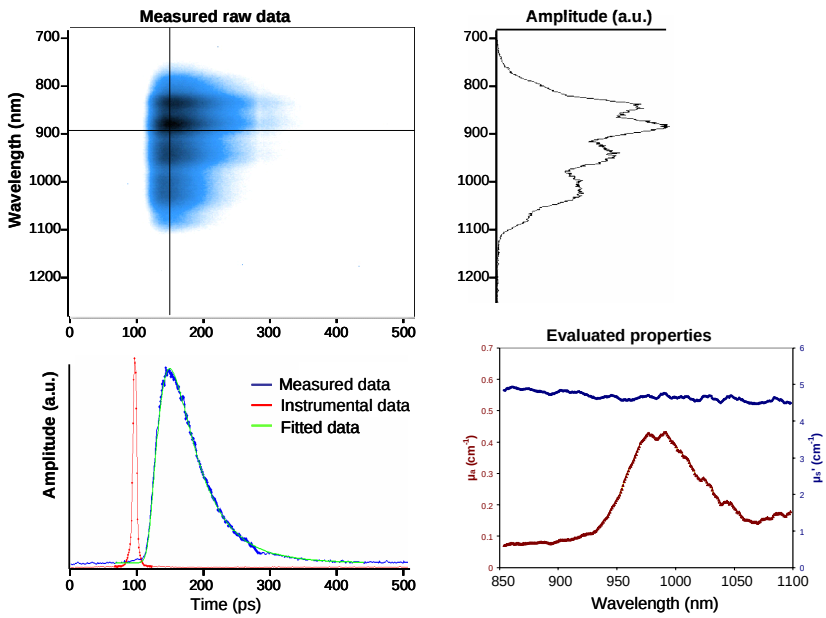

Fig. 3. A recorded data set is shown (upper left). Remitted light intensity is presented versus time along the horizontal axis and wavelength along the vertical axis. A spectral profile of the remitted light at a time gate around 150 ps is shown in the plot to the upper right, while the temporal dispersion of the detected light at 900 nm is illustrated in the lower left graph. In the latter plot, the instrumental response function (IRF) is also indicated (in red), together with the best obtainable fit (green curve). In the lower right plot, the optical properties evaluated from this image are shown as a function of wavelength.

#4822 - $15.00 US Received 16 July 2004; revised 16 August 2004; accepted 16 August 2004

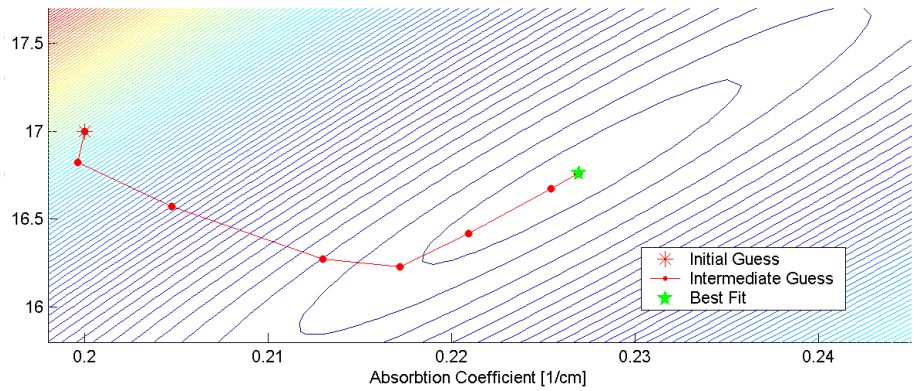

Fig. 4. Levenberg-Marquardt Minimization. The elliptical pattern is built up of equidistant iso-curves of the merit norm. The elliptical shape implies an apparent correlation between fitted parameter values, giving rise to certain limitations when trying to separate absorption from scattering.

3. Results and discussion

An estimation of accuracy in the evaluation of optical properties from the recordings of the system is given by correlating with those estimated for four phantoms, produced with different absorption and scattering properties. A correlation plot is presented in Fig. 5, illustrating the agreement between estimated and evaluated optical properties at 916 nm. The estimated values were obtained in agreement with integrating sphere measurements of thin slabs of the phantoms and time-resolved measurements at a specific wavelength using a time-correlated single photon counting system [33]. As can be seen the obtained values agree within approximately 10% with the estimated values for the absorption and within 20% for the scattering.

Spectra of optical properties from an apple fruit are illustrated in Fig. 6a. As can be seen the reduced scattering coefficient decreases almost linearly with increasing wavelength. By fitting the spectrum to the expression for reduced scattering coefficient as a function of wavelength, $\mu_s' = a\lambda^{-b}$, where b = 0.3, it is obvious from Mie theory that the size of the effective scattering centers in the apple are relatively large. The absorption spectrum is dominated by water absorption peaking around 975 nm.

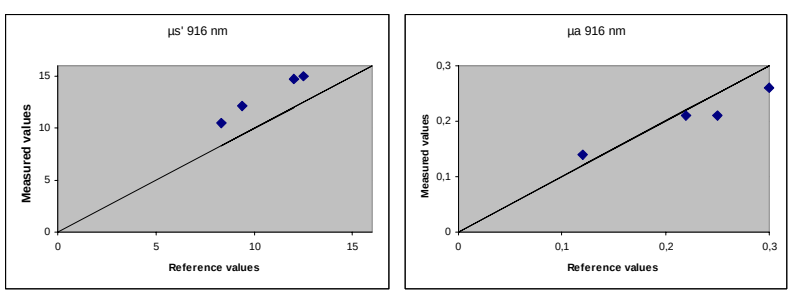

Fig. 5. Correlation plot for measured and estimated optical properties from five epoxy phantoms containing TiO_2 particles as scattering material and ink toner as absorber.

#4822 - $15.00 US Received 16 July 2004; revised 16 August 2004; accepted 16 August 2004

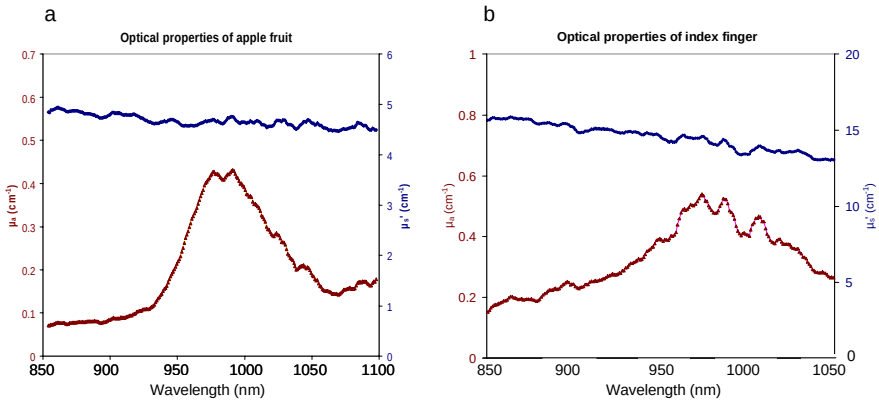

Fig. 6. Data evaluated from time-resolved diffuse (a) reflectance measurements on a green apple, and (b) transmission measurements through the tip of an index finger.

An example of results from a biomedical research related recording is given Fig. 6b. The spectra are recorded in transmission geometry for an index finger. The slope of the scattering is slightly higher than for the apple, indicating that the effective size of the scattering centers within the finger is smaller. Here, the b-factor is evaluated to be b = 0.9. The main absorber in the presented wavelength band is water. The absorption spectrum does not show any lipid content in the finger, which would have been visible close to 915 nm.

A last spectrum illustrates a typical pharmaceutical example. In Fig. 7 an evaluated absorption spectrum of a pharmaceutical tablet especially produced for these measurements in order to obtain a thin tablet and simple measurement geometry, is shown. The absorption spectrum is in good agreement with the active substance in the tablet [36]. The scattering coefficient for this tablet was about 500 cm^{-1}.

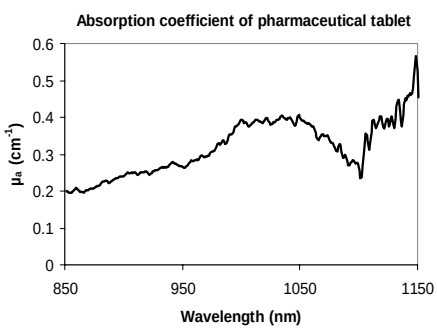

Fig. 8. Data evaluated from transmission measurements on a pharmaceutical tablet.

The source of the system developed is based on a light continuum generated in a crystal fiber. The crystal fiber technology is rapidly developing and key features of continuum generation in such fibers, such as spectral profile and bandwidth, are quickly improving. The system described in this paper is, however, relatively insensitive to the exact spectral profile of the continuum. As long as the light is sufficiently high at each wavelength of interest, the

#4822 - $15.00 US Received 16 July 2004; revised 16 August 2004; accepted 16 August 2004

optical properties can, as seen above, be obtained from a measurement. The detection unit of the system comprises a spectrometer and a streak camera. The spectrometer allows the recording of a wide spectral range, with a relatively high resolution. This is very important for most NIR spectroscopy applications. The streak-camera, on the other hand, provides a very high temporal resolution, enabling measurements of relatively low dispersion objects. As compared to a time-correlated single photon counting system used by several other groups in time-resolved diffuse remission spectroscopy, this system provides a unique combination of relatively short acquisition time in combination with high spectral and temporal resolution.

Acknowledgments

The authors would like to thank Fabien Chauchard, Cemagref, Montpellier, France, for assistance in the measurements and discussions regarding the fruit samples. We are also grateful to Anders Persson for keeping the performance of the laser at a very high level. The work was financially supported by AstraZeneca R&D Mölndal, Sweden, the Swedish Research Foundation, and the Swedish Research Council.

#4822 - $15.00 US Received 16 July 2004; revised 16 August 2004; accepted 16 August 2004

Paper II

Scatter correction of transmission near-infrared spectra by photon migration data: Quantitative analysis of solids

A. Abrahamsson, A. Löwgren, B. Strömdahl, T. Svensson, S. Andersson-Engels, J. Johansson and S. Folestad.

Applied Spectroscopy **59**, 1381-1387 (2005).

Scatter Correction of Transmission Near-Infrared Spectra by Photon Migration Data: Quantitative Analysis of Solids

CHRISTOFFER ÅBRAHAMSSON,* ALEXANDRA LÖWGREN, BIRGITTA STRÖMDAHL, TOMAS SVENSSON, STEFAN ANDERSSON-ENGELS, JONAS JOHANSSON, and STAFFAN FOLESTAD

Department of Physics, Lund Institute of Technology, P.O. Box 118, SE-221 00 Lund, Sweden (C.A., A.L., B.S., T.S., S.A.-E.); and AstraZeneca R&D Mölndal, SE-431 83 Mölndal, Sweden (J.J., S.F.)

The scope of this work is a new methodology to correct conventional near-infrared (NIR) data for scattering effects. The technique aims at measuring the absorption coefficient of the samples rather than the total attenuation measured in conventional NIR spectroscopy. The main advantage of this is that the absorption coefficient is independent of the path length of the light inside the sample and therefore independent of the scattering effects. The method is based on time-resolved spectroscopy and modeling of light transport by diffusion theory. This provides an independent measure of the scattering properties of the samples and therefore of the path length of light. This yields a clear advantage over other preprocessing techniques, where scattering effects are estimated and corrected for by using the shape of the measured spectrum only. Partial least squares (PLS) calibration models show that, by using the proposed evaluation scheme, the predictive ability is improved by 50% as compared to a model based on conventional NIR data alone. The method also makes it possible to predict the concentration of active substance in samples with other physical properties than the samples included in the calibration model.

Index Headings: **Scatter correction; Near-infrared spectroscopy; NIR spectroscopy; Partial least squares; PLS; Photon migration; Time-resolved spectroscopy; Diffusion.**

INTRODUCTION

Near-infrared (NIR) spectroscopy is an important tool for assessment of the chemical content of solid samples due to the fact that the samples can be analyzed directly in their native solid state. NIR spectroscopic measurements can be conducted both in transmission[1–4] and reflectance[5,6] mode, and the development of fiber optical probes[7–10] has enabled measurements directly in the reaction vessels, e.g., in a pharmaceutical process line.

Although the versatility and speed of NIR spectroscopic measurements has made it an important tool in process analytical chemistry, the technique has some limitations. One of the major drawbacks of NIR spectroscopy is its sensitivity to variations of the physical characteristics of the samples.[3,11] This is due to the fact that the measured absorbance follows the Beer–Lambert law and is therefore dependent on the concentration of the constituent to be quantified, but also on the path length of the light passing through the sample. The path length of the light passage between the light source and the detector is dependent on the physical parameters of the samples, e.g., sample thickness, particle size distribution, and sample compactness. In fact, when measuring on an intact tablet in the NIR wavelength range, the scattering is about 1000 times more prominent than the absorption,[12] which means that a small change in the physical parameters of the samples can alter the measured spectra to a larger extent than the alterations introduced by the variation in concentration of the sample constituents.

Several mathematical spectral pretreatment methods, e.g., standard normal deviation,[13] multiplicative scatter correction,[14] and orthogonal signal correction,[15] have all been proposed to correct NIR spectra in order to eliminate systematic variations unrelated to analyte concentrations. Despite the many efforts, it has still proven hard to incorporate samples from different batches or samples manufactured under different conditions into the same quantitative calibration model with acceptable results.

An alternative to mathematical pretreatment methods is to use a direct measurement of the scattering properties of the samples to correct conventional NIR spectra. Different measurement techniques have been developed to deconvolute the scattering and absorption properties of a sample. These techniques include time-resolved,[16] spatially resolved,[17] and integrating sphere measurements.[18] The techniques to measure the optical properties were developed primarily for biomedical applications but have also been used in some pharmaceutical applications. Scattering and absorption properties have been measured in order to calculate the effective sample size in diffuse reflectance NIR spectroscopy of powders[19,20] as well as for particle size analysis.[21] Measurements of the optical properties have also been used to make quantitative measurements of pharmaceutical powder blend homogeneity.[22]

When conducting time-resolved measurements a temporally very short light pulse is sent through the sample to be analyzed. The temporal shape of the pulse is altered when passing through the sample due to the dispersion of the light inside the sample. By analyzing the modified temporal shape of the pulse, the optical properties of that sample can be deduced.[23] A variety of different evaluation schemes have been developed for evaluating time-resolved data, ranging from simple evaluations like the final slope fitting[24] to more complex schemes like diffusion[25] and Monte Carlo models.[26]

The aim of this work was to introduce a methodology to improve quantitative assessments made from conventional NIR transmission data by using a scatter correction scheme based on the measurements of the actual scattering properties of the samples. To measure the scattering properties of the tablets in this work a novel broad-band time-resolved system was used in combination with dif-

Received 13 July 2005; accepted 24 August 2005.
* Author to whom correspondence should be sent. E-mail: christoffer.abrahamsson@fysik.lth.se.

0003-7028/05/5911-1381$2.00/0

fusion modeling of light transport. The results demonstrate the capability to deconvolute the absorption and scattering properties of pharmaceutical tablets using time-resolved spectroscopy. The quality of the quantitative assessments after the scatter correction was greatly improved, compared to assessments made directly from conventional NIR data. The improvements were especially large for samples with physical properties different from those covered by the calibration samples. The work also points out one possible direction for the development of NIR spectrometers, aiming at a system consisting of a standard NIR spectrometer in combination with a time-resolved diode-laser-based system at a few discrete wavelengths. Such a system would enable measurements of the absorption of samples without any contribution from scattering effects.

THEORY

Optical Properties of Turbid Media. The interaction between light and a turbid medium is governed by the optical properties of that medium. In this work the light will be assumed to be diffusely scattered and light transport will be modeled by the diffusion approximation.

The optical properties can be divided into absorption, primarily a measure of the chemical content of the sample, and scattering, dependent on the physical characteristics of the sample. The parameter used to describe the absorption of light is the absorption coefficient, μ_a, which is defined as the probability for absorption per unit length. The scattering of light is caused by variations of refractive index within the sample and is in the diffusion approximation described by the reduced scattering coefficient, μ_s', which is defined as the probability for an isotropic scattering event per unit length.

Diffusions Models. The measured time-resolved dispersion curves were analyzed using a solution of the radiative transport equation, under the diffusion approximation, for a semi-infinite slab.[27] The solution is based on the introduction of an isotropic point source in the sample at a distance z_0, equal to the inverse of μ_s' from the surface. This is applicable for many types of geometries as long as the solution is calculated for points far away from the source. Another restriction is that the reduced scattering coefficient must be much larger than the absorption coefficient for the diffusion approximation to be valid. Although single scattering events may not be isotropic, but rather be more prominent in specific directions, the validity of the diffusion model is dependent on the fact that the light is so vastly scattered that it loses its directionality and can be treated as isotropic. The diffusion approximation is valid when the distance between the light source and detector is larger than 10 times the mean free path of the photons in the sample,[28] which is greatly exceeded by the samples used in this work.

Since the refractive index changes at the surfaces of the slab, reflections will occur, and hence extrapolated boundaries, where the fluence rate equals zero, are introduced at a distance z_e from the real surface. Mirror sources are introduced around the extrapolated boundaries to fulfill the boundary condition.[29] In this study 30 mirror sources were used. At a time t and a radial distance r from the injection point, the transmittance through a slab is given by

$$T(r,t) = \frac{\exp\left(-\mu_a ct - \frac{r^2}{4Dct}\right)}{2(4\pi Dc)^{3/2}t^{5/2}} \times \sum_{m=-\infty}^{\infty}\left[z_{1,m}\exp\left(-\frac{z_{1,m}^2}{4Dct}\right) - z_{2,m}\exp\left(-\frac{z_{2,m}^2}{4Dct}\right)\right] \quad (1)$$

where

$$z_{1,m} = d(1-2m) - 4mz_e - z_0 \quad \text{for positive sources,}$$

$$z_{2,m} = d(1-2m) - (4m-2)z_e + z_0 \quad \text{for negative sources.}$$

where c is the speed of light, m is the number of the source, d is the thickness of the slab, and D is the diffusion coefficient given by

$$D = \frac{1}{3(\mu_a + \mu_s')} \quad (2)$$

An expression for steady-state transmission can be calculated by integrating the time-resolved expression over t, which gives

$$T(r) = \frac{1}{4\pi}\sum_{m=-\infty}^{\infty}\left(z_{1,m}(r^2+z_{1,m}^2)^{-3/2}\left\{1+\left[\frac{\mu_a(r^2+z_{1,m}^2)}{D}\right]^{1/2}\right\} \times \exp\left\{-\left[\frac{\mu_a(r^2+z_{1,m}^2)}{D}\right]^{1/2}\right\} - z_{2,m}(r^2+z_{2,m}^2)^{-3/2}\left\{1+\left[\frac{\mu_a(r^2+z_{2,m}^2)}{D}\right]^{1/2}\right\} \times \exp\left\{-\left[\frac{\mu_a(r^2+z_{2,m}^2)}{D}\right]^{1/2}\right\}\right) \quad (3)$$

EXPERIMENTAL

Samples. The tablets used in this work were produced in a cylindrical shape with flat end surfaces. The tablets had a diameter of 10 mm and thicknesses varied between 1.85 and 2.75 mm. All tablets had the same weight, and the thickness was varied by varying the compression force during the manufacturing process.

Three granulated materials with different concentration of active substance were used. The three granulated materials were sieved so that each tablet contained only particles of a certain size fraction. Two sieves were used, giving three different size fractions. The population investigated consisted of 82 tablets with approximately 9 tablets of each combination of particle size and concentration. The number of samples in the different batches is summarized in Table I. The different size fractions differed somewhat in concentration, but these differences were revealed by the reference analysis and therefore only made the concentration span of the samples larger.

As reference analysis, ultraviolet-absorption measurements were made on the tablets after they were dissolved

TABLE I. Overview of the number of measured tablets from the different batches.

		Sieve fraction (μm)		
		<150	150–400	>400
Nominal concentration (% weight)	28.5	9	10	9
	31.8	10	9	9
	34.9	9	8	9

in phosphate buffer pH 3.0.[30] The absorption was measured at 274 nm and the background at 550 nm on an HP 8453 UV/vis spectrometer (Agilent Technologies Sweden AB, Spånga, Sweden). From calibration samples, the content of active substance in the samples was calculated using the Beer–Lambert law. These values were used as reference values in the multivariate calibration models.

Time-Resolved Measurements. The time-resolved system used in this work has previously been described in detail.[31] Briefly, the experimental arrangement is depicted in Fig. 1. An Ar-ion laser pumped mode-locked Ti:Sapphire laser produced pulses shorter than 100 fs at a repetition rate of 80 MHz. The wavelength of the laser light was centered around 800 nm, and the energy of each pulse was 4 nJ. The light was focused into an index guiding crystal fiber (ICF) using a standard 40× microscope objective lens with a numeric aperture of 0.65. An optical isolator was used between the laser and the optics to prevent optical feedback into the laser due to reflections. A prism compressor was also used in the setup to compensate for the time dispersion caused by the different optical components. The ICF (Crystal Fibre A/S, Birkerod, Denmark) was 1 m long with a core diameter of 2 μm, manufactured to have zero dispersion at 760 nm. The dispersion properties of the fiber combined with the small core diameter resulted in a high peak power of the light through the entire fiber, yielding a widely spectrally broadened light emission due to nonlinear effects. The main broadening effects in the ICF were identified to be self-phase-modulation[32] and stimulated Raman scattering.[33] As a result of this, light pulses with almost the same temporal width as the laser, and with a spectral width spanning from 400 nm to at least 1200 nm, were accessible. However, the light distribution was not flat, but modulated with peaks with high intensities surrounded by wavelength regions with low intensities. The light from the output end of the ICF was focused by a lens onto the face of the tablet held into place by a circular iris holder, preventing stray light from reaching the detection system. The spot size on the tablet was approximately 2 mm. The light from the backside of the tablet was imaged onto the 250 μm slit of an imaging spectrometer, Chromex 250 IS (Bruker Optics Scandinavia AB, Taby, Sweden) coupled to a streak camera, Hamamatsu C5680 (Hamamatsu Photonics Norden AB, Solna, Sweden). The system measures a 600 nm broad wavelength region with a spectral resolution of 5 nm. The streak camera operated in synchro scan mode, allowing all light pulses to be collected. A small portion of the laser light was redirected by a beam splitter onto a photodiode that triggered the streak camera sweep. The system had a total temporal range of 2.1 ns with resolution of 4.5 ps. The instrumental response function was in the range of 30 ps when averaging over 300 s.

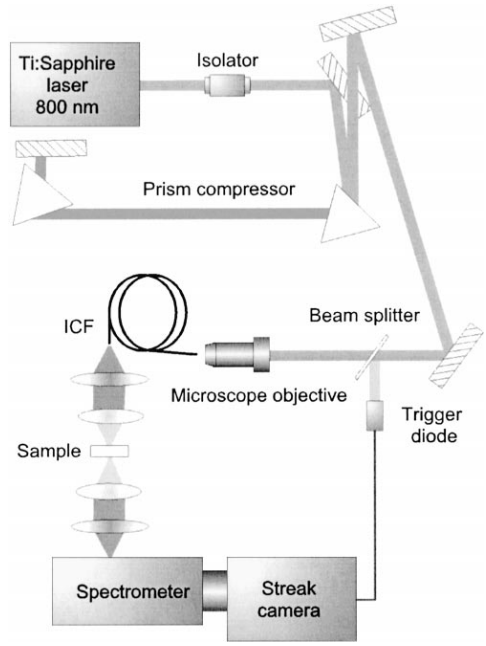

FIG. 1. Overview of the instrumentation used for the time-resolved measurements.

Conventional Transmission Near-Infrared Measurements. The conventional transmission NIR measurements were conducted on a Bomem MB 160 PH Fourier transform spectrometer (ABB Automation Technologies AB, Sollentuna, Sweden). The spectrometer was equipped with a tablet sampler making transmission measurements possible. The measurements were made in the wavelength range from 800 nm to 1500 nm with a resolution of 16 cm^{-1} in the entire range.

Deconvolution of Scattering and Absorption Properties of Samples Using Time-Resolved Measurements. The time-resolved data was evaluated for each wavelength individually in the wavelength region ranging from 800 to 1100 nm. The evaluation was made by fitting the measured time dispersion curves to the time-resolved diffusion model (Eq. 1), convolved with the instrumental response function (see Fig. 2). The dip at 275 ps in the photon migration data is due to detector sensitivity variations, but the effect is corrected before the evaluation. The data points included in the calculation were determined by two thresholds set to include all points with higher intensity than 20% of the peak intensity on the rising edge and higher than 10% on the falling edge. The evaluation algorithm used a Levenberg–Marquardt iterative procedure to extract μ_a and μ_s' from the data.

Scatter Correction of Conventional Transmission Near-Infrared Data. An overview of the complete scatter correction scheme is depicted in Fig. 3. The scattering

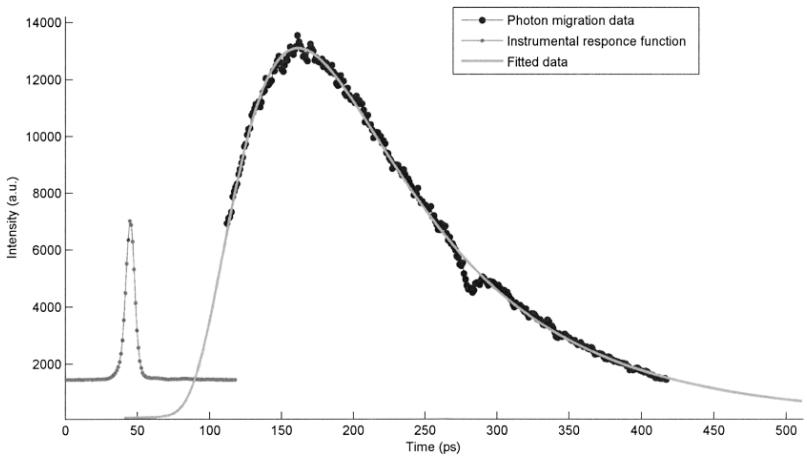

FIG. 2. An example of the evaluation of the time-resolved measurements, which was made by fitting the measured data to the time-resolved diffusion model. The measured data marked by the thicker line was used in the evaluation at this particular wavelength.

coefficients calculated from the time-resolved measurements at five wavelengths (855, 905, 955, 1005, and 1075 nm) were used in the scatter correction procedure. Using only five of all the available wavelengths had two objectives. First of all to mimic a simplified laser diode based system for *in situ* measurements, but also to facilitate the use of the other measured wavelengths to verify the correctness of the following steps of the evaluation scheme.

The scattering coefficients were calculated as an average over a 10 nm wide window to increase the signal-to-noise ratio. These values were used to calculate the scattering dependence on wavelength. The calculation was done by fitting the points to Eq. 4, which approximately describes the wavelength dependence of Mie scattering:[34]

$$\mu_s' = a\lambda^b \tag{4}$$

This approximation made it also possible to extrapolate the scattering coefficients into wavelength ranges not measurable by the present time-resolved system.

The extracted scattering coefficients from the Mie approximation were combined with the conventional NIR data and the steady-state diffusion model (Eq. 3) to extract the absorption coefficients in the entire wavelength range covered by the conventional NIR instrument (see Fig. 4). This calculation was also conducted using a Levenberg–Marquardt iterative procedure. The resulting absorption coefficients were independent of the path length of the light through the sample and therefore independent of the scattering properties of the sample.

Multivariate Calibrations. All multivariate calibration models were made in Simca-P 10.0 (Umetrics AB).

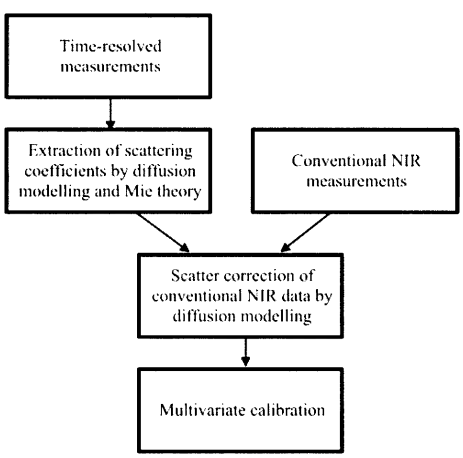

FIG. 3. Overview of the scatter correction procedure.

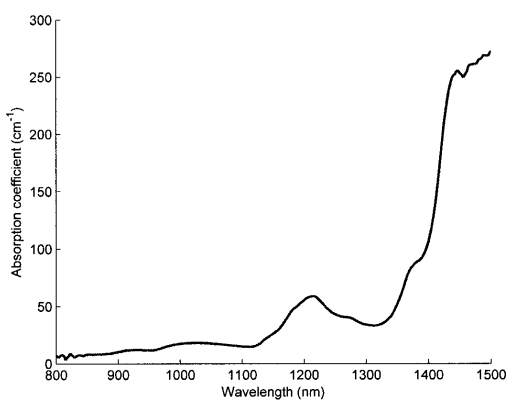

FIG. 4. The calculated absorption coefficients of a tablet from the batch with the highest nominal content of active substance and the medium sieve fraction.

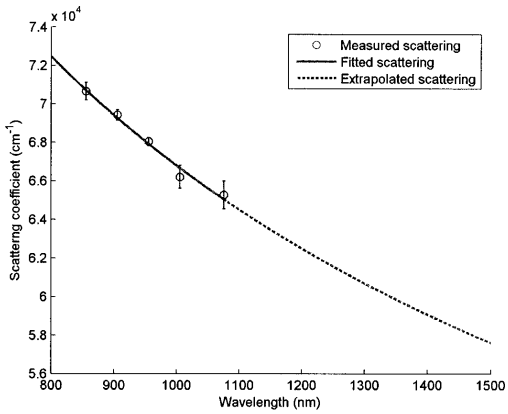

FIG. 5. A typical fit of the measured scattering to the equation defined by Mie theory. The measured scattering values are plotted to show the average and the standard deviation of ten measurements. The dotted line shows the extrapolation into longer wavelengths.

All spectra were mean centered before calculations and the number of principal components (PLSCs) selected in the models were as many as Simca-P 10.0 found suitable. The program uses the cross-validated predicted fraction for both X and Y to find the optimal number of PLSCs. In all models the samples not used in the calibration were used as a validation set, and the root mean square error of prediction value (RMSEP) (Eq. 5) was used to evaluate the performance of the different models.

$$RMSEP = \sqrt{\frac{\sum_{i=1}^{n} (\hat{y}_i - y_i)^2}{n}} \quad (5)$$

where $\hat{y}$ is the concentration of active substance predicted by the PLS model, y is the concentration of active substance measured by the reference analysis, and n is the number of samples. To get a better idea of the quality of the models, the RMSEP was divided by the mean concentration of the samples, giving the relative error in %.

RESULTS AND DISCUSSION

Deconvolution of Scattering and Absorption Properties of Samples Using Time-Resolved Data. The fitting of the time-resolved diffusion model to the time-resolved data was generally very good. The fit shown in Fig. 2 is typical for this step of the evaluations. A fit of the calculated scattering coefficients from the five wavelengths to the equation given by Mie theory is seen in Fig. 5. Values of b (see Eq. 4) were in the range from -0.25 to -0.5 for different samples.

After the scattering had been combined with the conventional NIR measurement and the steady-state diffusion model, the resulting absorption coefficients were compared to the absorption coefficients extracted from the time-resolved measurements alone. This comparison revealed that 70% of the samples showed a good agreement, with residuals below 10%, as seen in the left part of Fig. 6. The resulting 30% of the samples exhibit absorption coefficients that deviated from the absorption coefficients calculated directly from the time-resolved measurements. The deviations could be rather small, occurring just in limited wavelength regions, but some of the samples disagree completely, as seen in the right part of Fig. 6. The main source of error for this sometimes large deviation is thought to be errors introduced by an estimated time delay between the instrumental response function and the sample measurement, but also the signal-to-noise ratio in the evaluation of the scattering coefficients at the five wavelengths is crucial in order to obtain good results. The delay between the instrumental response function and sample measurements was calculated to be 15 ps. The delay occurs due to the insertion of a filter when measuring the instrumental response function, which was a necessity in order not to over-expose the detection system. Using this calculated delay gave unrealistic values of the absorption coefficients. Previous measurements on tissue phantoms, with known optical properties, have shown that by adding an extra 20

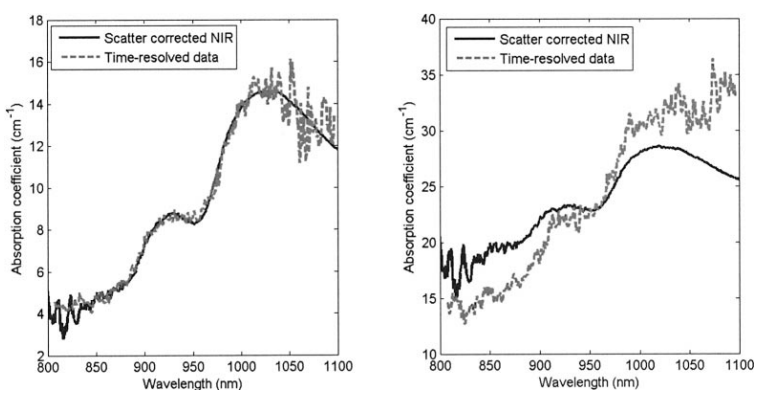

FIG. 6. Comparison between scatter corrected NIR spectra and absorption coefficient spectra calculated from time-resolved measurements.

ps to the calculated time delay, correct values of the absorption coefficient were gained. Therefore, a time delay of 35 ps was used in all evaluations. At this point, the reason for the extra time delay is not fully understood, but work to increase the understanding of the evaluation scheme is planned.

Quantitative Analysis Using Scatter Corrected Near-Infrared Data. To evaluate the data from the scatter correction scheme described above, a comparison with conventional NIR measurements was performed. The data from the scatter correction scheme will further on be referred to as the scatter corrected data. This to separate it from evaluations based on uncorrected conventional NIR data alone.

Basic Model. In order to compare the precision of the two methods, models based on half the data set were constructed and used to predict the other half. Both the calibration and validation sets included tablets from all nine batches. The model based on conventional NIR data resulted in an RMSEP value of 4.1% using five PLS components, while scatter corrected data resulted in an RMSEP value of 1.8% using six PLS components.

This evaluation shows that by correcting the conventional NIR data using time-resolved spectroscopy, the predictive ability of the constructed PLS models improved by more than 50%.

Models Based on Different Tablet Thicknesses. By building two different models, one only including the 17 thinnest tablets and one including only the 12 thickest tablets, a comparison of the robustness of the two methods was made. The validation sets contained the rest of the tablets, 65 and 70 samples respectively. To build a calibration model with that few samples, and to use it to predict samples with physical characteristics lying outside the parameter space spanned by the calibration samples, is troublesome when using conventional NIR data. The two models based on conventional NIR data showed the presumed quite poor predictive abilities, with RMSEP values of 5.2% and 11.2% for the models based on the thinnest and thickest tablets, respectively. The results from the scatter corrected data did not show the same drastic deterioration when compared to the basic model as the results from the conventional NIR data. When using scatter corrected data the RMSEP values for the two models were found to be 2.4% and 3.6% for the model based on the thinnest and thickest tablets, respectively.

This clearly shows that correcting conventional NIR data with time-resolved measurements at five wavelengths increases the robustness of the calibration models and makes it possible to predict samples with different physical dimensions than the tablets included in the calibration model (see Fig. 7).

Models Based on Tablets with Different Particle Size Distributions. To further compare the ability of the two techniques, all tablets manufactured from the largest particle size fraction (27 samples) were used as calibration set. When predicting the tablets made from the other two particle size groups the same kind of pattern as in the previous models was seen. The conventional NIR model gave prediction errors of 5.3% while the scatter corrected model showed a RMSEP value of 2.8%, further proving the robustness of the models based on scatter corrected data.

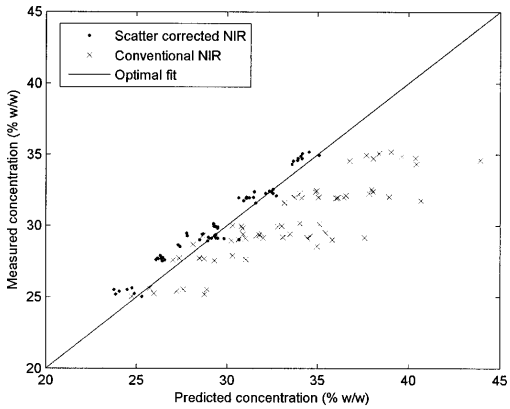

FIG. 7. Observed versus predicted values when predicting the 65 thickest tablets using a PLS models based on the 17 thinnest tablets. The scatter corrected data lies much closer to the line of optimal fit than the conventional NIR data.

Future Prospects. Although the instrumental setup for the time-resolved measurements used in this study only works in a research environment, the measurements and evaluations are conducted in a way that mimics a simplified laser diode based system. Such a system could be small and robust enough to be used for laboratory use as well as for on-line or at-line measurements in a process environment.

Combining a conventional NIR spectrometer with a simple time-resolved system could be an important step in making NIR spectroscopy more robust, making it possible to measure absorption spectra without any contribution from scattering effects. The technique might also be used for calibration transfer schemes[35,36] or other applications where additional information about the scattering properties of samples can complement conventional NIR data.

CONCLUSION

The scope of this work is a new methodology to correct conventional NIR data for scattering effects. The technique aims at measuring the absorption coefficient of the samples rather than the total attenuation, measured in conventional NIR spectroscopy. The main advantage of this is that the absorption coefficient is independent of the path length of the light inside the sample and therefore independent of the scattering effects.

The method is based on time-resolved spectroscopy and modeling of light transport by diffusion theory. This provides an independent measure of the scattering properties of the samples and therefore the path length of light. This yields a clear advantage over other preprocessing techniques, where scattering effects are estimated and corrected for by using the shape of the measured spectrum only.

Partial least squares calibration models show that, by using the proposed evaluation scheme, the predictive ability is improved by 50% as compared to a model based on conventional NIR data only. The method also makes

it possible to predict the concentration of active substance in samples with other physical properties than the samples included in the calibration model.

1. A. Eustaquio, P. Graham, R. D. Jee, A. C. Moffatt, and A. D. Trafford, Analyst (Cambridge, U.K.) **123,** 2303 (1998).
2. M. Dyrby, S. B. Engelsen, L. Norgaard, M. Bruhn, and L. Lundsberg-Nielsen, Appl. Spectrosc. **56,** 579 (2002).
3. P. Corti, G. Ceramelli, E. Dreassi, and S. Mattii, Analyst (Cambridge, U.K.) **124,** 755 (1999).
4. J. Gottfries, H. Depui, M. Fransson, M. Jongeneelen, M. Josefson, F. W. Langkilde, and D. T. Witte, J. Pharm. Biomed. Anal. **14,** 1495 (1996).
5. K. A. Martin, Appl. Spectrosc. Rev. **27,** 325 (1992).
6. R. B. Bruce, A. B. Mark, C. Show, Q. Xue-Zhi, and A. R. Priscilla, Pharm. Res. **13,** 616 (1996).
7. B. F. MacDonald and K. A. Prebble, J. Pharm. Biomed. Anal. **11,** 1077 (1993).
8. M. Andersson, O. Svensson, S. Folestad, M. Josefson, and K.-G. Wahlund, Chemom. Intell. Lab. Syst. **75,** 1 (2005).
9. J. Rantanen, H. Wikstrom, R. Turner, and L. S. Taylor, Anal. Chem. **77,** 556 (2005).
10. M. Blanco, J. Coello, A. Eustaquio, H. Iturriaga, and S. Maspoch, Anal. Chim. Acta **392,** 237 (1999).
11. M. Blanco, J. Coello, H. Iturriaga, S. Maspoch, and C. de la Pezuela, Analyst (Cambridge, U.K.) **123,** 135R (1998).
12. J. Johansson, S. Folestad, M. Josefson, A. Sparen, C. Abrahamsson, S. Andersson-Engels, and S. Svanberg, Appl. Spectrosc. **56,** 725 (2002).
13. R. J. Barnes, M. S. Dhanoa, and S. J. Lister, Appl. Spectrosc. **43,** 772 (1989).
14. P. Geladi, D. MacDougall, and H. Martens, Appl. Spectrosc. **39,** 491 (1985).
15. S. Wold, H. Antii, F. Lindgren, and J. Ohman, Chemom. Intell. Lab. Syst. **44,** 175 (1998).
16. S. Andersson-Engels, R. Berg, O. Jarlman, and S. Svanberg, Opt. Lett. **15,** 1179 (1990).
17. R. M. P. Doornbos, R. Lang, M. C. Aalders, F. W. Cross, and H. J. C. M. Sterenborg, Phys. Med. Biol. **44,** 967 (1999).
18. J. W. Pickering, S. A. Prahl, N. van Wieringen, J. F. Beek, H. J. C. M. Sterenborg, and M. J. C. van Gemert, Appl. Opt. **32,** 399 (1993).
19. O. Berntsson, T. Burger, S. Folestad, L. G. Danielsson, J. Kuhn, and J. Fricke, Anal. Chem. **71,** 617 (1999).
20. T. Pan and E. M. Sevick-Muraca, Anal. Chem. **74,** 4228 (2002).
21. Z. Sun, S. Torrance, F. K. McNeil-Watson, and E. M. Sevick-Muraca, Anal. Chem. **75,** 1720 (2003).
22. R. R. Shinde, G. V. Balgi, S. L. Nail, and E. M. Sevick-Muraca, J. Pharm. Sci. **88,** 959 (1999).
23. A. Pifferi, A. Torricelli, A. Bassi, P. Taroni, R. Cubeddu, H. Wabnitz, D. Grosenick, M. Möller, R. Macdonald, J. Swartling, T. Svensson, S. Andersson-Engels, R. van Veen, H. J. C. M. Sterenborg, J.-M. Tualle, H. L. Nghiem, S. Avrillier, M. Whelan, and H. Stamm, Appl. Opt. **44,** 2104 (2004).
24. S. K. Wan, Z. X. Guo, S. Kumar, J. Aber, and B. A. Garetz, J. Quant. Spectrosc. Radiat. Transfer **84,** 493 (2004).
25. S. J. Madsen, B. C. Wilson, M. S. Patterson, Y. D. Park, S. L. Jacques, and Y. Hefetz, Appl. Opt. **31,** 3509 (1992).
26. A. Pifferi, R. Berg, P. Taroni, and S. Andersson-Engels, Opt. Soc. Am. **32767,** 311 (1996).
27. M. S. Patterson, B. Chance, and B. C. Wilson, Appl. Opt. **28,** 2331 (1989).
28. K. M. Yoo, F. Liu, and R. R. Alfano, Phys. Rev. Lett. **64,** 2647 (1990).
29. R. C. Haskell, L. O. Svaasand, T.-T. Tsay, T.-C. Feng, M. S. McAdams, and B. J. Tromberg, J. Opt. Soc. Am. A **11,** 2727 (1994).
30. C. Abrahamsson, J. Johansson, A. Sparén, and F. Lindgren, Chemom. Intell. Lab. Syst. **69,** 3 (2003).
31. C. Abrahamsson, T. Svensson, S. Svanberg, S. Andersson-Engels, J. Johansson, and S. Folestad, Opt. Express **12,** 4103 (2004).
32. R. R. Alfano and S. L. Shapiro, Phys. Rev. Lett. **24,** 592 (1970).
33. S. Coen, J. D. Harvey, R. Leonhart, J. C. Knight, W. J. Wadsworth, and P. S. J. Russell, Opt. Lett. **26,** 1356 (2001).
34. F. Bevilacqua, A. J. Berger, A. E. Cerussi, D. Jakubowski, and B. J. Tromberg, Appl. Opt. **39,** 6498 (2000).
35. R. N. Feudale, N. A. Woody, H. Tan, A. J. Myles, S. D. Brown, and J. Ferre, Chemom. Intell. Lab. Syst. **64,** 181 (2002).
36. T. Fearn, J. Near Infrared Spectrosc. **9,** 229 (2001).

Paper III

Characterization of normal breast tissue heterogeneity using time-resolved near-infrared spectroscopy

T. Svensson, J. Swartling, P. Taroni, A. Torricelli, P. Lindblom, C. Ingvar and S. Andersson-Engels.

Physics in Medicine and Biology **50**, 2559-2271 (2005).

INSTITUTE OF PHYSICS PUBLISHING PHYSICS IN MEDICINE AND BIOLOGY

Phys. Med. Biol. **50** (2005) 2559–2571 doi:10.1088/0031-9155/50/11/008

Characterization of normal breast tissue heterogeneity using time-resolved near-infrared spectroscopy

Tomas Svensson[1], Johannes Swartling[1], Paola Taroni[2], Alessandro Torricelli[2], Pia Lindblom[3], Christian Ingvar[3] and Stefan Andersson-Engels[1]

[1] Department of Physics, Lund Institute of Technology, Box 118, SE-221 00 Lund, Sweden
[2] Politecnico di Milano, Piazza Leonardo da Vinci 32, I-210 33 Milan, Italy
[3] Department of Surgery, Lund University Hospital, SE-221 85 Lund, Sweden

E-mail: tomas.svensson@fysik.lth.se, js604@cam.ac.uk, paola.taroni@polimi.it, alessandro.torricelli@polimi.it, pia.lindblom@skane.se, christian.ingvar@skane.se and stefan.andersson-engels@fysik.lth.se

Received 11 November 2004
Published 18 May 2005
Online at stacks.iop.org/PMB/50/2559

Abstract

In recent years, extensive efforts have been made in developing near-infrared optical techniques to be used in detection and diagnosis of breast cancer. Variations in optical properties of normal breast tissue set limits to the performance of such techniques and must therefore be thoroughly examined. In this paper, we present intra- and intersubject as well as contralateral variations of optical and physiological properties in breast tissue as measured by using four-wavelength time-resolved spectroscopy (at 660, 786, 916 and 974 nm). In total, 36 volunteers were examined at five regions at each breast. Optical properties (absorption, μ_a, and reduced scattering, μ_s') are derived by employing diffusion theory. The use of four wavelengths enables determination of main tissue chromophores (haemoglobin, water and lipids) as well as haemoglobin oxygenation. Variations in all evaluated properties seen over the entire breast are approximately twice those for small-scale heterogeneity (millimetre scale). Intrasubject variations in optical properties are almost in all cases below 20% for μ_s', and 40% for μ_a. Overall variations in water, lipid and haemoglobin concentrations are all in the order of 20%. Oxygenation is the least variable of the quantities evaluated, overall intrasubject variations being 6% on average. Extracted physiological properties confirm differences between pre- and post-menopausal breast tissue. Results do not indicate systematic differences between left and right breasts.

1. Introduction

The development of optical methods for detection and diagnosis of breast cancer has been pursued with increasing efforts during recent years. Optical methods for non-invasive tumour detection are based on near-infrared (NIR) light, typically within 600–1000 nm, which has the ability to propagate through tissue and yield a detectable reflected or transmitted signal. The NIR signal provides information on absorption and scattering properties of tissue, as well as spatial distribution of structures in the breast. The absorption coefficient μ_a and the reduced scattering coefficient μ_s' can be determined. This can be done locally, by using a probe based on a number of optical fibres to deliver and collect the light (Cubeddu *et al* 1999, Cerussi *et al* 2002, van Veen *et al* 2004a), or by imaging techniques such as diffuse optical tomography (Gratton *et al* 1993, Colak *et al* 1999, McBride *et al* 2001, Hebden *et al* 2002, Li *et al* 2003, Yates *et al* 2005) or by scanning the source and detector fibres across the compressed breast to record a shadowgram type image analogous to x-ray mammography (Franceschini *et al* 1997, Grosenick *et al* 2003, Taroni *et al* 2004). A key concept in these optical methods is the spectral information that can be derived if several wavelengths are used. Absorption properties can be used to quantify concentrations of chromophores in the tissue, of which the four principal ones are non-oxygen-saturated haemoglobin, oxygen-saturated haemoglobin, water and lipids (Sevick *et al* 1991, Matcher *et al* 1995, Cubbedu *et al* 1999). The spectral shape of the reduced scattering coefficient can provide valuable information about size and distribution of tissue scatterers, which in turn can be used to extrapolate structure and cellular composition of the tissue (Beauvoit *et al* 1994, Mourant *et al* 1997, Nilsson *et al* 1998, Cerussi *et al* 2001, Srinivasan *et al* 2003, Pifferi *et al* 2004).

Several investigations have been carried out to determine the relations between optical and physiological properties of normal breast tissue. Studies utilizing optical techniques have shown that breast tissue characteristics correlate with factors such as age (Cubeddu *et al* 1999, Cerussi *et al* 2001, Srinivasan *et al* 2003, Shah *et al* 2001), hormonal cycle (Cubeddu *et al* 2000), menopause status (Shah *et al* 2001, Cerussi *et al* 2002) and body mass index (Pogue *et al* 2001, Cerussi *et al* 2002, Durduran *et al* 2002). A number of investigators have also shown differences in the NIR signal for cancerous lesions as compared to normal tissue or benign lesions (Andersson-Engels 1992, Fantini *et al* 1998, Tromberg *et al* 2000, Pogue *et al* 2001, Grosenick *et al* 2003, Taroni *et al* 2004). These papers present a variability in optical properties for different lesions. Other studies have investigated the variability in optical properties of normal breast tissue (Shah *et al* 2004, van Veen *et al* 2004a, Pogue *et al* 2004). Of these, only Shah *et al* (2004) emphasize intrasubject variations. The overall variability implies an overlap between optical properties of lesions and normal tissue, which most likely precludes detection formulae based on direct analysis of absolute values of measured optical properties. Most certainly, detection methods will therefore be based on relative observations such as ratios, comparisons between different parts of the breast, comparisons between left and right breasts, or image contrast and context analysis in the case of imaging modalities. For this development, it is of fundamental importance to possess knowledge of the intrinsic variations of optical properties within a breast and between left and right breasts.

In this paper, we present an extensive investigation of intra- and intersubject heterogeneity in optical and physiological properties of normal breast tissue. A total number of 36 volunteers were included in the study. Optical properties were measured using four-wavelength time-resolved spectroscopy (Swartling *et al* 2003, Pifferi *et al* 2005) following a protocol comprising five measurement areas on each breast. Small-scale variations (millimetre displacements) were investigated thoroughly. A similar protocol was used by Shah *et al* (2004), in an investigation based on frequency-domain measurements at a fixed fibre separation.

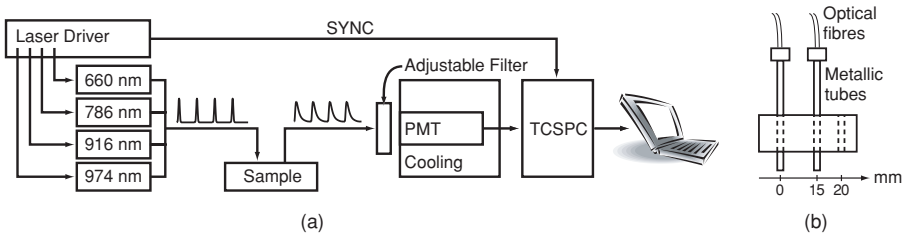

Figure 1. A schematic of the instrumentation in reflectance mode (a) and one of the probe while having 15 mm fibre separation (b).

In our study, most measurements were conducted using two different source and detector fibre separations, which means that different probing depths were used. This enables us to investigate spatial variation both laterally and axially.

2. Materials and methods

2.1. Instrumentation

All data were acquired using a compact and portable time-domain photon migration instrument primarily intended for spectroscopy of biological tissue in a clinical environment (Swartling *et al* 2003, Pifferi *et al* 2005). The system is based on diode laser technology and time correlated single photon counting (TCSPC). A laser driver (SEPIA PDL 808, PicoQuant, Germany) controls four pulsed diode lasers (LDH, PicoQuant at 660, 786, 916 and 974 nm). Wavelengths are chosen to enable monitoring of important tissue constituents (haemoglobin, water and lipids) and properties (tissue oxygenation). By separating the individual pulses in time (~ 6 ns), using electric cables of different lengths, it is possible to generate 4λ pulse trains at a repetition frequency up to 40 MHz. Diode lasers are coupled into 200 μm GRIN fibres (G 200/280 N, ART Photonics, Germany). A 4-1 coupler is used to couple all lasers into a 600 μm GRIN fibre (G 600/840 N, ART Photonics), which serves as the light source. A second 600 μm GRIN fibre collects light and delivers it to the detector. The length of these fibres were 1.95 m each. Since this work is based on diffuse reflectance measurements, these fibres were held by a probe that fixes them at a certain fibre separation (15 or 20 mm). The probe is made of a small metal block through which two metal tubes run (tubes may be moved to achieve proper separation). The metal tubes extend from the block, and optical fibres are inserted in these so that fibre endings are almost edge to edge with tube endings. The probe is held so that tube and fibre endings are in contact with the tissue. All parts are painted in mat black. Proper photon levels are achieved by sending collected light through an adjustable gradient ND filter. Remaining photons are sent into a cooled MCP-PMT (R3809-59, Hamamatsu Photonics, Japan). A TCSPC computer card (SPC-300, Becker & Hickl, Germany) is used to obtain time-dispersion curves. Lasers are typically operated at 1–2 mW generating pulses about 70 ps wide (FWHM). However, broadening in fibres and detector causes the instrument response function (IRF) to be about 100 ps wide. A schematic is given in figure 1.

2.2. Clinical procedure

Clinical data were collected at the Lund University Hospital adhering to a protocol approved by the local committee of ethics. Measurements were conducted during May and June 2003

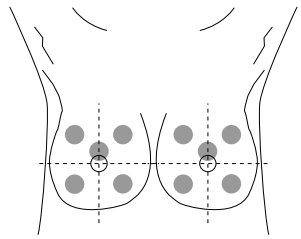

Figure 2. Location of measurement areas (five on each breast).

on in total 36 volunteers (29 pre-menopausal and 7 post-menopausal). Relevant medical information was collected in connection with the measurements. None of the volunteers had been diagnosed with malignant disease. All measurements were carried out while subjects were in a comfortable sitting posture. The probe was held by subjects themselves after careful instruction. Each breast was examined at five different areas: at the centre part of the four quadrants and just above the areolar area (denoted left/right (L/R) upper outer (UO), upper inner (UI), lower inner (LI), lower outer (LO) and upper areolar (UA)). Locations of measurement areas are illustrated in figure 2. Six out of the thirty-six volunteers were examined using only the 20 mm fibre separation, and following a more comprehensive protocol P1 where (i) five spatially separated measurements are performed within each area (small millimetre-scale probe displacements) and (ii) five spatially identical measurements (fixed probe geometry) are performed at the upper outer areas (RUO and LUO) to ensure/monitor stability. The remaining 30 volunteers were examined using two different fibre separations (15 and 20 mm) and a different protocol P2. In these cases each area was only measured once, except for the upper outer areas which were measured three times (spatially separated in the case of ROU and spatially identical in the case of LOU). Typically, a single measurement was completed within 20–30 s.

2.3. Modelling

Experimental data are modelled using the diffusion approximation of transport theory. The particular model used in this work is derived for the case of homogenous media in a semi-infinite geometry and employs a so-called extrapolated boundary condition (Haskell *et al* 1994, Hielscher *et al* 1995). The refractive index of tissue is assumed to be 1.4. Tissue optical properties are extracted by fitting solutions of the diffusion equation to experimental data. An example on how data may appear is given in figure 3. To avoid problems related to early photons, such as poor validity of the diffusion equation and stray light, fitting is limited to datapoints where the photon count exceeds 30% of the peak count on the rising flank (see figure 3). The trailing flank is cut where the photon count drops below 1% of the peak count. Discussions on appropriate fit regions are found in Hielscher *et al* (1995) and Cubeddu *et al* (1996). The best fit is reached iteratively using a Levenberg–Marquardt algorithm, where μ_s', μ_a and an overall amplitude (scale) factor are varied in order to minimize the χ^2 error norm. The temporal delay between IRF and experimental data is known and is thus not a free parameter. Each iteration involves a convolution between the theoretical time-dispersion curve and the IRF. The IRF is carefully measured before and after every set of measurements to ensure stability and, as mentioned above, since it is needed in data evaluation.

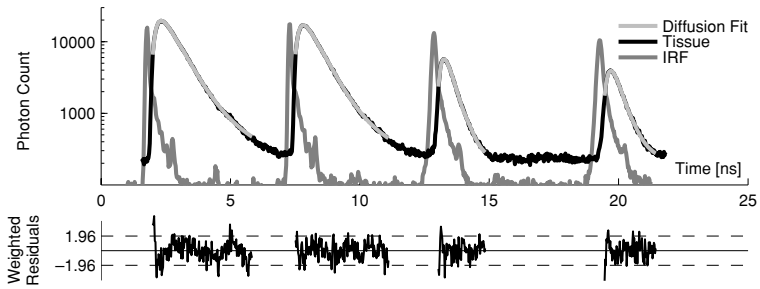

Figure 3. Example of time-resolved data. The 4λ pulsetrains correspond to (from left to right) 660, 786, 916 and 974 nm. Experimental curves (tissue) are partially hidden behind fitted diffusion curves, indicating reasonable fits. Residuals occasionally and non-systematically exhibit non-random patterns (as seen for 660 nm in this example). [−1.96, 1.96] is a 95% prediction interval for a standardized normal distribution.

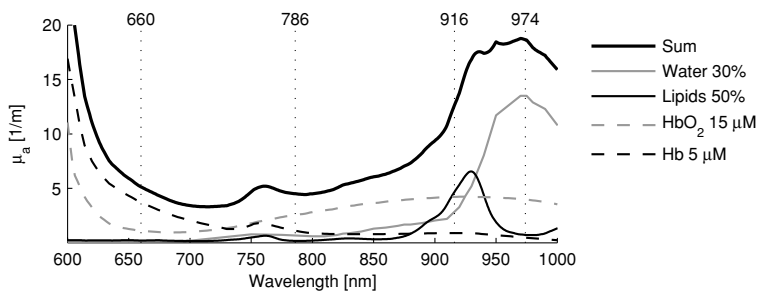

Figure 4. A typical breast tissue spectrum constructed from component spectra. Vertical dotted lines mark where diode lasers are positioned. Note that oxy-haemoglobin, lipid and water absorption exhibit comparable strengths in the range 900–950 nm.

Tissue constituents are determined using the four extracted absorption coefficients. The use of four wavelengths enables calculations of concentration for the four main chromophores in breast tissue: water, lipids, deoxy-haemoglobin (Hb) and oxy-haemoglobin (HbO_2). The assumption is that the observed absorption match a linear superposition of the four main component spectra, and that no other tissue constituents contribute to the absorption in this wavelength region. The haemoglobin spectra are taken from Prahl (2004), the water spectrum from Hale and Querry (1973) and the lipid spectrum from van Veen *et al* (2004b). An example of an interpreted breast spectrum composed of the four tissue chromophores in typical concentrations is shown in figure 4. Mathematically, concentrations are calculated by solving a set of linear equations

$$\boldsymbol{\mu}_\mathrm{a} = \boldsymbol{A} \cdot \boldsymbol{c} \quad \Rightarrow \quad \boldsymbol{c} = \boldsymbol{A}^{-1} \cdot \boldsymbol{\mu}_\mathrm{a} \tag{1}$$

where $\boldsymbol{\mu}_\mathrm{a}$ is a vector of extracted absorption coefficients at the four wavelengths, $\boldsymbol{A}$ a matrix of absorption coefficients for the four chromophores at the four wavelengths measured and $\boldsymbol{c}$ a vector of concentrations. Haemoglobin concentrations [Hb] and [HbO_2] are measured in μM, while water and lipid concentrations are measured in volume per cent (per cent relative to pure water and lipid, respectively). Oxygenation (S_tO_2) is determined by the ratio of [HbO_2] to total haemoglobin concentration [Hb] + [HbO_2] (THC). Error propagation is discussed in section 4.

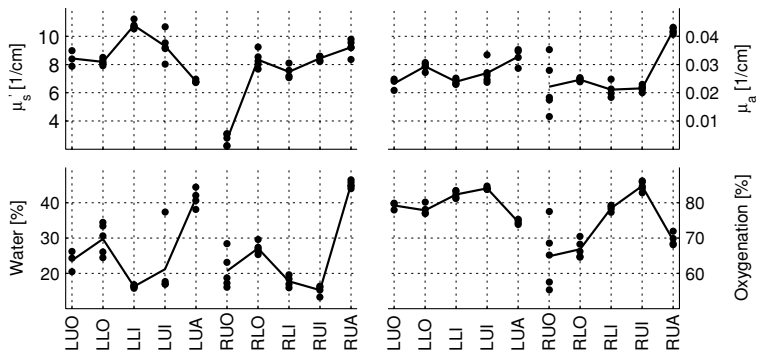

Figure 5. Derived optical (660 nm) and physiological parameters grouped by position, originating from one volunteer (age 33 years) examined according to protocol P1. In this particular case, extremely low scattering is extracted at one position (RUO). Markers correspond to extracted values within series of small-scale probe displacements. Lines join positional averages. Data from the left and right breasts are presented separately in each graph.

Table 1. Positional averages of optical and physiological properties (this study). Results are compared with values from recent literature. *N* states the number of subjects involved in the different studies. Optical properties, μ_s' and μ_a, are extracted at 785 or 786 nm.

	N	μ_s' (cm^{-1})	μ_a (cm^{-1})	THC (μM)	Oxygenation (%)
This study	36	8.0 ± 2.0	0.041 ± 0.021	17 ± 10	77 ± 8
Spinelli *et al* (2004)	>50	11.3 ± 2.1	0.037 ± 0.013	16 ± 5	66 ± 9
Grosenick *et al* (2003)	28	10.2 ± 1.6	0.039 ± 0.009	17 ± 8	74 ± 3
Durduran *et al* (2002)	52	8.5 ± 2.1	0.041 ± 0.025	34 ± 9	68 ± 8

2.4. Variational measures

Intrasubject variations are characterized using coefficients of variation (CV). The CV of a certain series $\{x_i\}$ is defined as the standard deviation divided by the mean: $\mathrm{CV}_x = \sigma_x/\overline{x}$. It is a unitless quantity stated in per cent.

The CV of a fixed geometry series states the variations induced mainly by instrumentation and measurement parameters, such as e.g. probe-skin pressure, as well as noise in the signal. The CV of a displacement series is a measure of the local intrasubject variation within different measurement areas. Overall intrasubject variation is, in this work, defined as the CV of the ten average values obtained for the ten different positions.

3. Results

An example of how extracted data may appear is given in figure 5. Here, a selection of data from one volunteer examined according to protocol P1 is presented. Average properties, based on all volunteers, are presented and compared to values from literature in table 1.

A statistical analysis of intrasubject variations for fixed geometries (F), small-scale displacements (D) and overall (O) is shown in figure 6. Variations in fixed geometry series are typically very small compared to variations in series where the probe is displaced, as long as the probe is held properly (no change in pressure or orientation). However, if probe-skin pressure or probe orientation is varied (still using a fixed position) variations

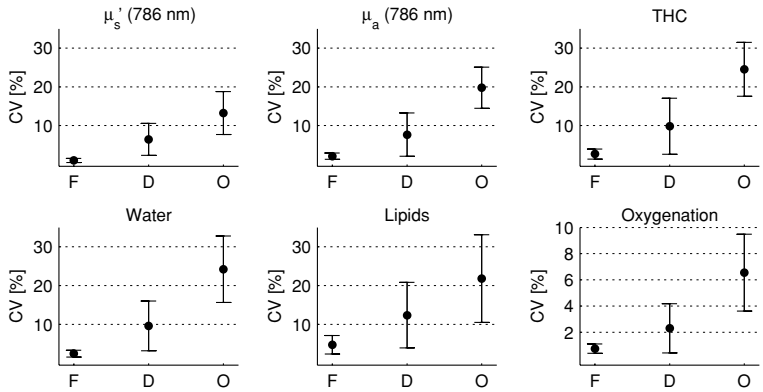

Figure 6. Intrasubject variation in fixed series (F, $m = 42$), displacement series (D, $m = 90$) and overall (O, $m = 36$), where m follows from study protocols and refers to the number of underlying series. Variations are given in CV (%). Dots represent the average intrasubject CV and error bars stretch out to $\pm\sigma$, where σ is the standard deviation of the CV distribution. Data are based on series from $n = 36$ volunteers.

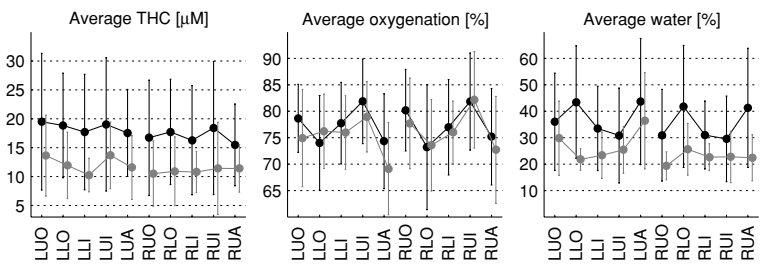

Figure 7. Average values versus measurement position. Volunteers are divided in two groups: pre-menopausal ($n = 29$, black) and post-menopausal ($n = 7$, grey). 20 mm fibre separation.

occasionally are in the same order. Derived optical and physiological properties indicate that the overall intrasubject variation is typically a factor of 2 greater than variations within displacement series (a factor of 4 in the case of S_tO_2). Overall intrasubject variations in μ_s' were $(14.0 \pm 6.5)\%$, $(13.2 \pm 5.6)\%$, $(15.1 \pm 5.5)\%$ and $(15.3 \pm 6.0)\%$, for 660, 786, 916 and 974 nm respectively. μ_a varied even more, and corresponding figures were $(23.1 \pm 8.3)\%$, $(19.8 \pm 5.3)\%$, $(11.8 \pm 3.6)\%$ and $(20.4 \pm 8.3)\%$ (the largest variation was 48.7% and was registered at 974 nm, but CVs above 40% were very rare). S_tO_2 displays the smallest overall intrasubject variation, being $(6.6 \pm 2.9)\%$ (in all cases below 14.2%).

In order to better understand these variations, the data were analysed to provide intersubject variation with respect to positional averages. Figure 7 shows the result for haemoglobin, oxygenation and water. In these graphs, pre-menopausal and post-menopausal volunteers are considered as two separate groups. Concentrations of haemoglobin and water were both approximately 1.5 times greater, on average, for pre-menopausal volunteers. On the other hand, lipid concentration was approximately 1.4 times greater for post-menopausal volunteers. Nonetheless, variations within the two groups cause overlap. No significant differences were noted neither for oxygenation levels or scattering levels (not shown).

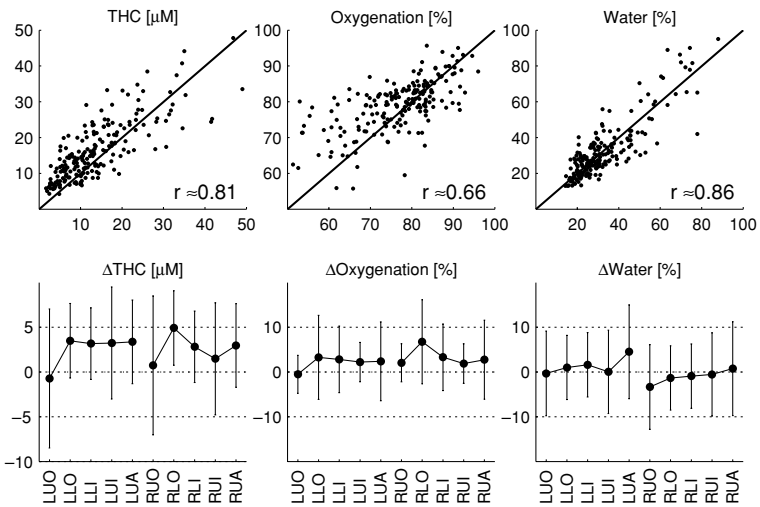

Figure 8. Upper row: scatter plots showing correlation between results obtained using different fibre separations (15 mm (x axis) and 20 mm (y axis)). Correlation coefficient r and diagonals are added for reference. Lower row: average difference, $\Delta = \Delta_{20-15}$, grouped on measurement position. Error bars stretch out to $\pm\sigma$.

By changing the separation between probe fibres, the influence of probing depth was examined. Correlations between data obtained for the two fibre separations are stated using the correlation coefficient r. Fairly strong correlations between the two ways of measuring were observed for all optical and physiological properties. Lowest correlation was found in scattering (on average $r = 0.51$). Correlations (r) were on average 0.78 for absorption, 0.67 for lipids and 0.86 for water. No significant differences were observed in the cases of lipids, water or scattering. However, as indicated in figure 8, extracted levels of oxygenation and haemoglobin tended to be systematically higher when using the larger fibre separation (20 mm).

Intrasubject variations between left and right breasts were examined by comparing corresponding measurements. The result does not indicate any significant systematic differences. Left–right asymmetry in a certain parameter p is measured using relative deviation Δ_{rel}

$$\Delta_{\text{rel}} = \frac{|p_{\text{left}} - p_{\text{right}}|}{(p_{\text{left}} + p_{\text{right}})/2} \tag{2}$$

where p_{left} and p_{right} are (mean) values derived at a certain measurement area. Δ_{rel} is a unitless quantity that states the deviation in % of the mean of the left and right parameter values. Results are presented in table 2.

4. Discussion

The main purpose of this study is to measure variations in tissue composition of normal breasts and discuss how such variations may influence the possibility of discriminating a possible tumour using optical methods. Nevertheless, it is important to note that fundamental optical and physiological properties derived in this study are in good agreement with previously

Table 2. Variations between the left and right breasts stated in relative deviation Δ_{rel} (% of mean). Values presented are means of the individual relative left–right deviation derived for all $n = 36$ volunteers (20 mm fibre separation).

	UO	LO	LI	UI	UA
THC	27	19	19	26	26
Oxygenation	6	8	5	5	9
Water	28	15	17	19	24
Lipid	24	36	20	22	26
Scattering (786 nm)	11	12	13	15	15

published data (see table 1). Deviations may be assigned to differences in measurement geometry. The statistical analysis of spatial variations within breast tissue, as measured in this study, is illustrated in figure 6. On average, variations once the probe was held fixed in the same position are small for all properties evaluated. Variations in these measurements are not believed to reflect any changes within the tissue structure, but rather variations in how the probe was applied to the tissue, mainly due to pressure variations, as well as uncertainties in the evaluation of the signals due to noise. As soon as the probe was displaced a few millimetres to include small-scale tissue variability, variations increased for all parameters. Interestingly, water, lipid and haemoglobin concentrations varied considerably more (a factor 5) than the oxygenation (as also reported by Shah *et al* (2004)). Variations in evaluated constituent concentrations are believed to be due to the heterogeneous structure of breast tissue even at this small scale (millimetres). The oxygenation of haemoglobin present in the probe volume is, however, less likely to alter for these small displacements. Oxygenation is high everywhere in normal breasts.

Variations in all evaluated properties seen over the entire breast are approximately twice those registered for small-scale displacements of the probe. The increased variability for these measurements can, at least partly, be explained by more systematic alterations in tissue structure and composition at different parts of the breast. Such variations are presented in figure 7. In general, strong overlaps exist between values for different locations. However, while total haemoglobin concentration is relatively even throughout the breast, oxygenation seems to be slightly higher in the upper inner area of the breast and lower in the upper areolar area. Shah *et al* (2004) report significantly lower oxygenation in areolar regions, but no significant variations among other regions. Worth noting is also that intrasubject variations in μ_a is a factor 2 smaller at 916 nm than at the other three wavelengths. This is related to the fact that lipids and water exhibit comparable absorption strengths in this region, and that these two constituents, to a large extent, replace each other (Pifferi *et al* 2004, Swartling *et al* 2005).

The data also show differences in total haemoglobin and water concentrations for pre- and post-menopausal women. Such changes are in accordance with known structural alterations of breast tissue after menopause (Shah *et al* 2004). However, one should also have in mind that there is a difference in age between the two groups. The mean ages for the two groups in this study are 37 and 52 years, respectively. In the material, it is also evident that the composition of the breast may be quite different in different persons. Intersubject variations are thus much higher than intrasubject variations (see figure 7).

Heterogeneity of breast tissue has previously been addressed by Shah *et al* (2004). Their investigation presents small-scale variations in the same order as our report. Overall heterogeneity is similar in the case of water, lipids, THC and oxygenation. However, Shah *et al* (2004) report on an overall heterogeneity less than 12% for μ_s' while we observe corresponding values up to approximately 20%. The generally good agreement in results was obtained despite

differences in measurement technique (time-domain versus frequency-domain), measurement geometry (probe design, sitting versus supine position) and possibly also in exact measurement positions.

By using two different distances between the source and detector fibres we probe different depths of the tissue (Patterson *et al* 1995). For time-resolved data the probing depth is also a function of the time the light has spent in the tissue. The evaluation of μ_s' in the fitting process is sensitive to the early portion of the light, while μ_a is mostly determined by the late light (Andersson-Engels *et al* 1992, Cubeddu *et al* 1996). This means that the extracted values of μ_s' and μ_a do not represent the exact same volume, even for the same fibre separation. Scattering values represent a shallow volume confined to the region between the two fibres, while the absorption values are derived from a larger volume deeper in the tissue. When performing measurements, for practical reasons, the probe had to be lifted between the measurements at 15 mm and 20 mm fibre separation. Repositioning of the probe could not be done with better accuracy than a few millimetres, which means that we can expect a random variation in the results of at least the same order of magnitude as that given by small displacements of the probe, as shown in figure 6. This is seen in the scatter plots in figure 8. The difference in effective probing volume for determination of μ_a and μ_s' may explain the lower degree of correlation for μ_s' ($r = 0.51$) compared to μ_a ($r = 0.78$). Moreover, we noted an average increase in both THC and S_tO_2 when increasing the fibre separation from 15 mm to 20 mm, as seen in figure 8. This may be interpreted as a higher haemoglobin concentration and oxygen saturation at larger depth, and is in agreement with the known structure of tissue: at short fibre separations, the probing volume is more affected by the skin layer, which has lower blood perfusion. Similar findings were reported by Pifferi *et al* (2004), where the fibre separation was increased from 20 to 40 mm.

All data presented in this study are based on rather superficial measurements on breasts, including skin, subcutaneous fat and breast tissue. This will often be the case in diagnostic procedures based on non-invasive optical spectroscopy. Due to the aim to measure local properties in the same spatial scale as would be of interest for tumour diagnostics, without relying on a tomographic algorithm, the interfibre distance is short. This results in a relatively large fraction of the probed tissue being occupied by subcutaneous fat, especially for women with high body mass index (BMI). Unfortunately, the material is not sufficiently large to make a correlation with BMI. However, Pifferi *et al* (2004) report that the kind of diffuse reflectance measurements employed in this paper provide representative values even for interior breast tissue. Whether this also hold for interior heterogeneity is unclear and is currently examined both in Lund and elsewhere.

In this work, breast spectra are sampled at four wavelengths. Since equally many (four) chromophores need to be taken into account, it is very important that all of the four derived absorption coefficients are accurate. According to basic perturbation theory, errors in $\boldsymbol{c}$ (denoted $\delta\boldsymbol{c}$) are related to errors in $\boldsymbol{\mu}_a$ (denoted $\delta\boldsymbol{\mu}_a$) as shown in (3).

$$\boldsymbol{c} = \boldsymbol{c}^{\text{true}} + \delta\boldsymbol{c} = \boldsymbol{A}^{-1} \cdot \left(\boldsymbol{\mu}_a^{\text{true}} + \delta\boldsymbol{\mu}_a\right) \quad \Rightarrow \quad \delta\boldsymbol{c} = \boldsymbol{A}^{-1} \cdot \delta\boldsymbol{\mu}_a. \tag{3}$$

Thus, influence of errors in extracted absorption coefficients may be examined by taking a closer look at the matrix $\boldsymbol{A}^{-1}$. Relative errors naturally depend on the tissue constitution of the particular breast (i.e. $\boldsymbol{c}^{\text{true}}$ and $\boldsymbol{\mu}_a^{\text{true}}$). By proper normalization of $\boldsymbol{A}^{-1}$ it is possible to determine a relative error propagation matrix, $\boldsymbol{E}$, that states component-wise relative error propagation (valid for a particular tissue composition). The normalization procedure is defined in 4, where diag$(\cdots)$ are diagonal 4×4 matrices.

$$\boldsymbol{E} = \boldsymbol{E}\left(\boldsymbol{A}^{-1}, \boldsymbol{c}^{\text{true}}, \boldsymbol{\mu}_a^{\text{true}}\right) = \text{diag}(1/\boldsymbol{c}^{\text{true}}) \cdot \boldsymbol{A}^{-1} \cdot \text{diag}\left(\boldsymbol{\mu}_a^{\text{true}}\right). \tag{4}$$

When considering breast tissue having the composition as shown in figure 4 one finds that

$$\boldsymbol{E} = \begin{pmatrix} 1.58 & -0.56 & -0.12 & 0.11 \\ -0.74 & 2.27 & -0.12 & -0.41 \\ 0.27 & -1.59 & 2.90 & -0.58 \\ 0.15 & -0.56 & -0.11 & 1.53 \end{pmatrix}. \tag{5}$$

Here, each column corresponds to a certain wavelength (660, 786, 916 and 974 nm, from left to right) and each row to a certain chromophore (Hb, HbO_2, lipids and water, from top to bottom). As an example, a + 1% error in μ_a at 786 nm will add a +2.27% error on HbO_2 concentration (when measuring on a tissue consisting of 50% lipids, 30% water, 5 μM Hb and 15 μM HbO_2). $\boldsymbol{E}$ gives an idea of the robustness of four-wavelength spectroscopy when applied to characterization of breast tissue. The diagonal dominance implies that each chromophore has its own main wavelength (this is also seen in figure 4). The relatively large numbers in the third row show that the derivation of lipid concentrations suffer the greatest sensitivity to errors. This is due to that lipid absorption normally does not dominate over other chromophores at any wavelength (this is exemplified in the breast spectra presented in figure 4). This is a possible explanation to why lipid levels, in comparison with other chromophore levels, exhibit larger variations within fixed series (see figure 6).

5. Conclusion

In summary, we have investigated the influence of normal spatial heterogeneities of breast tissue on optical and related physiological properties measured with a four-wavelength, time-resolved diffuse spectroscopy instrument. Variations in evaluated properties over all measurement areas were about twice as large as small-scale variations (mm displacements). Intrasubject variation was in almost all cases below 40% for μ_a and below 20% for μ_s'. In terms of the evaluated quantities of water, lipids and haemoglobin, the variation in these were all in the order of 20%, while the oxygen saturation exhibited a lower variation (6%). These numbers define a background variation that any modality for optical detection of breast cancer has to take into account. Furthermore, we did not see any evidence of systematic differences between contralateral breasts, although individual left–right asymmetry is often seen. The intersubject variation is larger than the intrasubject variation and is loosely correlated with menopause status, which confirms previous studies. Finally, measurements performed at different fibre separations, thus probing different depths, indicated an on average higher haemoglobin concentration at the larger fibre separation. Random variations were in this case comparable to those seen for small-scale displacements.

Acknowledgments

This work was financially supported by OPTIMAMM (European grant QLG1-2000-00690), MEDPHOT (European grant QLG1-2000-01464), CUSBO (European grant HPRI-CT-2001-00148) as well as the Swedish Research Council. The authors also wish to thank all volunteers for their participation.

References

Andersson-Engels S, Berg R and Svanberg S 1992 Effects of optical constants on time-gated transillumination of tissue and tissue-like media *J. Photochem. Photobiol.* B **16** 155–67

Beauvoit B, Kitai T and Chance B 1994 Contribution of the mitochondrial compartment to the optical properties of the rat liver: a theoretical and practical approach *Biophys. J.* **67** 2501–10

Cerussi A, Berger A J, Bevilacqua F, Shah N, Jakubowski D, Butler J, Holocombe R F and Tromberg B J 2001 Sources of absorption and scattering contrast for near-infrared optical mammography *Acta Radiol.* **8** 211–8

Cerussi A E, Jakubowski D, Shah N, Bevilacqua F, Lanning R, Berger A J, Hsiang D, Butler J, Holcombe R F and Tromberg B J 2002 Spectroscopy enhances the information content of optical mammography *J. Biomed. Opt.* **7** 60–71

Colak S B, van der Mark M B, 't Hooft G W, Hoogenraad J H, van der Linden E S and Kuijpers F A 1999 Clinical optical tomography and NIR spectroscopy for breast cancer detection *IEEE J. Sel. Top. Quantum Electron.* **5** 1143–58

Cubeddu R, D'Andrea C, Pifferi A, Taroni P, Torricelli A and Valentini G 2000 Effects of the menstrual cycle on the red and near-infrared optical properties of the human breast *Photochem. Photobiol.* **72** 383–91

Cubeddu R, Pifferi A, Taroni P, Torricelli A and Valentini G 1996 Experimental test of theoretical models for time-resolved reflectance *Med. Phys.* **23** 1625–33

Cubeddu R, Pifferi A, Taroni P, Torricelli A and Valentini G 1999 Noninvasive absorption and scattering spectroscopy of bulk diffusive media: an application to the optical characterization of human breast *Appl. Phys. Lett.* **74** 874–6

Durduran T, Choe R, Culver J P, Zubkov L, Holboke M J, Giammarco J, Chance B and Yodh A G 2002 Bulk optical properties of healthy female breast tissue *Phys. Med. Biol.* **47** 2847–61

Fantini S, Walker S A, Franceschini M A, Kaschke M, Schlag P M and Moesta K T 1998 Assessment of the size, position, and optical properties of breast tumors *in vivo* by noninvasive optical methods *Appl. Opt.* **37** 1982–9

Franceschini M A, Moesta K T, Fantini S, Gaida G, Gratton E, Jess H, Mantulin W W, Seeber M, Schlag P M and Kaschke M 1997 Frequency-domain techniques enhance optical mammography: initial clinical results *Proc. Natl. Acad. Sci. USA* **94** 6468–73

Gratton E, Mantulin W W, vandeVen M J, Fishkin J, Maris M B and Chance B 1993 A novel approach to laser tomography *Bioimaging* **1** 40–6

Grosenick D, Moesta K T, Wabnitz H, Mucke J, Stroszczynski C, Macdonald R, Schlag P M and Rinneberg H 2003 Time-domain optical mammography: initial clinical results on detection and characterization of breast tumors *Appl. Opt.* **42** 3170–86

Hale G M and Quearry M R 1973 Optical constants of water in the 200-nm to 200-μm wavelength region *Appl. Opt.* **12** 555–63

Haskell R C, Svaasand L O, Tsay T-T, Feng T-C, McAdams M S and Tromberg B J 1994 Boundary conditions for the diffusion equation in radiative transfer *J. Opt. Soc. Am.* A **11** 2727–41

Hebden J C, Bland T, Hillman E M C, Gibson A, Everdell N and Delpy D 2002 Optical tomography of the breast using a 32-channel time-resolved imager *OSA Biomedical Topical Meetings, OSA Technical Digest* pp 187–9

Hielscher A H, Jacques S L, Wang L H and Tittel F K 1995 The influence of boundary-conditions on the accuracy of diffusion-theory in time-resolved reflectance spectroscopy of biological tissues *Phys. Med. Biol.* **40** 1957–75

Li A *et al* 2003 Tomographic optical breast imaging guided by three-dimensional mammography *Appl. Opt.* **42** 5181–90

Matcher S J, Elwell C E, Cooper C E, Cope M and Delpy D T 1995 Performance comparison of several published tissue near-infrared spectroscopy algorithms *Anal. Biochem.* **227** 54–68

McBride T O, Pogue B W, Jiang S, Osterberg U L and Paulsen K D 2001 A parallel-detection frequency-domain near-infrared tomography system for hemoglobin imaging of the breast *in vivo Rev. Sci. Instrum.* **72** 1817–24

Mourant J R, Fuselier T, Boyer J, Johnson T M and Bigio I J 1997 Predictions and measurements of scattering and absorption over broad wavelength ranges in tissue phantoms *Appl. Opt.* **36** 949–57

Nilsson A M K, Sturesson C, Liu D L and Andersson-Engels S 1998 Changes in spectral shape of tissue optical properties in conjunction with laser-induced thermotherapy *Appl. Opt.* **37** 1256–67

Patterson M S, Andersson-Engels S, Wilson B C and Osei E K 1995 Absorption spectroscopy in tissue-simulating materials: a theoretical and experimental study of photon paths *Appl. Opt.* **34** 22–30

Pifferi A *et al* 2005 Performance assessment of photon migration instruments: the MedPhot protocol *Appl. Opt.* accepted

Pifferi A, Swartling J, Chikoidze E, Torricelli A, Taroni P, Bassi A, Andersson-Engels S and Cubeddu R 2004 Spectroscopic time-resolved diffuse reflectance and transmittance measurements of the female breast at different interfiber distances *J. Biomed. Opt.* **9** 1143–51

Pogue B W, Jiang S D, Dehghani H, Kogel C, Soho S, Srinivasan S, Song X M, Tosteson T D, Poplack S P and Paulsen K D 2004 Characterization of hemoglobin, water, and NIR scattering in breast tissue: analysis of intersubject variability and menstrual cycle changes *J. Biomed. Opt.* **9** 541–52

Pogue B W, Poplack S P, McBride T O, Wells W A, Osterman K S, Osterberg U L and Paulsen K D 2001 Quantitative hemoglobin tomography with diffuse near-infrared spectroscopy: pilot results in the breast *Radiology* **218** 261–6

Prahl S A 2004 http://omlc.ogi.edu/spectra/hemoglobin/summary.html

Sevick E M, Chance B, Leigh J, Nioka S and Maris M 1991 Quantitation of time- and frequency-resolved optical spectra for determination of tissue oxygenation *Anal. Biochem.* **195** 330–51

Shah N, Cerussi A, Eker C, Espinoza J, Butler J, Fishkin J, Hornung R and Tromberg B 2001 Noninvasive functional optical spectroscopy of human breast tissue *Proc. Natl Acad. Sci. USA* **98** 4420–5

Shah N, Cerussi A E, Jakubowski D, Hsiang D, Butler J and Tromberg B J 2004 Spatial variations in optical and, physiological properties of healthy breast tissue *J. Biomed. Opt.* **9** 534–40

Spinelli L, Torricelli A, Pifferi A, Taroni P, Danesini G M and Cubeddu R 2004 Bulk optical properties and tissue components in the female breast from multiwavelength time-resolved optical mammography *J. Biomed. Opt.* **9** 1137–42

Srinivasan S, Pogue B W, Jiang S D, Dehghani H, Kogel C, Soho S, Gibson J J, Tosteson T D, Poplack S P and Paulsen K D 2003 Interpreting hemoglobin and water concentration, oxygen saturation, and scattering measured *in vivo* by near-infrared breast tomography *Proc. Natl Acad. Sci. USA* **100** 12349–54

Swartling J, Pifferi A, Giambattistelli E, Chikoidze E, Torricelli A, Taroni P, Andersson M, Nilsson A and Andersson-Engels S 2003 Rigorous characterization of time-resolved diffuse spectroscopy systems for measurements of absorption and scattering properties using solid phantoms *Proc. SPIE* **5138** 80–7

Swartling J, Svensson J, Bengtsson D, Terike K and Andersson-Engels S 2005 Fluorescence spectra provide information on the depth of fluorescent lesions in tissue *Appl. Opt.* **44** 1934–41

Taroni P, Danesini G, Torricelli A, Pifferi A, Spinelli L and Cubeddu R 2004 Clinical trial of time-resolved scanning optical mammography at 4 wavelengths between 683 and 975 nm *J. Biomed. Opt.* **9** 464–73

Tromberg B J, Shah N, Lanning R, Cerussi A, Espinoza J, Pham T, Svaasand L O and Butler J 2000 Non-invasive *in vivo* characterization of breast tumors using photon migration spectroscopy *Neoplasia* **2** 26–40

van Veen R L P, Sterenborg H J C M, Marinelli A W K S and Menke-Pluymers M 2004a Intraoperatively assessed optical properties of malignant and healthy breast tissue used to determine the optimum wavelength of contrast for optical mammography *J. Biomed. Opt.* **9** 1129–36

van Veen R L P, Sterenborg H J C M, Pifferi A, Torricelli A and Cubeddu R 2004b Determination of VIS-NIR absorption coefficients of mammalian fat, with time- and spatially resolved diffuse reflectance and transmission spectroscopy *Biomedical Topical Meetings* (Washington: Optical Society of America)

Yates T D, Hebden J C, Gibson A P, Everdell N L, Arridge S R and Douek M 2005 Optical tomography of the breast using a multi-channel time-resolved imager *Phys. Med. Biol.* **50** 2503–17

Paper IV

Performance assessment of photon migration instruments: the MEDPHOT protocol

A. Pifferi, A. Torricelli, A. Bassi, P. Taroni, R. Cubeddu, H. Wabnitz, D. Grosenick, M. Möller, R. Macdonald, J. Swartling, T. Svensson, S. Andersson-Engels, R.L.P. van Veen, H.J.C.M. Sterenborg, J.M Tualle, H.L. Nghiem, S. Avrillier, M. Whelan and H. Stamm.

Applied Optics **44**, 2104-2114 (2005).

Performance assessment of photon migration instruments: the MEDPHOT protocol

Antonio Pifferi, Alessandro Torricelli, Andrea Bassi, Paola Taroni, Rinaldo Cubeddu, Heidrun Wabnitz, Dirk Grosenick, Michael Möller, Rainer Macdonald, Johannes Swartling, Tomas Svensson, Stefan Andersson-Engels, Robert L. P. van Veen, Henricus J. C. M. Sterenborg, Jean-Michel Tualle, Ha Lien Nghiem, Sigrid Avrillier, Maurice Whelan, and Hermann Stamm

We propose a comprehensive protocol for the performance assessment of photon migration instruments. The protocol has been developed within the European Thematic Network MEDPHOT (optical methods for medical diagnosis and monitoring of diseases) and is based on five criteria: accuracy, linearity, noise, stability, and reproducibility. This protocol was applied to a total of 8 instruments with a set of 32 phantoms, covering a wide range of optical properties.

OCIS codes: 170.5280, 170.7050, 220.4840, 350.4800, 000.3110.

1. Introduction

In the past decade, the field of photon migration has grown rapidly, attracting the interest of researchers in a number of applications in the biomedical field, spanning from optical mammography to muscle and brain oximetry, from tissue spectroscopy to the study of bone and joint diseases, and from optical characterization of photosensitizers to molecular imaging.[1–3] In addition to *in vivo* applications, in which interest has been strong, other fields have been pioneered, such as nondestructive characterization of agricultural products[4] or quality assessment of pharmaceutical tablets.[5] All these applications have fostered the development of a wide collection of instruments based on the detection of light propagated through turbid media. Different techniques are exploited, most of which can be classified as time resolved, frequency domain, or space resolved, although mixed approaches are possible. These instruments are operated at a single wavelength, at a few discrete wavelengths or, in some cases, over a wide continuous spectral range. Active theoretical research has led to the development of various theoretical models and algorithms for data analysis that are generally—but not exclusively—based on the transport equation under the diffusion approximation. Measurements can produce average values with a single source–detector pair set at a given interfiber distance ρ, projection images with a scanning approach, as well as topographic or tomographic images that exploit multiple source–detector schemes. Also, the acquisition time is quite different, ranging from few milliseconds for instruments monitoring fast changes in the optical properties up to 1 h for fully tomographic systems.

From this brief overview it is clear that photon migration instruments are quite different from one another in terms of technical approach, performance, theoretical model used for the analysis, and finaliza-

A. Pifferi (antonio.pifferi@fisi.polimi.it), A. Torricelli, A. Bassi, P. Taroni, and R. Cubeddu are with the Laboratorio Nazionale per l'Ottica Ultra-rapida e Ultra-intensa, Dipartimento di Fisica e Istituto di Fotonicae Nanotecnologie, Consiglio Nazionale delle Ricerche, Politecnico di Milano, Piazza Leonardo da Vinci 32, I-20133 Milan, Italy. H. Wabnitz, D. Grosenick, M. Möller, and R. Macdonald are with Physikalisch-Technische Bundesanstalt, Abbestrasse 2-12, D-10587 Berlin, Germany. J. Swartling, T. Svensson, and S. Andersson-Engels are with the Department of Physics, Lund University Medical Laser Centre, Lund Institute of Technology, P.O. Box 118, 22100 Lund, Sweden. R. L. P. van Veen and H. J. C. M. Sterenborg are with the Department of Radiation Oncology, Erasmus Medical Center, University Medical Center, Rotterdam, Westzeedijk 118, 3000 CA, The Netherlands. J.-M. Tualle, H. L. Nghiem, and S. Avrillier are with Laboratoire de Physique des Lasers CNRS UMR 7538, Institut Galilée, Université Paris 13, 99 Avenue J.-B. Clément, 93430 Villetaneuse, France. M. Whelan and H. Stamm are with the Institute for Health and Consumer Protection, European Commission Joint Research Centre, Ispra I-21020, Italy.

Received 26 July 2004; revised manuscript received 5 November 2004; accepted 5 November 2004.

0003-6935/05/112104-11$15.00/0

tion to a specific application. Nonetheless, there is common ground unifying all these systems: the physics of photon migration, which does not depend on the way photons are detected, and possibly also the typical outcomes from the measurement of the absorption (μ_a) and the reduced scattering (μ_s') coefficients.

This common ground makes it possible to use the same phantom to test and characterize quite diverse systems. The most common phantoms for studying photon migration are water-based solutions and resin-based solid samples. The former are water solutions of a diffusive medium—typically Intralipid, a lipid suspension used for the nutrition of hospitalized patients[6,7]—together with inks or dyes as absorbers.[8] Using jellifying agents[9] or transparent films,[10] one can construct heterogeneous structures. The water phantoms are inexpensive, and are easy and fast to prepare; however, they are perishable, difficult to exchange among different laboratories, and may differ between batches. The latter phantoms are based on resin with a scatterer added—typically titanium dioxide or calibrated microspheres—and a resin-soluble absorber.[11,12] These phantoms are solid, durable, and easy to machine and exchange; however, they are more cumbersome to prepare and, in some cases, to characterize. There has been much research on the design, testing, and characterization of phantoms, some of which have been circulated among different institutions.[13]

Conversely, less attention has been paid to the definition of common protocols for the performance assessment of instruments, which compared with other more mature fields, has no consensus on the most relevant tests and figures for the performance evaluation of photon migration setups. Most often, the system specifications are expressed in terms of those parameters that are directly related to the hardware implementation, such as temporal resolution or phase sensitivity, but that are not easily related to the measured parameters and cannot be compared among instruments based on different techniques but used for the same application. Also, the effect of the theoretical model or the fitting algorithm on the recovered properties is not often taken into account.

Various needs could potentially be addressed by use a common protocol. Obviously, it could be used to assess the instrument performances in a measurable way, possibly with a direct relation to the application requirements and to the limitations of the instrument in use. Then it could provide quality assurance during routine operation of the instrument, particularly during clinical trials for which studywide data consistency is crucial. Furthermore a common protocol could be seen as an aid during the development of new instruments or during the upgrade of existing ones, permitting the quantification of the effect of the technical interventions on the final outcome of the measurements. Finally, it can serve as a common basis for the comparison of different instruments and consequently of the measurement results.

The issue of the formulation of a common protocol has been undertaken within the European Thematic Network MEDPHOT (optical methods for medical diagnosis and monitoring of diseases).[14] This project sets a common discussion floor among 21 European partners from 8 countries on the development, testing, and application of biomedical optics instruments. One task of the project was devoted to the quality assessment of photon migration instruments, and the protocol presented in this paper was discussed, designed, and tested during regular project meetings as well as during interlaboratory visits.

In this paper we present the general concepts on which the protocol was designed, identify the relevant measurables, and define the assays that constitute the protocol. Then we describe the phantom kit chosen and constructed for the implementation of the protocol. Finally, we provide some examples derived from the application of the protocol to a wide collection of photon migration instruments.

The methods that are presented in the following sections are not necessarily new to the photon migration community. Some of the proposed assays are routinely used by many research groups, others are straightforward implementations of metrology concepts. What is novel here is the cumulative use of these assays together in a well-defined way and—most of all—the consensus reached among many institutions on the protocol's adoption as a common platform.

2. Definition of the MEDPHOT Protocol

A. General Concepts

The general concepts that we agree as the basis for the design of the protocol are the following:

- to define general procedures applicable to the whole class of photon migration instruments;
- to characterize instruments in terms of measurement results and not of hardware specifications;
- to specify physical parameters instead of clinical ones; and
- to identify a few fundamental assays that probe the key features of photon migration instruments.

The first point was motivated by the need to cover a wide set of photon migration instruments independently of the type of application or measurement technique. The second point was meant to permit the performance assessment of different instruments on the basis of the final outcome of the measurement (e.g., μ_a and μ_s') and not of hardware-dependent specifications. The instrument is considered here as a "black box" with respect to both acquisition and the analysis tools. The hardware specifications of the instruments obviously determine the quality of the measurements, yet the characterization is given in terms of those measurables that are effectively used for the application. The third point simply states that the systems should be validated against reproducible and quantifiable assays, whereas the clinical parameters, such as sensitivity and sensibility, are specific to a particular clinical study (and may also be af-

fected by the specific clinical protocol). Finally, the protocol should be based on a limited set of fundamental assays, which should identify the distinct and fundamental features of photon migration instruments. Particular aspects pertinent only to specific applications should be left aside so as not to overly complicate the definition and the use of the protocol with a cumbersome set of special cases. Instead, dedicated assays could be devised as add-ons to the proposed protocol in order to meet the demands of particular functions.

B. Measurables

Different quantities can be considered as output of a photon migration measurement. The most obvious ones are the optical properties expressed in terms of absorption and reduced scattering coefficients (μ_a, μ_s', respectively). Other quantities often used either for imaging (e.g., mammography) or for oximetry are the detected intensities, expressed as total cw intensity (I_{cw}) or time-gated intensity ($I_{\Delta t}$) in the case of time-resolved instruments. Frequency-domain instruments often produce results directly in terms of amplitude or phase changes. Furthermore, other quantities can be derived, such as tissue-constituent concentrations or normalized intensities.

According to the first criteria expressed above, we designed the protocol by focusing on μ_a and μ_s' as the fundamental measurables. However, the proposed protocol could, in principle, be applied to any other measurable.

We indicate here with x any measurand of the photon migration instrument. In particular, we denote x_{meas} as the measured value of the measurand. The true value of the measurand x_{true} cannot be assumed to be known, thus the conventionally true value x_{conv} is chosen instead.[15] The conventionally true value represents an estimate of x_{true} as derived either by the independent measurements or by a comparison of different instruments operated under optimal experimental conditions. The assessment of a reasonable estimate for x_{conv} is particularly challenging for photon migration phantoms, since often the optical characterization of individual constituents can hardly be performed or cannot be performed at all, as is discussed in Section 5. For a synthetic description of the optical properties of a given phantom, the nominal value x_{nom} is introduced, which corresponds to the optical properties of the phantom as predicted at the design stage for a given optical property. It is only a rough estimate of the measurand to be used only for labeling purposes.

C. Assay Definitions

The MEDPHOT protocol is composed of five assays:

- accuracy
- linearity
- noise
- stability
- reproducibility

The accuracy of the measurement is defined as the capability of the instrument for obtaining a value for the measurable quantity x_{meas} as close as possible to the conventionally true value x_{conv} under optimal experimental conditions [e.g., high signal-to-noise ratio, optical properties of the sample well within the validity range of the theoretical model, and so on]. This figure can be quantified by use of the relative error of the measurement, defined as

$$\varepsilon = \frac{x_{meas} - x_{conv}}{x_{conv}}. \quad (1)$$

This parameter is important for absolute measurements, i.e., whenever the effective value of an optical property or of a constituent concentration is of interest (e.g., to classify the results or to discriminate pathological from healthy regions) or when a tissue must be characterized (e.g., to derive physiological information about the tissue).

A linearity assay is performed by measurement of a set of phantoms combining M values for the absorber concentration (A_i, $i = 1 \ldots M$), with N values for the scatterer concentration (S_j, $j = 1 \ldots N$). For each measurable x_{meas}, an $M \times N$ matrix of measured values is obtained:

$$x_{meas,\,i,j} = f(A_i,\ S_j). \quad (2)$$

If both μ_a and μ_s' are taken as measurands, a total of four linearity plots can be obtained, showing the dependence of the measured μ_a or μ_s' against the conventionally true μ_a or μ_s'. This assay is important for relative measurements to check whether the system can follow changes in a given parameter without distortions. Also, it is crucial for spectroscopy to assure that the shape of the spectrum is preserved, resulting in a correct estimate of the relative abundance of tissue constituents. On the other hand, it can reveal absorption-to-scattering coupling, which can produce artifacts and cause deformations of the scattering spectrum.

The noise assay concerns the variability due to random effects and can be performed by repeating a series of measurements on the same phantom. In particular, we study the noise as a function of the detected optical signal energy E_{out}. For each selected level of the light energy collected from the sample E_{out}, the coefficient of variation CV of a certain number of repeated measurements is derived as

$$\mathrm{CV}(E_{out}) = \frac{\sigma(x)}{\langle x \rangle}, \quad (3)$$

where σ denotes the standard deviation for x_{meas}, calculated for a series of repeated measurements, and $\langle x \rangle$ denotes the corresponding average value.

It is also useful to represent the CV against the injected energy E_{in}. The plot $\mathrm{CV}(E_{in})$ can be used to determine the minimum energy that must be injected in that particular phantom (with given optical properties) to obtain a fluctuation of the measurement

(CV) below a certain threshold. The main drawback in using E_{in} instead of E_{out} is that the instrument characterization is uniquely related to the chosen phantom. Yet E_{out} can be derived from E_{in}, calculating the light attenuation caused by photon migration in the sample by means of the diffusion equation. Finally, the plot of the noise against the number of counts per curve is useful when one is dealing with a time-correlated single-photon counting (TCSPC) system, although it is completely insensitive to the overall coupling and detector efficiencies.

The noise of the measurement directly determines the sensibility of the instrument. In fact, the lowest detectable change in x_{meas} is related to the noise of x_{meas}. Clearly, the noise level is reduced for higher signal intensities and detection efficiencies, and thus the sensibility of the instrument depends on the amount of signal (energy) collected per each measurement point.

The stability assay can be performed by repetition of the measurement on the same phantom many times at subsequent time instants t_i without changing the experimental conditions. The corresponding plot

$$x_{meas} = f(t_i) \tag{4}$$

can reveal short- or long-term drifts of the system as well as unwanted fluctuations. Clearly, the injected energy E_{in} for each measurement must be high enough to set a low CV for x_{meas}, as characterized in the noise assay.

The reproducibility assay is performed by repetition of the measurement on the same phantom under the same experimental conditions on different days. The instrumental reproducibility is expressed as the CV of these measurements. This figure quantifies how the system is self-consistent over different days and permits the correlation of results obtained in different measurement sessions. It is particularly important in the case of clinical studies and whenever measurements obtained over the course of years must be pulled together. In these cases the reproducibility assay should be performed regularly throughout the study.

3. Phantom Kit

The MEDPHOT protocol can be applied by use of any phantom with stable, homogeneous, and controllable optical properties. Yet a specific set of solid phantoms was made on purpose for the MEDPHOT project and was circulated among partners to test the protocol. The phantom is based on epoxy resin, with TiO_2 powder as the scatterer and black toner as the absorber. The phantom recipe was taken from the work of Firbank *et al.*,[11] with the improvements introduced by Swartling *et al.*[16] The scheme of phantom fabrication is depicted in Fig. 1. Briefly, the necessary amounts of toner (black 46/I, part 885 983 06; Infotec, France) and TiO_2 powder (T-8141; Sigma-Aldrich, St. Louis, Missouri) were dispersed in the hardener (H179B; Nils Malmgren AB, Ytterby, Sweden) by sonicating for 20 min. This suspension was added to the resin (NM500; Nils Malmgren AB, Ytterby, Sweden) and stirred manually for 30 min. The mix was poured in the mold and set aside for 1 day at room temperature. Then the phantom was cured in the oven at 50 °C for 12 h, after which it could be machined into the proper shape and polished.

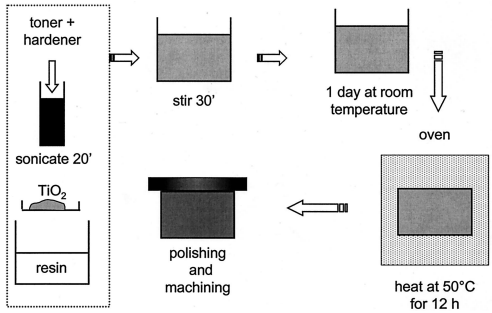

Fig. 1. Scheme of the fabrication of solid phantoms, following the recipe in Ref. 16.

A total of 32 homogeneous cylinders (4.5-cm height, 10.5-cm diameter) were constructed, combining 4 concentrations of TiO_2 powder with 8 concentrations of toner. The TiO_2 and toner concentrations were varied linearly in steps of $\sim 0.05\ cm^{-1}$ for μ_a and $5\ cm^{-1}$ for μ_s' at 800 nm. These phantoms were labeled with a letter and a number, in which the letter stands for the nominal scattering (A, B, C, D corresponding to $\mu_s' = 5, 10, 15, 20\ cm^{-1}$, respectively) and the number indicates the absorption (1, 2, 3, 4, 5, 6, 7, 8 correspond to $\mu_a = 0, 0.05, 0.10, 0.15, 0.20, 0.25, 0.30, 0.35\ cm^{-1}$, respectively).

In addition, three more phantoms were constructed with the same geometry and with identical nominal values of $\mu_a = 0.1\ cm^{-1}$ and $\mu_s' = 10\ cm^{-1}$ at 800 nm. These phantoms were labeled with T_x (T_a, T_b, T_c).

4. Systems Enrolled in the Study

A total of eight instruments, developed by research institutions in five countries, were enrolled in the first application of the MEDPHOT protocol. Table 1 summarizes the key aspects of the systems considered. The systems were grouped into three classes (spectroscopy, imaging, and monitoring) based on the finalization of the instrument-to-tissue optical characterization, on imaging through turbid media, or on monitoring of physiological changes of optical properties, respectively. Most of the instruments were implemented with time-resolved approaches. Two of them were based on cw techniques that exploit multidistance or interferometric measurements. Although no frequency-domain instrument was proposed for the test, the MEDPHOT protocol can be applied to that class of instrument as well. In the following paragraphs, we give a brief description of

Table 1. Classification, Measurement Technique, and Owner Partner of Instruments Characterized with the Proposed Protocol

Class	Technique	Partner	Instrument	Reference
Spectroscopy				
1	Time resolved	POLIMI[a]	Scanning tissue spectrometer	17
2	Space resolved	EMCR[b]	Multifiber tissue spectrometer	18
3	Time resolved	LLC[c]	Four-wavelength portable system	19
Imaging				
4	Time resolved	POLIMI[a]	Optical mammograph	20
5	Time resolved	PTB[d]	Optical mammograph	21
6	Time resolved	POLIMI[a]	Time-gated camera	22
Monitoring				
7	Interferometric	PARIS 13[e]	Oximeter	23
8	Time resolved	POLIMI[a]	Oximeter–functional imager	24

[a]Politecnico di Milano.
[b]Erasmus Medical Center Rotterdam.
[c]Lund University Medical Laser Center.
[d]Physikalisch-Technische Bundesanstalt.
[e]Université Paris 13.

each instrument, referring the reader to the appropriate references for more details.

Instrument 1 is a fully automated system for absorption and scattering spectroscopy of diffusive media.[17] It is based on mode-locked lasers (dye and Ti: sapphire lasers) that are continuously tunable in the 610–1050-nm range and on a detection stage for TCSPC. The maximum power is kept below 1 ÷ 10 mW, depending on the illuminating area, and the typical measurement time for a whole spectrum is ~15 min.

Instrument 2 is a portable cw-based system to derive absorption and scattering properties with a 0.6-nm resolution from 400 to 1100 nm.[18] Light from a 100-W halogen light source is coupled into the sample by means of an optical fiber. Diffuse remitted light from the sample is collected at nine different source–detection fiber distances and is coupled into a spectrograph and projected onto a cooled (−35 °C) CCD camera.

Instrument 3 is a time-domain system intended primarily for spectroscopy of biological tissue.[19] It is based on TCSPC technology and incorporates four pulsed picosecond diode lasers at 660, 786, 916, and 974 nm. The output power is 1–2 mW at each wavelength, and a single measurement is typically performed within 10–30 s.

Instrument 4 is a time-domain optical mammograph operated at four wavelengths (637, 785, 905, and 975 nm).[20] It produces images of the compressed breast both in craniocaudal and oblique projections by continuously scanning the breast at 1-mm intervals with the fibers in a tandem geometry. This instrument is based on picosecond diode lasers and two boards for TCSPC. The maximum laser power is a few milliwatts per each wavelength, and the acquisition time is 25 ms per measurement point, totaling ~5 min for a whole scan.

Instrument 5 is a time-domain optical mammograph for multiprojection imaging.[21] It is equipped with up to eight parallel detection channels, allowing one to measure transmittance through the compressed breast simultaneously on axis and for selected lateral offsets between sources and detectors. The breast is scanned sequentially in craniocaudal and mediolateral projection by use of a step size of 2.5 mm. The device employs four picosecond diode lasers (652, 684, 797, and 830 nm).

Instrument 6 is an imaging system based on a time-gated intensified CCD camera.[22] It permits the parallel acquisition of the time-dispersion curves either in reflectance or in transmittance geometry, over a wide area, and within a few seconds. It can be operated either with pulsed diode lasers or with mode-locked laboratory lasers.

Instrument 7 is an interferometric system that allows one to perform time-resolved measurements of the light scattered by the tissue.[23] The present version works at 780 nm, in reflectance geometry, with a source–detector separation of 1 cm.

Instrument 8 is a time-resolved tissue oximeter based on two diode lasers (690 and 820 nm) and PC boards for TCSPC.[24] It is implemented with 9 sources and 12 parallel detectors, permitting the acquisition of a whole combination of source–detector pairs in 1 s. The laser power is <1 mW per wavelength.

Data analysis is implemented by solving the transport equation under the diffusion approximation and by applying the extrapolated boundary conditions.[18,25,26]

5. Phantom Characterization

As a first step toward the optical characterization of the kit of solid phantoms, Fig. 2 shows the absorption coefficient [Fig. 2(a)] and the reduced scattering coefficient [Fig. 2(b)] obtained with all the instruments listed in Table 1 for the phantom B2, under the experimental conditions specified in the figure caption. There is a certain dispersion among the measurement points, although the spectral features of the absorption spectrum are similarly assessed by all the instruments. As expected, the absorption coefficient exhibits a rather flat plateau below 850 nm, owing mainly to the toner absorption, and higher peaks

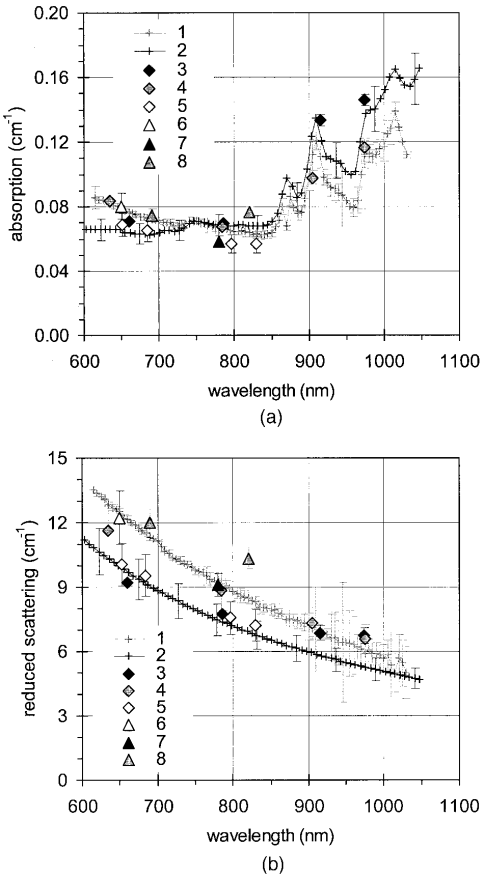

Fig. 2. Comparison of the estimate of (a) μ_a and (b) μ_s' obtained by the eight instruments on the phantom B2. The measurements are performed in transmittance geometry for instruments 4, 5, and 6; in reflectance geometry with $\rho = 2$ cm for instruments 1, 3, 7, and 8; and in reflectance geometry with ρ variable in the interval 0.2–1.8 cm in steps of 0.2 cm for instrument 2.

beyond 850 nm, ascribed to the resin contribution. The differences among instruments pertain mainly to the absolute values, whereas consistency in the spectral shape is maintained.

With respect to the scattering coefficient, all instruments detect, as expected, decreasing values of μ_s' with increasing wavelength. Again, there is a certain dispersion on the absolute estimate of μ_s', with minor variations in the slope of the spectrum.

Overall, comparing the results at wavelengths with at least three independent measurements within a 10-nm range, the average dispersion on μ_a is 10%, whereas the maximum discrepancy between two instruments is found at 970 nm, with a peak-to-peak difference of 32%. Correspondingly, the average dispersion on μ_s' is 13%, whereas the maximum discrepancy is 41% at 820 nm. The measurements were performed over a time period of ~6 months. The phantoms were not checked for long-term stability, and a small change in optical properties, particularly in the resin matrix, cannot be completely ruled out. Yet the intersystem differences in Fig. 2 are not chronologically correlated and thus cannot be ascribed to this problem.

The data in Fig. 2 are not sufficient for a robust characterization of the phantoms. The grand average of the measured optical properties does not necessarily converge to good conventionally true values, since most of the instruments are based on the same technical approach and might be affected by the same systematic errors. On the other hand, a direct assessment of the optical properties of the key phantom constituents is not straightforward. The reduced scattering coefficient produced by the TiO_2 particles is not easily derived. Also, the pure toner powder has nonnegligible scattering properties, which hamper a direct evaluation of its absorption coefficient. Yet we preferred it over other absorbers (e.g., organic dyes and inks) because it is not fluorescent and provides a rather flat absorption spectrum from 600 to 1100 nm.

The importance of obtaining robust and reliable estimates for the phantom optical properties forced us to explore other independent approaches as well as cross-validation tests. This task is nontrivial, owing to the need to derive the spectral properties continuously on a wide wavelength range and to the delicate procedure used to attain a reference standard. This research is still in progress, and the main goal of the present paper is to present the overall methodology of the five-assay protocol. So we decided to devote the characterization of the phantom kit to a specific study to be published in the near future.

To be able to show an example of the application of the accuracy assay, we derived an estimate of the phantom properties from the measurements obtained with system 1. This does not mean that we consider those results to be any better than the others. Neither do we assume that those numbers are conventional true optical properties. Rather, the use of the optical properties derived with the instrument 1 was performed with the sole purpose of producing an example of the accuracy test, as presented in the following paragraph. The absorption spectrum of resin was obtained by averaging the measurements of the phantoms with a null toner concentration (label 1). The toner contribution was assessed by subtracting and averaging the results of measurements performed on phantoms with close absorption values, e.g., average of $[\mu_a(B3) - \mu_a(B2)]$ and $[\mu_a(C3) - \mu_a(C2)]$. To this end, we considered only data obtained in the best experimental conditions in terms of signal and applicability of the diffusion approximation (phantoms B1–4, C1–4; interfiber distance 2–3 cm). The reduced scattering spectrum of the TiO_2 resin matrix was estimated by fitting the average spectra of a selection of phantoms with the power law spectral dependence of the scattering coefficient.[27,28] The optical properties of the phantom kit were calculated synthetically

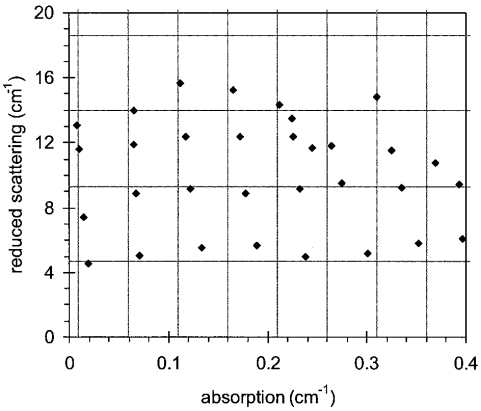

Fig. 3. Accuracy plot obtained with instrument 4 in a transmittance geometry at 785 nm on the whole phantom kit. Each diamond identifies the measured optical properties obtained for each of the 32 phantoms. The grid lines are set in correspondence to a first estimate of the conventionally true values for the phantom properties derived with the limitations described in Section 5.

every 5 nm by use of the optical properties of individual constituents estimated as described above. Thus the estimated μ_a and μ_s' are perfectly linear with the toner and TiO_2 concentrations, respectively.

6. Examples of Application of the MEDPHOT Protocol

The protocol was applied to all the instruments listed in Table 1. An example of a possible outcome of the accuracy assay is reported in Fig. 3, which shows the measured values of μ_a and μ_s' for the 32 solid phantoms, using instrument 4 at 785 nm in a transmittance geometry. The corresponding conventionally true values—obtained as described and with the limitations discussed in Section 5—are plotted as grid lines. Alternative representations are given in Tables 2 and Table 3, report the relative error ε for a measurement of μ_a and μ_s', respectively. In principle, the accuracy assay need not necessarily be applied to the whole kit of phantoms. It is sufficient to assess the

Table 2. Relative Error on the Estimate of μ_a [a]

	μ_s'			
μ_a	A (**4.7**)	B (**9.3**)	C (**14.0**)	D (**18.6**)
1 (**0.009**)	113%	66%	9%	−10%
2 (**0.059**)	19%	14%	9%	11%
3 (**0.109**)	22%	12%	7%	2%
4 (**0.159**)	19%	12%	8%	4%
5 (**0.209**)	14%	11%	8%	1%
6 (**0.260**)	16%	6%	2%	−14%
7 (**0.310**)	14%	8%	5%	−21%
8 (**0.360**)	10%	9%	3%	−14%

[a]The numbers in bold represent the conventionally true values for μ_a (phantoms 1–8) and μ_s' (phantoms A–D) in inverse centimeters.

Table 3. Relative Error on the Estimate of μ_s' [a]

	μ_s'			
μ_a	A (**4.7**)	B (**9.3**)	C (**14.0**)	D (**18.6**)
1 (**0.009**)	−2%	−20%	−17%	−30%
2 (**0.059**)	8%	−5%	−15%	−25%
3 (**0.109**)	18%	−2%	−11%	−16%
4 (**0.159**)	22%	−5%	−12%	−18%
5 (**0.209**)	7%	−2%	−11%	−23%
6 (**0.260**)	11%	2%	−16%	−28%
7 (**0.310**)	25%	−1%	−17%	−37%
8 (**0.360**)	30%	1%	−23%	−20%

[a]The numbers in bold represent the conventionally true values for μ_a (phantoms 1–8) and μ_s' (phantoms A–D) in inverse centimeters.

accuracy on a single phantom (e.g., any phantom T_x) that matches the optimal conditions for the instrument. This check provides the best system performance. Any deviation from this ideal behavior can be further explored with the linearity assay.

An example of a linearity assay is reported in Fig. 4. These data were obtained with instrument 3 at 786 nm in reflectance with $\rho = 2$ cm. If both μ_a and μ_s' are taken as measurands, a total of four linearity plots can be obtained, showing the dependence of the measured μ_a or μ_s' against the conventionally true μ_a or μ_s'. Each plot highlights a different aspect of the measurement. The plot of $\mu_{a,\,meas}$ versus $\mu_{a,\,conv}$ [Fig. 4(a)] displays the linearity characteristics of the system for absorption measurements. It is possible to derive information on the integral nonlinearity, the differential nonlinearity, and the linearity range of the system. Referring to the data presented in Fig. 4, one notes that the system is perfectly linear up to $\mu_a \leq 0.2\ cm^{-1}$, and then it starts deviating from linearity, reaching a maximum displacement (integral nonlinearity) of ~20% for $\mu_{a,\,conv} = 0.36\ cm^{-1}$. The plot of $\mu_{a,\,meas}$ versus $\mu_{s,\,conv}'$ [Fig. 4(b)] points out any coupling of the absorption coefficient to the scattering coefficient. With reference to the figure, we see that the trend lines are almost horizontal—at least for relative low-absorption properties, that is $\mu_a \leq 0.2\ cm^{-1}$—permitting the exclusion of scattering-to-absorption coupling in this range. Conversely, the plot of $\mu_{s,\,meas}'$ versus $\mu_{a,\,conv}$ [Figure 4(c)] investigates the opposite coupling of the scattering to the absorption coefficient. In Fig. 4(c) the tendency of $\mu_{s,\,meas}'$ to increase with increasing values of $\mu_{a,\,conv}$ is a clear indication of scattering-to-absorption coupling. The variation here is not dramatic (an increase of ~30% in μ_s' on the A series for an increase of μ_a from 0.1 to $0.3\ cm^{-1}$), yet it can produce bumps in the scattering spectrum for large changes in μ_a (e.g., around the water absorption peak). Finally, the plot of $\mu_{s,\,meas}'$ versus $\mu_{s,\,conv}'$ [Fig. 4(d)] shows the scattering linearity. In this figure the trend lines show an almost negligible offset (the intercept of the vertical axis is $<0.5\ cm^{-1}$ for most series).

An example of the noise on μ_a plotted as a function

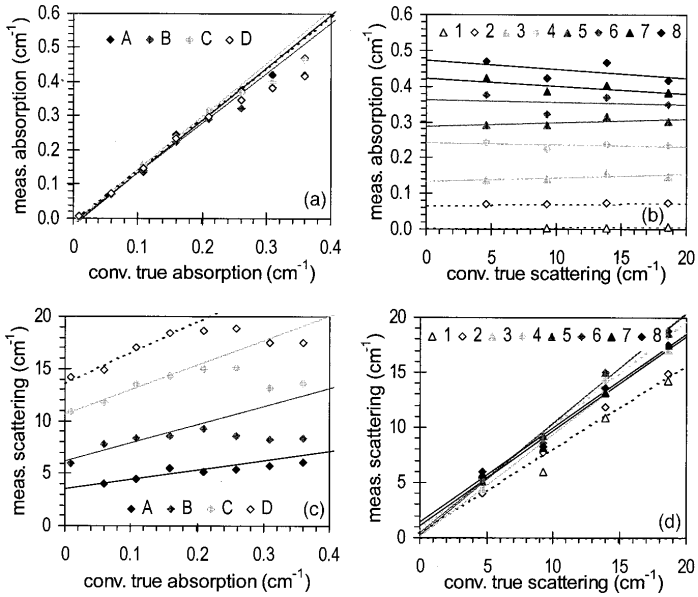

Fig. 4. Linearity plots obtained with instrument 3 in a reflectance geometry at 786 nm for $\rho = 2$ cm. Four different views of the data are presented, corresponding to the changes of $\mu_{a,\,meas}$ against (a) $\mu_{a,\,conv}$ and (b) $\mu_{s,\,conv}'$, as well as to the changes of $\mu_{s,\,meas}'$ against (c) $\mu_{a,\,conv}$ and (d) $\mu_{s,\,conv}'$. The letters and the numbers in the figure legends identify the scattering and absorption labels of the phantoms. The straight lines are linear interpolations on the first four points.

of the input energy E_{in} is shown in Fig. 5, again for instrument 4 at 635 nm, using the phantom T_a. In this case the assay is used to explore the consequence of using as-free parameters in the fitting procedure of both μ_a and μ_s' (dark gray); μ_a, μ_s' and a free time shift t_0 (black); or μ_a and t_0 while fixing μ_s' to a constant value (light gray). In the case of the (μ_a, μ_s') method, an energy of ~3.5 mJ is required to reach a noise level of 6%, which corresponds, for instance, to the typical absorption contrast foreseen in a given application. Conversely, using the free shift approach (μ_a, μ_s', t_0), the same noise level requires ~25 mJ (7 times more energy). The fixed approach (μ_a, t_0) is much more stable, requiring just 2 mJ, and can be of interest to follow small absorption changes under the assumption of a rather constant μ_s'.[29] Since the input power is often limited either by the safety regulations or by the available light power, the energy requirements can be easily related to the minimum acquisition time needed to achieve a given noise level. If the acquisition time is also fixed, the noise plot yields the noise level of the apparatus.

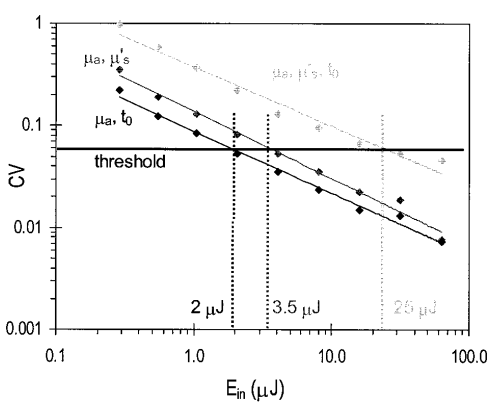

Fig. 5. Plot of the noise level for the measurement of μ_a expressed by the CV calculated for different values of the energy injected into the phantom. The data were obtained with instrument 4 in a transmittance geometry at 785 nm on the phantom T_a. The experimental measurements were fitted by use of as-free parameters μ_a and μ_s' (dark gray); μ_a, μ_s' and a free time shift t_0 (light gray); or μ_a and t_0 while fixing μ_s' (black).

Figure 6 shows an example of a stability assay obtained on the phantom T_a for instrument 8 operated at 690 nm in a reflectance geometry with an interfiber distance of 2 cm [Fig. 6(a)] and for instrument 4 at 635 nm in a transmittance geometry [Fig. 6(b)]. The time course is taken immediately after the instruments have been switched on, for a total of 2 h. The horizontal dashed lines represent a range of ±3% and ±10% with respect to the average value calculated in the last 30 min of the measurement period. For the first instrument [Fig. 6(a)], a reasonable warm-up time seems to be 30 min, after which the system is stable in the assessment of μ_a within ±3%, whereas the second one is still drifting after 1 h. Clearly, the stability requirements depend on the

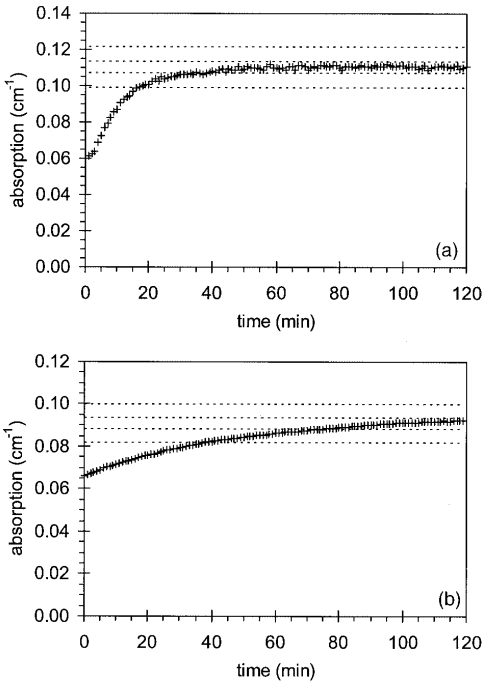

Fig. 6. Stability plot for μ_a obtained on the phantom T_a, using (a) instrument 8 at 690 nm, in a reflectance geometry, with ρ = 2 cm and (b) instrument 4 at 785 nm, in a transmittance geometry. The dashed lines correspond to $\pm 3\%$ and $\pm 10\%$ changes with respect to the average of μ_a over the last 30 min of measurement.

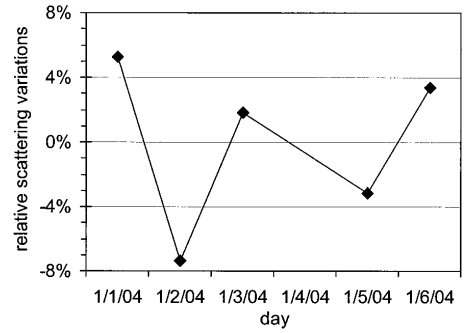

Fig. 7. Reproducibility plot for μ_a obtained on phantom T_a, using instrument 7 at 780 nm, in a reflectance geometry, with ρ = 1 cm. The plot represents the relative displacement of $\mu_{a,\,meas}$ obtained at each measurement day with respect to the average value calculated over 5 days.

overall duration of the measurement. Also, in the case of the second instrument, after 1 h the measurement is relatively stable within a few percent for a measurement session of 10 min. The ultimate cause of this deviation is the time-drift of the laser pulses. For constructing the plot of Fig. 6(b), we fitted the data by using the instrumental transfer function (ITF) recorded at the end of the trial. Thus this deviation can be compensated for by use of an ITF that is closer to the actual measurement period, or even better by continuous recording of the ITF as a reference pulse during the measurements.

Figure 7 displays an example of a reproducibility assay for a measurement of μ_s' over 5 different days. These data were obtained with instrument 7 on phantom T_a with ρ = 1 cm. All the experimental conditions were kept as constant as possible (e.g., allowing adequate warm-up time, keeping constant ambient light level, etc.). The data are presented as relative variations with respect to the average μ_s'. The average dispersion of the data is 5.2%, with a maximum displacement of 7.4%, which yields an indication of the day-by-day reproducibility and consistency of the measurements.

To permit an easy comparison of results among different instruments or even different releases of the same instrument, as well as to simplify the analysis and reporting tasks, we prepared a common reporting tool and implemented it as an Excel document. The fitted μ_a and μ_s' for the different assays are inserted together in a worksheet with some information related, e.g., to the phantom labels, assay type, measurement time, and so on. With minor actions from the user, a two-page printable summary report is produced, showing all relevant plots, as depicted in Fig. 8. The final section of the report contains some synthetic descriptors of the outcome of the assay, such as the median of the absolute error for the accuracy, the average deviation from linearity, the input energy required to yield a measurement with 1% noise, the slope and range of the stability plot after warm-up time, and the average value of the reproducibility. These numbers permit an immediate appraisal of the system performances as well as a fast and quantitative evaluation of an instrument upgrade.

It is clear that the proposed protocol does not cover all the features related to photon migration instruments. As specified in Section 1, some dedicated assays could be added to the protocol to properly assess issues specific to particular applications. This is the case, for instance, with imaging instruments, for which the aspect of spatial resolution is not encompassed by the MEDPHOT protocol and should be addressed with specific criteria and dedicated inhomogeneous phantoms. Nonetheless, it is also true that the problem of spatial resolution is somehow more linked to the physics of photon migration and to the algorithms used to produce the image rather than to the effective performances of the instruments, and it could possibly be derived from simulations or calculations. On the contrary, the visibility of a suspect lesion, quantified by the effective contrast, is directly related to the noise of the background, as defined the MEDPHOT protocol. Thus the assessment of the five

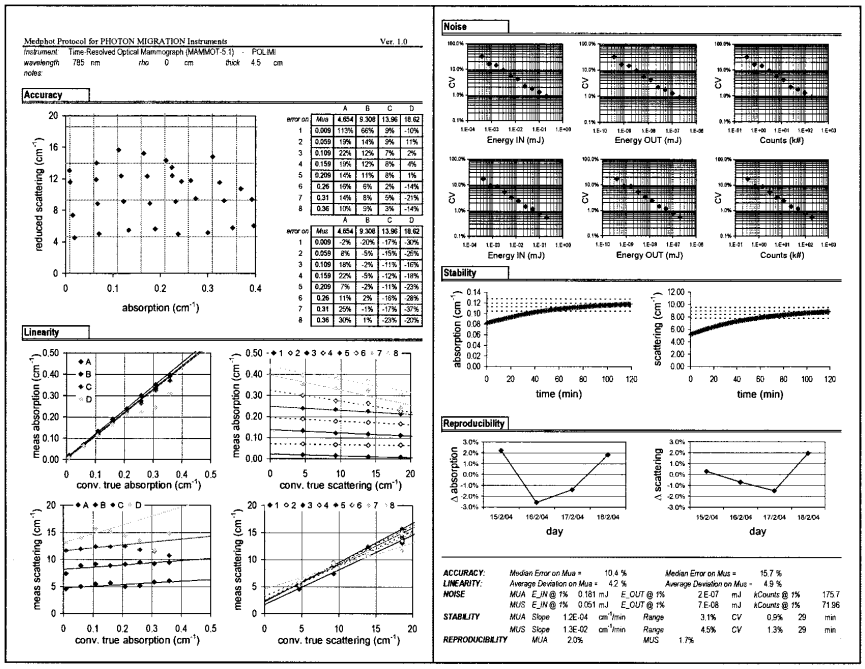

Fig. 8. Printout of the two-page reporting sheet, presenting general information on the instrument, the relevant figures of the MEDPHOT protocol, and some synthetic descriptors of the instrument performances derived from the five assays.

criteria described in this paper cover much of the key aspects of most instruments.

7. Conclusions

In conclusion, we have proposed a novel protocol for the performance assessment of photon migration instruments composed of five assays: accuracy, linearity, noise, stability, and reproducibility. The protocol was applied on a total of 8 instruments, from 5 different countries, using a kit of 32 solid phantoms covering a wide range of optical properties. We have shown examples of the applications of the protocol to encompass different aspects of a photon migration measurement that can be directly related to the needs of the specific application field of the instrument. A unified and quasi-automatic reporting tool permits objective, synthetic, and fast visualization of the protocol results. Research to obtain an accurate spectral characterization of the phantom kit is still in progress. As soon as this parallel study is finished, we will be able to circulate the phantom kit, the protocol specifications, and the reporting tool among the research groups interested in their use.

The study was partially supported by European Union grants QLG1-CT-2000-01464, QLG1-CT-2000-00690, and HPRI-CT-2001-00148.

References

1. *Biomedical Topical Meetings on CD-ROM* (Optical Society of America, Washington, D.C., 2004).
2. Special issue on Recent Developments in Biomedical Optics, Phys. Med. Biol. **49,** (2004).
3. Feature issue on Topics in Biomedical Optics, Appl. Opt. **10–11** (2005).
4. R. Cubeddu, C. D'Andrea, A. Pifferi, P. Taroni, A. Torricelli, G. Valentini, C. Dover, D. Johnson, M. Ruiz-Altisent, and C. Valero, "Nondestructive quantification of chemical and physical properties of fruits by time-resolved reflectance spectroscopy in the wavelength range 650–1000 nm," Appl. Opt. **40,** 538–543 (2001).
5. J. Johansson, S. Folestad, M. Josefson, A. Sparen, C. Abrahamsson, S. Andersson-Engels, and S. Svanberg, "Time-resolved NIR/Vis spectroscopy for analysis of solids: pharmaceutical tablets," Appl. Spectrosc. **56,** 725–731 (2002).
6. S. T. Flock, S. L. Jacques, B. C. Wilson, W. M. Star, and M. J. C. van Gemert, "Optical properties of Intralipid: a phantom medium for light propagation studies," Lasers Surg. Med. **12,** 510–519 (1992).
7. H. J. van Staveren, C. J. M. Moes, J. van Marle, S. A. Prahl, and M. J. C. van Gemert, "Light scattering in Intralipid-10% in the wavelength range of 400–1100 nm," Appl. Opt. **30,** 4507–4514 (1991).
8. S. J. Madsen, M. S. Patterson, and B. C. Wilson, "The use of India ink as an optical absorber in tissue-simulating phantoms," Phys. Med. Biol. **37,** 985–993 (1992).
9. R. Cubeddu, A. Pifferi, P. Taroni, A. Torricelli, and G. Valen-

tini, "A solid tissue phantom for photon migration studies," Phys. Med. Biol. **42,** 1971–1979 (1997).
10. S. Del Bianco, F. Martelli, F. Cignini, G. Zaccanti, A. Pifferi, A. Torricelli, A. Bassi, P. Taroni, and R. Cubeddu, "Liquid phantom for investigating light propagation through layered diffusive media," Opt. Express **12,** 2102–2111 (2004), http://www.opticsexpress.org.
11. M. Firbank, M. Oda, and D. T. Delpy, "An improved design for a stable and reproducible phantom material for use in near-infrared spectroscopy and imaging," Phys. Med. Biol. **40,** 955–961 (1995).
12. U. Sukowsky, R. Schubert, D. Grosenick, and H. Rinneberg, "Preparation of solid phantoms with defined scattering and absorption properties for optical tomography," Phys. Med. Biol. **41,** 1823–1844 (1996).
13. J. C. Hebden, D. J. Hall, M. Firbank, and D. T. Delpy, "Time-resolved optical imaging of a solid tissue-equivalent phantom," Appl. Opt. **34,** 8038–8047 (1995).
14. MEDPHOT Project, http://medphot.jrc.it.
15. ISO Draft Guide, "International Vocabulary of Basic and General Terms in Metrology (VIM)," ISO DGUIDE 99999 (2004).
16. J. Swartling, J. S. Dam, and S. Andersson-Engels, "Comparison of spatially and temporally resolved diffuse-reflectance measurement systems for determination of biomedical optical properties," Appl. Opt. **42,** 4612–4620 (2003).
17. R. Cubeddu, A. Pifferi, P. Taroni, A. Torricelli, and G. Valentini, "Non-invasive absorption and scattering spectroscopy of bulk diffusive media: an application to the optical characterization of human breast," Appl. Phys. Lett. **74,** 874–876 (1999).
18. R. L. P. van Veen, W. Verkruijsse, and H. J. C. M. Sterenborg, "Diffuse reflectance spectroscopy from 500 to 1060 nm by correction for inhomogenously distributed absorbers," Opt. Lett. **27,** 246–248 (2002).
19. J. Swartling, A. Pifferi, E. Giambattistelli, E. Chikoidze, A. Torricelli, P. Taroni, M. Andersson, A. Nilsson, and S. Andersson-Engels, "Rigorous characterization of time-resolved diffuse spectroscopy systems for measurements of absorption and scattering properties using solid phantoms," in *Photon Migration and Diffuse-Light Imaging*, D. A. Boas, ed., Proc. SPIE **5138,** 80–87 (2003).
20. A. Pifferi, P. Taroni, A. Torricelli, F. Messina, R. Cubeddu, and G. Danesini, "Four-wavelength time-resolved optical mammography in the 680–980-nm range," Opt. Lett. **28,** 1138–1140 (2003).
21. M. Moeller, H. Wabnitz, A. Kummrow, D. Grosenick, A. Liebert, B. Wassermann, R. Macdonald, and H. Rinneberg, "A four-wavelength multi-channel scanning time-resolved optical mammograph," in *Photon Migration and Diffuse-Light Imaging*, D. A. Boas, ed., Proc. SPIE **5138,** 290–297 (2003).
22. C. D'Andrea, D. Comelli, A. Pifferi, A. Torricelli, G. Valentini, and R. Cubeddu, "Time-resolved optical imaging through turbid media using a fast data acquisition system based on a gated CCD camera," J. Phys. D **36,** 1675–1681 (2003).
23. J.-M. Tualle, "E. Tinet, and S. Avrillier, "A new and easy way to perform time-resolved measurements of the light scattered by a turbid medium," Opt. Commun. **189,** 211–220 (2001).
24. A. Torricelli, V. Quaresima, A. Pifferi, G. Biscotti, L. Spinelli, P. Taroni, M. Ferrari, and R. Cubeddu, "Mapping of calf muscle oxygenation and haemoglobin content during dynamic plantar flexion exercise by multi-channel time-resolved near infrared spectroscopy," Phys. Med. Biol. **49,** 685–699 (2004).
25. M. S. Patterson, B. Chance, and B. C. Wilson, "Time-resolved reflectance and transmittance for the noninvasive measurement of tissue optical properties," Appl. Opt. **28,** 2331–2336 (1989).
26. R. C. Haskell, L. O. Svasaand, T. T. Tsay, T. C. Feng, M. S. McAdams, and B. J. Tromberg, "Boundary conditions for the diffusion equation in radiative transfer," J. Opt. Soc. Am. A **11,** 2727–2741 (1994).
27. A. M. K. Nilsson, C. Sturesson, D. L. Liu, and S. Andersson-Engels, "Changes in spectral shape of tissue optical properties in conjunction with laser-induced thermotherapy," Appl. Opt. **37,** 1256–1267 (1988).
28. J. R. Mourant, T. Fuselier, J. Boyer, T. M. Johnson, and I. J. Bigio, "Predictions and measurements of scattering and absorption over broad wavelength ranges in tissue phantoms," Appl. Opt. **36,** 949–957 (1997).
29. R. Cubeddu, A. Pifferi, P. Taroni, A. Torricelli, and G. Valentini, "Experimental test of theoretical models for time-resolved reflectance," Med. Phys. **23,** 1625–1633 (1996).

Paper V

Least-squares support vector machines modelization for time-resolved spectroscopy

F. Chauchard, S. Roussel, J.M. Roger, V. Bellon-Maurel,
C. Abrahamsson, T. Svensson, S. Andersson-Engels, S. Svanberg.

Applied Optics **44**, 7091-7097 (2005).

Least-squares support vector machines modelization for time-resolved spectroscopy

Fabien Chauchard, Sylvie Roussel, Jean-Michel Roger, Véronique Bellon-Maurel, Christoffer Abrahamsson, Tomas Svensson, Stefan Andersson-Engels, and Sune Svanberg

By use of time-resolved spectroscopy it is possible to separate light scattering effects from chemical absorption effects in samples. In the study of propagation of short light pulses in turbid samples the reduced scattering coefficient and the absorption coefficient are usually obtained by fitting diffusion or Monte Carlo models to the measured data by use of numerical optimization techniques. In this study we propose a prediction model obtained with a semiparametric modeling technique: the least-squares support vector machines. The main advantage of this technique is that it uses theoretical time dispersion curves during the calibration step. Predictions can then be performed by use of data measured on different kinds of sample, such as apples.

OCIS codes: 300.6500, 000.3860, 170.3660, 290.7050.

1. Introduction

Striking advances have been made in time-resolved spectroscopy (TRS).[1] Whereas conventional near-infrared spectroscopic measurements are influenced by light scattering in the sample, TRS deconvolutes absorption from scattering effects. The scattering properties of a sample depend on the physical properties of the samples, whereas the absorption is mostly dependent on the chemical composition of the samples. TRS was first developed for medical applications[2,3] but is now extended to other fields, such as pharmaceutical applications[4] and agricultural applications.[5,6] TRS uses short laser pulses of a few picoseconds to irradiate a sample. The light signal diffusively remitted by the sample at a given distance from the irradiation point is then temporally recorded.[7] The recordings can be made in either the reflection or the transmission mode. To measure the temporal signal at different wavelengths simultaneously, new techniques that use a streak camera for detection have been proposed. There are different ways to obtain light pulses with a broad wavelength profile; one is to use continuum generation by focusing a high power laser pulse in a cuvette of water.[8] The development of photonic crystal fibers has further simplified the instrumental setups for continuum generation.[9]

Once the two-dimensional signal is recorded, the reduced scattering coefficient (μ_s') and the absorption coefficient (μ_a) are obtained by linking the experimental data with theoretical or modeling data. This step is crucial to obtain the correct results, and many methods have been proposed. Three approaches are usually found: Monte Carlo simulations,[7,10] numerical optimizations,[11,12] and analytical descriptors of temporal dispersion.[13] Since the signal cannot be described by a linear equation, a nonlinear multivariate model is required. Semiparametric methods, such as kernel methods, provide more understandable models than artificial neural networks. Recently least-squares support vector machines (LSSVM)[14] methods have been developed and applied to near-infrared spectroscopy issues such as nonlinear discrimination[15,16] and quantitative predictions.[17]

Our aim here is to study LS SVM models calibrated only by use of theoretical data calculated from the diffusion equation in the reflectance mode. These models are then applied to predict the reduced scattering coefficient and the absorption coefficient of the experimental data.

F. Chauchard (fabien.chauchard@montpellier.cemagref.fr), J.-M. Roger, and V. Bellon-Maurel are with Information and Technologies for Agro-processes Cemagref, BP 5095, 34033 Montpellier, Cedex 1, France. S. Roussel is with Agrometrix, MINEA research parc, Cemagref, 361 rue Jean-Francois Breton, BP 5095, 34033 Montpellier, Cedex 1, France. C. Abrahamsson, T. Svensson, S. Andersson-Engels, and S. Svanberg are with the Department of Physics, Lund Institute of Technology, P.O. Box 118, Lund SE-221 00, Sweden.

Received 28 February 2005; revised manuscript received 10 May 2005; accepted 16 May 2005.

0003-6935/05/337091-07$15.00/0

2. Theory

A. Diffusion Equation

Photon transport in turbid media is described by the radiative transport equation[18]:

$$\frac{1}{c}\frac{\partial L(r,\ \mathbf{s},\ t)}{\partial t} + \mathbf{s}\cdot\nabla L\ (r,\ \mathbf{s},\ t) + (\mu_s + \mu_a)\, L(r,\ \mathbf{s},\ t) = \mu_s \int_{4\pi} L(r,\ \mathbf{s},\ t)p(\mathbf{s},\ \mathbf{s}')\mathrm{d}\omega' + Q(r,\ \mathbf{s},\ t). \quad (1)$$

Here L is the radiance at a given distance r from the irradiating source at time t and in direction $\mathbf{s}$; $p(\mathbf{s}, \mathbf{s}')$ is the Henyey–Greenstein phase function; $\mathrm{d}\omega'$ is the angle between the initial photon direction $\mathbf{s}$ and the new direction $\mathbf{s}'$; and c is the speed of light in vacuum. To solve this equation the sample geometry must be taken into account. In the case of a semi-infinite homogeneous medium measured in reflection, the solution is given by the time-resolved diffusion equation[7]

$$R(\rho,\ t) = (4\pi D v)^{-3/2}\, z_0 t^{-5/2} \exp(-\mu_a v t) \times \exp\left(-\frac{\rho^2 + {z_0}^2}{4Dvt}\right). \quad (2)$$

Here R is the signal measured at a given distance ρ at time t; D is the diffusion coefficient with $D(\lambda) = \{3[\mu_a(\lambda) + \mu_s'(\lambda)]\}^{-1}$; $z_0(\lambda) = [1/\mu_s']$ is the mean path; and v is the speed of light in the medium, assumed to be constant in the measured wavelength range. A theoretical database containing time-resolved curves can be easily obtained by use of Eq. (2). A model can be derived based on this database, which can then be used to predict μ_a and μ_s'.

B. Least-Squares Support Vector Machines Theory

LS SVM models constitute an alternate formulation of SVM regression[19] proposed by Suykens.[14] Whereas classical multivariate regression is built on variables (e.g., time data for TRS or wavelengths for spectroscopic data) LS SVM methods are based on a kernel matrix **K.** The raw data matrix $\mathbf{X}_{n,p}$ containing n samples with p variables (e.g., n time-resolved curves), is then replaced by the $\mathbf{K}_{n,n}$ kernel defined as

$$\mathbf{K} = \begin{pmatrix} k_{1,1} & \cdots & k_{1,n} \\ \vdots & \ddots & \vdots \\ k_{n,1} & \cdots & k_{n,n} \end{pmatrix}. \quad (3)$$

Here $k_{i,j}$ is given by the radial basis function

$$k_{i,j} = \exp\left(\frac{-\|\mathbf{x_i^T} - \mathbf{x_j^T}\|^2}{\sigma^2}\right), \quad (4)$$

and $\mathbf{x}_i^T$ is the time response for a TRS measurement. The variable space is hence replaced by a sample space of a high dimension where a sample is defined by its distance to the other samples contained in the database. The proper subspace for modeling is tuned with the σ^2 parameter. The higher the σ^2, the wider the Gaussian kernel. Put simply, $k_{i,j}$ represents the similarities between the $\mathbf{x}_i^T$ and the $\mathbf{x}_j^T$ time responses. The model equation is then

$$\hat{\mathbf{y}} = \mathbf{K}\boldsymbol{\beta} + \beta_0, \quad (5)$$

where $\hat{\mathbf{y}}$ is the predicted value, $\mathbf{K}$ is the kernel as defined by Eq. (3), $\boldsymbol{\beta}$ is the regression vector, and β_0 is the offset term. Furthermore, the LS SVM objective function takes into account the norm of the regression vector to increase the model robustness. The classical squared loss function is thus replaced by the following objective function:

$$\min(\mathbf{e}) = \min\left[\frac{\sum_{i=1}^{n}(y_i - \hat{y}_i)^2}{2} + \frac{1}{\gamma}\frac{(\boldsymbol{\beta}^{\mathrm{T}}\boldsymbol{\beta})}{2}\right], \quad (6)$$

where γ is a regularization parameter analogous to the regularization parameter of regularized artificial neural networks and is used to weigh β norm. Once σ^2 and γ are chosen, the model is trained after constructing the Lagrangian by solving the linear Karush–Kuhn–Tucker system:

$$\begin{bmatrix} 0 & \mathbf{l}_n^{\mathrm{T}} \\ \mathbf{l}_n & \mathbf{K} + \dfrac{\mathbf{I}}{\gamma} \end{bmatrix} \begin{bmatrix} \hat{b}_0 \\ \hat{\mathbf{b}} \end{bmatrix} = \begin{bmatrix} 0 \\ \mathbf{y} \end{bmatrix}, \quad (7)$$

where $\mathbf{I}$ refers to an $[n \times n]$ identity matrix and $\mathbf{l}_n$ is an $[n \times 1]$ unity vector. The solution of Eq. (7) can be found by use of most standard methods of solving sets of linear equations, such as the conjugate gradient descent.

3. Material and Methods

A. Instrumentation

Figure 1 depicts the experimental setup. The instrument has been described in detail elsewhere.[9] Briefly, a Ti:sapphire mode-locked laser, pumped by an Ar-ion laser, was used to generate 100 fs pulses centered around 800 nm with an 80 MHz repetition rate. The laser pulses were focused into a 100 cm long index guiding crystal fiber (ICF)(Crystal Fiber A/S, Copenhagen, Denmark). The broadband light pulses generated by nonlinear effects in the ICF ranged from 750 to 1100 nm. The light was then transferred by a set of lenses into a gradient-index fiber guiding the light to the sample. Another gradient fiber, with the distal tip 6 mm from the irradiating tip, was used to collect the light diffusively reflected by the sample. The fibers were put in contact with the sample. A streak camera (Hamamatsu Model C5680) coupled to an imaging spectrometer (Chromex Model 250IS) captured the reflected light as a function of time and wavelength $R(t, \lambda)$. The spectral resolution was 0.93

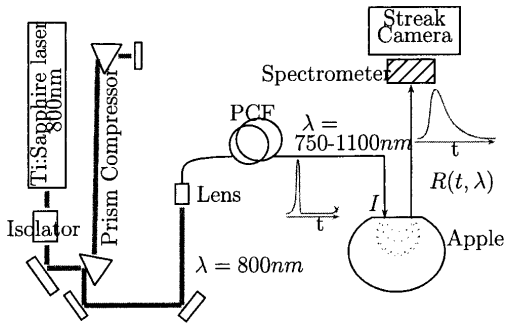

Fig. 1. Setup for TRS spectrum acquisition.

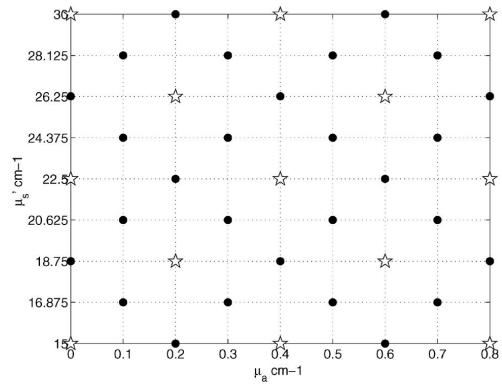

Fig. 2. (a) Values of μ_a and μ_s' for the training set: ★, calibration (A); ●, validation (B) for γ and σ^2 parameter tuning. (b) Four theoretical dispersion profiles.

nm distributed over 512 pixels while the temporal resolution was 2.93 ps in the span from 0 to 1900 ps, spread over 640 pixels.

B. Measured Samples

Fifteen Golden Delicious apples were measured with the TRS setup. A small part of the apple was carefully removed to create a flat surface for applying the fibers. The measurements were performed immediately after the preparation of the apples to avoid flesh drying. Prior to each sample measurement, we recorded an instrumental response function by connecting the transmitting and receiving fibers to each end of a thin metal tube. This instrumental response function was used to determine time zero of the streak camera response and to measure the dispersion of the measured pulse that is due to the system characteristics.

C. Least-Squares Support Vector Machines Model

The LS SVM model was derived by use of a theoretical calibration set. We obtained the dataset by using the diffusion equation for an interfiber distance of $\rho = 6$ mm and a time resolution of 2.93 ps. Each signal was normalized by division with its maximum to become independent of variations in the irradiating signal intensity level. To improve the model efficiency, the temporal window between $t = 43$ and 900 ps was selected, where the time dispersion curves with different optical properties were significantly different. To span the absorption and scattering variations of apples,[20] a mixture design was used as described in Fig. 2. To tune γ and σ^2 the training set was split into two subsets, one for calibration (subset A) and one for validation (subset B). After the two parameters were chosen, the final model was constructed by use of the whole theoretical dataset.

The LS SVM toolbox (LS SVM version 1.4[21]) was used with MATLAB 6.0 (The MathWorks, Incorporated, Natick, Massachusetts) to derive the LS SVM models. To evaluate the accuracy of this new method, we compared the predicted values of μ_a and μ_s' with the ones fitted to the diffusion equation by using a Levenberg–Marquardt algorithm (LMA) previously used for apple TRS measurements.[20]

4. Results and Discussion

A. Time-Resolved Spectroscopy Measurements

Figure 3(a) shows the instrumental response function. The continuum light pulses obtained were 300 nm wide (800–1100 nm). The temporal width was approximately 23 ps FWHM. The spectral profile was sensitive to changes in the laser intensity and variations in incoupling efficiency into the ICF. As a result, the spectral profile of the irradiating source changed from one sample measurement to another. The LS SVM model uses a temporal signal at a given wavelength. This response is normalized to obtain a maximum value of 1. Hence, source intensity variation from one sample measurement to another does not act on the model prediction efficiency. The recorded signal from one apple is depicted in Fig. 3(b). The temporal dispersion is high because of the scattering phenom-

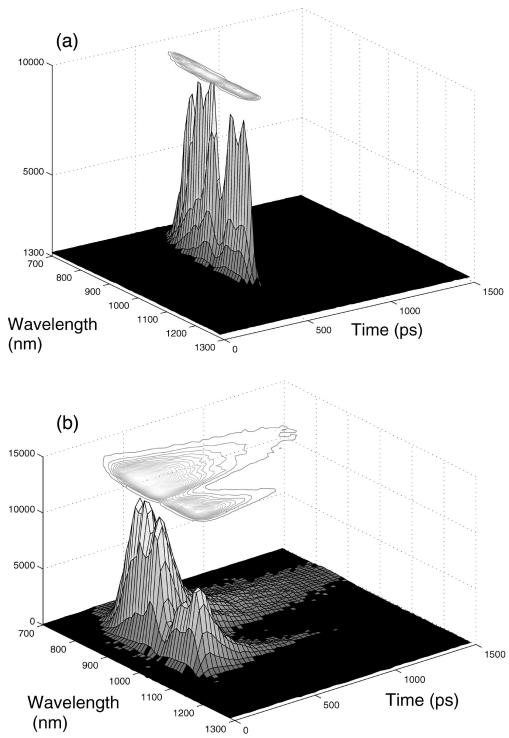

Fig. 3. Recording of two-dimensional time-resolved measurements: (a) multispectral light pulse for sample irradiation and (b) recorded signal for an apple.

ena inside the apple. Since the recorded signal-to-noise ratio was high enough in the region ranging from 800 to 1050 nm, this spectral window was selected for the study of optical properties of the apples.

B. Model Tuning

The optimization response surface for μ_a prediction is illustrated in Fig. 4. This surface represents the standard error of prediction on validation set B. The best prediction of μ_a was found for $\gamma = 50$ and $\sigma^2 = 500$. The μ_s' response surface (not presented here) gives an optimal solution for the same values. Since σ^2values are the same for both μ_a and μ_s', the kernel matrix is the same; this means that both models are built on the same subspace, allowing for the same degree of nonlinearities. Only the regression vectors are different for predicting μ_a and μ_s'. Low values of robustness criteria γ imply that regression vectors have a small norm that is necessary for a robust model.

C. Evaluation of Scattering and Absorption Coefficients for Experimental Data

Figure 5 shows a comparison of μ_a and μ_s' values predicted by the LMA and LS SVM for one apple. The absorption coefficient curves are similar, which

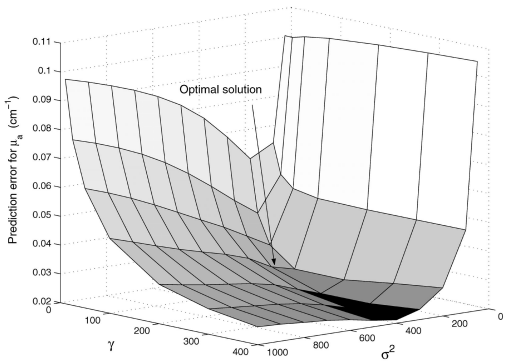

Fig. 4. Optimization surface for γ and σ^2 tuning for μ_a modelization.

proves the LS SVM prediction capabilities. In spite of the noise, the water peak is clearly visible at 970 nm as normally seen in conventional near-infrared spectra of fruits. With regard to the scattering coefficient the prediction values present an offset compared with the LMA results. This can be explained by the temporal dispersion shown in Fig. 6: the LS SVM model considers the irradiating peak as perfectly resolved in time (time width infinitely small), whereas the LMA takes the instrumental response into account in the calculations. Since the LMA is based on convolution, the predicted TRS curves are closer to the measured signal. However the LS SVM produce acceptable results. The LS SVM curves are above the LMA and are slightly peak shifted, which explains the offset previously observed between μ_s' values.

D. Prediction Performances

Figure 7 shows the LS SVM predicted values versus the LMA values of μ_a for the 15 apples (271 dispersion curves per sample). The determination coefficient of 0.96 is satisfactory, with a standard error of

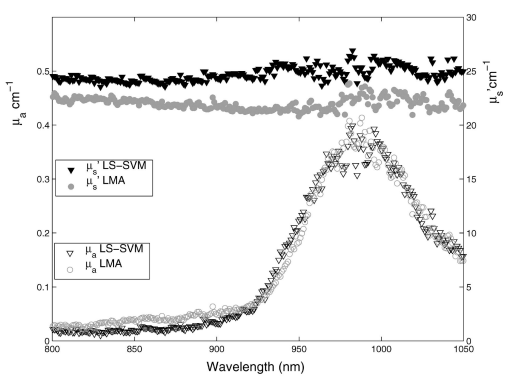

Fig. 5. Results for μ_a and μ_s prediction for an apple at all wavelengths.

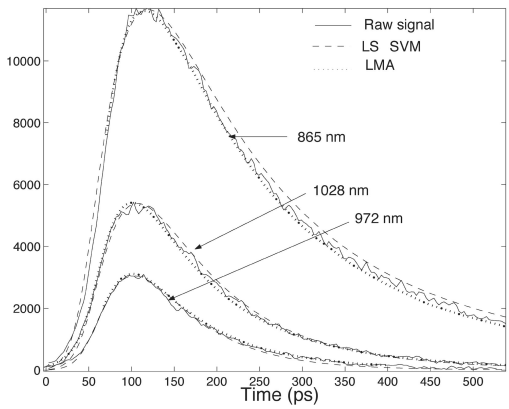

Fig. 6. Measured signal and fitted signals for three wavelengths.

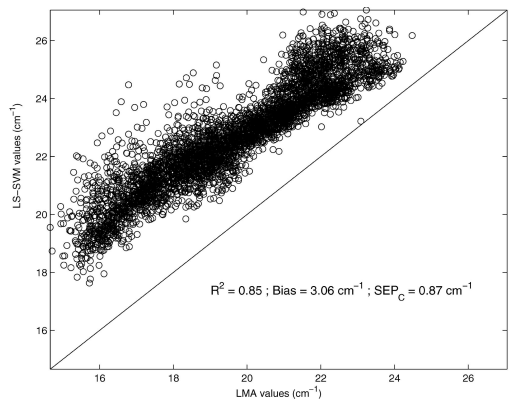

Fig. 8. Predicted performance of the μ_s' prediction model.

prediction of 0.02 cm^{-1}. It should be noted that there are no real reference values, but only reference values estimated by the LMA. Figure 8 shows a bias between LMA values and LS SVM predicted values for μ_s' determination. As explained in Subsection 4.C, this difference comes from the convolution process that is not used in the LS SVM. Since the determination coefficient is satisfactory (0.85), the model can easily be bias corrected by adding a constant (-3.06 cm^{-1}). However, this approach would consider LMA values as real reference values, although the LMA also has drawbacks and inaccuracies. For this reason, it would be more interesting to follow a more sophisticated approach, integrating a convolution process when building the database. In this case, the model would be calibrated on theoretical curves obtained by convoluting the diffusion equation with the instrumental response function. Of course, this method is more time-consuming since the model must be designed for each sample. When this approach is followed the prediction plot gives the results shown in Fig. 9. As assumed, the bias is reduced but is not small enough to be neglected. Furthermore, the correlation coefficient between LMA and LS SVM values decreases to 0.75. The noise in the measured data acts differently in the two methods since they have different bases. A visual curve analysis [Fig. 10(a)] is not accurate enough to be used to judge the differences between method performance. For this reason, the determination coefficient between the raw signal and the two estimated signals are presented for each wavelength in Fig. 10(b). The temporal curves calculated with the LS SVM predicted coefficient clearly have high performance ($r^2 > 0.99$), which is close to those calculated with the LMA. This tends to prove the accuracy of the proposed approach.

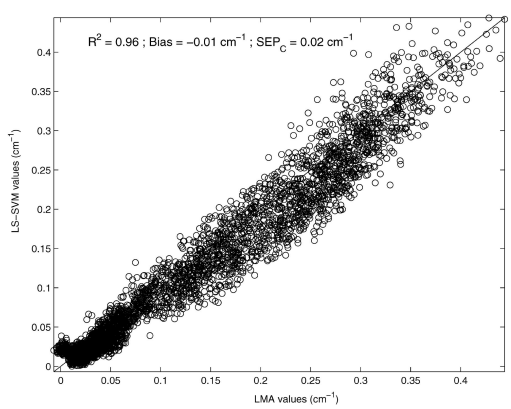

Fig. 7. Predicted performance of the μ_a prediction model.

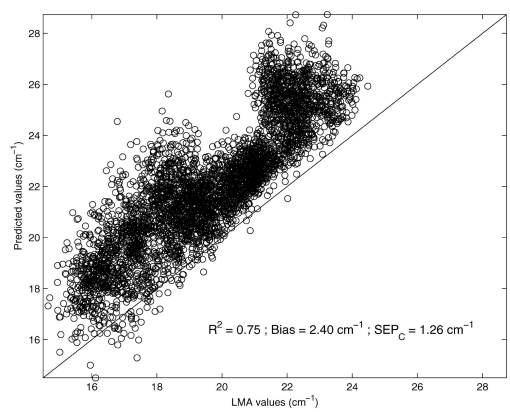

Fig. 9. Predicted performance of the μ_s' prediction model with a convolution approach.

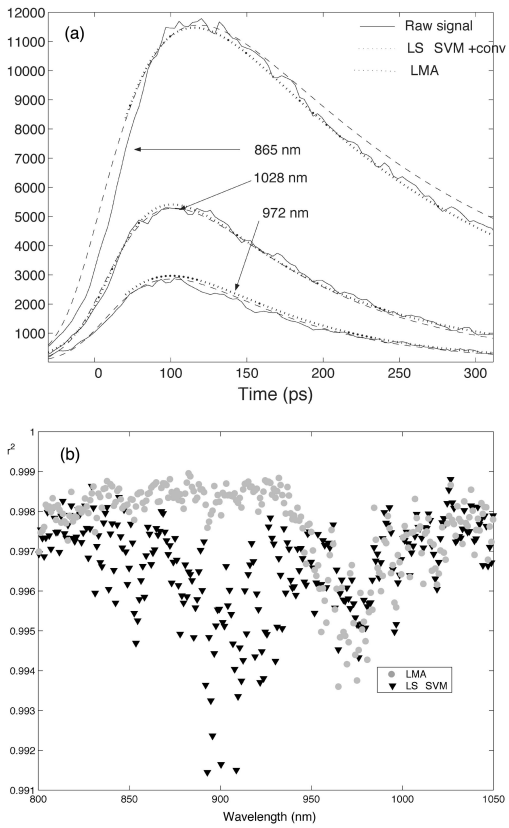

Fig. 10. Measured signal and fitted signals with the LS SVM obtained with convolution and determination coefficients: (a) predicted signals for three wavelengths and (b) r^2 between curves for each wavelength.

5. Conclusion

Thanks to its performance, the LS SVM model can be applied to time-resolved data for extraction of absorption and scattering coefficients. The model we have proposed in this paper has two main advantages. The first is that it can be used on any diffusing sample with $\mu_a < 0.08\ \mathrm{cm}^{-1}$ and $1.5\ \mathrm{cm}^{-1} < \mu_s' < 3\ \mathrm{cm}^{-1}$ (but a larger model can be calibrated) such as for human tissues. The second is that, since the model uses only 41 time-resolved curves, it can easily be integrated into an embedded sensor for industrial use. Even if the model performance is already interesting, the method can be improved by integration of a convolution process into the database construction. For optimization, data smoothing can be applied to the raw data.

The LS SVM could also be used with a database of Monte Carlo data. This would be interesting for measurement geometries for which the diffusion approximation is not valid, e.g., where the source and the detection fibers are situated close to each other or when the boundary conditions are too complex to be solved analytically.

As TRS transmission measurements produce the same type of curves as the reflection geometry, the LS SVM model can also be derived and applied efficiently to transmission data (slab geometry). We also believe that LS SVM modeling would be of great interest for spatially resolved spectroscopy and phase modulation spectroscopy.

This research was supported by the Integrated Initiative of Infrastructure project LASERLAB-EUROPE, contract RII3-CT-2003-506350.

References

1. B. Chance, J. Leigh, H. Miyake, D. Smith, S. Nioka, R. Greenfeld, M. Finander, K. Kaufmann, W. Levy, and M. Young, "Comparison of time-resolved and unresolved measurements of deoxyhemoglobin in brain," Proc. Natl. Acad. Sci. USA **85,** 4971–4975 (1988).
2. S. L. Jacques, "Time-resolved propagation of ultrashort laser pulses within turbid tissues," Appl. Opt. **28,** 2223–2229 (1989).
3. S. Andersson-Engels, R. Berg, S. Svanberg, and O. Jarlman, "Time-resolved transillumination for medical diagnostics," Opt. Lett **15,** 1179–1181 (1990).
4. J. Johansson, S. Folestad, M. Josefson, A. Sparen, C. Abrahamsson, S. Andersson-Engels, and S. Svanberg, "Time-resolved NIR/Vis spectroscopy for analysis of solids: pharmaceutical tablets," Appl. Spectrosc. **56,** 725–731 (2002).
5. P. E. Zerbini, M. Grassi, R. Cubeddu, A. Pifferi, and A. Torricelli, "Nondestructive detection of brown heart in pears by time-resolved reflectance spectroscopy," Postharvest Biol. Technol. **25,** 87–97 (2002).
6. J. Johansson, R. Berg, A. Pifferi, S. Svanberg, and L. Bjorn, "Time-resolved studies of light propagation in *Crassula* and *Phaseolus* leaves," Photochem Photobiol. **69,** 242–247 (1999).
7. M. S. Patterson, B. Chance, and B. C. Wilson, "Time-resolved reflectance and transmittance for the noninvasive measurement of tissue optical properties," Appl. Opt. **28,** 2331–2336 (1989).
8. S. Andersson-Engels, R. Berg, A. Persson, and S. Svanberg, "Multispectral tissue characterization with time-resolved detection of diffusely scattered white light," Opt. Lett. **18,** 1697–1699 (1993).
9. C. Abrahamsson, T. Svensson, S. Svanberg, S. Andersson-Engels, J. Johansson, and S. Folestad, "Time and wavelength resolved spectroscopy of turbid media using light continuum generated in a crystal fiber," Opt. Express **12,** 4103–4112 (2004).
10. T. J. Farrell, M. S. Patterson, and B. Wilson, "A diffusion theory model of spatially resolved, steady-state diffuse reflectance for the noninvasive determination of tissue optical properties *in vivo,*" Med. Phys. **19,** 879–888 (1992).
11. R. Cubeddu, A. Pifferi, P. Taroni, A. Torricelli, and G. Valentini, "Experimental test of theoretical models for time resolved reflectance," Med. Phys. **23,** 1625–1633 (1996).
12. S. J. Madsen, B. C. Wilson, M. S. Patterson, Y. D. Park, S. L. Jacques, and Y. Hefetz, "Experimental tests of a simple diffusion model for the estimation of scattering and absorption coefficients of turbid media from time resolved diffuse reflectance measurements," Appl. Opt. **31,** 3509–3517 (1992).
13. L. Leonardi and D. H. Burns, "Quantitative constituent measurements in scattering media from statistical analysis of photon time-of-flight distributions," Anal. Chim. Acta **348,** 543–551 (1997).
14. J. A. K. Suykens, T. Van Gestel, J. De Brabanter, B. De Moor, and J. Vandewalle, *Least Squares Support Vector Machines* (World Scientific, 2002).

15. A. I. Belousov, S. A. Verzakov, and J. von Frese, "Applicational aspects of support vector machines," J. Chemom. **16,** 482–489 (2002).
16. R. Goodacre, "Explanatory analysis of spectroscopic data using machine learning of simple, interpretable rules," Vib. Spectrosc. **32,** 33–45 (2003).
17. F. Chauchard, R. Cogdill, S. Roussel, J. M. Roger, and V. Bellon-Maurel, "Application of LS-SVM to non-linear phenomena in NIR spectroscopy: development of a robust and portable sensor for acidity prediction in grapes," Chemom. Intell. Lab. Syst. **71,** 141–150 (2004).
18. A. Ishimaru, *Wave Propagation and Scattering in Random Media* (Academic, 1978).
19. V. Vapnik and A. Lerner, "Pattern recognition using generalized portrait method," Autom. Remote Control **24,** 774–780 (1963).
20. R. Cubeddu, C. D'Andrea, A. Pifferi, P. Taroni, A. Torricelli, G. Valentini, C. Dover, D. Johnson, M. Ruiz-Altisent, and C. Valero, "Nondestructive quantification of chemical and physical properties of fruits by time-resolved reflectance spectroscopy in the wavelength range 650–1000 nm," Appl. Opt. **40,** 538–543 (2001).
21. LS SVMs toolbox, www.esat.kuleuven.ac.be/sista/lssumlab/.

Paper VI

In vivo optical characterization of human prostate tissue using near-infrared time-resolved spectroscopy

T. Svensson, S. Andersson-Engels, M. Einarsdóttír and K. Svanberg.
Journal of Biomedical Optics **12**, 014022 (2007).

Journal of Biomedical Optics 12(1), 014022 (January/February 2007)

In vivo optical characterization of human prostate tissue using near-infrared time-resolved spectroscopy

Tomas Svensson
Stefan Andersson-Engels
Lund University
Department of Physics
SE-221 00 Lund
Sweden

Margrét Einarsdóttír
Katarina Svanberg
Lund University Hospital
Department of Oncology
SE-221 00 Lund
Sweden

Abstract. The development of photodynamic therapy into a modality for treatment of prostate cancer calls for reliable optical dosimetry. We employ, for the first time, interstitial time-resolved spectroscopy to determine *in vivo* optical properties of human prostate tissue. Nine patients are included in the study, and measurements are conducted prior to primary brachytherapy treatment of prostate cancer. Intrasubject variability is examined by measuring across three tissue volumes within each prostate. The time-resolved instrumentation proves its usefulness by producing good signal levels in all measurements. We are able to present consistent values on reduced scattering coefficients (μ_s'), absorption coefficients (μ_a), and effective attenuation (μ_{eff}) at the wavelengths 660, 786, and 916 nm. At 660 nm, μ_s' is found to be 9 ± 2 cm^{-1}, and μ_a is 0.5 ± 0.1 cm^{-1}. Derived values of μ_{eff} are in the range of 3 to 4 cm^{-1} at 660 nm, a result in good agreement with previously published steady state data. Total hemoglobin concentration (THC) and oxygen saturation are spectroscopically determined using derived absorption coefficients. Derived THC values are fairly variable (215 ± 65 μM), while derived values of oxygen saturation are gathered around 75% (76 ± 4%). Intrasubject variations in derived parameters correlate (qualitatively) with the heterogeneity exhibited in acquired ultrasound images. [DOI: 10.1117/1.2435175]

Keywords: human prostate; hemoglobin; photon migration; time-resolved spectroscopy; optical properties; *in vivo*.

Paper 06239R received Sep. 5, 2006; revised manuscript received Nov. 7, 2006; accepted for publication Nov. 8, 2006; published online Jan. 25, 2007.

1 Introduction

Interest in optical characteristics of the human prostate is mainly related to recent efforts in developing photodynamic therapy (PDT) into a modality for treatment of localized prostate cancer. Initial preclinical work on PDT of prostate carcinoma appeared during the 1980s (Refs. 1 and 2) and (first) clinical work was published[3] as early as 1990. For the development and optimization of the technique, several studies have since been performed on canine[4–6] and rat[1,7] models. Clinical results from various research groups are now available.[8–13] Altogether, these results have shown a great potential of PDT in the management of prostate cancer.[14,15]

PDT, in general, relies on a process where light excites (i.e., activates) a photosensitizer, which induces cytotoxic oxygen species. Thus, PDT relies on the presence of light, a photosensitizer, and oxygen. The corresponding dosimetry is therefore a complex matter, involving measurement and/or prediction of sensitizer and oxygen concentrations as well as light fluence (light dose). Since full treatment of diseased regions is crucial, these issues must be carefully addressed. Accordingly, PDT dosimetry has been the main focus of numerous papers (see, e.g., Star[16]), of which a few are closely related to the particular case of PDT of prostate cancer.[17–21] One fundamental aspect in this context is the tissue optical properties, e.g., absorption and scattering coefficients. Not only do they together determine the light dose distribution, but *in vivo* access to absorption coefficients can be used to estimate, for example, sensitizer concentrations, hemoglobin concentration, and tissue oxygenation. In addition, due to dynamic changes during PDT treatment, it is sometimes argued that on-line monitoring is required to achieve optimal treatment.[22,23]

For the case of prostate tissue, several papers have addressed the issue of optical properties, e.g., the effective attenuation coefficient μ_{eff} and in some cases also absorption and reduced scattering coefficients μ_a and μ_s', respectively.[4,18,24–31] Most of them rely on interstitial fiber optic steady state fluence rate measurements at multiple source-detector separations. By measuring relative fluence rate in a range of source-detector separations larger than a few millimeters (i.e., the diffuse regime), the diffusion approximation of light transport can be employed to determine μ_{eff}. Since μ_{eff} depends on both μ_a and μ_s', additional data is required to reach information on absorption and scattering separately.

Address all correspondence to Tomas Svensson, Department of Physics, Lund University, Box 118, SE-221 00 Lund, Sweden; Phone: +46-46-2223120; Fax: +46-46-2224250; E-mail: tomas.svensson@fysik.lth.se

1083-3668/2007/12(1)/014022/10/$25.00 © 2007 SPIE

One option is to determine $\mu_t' = \mu_a + \mu_s'$ by measuring relative radiance at multiple, but short, source-detector separations.[32] A second option, avoiding the need of short source-detector separations, is to measure absolute (instead of relative) fluence rate in the diffuse regime.[33] Data evaluation, by means of curve fitting, then yields μ_{eff} and μ_s'. Hence, both options enable estimation of absorption and scattering coefficients.

Previously published values on optical properties of the human prostate, together with the results obtained in this study, are given in Sec. 3. The first published work presents *ex vivo* steady state measurements of μ_{eff} and $\mu_t' = \mu_a + \mu_s'$, at 633 nm, in three whole, nonmalignant human prostates.[24] Another *post mortem* study estimates prostate optical properties (μ_a, scattering coefficient μ_s, scattering anisotropy g, and μ_s') at 1064 nm, by measuring through thin prostate slices.[25] *In vivo* effective attenuation in prostates diagnosed with benign prostatic hyperplasia (BPH) or prostatic carcinoma (PC) has been estimated at 630, 633, and 665 nm, by employing steady state fluence rate measurements.[26,28,29] Other studies rely on absolute fluence rate measurements to determine both absorption and scattering coefficients. By measuring fluence rates along a linear channel (5 mm away from the source fiber), one such study presents optical properties at 732 nm, before and after motexafin-lutetium-mediated PDT of locally recurrent prostate cancer.[34] In a similar study, optical fibers are kept fixed (five source fibers and three detector fibers), and absolute fluence rate data is collected for 15 source-detector separations (at 762 nm). Measurements were in that case performed in connection with TOOKAD-mediated PDT of recurrent prostate cancer.[30] Regarding hemoglobin monitoring in human subjects, only very limited data have been published.[30,31]

This study employs interstitial time-resolved spectroscopy to characterize human prostate tissue *in vivo*. Conceptually, this approach is very different from those chosen in previously published work related to prostate tissue. By analyzing the temporal broadening of picosecond laser pulses due to propagation through tissue, this technique provides reliable estimations of absorption and reduced scattering coefficients. The use of multiple wavelengths enables spectroscopic determination of total hemoglobin concentration (THC) and oxygen saturation (S_tO_2). The technique has previously been used in various areas of biomedical optics.[35–39]

The aim of the paper is to provide information on parameters of dosimetric importance, as well as to introduce time-resolved spectroscopy as a tool in PDT research. In particular, the aim is to achieve separate information on μ_a and μ_s', as well as quantitative information on hemoglobin parameters. We also wish to give a proper indication on intra- and inter-subject variation, for the case of untreated prostate cancer. These parameters are important for PDT dosimetry calculations, and are not extensively explored in previous studies.

Nine patients diagnosed with prostate cancer were included in the study, and all measurements were performed before primary treatment. By inserting three optical fibers, three tissue volumes were probed, yielding information on prostate tissue heterogeneity.

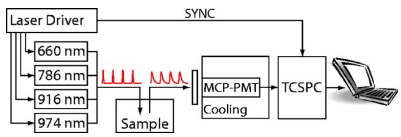

Fig. 1 Schematic of the instrumentation in interstitial mode.

2 Material and Methods

2.1 *Instrumentation*

Time-resolved data were acquired using a compact ($50 \times 50 \times 30$ cm) and portable time-domain photon migration instrument primarily intended for spectroscopy of biological tissues in clinical environments.[39,40] A schematic illustration is given in Fig. 1.

The system is based on diode laser technology and time-correlated single-photon-counting (TCSPC). A laser driver (SEPIA PDL 808, PicoQuant, Germany) controls four pulsed diode lasers (LDH, PicoQuant at 660, 786, 916, and 974 nm). Wavelengths are chosen to enable monitoring of important tissue constituents (hemoglobin, water, and lipids) and properties (tissue oxygenation). Lasers are typically operated at 1 to 2 mW, generating pulses about 70 ps wide (FWHM). Four wavelength pulse trains are generated at a repetition frequency of 40 MHz. This is accomplished by separating the individual pulses in time (~6 ns), using electric cables of different lengths.

The light emitted from each diode laser is individually coupled into a separate 200-μm graded-index (GRIN) fiber (G 200/280 N, ART Photonics, Germany). A four-to-one coupler is used to couple all light into a single 600-μm GRIN fiber (G 600/840 P, ART Photonics), which serves as the light source. A second fiber collects light and delivers it to the detector. Each of these two fibers is approximately 2 m long. To fit into 1-mm inner diameter brachytherapy needles, a thin polyimide layer acts as the only fiber coating at the fiber endings. Remaining parts are protected in polyolefin tubing.

Proper photon levels are achieved by sending collected light through an adjustable gradient neutral density (ND) filter. Remaining photons are sent to a cooled microchannel plate photomultiplier tube (MCP-PMT; R3809-59, Hamamatsu Photonics, Japan). A TCSPC computer card (SPC-300, Becker&Hickl, Germany) is used to obtain time-dispersion histograms with channel widths of approximately 25 ps.

Broadening in the fibers and the detector yields an instrument response function (IRF) that is about 100 ps wide. The IRF is measured by inserting source and detector fibers into a chamber so that the end facets are separated by 150 mm and face each other. The chamber is made of black delrin, and contains a pinhole that is inserted between the two fibers to block reflected stray light.

2.2 *Modeling*

Experimental data are modeled using the diffusion approximation of transport theory. More specifically, data are fitted to the analytical solution of the time-dependent diffusion equation for the case of a homogenous and infinite medium.[41]

Accordingly, the fluence rate Φ due to a infinitely short light pulse from an isotropic point source can be written as

$$\Phi(r,t) = c' E_0 (4\pi c' D t)^{-3/2} \exp\left(- \frac{r^2}{4c'Dt} - \mu_a c' t \right), \quad (1)$$

where E_0 is the pulse energy, r is the distance from the point source, c' is the speed of light within the material, and D is the diffusion coefficient. The refractive index is assumed to be $n=1.4$. To comply with recent work concerning the diffusion coefficient, it is defined as in Eq. (2), rather than in the traditional (absorption-dependent) way[42,43]:

$$D = \frac{1}{3\mu_s'}. \quad (2)$$

The form of Eq. (1) enables deduction of both μ_s' and μ_a from experimental data without requiring absolute measurements of light fluence. This is achieved by considering temporal shapes only. That is, experimental data are fitted using an expression similar to that given in Eq. (1), but in which amplitude information is contained in a free parameter k. This expression is given as

$$y(\mu_a, \mu_s', k, t) = k\, t^{-3/2} \exp\left(- \frac{3\mu_s' r^2}{4c't} - \mu_a c' t \right). \quad (3)$$

The best fit is reached iteratively using a Levenberg-Marquardt algorithm, where μ_s', μ_a, and k are varied to minimize a χ^2 error norm.[44] Final values of μ_s' and μ_a are then estimations of the reduced scattering coefficient and absorption coefficient, respectively. Note that the IRF, being about 100 ps wide, cannot be regarded as infinitely short in comparison to the tissue response. Therefore, each iteration in the curve-fitting procedure involves a convolution of analytical data and IRF. It should also be noted that fitting is performed using the part of experimental data between times given by the 50% of maximum on the rising edge, and 20% on the falling edge (see Fig. 5 in Sec. 3).

The previous studies of human prostate optical properties mentioned in the introduction used the same theoretical framework. However, by employing steady state techniques, they rely on a stationary solution rather that the time-dependent solution given in Eq. (1). The stationary solution of the diffusion equation for an infinite homogenous medium is given as

$$\Phi(r) = \frac{3\mu_s' P_0}{4\pi r} \exp(-\mu_{eff} r). \quad (4)$$

Here, P_0 is the power of the point source, r is the distance from the source, and μ_{eff} the effective attenuation. The effective attenuation is defined as

$$\mu_{eff} = (\mu_a / D)^{1/2} = (3\mu_a \mu_s')^{1/2} \quad (5)$$

From the form of Eq. (4), we see that μ_{eff} can be deduced from relative fluence measurements at multiple source detector separations. Only if absolute fluence rate is measured, it can be used to get information on reduced scattering and absorption separately. Absolute measurement of fluence rate in living tissue is of course a difficult matter (especially in interstitial settings). Note also that μ_{eff} is a primary parameter when using the steady state technique. Time-resolved experiments provide estimations of μ_a and μ_s' which in a second step can be used to calculate μ_{eff}.

Table 1 Extinction and absorption coefficients of tissue chromophores.

	Unit	660 nm	786 nm
Pure water	cm^{-1}	0.0036	0.0222
Pure lipid	cm^{-1}	0.0042	0.0036
Hb	$cm^{-1}/\mu M$	0.0074	0.0022
HbO_2	$cm^{-1}/\mu M$	0.00074	0.0017

2.3 *Hemoglobin Spectroscopy*

The spectroscopic evaluation employed in this study assumes that the absorption exhibited by prostate tissue originates from oxy- and deoxyhemoglobin (Hb and HbO_2, respectively), water, and lipids. Since high absorption prevented the use of 974-nm data (see Sec. 3), water and lipid concentrations could not be estimated. Instead, absorption coefficients at 660 and 786 nm were used to extract oxy- and deoxyhemoglobin concentrations ($[HbO_2]$ and [Hb], respectively). In this procedure, the prostate was assumed to contain 70% water and 10% lipids (note that due to relatively low absorption of water and lipids at 660 and 786 nm, the choice of these values is of very little importance). The extinction coefficients of these chromophores were taken from literature[45–47] and are presented in Table 1.

In a second step, total hemoglobin concentration and oxygen saturation are calculated from $[HbO_2]$ and [Hb].

2.4 *Clinical Procedure*

Clinical data were collected at the Lund University Hospital adhering to a protocol approved by the regional ethics committee. All nine patients involved in the study were undergoing primary treatment of prostate cancer. Measurements were performed in connection with brachytherapy (low-dose seed implantation). This fact limits our study to patients suitable for this treatment, that is, patients fulfilling the following requirements: (1) Gleason index <6, (2) prostate specific antigen (PSA) <10, (3) no tumor obstruction of urethra, and (4) prostate volume of the order of 20 to 40 cm^3. Such patients are often referred to as low-risk patients.

This type of brachytherapy of prostate cancer involves permanent implantation of radioactive seeds (internal radiotherapy). The procedure takes place in an operating theater, while patients are under general anesthesia. At the Lund University Hospital, the first step in this procedure is to image the prostate gland using transrectal ultrasound. When the physician has marked important boundaries in these images (prostate, urethra, and rectum), a radiotherapist performs dosimetric calculations. Dosimetric calculations open a time window of about 20 min in which the time-resolved measurements were performed without interfering with the routine proce-

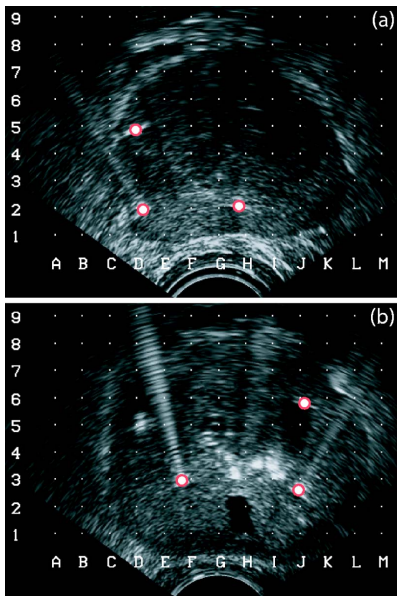

Fig. 2 Two ultrasound images showing three needles inserted into the prostate. For clarity, the needles are marked by circles. Shadows behind the needles are due to their high reflectivity. The fairly homogenous image (a) originates from patient 5, while the heterogenous structure in (b) was exhibited by patient 6.

dures. Three standard brachytherapy needles were then inserted, all to the same depth (using transrectal ultrasound guidance). A standard transperineal brachytherapy needle matrix handles lateral positioning (5×5-mm grid spacing). Three sterilized optical fibers were inserted through the three needles so that they were located edge to edge with the needle tips (this positioning is achieved by premarking the fibers). Fiber separations are inferred from ultrasound images (B-K Medical Hawk 2102 EXL with transducer 8658-T operating at 6.5 to 7.5 MHz). Figure 2 shows two authentic ultrasound images.

By using three needles, it is possible to probe three fairly nonoverlapping prostate tissue volumes. Fiber separations were in the range of 10 to 30 mm. The three fiber separations used within each patient were chosen to differ, and typically set in a triangular pattern to approximately 15, 20, and 25 mm. The longest fiber separation corresponds to a more central volume of the prostate, bordering the urethra. Typical fiber positioning is schematically illustrated in Fig. 3. In addition, this figure also indicates sampling volumes by displaying[48] PHDs.

Since the instrumentation used in this study supports only one source and one detector fiber at a time, three sequential measurements must be performed. The total data acquisition time was approximately 3 min per patient (1 min per tissue volume). To detect unexpected changes during data acquisition, measurements were performed in 1 s increments. After

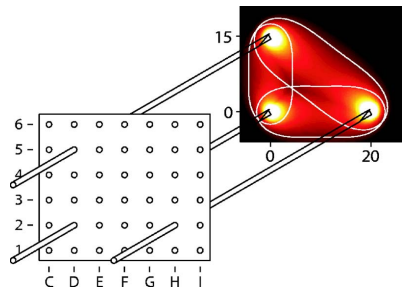

Fig. 3 Schematic drawing of fiber positioning [compare with Fig. 2(a)]. The needle template has 5-mm grid spacing. Three optical fibers are inserted to the same depth. Fiber separations are 15, 20, and 25 mm. The three tissue volumes being probed are indicated using calculations of photon-hitting densities (PHDs) at the plane of fiber tips (μ_s'=8.7 and μ_a=0.49 cm^{-1}). Isocurves indicate where the PHD is 50% of the value exhibited halfway between source- and detector fibers.

completion of the tissue measurements, the IRF is measured using the same set of fibers. To ensure system stability (e.g., avoid drifts due to temperature changes), this step is conducted while the system is in the operating theater.

3 Results

Analysis of collected data reveals that time-resolved spectroscopy can provide consistent optical and physiological characteristics of human prostate tissue. Data were collected at four wavelengths: 660, 786, 916, and 974 nm. For each patient and wavelength, raw data consist of three dispersion curves (tissue response) corresponding to the three utilized fiber separations (in total, 27 time-resolved data sets from nine patients). Since the fiber separations within a patient are chosen to be different, e.g., 15, 20, and 25 mm, the obtained curves are significantly different. For the range of fiber separations used in this study, most detected light travels a time less than 1.5 ns through tissue (corresponding to maximum path lengths of about 30 cm). An example of raw data, for the case of 660 nm, is given in Fig. 4.

By means of curve fitting, optical properties were extracted for 660, 786, and 916 nm from all 27 time-resolved data sets. Unfortunately, high absorption at 974 nm prevented analysis of data acquired at that wavelength. A typical fitting example, for the case of 786 nm, is shown in Fig. 5.

A summary of the results of this study is given in Table 2, in which previously published data are presented for comparison. A detailed report on measured optical (at 660 and 786 nm) and physiological characteristics are given in Table 3. In the following, graphical representation of data from Table 3 is used to illustrate and support further analysis.

No pronounced correlation between estimated values of μ_a and μ_s' was seen for any wavelength, implying that results do not suffer from μ_s' to μ_a crosstalk. This is shown in Fig. 6, where results from 660 nm are presented. A general comment is, however, helpful in interpreting the pattern shown. Three measurements (21.5 and 26.4 mm from patient 6, and 25.0 mm from patient 8) resulted in very low values of both

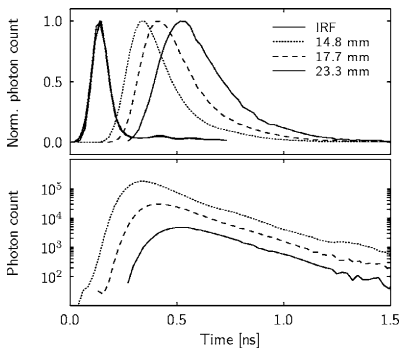

Fig. 4 Acquired time-resolved data at 660 nm for patient 5 (after background subtraction). Data are shown in both linear (upper axes, normalized) and logarithmic scale (lower axes). Corresponding 660-nm IRFs are also shown. Input laser pulses are broadened from 90 ps (IRF) to 222 (14.8), 264 (17.7), and 291 ps (23.3 mm).

absorption and reduced scattering (leading to a THC less than 100 μM). In these cases, note that an extremely low degree of bleeding was noted during the measurements (almost no blood stains on the used fibers, while the average fiber was heavily stained after a measurement). Thus, it is likely that these measurement outcomes correspond to a particular tissue composition, rather than a systematic error such as μ_s' to μ_a crosstalk.

The influence of fiber separation on derived optical properties is illustrated in Fig. 7. Although derived optical properties show no strict dependence on the fiber separation, there might be a tendency toward measuring lower μ_a and μ_s' for large fiber separations. Such a tendency may be related to the fact that the longest fiber separation (for each patient) corresponds to a central prostate volume, while the two shorter correspond to outer volumes. For comparison, note that studies on intralipid phantoms having prostate-like optical properties were performed. In these, the selection of fiber separation had no systematic influence on derived optical properties.

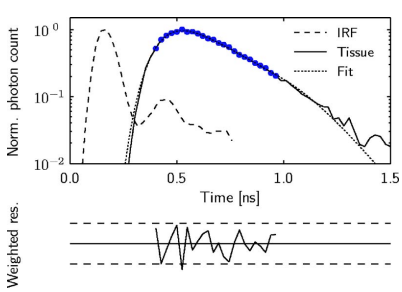

Fig. 5 Fitting of 786-nm time-resolved data from patient 4 (26.5-mm fiber separation). Dispersion data used in fitting are marked by solid dots. Weighted residuals are shown below, together with the zero level (solid line) and the [−1.96,1.96] prediction interval of standardized normal distributions (dashed lines).

As we can see in Fig. 8, derived hemoglobin concentrations show a behavior similar to that of μ_a, while oxygen saturation showed no correlation to utilized fiber separation.

Turning to inter- and intrapatient variations, an important general observation is that patients 2 to 5 exhibited homogenous ultrasound images, while obvious inhomogeneities due to calcifications are found in images from patients 1 and 6 to 9. As we can see in Figs. 9–11, this fact correlates to measured intrasubject variations. A second general observation is that all derived parameters, except oxygen saturation, can be subject to a fairly large spread, even within individual patients. Figure 9 presents inter- and intrapatient variations of 660-nm optical properties.

Effective attenuation, being an important parameter in PDT dosimetry, was calculated from extracted μ_a and μ_s' and is presented in Fig. 10.

Hemoglobin concentrations and oxygen saturation were spectroscopically determined using absorption coefficients as measured at 660 and 786 nm. As we can see in Fig. 11, THC exhibit substantial inter- and intrasubject variations. Oxygen saturation, on the other hand, displays only minor variations.

One alternative to deriving hemoglobin concentrations from 660- and 786-nm data only, would be to include 916-nm data (still assuming that the prostate contains 70% water and 10% lipids). If this procedure is followed, resulting THC values deviate by +1.5±8.7%, and S_tO_2 by +1.1±4.1% from the values calculated from 660- and 786-nm data only. In terms of overall impact, derived THC changes from 215±65 to 215±56 μM (the rounded average is coincidentally conserved), and S_tO_2 from 76±4 to 77±4%. These fairly small changes can also be understood by analyzing the difference between measured 916-nm μ_a, and the predicted 916-nm μ_a, as calculated from derived hemoglobin levels (estimated from 660- and 786-nm data) in combination with the assumption of 70% water and 10% lipids. Such analysis show that measured 916-nm μ_a deviates by 2±11% from predicted values.

A synthetic absorption spectra can be constructed using derived hemoglobin concentrations and assumed concentrations of water and lipids. Figure 12 presents the average composite absorption spectra of the prostate, as derived in this study.

4 Discussion

Reliable optical dosimetry is an important issue in the development of PDT into a modality for treatment of prostate can-

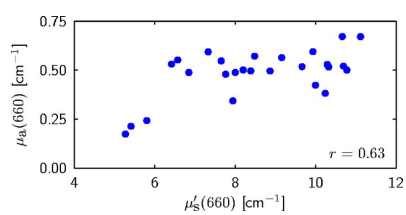

Fig. 6 Scatterplot showing correlation between derived μ_s' and μ_a at 660 nm. The three points in the lower left correspond to the three measurement cases exhibiting a low degree of bleeding and low THC (r=0.31 if disregarded).

Table 2 Optical properties (given in inverse centimeters) of human prostate tissue as reported in various published studies; the number of involved patients is also given (*N*); note differences regarding wavelength.

Study	Description	λ (nm)	*N*	μ_a	μ_s'	μ_{eff}
Pantelides et al.[24] (1990)	*ex vivo* steady state data, normal whole prostates	633	3	0.7±0.2	8.6±0.5	4.3±0.5
Whitehurst et al.[26] (1994)	*in vivo* steady state data, untreated BPH and PC	633	11			3.6±0.2
Lee et al.[28] (1995)	*in vivo* steady state data, untreated BPH and PC	633	11			3.9±0.5
Lee et al.[28] (1995)	*in vivo* steady state data, untreated BPH and PC	665	11			3.2±0.5
Lee et al.[29] (1999)	*in vivo* steady state data, untreated PC	630	7			3.5±0.7
This study	*in vivo* time-resolved data, untreated PC	660	9	0.5±0.1	8.7±1.9	3.6±0.8
Weersink et al.[30] (2005)	*in vivo* steady state data, recurrent PC	762	22	0.4±0.2	3.4±1.6	2.0±0.6
Zhu et al.[34] (2005)	*in vivo* steady state data, recurrent PC	732	13	0.4±0.2	11.8±8.2	3.3±0.5
This study	*in vivo* time-resolved data, untreated PC	786	9	0.4±0.1	7.1±1.6	2.9±0.7
This study	*in vivo* time-resolved data, untreated PC	916	9	0.6±0.1	7.7±1.8	3.8±0.8
Essenpreis et al.[25] (1992)	*ex vivo* integrating sphere data, normal prostates	1064		1.5±0.2	6.4	

cer. Whether reliable dosimetry means on-line monitoring of certain parameters, individual pretreatment planning, or general knowledge on intra- and intersubject variations remains an open question. By employing time-resolved spectroscopy, this study was able to generate estimations of optical and physiological characteristics (μ_a, μ_s', μ_{eff}, total hemoglobin concentration, and oxygen saturation) for all involved patients, and thus providing a reliable indication on intra- and intersubject variations for the case of untreated prostate cancer. In fact, as we can see in Table 3, all measurements resulted in quality data. In addition, by requiring only two fixed fibers for a single measurement, the time-resolved technique is accompanied with fairly simple clinical procedures.

Calculations of PHDs suggest that sampling volumes are kept within the prostate. Results are consistent and imply that the prostates of the patient group under consideration exhibit moderate intra- and intersubject variations. However, the fol-

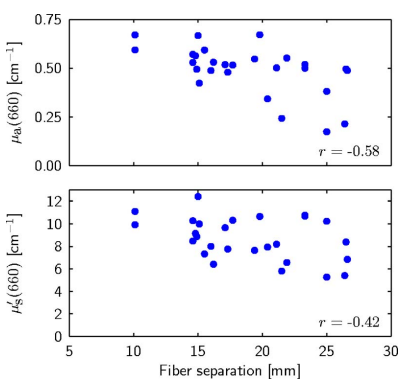

Fig. 7 Scatterplot showing the correlation between utilized fiber separation and derived optical properties at 660 nm. Correlation coefficients *r* are added for reference. The three points with $\mu_a < 0.25$ correspond to the three measurement cases exhibiting a low degree of bleeding and low THC.

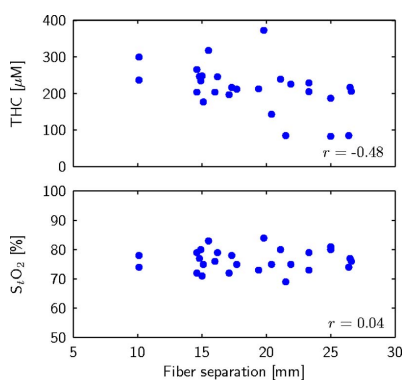

Fig. 8 Scatterplot showing the correlation between utilized fiber separation and THC and S_tO_2, respectively. Correlation coefficients *r* are added for reference.

Table 3 Detailed report on optical and physiological characteristics of human prostate tissue *in vivo*, as measured by our time-resolved instrumentation; prostate volumes (V) are determined from ultrasound images.

				Optical properties (cm^{-1})				Physiological properties	
Patient	Age (yr)	V (cm^3)	Fiber sep. (mm)	$\mu_a(660)$	$\mu_s'(660)$	$\mu_a(786)$	$\mu_s'(786)$	THC (μM)	S_tO_2 (%)
1	57	41	10.1	0.67	11.1	0.56	9.1	300	78
			14.9	0.50	8.9	0.44	6.7	235	80
			17.3	0.48	7.8	0.41	6.6	217	78
2	69	23	10.1	0.59	9.9	0.45	8.6	237	74
			15.1	0.42	10.0	0.34	8.5	177	75
			17.1	0.52	9.7	0.38	7.2	197	72
3	58	26	14.6	0.53	10.3	0.39	8.3	204	72
			21.9	0.55	6.6	0.43	4.7	226	75
			26.6	0.49	6.8	0.39	5.4	206	76
4	70	40	14.6	0.57	8.5	0.50	7.0	266	79
			21.1	0.50	8.2	0.45	6.5	239	80
			26.5	0.50	8.4	0.41	6.4	217	77
5	70	33	14.8	0.56	9.2	0.47	7.4	247	77
			17.7	0.52	10.3	0.40	8.3	212	75
			23.3	0.52	10.7	0.39	8.3	205	73
6	69	36	16.0	0.49	8.0	0.39	6.7	204	76
			21.5	0.24	5.8	0.17	4.6	85	69
			26.4	0.21	5.4	0.17	4.6	85	74
7	67	24	15.5	0.59	7.3	0.59	6.4	318	83
			19.8	0.67	10.6	0.68	10.0	373	84
			23.3	0.50	10.8	0.43	8.9	229	79
8	68	31	16.2	0.53	6.4	0.46	6.0	246	79
			20.4	0.34	7.9	0.28	6.4	143	75
			25.0	0.17	5.3	0.17	4.5	83	80
9	63	26	15.0	0.67	12.4	0.47	10.1	248	71
			19.4	0.55	7.7	0.41	6.5	213	73
			25.0	0.38	10.2	0.35	9.3	187	81
Average	66	31	19	0.49	8.7	0.41	7.1	215	76
Standard deviation	5	7	5	0.13	1.9	0.12	1.6	65	4

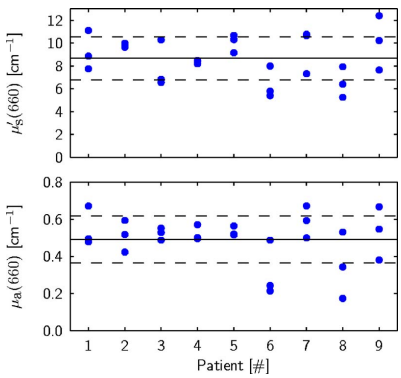

Fig. 9 Inter- and intrapatient variations in 660-nm optical properties. Patients 2 to 5 exhibited homogenous ultrasound images. Solid lines marks the average values, and dashed lines correspond to ± one standard deviation.

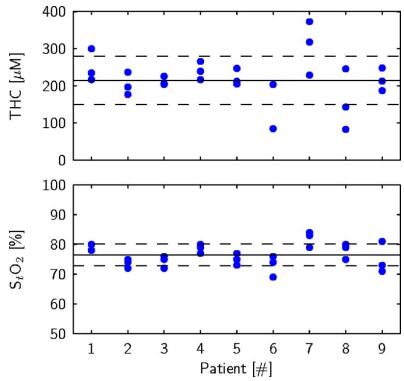

Fig. 11 Inter- and intrapatient variations in hemoglobin parameters. Patients 2 to 5 exhibited homogenous ultrasound images. Solid lines mark the average values, and dashed lines correspond to ± one standard deviation.

lowing observation calls for a separate discussion: derived μ_s' at 916 nm exceeds those at 786 nm in 23 out of 27 measurements. According to the general theory of tissue optics, a reduction of μ_s' is expected. Such behavior was only seen in 4 out of 27 measurements (three out of nine patients). The explanation is very likely to be related to the high absorption and low scattering at 916 nm. In fact, analysis of Monte Carlo simulations indicates a breakdown of diffusion approximation in this regime. Derived μ_s' is closely related to the rising flank of the dispersion curve (early photons), and may be particularly sensitive. Another aggravating circumstance is that such optical properties yield a low degree of broadening (and thus fewer data points), which in turn reduces the performance of the fitting procedure. Refined data evaluation may solve this problem, one option being implementation of Monte-Carlo-based evaluation.

When comparing our results to previously published data, two important facts must be noted. First, differences in patient groups must be taken into account (e.g., untreated or recurrent prostate cancer). The prostate physiology changes drastically upon radiation therapy. An experienced physician can feel such differences during the insertion of brachytherapy needles. Second, previous studies of prostate tissue have employed steady state techniques. Note that the ambiguous appearance of published steady state μ_s' data may indicate a difficulty in separating absorption and scattering using steady-state techniques (cf the published values of μ_s' stated in Table 2). Unfortunately, differences in patient groups prevent these results from being compared to the results of this study. It would thus be very interesting to employ time-resolved spectroscopy also in cases of locally recurrent prostate cancer. On the other hand, in the 600-nm range, μ_{eff} were measured using steady state techniques in patient groups similar to ours. In this respect, the two techniques seem to produce similar data (most derived μ_{eff} values are between 3 and 4 cm^{-1}).

To discuss the correctness of our approach, a few general remarks are given in the following. First, the model used in this study is valid for photon fluence rates. Detected light is collected by cleaved optical fibers, and is thus not a direct measure of fluence rate. Since data evaluation considers only temporal shapes, this fact is, however, not a source of error if the proportionality constant between actual fluence rate and collected light is the same for all photon times of flight. Moreover, the model applies for homogenous media. The prostate

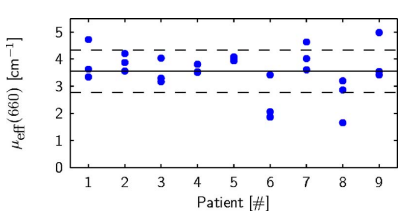

Fig. 10 Inter- and intrapatient variations in 660-nm effective attenuation. Patients 2 to 5 exhibited homogenous ultrasound images. The solid line mark the average value, and dashed lines correspond to ± one standard deviation.

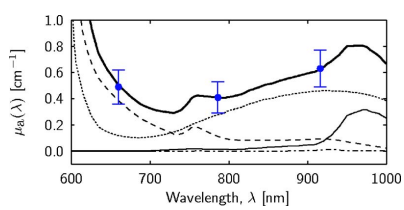

Fig. 12 Synthetic average absorption spectra (bold solid) together with derived absorption coefficients at 660, 786, and 916 nm (mean ± standard deviation). It is constructed using 215 μM THC at 76% oxygen saturation, 70% water and 10% lipids. Contribution spectra are also shown: 51.6-μM Hb (dashed), 163.4-μM HbO_2 (dotted), 70% water (solid), and 10% lipid (dash-dotted).

is, of course, heterogenous, and out of all detected photons, those that have traveled through regions of low attenuation will be overrepresented. One should therefore be careful in interpreting the derived values as true volume averages.

Second, the choice of data range involved in curve fitting occasionally has an influence on the outcome. Finding an optimal fitting range is, however, a complex issue, since the correctness of our model varies with the photon time of flight. For example, early photons are often disregarded since diffusion theory does not describe them very well. In this study, we focus on regions with fairly high photon count rates by choosing to cut the tail of late photons at 20% of maximum (see Sec. 2.2). The reason why later photons are excluded is to avoid a region with many data points at a low signal level, where even small absolute systematic measurement/model errors will have a significant impact on fitted parameters.

Third, as we can see in Eq. (3), the fiber separation is an important parameter in time-resolved spectroscopy. The inferring of fiber separations from ultrasound images is, of course, afflicted with some errors. However, it is unlikely that the error between true and measured separation, r_{true} and r_{meas}, respectively, exceeds 1 mm. From Eq. (3), one finds that errors in fiber separation will produce errors only in derived reduced scattering coefficients. The optimal fit is expected when μ_s' is selected so that

$$\mu_s' r_{\text{meas}}^2 = \mu_s'(r_{\text{true}} + \delta r)^2 = \mu_{s,\text{true}}' r_{\text{true}}^2, \tag{6}$$

where $\mu_{s,\text{true}}'$ is the true reduced scattering coefficient, and δr is the error in fiber separation. The impact of uncertainties regarding fiber separation can be described by the tuning coefficient

$$\gamma_r = \left.\frac{\partial \mu_s'}{\partial \delta r}\right|_{\delta r=0} = \frac{-2\mu_{s,\text{true}}'}{r_{\text{true}}}, \tag{7}$$

which states the change in derived reduced scattering coefficients due to (small) errors in fiber separation. For the case of $\mu_{s,\text{true}}'=8.7\ \text{cm}^{-1}$ and $r_{\text{true}}=20$ mm, one finds that $\gamma_r = 0.87\ \text{cm}^{-1}/\text{mm}$. Hence, a nonnegligible part of the intrasubject variations in derived reduced scattering coefficients may be assigned to errors in fiber separation. However, correlation with ultrasound heterogeneity and the large variations measured in some patients imply that there are significant inherent intrasubject variations.

Finally, the time-resolved approach, in contrast to steady state techniques, should be rather insensitive to bleedings around the needle tips. These bleedings can be thought of as random filters, and may therefore disturb measurements of fluence rate. However, all detected photons must pass the region of bleeding, leaving the temporal shape unchanged.

5 Summary

This study clearly shows that time-resolved spectroscopy is a suitable tool for accessing information on human prostate tissue *in vivo*. By producing consistent estimations of absorption (μ_a), reduced scattering (μ_s'), effective attenuation (μ_{eff}), hemoglobin concentrations, and tissue oxygenation, this technique was able to generate the most complete *in vivo* optical characterization of human prostate tissue published so far. By measuring across three tissue volumes in each prostate, both inter- and intrasubject variations were examined. All derived parameters, with the exception of tissue oxygen saturation, are subject to fairly large intrasubject variation. Interestingly, these variations correlate with the heterogeneity exhibited by acquired ultrasound images.

Acknowledgments

The authors wish to thank the brachytherapy team at the Lund University Hospital, especially Ola Bratt, Inger-Lena Lamm, Per Munck af Rosenschöld, Jonas Nilsson, and Pia Nilsson, for friendly and professional cooperation. We are also grateful to Christoffer Abrahamsson, Ann Johansson, and Johannes Swartling for fruitful discussions, as well as to Johan Stensson for technical assistance during measurements.

References

1. M. S. McPhee, C. W. Thorndyke, G. Thomas, J. Tulip, D. Chapman, and W. H. Lakey, "Interstitial applications of laser irradiation in hematoporphyrin derivative-photosensitized dunning r3327 prostate cancers, *Lasers Surg. Med.* **4**(1), 93–98 (1984).
2. J. L. Camps, S. K. Powers, W. C. Beckman, J. T. Brown, and R. M. Weissman, "Photodynamic therapy of prostate-cancer: an in vitro study," *J. Urol. (Baltimore)* **134**(6), 1222–1226 (1985).
3. T. Windahl, S. O. Andersson, and L. Lofgren, "Photodynamic therapy of localized prostatic cancer," *Langmuir* **336**(8723), 1139–1139 (1990).
4. L. K. Lee, C. Whitehurst, Q. Chen, M. L. Pantelides, F. W. Hetzel, and J. V. Moore, "Interstitial photodynamic therapy in the canine prostate," *Br. J. Urol.* **80**(6), 898–902 (1997).
5. Q. Chen, Z. Huang, D. Luck, J. Beckers, P. H. Brun, B. C. Wilson, A. Scherz, Y. Salomon, and F. W. Hetzel, "Preclinical studies in normal canine prostate of a novel palladium-bacteriopheophorbide (WST09) photosensitizer for photodynamic therapy of prostate cancer," *Photochem. Photobiol.* **76**(4), 438–445 (2002).
6. R. Sroka, D. Zaak, M. Hoppner, R. Muschter, R. Knuchel, A. Perlmutter, and A. Hofstetter, "*In vivo* investigations of photodynamic therapy by means of 5-ALA induced PPIX on canine prostates," *Med. Laser Appl.* **18**(1), 87–90 (1992).
7. D. Zaak, R. Sroka, et al., "Photodynamic therapy of prostate cancer by means of 5-aminolevulinic acid-induced protoporphyrin IX—*in vivo* experiments on the dunning rat tumor model," *Urol. Int.* **72**(3), 196–202 (2004).
8. A. M. Ronn, M. Nouri, L. A. Lofgren, B. M. Steinberg, A. Westerborn, T. Windahl, M. J. Shikowitz, and A. L. Abramson, "Human tissue levels and plasma pharmacokinetics of temoporfin (Foscan(R), mTHPC)," *Lasers Med. Sci.* **11**(4), 267–272 (1996).
9. D. Zaak, R. Sroka, M. Hoppner, W. Khoder, O. Reich, S. Tritschler, R. Muschter, R. Knuchel, and A. Hofstetter, "Photodynamic therapy by means of 5-ALA induced PPIX in human prostate cancer—preliminary results," *Med. Laser Appl.* **18**(1), 91–95 (2003).
10. T. Nathan, D. Whitelaw, et al., "Photodynamic therapy for prostate cancer recurrence after radiotherapy: a phase I study," *J. Urol. (Baltimore)* **168**(4), 1427–1432 (2002).
11. K. Verigos, D. C. H. Stripp, et al., "Updated results of a phase I trial of motexafin lutetium-mediated interstitial photodynamic therapy in patients with locally recurrent prostate cancer," *J. Environ. Pathol. Toxicol. Oncol.* **25**(1–2), 373–387 (2006).
12. K. L. Du, R. Mick, et al., "Preliminary results of interstitial motexafin lutetium-mediated PDT for prostate cancer," *Lasers Surg. Med.* **38**(5), 427–434 (2006).
13. C. M. Moore, T. R. Nathan, W. R. Lees, C. A. Mosse, A. Freeman, M. Emberton, and S. G. Bown, "Photodynamic therapy using meso tetra hydroxy phenyl chlorin (mTHPC) in early prostate cancer," *Lasers Surg. Med.* **38**(5), 356–363 (2006).
14. C. M. Moore, I. M. Hoh, S. G. Bown, and M. Emberton, "Does photodynamic therapy have the necessary attributes to become a future treatment for organ-confined prostate cancer?" *BJU Int.*, **96**(6), 754–758 (2005).

15. J. H. Pinthus, A. Bogaards, R. Weersink, B. C. Wilson, and J. Trachtenberg, "Photodynamic therapy for urological malignancies: past to current approaches," *J. Urol. (Baltimore)* **175**(4), 1201–1207 (2006).
16. W. M. Star, "Light dosimetry *in vivo*," *Phys. Med. Biol.* **42**(5), 763–787 (1997).
17. C. Whitehurst, M. L. Pantelides, J. V. Moore, and N. J. Blacklock, "Optimization of multifiber light delivery for the photodynamic therapy of localized prostate-cancer," *Photochem. Photobiol.* **58**(4), 589–593 (1993).
18. Q. Chen and F. Hetzel, "Laser dosimetry studies in the prostate," *J. Clin. Laser Med. Surg.* **16**(1), 9–12 (1998).
19. L. Lilge, N. Pomerleau-Dalcourt, A. Douplik, S. Selman, R. Keck, M. Szkudlarek, M. Pestka, and J. Jankun, "Transperineal *in vivo* fluence-rate dosimetry in the canine prostate during SnET2-mediated PDT," *Phys. Med. Biol.* **49**(14), 3209–3225 (2004).
20. M. D. Altschuler, T. C. Zhu, J. Li, and S. M. Hahn, "Optimized interstitial PDT prostate treatment planning with the Cimmino feasibility algorithm," *Med. Phys.* **32**(12), 3524–3536 (2005).
21. J. Jankun, R. W. Keck, E. Skrzypczak-Jankun, L. Lilge, and S. H. Selman, "Diverse optical characteristic of the prostate and light delivery system: implications for computer modelling of prostatic photodynamic therapy," *BJU Int.* **95**(9), 1237–1244 (2005).
22. J. Jankun, L. Lilge, A. Douplik, R. W. Keck, M. Pestka, M. Szkudlarek, P. J. Stevens, R. J. Lee, and S. H. Selman, "Optical characteristics of the canine prostate at 665 nm sensitized with tin etiopurpurin dichloride: need for real-time monitoring of photodynamic therapy," *J. Urol. (Baltimore)* **172**(2), 739–743 (2004).
23. A. Johansson, T. Johansson, M. Soto Thompson, N. Bendsoe, K. Svanberg, S. Svanberg, and S. Andersson-Engels, "*In vivo* measurement of parameters of dosimetric importance during photodynamic therapy of thick skin tumors," *J. Biomed. Opt.* **11**(3), 034029 (2006).
24. M. L. Pantelides, C. Whitehurst, J. V. Moore, T. A. King, and N. J. Blacklock, "Photodynamic therapy for localized prostatic cancer—light penetration in the human prostate-gland," *J. Urol. (Baltimore)* **143**(2), 398–401 (1990).
25. M. Essenpreis, "Thermally induced changes in optical properties of biological tissues," Ph.D. Thesis, University College London (1992).
26. C. Whitehurst, M. L. Pantelides, J. V. Moore, P. J. C. Brooman, and N. J. Blacklock, "*In vivo* laser-light distribution in human prostatic-carcinoma," *J. Urol. (Baltimore)* **151**(5), 1411–1415 (1994).
27. Q. Chen, B. C. Wilson, S. D. Shetty, M. S. Patterson, J. C. Cerny, and F. W. Hetzel, "Changes in *in vivo* optical properties and light distributions in normal canine prostate during photodynamic therapy," *Radiat. Res.* **147**(1), 86–91 (1997).
28. L. K. Lee, C. Whitehurst, M. L. Pantelides, and J. V. Moore, "*In situ* comparison of 665 nm and 633 nm wavelength light penetration in the human prostate gland," *Photochem. Photobiol.* **62**(5), 882–886 (1995).
29. L. K. Lee, C. Whitehurst, M. L. Pantelides, and J. V. Moore, "An interstitial light assembly for photodynamic therapy in prostatic carcinoma," *BJU Int.* **84**(7), 821–826 (1999).
30. R. A. Weersink, A. Bogaards, M. Gertner, S. R. H. Davidson, K. Zhang, G. Netchev, J. Trachtenberg, and B. C. Wilson, "Techniques for delivery and monitoring of TOOKAD (WST09)-mediated photodynamic therapy of the prostate: clinical experience and practicalities," *J. Photochem. Photobiol., B* **79**(3), 211–222 (2005).
31. T. C. Zhu, J. C. Finlay, and S. M. Hahn, "Determination of the distribution of light, optical properties, drug concentration, and tissue oxygenation *in vivo* in human prostate during motexafin lutetium-mediated photodynamic therapy," *J. Photochem. Photobiol., B* **79**(3), 231–241 (2005).
32. D. R. Doiron, L. O. Svaasand, and A. E. Profio, "Light dosimetry in tissue: application to photoradiation therapy," *Appl. Spectrosc.* **160**, 63–76 (1983).
33. A. Dimofte, J. C. Finlay, and T. C. Zhu, "A method for determination of the absorption and scattering properties interstitially in turbid media," *Phys. Med. Biol.* **50**(10), 2291–2311 (2005).
34. T. C. Zhu, A. Dimofte, J. C. Finlay, D. Stripp, T. Busch, J. Miles, R. Whittington, S. B. Malkowicz, Z. Tochner, E. Glatstein, and S. M. Hahn, "Optical properties of human prostate at 732 nm measured during motexafin lutetium-mediated photodynamic therapy, *Photochem. Photobiol.* **81**(1), 96–105 (2005).
35. A. H. Barnett, J. P. Culver, A. G. Sorensen, A. Dale, and D. A. Boas, "Robust inference of baseline optical properties of the human head with three-dimensional segmentation from magnetic resonance imaging," *Appl. Opt.* **42**(16), 3095–3108 (2003).
36. C. Abrahamsson, A. Löwgren, B. Strömdahl, T. Svensson, S. Andersson-Engels, J. Johansson, and S. Folestad, "Scatter correction of transmission near-infrared spectra by photon migration data: quantitative analysis of solids," *Appl. Spectrosc.* **59**(11), 1381–1387 (2005).
37. P. Taroni, A. Torricelli, L. Spinelli, A. Pifferi, F. Arpaia, G. Danesini, and R. Cubeddu, "Time-resolved optical mammography between 637 and 985 nm: clinical study on the detection and identification of breast lesions," *Phys. Med. Biol.* **50**(11), 2469–2488 (2005).
38. Y. Hoshi, M. Shimada, C. Sato, and Y. Iguchi, "Reevaluation of near-infrared light propagation in the adult human head: implications for functional near-infrared spectroscopy," *J. Biomed. Opt.* **10**(6), 064032 (2005).
39. T. Svensson, J. Swartling, P. Taroni, A. Torricelli, P. Lindblom, C. Ingvar, and S. Andersson-Engels, "Characterization of normal breast tissue heterogeneity using time-resolved near-infrared spectroscopy," *Phys. Med. Biol.* **50**(11), 2559–2571 (2005).
40. A. Pifferi, A. Torricelli, A. Bassi, P. Taroni, R. Cubeddu, H. Wabnitz, D. Grosenick, M. Moller, R. Macdonald, J. Swartling, T. Svensson, S. Andersson-Engels, R. L. P. van Veen, H. J. C. M. Sterenborg, J. M. Tualle, H. L. Nghiem, S. Avrillier, M. Whelan, and H. Stamm, "Performance assessment of photon migration instruments: the MEDPHOT protocol," *Appl. Opt.* **44**(11), 2104–2114 (2005).
41. M. S. Patterson, B. Chance, and B. C. Wilson, "Time resolved reflectance and transmittance for the noninvasive measurement of tissue optical-properties," *Appl. Opt.* **28**(12), 2331–2336 (1989).
42. T. Nakai, G. Nishimura, K. Yamamoto, and M. Tamura, "Expression of optical diffusion coefficient in high-absorption turbid media," *Phys. Med. Biol.* **42**(12), 2541–2549 (1997).
43. T. Durduran, A. G. Yodh, B. Chance, and D. A. Boas, "Does the photon-diffusion coefficient depend on absorption?" *J. Opt. Soc. Am. A* **14**(12), 3358–3365 (1997).
44. W. Press, S. Teukolsky, W. Vetterling, and B. Flannery, *Numerical Recipes in C: The Art of Scientific Computing*, 2nd ed., Cambridge University Press, Cambridge (1992).
45. G. M. Hale and M. R. Querry, "Optical-constants of water in 200-nm to 200-mum wavelength region," *Appl. Opt.* **12**(3), 555–563 (1973).
46. R. L. P. van Veen, H. J. C. M. Sterenborg, A. Pifferi, A. Torricelli, E. Chikoidze, and R. Cubeddu, "Determination of visible near-IR absorption coefficients of mammalian fat using time- and spatially resolved diffuse reflectance and transmission spectroscopy," *J. Biomed. Opt.* **10**(5), 054004 (2005).
47. S. Prahl, "Optical absorption of hemoglobin," URL http://omlc.ogi.edu/spectra/hemoglobin/index.html(2006).
48. J. C. Schotland, J. C. Haselgrove, and J. S. Leigh, "Photon hitting density," *Appl. Opt.* **32**(4), 448–453 (1993).

Paper VII

Noninvasive characterization of pharmaceutical solids by diode laser oxygen spectroscopy

T. Svensson, L. Persson, M. Andersson, S. Svanberg,
S. Andersson-Engels, J. Johansson, and S. Folestad.

Applied Spectroscopy **61**, 784-786 (2007).

Noninvasive Characterization of Pharmaceutical Solids by Diode Laser Oxygen Spectroscopy

TOMAS SVENSSON,* LINDA PERSSON, MATS ANDERSSON, SUNE SVANBERG, STEFAN ANDERSSON-ENGELS, JONAS JOHANSSON, and STAFFAN FOLESTAD

Department of Physics, Lund University, Sweden (T.S., L.P., M.A., S.S., S.A.-E.); and Astra Zeneca R&D, Mölndal, Sweden

Index Headings: **Oxygen spectroscopy; Light scattering; Porosity.**

INTRODUCTION

Characterization of solid pharmaceuticals, ranging from monitoring of solid-state reactions to understanding tablet dissolution, is of great interest for pharmaceutical science.[1] The quality of the finished product highly depends on knowledge about the pharmaceutical materials used and the different unit operations involved in manufacturing of pharmaceuticals. Thus, availability of appropriate and reliable tools for measurements of physical and chemical properties of drug materials *in situ* during chemical and physical processing is a key for optimized processing. In early stages of pharmaceutical development a whole range of techniques for characterization of the solid state is available, addressing, for example, particle size and shape, density, porosity, calorimetry, thermo-mechanical properties, specific area, and crystallinity.[2] However, most of these techniques are slow and not well suited for fast laboratory-based or process applications. Process analytical technology (PAT) is a term describing a holistic approach to pharmaceutical manufacturing based on in-depth understanding through advanced process sensors and modeling tools.[3] In order to succeed with this, new tools are needed, e.g., with capability to directly measure physico-chemical attributes *in situ* of the mechanical process. In this context, tools based on spectroscopic techniques offer obvious advantages owing to their speed, compactness, versatility, and ability to perform noninvasive analysis.

By employing the spectroscopic technique referred to as gas in scattering media absorption spectroscopy (GASMAS), it is possible to extract information related to gas dispersed within highly scattering (turbid) materials.[4] In our case, the key is contrast between the sharp (GHz) absorption features of molecular oxygen located around 760 nm and the broad absorption features related to tablet bulk material. The technique is based on high-resolution diode laser absorption spectroscopy, and its main principle is illustrated in Fig. 1. Light is injected into a highly scattering sample, often utilizing optical fibers. The actual path length distribution of transmitted photons will depend on the scattering properties of the sample. Due to significant multiple scattering, the average photon path length greatly exceeds sample dimensions. For example, the average path length of photons that have traveled through a pharmaceutical tablet typically exceeds 10 cm.[5] During passages through air-filled pores, photons in resonance with an absorption line in the A-band of molecular oxygen can be absorbed. Oxygen absorption can be distinguished from bulk absorption due to the extremely narrow absorption features (GHz) exhibited by free gases. To resolve such narrow features, high-resolution spectroscopy must be employed. The resulting absorption signal depends on both the oxygen content and the scattering properties (photons path lengths) of the sample. Indirectly, it is thus related to mechanical properties such as porosity and particle size.

The GASMAS technique has previously been used to study the gas content in, for example, polystyrene foam, wheat flour, granulated salt, wood materials, fruit, and human sinuses.[4,6–9] Gas exchange dynamics has been studied by placing samples of wood and fruit in nitrogen atmospheres and monitoring the re-invasion of oxygen.[7,8]

In this paper we show the potential of using GASMAS for determination of physical and structural parameters of pharmaceutical solids. We present results from a study of pharmaceutical tablets made from two different sieve fractions (particle size distributions) and with different compression forces. In addition, the prospects of a broader use of this technique for pharmaceutical analysis are discussed.

EXPERIMENTAL

Instrumentation. A simplified schematic of the setup is given in Fig. 2. The instrumentation and corresponding data evaluation has been described in detail elsewhere.[10] Briefly, a temperature stabilized distributed feed-back (DFB) diode laser (NanoPlus, Germany) is repetitively wavelength tuned over one of the narrow absorption lines in the oxygen A-band (R11Q12, 760.445 nm vacuum wavelength). The DFB diode laser is pigtailed using a single-mode (SM) optical fiber, yielding an output of about 4 mW. Sensitivity was vastly increased by employing wavelength modulation spectroscopy (WMS), in this case implemented by imposing an $f = 9$ kHz harmonic modulation on the laser diode injection current. A 90/10% fiber splitter (Laser2000, Sweden) is used create a double-beam arrangement (reference and sample arm), allowing balanced detection. This maneuver is important in order to minimize the influence of optical interference fringes. The lower intensity optical fiber is immediately directed to a silicon photodiode (PIN-10DP/SB, UDT Sensors), producing a reference signal. The other fiber guides light to our sample (e.g., tablet).

Samples were placed in contact with a long-pass filter (Schott RG715), which in turn was placed directly on top of a photomultiplier tube (PMT, 5070A, Hamamatsu) detecting diffuse transmittance. The long-pass filter in combination with the PMT sensitivity fall-off effectively suppressed unwanted ambient light. Signals from the reference and sample detectors are sent to lock-in amplifiers detecting at the second harmonic ($2f$) of the modulation frequency f. The $2f$ signal is normalized

Received 17 January 2007; accepted 7 May 2007.
* Author to whom correspondence should be sent. E-mail: tomas.svensson@fysik.lth.se.

0003-7028/07/6107-000000$2.00/0

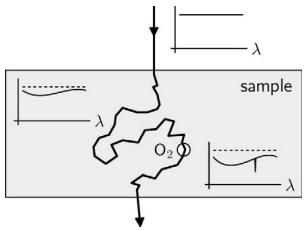

FIG. 1. The principle of GASMAS. The key is the contrast between the sharp absorption features of free gases (e.g., oxygen) and the broad absorption features related to bulk material. This is illustrated by the change in absorption spectra along a particular photon path. The gas absorption is typically much weaker than bulk absorption and is thus exaggerated in the graph.

using direct detector signals. Software-based balanced detection is employed to remove contributions originating from optical interference fringes. In addition, vibrators positioned close to the sample were used to further suppress such effects.

Data Evaluation. Acquired $2f$ signals are evaluated using curve fitting of an experimental long-path recording of the oxygen absorption feature. This recording was performed using the same setup as for tablet measurements. The oxygen imprint is measured in terms of mm of equivalent path length through air, L_{eq}. That is, if $L_{eq} = 10$ mm, the oxygen absorption exhibited by the turbid sample equals that of a 10 mm path length through ambient air. The absolute relation between the $2f$ signal and the equivalent path length is established experimentally by means of a standard addition calibration. In this particular case, the standard addition involves adding known path lengths of air to the sample arm. A detailed description of these procedures is found in a previous publication.[10]

Pharmaceutical Samples. Measurements were performed on 22 model tablets with microcrystalline cellulose as the main constituent, manufactured using a wet granulation process.[11] The influence of particle size distribution was studied by sieving the granulate, producing two different batches consisting of 11 tablets each (particle sizes: <150 μm and >400 μm). The tablets were compressed manually into various thicknesses (3–4 mm). The tablets were round, without score or engravings, and had a 10 mm diameter.

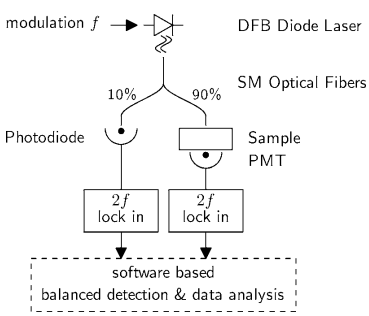

FIG. 2. Simplified schematic of the setup. A 90/10% optical fiber splitter is used to achieve the double-beam arrangement typical of applications requiring high sensitivity. Lock-in amplifiers detect at the second harmonic of the modulation frequency f. Software algorithms handle balanced detection and data evaluation.

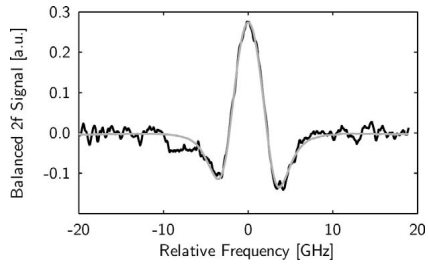

FIG. 3. Data obtained for a 3.38 mm thick tablet from PS > 400 μm. The $2f$ signal after balanced detection (black) is shown together with a fitted oxygen absorption signature (grey). The signal corresponds to an L_{eq} of 17.4 mm. The optical frequency is given relative to the oxygen absorption line (760.445 nm). The corresponding wavelength range is 760.41–760.48 nm, where the lower wavelength is to the right.

RESULTS

Examined tablets exhibited oxygen absorption corresponding to 5–50 mm propagation through ambient air. A typical example of the acquired $2f$ absorption signature is given in Fig. 3. To illustrate that obtained signals are related to oxygen absorption, additional nitrogen atmosphere experiments was performed. Tablets were then stored for several hours in plastic bags filled with nitrogen. When inserting them into the setup (while still in their plastic bags), obtained signals exhibited nothing but the ordinary 3 mm L_{eq} noise floor. When the plastic bags was opened and ventilated, the expected signal quickly appeared. This oxygen re-invasion could, however, not be temporally resolved.

The overall influence of tablet compression and particle size is shown in Fig. 4. Here, each tablet was measured four times consecutively, and the average derived L_{eq} is presented. The acquisition time was 25 s in each of the four measurements, and the standard deviation in these sets of four repetitions was on average 0.8 mm (<150 μm) and 1.0 mm (>400 μm). However, these measures of uncertainty do not include

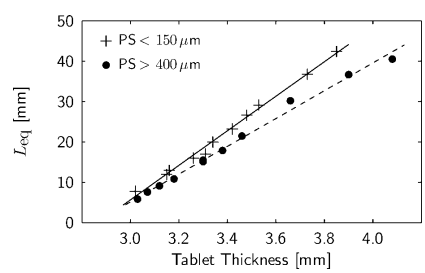

FIG. 4. Equivalent path length L_{eq} versus tablet thickness. Shown values are averages from four consecutive measurements. All tablets have the same weight (300 mg) and diameter (10 mm), but intentional variations in applied compression force yielded variations in tablet thickness.

systematic errors due to optical interference fringes that remain after balanced detection. The systematic errors due to such fringes can be estimated by looking at the amplitude of interference noise in spectral regions free from oxygen absorption (consider, for example, the 10–20 GHz range in Fig. 3). Furthermore, this noise was found to be stable between the four consecutive measurements. In the current configuration, optical noise remaining after balanced detection limits the accuracy to about 3 mm L_{eq}. This corresponds to an optical absorption fraction of 7.5×10^{-5}.

In the range of examined tablet thicknesses, there is a highly linear relation between tablet thickness and equivalent path length. It is also clear that in case of comparable thickness, tablets manufactured from the smaller granule particles ($<$150 μm) exhibited the largest oxygen absorption.

DISCUSSION

Our results clearly show that it is possible to detect oxygen dispersed within pharmaceutical tablets. Hence, a new tool is available for characterization of pharmaceutical solids. Using the GASMAS technique, parameters such as porosity and particle size may be determined in raw materials as well as finished tablets. This may in turn lead to a better optimization of pharmaceutical manufacturing processes. Required instrumentation involves standard components and is simple and fairly compact. Further development is expected to improve data quality.

The porosity of pharmaceutical tablets is normally estimated by employing mercury intrusion porosimetry.[12] This method has several limitations: it is a destructive technique, it includes hazardous handling of mercury, and it is not suitable for fast laboratory-based or on-line analysis. Furthermore, mercury porosimetry is only sensitive to open pores, while the presented technique is sensitive to all pores containing oxygen. It would thus be of interest to compare results from this technique with results from mercury porosimetry. Moreover, this will also provide opportunities for accessing functional properties such as tablet hardness. Preliminary data on such parameters has been shown before.[13,14]

In addition to the results reported here, we propose monitoring of gas diffusion dynamics. It would be attractive to study oxygen reinvasion in samples that have been placed in, for example, a pure nitrogen environment or a vacuum chamber. Such dynamic experiments have been successfully demonstrated in, for example, wood and fruit materials.[7,9] In addition, we propose GASMAS measurements on tablets in blister packages, allowing study of gas exchange through blister materials.

Although the oxygen absorption signal clearly correlates to relevant physical parameters, a detailed understanding of the interaction of near-infrared light with the turbid sample requires further studies. The signal is influenced by both oxygen concentration and photon path length, both being unknown quantities and adding to the total response. It would thus be of great interest to separate these effects in future research. Such a separation is possible by combining GASMAS with time- or frequency-domain photon migration techniques.[6] These techniques are frequently used in biomedical optics, but have also been applied to pharmaceutical solids.[5,15] More such work is forthcoming.

1. D. E. Bugay, Adv. Drug Delivery Rev. **48,** 43 (2001).
2. D. C. Lee and M. Webb, Eds., *Pharmaceutical Analysis* (Blackwell Publishing, Oxford, 2003), 1st ed.
3. J. Workman, M. Koch, and D. J. Veltcamp, Anal. Chem. **75,** 2859 (2003).
4. M. Sjöholm, G. Somesfalean, J. Alnis, S. Andersson-Engels, and S. Svanberg, Opt. Lett. **26,** 16 (2001).
5. J. Johansson, S. Folestad, M. Josefson, A. Sparén, C. Abrahamsson, S. Andersson-Engels, and S. Svanberg, Appl. Spectrosc. **56,** 725 (2002).
6. G. Somesfalean, M. Sjöholm, J. Alnis, C. af Klinteberg, S. Andersson-Engels, and S. Svanberg, Appl. Opt. **41,** 3538 (2002).
7. J. Alnis, B. Anderson, M. Sjöholm, G. Somesfalean, and S. Svanberg, Appl. Phys. B **77,** 691 (2003).
8. L. Persson, K. Svanberg, and S. Svanberg, Appl. Phys. B **82,** 313 (2006).
9. L. Persson, H. Gao, M. Sjöholm, and S. Svanberg, Opt. Laser. Eng. **44,** 687 (2006).
10. L. Persson, F. Andersson, M. Andersson, and S. Svanberg S, Appl. Phys. B DOI:10.1007/s00340-007-2593-y (2007).
11. A. Sparén, M. Malm, M. Josefson, S. Folestad, and J. Johansson, Appl. Spectrosc. **56,** 586 (2002).
12. J. M. Haynes and P. Rossi-Dori, Eds., *Principles and Applications of Pore Structural Characterization* (Arrowsmith, Bristol, 1985).
13. T. Svensson, J. Johansson, S. Andersson-Engels, S. Svanberg, and S. Folestad, "Non-invasive determination of porosity in solids by diode laser oxygen spectroscopy: application to pharmaceutical tablets", Poster \#562 at FACSS 2004 (Portland, OR, Oct 3–7, 2004).
14. J. Johansson, S. Folestad, S. Svanberg, M. Sjöholm, G. Somesfalean, C. Abrahamsson, and S. Andersson-Engels, "Method for analysing a pharmaceutical sample", international patent PCT no. WO 03/078983 (2003).
15. Z. G. Sun, S. Torrance, F. K. McNeil-Watson, and E. M. Sevick-Muraca, Anal. Chem. **75,** 1720 (2003).

Paper VIII

Non-intrusive optical study of gas and its exchange in human maxillary sinuses

L. Persson, M. Andersson, T. Svensson, M. Cassel-Engquist, K. Svanberg, and S. Svanberg.

Proc. of SPIE: Diagnostic Optical Spectroscopy in Biomedicine IV **6628**, 662804 (2007).

Non-intrusive optical study of gas and its exchange in human maxillary sinuses

L. Persson[a], M. Andersson[a], T. Svensson[a], M. Cassel-Engquist[a], K. Svanberg[b], and S. Svanberg[a]

[a]Division of Atomic Physics, Lund University, P.O. Box 118, SE-221 00 Lund, Sweden
[b]Department of Oncology, Lund University Hospital, SE-221 85 Lund, Sweden

ABSTRACT

We demonstrate a novel non-intrusive technique based on tunable diode laser absorption spectroscopy to investigate human maxillary sinuses *in vivo*. The technique relies on the fact that free gases have much sharper absorption features (typical a few GHz) than the surrounding tissue. Molecular oxygen was detected at 760 nm. Volunteers have been investigated by injecting near-infrared light fibre-optically in contact with the palate inside the mouth. The multiply scattered light was detected externally by a handheld probe on and around the cheek bone. A significant signal difference in oxygen imprint was observed when comparing volunteers with widely different anamnesis regarding maxillary sinus status. Control measurements through the hand and through the cheek below the cheekbone were also performed to investigate any possible oxygen offset in the setup. These provided a consistently non-detectable signal level. The passages between the nasal cavity and the maxillary sinuses were also non-intrusively optically studied, to the best of our knowledge for the first time. These measurements provide information on the channel conductivity which may prove useful in facial sinus diagnostics. The results suggest that a clinical trial together with an ear-nose-throat (ENT) clinic should be carried out to investigate the clinical use of the new technique.

Keywords: Diode lasers, Near infrared spectroscopy, Absorption, Molecular oxygen, Medicine, Human sinuses

1. INTRODUCTION

In addition to the mouth and nasal cavities, the human head comprises further air volumes, all connected to the nose and the epipharyngeal area by venting channels. The middle ear, the frontal and maxillary sinuses are such air-filled volumes that are all quite vulnerable to infection (conditions called otitis and sinusitis, respectively). The cavities may then be filled with swollen mucosa, mucus and pus, and treatment with antibiotics is frequently considered appropriate. Each sinus is connected by a channel with a mucous membrane lining to the nose for free exchange of air and mucus. Anything that causes a swelling in the nose such as an infection, an allergic reaction, or another type of immune reaction, can affect the sinuses. With any of these above mentioned conditions, these passages may be blocked. In view of the many million patients suffering from this type of infection, improved diagnostic tools, complementing or replacing ultra-sound and CT scans are desirable.[1–6]

Recently, we reported on a new technique for assessing the sinuses relying on the monitoring of the oxygen absorption at about 760 nm. The absorption features are more then a factor of 1000 sharper than the spectral signatures of the tissues. In the first study, a faint oxygen signal could be observed in a backscattering geometry for the frontal sinuses of a healthy volunteer.[7] We have now explored the technique in a transmission geometry probing the maxillary (cheek) sinuses by injection of light using fibre optics in contact with the palate, and detecting the diffusely scattered light emerging out through the cheek bone. Strong signal differences in oxygen imprint between two volunteers with widely different anamnesis regarding maxillary sinus status were observed. By improved handling of noise and detrimental interference fringes, we now obtained prominent signals, which also allowed a dynamic study of gas exchange through the venting channels. Sinus ventilation studies have previously been performed by radioactive tracer gases, such as Xe^{133}, in combination with single photon emission computed tomography (SPECT).[8] Another method attempted is to use stable xenon inhalation followed by computer tomography (CT).[9]

E-mail: linda.persson@fysik.lth.se

Diagnostic Optical Spectroscopy in Biomedicine IV, edited by Dietrich Schweitzer, Maryann Fitzmaurice,
Proc. of SPIE-OSA Biomedical Optics, SPIE Vol. 6628, 662804, © 2007 SPIE-OSA · 1605-7422/07/$18

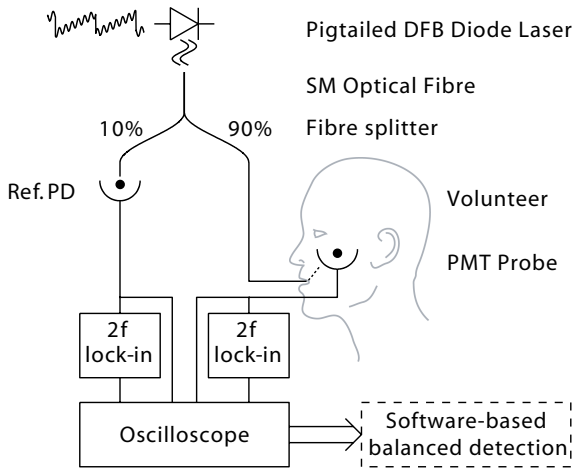

Figure 1. Schematic drawing of experimental arrangement for tunable diode laser gas absorption spectroscopy of oxygen probing the human maxillary sinuses.

In the following section the experimental setup, the data evaluation and the measurement procedure will be discussed. Results from two volunteers with widely different anamnesis regarding maxillary sinus status will then be shown. At the end conclusions of the presented work will be drawn. An outlook of future work will then be discussed.

2. MATERIAL AND METHOD

2.1. Experimental setup

A schematic drawing of the arrangement used in this study is shown in Fig. 1. The setup is based on a distributed feedback (DFB) diode laser that is single-mode (SM) fibre-pigtailed and thermoelectrically cooled (Nanoplus, Germany). The laser operates with an output power of about 4 mW. The light was scanned across the R11Q12 molecular oxygen absorption line at 760.445 nm (vacuum wavelength) by supplying a 4 Hz saw-tooth ramp to the laser driver current. A 9 kHz sinus-shaped wave was superimposed on the laser driver current in a wavelength modulation scheme to achieve sensitive detection.

The light from the fibre was split 90/10(%) with a single-mode fibre-coupled beamsplitter (Laser2000, Sweden) to allow balanced detection. The fibre carrying the lower intensity was directly guided to a photo diode, PD, (10DP/SB, OSI Optoelectronics), producing the reference signal. The other fibre part (90% of the intensity) was positioned on the palate inside the mouth. The light then travels through the tissue with a fraction part of it crossing the maxillary sinuses. The multiply scattered light was detected by a photomultiplier tube, PMT, (5070A, Hamamatsu) at different locations on the cheek bone by a handheld probe. This signal is denoted as the sample signal. The two signals were each split into two parts; one of the parts was directly connected to an oscilloscope remote controlled, called the direct signal, while the other parts was first sent via a lock-in amplifier (5209, EG&G Princeton Applied Research), where the 2f signal was detected.

2.2. Data evaluation

To suppress noise and perturbations, like optical interference fringes, software based balanced detection was used. These procedures have been described in detail elsewhere.[10] Briefly, the two detected 2f signals are first normalised with the direct signals. A set of parameters is then estimated by comparing the normalised reference signal and the normalised sample signal at frequency regions outside the expected oxygen imprint. A matched version of the reference signal is then subtracted from the sample signal over the whole frequency scan.

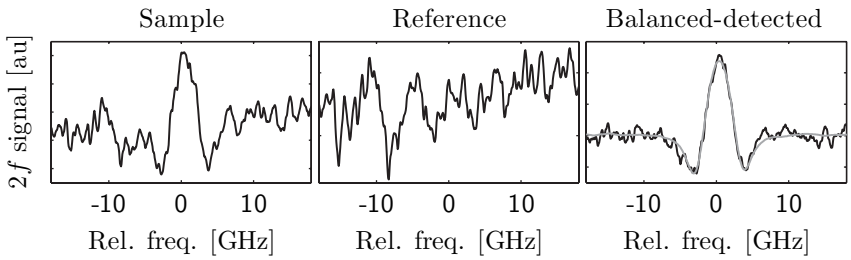

Figure 2. Typical recorded signals in this study from the sample detector (to the left) and the reference detector (center). The balanced-detection signal is also included with a fitted ideal function (to the right). The signal corresponds to an L_{eq} of 25 mm corresponding to an absorption fraction of $3.8 \cdot 10^{-4}$.

Once a balanced-detection signal is computed, an ideal signal is fitted to it. This signal obtained from a measurement where the oxygen imprint is many orders larger than the noise, created by measuring over an air distance of several meters. Fig. 2 shows typical recorded signals. To the left a signal from the sample detector is shown, in the center a corresponding signal from the reference detector is given, and to the right the computed balanced-detection signal is included together with the fitted ideal signal.

A quantity called the equivalent mean path length, L_{eq}, was estimated from the amplitude of the balanced-detection signal. This quantity corresponds to how far light has to travel in ambient air to achieve the observed absorption imprint. The calibration was done by employing the standard-addition method.[7, 10] The signal shown in Fig. 2 corresponds to an L_{eq} of 25 mm. We note that the L_{eq} signals depend on the gas concentration as well as the effective light path way that becomes an undefined quantity in a scattering medium. However, as we shall see, this difficulty can be suppressed under certain conditions.

2.3. Measurement procedure

Measurements were performed on two volunteers; one with constantly recurring sinus problems (Volunteer I) the other one with no history of such problems (Volunteer II). A CT image of Volunteer I is shown in Fig. 3a. It can clearly be seen that the left maxillary sinus is completely filled with inflamed swollen mucosa while the right one is only partly filled.

Four different measurements are presented in this study and are listed below:

Signal levels: The L_{eq} was measured on both volunteers in the left and right maxillary sinuses. The fibre was placed on the palate inside the mouth in close proximity to the particular sinus. The light was detected at two different locations; on the cheek bone and translated towards the nose (about 2 cm). Measurements were performed once a day during about a week.

Control: Two types of reference measurements were performed to investigate any possible L_{eq} offset in the current setup. The signal was measured through the cheek and the hand of the volunteers. In the case of reference measurements through the cheek, the fibre was placed inside the mouth in contact with the cheek and the detector was positioned on the opposite side of the cheek. In the case of reference measurements through the hand, the fibre was placed in contact with the palm and the detector was positioned on the opposite side of the hand.

Reproducibility: The reproducibility of the measured L_{eq} values was also investigated for Volunteer II. 10 measurements were done on the each sinuses by removing the detector and fibre between each recording. Measurements were done for the both the detector positions explained above.

Gas exchange: To study the ostia function (ventilation between nasal cavity and sinus cavity) L_{eq} was measured continuously during inhalation of non-ambient air (pure nitrogen). Data was collected for about 3.5 min;

1 min before flushing with nitrogen, 30 s during nitrogen flush through the nostril and for about about 2 min after terminating the flush, all the time pursuing normal mouth breathing. Each recorded signal was averaged for about 15 s. Measurements were performed on both the left and right maxillary sinuses on Volunteer I and II.

3. RESULT

Signal levels

The average measured L_{eq} values from the two volunteers together with error bars corresponding to two standard deviations are shown in Fig. 3b. It was observed that similar values were measured at the different detector locations. This is consistent with the results from Monte Carlo simulations of the signal strengths.[11,12] In the figure it can be seen that Volunteer I exhibits a small signal on the right sinus ($L_{eq} \approx 10$ mm) while nothing was detectable on the left side. The setup presented has a detection limit of L_{eq} of about 2 mm, corresponding to an absorption fraction of $3 \cdot 10^{-5}$.[10] In contrast to the measurements performed on Volunteer I, a much larger signal was observed on Volunteer II in both the right ($L_{eq} \approx 26$ mm) and left sinus ($L_{eq} \approx 20$ mm). Clearly, a significant difference on the oxygen imprint could be observed between the volunteer with constantly recurring sinus problems and the volunteer with no history of such problems.

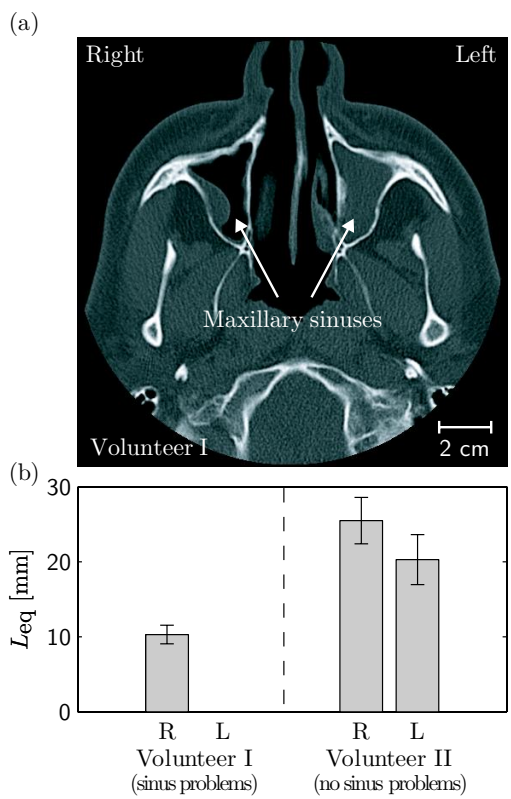

Figure 3. a) A CT image of Volunteer I with constantly recurring sinus problems. b) Signal levels study - Measured L_{eq} for both volunteers on the right and left maxillary sinus (Volunteer I with constantly recurring sinus problems, Volunteer II with no history of such problems).

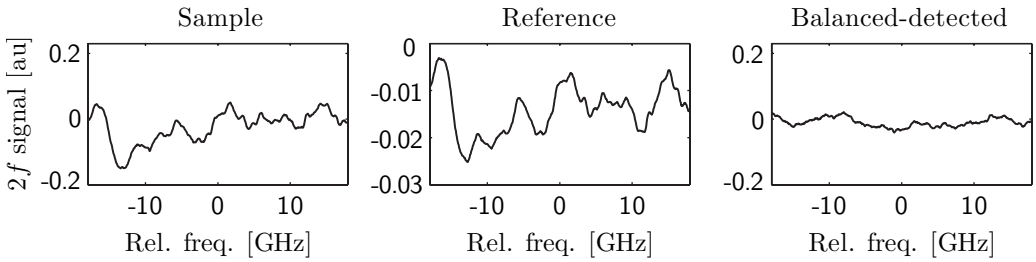

Figure 4. Control study - Typical recorded signals in this study from the sample detector (to the left) and the reference detector (center) when performing reference measurements. The fibre has been placed inside the mouth in contact with the cheek and the detector has been positioned on the opposite side of the cheek. The balanced-detection signal is also included. The remaining noise floor corresponds to about a L_{eq} of 2 mm (absorption fraction of $3 \cdot 10^{-5}$).

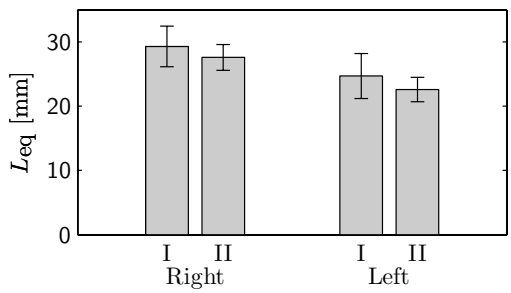

Figure 5. Reproducibility study - Average L_{eq} together with two standard deviations obtained from 10 measurements at each detector position (I : Cheek bone, II : Towards nose) and maxillary sinus for Volunteer II. The fibre and the detector were removed in between each recording.

Control

Before each measurement two reference measurements were performed. These measurements resulted in a consistently non-detectable signal providing the information that no oxygen offset is present in the setup. In our case a non-detectable signal corresponds to a L_{eq} of less than 2 mm as previously mentioned.[10] In Fig. 4 typical signals when performing reference measurements can be seen. From the balanced-detection signal the remaining noise floor can be observed.

Reproducibility

Fig. 5 shows the average L_{eq} together with error bars corresponding to two standard deviations obtained from 10 measurements at each detector position (I : Cheek bone, II : Towards nose) and maxillary sinus for Volunteer II when removing the detector and fibre between each recording. As can be seen, the standard deviation corresponds to about 10% for each position.

Gas exchange

Gas exchange studies were performed on both volunteers. No change could be observed in Volunteer I, while Volunteer II showed a decrease of signal when the nose cavity was flushed with pure nitrogen through a plastic tube positioned at the opening of the nostril. In Fig. 6 the invasion of N_2 in the right maxillary sinus of Volunteer II can be seen. The reinvasion of oxygen into the sinus can as well be observed when terminating the N_2 flush. During the measurements the fibre was placed on the palate, and the detector on the right cheek bone without

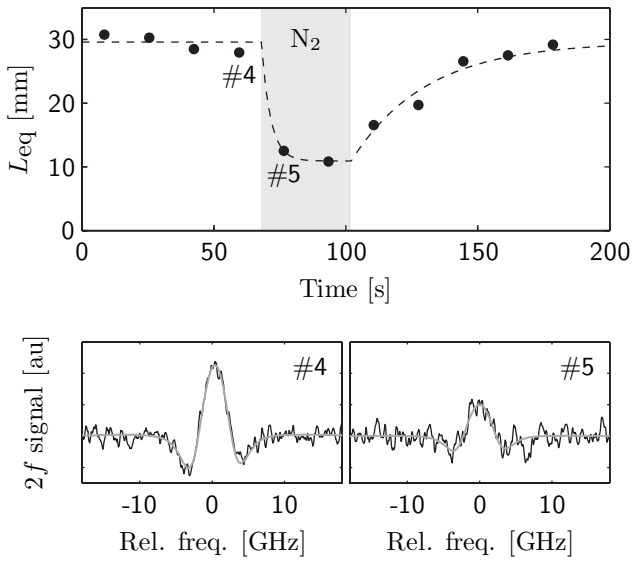

Figure 6. Gas exchange study - The measured L_{eq} (solid dots) together with a trend line (dashed line) in the right maxillary sinus of Volunteer II having no history of sinus problems. The oxygen level is first measured, N_2 is then flushed into the nasal cavity through the nostril and the invasion of the gas in the sinus is measured. The reinvasion of air is then recorded after terminating the N_2 flush. Two balanced-detection signals are also included in the figure; one before and one during N_2 flush.

being moved. Signals were averaged for about 15 s corresponding to the spacing between the measurement points. Two balanced-detection signals are also included in the figure; one signal before the gas is flushed and one during flushing. A reduction of about 2/3 was obtained in the signal for the case presented. More experiments with the same procedure have been performed showing different reductions depending on the N_2 flow.

4. CONCLUSION AND OUTLOOK

The technique described allows the monitoring of free oxygen gas in human sinuses, both in backscattering geometry, as demonstrated in Ref. [7] for the frontal sinuses, and in transmission geometry for the maxillary sinuses, as shown above. Actually, hybrids, where light is injected through the orbital wall close to the upper eye lid and the emerging light is detected against the forehead, or light is injected from the outside below the cheek bone and detected above the cheek bone have proved to be feasible, yielding strong signals, without the need of internal light injection.[13]

A person with sinus problems could readily be distinguished from a non-affected person also when varying scattering conditions were not accounted for. The degree of scattering, however, do not influence the data when the time constants for gas flow through the connecting channels are studied, since only the relative time variation of the signal is recorded. Like-wise, by forming a ratio between signals due to two gases interrogated at similar wavelengths, unknown scattering factors may be taken into account. Referencing around 935 nm to water vapor in the cavity, with its concentration determined only by the temperature (naturally thermostated to approximately 37^{o}C), it should be possible to directly determine the concentration of oxygen in the sinus, which might be related to the type of infection present.[13] Monitoring of free water vapor in scattering media was recently demonstrated in connection with wood drying.[14]

Based on the promising results reported here, a clinical study with well diagnosed patients, for which CT images are available, will be performed. This will be carried out together with an ear-nose-throat (ENT) clinic.

We anticipate, that a new and powerful non-intrusive optical method can be developed for assisting in fast and improved diagnostics of the common sinus problems, which frequently are abated with antibiotics, on sometimes uncertain grounds.

ACKNOWLEDGMENTS

The authors are grateful for fruitful discussions with N.G. Holmer, L. Malm, and M. Jannert. This research was supported by the Swedish Research Council, the Medical Faculty, Lund University, and the Knut and Alice Wallenberg Foundation.

REFERENCES

1. Health Matters, Sinusitis, Nat. Inst. of Allergy and Infectious Diseases, US Dept. of Health and Human Services, Bethesda (2005).
2. P. Stierna, G. Karlsson, I. Melén, and M. Jannert, "Aspect on Sinusitis - Diagnosis and threatment in adults," Proceedings from Meeting of the Swedish Association of Otorhinolaryngologists, HNS, Stockholm (1995).
3. M. Mafee, "Modern imaging of paranasal sinuses and the role of limited sinus computerized tomography; considerations of time, cost and radiation," *Ear Nose Throat J.* **73,** 532–534 (1994).
4. S. Zinreich, "Progress in sinonasal imaging," *Ann. Oto. Rhinol. Laryn.* **196,** 61–65 (2006).
5. D. Leopold, S. Zinreich, B. Simon, M. Cullen, and C. Marcucci, "Xenon-enhanced computed tomography quantifies normal maxillary sinus ventilation," *Otolaryngol. Head Neck Surg.* **122,** 422–424 (2000).
6. R. Rizzi, I. Dimitrov, A. Thompson, G. Jones, T. Gentile, M. Ishii, R. Reddy, M. Schnall, and J. Leigh, "MRI of hyperpolarized ^{3}He in human paranasal sinuses," *Magn. Reson. Med.* **39,** 865–868 (1998).
7. L. Persson, K. Svanberg, and S. Svanberg, "On the potential of human sinus cavity diagnostics using diode laser gas spectroscopy," *Appl. Phys. B* **82,** 313–317 (2006).
8. B. Paulsson, J. Dolanta, P. Ohlin, I. Larsson, and S. Lindberg, "Paranasal sinus ventilation in healthy subjects and in patients with sinus disease evaluated with the 133-Xenon washout technique," *Ann. Oto. Rhinol. Laryn.* **110,** 667–674 (2001).
9. D. Leopold, S Zinreich, B Simon, M Cullen, and C. Marcucci, "Xenon-enhanced computed tomography quantifies normal maxillary sinus ventilation ," *Otolaryn. Head Neck* **122,** 422–424 (2000).
10. L. Persson, F. Andersson, M. Andersson and S. Svanberg, "Approach to optical interference fringes reduction in diode laser absorption spectroscopy," *Appl. Phys. B* **87,** 523–530, (2007).
11. E. Kristensson and L. Simonsson, M.Sc. Thesis, Lund Institute of Technology, Lund Reports on Atomic Physics LRAP-361, LTH, Sweden (2006).
12. L. Persson, E. Kristensson, L. Simonsson, and S. Svanberg, "Monte Carlo simulations of optical human sinusitis diagnostics," *J. Bio. Med. Opt*, in press (2007).
13. L. Persson, M. Andersson, Märta Cassel-Engquist, K. Svanberg, and S. Svanberg, "Gas monitoring in human sinuses using tunable diode laser spectroscopy," *Manuscript in preparation*, (2007).
14. M. Andersson, L. Persson, M. Sjöholm, and S. Svanberg, "Spectroscopic studies of wood-drying processes," *Optics Express* **14,** 3641–3653, (2006).

Paper IX

Flexible lock-in detection system based on synchronized computer plug-in boards applied in sensitive gas spectroscopy

M. Andersson, L. Persson, T. Svensson, S. Svanberg.

Review of Scientific Instruments **78**, 113107 (2007).

REVIEW OF SCIENTIFIC INSTRUMENTS **78**, 113107 (2007)

Flexible lock-in detection system based on synchronized computer plug-in boards applied in sensitive gas spectroscopy

Mats Andersson, Linda Persson, Tomas Svensson, and Sune Svanberg[a)]
Atomic Physics Division, Lund University, P.O. Box 118, S-221 00 Lund, Sweden

(Received 3 July 2007; accepted 22 October 2007; published online 26 November 2007)

We present a flexible and compact, digital, lock-in detection system and its use in high-resolution tunable diode laser spectroscopy. The system involves coherent sampling, and is based on the synchronization of two data acquisition cards running on a single standard computer. A software-controlled arbitrary waveform generator is used for laser modulation, and a four-channel analog/digital board records detector signals. Gas spectroscopy is performed in the wavelength modulation regime. The coherently detected signal is averaged a selected number of times before it is stored or analyzed by software-based, lock-in techniques. Multiple harmonics of the modulation signal ($1f$, $2f$, $3f$, $4f$, etc.) are available in each single data set. The sensitivity is of the order of 10^{-5}, being limited by interference fringes in the measurement setup. The capabilities of the system are demonstrated by measurements of molecular oxygen in ambient air, as well as dispersed gas in scattering materials, such as plants and human tissue. © *2007 American Institute of Physics.*
[DOI: 10.1063/1.2813346]

I. INTRODUCTION

Analog lock-in techniques for tunable diode laser spectroscopy have been used for decades to improve the performance in the detection of trace gases.[1–4] Originally, desktop, lock-in amplifiers were used in combination with mechanically chopped light. Today, external signal generators are used to superimpose sine wave modulation signals on the laser operation current. The modulation signal also acts as phase reference and is fed to an analog, lock-in amplifier. This lock-in amplifier is then capable of filtering out harmonic components generated when light passes an absorbing sample/gas cell. Absorption lines are scanned across by superimposing a low-frequency triangular or sawtooth ramp on the operating current of the laser. The major reason for using lock-in detection is to suppress noise by moving the detection frequency to a range that is normally less affected by noise (above 1 kHz).[5] In the 1980s, modulation techniques such as wavelength-,[6] frequency-,[7] and two-tone frequency[8] modulation schemes were developed. Normally, direct absorption measurements (baseband detection) give a detection limit of 10^{-3}–10^{-4}, while modulation techniques such as wavelength and frequency modulations, give a detection limit of 10^{-6} or better.[9] Over the past 10 years digital amplifiers have been used and, currently, small digital-signal-processing based lock-in solutions are being developed and used.[10,11]

Even if the use in spectroscopy of modulation techniques, based on phase-sensitive detection, is straightforward, it is normally not easy to analyze and probe the raw signal, due to sources of error that affect the gas imprint signal before the lock-in detection has been implemented. This is because the detected gas imprint signal is weak and markedly affected by noise. Thus, data from the lock-in amplifier need to be averaged for several seconds or minutes in order to achieve the needed signal-to-noise ratio (SNR). It is often not possible to average the raw signal without degradation. This is due to unavoidable trigger jitter. Moreover, since lock-in detection normally takes place in real time, another drawback is that the influence of a change in lock-in settings (for example, the selection of harmonic) cannot be evaluated later on. In addition to the lock-in technique, methods to improve the signal include balanced detection,[12] coherent sampling,[13] waveform averaging,[14] and high-pass filtering prior to lock-in detection.[13]

Coherent sampling is a well-known technique, commonly used in spectrum analysis and signal processing for acoustics and telecom research and development. In coherent sampling, a master clock is used to create modulation waveforms and to control the sampling process of the detector signal. Coherent sampling requires that an integer number of wanted waveforms exist in the acquired data set and that the ratios between the sampling and the modulation frequencies (both laser scanning and laser modulation signals) are integers.[15–17] With this technique a number of scanned signals can be averaged before the lock-in detection is carried out. Periodic noise such as power supply ripple and external optical noise from fluorescent lamps, etc., which does not fulfill the requirements above, is averaged out (the coherent sampling process acts as a comb filter) together with nonperiodic noise. It should be noted that coherent sampling facilitates complete postdata processing. For example, this means that applications which previously required several lock-in amplifiers, can now be realized using coherent data acquisition and subsequent harmonic demodulation at desired harmonics (e.g., $1f$ and $2f$). In addition, high-pass filtering can increase the dynamic range further, since it suppresses most of the low-frequency content (e.g., below the $1f$ frequency).

[a)]Electronic mail: sune.svanberg@fysik.lth.se

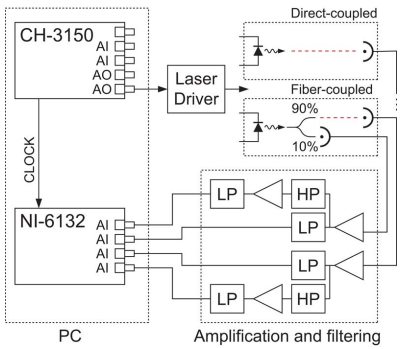

FIG. 1. The direct-coupled and the fiber-coupled experimental setups for measurement on ambient air by the use of VCSEL lasers. The lasers are modulated by an arbitrary waveform that is generated in a data acquisition board (CH-3150, Exacq Technologies). The amplified and high-pass filtered signals from the sample and the reference detectors are sampled coherently and synchronically by a four channel A/D board (NI-6132, National Instruments). See text for more details.

This article describes the construction of a compact and flexible digital lock-in detection system based on two plug-in boards for a standard computer. By employing coherent sampling, raw data storage and postdata processing in the time or frequency domain are made possible. The system can be used for both traditional trace gas analysis, and the more recently introduced high-speed combustion gas analysis requiring scan rates of 100 Hz or more. Experimental arrangements and data acquisition architecture are described in Sec. II. The required analog/digital (A/D)resolution is also discussed. The calibration and applications of the system are presented in Secs. III and IV. Finally, advantages of using a detection system based on coherent sampling and plug-in boards are discussed, and several examples of measurements are given.

II. MATERIALS AND METHODS

A. Optical setup

An overview of the optical setup is shown in Fig. 1. Two different vertical cavity surface emitting lasers (VCSELs) are used alternatingly, and correspond to two different experimental configurations. The *direct-coupled setup* is based on a standard single-mode VCSEL (ULM763-03-TN-S46FOP, Ulm Photonics) with a maximal output of 0.3 mW, operating at 0.25 mW at the sample. The wavelength is scanned across the P11P11 oxygen line at 764.281 nm (vacuum wavelength). The second configuration is referred to as the *fiber-coupled setup*, and employs a pigtailed, single-mode VCSEL (L2K-P760-LD-SM, Laser2000, Sweden) with a maximum output power of 0.2 mW, operating at 0.085 mW at the sample. The wavelength is scanned across the R15Q16 oxygen line at 760.094 nm (vacuum wavelength). After the pigtailed laser, the light is split by a 10/90(%), single-mode fiber splitter (Laser2000, Sweden). The smaller fraction is guided to a reference detector, while the main part is either propagated through ambient air (for calibration purposes, see Sec. III), or guided to a scattering and absorbing sample. A collimating lens package (CFC-5-760, Thorlabs) is used in the case of measurements in ambient air.

The laser frequency is scanned over the absorption lines by ramping the operating current, which is provided by a standard VCSEL current controller (LDC200, Thorlabs). This is done by using a triangular waveform of 130 Hz. A temperature controller (TED200, Thorlabs) ensures general temperature stability. Wavelength modulation is achieved by superimposing a sinusoidal modulation of 133 kHz on the triangular ramping signal. The ramping and modulation signals are created in a peripheral component interconnect (PCI)-based, 12 bit arbitrary waveform generator (CH-3150, Exacq Technologies). Its internal clock is used not only to clock out such waveforms, but also to externally clock the A/D converters (2.496 MHz), via a short coaxial cable, on a second computer board (NI-6132, National Instruments). It is this man euver that implements coherent sampling.

In the fiber-coupled setup, the light beams enter two detectors with built-in transimpedance amplifiers (UDT-455LN, OSI Optoelectronics). In the direct-coupled setup, only one of the above-mentioned detectors is used. In the present case, the gain of the amplifiers is set to 10^3 in order to fulfill a bandwidth of about 1 MHz. Both the sample and the reference signals are amplified by a factor of up to 1000 by an external amplifier in order to minimize external noise and for full utilization of the dynamic range of the AD converter. The reference and the sample signals are also filtered by a second-order, high-pass filter (50 kHz cutoff frequency), and amplified once more by a factor of 100. Measurements on scattering samples, such as bamboo or human tissue, require a large-area detector due to the fact that incident light is scattered and absorbed by the sample. In this case, the default sample detector is replaced by a cooled, large-area ($\varnothing = 10$ mm) avalanche photodiode (APD) module (SD 394-70-72-661, Advanced Photonix).

The advantage of using wavelength modulation techniques was estimated by measuring the relative intensity noise (RIN) of the direct-coupled laser and comparing the noise floor level at low frequency and at the laser modulation frequency. RIN is defined in a 1 Hz bandwidth, and expressed in decibels, as

$$\mathrm{RIN} = 20 \log_{10} \frac{V_{\mathrm{noise}}}{V_{\mathrm{average}}},$$

where V_{noise} is the spectral noise root-mean-square (rms) voltage and V_{average} is the averaged rms voltage corresponding to the averaged optical power recorded at the optical detector.[18] The RIN measurement was done by measuring the noise spectrum of the recorded detector signal with the laser turned on without any modulation or ramp signal. As shown in Fig. 2, the noise level at 133 kHz is about 20 dB (ten times) lower than the low-frequency noise level and gives information on the expected improvement in performance when the wavelength modulation technique is used. The decrease in the performance of a tunable diode laser system based on direct detection is due to flicker noise from the laser. In Fig. 2 the dynamic range achieved is about 126 dB (2.0×10^6) at 133 kHz frequency. According to the data

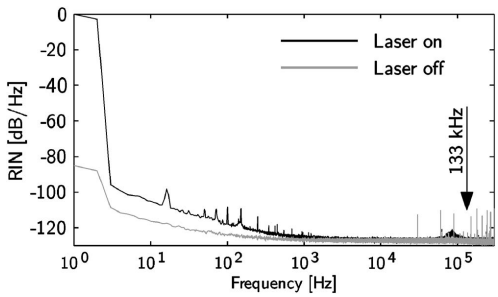

FIG. 2. Laser relative intensity noise (RIN) measurement with a spectral resolution of 1 Hz. Sensor data are recorded by a 14 bit data acquisition card at 600 kS/s over 100 s. The figure shows a power spectrum (RIN measurement) of the recorded detector data with and without unmodulated laser light turned on.

sheet of the laser the RIN value at 1 GHz is about −120 to −130 dB/Hz which sets the performance limit of a spectroscopy system based on this laser. As can be seen in the figure, any further improvement of the dynamic range is limited by the 14 bit data acquisition card since the noise floor is almost the same when the laser is turned off. Further, a detection limit of 10^{-6} requires the system to have a dynamic range of about 120 dB (1×10^{6}). To be able to resolve such a weak signal, a high-pass filter is mounted close to the detector to suppress any signal below the modulation frequency.

B. Data acquisition

A software program, based on LabVIEW, controls the arbitrary waveform acquisition board (CH-3150). First, the scanning and modulation signals to the laser are created and loaded to the board. During the run, the computer central processing unit (CPU) is free to carry out other tasks since the workload of the arbitrary waveform generator is handled by the board itself. All signals are sampled synchronously and coherently to the laser modulation waveforms by the externally clocked, four channel, 14 bit A/D converter PCI board (NI-6132). Sample data blocks that correspond to one scan are added in a data vector created in LabVIEW. Normally, 130 7800 scans (1–60 s) are carried out before averaged data, which are vector data divided by the number of scans, are stored on disk and/or are lock-in detected in the computer by a lock-in detection software module (LOCK-IN toolkit for LabVIEW, National Instruments). The phase reference, used by the lock-in detection module, is created by software. The first and the second channels record the signals from the sample detector (raw signal and high-pass filtered raw signal), while the third and the fourth channels record the signals from the reference detector (reference signal and high-pass filtered reference signal). These two last channels are used only in the fiber-coupled setup; see Fig. 1.

To illustrate the potential of a digital lock-in detection system, based on wavelength modulation and coherent sampling, a measurement based on the direct-coupled setup was performed over a distance of 10 cm in ambient air. Figure 3(a) presents the direct signal recorded, where the

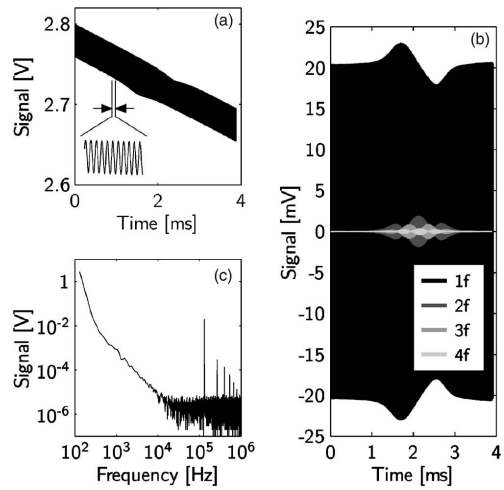

FIG. 3. Typical behavior of the recorded signal for a measurement of oxygen, based on wavelength modulation techniques, for 10 cm of air; 130 (1*s*) synchronous averages. (a) shows the signal from the detector when the laser is scanned about 25 GHz, (b) shows the bandpass-filtered detector signals (three-pole Butterworth, 4 kHz bandwidth) of the detector signal, (c) shows the spectral peak voltages based on an FFT of the detector signal presented in (a). The spectral resolution of the FFT is 130 Hz. See text for more details.

residual amplitude modulation (RAM) signal is clearly seen as a sine wave signal that is present during a scan.[20] The RAM signal occurs because the change in frequency is caused by a change in diode driving current and so altering the output power of the diode laser. In the middle of the frequency scan, the absorption line (P11P11) is crossed, resulting in amplitude changes of the direct signal, and overtones are created ($2f, 3f, 4f, \ldots$). The amplitude of the RAM signal (40 mV_{pp}) is about 1.5% of the dc level of the signal (2.7 V). The recorded, direct signal was filtered by four software-based, bandpass filters (center frequency at 1*f*, 2*f*, and 4*f*) and the data are presented in Fig. 3(b). This figure shows that the 2*f* signal (4 mV_{pp}) is weaker than the 1*f* signal (6 mV_{pp}) but still of similar amplitude compared to the dip in the direct signal since the amplitude of the 2*f* signal is about 0.1% of the amplitude of the direct signal. The amplitude of the harmonic signals is highly dependent on the modulation index that in this case is set to 2.2.[6] The modulation index is the ratio between the modulation excursion in frequency and the half width at half maximum of the absorption feature. The expected fractional absorption can be used to calculate the dynamic range of the system required. The absorption fraction for 10 cm of air corresponds to 2.45×10^{-3}. It is also shown that the 3*f* and 4*f* signals (1.8 mV_{pp}, respectively, 0.7 mV_{pp}) are weak and that the RAM signal is strong compared to the peak to peak of the 1*f* signal.

To get an overview of the signal spectrum recorded, a fast Fourir transform (FFT) of the data presented in Fig. 3(a) was carried out and is presented in Fig. 3(c). The figure shows that the 1*f* signal (20 mV_{pp} at 133 kHz) is about a

factor of 100 weaker than the averaged signal from the detector (2.7 V). It is also shown that the system SNR, for 130 averages, is about 3×10^5. The SNR is measured at 133 kHz and with a measurement bandwidth of 130 Hz. Normally, SNRs are expressed on a logarithmic (dB) scale according to

$$\mathrm{SNR} = 20\log_{10}\frac{V_{\mathrm{signal}}}{V_{\mathrm{noise}}},$$

where V_{signal} is the averaged detector rms voltage level and V_{noise} is the rms voltage level of measured noise. A SNR of 3×10^5 corresponds to a SNR of about 110 dB. If a high-pass filter is introduced, which suppresses signals below the $1f$ frequency, the A/D dynamic range required decreases by a factor of about 100, as shown in Fig. 3(c).

C. The impact of the A/D converter resolution

The direct-coupled setup was used to study the impact the resolution of an A/D converter has on a coherent measurement system for spectroscopy. A number of streaming and scanning $2f$ detection measurements were performed for a distance in ambient air of 10 mm. This corresponds to a fractional absorption of 2.45×10^{-4}. Four measurements, each recording for 1 min (7800 scans) were done. The sample signal and high-pass sample signal were streamed to a hard disk at 2.469 MS/s. Raw data were stored for each measurement, with different resolutions corresponding to 8, 10, 12, and 14 bits of the A/D converter. By default, the A/D board has a 14 bit resolution but this can be decreased by software during a streaming measurement (based on an application example provided by National Instruments). Thus, the impact of different A/D converter resolutions could be studied. The streamed data were read from the disk, averaged, and lock-in detected. In Fig. 4 the $2f$ signals for a resolution of 8 and 14 bits are presented.

As can be seen on the left-hand side of Fig. 4 and 8 bit A/D converter cannot resolve the oxygen absorption line even though 100 averages are performed. An absorption dip of 2.45×10^{-4} requires a dynamic range of the A/D converter of about 72 dB $[20\log(1/2.45\times10^{-4})]$ to reach an SNR of unity. However, an 8 bit A/D converter has a dynamic range of only about 48 dB and this is too poor to resolve absorption lines in this test setup even though long time averaging is used. If more bits are used the absorption dip can be resolved, even with few or no data averages. 14 bits are enough to resolve an absorption dip of 2.45×10^{-4} since its theoretical dynamic range is about 86 dB. The 100 averages increase the dynamic range by an additional factor of 10 (20 dB).

The performance can be increased by the use of dithering[21] or high-pass filtering,[19] as shown on the right-hand side of Fig. 4. It can be seen that similar performance is reached regardless of whether an 8 bit or a 14 bit AD converter is used. If high-pass filtering is used it should be possible to detect a weak absorption line $(1\times10^{-6}$–$1\times10^{-8})$ by using a 14 bit or a 16 bit A/D converter. On the right-hand side of Fig. 4, it can also be seen that single scan data are not *a priori* improved by introducing more bits. This is due to the fact that data from one scan are greatly affected by mechanical vibrations introduced by vibration motors. Small vibration motors are mounted in the test setup in order to shake the laser and the detector to minimize persistent optical fringe generation, a well-known detrimental factor in diode laser spectroscopy.[22]

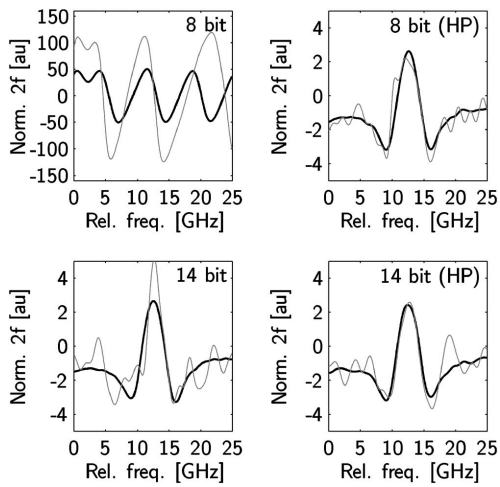

FIG. 4. Streaming measurements on 1 cm of ambient air (fractional absorption of 2.45×10^{-4}) with the direct-coupled setup based on different A/D resolutions and signal filtering. The $2f$ signal for the P11P11 oxygen line at about 764.3 nm is measured for two different average settings: 1 (gray line) and 100 averages (black line). On the left, the $2f$ signal, based on $2f$ detection of the sample signal, is shown for different A/D resolutions and measurement times. On the right, similar data based on $2f$ lock-in-detected, high-pass filtered, sample signals are shown.

III. CALIBRATION OF THE SYSTEM

The standard addition method was used to calibrate and to test the linearity and noise behavior of the system. The method is based on adding a known distance through ambient air between the laser and the detector and monitoring the amplitude of the $2f$ signal, divided by the dc level of the direct signal.[22] The signal increases linearly as is also shown in Fig. 5. The estimated air offset of 4 mm, in the direct-coupled setup, is due to the fact that it is not possible to mount the detector directly connected to the laser in the direct-coupled setup. The estimated air offset of 14 mm in the fiber-coupled setup is due to air inside the collimator package used. It is possible to evaluate $1f$–$4f$ signals from one measurement data file, since data are recorded synchronously almost 20 times for each period of the modulation signal. The figure also shows typical recorded signals of the $2f$ signal for a distance through air of about 35 mm for the fiber-coupled and the direct-coupled setups. As shown in Fig. 5(b), the $2f$ sample signal in the fiber-coupled setup is markedly distorted. The distortion is due to optical interference effects which occur frequently in pigtailed lasers. Periodic noise and fringes can be handled by using balanced detection.[22] By detecting both the sample and reference beams synchronously, a balanced $2f$ detection signal is evaluated, as shown in Fig. 5(b).

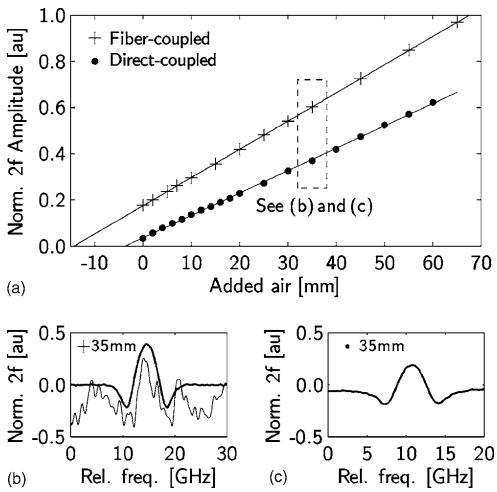

FIG. 5. (a) Standard addition measurement results from the direct-coupled and fiber-coupled measurement setups. Ten measurements (20 s measurement time) were made at each air distance, ranging from 0 to 65 mm. (b) Typical behavior of the $2f$ signal in the fiber-coupled setup for a distance through air of about 35 mm. The figure shows the $2f$ signal of the sample signal (thin line) and the evaluated balanced signal (bold line). (c) Typical behavior of the $2f$ signal in the direct-coupled setup for a distance through air of about 35 mm.

IV. APPLICATIONS

A. Gas discharge measurements on a bamboo stalk

To show the strength of using the digital lock-in detection system, we performed test measurements. The oxygen content inside a bamboo stalk was measured. Similar studies on wood have been carried out previously, using a traditional spectroscopy setup, based on desktop analog lock-in amplifiers.[23,24] The purpose of our measurements was to show how the hollow compartment inside a bamboo stalk interacts with ambient air. The stalk of a bamboo consists of hollow, jointed compartments. We performed measurements on a 23 cm long stalk with an inner diameter of 11 mm. The external diameter was approximately 18 mm. Before the measurement was started, the bamboo stalk was exposed to a nonambient gas by placing it for 72 h in a bag containing nitrogen. Figure 6 shows the direct-coupled setup measurement arrangement and also the experimental data, showing that the discharge of nitrogen has a time constant of about 30 min.

The light reaching the APD detector is in the range of only 0.3 μW or 0.1% of the emitted light from the laser. Initial measurements showed noisy signals, and no pure $2f$ signal could be detected for 20 s of averaging. This is due to interference fringes that appear between the laser, the bamboo stalk, and the detector. Small vibration motors were mounted on the laser and the detector in order to shake the test setup to minimize persistent fringe generation that otherwise overrides the $2f$ oxygen signal. Even though each measurement point in Fig. 6 is based on 20 s of averaging (2600 scans), measurement data still fluctuate. This could be

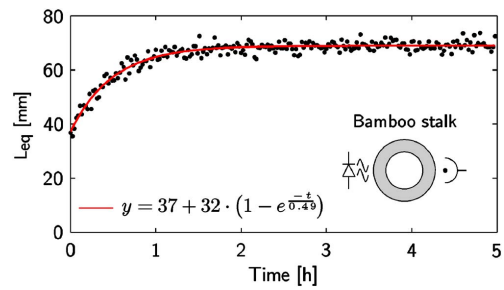

FIG. 6. (Color online) Measurement on nitrogen discharge in a bamboo stalk with a diameter of 18 mm. As shown in the figure, the $2f$ signal starts at an offset that corresponds to 37 mm of ambient air. This is partially because the stalk is mounted at a certain distance from the laser and the detector. Thus, light also passes through ambient air, not only through the stalk.

the result of changing motor speed, backscattered light, interference fringes, etc., which add noise and intensity fluctuations.

B. Measurements on the human frontal sinus

Human frontal sinuses are air-filled cavities in the frontal bone. Measurements on these sinuses, on a healthy volunteer, were performed with the fiber-coupled setup. This setup was chosen since the measurement requires a device that can be positioned at any point on the human body. The tip of the fiber was positioned onto the caudal part of the frontal bone while the APD detector was positioned on the forehead about 3 cm from the fiber. The light that reaches the APD detector was in the range of only 0.15 μW or 0.2% of the emitted light from the laser. Measurements, based on 60 s of averaging, show a $2f$ signal that corresponds to an distance through ambient air of 13 mm. The result is in agreement to that reported in Ref. 25. As expected, the SNR of the $2f$ signal is

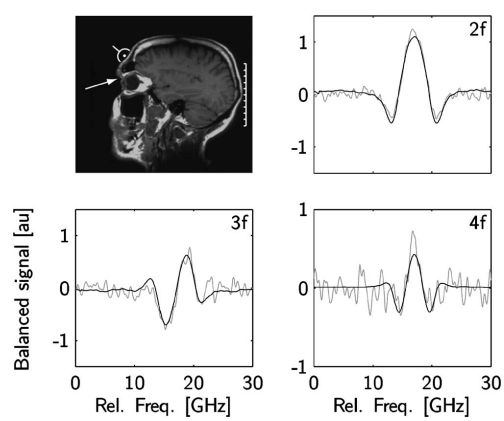

FIG. 7. Measurement on frontal sinuses on a healthy volunteer. The strength of the signal corresponds to a distance through ambient air of 13 mm. The figure shows the behavior of the $2f$–$4f$ signals for one measurement (60 s averaging). See text for more details.

higher than for the $3f$ and $4f$ signals, as shown in Fig. 7. The measurement time, to produce a signal of an acceptable signal, should be 10–30 s. Commonly, fringes dominate the noise floor and in some cases the $4f$ signal contains less such noise than the $2f$ signal.[26] Thus, the $4f$ signal may be a better choice for data analysis in the case of large interference fringes. However, the $4f$ analysis requires more light or less attenuation by the sample. This is due to the fact that the signal level of the $4f$ signal is lower than the $2f$ signal by a factor of 5, as shown in Fig. 3.

V. DISCUSSION

The CH-3150 board was chosen because it has a fast arbitrary generator onboard, which can be used to modulate the laser. Any modulation frequency from dc to several megahertz can be created without loading the computer central processor unit (CPU). The two analog input channels onboard can be used to coherently sample the detector signals at the same time. Thus, this board would be adequate to develop a flexible, powerful, cheap, and compact system for trace gas analysis. This system can be used in general gas spectroscopy and in applications with fast changing environments such as in combustion, requiring a ramping frequency of the order of 1 kHz. However, since four input channels were required for balanced detection to suppress fringes, a second board was introduced (NI-6132) that contains four synchronized A/D converters clocked by the CH-3150 board. The clock signal and the waveform sync signal were fed to the A/D board via two coaxial cables mounted inside the computer. This action was taken to suppress noise and prevent cross-talk between the clock and the detector signals.

Even though this system can be run incoherently, like an ordinary, personal computer (PC)-based, lock-in detection system, coherent sampling is used since this avoids the requirement that lock-in data are real-time data. Data can thus be averaged in real time coherently and can be processed after the averaging is finished or stored for later analysis. The user is free to analyze the data in the time or the frequency domain. This provides the possibility of analyzing signals from several channels and performing baseband analysis and lock-in detection ($1f$–$4f$) on the same data set. The current solution corresponds to the performance of standardized, digital lock-in amplifiers. However, with this setup, baseband detection, $1f$–$4f$ detection, and fast ramp frequencies (4 Hz–1 kHz) could be used by running different software applications without any changes having to be made in the hardware. The solution is compact and installed in an ordinary PC.

If higher performance is needed, high-pass filtering of the detector signal increases the dynamic range of the signal detection, since most of the low-frequency signals (below $1f$) are thus suppressed. When this technique is used, the resolution requirement of the A/D converter is not critical. A 12–16 bit A/D converter should be adequate even for applications requiring a fractional absorbance of about 1×10^{-7}. The output resolution of the D/A converter is 12 bits, which adds quantization noise even though the CH-3150 board has analog reconstruction filters onboard. It is difficult to estimate how this limitation affects the resolution of the system since amplitude noise at the laser input is converted into amplitude and frequency variations in the laser at the same time.

Another way to improve the performance of the system is to replace the current data acquisition (DAQ) boards with boards with higher resolution. As an example, a second measurement was performed to measure the laser noise using a 24 bit data acquisition board (NI-4472, National Instruments). The use of this board resulted in lowering the noise floor at 10 kHz by an additional 30 dB. However, this board is too slow (about 100 kHz sampling frequency) for combustion measurements, for instance, and it is not possible to clock it externally. Thus, this board cannot be used in a coherent sampling system. It is also possible to add input channels by replacing the A/D board with a board with eight input channels, for example. If a cheaper solution is needed, standardized external sound cards can be used. Today, these devices have excellent performance with 24 bit resolution A/D and D/A converters. The only drawbacks are that the sampling clock is limited to 196 kHz and no dc level can be measured. However, this solution may be adequate for some applications.

VI. SUMMARY

By the use of plug-in boards for standardized computers, a powerful and flexible detection system for gas spectroscopy was developed. One of the greatest advantages of the system is that raw data, from a number of channels, can be streamed and stored on disk by the use of standardized software. There is no need for specially designed computers, field-programmable gate arrays, or embedded solutions. Coherent sampling allows the raw data to be analyzed in real time or postprocessed in the time or frequency domain. In our experience the current system is limited by interference fringes in the optical setup.

ACKNOWLEDGMENTS

This work was supported by the Swedish Research Council and the Knut and Alice Wallenberg Foundation. The authors are grateful for Lars Rippe for sharing his expertise in measurement technology.

[1] P. Werle, Spectrochim. Acta, Part A **54**, 197 (1998).
[2] G. Galbács, Appl. Spectrosc. Rev. **41**, 259 (2006).
[3] M. Allen, Meas. Sci. Technol. **9**, 545 (1998).
[4] K. Song and E. C. Jung, Appl. Spectrosc. Rev. **38**, 395 (2003).
[5] D. T. Cassidy and J. Reid, Appl. Opt. **21**, 1185 (1982).
[6] J. Reid and D. Labrie, Appl. Phys. B: Photophys. Laser Chem. **26**, 203 (1981).
[7] G. C. Bjorklund, Opt. Lett. **5**, 15 (1980).
[8] D. T. Cassidy and J. Reid, Appl. Phys. B: Photophys. Laser Chem. **29**, 279 (1982).
[9] J. Silver, Appl. Opt. **31**, 707 (1992).
[10] R. Alonso, F. Villuendas, J. Borja, L. A. Barragn, and I. Salinas, Meas. Sci. Technol. **14**, 551 (2003).
[11] A. Gnudi, L. Colalongo, and G. Baccarani, Proceedings of the European Solid-State Circuits Conference, 1999 (unpubished).
[12] P. Vogel and V. Ebert, Appl. Phys. B: Lasers Opt. **72**, 127 (2001).
[13] T. Fernholz, H. Teichert, and V. Ebert, Appl. Phys. B: Lasers Opt. **75**, 229 (2002).
[14] P. Werle, R. Miicke, and F. Slemr, Appl. Phys. B: Lasers Opt. **57**, 131

(1993).
[15] R. Rosing, H. Kerkhoff, R. Tangelder, and M. Sachdev, J. Electronic Testing: Theory and Applications **14**, 67 (1999).
[16] P. Heinonen, T. Saramaki, J. Malmivuo, and Y. Neuvo, IEEE Trans. Circuits Syst. **31**, 438 (1984).
[17] M. E. Takanen, Ph.D. Thesis, Helsinki University of Technology, 2005.
[18] C. Thibon, F. Dross, A. Marceaux, and N. Vodjdani, IEEE Photon. Technol. Lett. **17**, 1283 (2005).
[19] R. Engelbrecht, Spectrochim. Acta, Part A **60**, 3291 (2004).
[20] X. Zhu and D. T. Cassidy, J. Opt. Soc. Am. B **14**, 1945 (1997).
[21] J. Reid, M. El-Sherbiny, B. K. Garside, and E. A. Ballik, Appl. Opt. **19**, 3349 (1980).
[22] L. Persson, F. Andersson, M. Andersson, and S. Svanberg, Appl. Phys. B: Lasers Opt. **87**, 523 (2007).
[23] M. Sjöholm, G. Somesfalean, J. Alnis, S. Andersson-Engels, and S. Svanberg, Opt. Lett. **26**, 16 (2001).
[24] J. Alnis, B. Anderson, M. Sjholm, G. Somesfalean, and S. Svanberg, Appl. Phys. B: Lasers Opt. **77**, 691 (2003).
[25] L. Persson, M. Andersson, M. Cassel-Engquist, K. Svanberg, and S. Svanberg, J. Biomed. Opt. **12**, 053001 (2007).
[26] P. Kluczynski and O. Axner, Appl. Opt. **38**, 5803 (1999).

Paper X

White Monte Carlo for Time-resolved Photon Migration

E. Alerstam, S. Andersson-Engels, and T. Svensson.
Journal of Biomedical Optics **13**, 041304 (2008).

Journal of Biomedical Optics 13(4), 041304 (July/August 2008)

White Monte Carlo for time-resolved photon migration

Erik Alerstam
Stefan Andersson-Engels
Tomas Svensson
Lund University
Department of Physics
Sweden

Abstract. A novel scheme for fully scalable White Monte Carlo (WMC) has been developed and is used as a forward solver in the evaluation of experimental time-resolved spectroscopy. Previously reported scaling problems are avoided by storing detection events individually, turning spatial and temporal binning into post-simulation activities. The approach is suitable for modeling of both interstitial and noninvasive settings (i.e., infinite and semi-infinite geometries). Motivated by an interest in *in vivo* optical properties of human prostate tissue, we utilize WMC to explore the low albedo regime of time-domain photon migration—a regime where the diffusion approximation of radiative transport theory breaks down, leading to the risk of overestimating both reduced scattering (μ_s') and absorption (μ_a). Experimental work supports our findings and establishes the advantages of Monte Carlo–based evaluation. [DOI: 10.1117/1.2950319]

Keywords: Monte Carlo; photon migration; time-resolved spectroscopy (TRS); optical properties; human prostate.

Paper 07390SSR received Sep. 18, 2007; revised manuscript received Nov. 13, 2007; accepted for publication Nov. 16, 2007; published online Jul. 9, 2008.

1 Introduction

Many applications within the field of biomedical optics rely either on the capability of performing, or the availability of, accurate measurements of optical properties of highly scattering materials. This is reflected by the massive development of theory related to light propagation in turbid media (photon migration), and the numerous techniques available for characterisation of such materials.

Time-resolved spectroscopy (TRS) is one of several techniques available for assessing optical properties of turbid media. By studying the broadening of short (picosecond) light pulses, it allows determination of both the absorption coefficient (μ_a) and the reduced scattering coefficient (μ_s') without the need of absolute measurements of light intensities. At first, time-resolved photon migration was investigated and evaluated using the diffusion approximation of radiative transport theory.[1] Although proven useful in numerous cases, the diffusion modeling was found erroneous at low albedos or close to radiation sources.[2,3] Unfortunately, several tissue types exhibit optical properties in the range where the use of the diffusion approximation may be questioned. The human prostate is one example,[4,5] exhibiting reduced scattering below 10 cm^{-1} and absorption above 0.3 cm^{-1}.

In order to extend the range of optical properties and source-detector separations over which TRS can provide accurate data, methods for Monte Carlo-based modeling were developed. Introduced to the field of biomedical optics and photon migration by Wilson and Adam,[6] Monte Carlo (MC) simulation has become the gold standard for modeling of light propagation in tissue optics.[7] Besides modeling spatially and temporally resolved light distribution, MC has proven useful in, for example, fluorescence modeling[8] and Raman spectroscopy.[9]

Traditionally, MC was performed for a particular set of optical properties at a time. Since the simulation is time-consuming, it is thus not useful as a forward solver in reverese problems, for instance, during evaluation of experimental data (iterative curve-fitting). This obstacle lead to the development of White Monte Carlo (WMC),[10–12] in which a single simulation in combination with proper rescaling ensures coverage of a wide range of optical properties. The main feature in WMC, making it feasible for use as a forward model in an iterative solver, is illustrated in Fig. 1.

During MC simulations of light propagation in homogeneously scattering and nonabsorbing media, photon paths are determined only by the scattering phase-function, the scattering coefficient, and the sequence of random numbers generated by the simulation program. For a given phase function, and considering a particular sequence of random numbers, the photon path will scale linearly with the scattering coefficient, μ_s. The recording of photon paths and corresponding time-of-flights thus allows post-simulation transformation, from the scattering coefficient used during simulation, to an arbitrary. Furthermore, the impact of nonzero absorption can be imposed post-simulation simply by giving photons different weights w_a according to the Beer-Lambert law of attenuation. This weight is stated in Eq. (1), where c' is the speed of light within the media:

$$w_a = \exp(-\mu_a c' t). \tag{1}$$

This means that a single Monte Carlo simulation can be used to extract photon time-of-flight distribution not only for dif-

Address all correspondence to: Tomas Svensson, Lund University, Department of Physics, Lund, Sweden.

1083-3668/2008/13(4)/041304/10/$25.00 © 2008 SPIE

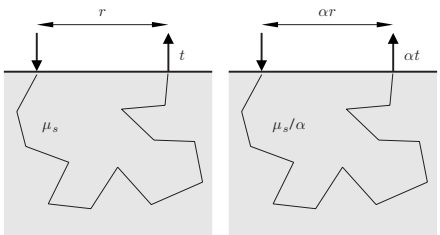

Fig. 1 In WMC, the shapes of the photon paths are determined only by the phase scattering function and the sequence of random numbers. Paths generated by simulations in nonabsorbing media can hence be linearly scaled to apply for different values of μ_s. The illustration is adapted from Ref. 12.

ferent source-detector separations, but also for different optical properties μ_s' and μ_a.

The preceding theory has been discussed in several papers.[8,10–15] Graaff et al. suggested a limited scalable Monte Carlo technique where the optical properties of simulations in slab geometries could be scaled as long as the total attenuation coefficient was held constant.[13] Two groups simultaneously and independently extended the theory of Graaff et al. Kienle and Patterson suggested a scalable Monte Carlo technique for infinite and semi-infinite homogeneously scattering media and used independent (reference) MC simulations for verification of its performance in the semi-infinite case.[10] Pifferi et al. suggested a similar approach,[11,12] proposing scalability in both μ_a and μ_s'. In practice, however, they based their evaluation on interpolation between MC simulations carried out at different μ_s, thus utilizing scalability in μ_a only. On the other hand, their work included evaluation of experimental time-resolved transmittance in the slab geometry (a geometry not allowing μ_s rescaling). Swartling et al. showed the usefulness of the WMC approach in fluorescence emission spectra modeling.[8] Swartling also raised the important question regarding the equivalency of WMC and traditional MC.[14] Xu et al. demonstrated the superior performance of WMC over different light propagation models as a forward model for evaluation of frequency domain data (generated by a traditional Monte Carlo program[15]). In the same paper, Xu et al. demonstrated scaling of data from an absorbing media using the weighting relationships from traditional Monte Carlo. Xu et al. also reported the so-called *scaling effect* as being the major inconvenience in WMC-based data evaluation. This inconvenience originates from the fact that scaling in μ_s is accompanied by a scaling of temporal and spatial bin size, resulting in a need for data resampling and a limited range in scalability.

Motivated by an interest in *in vivo* optical characterization of human prostate tissue, this work is aimed at providing a scheme for fully scalable WMC for time-domain photon migration and demonstrating its value in evaluation of experimental data in the low albedo regime of photon migration. The approach is useful in both infinite and semi-infinite geometries, featuring individual storage of the spatial location and the time-of-flight for all potential detection events. Since this allows post-scaling binning (temporal, as well as spatial),

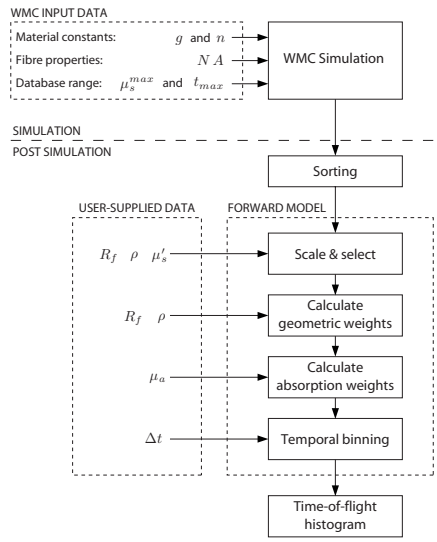

Fig. 2 A flowchart of the WMC scheme used. The WMC simulation program performs the simulation in either infinite or semi-infinite homogenously scattering media, using user-supplied WMC input data. The resulting database is sorted and stored to be used later by the forward model. The forward model rescales the database data and generates time-of-flight histograms corresponding to parameters supplied by the user. These parameters include the radius R_f of the involved optical fibers, the source-detector separation ρ, the optical properties μ_s' and μ_a, and the desired temporal channel width Δt. As this fast forward model is incorporated in the forward solver, the method can be used to evaluate experimental time-domain data.

it eliminates the need for the data resampling otherwise accompanying μ_s scaling. It also allows an accurate account for finite extension of source and detector areas (e.g., optical fiber diameters).

2 Materials and Methods

2.1 *White Monte Carlo*

A WMC model was developed to serve as the forward model for evaluation of fiber-based time-resolved spectroscopy under interstitial as well as under noninvasive conditions (i.e., infinite and semi-infinite geometry). The model consists of a simulation program written in C and a set of MATLAB scripts performing post-simulation processing. The main objectives were to retain full scalability in both μ_s' and μ_a, while avoiding scaling inconveniences by moving spatial and temporal binning to post-simulation. This eliminates the need for any temporal resampling and allows accurate convolutions to properly account for the finite size (radius R_f) and light distribution of optical fibers. A schematic illustration of the WMC model is given in Fig. 2. Apart from selecting simulation geometry, the user has to provide the WMC simulation program with a few input parameters. The refractive index n, the anisotropy factor g, and the numerical aperture NA of the involved optical fibers are material parameters specific to a

particular simulation. The simulation is run at the specified scattering level μ_s^{max} but is always terminated when time reaches t_{max}. This notation is used because μ_s^{max} defines the maximum scattering coefficient for which the resulting database can provide valid data throughout the time interval $[0, t_{max}]$. Generally, scaling to a certain scattering $\mu_s = \mu_s^{max}/\alpha$ results in data valid in the time interval $[0, \alpha t_{max}]$.

2.1.1 *Simulation program*

The WMC simulation program was written in ANSI C, adapting some parts from the *de facto* standard MC simulation program multi-layer Monte Carlo (MCML[7]). As the photon propagation is similar to traditional MC, we refer to the work of Wang et al.[7] and Prahl et al.[16] for basic Monte Carlo theory. Here, we present features differing from their work.

An important change is the adaptation of a state-of-the-art pseudo-random number generator, the Mersenne twister by Saito and Matsumoto.[17] The implementation used was the double-precision SIMD-oriented fast Mersenne twister (dSIMD) version 1.2.1, featuring a $2^{132049}-1$ period, documented excellent equidistribution properties, and fast random number generation. The entire 32-bit output of the *time ()* function in C was used to seed the generator.

Photons are launched from the origin of a Cartesian coordinate system (as in MCML). The launch direction is in the positive z direction (downward) with the addition of a deflection angle, θ, representing the emission cone of the source fiber, defined by the NA of the fiber, $\theta_{max} = \arcsin(NA/n)$. The angular distribution is assumed flat, i.e., $\cos\theta = 1 - \xi(1 - \cos\theta_{max})$, where ξ is a random number, $\xi \epsilon [0,1)$. Although unnecessary in a cylindrically symmetric problem, the azimuthal angle φ is also randomized, $\varphi = 2\pi\xi$, where $\xi \epsilon [0,1)$. Note that taking the angular distribution of the source fiber into account prevents post-simulation scaling of the refractive index. Thus, different WMC simulations are required in order to handle different fiber *NA*, as well as different refractive indices.

The step size, Δs, is calculated using the scattering coefficient instead of the total attenuation coefficient. It is defined in Eq. (2):

$$\Delta s = \frac{-\ln(\xi)}{\mu_s^{\max}}, \tag{2}$$

where ξ is a random variable, $\xi \epsilon (0,1]$, implying $\Delta s \epsilon [0,\infty)$. As in MCML, the actual photon scattering is simulated using the Henyey-Greenstein phase function.

The photon detection scheme assumes that the source and detector optical fibers are parallel, having their tips in the same plane (a plane to which the fibers are also assumed to be orthogonal). This corresponds to the settings followed in the interstitial clinical measurements on human prostate tissue presented in Ref. 5, where optical fibers are inserted to the same depth. Regardless of whether simulations are performed in the infinite or semi-infinite geometry, a potential photon detection event requires that a photon path crosses the source-detector plane.

In the case of an infinite medium, photons passing upward through the source-detector plane, being within the acceptance cone of the detector fiber, may be detected. Such a crossing is referred to as a *detection event* and is always registered by storing its radial distance from the source r, as well as its total time-of-flight t. For memory conservation, storing is done using 32-bit floating point variables. Since the photon is propagating in an infinite medium, and since the position of the detector fiber is undefined, the photon is, however, not terminated at this point. Instead, photon termination occurs only when the time reaches t_{max}. Note that this implies that a single photon may generate multiple detection events. These events are considered independent by the proposed WMC scheme, inducing a small error in generated time-of-flight histograms. This issue is further discussed in Sec. 2.1.3.

For the case of a semi-infinite geometry, the source-detector plane equals the medium boundary. Photons escaping the medium at an angle within the acceptance cone of the detector fiber generate detection events, i.e., r and t are recorded. Here, a notable difference from traditional Monte Carlo in semi-infinite geometries is that partial reflections are not allowed by WMC (the weight of the photons are not monitored). Instead, the reflection coefficient is compared to a random number, and the photons are either reflected or transmitted and terminated. Note that this also means that the semi-infinite detection geometry does not suffer from the risk of double-detecting photons. Note also that photons are terminated not only upon boundary crossing, but also when the time exceeds the predefined maximum time-of-flight t_{max}.

2.1.2 *Post-simulation processing*

The database of detection events (r, t pairs) from the simulation are sorted with respect to r. This is done using the fast {$O[n\log(n)]$ worst-case time complexity} in-place sorting algorithm Combsort11.[18] The $O(1)$ memory usage of the Combsort11 algorithm enables sorting and usage of databases of sizes close to the physical memory of the computer used.

The sorted database is used by a MATLAB function generating photon time-of-flight distributions. This function is employed as the forward model in an iterative solver and is called with the following input parameters: μ_a and μ_s' being the optical properties corresponding to the resulting time-of-flight distribution, the temporal channel width Δt, source-detector separation ρ, and the fiber radius R_f (experiments typically involve two identical fibers). The first task is to calculate the scaling coefficient $\alpha = \mu_s^{max}/\mu_s (\alpha \geq 1)$. The r, t pairs within the spatial interval $\rho - 2R_f < \alpha r < \rho + 2R_f$ are extracted and scaled ($r' = \alpha r$, $t' = \alpha t$). As the r, t pairs are sorted with respect to r, the selecting process turns into a simple task of finding the borders of the spatial interval, which is done quickly using a standard binary search algorithm. The interval itself is motivated by the convolution of each detection event with the size of the source fiber combined with the size of the detector fiber. A photon will hence contribute to the time dispersion histogram as soon as its distance to the center of the detector fiber is less than $2R_f$. Each photon detection event is assigned a weight, $w_f(r')$, according to its spatial position. This weight is based on the overlap between two circles of radius R_f, one centered at the detection event and one centered at the detector location. More precisely, the weight is reached after integration over all origin-to-detector angles (rotating the detector circle around the z axis). This is similar to work by Wang et al.[19] and Prahl.[20] As the fiber radius and the

source-detector separation is known when evaluating data, the weight $w_f(r')$ can be precalculated, and the computationally costly integrals do not have to be evaluated for each photon. A uniform near-field irradiance distribution of the fibers was assumed in this work, although any distribution could be utilized with minimal modifications.

The photon detection events are also assigned a weight due to absorption, $w_a(t')=\exp(-\mu_a c' t')$, where c' is the local speed of light. The total weight for each detection event is thus $w_{tot}=w_f \cdot w_a$.

The final step is a simple matter of creating a weighted histogram of the (t', w_{tot}) data, where the temporal channel width, Δt, can be specified by the user.

2.1.3 *Entangled detection events*

As mentioned earlier, a single photon may generate multiple detection events (a primary event, a secondary event, and so on). All such events should contribute to the final time-of-flight histogram (given that they are located within the detection range $\rho-2R_f<r'<\rho+2R_f$). However, if the spatial distance between two such events is less than $2R_f$, their weights cannot be considered independent, and there is a risk for erroneous additions of weight to the final histogram. The worst case is if the two events coincide spatially (zero event distance), a case in which the entire weight contributed by the secondary event is erroneous. In contrast, when the spatial event separation is $2R_f$ or greater, none of its contribution is erroneous. For event separations between zero and $2R_f$, the matter is nontrivial. In general, the erroneously added weight decreases with event separation. An estimate of the total amount of erroneous weight is reached by studying the multiple detection events occurring during the WMC simulations. For the case of $\mu_s'=10\ \mathrm{cm}^{-1}$, $g=0.7$, $NA=0.29$, and $R_f=0.3$ mm, we found that 0.5% of the primary events are accompanied by a secondary event less than $2R_f$ away (and only 0.1% within R_f). Assuming that all corresponding weight is erroneous (clearly an exaggeration of the problem), we can note that the final photon time-of-flight histogram contains less than 0.5% erroneous weight. Although this suggests that the problem of entangled detection events is insignificant, it may deserve further attention.

2.1.4 *Verification*

In an effort to validate the WMC simulation program code and the implementation of the scaling relationships, the open source program MCML was carefully modified to monitor the time-of-flight histograms of photons leaving a homogenously scattering, semi-infinite medium. The photon weights leaving the medium within the 1-mm-wide spatial bins, centered around 10, 15, and 20 mm, were recorded with 10-ps temporal resolution. 10^8 photons were simulated at $g=0.7$ and $n=1.33$ for all combinations of $\mu_s'=5$, 10 cm^{-1} and $\mu_a=0.1$, 0.5 cm^{-1}.

2.2 *Time-Resolved Instrumentation*

Time-resolved photon migration experiments were conducted using a compact ($50\times50\times30\ \mathrm{cm}^3$) and portable time-domain photon migration instrument primarily intended for spectroscopy of biological tissues in clinical environments. Detailed information on the instrumentation can be found in previous publications.[5,21,22] Briefly, the system is based on pulsed diode laser technology and time correlated single photon counting (TCSPC). Four pulsed diode lasers (at 660, 786, 830, and 916 nm, respectively) generate pulses having a FWHM of about 70 ps, the average power being 1 to 2 mW. Light is injected into the sample and collected using 600-μm GRIN optical fibers ($NA=0.29$). A fast MCP-PMT together with a TCSPC computer card is used to obtain photon time-of-flight histograms. Broadening in fibers and detector yields an instrument response function (IRF) of about 100-ps FWHM. The IRF is measured by putting the fiber ends face to face with a thin paper coated on both sides with black toner, similar to the IRF measurements proposed by Schmidt et al.[23] A schematic illustration of the setup is given in Fig. 3.

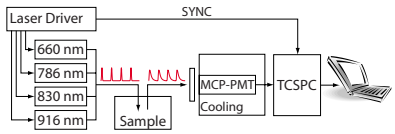

Fig. 3 A schematic of the instrumentation in interstitial mode.

2.3 *Experiment*

In order to compare diffusion-based and WMC-based evaluation of experimental data, measurements were performed on tissue phantoms based on Intralipid (Fresenius Kabi 200 mg/ml) and ink (1:100 stock solution of Pelikan Fount India ink).[24]

Two measurement series were performed: one added absorber series using ink,[25] and one added scatterer series using Intralipid.[26,27] Neglecting the minor volume change occurring during these measurement series, we can qualitatively expect a constant scattering and linearly increasing absorption in the added absorber series. In addition, when extrapolating of derived μ_a toward the zero ink level, the absorption should be close to the absorption exhibited by pure water.

Similarly, the added scatterer series should yield a constant absorption, linearly increasing scattering. Extrapolation of the derived scattering coefficient toward the zero Intralipid level should yield a zero scattering (at least if ink scattering is negligible).

The added absorber series was performed on a phantom based on 577 ml water and 22 ml Intralipid. Measurements were performed at 2 to 8 ml total volume of added ink solution (1-ml increments). The added scatterer series was performed on a phantom based on 577 ml water and 4 ml ink solution. Measurements were performed at 10 to 24 ml added volume of Intralipid (in 2-ml increments). A cylindrical plastic container, $\varnothing=110$-mm and height=70 mm, was used to hold the phantoms during mixing and measurements. The container was placed on a magnetic stirrer, utilized for mixing of the phantoms after each addition of ink or Intralipid. Fibers were placed in parallel at 30-mm depth in the center of the phantom, separated 14.7 mm, center to center. Data acquisition was performed for 30 s for each measurement, and the IRF was measured before, after, and occasionally between the measurements (monitoring potential temporal drifts in the system).

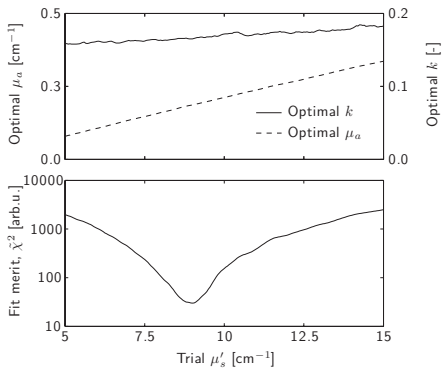

Fig. 4 WMC fitting procedure of the experimental data featuring the 2-ml added ink absorption series measurement at 660 nm, ρ =14.7 mm.

2.4 *Modeling*

The agreement between the diffusion approximation and MC is investigated by fitting analytical solutions of the diffusion equation to the impulse responses as delivered by WMC (along the lines of, e.g., Refs. 3 and 12). Such diffusion modeling is based on iterative nonlinear Levenberg-Marquardt curve fitting, in which μ_a, μ_s', and an amplitude factor, k, are varied in order to minimise a χ^2 merit function.[3,28] For the interstitial case (infinite geometry, see, e.g., Ref. 1), the form of the diffusion-based impulse response is stated in Eq. (3):

$$y(\mu_a,\mu_s',k,t) = kt^{-3/2}\exp\left(-\frac{3\mu_s'\rho^2}{4c't}-\mu_a c't\right), \qquad (3)$$

where ρ is the source-detector separation, and c' is the speed of light in the sample. To reach this expression, we use the absorption-independent definition of the diffusion coefficient, $D=(3\mu_s')^{-1}$. During evaluation of experimental data, the procedure described earlier involves a convolution with the system IRF.

When WMC is used for modeling, the fitting procedure is based on an exhaustive search over μ_s'. That is, for each value in a set of trial values of μ_s', the optimal choice of μ_a and k is determined in a suboptimization procedure. The suboptimized error norm, $\tilde{\chi}^2(\mu_s')$, is given in Eq. (4):

$$\tilde{\chi}^2(\mu_s') = \min_{k,\mu_a}\{\chi^2(k,\mu_a,\mu_s')\}, \qquad (4)$$

and is thus to be exhaustively searched on some appropriate μ_s' grid. In this work, $\tilde{\chi}^2(\mu_s')$ is evaluated in steps of 0.05 cm^{-1}. An example of this procedure is given in Fig. 4.

This article uses an MC database for infinite geometries (interstitial measurements) consisting of about 8×10^7 detection events, originating from a simulation of 2×10^8 photons. The database for semi-infinite evaluations is of a similar size, resulting from a simulation of 10^9 photons. Both these databases are based on simulations where g=0.7, n=1.33, NA =0.29, μ_s^{max}=90 cm^{-1}, and t_{max}=2 ns. A single forward modeling (that is, a generation of a time-of-flight histogram from the previously stored database) can be performed in less than one second. Using the exhaustive search described earlier, the best fit is found in approximately 15 s.

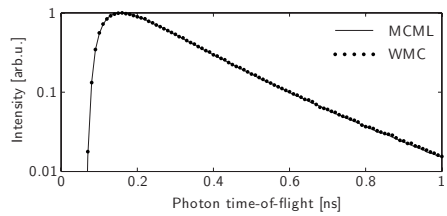

Fig. 5 Illustration of the agreement between MCML and the proposed WMC. In this particular case, the source-detector separation is 15 mm, μ_s'=5 cm^{-1}, and μ_a=0.1 cm^{-1}.

It should also be noted that, unless otherwise stated, all evaluations are based on fittings in the temporal range defined by the 50% level (of peak maximum) on the rising flank and the 20% level on the tail.

3 Results

3.1 *White Monte Carlo Performance*

The performance of our WMC approach was investigated and verified for the case of diffuse reflectance by comparing its output with that of MCML. The optical properties examined were combinations of μ_s'=5, 10 cm^{-1} and μ_a=0.1, 0.5 cm^{-1}, as described in Sec. 2.1.4. Evaluating the time-resolved MCML data with WMC shows only minor differences, despite major differences in for example spatial binning. The relative difference between derived optical properties and MCML input parameters was only $1\pm4\%$ in absorption, and $0\pm2\%$ for reduced scattering (mean $\pm$ st.dev.). An illustration of this agreement is shown in Fig. 5.

3.2 *WMC Versus Diffusion Modeling*

That the use of diffusion modeling is questionable in the low albedo regime is easily shown by simple visual comparison of the impulse responses as delivered by the diffusion approximation and WMC, respectively. An example of this is given in Fig. 6, using optical properties encountered in the human prostate (at wavelengths in the range 650 to 900 nm).

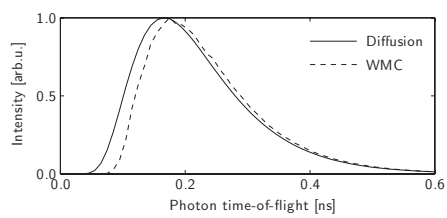

Fig. 6 Illustration of the breakdown of the diffusion approximation in the low albedo regime of photon migration. In this particular case, the data correspond to an infinite (interstitial) geometry using a 15-mm source-detector separation, with μ_s'=7.5 cm^{-1}, and μ_a=0.5 cm^{-1}.

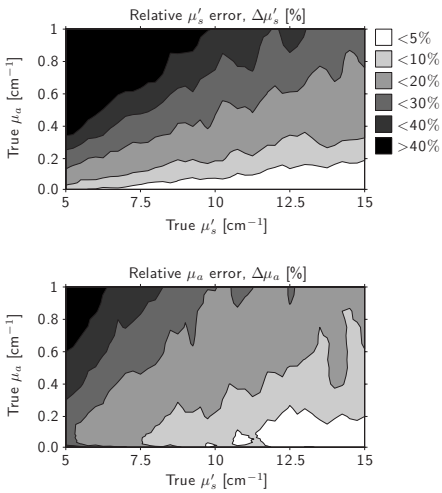

Fig. 7 Relative errors due to diffusion modeling. Since the relative errors are positive throughout the examined range, diffusion modeling results in overestimation of both scattering and absorption. Fitting is performed between the 50% level (of peak maximum) on the rising flank and the 20% level on the tail. The gray scale applies to both graphs.

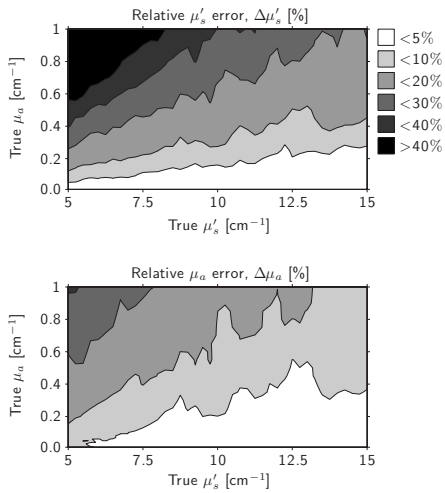

Fig. 8 Relative errors due to diffusion modeling when fitting is performed between the 80% level (of peak maximum) on the rising flank and the 1% level on the tail. As in Fig. 7, diffusion modeling results in overestimation of both scattering and absorption. The gray scale applies to both graphs.

In order to quantitatively investigate the performance of diffusion modeling for the range of optical properties explored in this work, the analytical expression for the diffusion-based impulse response was fitted to data delivered by WMC (at 10-ps time resolution). In order to mimic the experimental conditions, where the system IRF must be accounted for, data was convoluted with a synthetic, 70-ps FWHM Gaussian prior to curve fitting. The parameter space covered in this investigation was:

$$0.01 \leqslant \mu_a \leqslant 1,$$

$$5 \leqslant \mu_s' \leqslant 15 \quad [\mathrm{cm}^{-1}].$$

In order to allow direct comparison with the diffusion modeling used in our previous work on *in vivo* characterization of human prostate tissue,[5] fitting was performed in the range defined by the 50% level (of peak maximum) on the rising flank, down to 20% on the tail. The WMC parameters, μ_{WMC} are considered as true optical properties, and relative errors in derived optical properties due to diffusion modeling are calculated as given in:

$$\Delta\mu = \frac{\mu_D - \mu_{WMC}}{\mu_{WMC}}, \tag{5}$$

where μ_D denotes the optical properties as derived by diffusion modeling. The result is shown in Fig. 7 and suggests that diffusion modeling will result in fairly large overestimations of both μ_a and μ_s'.

The influence of the selection of fit range has been discussed in several articles.[3,12,29] To address this issue, we present the performance of time-domain diffusion modeling also for the case of fitting in the range defined by the 80% level (of peak maximum) on the rising flank, down to the 1% level on the tail. The results are shown in Fig. 8. Although the use of a reduced fit range slightly improves the performance of diffusion modeling, it is clear that significant overestimation remains.

In order to predict the outcome of the experimental procedures described in Sec. 2.3, we employ diffusion modeling to interpret sets of WMC data where (1) μ_s' is kept constant, while μ_a gradually increases (added absorber series), and (2) μ_a is kept constant, while μ_s' gradually increases (added scatterer series). These two simulation series correspond to two-dimensional (2-D) sections in the three-dimensional (3-D) maps shown in Figs. 7 and 8. The outcome is shown in Figs. 9 and 10, clearly revealing the increasing model errors as we move further and further into the low albedo regime. For the added absorber series, note especially that the slope encountered in derived μ_a is steeper than the true increase, and that the constancy of μ_s' is replaced by a fairly linear increase. For the added scatterer series at μ_a=0.5 cm^{-1}, note the offset-like pattern for μ_s', as well as the remarkably poor agreement between true and derived μ_a at low values of μ_s'.

3.3 *Experimental Results*

The experimental results from the added absorber series, evaluated using both diffusion theory and WMC, are presented in Fig. 11. Here, derived μ_a appears to increase linearly when employing WMC evaluation, while diffusion

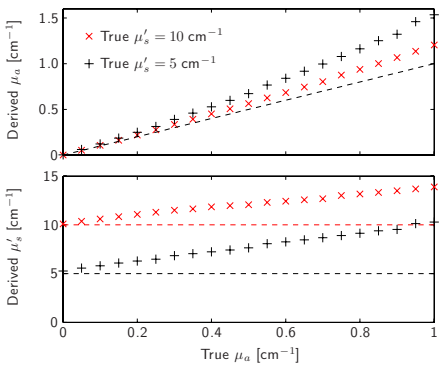

Fig. 9 Derived optical properties for two levels of μ_s' when diffusion modeling is used to interpret WMC data (corresponds to the added absorber series).

modeling appears to introduce a slight nonlinear increase. In addition, and in good agreement with the predictions presented in Sec. 3.2, diffusion evaluation gives rise to a steeper slope. Linear extrapolation of the WMC-derived absorption coefficient to the zero ink level produces estimations of background absorption as stated in Table 1. Turning to derived scattering, WMC produces almost constant estimations of μ_s', whereas diffusion theory undergoes a significant increase as more ink is added. Also this phenomenon agrees with our predictions.

The results from the added scatterer series are shown in Fig. 12. As predicted by our simulations, absorption coefficients derived with diffusion theory decrease heavily with the volume of added Intralipid. In contrast, μ_a remains constant when derived using WMC evaluation. Also, when turning the attention to scattering, the predictions from Sec. 3.2 hold. Although the response is linear, diffusion modeling produces significantly larger values of μ_s', in an offset-like manner

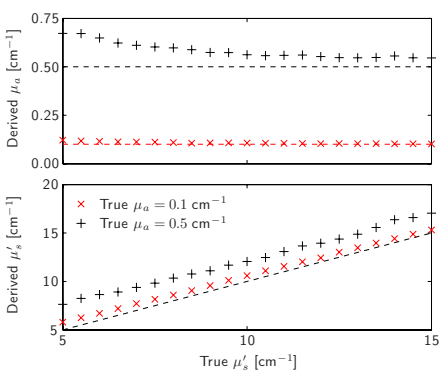

Fig. 10 Derived optical properties for two levels of μ_a when diffusion modeling is used to interpret WMC data (corresponds to the added scatterer series).

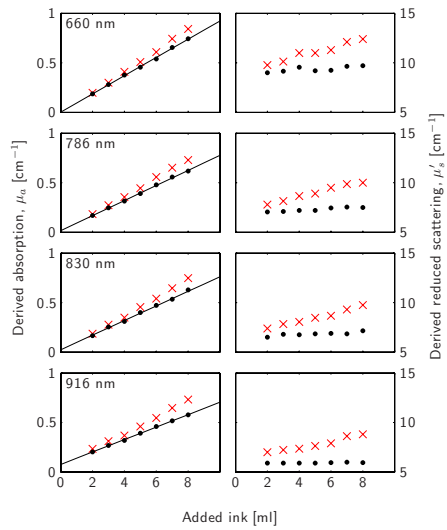

Fig. 11 The results from the added absorber series (adding ink to a liquid Intralipid phantom). Derived optical properties are given both for diffusion-based evaluation (crosses) and WMC-based evaluation (circles). The results are to be compared with the simulation results presented in Fig. 9.

(clearly not approaching zero scattering when extrapolating the Intralipid content to the zero level). A small offset is present also for WMC evaluation and may be related to ink scattering or temporal drifts.

When using the μ_s' slope (as provided by linear regression) to estimate the scattering of Intralipid, WMC evaluation yields values in good agreement with the levels reported by van Staveren et al.,[26] as shown in Table 2.

4 Discussion

This work establishes White Monte Carlo as a tool for evaluation of experimental time-resolved photon migration. At the

Table 1 Background absorption extrapolated from added absorber measurements (evaluated using WMC). As water is the principal absorber in the ink-free phantom, water absorption coefficients are stated for reference.

	μ_a(cm^{-1})	
λ(nm)	$\mu_a(0)$	Water
660	0.002	0.004
786	0.016	0.022
830	0.024	0.029
916	0.077	0.091

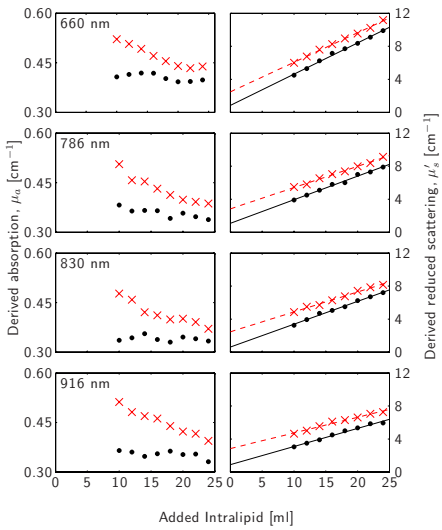

Fig. 12 The results from the added scatterer series (adding further Intralipid to a liquid phantom based on ink and Intralipid). Derived optical properties are given both for diffusion-based evaluation (crosses) and WMC-based evaluation (circles). The results are to be compared with the simulation results presented in Fig. 10.

same time, we clearly show that the diffusion approximation of light propagation should be used with great care when evaluating time-resolved spectroscopy in highly absorbing turbid media. For example, regardless of the fitting range used, the errors in derived optical properties due to diffusion modeling are about 10% or more in the regime of interest when modeling light propagation in the human prostate. Our hope is that this development will promote accurate assessment of, for example, the *in vivo* optical properties of human prostate tissue.

The minor differences observed when comparing MCML and WMC indicate that our approach, including both simulation and scaling procedures, is valid. The small discrepancies can be explained either by differences in spatial sampling or by limited photon statistics (signal to noise). It should be noted that the generated MCML data sets correspond to an infinitely small source and equal weighting of all photons appearing at a radial distance within 0.5 mm from the source-detector separation ρ. In contrast, our WMC simulations assumed that the source and detector fibers had a radius of 0.3 mm, performing individual photon weighting based on the spatial (radial) location of the detection event. Furthermore, the numerical apertures of the involved optical fibers were also accounted for. In fact, the limited differences suggest that the elaborate procedures used in order to take source and detector characteristics into account might be unnecessary. However, there might exist regimes of optical properties, or source-detector separations, where this still is a valuable approach. In this context, it should also be mentioned that the use of fixed acceptance cones (rather than *NA*-based) would allow scalability also with respect to the refractive index.

Table 2 Scattering of 200 mg/l Intralipid.

	μ_s'[cm^{-1}/(ml/l)]	
λ(nm)	This Work	Van Staveren et al.[26]
660	0.227	0.25
786	0.171	0.20
830	0.166	0.19
916	0.138	0.17

The inability of scaling Monte Carlo simulations with respect to the anisotropy factor g has been discussed in earlier work on White Monte Carlo.[10,12] The question is how a discrepancy between the actual g and the value used in simulations will influence derived values of μ_a and μ_s'. However, light propagation in the photon migration regime is known to fall under similarity as long as $\mu_s'=(1-g)\mu_s$ is conserved.[30] This means that an exact knowledge of g is not crucial and that a single WMC database may be used to model materials exhibiting different anisotropies. Pifferi et al.[12] argue that when using diffuse reflectance to solve for μ_s', the influence of the exact value of g is small at least as long as $0.7<g<0.9$. Similar findings are reported by Kienle and Patterson,[10] who concluded similarity in diffuse reflectance for short fiber separations (2.25 to 4.75 mm) as long as $g>0.8$.

The WMC-based data evaluation of the added absorber and added scatterer series removes the expected, but erroneous, patterns in derived optical properties exhibited when basing modeling on diffusion theory. In the added absorber series, WMC produces a highly linear increase in derived μ_a and a constant level of μ_s'. Extrapolating measured μ_a indicates a background absorption close to that of pure water. For the case of the added scatterer series, WMC evaluation results in a linearly increasing μ_s' together with a constant level of absorption. The small offsets in derived μ_s' when extrapolating toward the zero Intralipid level remains unexplained and may originate from temporal drifts and/or a nonzero scattering contribution from ink. In total, this forms a strong argument that the proposed WMC approach provides accurate estimations of optical characteristics. This is further supported by the fact that generated estimations of Intralipid scattering are in good agreement with previously published values (as shown in Table 2). However, a more detailed and quantitative discussion on accuracy is aggravated by the uncertainties in the optical properties of the utilized optical phantoms. The scattering of Intralipid is somewhat debated and may depend on batch-to-batch variations.[26,27] Moreover, ink is known to scatter light, making it difficult to accurately assess its absorption.[25]

Regarding the fit range, it has been shown that early photons should be excluded when using diffusion as the forward model. Cubeddu et al.[29] suggest the use of the range between the 80% level (of peak maximum) on the rising flank down to the 1% level on the tail (80/1). In this work, we mainly use a

50/20 range. This is to allow direct comparison with previously published modeling of *in vivo* time-resolved spectroscopy of the human prostate.[5] Although such a choice might be questioned, the 80/1 fitting range still suffers from significant model errors. This in combination with the availability of WMC evaluation renders further discussions on the optimal range for diffusion-based modeling somewhat irrelevant.

Furthermore, we would like to call for some attention regarding the step-sizes used in Monte Carlo simulations. Swartling questions whether the White Monte Carlo approach, including all scalable Monte Carlo approaches based on simulations in nonabsorbing media, is equivalent to the *de facto* standard Monte Carlo approach.[14] Conventional Monte Carlo utilizes an average step-size of $1/\mu_t = 1/(\mu_a + \mu_s)$, whereas a WMC approach uses a $1/\mu_s$ average step-size. This means that the photon paths generated by the two methods will differ if μ_a is nonzero. Since traditional Monte Carlo for light propagation in turbid media assumes that scattering dominates absorption ($\mu_s \gg \mu_a$, high albedo), this has not been considered as an important source of discrepancy.[31] Furthermore, the methods for reduction of photon weights differ. Traditional MC reduces the photon weight by a factor of a at each scattering event [$a = \mu_s/(\mu_a + \mu_s)$ being the albedo], while WMC follows the conventional Beer-Lambert law of absorption. Swartling argues that the two ways of absorbing weight are equivalent at the extremes, that is, when $a \to 1$ or $a \to 0$, but notes that equivalence is not guaranteed in the intermediate region where $\mu_s \approx \mu_a$. Since WMC does not rely on the high albedo assumption, this method should be more reliable in the regime when scattering and absorption coefficients are of comparable magnitude. (For an example of non-white MC without being based on the high albedo assumption, we refer to the work of Farina et al.[32]). In most types of biological tissue, the difference between traditional MC and WMC can, however, be disregarded.

Finally, it should be noted that if the Monte Carlo approach described in this work is considered for use in steady-state investigations, the procedures for photon termination deserve extra attention. Terminating photons when the time-of-flight exceeds t_{max} may impose errors during steady-state analysis of generated WMC databases.

5 Conclusion

We have developed a quick and accurate scheme for Monte Carlo–based evaluation of experimental time-resolved spectroscopy of highly scattering materials. We show, for the first time, evaluations of experimental interstitial time-domain photon migration using fully scalable White Monte Carlo. The great value of this approach is demonstrated in a regime where diffusion-based modeling results in fairly large errors (overestimations of both μ_s' and μ_a). The relevance of this regime is, for example, motivated by the recent interest in the optical properties of human prostate tissue, where $\mu_a > 0.3$ cm^{-1} and $\mu_s' < 10$ cm^{-1}.

Acknowledgments

We gratefully acknowledge financial support from the Wallenberg Foundation and through the EC Grant Nano-UB Sources (IST-2005-017128).

References

1. M. S. Patterson, B. Chance, and B. C. Wilson, "Time resolved reflectance and transmittance for the noninvasive measurement of tissue optical-properties," *Appl. Opt.* **28**(12), 2331–2336 (1989).
2. S. T. Flock, M. S. Patterson, B. C. Wilson, and D. R. Wyman, "Monte Carlo modeling of light-propagation in highly scattering tissues: I. model predictions and comparison with diffusion-theory," *IEEE Trans. Biomed. Eng.* **36**(12), 1162–1168 (1989).
3. A. H. Hielscher, S. L. Jacques, L. H. Wang, and F. K. Tittel, "The influence of boundary-conditions on the accuracy of diffusion-theory in time-resolved reflectance spectroscopy of biological tissues," *Phys. Med. Biol.* **40**(11), 1957–1975 (1995).
4. M. L. Pantelides, C. Whitehurst, J. V. Moore, T. A. King, and N. J. Blacklock, "Photodynamic therapy for localized prostatic cancer—light penetration in the human prostate-gland," *J. Urol. (Baltimore)* **143**(2), 398–401 (1990).
5. T. Svensson, M. Einarsdóttír, K. Svanberg, and S. Andersson-Engels, "*In vivo* optical characterization of human prostatic tissue using near-infrared time-resolved spectroscopy," *J. Biomed. Opt.* **12**(1), 014022 (2007).
6. B. C. Wilson and G. Adam, "A Monte Carlo model for the absorption and flux distributions of light in tissue," *Med. Phys.* **10**(6), 824–830 (1983).
7. L. H. Wang, S. L. Jacques, and L. Q. Zheng, "MCML Monte Carlo modeling of light transport in multilayered tissues," *Comput. Methods Programs Biomed.* **47**(2), 131–146 (1995).
8. J. Swartling, A. Pifferi, A. M. K. Enejder, and S. Andersson-Engels, "Accelerated Monte Carlo models to simulate fluorescence spectra from layered tissues," *J. Opt. Soc. Am. A* **20**(4), 714–727 (2003).
9. N. Everall, T. Hahn, P. Matousek, A. W. Parker, and M. Towrie, "Photon migration in Raman spectroscopy," *Appl. Spectrosc.* **58**(5), 591–597 (2004).
10. A. Kienle and M. S. Patterson, "Determination of the optical properties of turbid media from a single Monte Carlo simulation," *Phys. Med. Biol.* **41**(10), 2221–2227 (1996).
11. A. Pifferi, R. Berg, P. Taroni, and S. Andersson-Engels, "Fitting of time-resolved reflectance curves with a Monte Carlo model," in *Trends in Optics and Photonics: Advances in Optical Imaging and Photon Migration* (1996).
12. A. Pifferi, P. Taroni, G. Valentini, and S. Andersson-Engels, "Real-time method for fitting time-resolved reflectance and transmittance measurements with a Monte Carlo model," *Appl. Opt.* **37**(13), 2774–2780 (1998).
13. R. Graaff, M. H. Koelink, F. F. M. Demul, W. G. Zijlstra, A. C. M. Dassel, and J. G. Aarnoudse, "Condensed Monte Carlo simulations for the description of light transport," *Appl. Opt.* **32**(4), 426–434 (1993).
14. J. Swartling, "Biomedical and atmospheric applications of optical spectroscopy in scattering media," PhD Thesis, Lund University (2002).
15. H. P. Xu, T. J. Farrell, and M. S. Patterson, "Investigation of light propagation models to determine the optical properties of tissue from interstitial frequency domain fluence measurements," *J. Biomed. Opt.* **11**(4), 041104 (2006).
16. S. A. Prahl, M. Keijzer, S. L. Jacques, and A. J. Welch, "A Monte Carlo model of light propagation in tissue," in *Dosimetry of Laser Radiation in Medicine and Biology*, G. J. Müller and D. H. Sliney, eds., **IS 5**, SPIE, Bellingham, WA, 102–111 (1989).
17. M. Saito and M. Matsumoto, "SIMD-oriented fast Mersenne twister: a 128-bit pseudorandom number generator," in *MCQMC 2006 Proc.* (2006).
18. S. Lacey and R. Box, "A fast, easy sort," *BYTE* **16**(4), 315 (1991).
19. L. Wang, S. L. Jacques, and L. Zheng, "CONV-convolution for responses to a finite diameter photon beam incident on multi-layered tissues," *Comput. Methods Programs Biomed.* **54**, 141–150 (1997).
20. S. A. Prahl, "Light transport in tissue," PhD Thesis, Univ. Texas Austin (1988).
21. T. Svensson, J. Swartling, P. Taroni, A. Torricelli, P. Lindblom, C. Ingvar, and S. Andersson-Engels, "Characterization of normal breast tissue heterogeneity using time-resolved near-infrared spectroscopy," *Phys. Med. Biol.* **50**(11), 2559–2571 (2005).
22. A. Pifferi, A. Torricelli, et al., "Performance assessment of photon migration instruments: the MEDPHOT protocol," *Appl. Opt.* **44**(11), 2104–2114 (2005).
23. F. E. W. Schmidt, M. E. Fry, E. M. C. Hillman, J. C. Hebden, and D.

T. Delpy, "A 32-channel time-resolved instrument for medical optical tomography," *Rev. Sci. Instrum.* **71**(1), 256–265 (2000).
24. B. W. Pogue and M. S. Patterson, "Review of tissue simulating phantoms for optical spectroscopy, imaging, and dosimetry," *J. Biomed. Opt.* **11**(4), 041102 (2006).
25. S. J. Madsen, M. S. Patterson, and B. C. Wilson, "The use of india ink as an optical absorber in tissue-simulating phantoms," *Phys. Med. Biol.* **37**(4), 985–993 (1992).
26. H. J. van Staveren, C. J. M. Moes, J. van Marle, S. A. Prahl, and M. J. C. Vangemert, "Light scattering in intralipid-10-percent in the wavelength range of 400–1100 nm," *Appl. Opt.* **30**(31), 4507–4514 (1991).
27. S. T. Flock, S. L. Jacques, B. C. Wilson, W. M. Star, and M. J. C. Vangemert, "Optical properties of intralipida phantom medium for light-propagation studies," *Lasers Surg. Med.* **12**(5), 510–519 (1992).
28. C. Abrahamsson, T. Svensson, S. Svanberg, S. Andersson-Engels, J. Johansson, and S. Folestad, "Time and wavelength resolved spectroscopy of turbid media using light continuum generated in a crystal fiber," *Opt. Express* **12**(17), 4103–4112 (2004).
29. R. Cubeddu, A. Pifferi, P. Taroni, A. Torricelli, and G. Valentini, "Experimental test of theoretical models for time-resolved reflectance," *Med. Phys.* **23**(9), 1625–1633 (1996).
30. R. Graaff, J. G. Aarnoudse, F. F. M. Demul, and H. W. Jentink, "Similarity relations for anisotropic scattering in absorbing media," *Opt. Eng.* **32**(2), 244–252 (1993).
31. S. L. Jaques and L. Wang, "Monte Carlo modeling of light transport in tissues," Chapter 4, *Optical-Thermal Response of Laser-Irradiated Tissue*, pp. 73–100, Plenum Press, New York, (1995).
32. B. Farina, S. Saponaro, E. Pignoli, S. Tomatis, and R. Marchesini, "Monte Carlo simulation of light fluence in tissue in a cylindrical diffusing fiber geometry," *Phys. Med. Biol.* **44**, 1–11 (1999).

Paper XI

High sensitivity gas spectroscopy of porous, highly scattering solids

T. Svensson, M. Andersson, L. Rippe, J. Johansson, S. Folestad, and S. Andersson-Engels.

Optics Letters **33**, 80-82 (2008).

80 OPTICS LETTERS / Vol. 33, No. 1 / January 1, 2008

High sensitivity gas spectroscopy of porous, highly scattering solids

Tomas Svensson,[1,*] Mats Andersson,[1] Lars Rippe,[1] Jonas Johansson,[2] Staffan Folestad,[2] and Stefan Andersson-Engels[1]

[1]*Department of Physics, Lund University, SE-221 00 Lund, Sweden*
[2]*Astra Zeneca Research and Development, SE-431 83 Mölndal, Sweden*
[*]*Corresponding author: tomas.svensson@fysik.lth.se*

Received October 23, 2007; revised November 20, 2007; accepted November 20, 2007;
posted November 29, 2007 (Doc. ID 88933); published December 21, 2007

We present minimalistic and cost-efficient instrumentation employing tunable diode laser gas spectroscopy for the characterization of porous and highly scattering solids. The sensitivity reaches 3×10^{-6} (absorption fraction), and the improvement with respect to previous work in this field is a factor of 10. We also provide the first characterization of the interference phenomenon encountered in high-resolution spectroscopy of turbid samples. Revealing that severe optical interference originates from the samples, we discuss important implications for system design. In addition, we introduce tracking coils and sample rotation as new and efficient tools for interference suppression. The great value of the approach is illustrated in an application addressing structural properties of pharmaceutical materials. © 2007 Optical Society of America

OCIS codes: 300.6320, 120.6200, 290.4210, 170.7050, 170.5280, 120.4290.

High-resolution diode laser absorption spectroscopy (TDLAS) is a well established tool for selective and sensitive gas analysis and has proved its value in many areas of science, as well as in industrial applications [1,2]. The sensitivity of the technique is often improved by employing various noise reduction schemes, such as wavelength modulation spectroscopy (WMS) [3,4]. Since 2001, TDLAS and WMS have also been used for the sensing of gases dispersed within highly scattering media [5]. This approach, often referred to as gas in scattering media absorption spectroscopy (GASMAS), has since then been successfully used for the characterization of various materials, such as polystyrene foam [5,6], wood [7], fruit [8], biological tissue [9], and pharmaceutical solids [10]. However, GASMAS experiments suffer from a much lower sensitivity than the traditional use of TDLAS. By traditional use, we refer to setups with well-defined beam lines together with known and controllable interaction length (often using gas cells). In such a setup, sensitivities are often in the 10^{-7} range. In contrast, measurements of gas content in highly scattering solid samples involve dealing with severe backscattering, heavy attenuation, diffuse light, and uncontrollable and unknown interaction lengths. Sensitivities better than $\sim5\times10^{-5}$ have never been reported until now. In the case of oxygen sensing at ~760 nm, an absorption fraction of 5×10^{-5} corresponds to more than a 1 mm path length in ambient air (1 mm L_{eq}). It should also be noted that these results have been achieved by imposing vibrations on the experimental setup (averaging out interference fringes). However, limited effort has been directed toward the understanding of the limitations in GASMAS.

In this Letter we have focused on understanding and restraining the negative effects of multiple scattering and have obtained a tenfold increase in GASMAS sensitivity in this way, reaching down to absorption fractions of 3×10^{-6} (a 1σ measure at 60 s acquisition time, see Figs. 3 and 4). In addition, this is the first detailed characterization of GASMAS performance, as well as the first investigation of the optical interference phenomena that limits measurement quality. Our findings have important implications for the design of GASMAS instrumentation. Finally, the gained sensitivity is sufficient to fully match the needs in most applications, and thus makes the technique very attractive.

We employ a minimalistic, single-beam WMS-TDLAS instrumentation based on oxygen sensing with a vertical-cavity surface-emitting laser (VCSEL). The instrumentation is schematically described in Fig. 1. Briefly, a 0.3 mW VCSEL (V-763-OXY-MTE, Laser Components) is wavelength tuned over one of the absorption lines in the R branch of molecular oxygen [R9Q10, 760.654 nm vacuum wavelength, peak absorption coefficient $\mu_a=2.83\times10^{-5}\,\mathrm{mm}^{-1}$ in ambient air, according to high-resolution transmission molecular absorption database (HITRAN)]. The modulation signal is created by an arbitrary waveform generator (AWG) (CH-3150, Exacq Technologies) running at 19.3536 MS/s, and

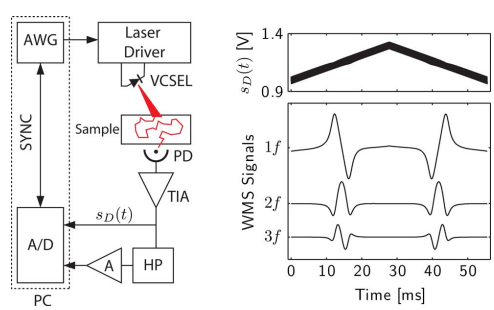

Fig. 1. (Color online) Schematic of the WMS-TDLAS instrumentation, together with sensor and WMS signals (obtained in ambient air measurements).

0146-9592/08/010080-3/$15.00

consists of a triangular ramp (at 18 Hz) that provides a linear frequency sweep and a superimposed harmonic oscillation (18.432 kHz) that allows WMS. In contrast to earlier work, neither optical fibers nor collimating optics are involved. Thus, a divergent beam is injected into our samples (multiple scattering renders collimation superfluous). Light is detected using a 5.6 mm × 5.6 mm large-area photodiode (S1337-66BR, Hamamatsu Photonics), and the resulting detector signal is amplified using a low noise transimpedance amplifier (TIA) (DLPCA-200, FEMTO Messtechnik). Data are sampled at 2.4192 MS/s using an analog-to-digital (A/D) board (NI-6132, National Instruments). For improved sensitivity, a high-pass (HP) filtered and amplified (A) version of the detector signal is also sampled. Laser modulation and data acquisition are synchronized, allowing scan averaging and powerful data postprocessing (without the need of lock-in amplification). This approach has been described by Fernholz *et al.* [11]. Although the technique inherently provides multiharmonic WMS detection, all data presented here are based on the second harmonic ($2f$) only. Measurements in ambient air (without a scattering material between laser and detector) show that the system sensitivity is 1×10^{-6} or better (60 s acquisition time). The system is carefully calibrated in ambient air, and obtained WMS signals are later used as absolute references during quantitative analysis of GASMAS data (i.e., curve fitting using a known experimental WMS signal provides the GASMAS L_{eq}). Furthermore, as expected from WMS theory, the intensity-corrected $2f$ WMS peak signal is observed to be ~0.3 times the actual absorption fraction [12].

The system performance in GASMAS is characterized by the use of highly scattering, nonporous epoxy samples (10 mm diameter and 3 mm thick) [13]. These samples were manufactured to mimic the optical properties of pharmaceutical solids. By employing photon time-of-flight spectroscopy and diffusion modeling, the reduced scattering coefficient was estimated to ~40 mm^{-1} and the absorption coefficient to $\sim 5 \times 10^{-3}$ mm^{-1} (the average optical path length in transmission is of the order of 100 mm). GASMAS measurements on such samples are expected to exhibit oxygen absorption only to the extent of the optical path length offset (space between VCSEL and sample surface). However, even when the path length offset is several millimeters, the registered WMS signal as acquired under static conditions exhibits nothing but a severe optical interference pattern. That the observed signal really is an optical interference pattern is inferred from the symmetry with respect to the triangular scan. Measurements over several minutes reveal that this pattern is stable. However, any small adjustment of either sample or laser position causes a complete change of the interference. This means that mechanical dithering enables us to convert this random (but stable) interference pattern into true interference noise and suppress it by means of waveform averaging.

To quantify interference, the WMS scan was adjusted to place the oxygen absorption imprint in the edge of our scans (close to the top of the triangular scan). We then use the standard deviation of the interference signal (in the region of no oxygen imprint), I_σ, as a measure of interference level. Figure 2(a) illustrates this procedure, and Figs. 2(b) and 2(c) show how I_σ is influenced by the laser-sample separation. Interestingly, shown in Fig. 2(b), the interference level does not decrease much as the laser is moved further away from the sample. Even when a 75 mm path is added, yielding an absorption fraction of $\sim 2 \times 10^{-3}$ and a WMS peak of 6×10^{-4}, the oxygen imprint is heavily distorted by random interference. If the sample is removed (and replaced by a filter to ensure similar intensity), the I_σ level drops more than 1 order of magnitude. These experiments rule out the possibility that the random interference signal is due to optical feedback into the VCSEL. Instead, it is clear that the observed random interference is due to the sample. The slight increase in I_σ for short distances can possibly be assigned to changes in injection spot size.

The fact that both the utility signal (oxygen absorption) and the limiting random interference signal are generated inside the sample has important implications for the design of GASMAS instrumentation. For example, the dual beam approach used in our previous work on pharmaceutical characterization [10], should not be capable of efficient interference suppression in GASMAS. This is in agreement with our experiences from that work, where we found it essential to impose vibrations to reveal the oxygen imprint.

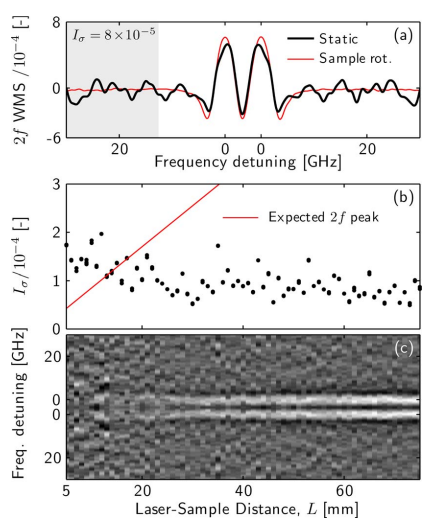

Fig. 2. (Color online) Optical interference encountered in GASMAS is exemplified in (a) (75 mm added path). There, we also show the signal measured with sample rotation (a procedure described below). Influence of the laser-sample distance is presented quantitatively in (b). The increase in the oxygen signal as L is increased is shown in (c), using a free-space oxygen response as reference (right side of image).

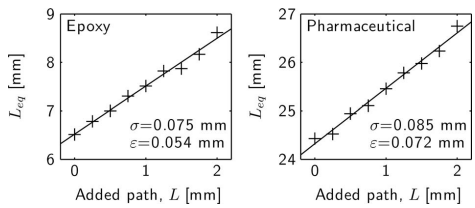

Fig. 3. Sensitivity analysis by means of standard addition and sample rotation. Residual standard deviation σ, and average absolute deviations, ε, for linear regression are stated. In epoxy measurements, the obtained signal originates from the ambient air path between laser and sample. Since the same path offset is present in the pharmaceutical data, the oxygen imprint for the tablet is ~18 mm L_{eq}.

To overcome the random interference described above, we now propose the use of sample rotation and tracking coils as efficient tools for interference to noise conversion. Tracking coils consists of a lens mounted close to two coils, allowing adjustment of the lens position, and is found in virtually all CD players. If the sample shape renders rotation impossible or inconvenient, this device can be positioned between the laser and the sample. By seeding the coils with appropriate signals, it allows controlled beam dithering as an alternative to sample rotation. Data presented below are acquired using ~1 turn/s sample rotations or low frequency (<100 Hz) feeding of tracking coils.

To measure system performance, we conducted two independent experiments. The first is based on the standard addition technique normally used in chemical analysis (determination of concentrations in unknown samples). It involves adding ambient air path lengths between the laser and the sample and the monitoring of the change in oxygen absorption. The second method involves repeated measurements and calculations of Allan deviation [14]. This experiment was conducted using both the epoxy sample discussed above and the pharmaceutical tablets. The outcome of the standard addition is exemplified in Fig. 3, indicating a sensitivity of ~0.1 mm L_{eq} for an acquisition time of 60 s (corresponding to an absorption fraction of 3×10^{-6}). Allan deviations for three measurement cases are shown in Fig. 4. Knowing that the absorption imprint remains hidden if no mechanical dithering is employed, this figure clearly shows the effectiveness of sample rotation and beam dithering.

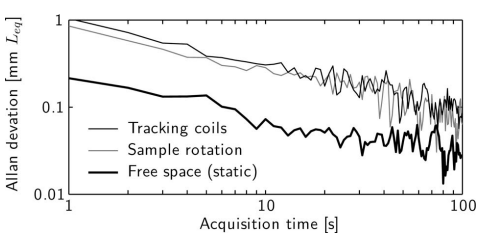

Fig. 4. Allan deviation based on 400 consecutive 1 s measurements. Data shown are from measurements on a pharmaceutical tablet under sample rotation (L_{eq}=25.8 mm), the epoxy sample with tracking coil beam dithering (L_{eq} =20.7 mm), as well from free-space measurements (no scattering sample present, L_{eq}=76.5 mm).

Utilizing very simple instrumentation, this work clearly demonstrates the first submillimeter GASMAS measurements. Furthermore, repeated measurements on more than ten different pharmaceutical tablets show that the day-to-day reproducibility is ~0.3 mm L_{eq} (presumably limited by laser positioning). The high sensitivity in combination with excellent reproducibility and simplistic instrumentation provide both scientific and industrial potential. The use of the proposed approach for characterization of pharmaceutical materials will be described in detail in a forthcoming article [15]

The authors acknowledge the enthusiastic support offered by Sune Svanberg.

References

1. I. Linnerud, P. Kaspersen, and T. Jæger, Appl. Phys. B **67**, 297 (1998).
2. P. A. Martin, Chem. Soc. Rev. **31**, 201 (2002).
3. P. Kluczynski, J. Gustafsson, Å. Lindberg, and O. Axner, Spectrochim. Acta, Part B **56**, 1277 (2001).
4. J. A. Silver, Appl. Opt. **31**, 707 (1992).
5. M. Sjöholm, G. Somesfalean, J. Alnis, S. Andersson-Engels, and S. Svanberg, Opt. Lett. **26**, 16 (2001).
6. G. Somesfalean, M. Sjöholm, J. Alnis, C. af Klinteberg, S. Andersson-Engels, and S. Svanberg, Appl. Opt. **41**, 3538 (2002).
7. M. Andersson, L. Persson, M. Sjöholm, and S. Svanberg, Opt. Express **14**, 3641 (2006).
8. L. Persson, H. Gao, M. Sjöholm, and S. Svanberg, Opt. Lasers Eng. **44**, 687 (2006).
9. L. Persson, M. Andersson, M. Cassel-Engquist, K. Svanberg, and S. Svanberg, J. Biomed. Opt. **12**, 054001 (2007).
10. T. Svensson, L. Persson, M. Andersson, S. Svanberg, S. Andersson-Engels, J. Johansson, and S. Folestad, Appl. Spectrosc. **61**, 784 (2007).
11. T. Fernholz, H. Teichert, and V. Ebert, Appl. Phys. B **75**, 229 (2002).
12. R. Arndt, J. Appl. Phys. **36**, 2522 (1965).
13. M. Firbank and D. T. Delpy, Phys. Med. Biol. **38**, 847 (1993).
14. P. Werle, R. Miicke, and F. Slemr, Appl. Phys. B **57**, 131 (1993).
15. T. Svensson, M. Andersson, L. Rippe, S. Svanberg, S. Andersson-Engels, J. Johansson, and S. Folestad, "VCSEL-based oxygen spectroscopy for structural analysis of pharmaceutical solids," Appl. Phys. B (to be published).

Paper XII

VCSEL-based oxygen spectroscopy for structural analysis of pharmaceutical solids

T. Svensson, M. Andersson, L. Rippe, S. Svanberg,
S. Andersson-Engels, J. Johansson, and S. Folestad.

Applied Physics B **90**, 345-354 (2008).

Appl. Phys. B (2008)
DOI: 10.1007/s00340-007-2901-6

Applied Physics B
Lasers and Optics

T. SVENSSON[1,✉]
M. ANDERSSON[1]
L. RIPPE[1]
S. SVANBERG[1]
S. ANDERSSON-ENGELS[1]
J. JOHANSSON[2]
S. FOLESTAD[2]

VCSEL-based oxygen spectroscopy for structural analysis of pharmaceutical solids

[1] Department of Physics, Lund University, P.O. Box 118, 22100 Lund, Sweden
[2] Astra Zeneca R&D, Mölndal, Sweden

Received: 6 September 2007

ABSTRACT We present a minimalistic and flexible single-beam instrumentation based on sensitive tunable diode laser absorption spectroscopy (TDLAS) and its use in structural analysis of highly scattering pharmaceutical solids. By utilising a vertical cavity surface emitting laser (VCSEL) for sensing of molecular oxygen dispersed in tablets, we address structural properties such as porosity. Experiments involve working with unknown path lengths, severe backscattering and diffuse light. These unusual experimental conditions has led to the use of the term gas in scattering media absorption spectroscopy (GASMAS). By employing fully digital wavelength modulation spectroscopy and coherent sampling, system sensitivity in ambient air experiments reaches the 10^{-7} range. Oxygen absorption exhibited by our tablets, being influenced by both sample porosity and scattering, was in the range 8×10^{-5} to 2×10^{-3}, and corresponds to 2–50 mm of path length through ambient air (L_{eq}). The day-to-day reproducibility was on average 1.8% (0.3 mm L_{eq}), being limited by mechanical positioning. This is the first time sub-millimetre sensitivity is reached in GASMAS. We also demonstrate measurements on gas transport on a 1-s time scale. By employing pulsed illumination and time-correlated single-photon counting, we reveal that GASMAS exhibits excellent correlation with time-domain photon migration. In addition, we introduce an optical measure of porosity by relating oxygen absorption to average photon time-of-flight. Finally, the simplicity, robustness and low cost of this novel TDLAS instrumentation provide industrial potential.

PACS 42.62.Fi; 39.30.+w; 78.55.Mb; 42.62.Cf; 87.64.Cc

1 Introduction

Pharmaceutical sciences employ numerous methods in order to measure, characterise and understand properties of solid pharmaceutical materials. While many of these methods are highly sophisticated and accurate, they are at the same time often slow and destructive to the sample. Out of numerous examples in this field, mercury porosimetry is for example used to assess voids and pores in physical structures such as tablets. Other examples of commonly used methods are tablet disintegration and dissolution, which are used to assess functional properties of dosage forms such as tablets and capsules. In recent years, the introduction of new tools for fast and non-destructive pharmaceutical analysis has received increased attention. Ultimately these tools can be applied to conduct measurements even in situ during physical, chemical and bioprocessing. In particular, implementation of real-time control of quality, commonly referred to as process analytical technology (PAT), rests on access to reliable and rapid measurement techniques. Moreover, in pharmaceutical development, formulation development times are continuously shortened, which is why pharmaceutical analysis can no longer afford to rely solely on traditional technologies that require hours to days for results to be produced. In this overall context of solid pharmaceutical materials, optical spectroscopy offers a whole range of useful analytical alternatives. These optical spectroscopy based techniques can be used for various tasks, depending on the sample type and the analytical requirements. Moreover, most of the optical spectroscopic techniques are non-destructive, fast and can easily be automated. Solid samples can thus be analysed in their native state without any sample preparation.

In this paper we establish gas in scattering media absorption spectroscopy (GASMAS [1]) as a tool for characterisation of pharmaceutical solid materials. This comprises characterisation of a novel GASMAS instrumentation and further characterisation of the measurement principle. The pharmaceutical solid materials used as model materials in this study typically exhibit strong optical scattering and are therefore representative of other materials with similar properties. Furthermore, potential applications of GASMAS are explored and are here mainly focused on pharmaceutical tablets. From a generic perspective, pharmaceutical tablets are typically constituted from primary particles or aggregated primary particles that have been compressed together. Measurements on this composite where the analytical signal reflects voids and pores in the physical structure could therefore carry key information on the solid sample properties. Ultimately, these may also be indicative of mechanical and functional properties of the composite sample.

The GASMAS tool developed in this study is based on high-resolution tunable diode laser absorption spectroscopy (TDLAS), and is in this case used to detect molecular oxygen located within the voids and pores of the pharmaceutical

✉ Fax: +46-46-2224250, E-mail: tomas.svensson@fysik.lth.se

tablet samples. The concept of GASMAS was introduced in 2001 [1], and takes advantage of contrast between the sharp (GHz) absorption features of gases and the broad absorption features related to the solid state. It simply utilises the fact that a gas phase absorption imprint can be measured even after propagation through a highly scattering solid material. It should be noted that the magnitude of this absorption imprint is related to both actual sample porosity and scattering properties (optical path length). The technique has previously been successfully used for characterisation of various materials, such as polystyrene foam [1, 2], wood [3, 4], fruit [5] and biological tissue [6–8].

TDLAS is a well-established optical technique for sensitive, selective and accurate measurements of gas concentrations. For increased sensitivity, the technique is often accompanied by noise-reduction schemes such as wavelength-modulation spectroscopy (WMS) [9]. Further refinements include for example digital phase sensitive detection with inherent noise suppression by means of coherent sampling [10]. In recent years, TDLAS has proved its practical value in various applications [12–15]. Its traditional configuration involves well-defined beam lines and known interaction lengths (often using gas cells), while this work deals with detection of gases dispersed within highly scattering samples. This involves working with unknown path-length distributions, severe backscattering and diffuse light. It is these rather unusual and aggravating experimental conditions that motivate the use of the acronym GASMAS.

We recently showed the potential of GASMAS in pharmaceutical applications [16, 17]. In [17], we utilised a fibre-optic, dual-beam WMS arrangement for oxygen spectroscopy using a pigtailed distributed feedback (DFB) diode laser, a photomultiplier tube (PMT) for optical detection of transmitted light and traditional analogue lock-in amplification for second-harmonic detection. We now introduce a minimalistic single-beam instrumentation for oxygen sensing using a vertical cavity surface emitting laser (VCSEL) and a large-area photodiode. We employ fully digital WMS in combination with coherent sampling, allowing powerful post-processing of non-reduced detector signals. The technical improvements with respect to earlier work on GASMAS are significant, in terms of simplicity, robustness, cost, speed and sensitivity. The limitations of GASMAS are further discussed in [18] (in which we present related data). In the present work we also, for the first time, present a careful experimental comparison between GASMAS and photon migration. This complementary approach has been used in earlier work by our group for proof of principle measurements of gas concentrations and porosity [2]. Briefly, we access photon time-of-flight distributions by measuring the temporal broadening exhibited by short (ps) laser pulses that have propagated through our samples. By relating the oxygen absorption to the path-length information provided by these time-of-flight experiments, we take the first step towards optical porosimetry.

2 Materials and methods

2.1 *WMS principle*

WMS and TDLAS have been extensively studied, both experimentally and theoretically [19, 20]. It is beyond the scope of this article to provide any detailed description here. Very briefly, WMS is a high-resolution laser absorption technique, in which the absorption signal is moved to higher detection frequencies in order to avoid low-frequency noise of system components. In TDLAS, this is realised by scanning a sinusoidally frequency-modulated diode laser over some narrow (e.g. gas-phase) absorption feature. This feature acts as a non-linear transfer function, producing a periodic but not perfectly sinusoidal variation in transmission (i.e. harmonic generation takes place, overtones are generated). A WMS signal measures the temporal evolution in the amplitude of the harmonic frequencies, and has traditionally been acquired using lock-in amplification. The usefulness comes with the fact that the WMS signal is proportional to the absorption (and thus gas concentration, in the case of weak absorption).

2.2 *TDLAS instrumentation*

The oxygen spectroscopy is based on conventional high resolution tunable diode laser absorption spectroscopy (TDLAS) in combination with coherent sampling. An overview is shown in Fig. 1. A vertical cavity surface emitting laser (SPECDILAS V-763-OXY-MTE, Laser Components, Germany) is wavelength tuned over one of the absorption lines in the *R* branch of molecular oxygen (R9Q10, 760.654-nm vacuum wavelength, peak absorption coefficient $\mu_a = 2.83 \times 10^{-5}\,\mathrm{mm}^{-1}$ in ambient air [21]). Oxygen sensing using such lasers is well studied [22, 23]. A temperature controller (TED200, Thorlabs, NJ, USA) keeps temperature stable (in this case, at about 35 °C), and the 4-mA-level operation current is provided via a VCSEL current controller (LDC200V, Thorlabs, NJ, USA). The diode laser is modulated using a digital arbitrary waveform generator (CH-3150, Exacq Technologies, USA) running at 19.3536 MS/s. The modulation signal consists of a triangular ramp (at 18 Hz) that provides a linear frequency sweep, and a superimposed harmonic oscillation (18.432 kHz) that allows wavelength-modulation spectroscopy. A relative frequency scale is determined using an etalon with a free spectral range of 2.41 GHz. The sinusoidal modulation amplitude is chosen in order to maximise the $2f$ WMS signal (achieved at a laser frequency modulation amplitude of about 3.3 GHz). Light is detected using an unbiased 5.6 mm × 5.6 mm PN photodiode (S1337-

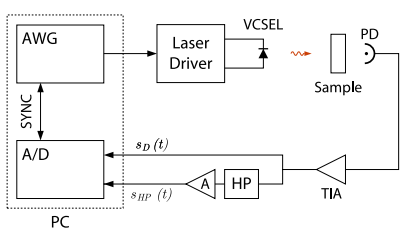

FIGURE 1 System overview. A VCSEL is modulated using an arbitrary waveform generator (AWG), and light is collected by a photodiode (PD). An external transimpedance amplifier (TIA) converts the photocurrent, and the resulting voltage signal is sampled coherently using an A/D board. Sensitivity is increased by using a second channel to record a high-pass (HP) filtered and amplified (A) signal version. A standard PC controls both the AWG and the A/D board

66BR, Hamamatsu Photonics, Japan). The photodiode is directly connected to a short (20 cm) high quality coaxial cable (LMR-100A, Times Microwaves), and mounted in a cylindrical piece of black Delrin. The photocurrent is converted and amplified using a low-noise transimpedance amplifier (TIA; DLPCA-200, FEMTO Messtechnik, Germany, running on its low-noise setting only). After this photodiode front end, the signal is split in two. One part is sent for high-pass filtering and amplification (using a Stanford Research SR560 running ac coupled with a 12 dB/octave 300 Hz high-pass (HP) filter and an output amplification g_{HP} typically set to 50), while the other part is left unaltered. The resulting signals, denoted $s_{\mathrm{D}}(t)$ and $s_{\mathrm{HP}}(t)$, are coherently sampled (2.4192 MS/s) using an A/D board (NI-6132, National Instruments) and stored to disk for later data processing. Although most experiments involve averaging of a certain number of scans (18 averages for a 1 s acquisition time), scan-by-scan acquisition (data streaming) is possible. The coherent sampling is achieved by synchronisation of the arbitrary waveform generator and the A/D board [7], and acts as a narrow-band comb filter filtering out frequencies not periodic with sampling. Furthermore, to allow high-quality harmonic detection of the modulation frequency and overtones, the modulation frequency is an exact integer of the scan frequency [10, 11]. Moreover, the concept of coherent sampling allows flexible and powerful data post-processing, avoiding for example traditional pre-configured lock-in amplification.

2.3 *Pharmaceutical samples*

The pharmaceutical samples examined in this work are model tablets with microcrystalline cellulose (MCC) as the main constituent, manufactured using a wet granulation process. The resulting granulate was sieved in order to create three batches of different particle size distributions. The three particle size (PS) distributions are denoted A, B and C, containing granules with particle size $< 150\,\mu$m, 150–400 μm and $> 400\,\mu$m, respectively. The granulate batches were used to produce 51 (17 from each particle size distribution) cylindrical tablets with a diameter of 10 mm, and a total weight of 300 mg. Tablets were compressed manually, and at different compression forces, yielding tablets with thicknesses from 2.8 to 4.2 mm. Each tablet is denoted according to its thickness, so that $A_{3.15}$ refers to a tablet made from particle size distribution A, being 3.15-mm thick. It should be noted that the average refractive index of a tablet depends on its thickness. Assuming that MCC has a refractive index of $n_{\mathrm{mcc}} = 1.5$ [24] and a true density of about $\varrho = 1.5\,\mathrm{mg/mm^3}$ [25], the average refractive index of a $m = 300$ mg tablet of thickness d is expected to follow the relation

$$n(d) = 1 + (n_{\mathrm{mcc}} - 1)\frac{m}{5^2 \pi d \varrho}\,. \qquad (1)$$

2.4 *Non-porous reference sample*

A TiO_2-based epoxy phantom was made, serving as a non-porous highly scattering reference sample. Such phantoms are frequently used in the field of photon migration [26]. Its bulk scattering properties are similar to the properties of the pharmaceutical samples discussed in Sect. 2.3. Time-of-flight data, supporting this statement, are shown in Fig. 10.

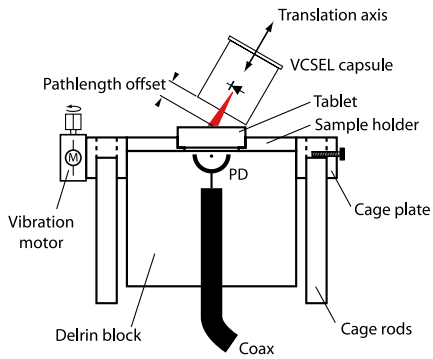

FIGURE 2 An illustration of the experimental configuration. The sample holder and tablet are made to rotate together by action of the vibrator

2.5 *Experimental configuration*

Two kinds of measurements are described in the present paper (measurements with and without scattering samples). General system performance is characterised using free-space standard addition experiments. In these, the VCSEL is directed towards the photodiode in an on-axis configuration. Except for the occasional use of a thin pinhole (2-mm diameter) and thin (0.05 mm) filter sheets, nothing but ambient air is present in the beam path (no collimation takes place). The diode laser holder is mounted on either a translation stage or a rail carrier. The 1 mm/turn translation stage allows accurate on-axis translation of the VCSEL over a 70-mm range. The rail requires manual positioning of rail carriers using a mm scale, causing fairly inaccurate positioning while allowing a 0–230-mm translation range. Note that since no collimating lens is involved, the 12° FWHM divergence of the laser diode results in significant changes in detected intensity upon translation.

A small vibration motor is attached to the cage system mechanics that hold the detector Delrin block, and a second is attached to the diode laser mount. These are turned on mainly to minimise the influence of backscattering into the diode laser and optical interference fringes (often crucial for sensitive measurements on highly scattering samples).

In measurements on pharmaceutical samples (cylindrical tablets), the laser is tilted 30° with respect to the detector surface (avoiding specular reflection). Tablets are placed in a thin (2 mm) circular sample holder made from black Delrin. The tablet rests on a thin (0.1-mm thick, 1-mm wide) flange, making a 8-mm-diameter area of the tablet visible to the detector. The detector Delrin block is mounted firmly to a cage plate (Linos cage mounting system, Germany), which in turn rests loosely on cage rods. The sample holder rests freely on top of the detector, and is kept in place by the walls of the cage plate (the detector surface is 2 mm below the cage-plate top). The situation is illustrated in Fig. 2. This configuration allows us to rotate the tablet using simple momentum transfer from the rotating vibration motor, to the sample holder and

tablet (a similar phenomenon is utilised in conventional vibratory feeders). During measurements, the VCSEL is lowered in order to be as close to the sample as possible. This positioning is done manually, but variations in path-length offset (see Fig. 2) are expected to be less than 0.5 mm.

2.6 *Signal processing*

The utilised procedures for signal processing of the fully digital WMS data are similar to those proposed by Fernholz et al. [10]. Readers lacking a more detailed description are referred to their extensive discussion. In the case of weak absorption, the direct signal collected by our system, $s_{\mathrm{D}}(t)$, will appear very similar to the waveform used for laser modulation. This is illustrated in Fig. 3a. Please note the contrast with respect to traditional lock-in-based data acquisition, in which a single channel only measures a certain frequency. However, as can be seen in Fig. 3b, the power spectrum reveals that harmonic generation has occurred (for improved sensitivity, we have now turned to $s_{\mathrm{HP}}(t)$). By performing band-pass filtering we can determine where, within our scan, the overtones are generated (see Fig. 3c). The first step towards a WMS signal is to filter out the positive frequencies around one of the harmonic frequencies. This is done in the Fourier domain using a super-Gauss window, and the corresponding Fourier domain signal $S_{nf}(\omega)$ is defined as

$$S_{nf}(\omega) = \mathfrak{F}\{s_{\mathrm{HP}}(t)\} \times \exp\left(-\left(\frac{\omega - n \times \omega_{\mathrm{m}}}{\delta\omega}\right)^8\right). \qquad (2)$$

Here, $\mathfrak{F}$ symbolises the time-discrete Fourier transform, n specifies the harmonic order ($1f$, $2f$, $3f$, etc.), ω_{m} is the modulation frequency and $\delta\omega$ is the super-Gauss width (in this work set to 1 kHz, ordinary frequency). The next step is to down convert the resulting signal so that the selected harmonic frequency becomes the zero frequency. The corresponding signal is denoted S^0_{nf}, and the procedure is defined as

$$S^0_{nf}(\omega) = S_{nf}(\omega + n \times \omega_{\mathrm{m}})\,. \qquad (3)$$

The signal is then transformed back into the time domain, and since negative frequencies were removed we end up with a complex signal $y^+(t)$:

$$y^+_{nf}(t) = \mathfrak{F}^{-1}\{S^0_{nf}(\omega)\}\,. \qquad (4)$$

For the cases of $1f$ ($n = 1$) and $2f$ ($n = 2$), this signal is exemplified in Fig. 3d and e using so-called phase plots. In such a phase plot, a pure sinusoidal signal would appear as a single dot, whose absolute value tells us its amplitude, and whose angle tells us its phase. The $1f$ signal is close to being a single frequency due to the residual amplitude modulation (RAM) that accompanies frequency modulation (FM) of diode lasers. The absorption signal shows up only as a small distortion, and is shown in the inset of Fig. 3d. There, the angle $\alpha_1 = -109.2°$ tells us the phase of the RAM. The angle $\beta_1 = -123.6°$ states the phase of the absorption-related $1f$ signal. The phase difference between RAM and FM is given by $\varphi = \alpha_1 - \beta_1 = 14.4°$. Due to the linearity of the VCSEL scan, no RAM is visible in y^+_{2f}. The phase of the $2f$ signal is easily identified from the phase plot, and is denoted β_2.

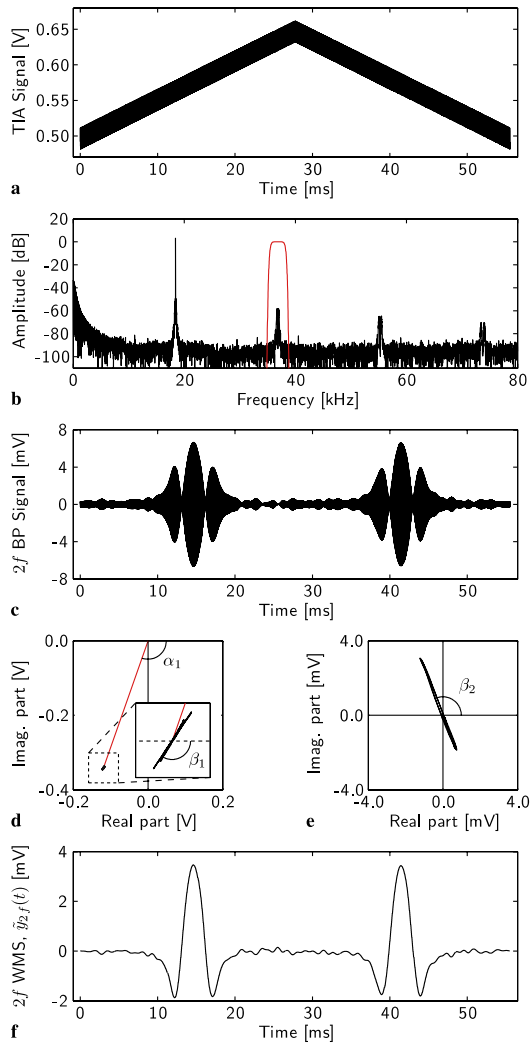

FIGURE 3 Summary of signal processing, exemplified using experimental data from tablet $A_{3.31}$: (**a**) TIA output signal, (**b**) spectrum of the HP-filtered signal $s_{\mathrm{HP}}(t)$ together with the super-Gauss window for $2f$ filtering, (**c**) band-passed (BP) version of the HP signal, (**d**) $1f$ phase plot, (**e**) $2f$ phase plot and (**f**) $2f$ WMS signal. Note that the factor two difference between (**c**) and (**f**) is due to the fact that the WMS signal is based on positive frequencies only. This particular signal corresponds to the oxygen absorption from a 28-mm path length in ambient air

The real WMS signal, exemplified in Fig. 3f, is reached after offset removal and phase adjustment, as shown by

$$\tilde{y}_{nf}(t) = \mathrm{Re}\left\{\left(y^+_{nf} - \mathrm{mean}\left(y^+_{nf}\right)\right) \times \exp(-\mathrm{i}\beta_n)\right\}. \qquad (5)$$

Furthermore, in order to account for the broadband sample transmissivity, an intensity-corrected WMS signal is created

by normalisation with respect to the triangular scan signal from the direct signal, $U_{\mathrm{scan}}(t)$. The scan signal is determined by separate fitting of two first-order polynomials to the two sides of the triangular signal (avoiding regions with oxygen imprint). In order to obtain a signal strength that can be compared directly with physical absorption fraction, we also take the extra gain of the HP signal, g_{HP}, into account. We also multiply by a factor of two in order to compensate for the loss of the negative-frequency amplitude. The signal is defined as

$$y_{nf}(t) = 2 \times \frac{\tilde{y}_{nf}(t)}{g_{\mathrm{HP}} \times U_{\mathrm{scan}}(t)} \,. \tag{6}$$

Quantitative analysis of intensity-corrected WMS signals is based on reference recordings made using a known path length through ambient air. The underlying model includes a second-order baseline correction, and is given by

$$y(t) = p_0 + p_1 t + p_2 t^2 + c \times y_{\mathrm{ref}}(t - t_0) \,. \tag{7}$$

Here, $y(t)$ and $y_{\mathrm{ref}}(t)$ refer to the intensity-corrected WMS signals. The coefficient c tells us how much of the reference signal is needed to explain $y(t)$. The shift parameter t_0 is included in order to take drifts in temperature and operation current into account. If speed is of high priority, the noise sensitivity may decrease if t_0 is kept fixed. The polynomial coefficients, the WMS amplitude coefficient c and the shift t_0 are determined by employing Levenberg–Marquardt non-linear curve fitting. The left- and right-hand sides of the triangular scan are analysed separately, eliminating the potential problem of differences in VCSEL tuning characteristics. The average of the two derived amplitude coefficients is used to describe each sample. The equivalent path length in ambient air, L_{eq}, corresponding to $y(t)$ is calculated according to (8), where c denotes the average amplitude coefficient:

$$L_{\mathrm{eq}} = c \times L_{\mathrm{ref}} \,. \tag{8}$$

2.7 *Time-of-flight instrumentation*

Knowledge concerning interaction path length is always an important part in understanding absorption signals. This is particularly important for the case of pharmaceutical solids, where massive light scattering causes photon path lengths to greatly exceed sample dimensions [27]. We are able to determine the photon time-of-flight by employing picosecond diode laser technology and time-correlated single-photon counting (TCSPC). A schematic of the instrumentation and the experimental setup is given in Fig. 4, and a detailed description can be found in a previous publication [28]. Briefly, picosecond pulses from a 786-nm diode laser (LDH, PicoQuant, Germany) are sent onto the centre of the cylindrical pharmaceutical tablet using a 600-μm graded-index optical fibre (G 600/840 P, ART Photonics, Germany). The temporally broadened pulses are collected centrally on the back side using a second fibre. To ensure that appropriate photon levels reach the cooled microchannel plate photomultiplier tube (MCP-PMT; R3809-59 Hamamatsu Photonics, Japan), collected light is first sent through an adjustable gradient neutral density filter. A TCSPC computer card (SPC-300, Becker&Hickl, Germany) is used to obtain photon time-of-flight histograms.

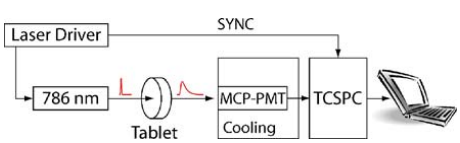

FIGURE 4 A schematic of the time-of-flight instrumentation

If the refractive index is known or estimated, the photon path lengths are readily available from the time-of-flight distribution. Material properties, such as average bulk absorption and reduced scattering, can be estimated using for example Monte Carlo simulation or the diffusion approximation of light propagation in highly scattering media [29, 30]. Note that these parameters are of no particular interest in this work, in which photon migration is employed only to determine path lengths.

3 Results

3.1 *TDLAS system performance*

The performance of the TDLAS system was tested by performing on-axis free-space standard addition experiments, in which known path lengths L of ambient air were added to the path between laser and detector. The laser mount was placed on a translation stage, and initially placed as close to the detector as possible (the resulting offset ΔL was about 1 mm). In a first series, data was acquired in 5-mm increments in the range 5–50 mm of added air, and with a thin pinhole put on top of the detector. The acquisition time was 10 s, the TIA gain was 10^4 V/A and the corresponding TIA bandwidth was 500 kHz. The resulting WMS signals are measured relative to the final 50-mm added air measurement ($y_{\mathrm{ref}} = y_{50\ \mathrm{mm}}$). When taking a possible offset ΔL into account, while disregarding geometrical imperfections, and using the recording of added path length L_{ref} as reference, the derived WMS amplitude coefficient c is expected to follow the expression

$$c(L) = \frac{L + \Delta L}{L_{\mathrm{ref}} + \Delta L} \,. \tag{9}$$

Fitting obtained $2f$ amplitude coefficients to this relation indicates that the offset ΔL was 3.31 mm. The residual standard deviation, denoted σ, was 1.09×10^{-3} and corresponds to $1.09 \times 10^{-3}(50\,\mu\mathrm{m} + 3.31\,\mu\mathrm{m}) \simeq 58\,\mu\mathrm{m}$. The average absolute deviation, denoted ε, from the fitted absolute reference model corresponds to 47 μm. The data are shown in Fig. 5a. Conventional linear regression yields $c_{2f} = 0.0188L + 0.0616$ and an offset of $\Delta L = 3.28$ mm ($y = 0$ intercept). The average absolute deviation is in the regression case 41 μm, and the degree of explanation was $R^2 = 99.999\%$. The small differences between these two fitted models can be assigned to noise in the reference dataset, geometrical effects, as well as to imperfections in on-axis alignment.

Although the linearity in this first series was more than satisfying, the unexpected offset called for further examination. In a second series, the acquisition time was increased to 60 s, and data were taken in the range 0–2.6 mm, in 0.2-mm

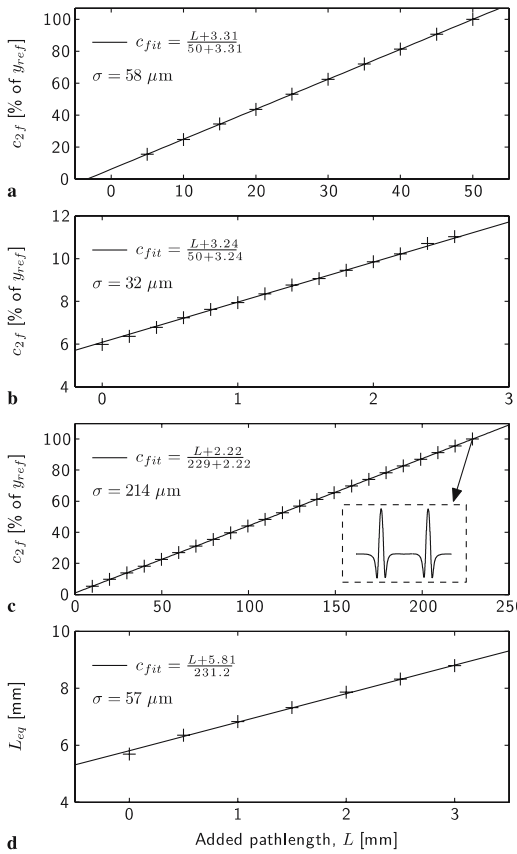

FIGURE 5 Standard addition data. The standard deviation of the residuals, denoted σ, are given in μm. (**a**) Linearity test using translator, TIA gain 10^4 and acq. time 10 s; (**b**) sensitivity test using translator, TIA gain 10^4 and acq. time 60 s; (**c**) recording of reference for scattering samples, using a rail carrier, TIA gain 10^6 and acq. time 60 s; (**d**) translator series with non-porous, highly scattering epoxy tablet, TIA gain 10^6 and acq. time 60 s

increments. Note, however, that the same reference was used (50-mm added air, 10-s acquisition time). The result is presented in Fig. 5b. The fitted offset ΔL was in this case 3.24 mm, and the average absolute deviation corresponds to 24 μm. Again, conventional linear regression provides similar results. The fitted line is $c_{2f} = 0.0193L + 0.0602$ (producing a ΔL estimation of 3.12 mm), the average absolute deviations about 18 μm and the degree of explanation 99.94%.

The simple standard addition experiments described above demonstrate a path-length sensitivity in the 25-μm range. An ambient air distance of 25 μm corresponds to an absorption fraction of 10^{-7}. In addition, these experiments also show that the capsule containing the VCSEL contains oxygen, and not only a mixture of helium and argon (as stated by the manufacturer).

The standard addition procedures described above provide valuable information on system performance. However, the insertion of a highly scattering sample in between the VCSEL and the photodiode causes a major change in measurement conditions. Light levels reaching the detector drop (requiring us to set the TIA gain to 10^6 V/A, giving us a 200-kHz bandwidth), and the VCSEL is subject to sample backscattering. In addition, the tilting of the laser introduces small uncertainties in path-length offset. These new conditions were examined in a small-scale standard addition series using the non-porous epoxy tablet described in Sect. 2.3. The resulting WMS signals were measured relative to a new reference dataset. This reference dataset was acquired in a free-space standard addition series in the range 10–230 mm of added air, using the new TIA settings and a 60-s acquisition time. In this series, it should be noted that no pinhole was present in the beam path (however, filter sheets were used to maintain proper intensity levels). The reference WMS signal and the underlying standard addition series are shown in Fig. 5c. The difficulties in manual positioning of the slider (using the rail mm scale) cause significantly larger deviations than before ($\varepsilon = 190$ μm). Thus, this series is not a proper indication of system performance. The linearity, however, is excellent. All measurements in this series are evaluated using the final 229-mm added air dataset ($y_{\text{ref}} = y_{229}$). Modelling of $2f$ data according to (9) yields $\Delta L = 2.2$ mm, and linear regression suggests $\Delta L = 2.4$ mm ($\varepsilon = 109$ μm, $R^2 = 99.9995\%$). The different offset with respect to the above-described series (Fig. 5a and b) is explained by geometrical differences (removal of the pinhole, as well as repositioning of the detector to compensate for the initial path-length offset due to the distance between the detector surface and the VCSEL-can front glass). When looking at other harmonics, the degrees of explanation were 99.9956% ($1f$), 99.9994% ($3f$), 99.9987% ($4f$), 99.9981% ($5f$) and 99.9936% ($6f$). The use of harmonics other than $2f$ is not further discussed in this work. Finally, the reference dataset from the above experiment has been used in all measurements on pharmaceutical samples presented in this work (serving as an absolute reference at $229 + 2.2 = 231.2$ mm L_{eq}).

The measurement series on the epoxy tablet was carried out following the configuration shown in Fig. 2, investigating added path lengths in the range 0–3 mm (0.5-mm increments). In the initial measurement, due to the 30° tilt, there is a path length of about 3 mm of ambient air between the VCSEL front glass and the detector surface. Adding this to the additional 2–3 mm equivalent path length inside the VCSEL capsule, we thus expect to register a WMS signal corresponding to 5–6 mm. The results of the epoxy tablet standard addition are shown in Fig. 5d. When using an absolute reference in a standard addition series, the signal is expected to follow the expression given in (10), rather than the expression given in (9):

$$c(L) = \frac{L + \Delta L}{L_{\text{ref}}} \,. \tag{10}$$

Using this model, the initial offset is estimated to be 5.8 mm ($\varepsilon = 38$ μm). Linear regression suggests an offset of 5.7 mm ($\varepsilon = 41$ μm, $R^2 = 99.8\%$). Both results are in good agreement with the expected 5–6 mm. Since the same offset is expected in measurements on the pharmaceutical tablets, an L_{eq} offset of 5.8 mm will be subtracted from all such measurements.

3.2 *Pharmaceutical GASMAS*

Although about 200 μW is directed onto the surface of the various tablets, severe scattering results in detected powers in the 0.5–5 μW range (see Fig. 6). A detected power of 1 μW corresponds to a photodiode current of about $I = 0.5$ μA, or $N = 3.1 \times 10^{12}$ electrons per second. The electrical shot noise in a one-second measurement results in a signal to noise ratio of $\mathrm{SNR} = N/\sqrt{N} = \sqrt{N} = 1.7 \times 10^6$. The shot-noise-equivalent small change in electron flow is then $\Delta N = \sqrt{N}$, and corresponds to an absorption fraction of $\Delta N/N = 1/\mathrm{SNR} = 5.7 \times 10^{-7}$. This can be considered as the 1-s shot-noise limit of our measurements of oxygen absorption fraction. Since we only interact with the oxygen absorption line in about 10% of the time (the WMS scan covers more than the oxygen absorption feature), our TDLAS acquisition time of 1 s corresponds to a 0.1-s effective measurement time (approximately). Such a consideration yields a shot-noise limit, for a TDLAS acquisition time of 1 s, of about $5.7 \times 10^{-7}/\sqrt{0.1} = 1.8 \times 10^{-6}$ (0.06 mm L_{eq}). Note, however, that the input voltage of the TIA (4 nV/$\sqrt{\mathrm{Hz}}$) in combination with the large capacitance of our photodiode (380 pF) limits our detection to about 50% above shot noise.

If the setup is run under static conditions (vibrators turned off), oxygen imprints are completely hidden in random interference signals. These problematic effects are described in [18]. However, tablet rotation ensures that high quality gas absorption data may be obtained in a matter of seconds (by means of waveform averaging). The influence of acquisition time was examined using Allan deviation, and is shown in Fig. 7. The Allan deviation is an often used measure of the system detection limit, as well as an indicator of optimal acquisition times [31]. In this case, it suggests that the system is stable over at least 60 s, and that the detection limit is in the order of 0.1 mm L_{eq} (for 60-s measurements on highly scattering solids).

Typical WMS signals are shown in Fig. 8. The magnitude and shape of intensity-corrected WMS signals are in good agreement with what is expected from multi-harmonic detection [20, 32]. For example, the observed ratio between the intensity-corrected peak height and the derived absorption fraction is about 0.4 for $1f$ and 0.3 for $2f$ (here, the absorption fraction is assumed to be $(23.2 + 5.8)2.83 \times 10^{-5} = 8.2 \times 10^{-4}$). Note also that despite the background exhibited in $1f$ and the noise in $6f$, the spread in derived L_{eq} between different harmonics is only 1.5% (coefficient of variation).

Measurements were performed on in total 54 tablets (17 tablets from each particle size). As can be seen in Fig. 9, the oxygen absorption due to tablet transmission is in the range 2–50 mm L_{eq}, corresponding to absorption fractions in the range 8×10^{-5} to 2×10^{-3}. As in data on transmitted power and (see Sect. 3.3, below) average time-of-flight, tablets made from the smallest granule particles stand out.

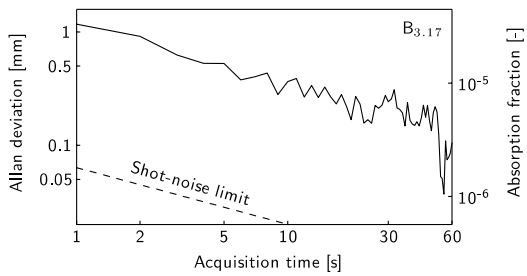

FIGURE 7 Allan deviation versus acquisition time for tablet $B_{3.17}$, illustrated using a log–log graph and stated in mm of equivalent path length (L_{eq}). Corresponding absorption fraction (absorbance) is also shown. The plot is based on a 3-min scan-by-scan acquisition (3240 scans individually stored, yielding 1.5 Gb of binary data). During data evaluation, the spectral shift t_0 was fixed. The shot-noise limit is given for reference (*dashed line*)

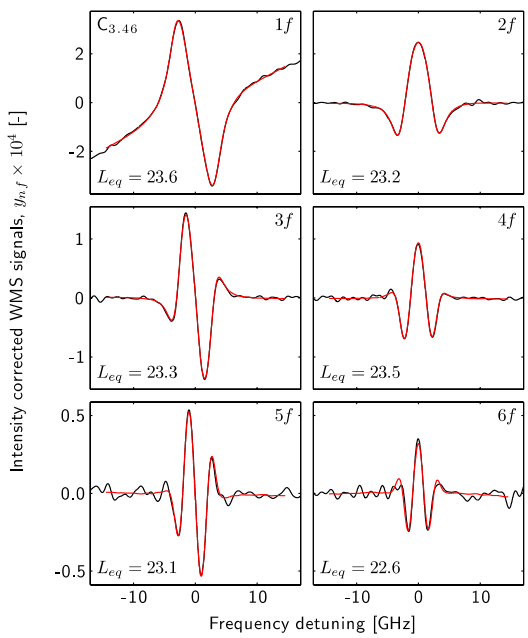

FIGURE 8 $1f$–$6f$ WMS signals from the pharmaceutical tablet $C_{3.46}$ (*black*) together with fitted reference data (*red*). A separate L_{eq} is stated for each harmonic (the 5.8-mm offset removed). The acquisition time was 60 s. Signals shown are from the left-hand side of the triangular scan. An L_{eq} of 23.2 mm corresponds to an absorption fraction of 6.6×10^{-4}

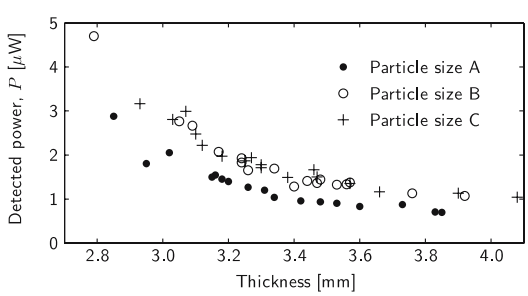

FIGURE 6 Detected power, P, versus tablet thickness. P is calculated from average TIA output voltage U_{avg} according to $P = U_{\mathrm{avg}}/(g \times \eta)$, where $g = 10^6$ V/A is the TIA gain and $\eta = 0.475$ A/W is the sensor responsivity at 760 nm. Since the VCSEL output is in the order of 200 μW, tablet transmission is in the order of 1%

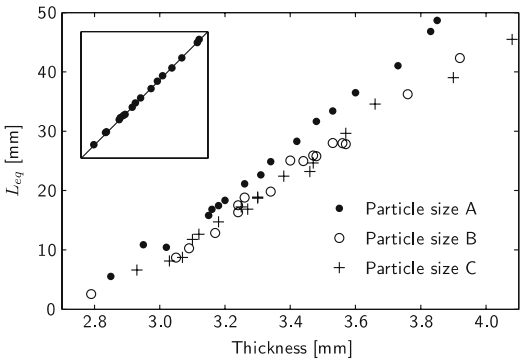

FIGURE 9 Outcome of measurements of pharmaceutical tablets. L_{eq} is calculated from the $2f$ WMS signal using the 231.2-mm absolute reference: $L_{\mathrm{eq}} = 231.2c_{2f} - 5.8$. Day-to-day reproducibility was tested by repeated measurements on type A tablets. The *inset* shows a scatter plot of two such repetitions, illustrating the excellent reproducibility. The average absolute difference between these measurements was only 0.3 mm (average reproducibility 1.8%). The largest difference was 0.56 mm, and was obtained for $A_{3.53}$. Note the similarity in pattern with the time-of-flight data in Fig. 10b

Furthermore, repeated measurements verify good day-to-day reproducibility (on average 1.8%, or 0.29 mm L_{eq}). Thus, the somewhat irregular/noisy pattern in Fig. 9 should be assigned to individual tablet variation, and not to measurement uncertainty. This conclusion is also supported by the time-of-flight data presented in Sect. 3.3, exhibiting a very similar pattern.

3.3 *Time-of-flight analysis*

The mean time-of-flight $\bar{t}$ ranged from 0.4 to 1.1 ns for the different tablets. Time-of-flight distributions for the two most extreme tablets are shown in Fig. 10a. The response for the epoxy tablet is also shown.

The overall result is presented in Fig. 10b. All tablets were measured twice (different days), and the time-of-flight measurements proved to be highly reproducible. The maximum difference between two repetitions was registered for $B_{3.57}$, being only 1.5% (0.016 ns). Any outlier appearance in Fig. 10 (for example, for tablets such as $A_{2.95}$, $A_{3.73}$ or $B_{3.40}$) should thus not be assigned uncertainties in time-of-flight measurements. Assuming that the average refractive index can be approximated using (1), the average photon path length is about 80 mm for $B_{2.79}$ and 250 mm for $A_{3.83}$.

Tablet bulk absorption and scattering can be estimated using the diffusion approximation of light propagation in highly scattering media. Assuming that our tablets can be approximated as infinite slabs, we found that the reduced scattering coefficients are in the order of 50 mm^{-1}, while the absorption coefficients are in the order of 3×10^{-3} mm^{-1}. These numbers are rough estimates of bulk optical properties, and are presented only to give an idea of the diffusive light propagation in these pharmaceutical samples. They can also be compared with the absorption coefficient in ambient air due to the R9Q10 absorption line of molecular oxygen, i.e. 2.83×10^{-5} mm^{-1} at 760.654 nm. Thus, the oxygen absorption is approximately a factor 100 lower than the bulk absorption.

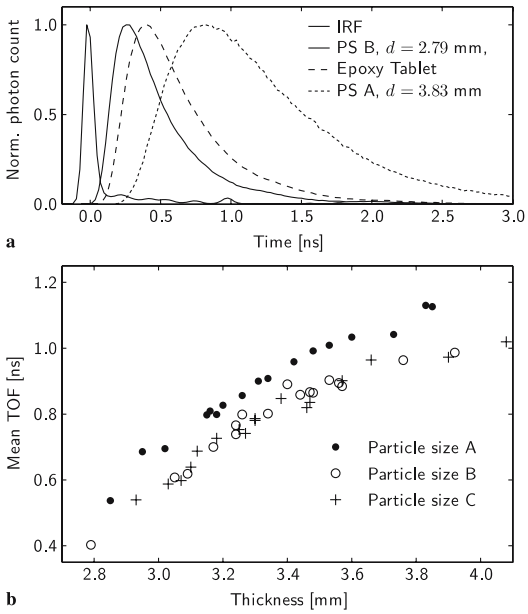

FIGURE 10 (**a**) Time-of-flight data for the two tablet extremes $B_{2.79}$ ($\bar{t} = 0.4$ ns) and $A_{3.83}$ ($\bar{t} = 1.1$ ns), as well as for the epoxy tablet ($\bar{t} = 0.6$ ns). The instrument response function (IRF) is about 85 ps (FWHM). (**b**) Mean time-of-flight (TOF) versus tablet thickness. All tablets were measured twice (different days, reproducibility in all cases better than 0.016 ns), and the average of these two values is presented. Note the similarity in pattern with the GASMAS data in Fig. 9

3.4 *Towards optical porosimetry*

The first step towards optical porosimetry is realised by forming the ratio between derived L_{eq} and average photon path length. The average photon path length, L_{tof}, is calculated from the average time-of-flight $\bar{t}$ according to (11), where $n(d)$ is the average tablet refractive index (estimated using (1)), and c is the speed of light in vacuum:

$$L_{\mathrm{tof}} = \frac{c}{n(d)} \times \bar{t}\,. \tag{11}$$

The result is shown in Fig. 11, and suggests porosities between 5 and 20%.

3.5 *Gas dynamics*

Gas exchange dynamics were studied by measuring the reinvasion of oxygen after nitrogen flushing (along the lines presented e.g. in [1, 3, 5]). A small plastic enclosure was put above the tablet and sample holder, and the region was flushed with nitrogen. There was 3–5 mm between laser front glass and tablet, most of it being within the enclosure. Approximately 60 s after the data-streaming start (scan-by-scan data acquisition), flushing was aborted and a quick air blow was applied to the area. During data evaluation, the spectral shift t_0 was fixed. The experimental outcome is shown in Fig. 12, and reveals that the gas exchange occurs within a few seconds.

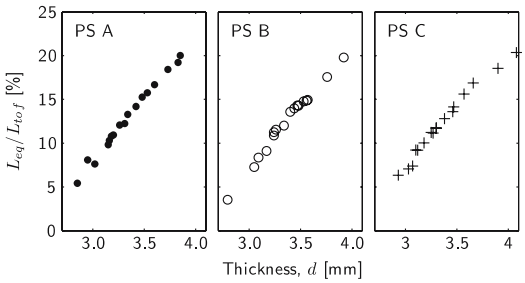

FIGURE 11 An optical measure of porosity is reached by normalising the derived L_{eq} with the average photon path length $L_{\text{tof}} = c\bar{t}/n(d)$

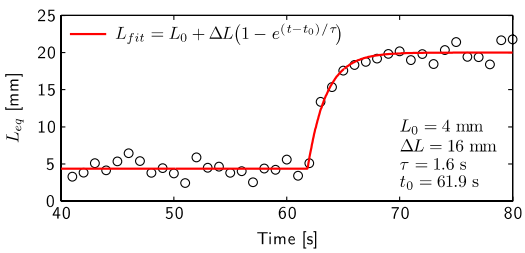

FIGURE 12 Streamed data showing gas dynamics in tablet $B_{3.17}$ ($L_{\text{eq}} = 12.9$ mm). Each data point is based on the average of 18 consecutive scans (1-s acquisition time). The tablet was put under a plastic enclosure, and the region was flushed with N_2. Flushing was aborted approximately 60 s after data-acquisition start

4 Discussion

This paper presents a minimalistic instrumentation for sensitive gas spectroscopy, and its use in pharmaceutical characterisation. It also presents significant improvements of GASMAS in general. For example, this is the first paper showing sub-millimetre sensitivity in measurements on scattering samples (see for example Fig. 5d, where the sensitivity is better than 0.1 mm L_{eq}).

Although the present instrumentation is cost efficient and outperforms the dual-beam fibre-optic instrumentation used in our first article on pharmaceutical characterisation, a fibre-optic approach may have advantages with respect to in situ access and light delivery. With respect to the previous work on pharmaceutical GASMAS [28], it should also be remembered that the present work includes several significant improvements that can be utilised also in systems based on fibre optics. These improvements include replacing the photomultiplier tube with a photodiode, incorporating a high-quality transimpedance amplifier, implementing synchronised and coherent sampling and employing sample rotation.

The obtained results demonstrate that accurate measurements of oxygen content in pharmaceutical materials on a second time scale is feasible. The fact that GASMAS is an all-optical characterisation of pharmaceutical materials makes it ideal for in-line/on-line analysis of pharmaceutical solids. Although it was used here to demonstrate prediction of porosity in tablets, the applicability of GASMAS extends to all solid materials such as powders, granulates and finished products and is expected to be highly useful as a general sensor of material transformations during pharmaceutical manufacturing.

The results presented also show that GASMAS depends on both actual tablet porosity and scattering properties. This is apparent in Fig. 9, where it can be seen that the tablets made from the smallest particle size (particle size *A*) exhibit larger oxygen absorbance. Since all tablets have the same weight (300 mg), this phenomenon can only be assigned to differences in light propagation. This is further verified by the use of photon time-of-flight experiments; see Fig. 10. This figure shows that type *A* tablets exhibit longer photon path lengths. Furthermore, the obvious pattern similarity between this time-of-flight data and the GASMAS L_{eq} data in Fig. 9 clearly shows that the somewhat noisy appearance in these two figures is due to tablet variations, not measurement uncertainties. This is further supported by the excellent reproducibility of both techniques, as well as by the outcome of the normalisation procedure used to introduce an optical measure of porosity (see Fig. 11). The smooth dependence exhibited by the $L_{\text{eq}}/L_{\text{tof}}$ ratio suggests that we, to a large extent, have compensated for tablet-specific variations in scattering properties. Furthermore, still referring to Fig. 11, the proposed measure of porosity gives similar results for the different particle size distributions. This is expected, since all tablets are made of 300-mg tablet material. However, regarding optical porosimetry, it is not evident that the ratio between equivalent path length L_{eq} and average photon path length is a proper estimation of true porosity. Such a claim would neglect the possibility that light prefers to travel in either pores or solid material. This fact also suggests that GASMAS in combination with time-of-flight spectroscopy may provide fundamental understanding of light propagation in scattering media. If the material density is well defined, the sample weight may provide true porosity (not the case for pharmaceutical materials, however). Now, if the optical measure of porosity differs from this direct measure of porosity, we may estimate with what preference the light travels in the solid material.

This paper does not provide information on the influence of light injection spot size, injection location and detection geometry. These issues deserve further attention. For example, if light is injected centrally, a larger absorption imprint would be encountered if one were to detect only peripherally transmitted light (rather than the detection of more or less all transmitted light, as in this work). In this context, it should also be noted that the average time-of-flight is measured using centrally detected light, while the GASMAS signal is based on light from a larger area.

Although the instrumentation and data evaluation used in this work exhibit very good performance, a few technical issues deserve some comments. First, it was noted that the response of the large-area photodiode depends on the illumination area. When comparing $2f$ optical to electrical modulation transfer, a 3% difference was noted for the cases of full detector illumination and central illumination (using a pinhole with 2-mm diameter). This should, however, be a minor problem, since the reference WMS signal was acquired under full detector illumination and the light transmitted through our samples is diffuse. Second, it should be noted that the mechanical setup sets limits to what one can expect in terms of performance. When detecting oxygen absorption in ambient

air environments, all mechanical instabilities cause uncertainties in interaction path length. We now show a day-to-day reproducibility in the order of 0.3 mm L_{eq}, and we expect that this is limited by the positioning of the diode laser. This is due to the fact that the laser position is adjusted between all measurements, and the accompanying uncertainty in path-length offset is probably in the order of the actual GASMAS reproducibility. It is likely that improvements would require a more dedicated mechanical setup (especially in an instrumentation introducing mechanical vibrations). Third, the use of rotational motors for the introduction of vibrations and rotation may not be an optimal solution, and we are exploring other alternatives for mechanical dithering. For GASMAS in general, further work is needed in order to characterise and understand the random interference signal that forces us to introduce vibrations and sample rotation. Fourth, the VCSEL output power is only about 200 μW, and the use of a more powerful DFB diode laser may allow faster measurements.

A natural future development of GASMAS would be to combine it with frequency-domain photon-migration technology, rather than the time-domain equivalent used in the present work. While the instrumentation needed for measurements of photon time-of-flight is complex and expensive, its Fourier-domain equivalent is less demanding and can to a large extent rely on the instrumentation already used for GASMAS recordings. There, photon path lengths may be measured by intensity modulating the laser in the 100-MHz regime, and measuring phase shifts due to sample transmission.

5 Conclusion

A fully digital, minimalistic, robust and cost-efficient instrumentation for sensitive single-beam tunable diode-laser absorption spectroscopy (TDLAS) has been developed. The system allows multi-harmonic detection, and scan-by-scan data streaming. Targeting molecular oxygen in ambient air environments, system sensitivity reaches into the 10^{-7} regime. We report on its use in gas in scattering media absorption spectroscopy (GASMAS) for structural characterisation of highly scattering pharmaceutical tablets. Resulting data is highly reproducible, and shows that the GASMAS signal depends on both actual tablet porosity and scattering properties. The observed oxygen absorption fractions are in the range 8×10^{-5} to 2×10^{-3}, and correspond to 2–50 mm of path length through ambient air (L_{eq}). The instrumentation is capable of adequate-quality measurements in a single second, allowing studies of gas exchange dynamics. In addition, the GASMAS data are, for the first time, carefully correlated with time-domain photon migration. Average path lengths range from 80 to 250 mm. The excellent co-variation of the two techniques shows that GASMAS is capable of sensing tablet variations. By combining the two techniques, we can introduce an optical measure of porosity. The proposed measure suggests porosities in the 5%–20% range. Finally, these satisfying results in combination with the simplistic TDLAS instrumentation provides industrial potential, especially in process analytical technology (PAT).

ACKNOWLEDGEMENTS The authors wish to thank Johan Mauritsson for sharing knowledge in Fourier analysis from the world of attophysics.

REFERENCES

1 M. Sjöholm, G. Somesfalean, J. Alnis, S. Andersson-Engels, S. Svanberg, Opt. Lett. **26**, 16 (2001)
2 G. Somesfalean, M. Sjöholm, J. Alnis, C. af Klinteberg, S. Andersson-Engels, S. Svanberg, Appl. Opt. **41**, 3538 (2002)
3 J. Alnis, B. Anderson, M. Sjöholm, G. Somesfalean, S. Svanberg, Appl. Phys. B **77**, 691 (2003)
4 M. Andersson, L. Persson, M. Sjöholm, S. Svanberg, Opt. Express **14**, 3641 (2006)
5 L. Persson, H. Gao, M. Sjöholm, S. Svanberg, Opt. Lasers Eng. **44**, 687 (2006)
6 L. Persson, K. Svanberg, S. Svanberg, Appl. Phys. B **82**, 313 (2006)
7 M. Andersson, L. Persson, T. Svensson, S. Svanberg, Rev. Sci. Instrum. **78**, 113 107 (2007)
8 L. Persson, M. Andersson, M. Cassel-Engquist, K. Svanberg, S. Svanberg, J. Biomed. Opt. **12**, 054 001 (2007)
9 J.A. Silver, Appl. Opt. **31**, 707 (1992)
10 T. Fernholz, H. Teichert, V. Ebert, Appl. Phys. B **75**, 229 (2002)
11 Maxim, Appl. Note 1040 (2002)
12 I. Linnerud, P. Kaspersen, T. Jæger, Appl. Phys. B **67**, 297 (1998)
13 M.G. Allen, Meas. Sci. Technol. **9**, 545 (1998)
14 E. Schlosser, J. Wolfrum, L. Hildebrandt, H. Seifert, B. Oser, V. Ebert, Appl. Phys. B **75**, 237 (2002)
15 G.B. Rieker, H. Li, X. Liu, J.B. Jeffries, R.K. Hanson, M.G. Allen, S.D. Wehe, P.A. Mulhall, H.S. Kindle, Meas. Sci. Technol. **18**, 1195 (2007)
16 J. Johansson, S. Folestad, S. Svanberg, M. Sjöholm, G. Somesfalean, C. Abrahamsson, S. Andersson-Engels, Int. Patent No. PCT WO 03/078983 (2003)
17 T. Svensson, L. Persson, M. Andersson, S. Svanberg, S. Andersson-Engels, J. Johansson, S. Folestad, Appl. Spectrosc. **61**, 784 (2007)
18 T. Svensson, M. Andersson, L. Rippe, J. Johansson, S. Folestad, S. Andersson-Engels, Opt. Lett. **33**, 80 (2008)
19 D.S. Bomse, A.C. Stanton, J.A. Silver, Appl. Opt. **31**, 718 (1992)
20 P. Kluczynski, J. Gustafsson, Å. Lindberg, O. Axner, Spectrochim. Acta B **56**, 1277 (2001)
21 L.S. Rothman, D. Jacquemart, A. Barbe, D. Chris Benner, M. Birk, L.R. Brown, M.R. Carleer, C. Chackerian Jr., K. Chance, L.H. Coudert, V. Dana, V.M. Devi, J.-M. Flaud, R.R. Gamache, A. Goldman, J.-M. Hartmann, K.W. Jucks, A.G. Maki, J.-Y. Mandin, S.T. Massie, J. Orphal, A. Perrin, C.P. Rinsland, M.A.H. Smith, J. Tennyson, R.N. Tolchenov, R.A. Toth, J. Vander Auwera, P. Varanasi, G. Wagner, J. Quant. Spectrosc. Radiat. Transf. **96**, 139 (2005)
22 H.P. Zappe, M. Hess, M. Moser, R. Hovel, K. Gulden, H.P. Gauggel, F.M. di Sopra, Appl. Opt. **39**, 2475 (2000)
23 P. Vogel, V. Ebert, Appl. Phys. B **72**, 127 (2001)
24 L. Bergström, S. Stemme, T. Dahlfors, H. Arwin, L. Ödberg, Cellulose **6**, 1 (1999)
25 C. Sun, J. Pharm. Sci. **94**, 2132 (2005)
26 B.W. Pogue, M.S. Patterson, J. Biomed. Opt. **11**, 041 102 (2006)
27 J. Johansson, S. Folestad, M. Josefson, A. Sparen, C. Abrahamsson, S. Andersson-Engels, S. Svanberg, Appl. Spectrosc. **56**, 725 (2002)
28 T. Svensson, M. Einarsdóttír, K. Svanberg, S. Andersson-Engels, J. Biomed. Opt. **12**, 014 022 (2007)
29 D. Contini, F. Martelli, G. Zaccanti, Appl. Opt. **36**, 4587 (1997)
30 F. Martelli, D. Contini, A. Taddeucci, G. Zaccanti, Appl. Opt. **36**, 4600 (1997)
31 P. Werle, R. Miicke, F. Slemr, Appl. Phys. B **57**, 131 (1993)
32 R. Arndt, J. Appl. Phys. **36**, 2522 (1965)

Paper XIII

Towards accurate in vivo spectroscopy of the human prostate

T. Svensson, E. Alerstam, M. Einarsdóttír, K. Svanberg, and S. Andersson-Engels.

Journal of Biophotonics **1**, in press (2008).

Towards Accurate *In Vivo* Spectroscopy of the Human Prostate

Tomas Svensson[1], Erik Alerstam[1], Margrét Einarsdóttír[2], Katarina Svanberg[2], and Stefan Andersson-Engels[1]
[1] *Department of Physics*
Lund University, Sweden and
[2] *Department of Oncology*
Lund University Hospital, Sweden
(Dated: June 5, 2008)

The recent interest in photodynamic therapy of human prostate cancer is accompanied by a need for techniques for *in vivo* monitoring of optical and physiological characteristics. We propose time-of-flight (TOF) spectroscopy in combination with Monte Carlo evaluation as a reliable optical technique for quantitative assessment of absorption, scattering, hemoglobin content and tissue oxygenation in the human prostate. For the first time, we demonstrate Monte Carlo-based evaluation of *in vivo* TOF photon migration data. We show that this approach is crucial in order to avoid the large errors associated with the use of time-resolved diffusion theory of light propagation in prostate-like tissues. This progress also allows us to present the first *in vivo* scattering spectroscopy of human prostate tissue. Furthermore, TOF spectroscopy, in contrast to the more common steady-state approach, is insensitive to bleedings, and has been found highly reliable (100% success rate).

Photodynamic therapy (PDT) is considered as a promising modality for treatment of prostate cancer [1, 2]. Clinical work was performed as early as 1990 [3], and several investigators have since then made efforts in bringing this therapy into the clinic [4–6]. PDT relies on the presence of photosensitiser, oxygen and light. Light is used to activate (excite) the photosensitiser, which then can produce cytotoxic substances and thus cause tissue destruction. Important issues are light dosimetry, photosensitiser concentrations and the availability of oxygen [7]. In this context, it is important to assess optical properties (scattering and absorption), as well as tissue oxygenation and sensitizer concentrations. Other applications of *in vivo* spectroscopy involves predicting response to chemotherapy or radiotherapy of cancer [8].

So far, the main methodology for assessment of *in vivo* optical properties of the prostate has been steady-state light fluence rate measurements in combination with diffusion modelling [9–11]. When utilising multiple source-detector separations, this approach should allow deduction of tissue effective attenuation (μ_{eff}). If the fluence rate is measured in absolute units (that is, in W/m^2), the technique theoretically allow quantification of both absorption and reduced scattering coefficients (μ_{a} and μ'_{s}, respectively). However, it is often difficult to realise absolute measurements *in vivo*. In addition, steady-state fluence rate measurements are aggravated by the localised bleedings caused by needle insertion, preventing proper quantitative derivation of optical and physiological parameters [10]. To resolve these difficulties, Svensson *et al.* recently introduced time-of-flight (TOF) spectroscopy as a tool for interstitial *in vivo* spectroscopy [12]. By analysis of the temporal dispersion of picosecond laser pulses, this technique allows quantification of μ_{a} and μ'_{s}. Since pulse shapes, rather than fluence rate levels, are evaluated, this quantification is found to be insensitive to local bleedings at the fibre tips. In [12], recorded photon TOF distributions were evaluated using time-domain diffusion theory of light propagation. Involving measurements at 660, 786 and 916 nm, the technique was found highly reliable, providing consistent data and good signal-to-noise for 27 measurements in 9 patients (100% success rate). However, the scattering spectroscopy in this study produced somewhat unexpected results. While Mie theory tells us that μ'_{s} is expected to decrease with wavelength, the derived μ'_{s} exhibited an increase from 786 to 916 nm. The authors suggested that this behaviour is due to a breakdown of diffusion theory, and that Monte Carlo-based evaluation may resolve the issue.

We recently developed a scheme for Monte Carlo evaluation of TOF spectroscopy, significantly improving the accuracy in the range of optical properties exhibited by the human prostate [13]. There, it was shown that time-resolved diffusion theory is indeed not a proper model for light propagation in this context. We also reported that the erroneous behaviour of the scattering spectroscopy in [12] was partly due to an inappropriate procedure for measurement of the instrumental response function (IRF), and not only due to modelling errors. Unfortunately, this prevents us from re-evaluating old data.

In this work, we present the first *in vivo* optical spectroscopy of the human prostate based on Monte Carlo evaluation. In addition, to our knowledge, it is the first time that Monte Carlo modelling is used for evaluation of *in vivo* TOF data in general. The results presented are based on previously unpublished clinical measurements. The refined IRF recordings in combination with the significant improvements in modelling suggests that our approach is not only reliable, but also accurate. Having overcome the problems affecting Ref. [12], we now present the first scattering spectroscopy of the human prostate. It should also be noted that the approach proposed in this letter should be applicable in other areas of *in vivo* spectroscopy.

Measurements were performed in connection with brachytherapy of prostate cancer, taking place during the dosimetry planning (between ultrasound mapping and

treatment). The presented data originate from two patients, referred to as patient A and B. Three sequential measurements, at three different fibre separations (typically within the range of 10-25 mm), are carried out for each patient. Patient A was eligible for seeds implantation as primary therapy of prostate cancer, thus belonging to the patient group examined in Ref [12]. In contrast, patient B had received external radiotherapy prior to our measurements, and was about to undergo high dose rate (HDR) brachytherapy.

Details on the instrumentation and the clinical procedures can be found in the previous publication [12]. Briefly, the system is based on pulsed diode laser technology and time correlated single photon counting (TCSPC). Four pulsed diode lasers (at 660, 786, 830, and 916 nm) produce pulses having a FWHM of about 70 ps (1-2 mW average power). Light is injected and collected interstitially using two optical fibers. Collected light is sent to an MCP-PMT, which together with a TCSPC computer card is used to obtain photon TOF histograms (24.4 ps time resolution). Our recently developed scheme for Monte Carlo-based evaluation is used for derivation of μ_a and μ_s' [13]. The scheme is based on so called White Monte Carlo (a single and scalable Monte Carlo simulation at zero absorption). In order to allow comparison with our previous work, evaluations are based on the temporal range defined by the 50% level (of peak maximum) on the rising flank, and the 20% level on the tail (50/20 fit range). Due to the model improvement, we expect that an extension of this range will improve evaluation performance. In particular, and in contrast to diffusion modelling, this improvement is expected also when including earlier photons. The derived scattering properties are further analysed by employing Mie theory [14]. This involves fitting an exponential $a \times (\lambda/\mu\text{m})^b$ to the derived μ_s' coefficients. Here, a is proportional to the density of scatterers, and b is related to the scatterer size. Furthermore, the four derived absorption coefficients are used for hemoglobin spectroscopy. The procedure is the same as in Ref. [12], and involves matching the observed absorption with a linear combination of the oxy- and deoxyhemoglobin spectra, while assuming that the prostate contains 70% water and 10% lipids. The outcome is stated in terms of total hemoglobin content (THC) and tissue oxygen saturation S_tO_2.

An example of raw TOF data from a prostate measurement is shown in Fig. 1. By highlighting the discrepancy between Monte Carlo and diffusion modelling, this figure also illustrates the breakdown of diffusion theory.

Derived THC ranges from 125 to 210 μM, and S_tO_2 from 67 to 78%. To exemplify prostate spectroscopy, the derived μ_s' and μ_a spectra from patient B (16.4 mm fibre separation), using both Monte Carlo and diffusion theory, are shown in Fig. 2. It is evident that the use of diffusion modelling results in significant overestimation of both μ_s' and μ_a. The magnitude of the overestimation increases with increasing absorption and decreasing scattering, i.e. when moving further towards the low albedo

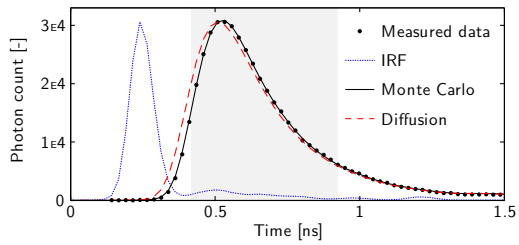

FIG. 1: Raw TOF data from Patient A (18.0 mm fibre separation, 830 nm). The measured data (markers) and IRF (dotted) are shown as recorded. The best fit using Monte-Carlo modelling (convolved with the IRF) is also shown (solid), yielding $\mu_s' = 7.4$ cm^{-1} and $\mu_a = 0.34$ cm^{-1}. The discrepancy between MC and diffusion is illustrated by providing the response for these optical properties as predicted by diffusion theory (dashed, arbitrary units). Note that the curve generated by Monte-Carlo modelling provides a good fit, even outside of the data subset used for evaluation (grey background).

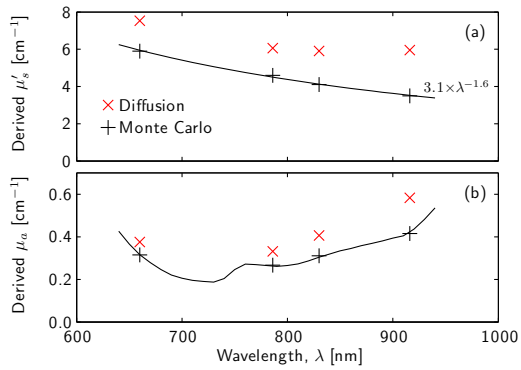

FIG. 2: Four-wavelength prostate spectroscopy illustrated using a measurement on patient B (16.4 mm fibre separation). The solid line in (b) is constructed from constituent chromophore spectra using the derived hemoglobin concentrations (THC 135 μM and S_tO_2 76 %). Note the severe overestimations related to diffusion modelling.

regime. This behaviour was found in all 6 measurements, and is in good agreement with previously published results [13]. Regardless of the evaluation method, the previously reported increase in μ_s' from 786 to 916 nm is cancelled, showing the importance of the improved procedure for IRF recordings. However, it is obvious that Monte Carlo evaluation is crucial in order to avoid errors related to time-domain diffusion modelling. Note, for the case of diffusion modelling, that the higher absorption at 916 nm generates a relatively larger overestimation of μ_s' than at 830 nm, eliminating the expected decrease in scattering. In the particular measurement shown in Fig. 2, diffusion modelling results in μ_s' errors of 25-70%,

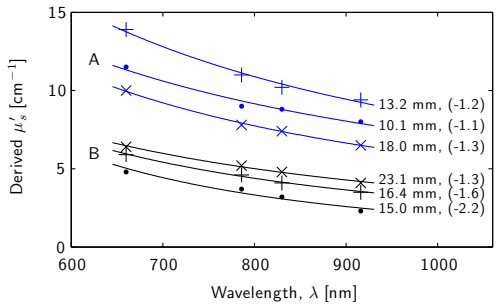

FIG. 3: Derived μ_s' for all measurements in patient A and B (markers), together with fitted $a \times (\lambda/\mu\text{m})^b$ curves (solid lines). The fiber separations were 10.1, 13.2 and 18.0 mm for patient A, and 15.0, 16.4 and 23.1 mm for patient B. Derived b coefficients are given within parentheses, while a is the μ_s' expected at $\lambda = 1$ μm.

and μ_a errors of 20-40%. These gross overestimations of derived scattering and absorption coefficients clearly illustrates the need for refined evaluation schemes, such as the novel White Monte Carlo approach used in this work.

The scattering spectroscopy is presented Fig. 3. As expected from Mie theory and tissue optics, the scattering decreases with wavelength in all six measurements. The magnitude of fitted b coefficients is comparable to what has been reported in for example breast tissue [16]. It should be noted that low scattering in combination with high absorption (for example $\mu_s' = 2.3$ and $\mu_a = 0.34$ at 916 nm for the 15.0 mm fibre separation) results in limited pulse broadening, leaving few datapoints available for data evaluation. Extending the fit range, or increasing the time resolution, may improve robustness (especially for measurements at longer wavelengths and shorter fibre separations, *i.e.* cases where detected pulses are relatively short).

The use of additional wavelengths, or even broadband radiation, is of course desirable and would increase spectroscopic precision. Broadband (white) light systems have been used for time-resolved spectroscopy in for example pharmaceutical characterisation [15] and breast tissue spectroscopy [16]. The recent development of compact broadband picosecond sources open for the possibility of broadband TOF spectroscopy even in demanding clinical settings [17]. Furthermore, the frequency domain correspondent of TOF spectroscopy provides a technical alternative [8]. Regardless of the technical solution, the photon migration model should be selected with care. Our experience is that it may be hard to judge model quality simply by inspection of obtained fits or residual patterns. For example, the diffusion model used in Ref. [12] appears to fit fairly well with obtained TOF histograms data although this is clearly shown not to be the case in Ref. [13]. The problem is not evident even when derived absorption coefficients are used for tissue chromophore spectroscopy.

In conclusion, we have reported on significant progress in *in vivo* spectroscopy of the human prostate. The use of Monte Carlo evaluation was shown to be a major leap forward in terms of accuracy, and the importance of appropriate photon migration modelling in TOF spectroscopy has been clearly illustrated. Given the advantages of the presented approach, it should prove useful in various applications of *in vivo* spectroscopy.

[1] C. M. Moore, I. M. Hoh, S. G. Bown, and M. Emberton, BJU Int. **96**, 754 (2005).
[2] J. H. Pinthus, A. Bogaards, R. Weersink, B. C. Wilson, and J. Trachtenberg, J. Urol. 175, 1201 (2006).
[3] T. Windahl, S. O. Andersson, and L. Lofgren, Lancet 336, 1139 (1990).
[4] T.R. Nathan, D.E. Whitelaw, S.C. Chang, W.R. Lees, P.M. Ripley, H. Payne, L. Jones, M.C. Parkinson, M. Emberton, A.R. Gillams, A.R. Mundy, and S.G. Bown, J. Urol. 168, 1427 (2002).
[5] K. Verigos, D. C. H. Stripp, R. Mick, T. C. Zhu, R. Whittington, D. Smith, A. Dimofte, J. Finlay, T. M. Busch, Z. A. Tochner, S. B. Malkowicz, E. Glatstein, and S. M. Hahn, J. Environ. Pathol. Toxicol. Oncol. 25, 373 (2006).
[6] C. M. Moore, T. R. Nathan, W. R. Lees, C. A. Mosse, A. Freeman, M. Emberton, and S. G. Bown, Laser Surg. Med. 38, 356 (2006).
[7] B. C. Wilson, M. S. Patterson, and L. Lilge, Laser Med. Sci. 12, 182 (1997).
[8] A. Cerussi, D. Hsiang, N. Shah, R. Mehta, A. Durkin, J. Butler, and B. J. Tromberg, P. Natl. Acad. Sci. USA 104, 4014 (2007).
[9] L. K. Lee, C. Whitehurst, M. L. Pantelides, and J. V. Moore, Photochem. Photobiol. 62, 882 (1995).
[10] T. C. Zhu, A. Dimofte, J. C. Finlay, D. Stripp, T. Busch, J. Miles, R. Whittington, S. B. Malkowicz, Z. Tochner, E. Glatstein, and S. M. Hahn, Photochem. Photobiol. 81, 96 (2005).
[11] R. A. Weersink, A. Bogaards, M. Gertner, S. R. H. Davidson, K. Zhang, G. Netchev, J. Trachtenberg, and B. C. Wilson, J. Photoch. Photobio. B 79, 211 (2005).
[12] T. Svensson, S. Andersson-Engels, M. Einarsdttr, and K. Svanberg, J. Biomed. Opt. 12, 014022 (2007).
[13] E. Alerstam, S. Andersson-Engels, and T. Svensson, J. Biomed. Opt., in press (2007).
[14] J. R. Mourant, T. Fuselier, J. Boyer, T. M. Johnson, and I. J. Bigio, Appl. Opt. 36, 949 (1997).
[15] C. Abrahamsson, T. Svensson, S. Svanberg, S. Andersson-Engels, J. Johansson, and S. Folestad, Opt. Express 12, 4103 (2004).
[16] A. Pifferi, J. Swartling, E. Chikoidze, A. Torricelli, P. Taroni, A. Bassi, S. Andersson-Engels, and R. Cubeddu, J. Biomed. Opt. 9, 1143 (2004).
[17] A. Bassi, A. Farina, C. D'Andrea, A. Pifferi, G. Valentini, and R. Cubeddu, Opt. Express 15, 14482 (2007).

Paper XIV

Improved accuracy in time-resolved diffuse reflectance spectroscopy

E. Alerstam, S. Andersson-Engels and T. Svensson.

Optics Express **16**, 10434-10448 (2008).

Improved accuracy in time-resolved diffuse reflectance spectroscopy

Erik Alerstam, Stefan Andersson-Engels and Tomas Svensson

Department of Physics, Lund University
Sweden
erik.alerstam@fysik.lth.se

Abstract: Significant improvements in the accuracy of time-resolved diffuse reflectance spectroscopy are reached by using a Monte Carlo scheme for evaluation of measured photon time-of-flight distributions. The use of time-resolved diffusion theory of photon migration, being the current standard scheme for data evaluation, is shown defective. In particular, the familiar problem sometimes referred to as absorption-to-scattering coupling or crosstalk, is identified as an error related to the breakdown of the diffusion approximation. These systematic errors are investigated numerically using Monte Carlo simulations, and their influence on data evaluation of experimental recordings are accurately predicted. The proposed Monte Carlo-based data evaluation avoids these errors, and can be used for routine data evaluation. The accuracy and reproducibility of both MC and diffusion modeling are investigated experimentally using the MEDPHOT set of solid tissue-simulating phantoms, and provides convincing arguments that Monte Carlo-based evaluation is crucial in important ranges of optical properties. In contrast to diffusion-based evaluation, the Monte Carlo scheme results in optical properties consistent with phantom design. Since the MEDPHOT phantoms are used for international comparisons and performance assessment, the performed characterization is carefully reported.

OCIS codes: (170.5280) Photon migration; (300.6500) Spectroscopy, time-resolved; (170.6510) Spectroscopy, tissue diagnostics; (170.7050) Turbid media; (290.1990) Diffusion; (160.4760) Optical properties

References and links

1. B. Chance, S. Nioka, J. Kent, K. Mccully, M. Fountain, R. Greenfeld, and G. Holtom, "Time-resolved spectroscopy of hemoglobin and myoglobin in resting and ischemic muscle," Anal. Biochem. **174**, 698–707 (1988).
2. B. Chance, J. Leigh, H. Miyake, D. Smith, S. Nioka, R. Greenfeld, M. Finander, K. Kaufmann, W. Levy, M. Young, P. Cohen, H. Yoshioka, and R. Boretsky, "Comparison of time-resolved and time-unresolved measurements of deoxyhemoglobin in brain," P. Natl. Acad. Sci. USA **85**, 4971–4975 (1988).
3. A. Pifferi, J. Swartling, E. Chikoidze, A. Torricelli, P. Taroni, A. Bassi, S. Andersson-Engels, and R. Cubeddu, "Spectroscopic time-resolved diffuse reflectance and transmittance measurements of the female breast at different interfiber distances," J. Biomed. Opt. **9**, 1143–1151 (2004).
4. T. Svensson, S. Andersson-Engels, M. Einarsdóttír, and K. Svanberg, "In vivo optical characterization of human prostate tissue using near-infrared time-resolved spectroscopy," J. Biomed. Opt. **12**, 014022 (2007).
5. A. Gibson, J. Hebden, and S. Arridge, "Recent advances in diffuse optical imaging," Phys. Med. Biol. **50**, R1–R43 (2005).
6. C. Abrahamsson, A. Löwgren, B. Strömdahl, T. Svensson, S. Andersson-Engels, J. Johansson, and S. Folestad, "Scatter correction of transmission near-infrared spectra by photon migration data: Quantitative analysis of solids," Appl. Spectrosc. **59**, 1381–1387 (2005).
7. F. Pandozzi and D. Burns, "Power law analysis estimates of analyte concentration and particle size in highly scattering granular samples from photon time-of-flight measurements," Anal. Chem. **79**, 6792–6798 (2007).
8. T. Svensson, M. Andersson, L. Rippe, S. Svanberg, S. Andersson-Engels, J. Johansson, and S. Folestad, "VCSEL-based oxygen spectroscopy for structural analysis of pharmaceutical solids," Appl. Phys. B **90**, 345–354 (2008).

9. K. Yoo, F. Liu, and R. Alfano, "When does the diffusion-approximation fail to describe photon transport in random-media," Phys. Rev. Lett. **64**, 2647–2650 (1990).
10. R. Haskell, L. Svaasand, T. Tsay, T. Feng, and M. Mcadams, "Boundary-conditions for the diffusion equation in radiative-transfer," J. Opt. Soc. Am. A **11**, 2727–2741 (1994).
11. A. Hielscher, S. Jacques, L. Wang, and F. Tittel, "The influence of boundary-conditions on the accuracy of diffusion-theory in time-resolved reflectance spectroscopy of biological tissues," Phys. Med. Biol. **40**, 1957–1975 (1995).
12. R. Cubeddu, A. Pifferi, P. Taroni, A. Torricelli, and G. Valentini, "Experimental test of theoretical models for time-resolved reflectance," Med. Phys. **23**, 1625–1633 (1996).
13. A. Kienle and M. Patterson, "Improved solutions of the steady-state and the time-resolved diffusion equations for reflectance from a semi-infinite turbid medium," J. Opt. Soc. Am. A **14**, 246–254 (1997).
14. E. Alerstam, S. Andersson-Engels, and T. Svensson, "White Monte Carlo for time-resolved photon migration," J. Biomed. Opt. (to be published).
15. R. Graaff, M. Koelink, F. Demul, W. Zijlstra, A. Dassel, and J. Aarnoudse, "Condensed Monte Carlo simulations for the description of light transport," Appl. Opt. **32**, 426–434 (1993).
16. A. Kienle and M. Patterson, "Determination of the optical properties of turbid media from a single Monte Carlo simulation," Phys. Med. Biol. **41**, 2221–2227 (1996).
17. A. Pifferi, R. Berg, P. Taroni, and S. Andersson-Engels, "Fitting of Time-resolved reflectance curves with a Monte Carlo model," in *Trends in Optics and Photonics: Advances in Optical Imaging and Photon Migration*, vol. 2, pp. 311–314 (Optical Society of America, 1996).
18. T. Svensson, E. Alerstam, M. Einarsdóttír, K. Svanberg, and S. Andersson-Engels, "Towards accuracte *in vivo* spectroscopy of the human prostate," J. Biophoton. DOI: 10.1002/jbio.200710025 (posted 24 April 2008, in press).
19. A. Pifferi, A. Torricelli, A. Bassi, P. Taroni, R. Cubeddu, H. Wabnitz, D. Grosenick, M. Moller, R. MacDonald, J. Swartling, T. Svensson, S. Andersson-Engels, R. van Veen, H. Sterenborg, J. Tualle, H. Nghiem, S. Avrillier, M. Whelan, and H. Stamm, "Performance assessment of photon migration instruments: the MEDPHOT protocol," Appl. Opt. **44**, 2104–2114 (2005).
20. A. Pifferi, A. Torricelli, P. Taroni, D. Comelli, A. Bassi, and R. Cubeddu, "Fully automated time domain spectrometer for the absorption and scattering characterization of diffusive media," Rev. Sci. Instrum. **78**, 053103 (2007).
21. B. Pogue and M. Patterson, "Review of tissue simulating phantoms for optical spectroscopy, imaging and dosimetry," J. Biomed. Opt. **11**, 041102 (2006).
22. L. Spinelli, F. Martelli, A. Farina, A. Pifferi, A. Torricelli, R. Cubeddu, and G. Zaccanti, "Calibration of scattering and absorption properties of a liquid diffusive medium at NIR wavelengths. Time-resolved method," Opt. Express **15**, 6589–6604 (2007).
23. M. Firbank, M. Oda, and D. Delpy, "An improved design for a stable and reproducible phantom material for use in near-infrared spectroscopy and imaging," Phys. Med. Biol. **40**, 955–961 (1995).
24. J. Swartling, J. S. Dam, and S. Andersson-Engels, "Comparison of spatially and temporally resolved diffuse-reflectance measurement systems for determination of biomedical optical properties," Appl. Opt. **42**, 4612–4620 (2003).
25. A. Pifferi, P. Taroni, G. Valentini, and S. Andersson-Engels, "Real-time method for fitting time-resolved reflectance and transmittance measurements with a Monte Carlo model," Appl. Opt. **37**, 2774–2780 (1998).
26. R. Graaff, J. Aarnoudse, F. Demul, and H. Jentink, "Similarity relations for anisotropic scattering in absorbing media," Opt. Eng. **32**, 244–252 (1993).
27. K. Furutsu and Y. Yamada, "Diffusion-approximation for a dissipative random medium and the applications," Phys. Rev. E **50**, 3634–3640 (1994).
28. M. Bassani, F. Martelli, G. Zaccanti, and D. Contini, "Independence of the diffusion coefficient from absorption: Experimental and numerical evidence," Opt. Lett. **22**, 853–855 (1997).
29. T. Nakai, G. Nishimura, K. Yamamoto, and M. Tamura, "Expression of optical diffusion coefficient in high-absorption turbid media," Phys. Med. Biol. **42**, 2541–2549 (1997).
30. T. Durduran, A. Yodh, B. Chance, and D. Boas, "Does the photon-diffusion coefficient depend on absorption?" J. Opt. Soc. Am. A **14**, 3358–3365 (1997).
31. L. Marti-Lopez, J. Hebden, and J.-L. Bouza-Dominguez, "Estimates of minimum pulse width and maximum modulation frequency for diffusion optical tomography," Opt. Laser Eng. **44**, 1172–1184 (2006).

1. Introduction

Photon time-of-flight spectroscopy (TOFS), also known as time-resolved spectroscopy, is a well established technique for characterization of scattering media. Its ability to accurately and quantitatively assess both absorption and scattering is extensively utilized in the field of biomedical optics. Applications include *in vivo* determination of physiological and optical parameters of muscle [1], the human brain [2], breast tissue [3], and human prostate tissue [4]. Furthermore, TOFS is an important tool in the emerging field of optical tomography [5]. A slightly differ-

ent area of application is pharmaceutical analysis, where TOFS has been used for analysis of chemical composition and physical properties [6, 7, 8].

Modeling of light propagation in scattering materials (*i.e.* photon migration) is a fairly complex matter. The photon time-of-flight (TOF) distribution, as recorded in TOFS, depends on refractive index, absorption and scattering coefficients, scattering anisotropy, sample geometry and boundary conditions, as well as on the size and location of source and detector. The complexity of this problem is reflected in the fact that Monte Carlo (MC) simulation is the gold standard for photon migration modeling. MC allows direct simulation of radiative transport theory, and is therefore considered highly accurate. The difficulties connected with the use of MC for data evaluation have, however, prevented it from becoming a tool for routine data analysis. This is especially the case in TOFS, where most photon migration modeling is based on the diffusion approximation of radiative transport theory. In simple geometries, diffusion theory supplies analytical expressions for photon TOF distributions, and dramatically simplifies data evaluation.

As early as 1990, Yoo *et al.* pointed out that time-domain diffusion theory is incapable of describing the propagation of light pulses in many materials of physical interest [9]. Since then several authors have investigated the validity of time-domain diffusion theory, and its dependence on how boundary conditions are taken into account [10]. Hielscher *et al.* concluded that the theory fails in reproducing the results from MC simulations of diffuse reflectance, and that the determination of reduced scattering coefficients suffer from particularly large errors [11]. Similar findings are reported by Cubbedu *et al.* who concluded that the model performance varies with the range of optical properties, as well as on experimental configuration [12]. Kienle *et al.* refined the diffusion models used for time-resolved diffuse reflectance, but reported that significant deviations from MC remains [13]. The three above cited publications clearly shows that diffusion modeling fails in describing time-resolved diffuse reflectance in important ranges of optical properties, regardless of how boundary conditions are treated. Despite these findings, diffusion modeling has remained the standard tool for data evaluation in TOFS.

In general, the validity of diffusion modeling decreases with increasing absorption, decreasing scattering, and decreased source-detector separation. Motivated by the high absorption and low scattering encountered in human prostate [4], we recently developed a scheme for Monte Carlo evaluation of TOFS data [14]. The developed scheme is referred to as White Monte Carlo (WMC), and is based on early ideas of the scalability of Monte Carlo simulations [15, 16, 17]. The speed and flexibility of the WMC approach makes it suitable for routine evaluation of TOFS in both reflectance and interstitial configurations, over a wide range of optical properties. The superior performance of WMC-based data evaluation has been carefully verified for the interstitial geometry, both theoretically and experimentally using liquid phantoms (intralipid and ink). More recently, WMC modeling has been used to significantly improve the accuracy of *in vivo* TOFS characterization of prostate tissue [18].

WMC evaluation is of interest also for the important case of diffuse reflectance, especially since Monte Carlo accurately can account for boundary effects. The present work aims at giving both experimental and theoretical evidence that WMC-based data evaluation significantly improves the performance of time-resolved diffuse reflectance (*i.e.* reflectance TOFS). It also aims to explain and quantify the model-related errors induced by diffusion modeling of diffuse reflectance. In particular, WMC is shown to avoid and explain the previously reported artifacts of TOFS referred to as absorption-to-scattering coupling or crosstalk [19, 20]. Experimental work is carried out on the solid phantoms prepared by Pifferi *et al.* that originally was intended for use in an international comparison of photon migration instrumentation (the MEDPHOT phantoms) [19]. Since WMC modeling is shown superior to diffusion modeling, the characterization of these phantoms is an important part of the results of the present article. Several authors have stressed the importance of calibrated and characterized reference phantoms [19, 21, 22], and we argue that the data presented here is, up to now, the most accurate assessment of the optical properties (absorption and reduced scattering) of these phantoms.

2. Materials and methods

2.1. Time-of-flight instrumentation

Photon time-of-flight experiments were conducted using a compact (50x50x30 cm^3) and portable time-domain photon migration instrument primarily intended for spectroscopy of biological tissues in clinical environments. Detailed information on the instrumentation can be found in previous publications [4]. Briefly, the system is based on pulsed diode laser technology and time correlated single photon counting (TCSPC). Four pulsed diode lasers (at 660, 786, 830 and 916 nm) generate 70 ps FWHM pulses (average power 1-2 mW). Light is injected into the sample and collected using 600 μm GRIN optical fibres. The collected light is sent to a fast MCP-PMT connected to a TCSPC-card that records the time-of-flight histograms with 24.4 ps time resolution. The instrument response function (IRF) is measured by putting the two fibre ends face-to-face with a thin paper coated on both sides with black toner. The total broadening of the system yields an IRF of approximately 100 ps FWHM.

2.2. The MEDPHOT phantom kit

This study utilized the MEDPHOT phantom kit, a collection of 32 solid cylinders (4.5 cm thick, 10.5 cm diameter) with different scattering and absorption properties. These epoxy-based solid phantoms were fabricated as a part of the MEDPHOT protocol, intended to be circulated among research groups, to allow comparison of the performance of different instruments. The phantoms were manufactured to combine four concentrations of scatterer (TiO_2 powder) with eight concentrations of absorber (toner) in linear and equally spaced steps. The phantoms are labeled with a letter and a number, where the letter indicate the nominal scattering (A, B, C and D, corresponding to μ_s'= 5, 10, 15 and 20 cm^{-1}, respectively, at 800 nm) and the number indicate the nominal absorption (1, 2, 3, 4, 5, 6, 7, 8 corresponding to μ_a= 0, 0.05, 0.10, 0.15, 0.20, 0.25, 0.30, 0.35 cm^{-1}, respectively, at 800 nm)[19]. The refractive index of the resin matrix was assumed to be $n = 1.55$ [23]. Also (owing the Monte-Carlo based evaluation method), the anisotropy factor of the TiO_2 had to be estimated. Based on integrating sphere measurements by Swartling *et al.* [24], on the same brand of TiO_2 powder (T-8141; Sigma-Aldrich, St. Louis, Missouri) the anisotropy factor, *g*, was assumed to be 0.75, which is large enough for the similarity relation to apply, i.e. independence of *g* on the derived μ_s' [25, 26].

Unfortunately the phantom A8 was missing when the phantoms were shipped to us and our measurements hence do not include this phantom.

2.3. Experimental

The measurements were performed by putting the optical fibres (guided by thin stainless steel tubes) in contact with the sample. The fibre separation was fixed at ρ =15 mm (center to center), and the positioning of the fibre pair on the phantom was random (somewhere in the middle of the phantom). The space between the fibres was occupied by a simple light-trap (black paper folded several times in contact with the phantom somewhere in between the fibres) to minimize the possibility of light-leakage into the collecting fibre. For the same reason, all adjacent surfaces were covered in black paper. Data were collected for 30 seconds for each measurement.

To minimize the temporal drifts, all measurements were conducted in a temperature stabilized lab where the system had been running for several hours prior to each measurement session. The temperature in the lab, as well as inside the system, was monitored to ensure stability during the measurements. The IRF was recorded approximately every 15 minutes during measurements as well as prior to and after each session. The phantoms were measured in random order independently on three occasions (2007-12-21 and twice 2008-01-08, 1.5 hours apart), denoted run 1, run 2 and run 3 in chronological order (represented by circles, diamonds and squares respectively throughout the figures in this work).

2.4. Modeling

This work utilizes two different forward models for photon propagation for data evaluation and mutual comparison, the Monte-Carlo based White Monte Carlo (WMC) model [14] and the diffusion approximation of radiative transport theory, utilizing the extrapolated boundary condition (EBC diffusion) [10, 13]. Since the fibre separation is significantly smaller than the phantom dimensions, it is assumed that the phantoms can be treated as semi-infinite.

The WMC model has been extensively explained in [14]. Briefly, the scheme is based on the scalability of Monte-Carlo simulations in certain geometries, *e.g.* infinite and semi-infinite homogenously scattering media. Hence a single simulation, comprising several billion photons, is performed and the resulting photon distribution can be scaled to the desired μ_s' and μ_a. The approach provides a fast and accurate equivalent to traditional Monte Carlo that can be used as a forward photon propagation model. The input parameters for the database-simulation used in this work were: Semi-infinite media, μ_s^{max}=90 cm^{-1}, t_{max}=2 ns, NA=0.29, n=1.55, g=0.75 and 6×10^9 photons. During this simulation, the photons are simulated at $\mu_s=\mu_s^{max}$ in an absorptionless media ($\mu_a=0$). Photons are terminated when they escape the media or when the simulated time-of-flight exceeds t_{max}. This results in a time interval [0,t_{max}] where the time-of-flight distribution is valid. However, during spatial (*i.e.* μ_s) scaling from μ_s^{max} to μ_s this time interval also scales as [0,αt_{max}] where $\alpha=\mu_s^{max}/\mu_s$. This implies that WMC will be a less advantageous when the resulting pulses are broad in time, *i.e.* at high scattering and low absorption.

During WMC evaluation of time-of-flight data, the fitting procedure is based on an exhaustive search over a pre-defined μ_s' interval with a finite resolution, $\Delta\mu_s'$. For each μ_s' value, the optimal values of μ_a and a free amplitude parameter, k are determined using a Marquard-Levenberg minimization of the error norm:

$$\tilde{\chi}^2(\mu_s')=\min_{k,\mu_a}\left\{\chi^2(k,\mu_a,\mu_s')\right\}. \tag{1}$$

In this work, a μ_s' resolution of $\Delta\mu_s'$=0.05 cm^{-1} was used.

The impulse response of a semi-infinite media, modeled using the diffusion approximation of radiative transport theory with the extrapolated boundary condition (EBC-diffusion) is given by Eq. 2 [10, 13].

$$R(\rho,t)=a(n)\Phi(\rho,z=0,t)+b(n)R_f(\rho,t), \tag{2}$$

where ρ is the source-detector separation, and the coefficients $a(n)$ and $b(n)$ are dependent on the refractive index of the medium. The reflectance (Eq. 2) is the sum of two terms, the fluence rate, Φ, and the flux, R_f, weighted by a and b. The two terms are given in Eq. 3 and Eq. 4 respectively.

$$\Phi(\rho,z=0,t)=\frac{c'}{(4\pi Dc't)^{3/2}}\exp(-\mu_a c't)\left[\exp\left(\frac{-{r_1}^2}{4Dc't}\right)-\exp\left(\frac{-{r_2}^2}{4Dc't}\right)\right], \tag{3}$$

$$R_f(\rho,t)=\frac{1}{2}\frac{1}{(4\pi Dc')^{3/2}}t^{-5/2}\exp(-\mu_a c't)\left[z_0\exp\left(\frac{-{r_1}^2}{4Dc't}\right)+(z_0+2z_b)\exp\left(\frac{-{r_2}^2}{4Dc't}\right)\right], \tag{4}$$

Here, ${r_1}^2={z_0}^2+\rho^2$ is the squared distance to the positive source, ${r_2}^2=(z_0+2z_b)^2+\rho^2$ the squared distance to the negative source, and c' is the speed of light in the medium. In this work, the diffusion coefficient, D, is defined in the absorption-independent way [27, 28, 29, 30], $D=(3\mu_s)^{-1}$. The two distances z_0 and z_b related to the source mirroring of EBC are given by:

$$z_0=\frac{1}{\mu_a+\mu_s'}, \tag{5}$$

$$z_b = \frac{1+R_{eff}(n)}{1-R_{eff}(n)}2D, \tag{6}$$

where $R_{eff}(n)$ is the effective reflection coefficient which is dependent on the refractive index of the medium. Using Eq. 2.3.5 and 2.3.7 of [10] to calculate R_{eff} for $n = 1.55$ yields $R_{eff} = 0.599$. The a and b coefficients are calculated using Eq. 7 of [13], resulting in $a(1.55) = 0.094$ $b(1.55) = 0.251$.

When the diffusion approximation is employed for data evaluation, an optimal fit between experimental data and $kR(\rho,t)$ is reached iteratively by employing Levenberg-Marquardt optimization (in which μ_s', μ_a, and the free amplitude parameter k are adjusted).

It should be noted that during the iterative data-fitting procedure of both the EBC-diffusion and the WMC model, the impulse responses provided by the models are convoluted with the recorded IRF. To minimize the effect of an uncertainty in the recorded IRF all data below 20% of the peak intensity is not used during the fitting procedure. In addition, during EBC-diffusion fitting, all data below 80% on the leading edge is disregarded as diffusion modeling is known to be a poor model for early photons [9, 12, 13]. The remaining data used during fitting is said to be within the fitting range. For simplicity, fitting ranges are denoted by the above stated percentages, *e.g.* EBC-diffusion uses a 80/20 fitting range while WMC uses a 20/20 fitting range.

During evaluation of experimental data the data points were weighted with the square-root of the signal given the normal distributed noise. During diffusion-based evaluation of WMC data, all data points were equally weighted (the noise characteristics of WMC simulations are not directly comparable to that of experimental recordings).

Finally, note that the two above mentioned models apply for reflectance in semi-infinite geometries, while the phantoms have a finite diameter and a finite thickness. However, since the fibre separation is significantly smaller than the phantom dimensions, it is assumed that the phantoms can be treated as semi-infinite. In fact, Monte Carlo simulation in an infinite geometry for a worst case scenario ($\mu_s' = 3$ cm^{-1} and $\mu_a = 0$ cm^{-1}, *i.e.* both lower scattering and lower absorption than our phantoms) shows that none of the photons that are detected at $\rho = 15$ mm and fall within the 20/20 fit range would have been affected by changing the geometry from a semi-infinite half-space to the actual phantom geometry. This was concluded by tracking 2×10^8 photons and recording their maximum depth and maximum radial excursion (4×10^5 photons contributed to the TOF distribution at $\rho = 15$ mm). Note, however, that if longer time-of-flights are included (*e.g.* when the fit range is extended), phantom boundaries may become an issue.

3. Results

Motivated by the fact the optical properties of the MEDPHOT phantoms commonly are characterized at around 800 nm, the presentation of experimental results in this section focus on the measurements at 786 nm. The results do however apply to all four measured wavelengths, and all data is enclosed in the Appendix. Note also that the simulation results apply to all wavelengths.

3.1. WMC versus the EBC diffusion model

In order to quantify the errors related to the use of EBC diffusion modeling, the corresponding TOF distributions were fitted to the TOF histograms delivered by the WMC model. The WMC-model, being equivalent to traditional Monte Carlo, is considered the gold standard, *i.e.* the optical properties used by the WMC model, μ_{WMC}, are considered true optical properties. To provide results comparable to our experimental results a 80/20 fitting range was used, and the temporal channel width was 24.4 ps (equal to the experimental channel width, see Sect. 2.1). Furthermore, to make the results applicable to actual measured data, both the WMC and

diffusion-based TOF distributions were convoluted (during the fitting procedure) with an IRF from our system. The same IRF was used in all convolutions (note that this eliminates the IRF measurement uncertainty that may aggravate real measurements). To verify that the results obtained were not dependent on the specific IRF used, the procedure was repeated with a 100 ps FWHM Gaussian, representing an almost ideal IRF, showing only minor differences.

The parameter space covered, *i.e.* the parameter spaced used to extract TOF distributions from the WMC-model, was:

$$0.01 \leq \mu_a \leq 0.75 \ [\mathrm{cm}^{-1}]$$
$$2 \leq \mu_s' \leq 18 \quad [\mathrm{cm}^{-1}]$$

The fibre separation and refractive index were fixed at $\rho = 15$ mm and $n = 1.55$.

The relative error in derived optical properties is defined as:

$$\Delta\mu = \frac{\mu_D - \mu_{WMC}}{\mu_{WMC}}, \tag{7}$$

where μ_D is the optical properties derived when employing data evaluation based on the EBC diffusion model. The corresponding error map is shown in Fig. 1. The results are similar to those presented for infinite media in Ref. [14], indicating that the presence of a boundary does not significantly worsen the performance of diffusion based modeling when using a reasonable boundary condition. In this context, it is also interesting to study the case of an ideal TOFS-system, *i.e.* one that exhibits an infinitely short IRF so that true impulse responses can be studied. An error map for impulse responses is shown in Fig. 2.

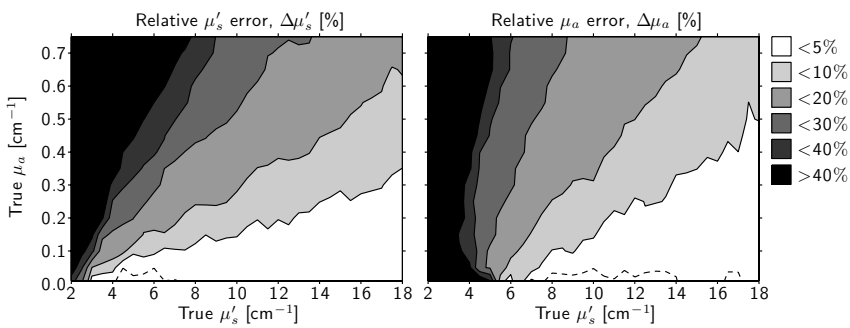

Fig. 1. Relative errors due to EBC diffusion modeling when using a 80/20 evaluation range, and involving a convolution with an IRF recorded by our TOFS system. The dashed line indicates the zero relative error and hence the border between overestimation and underestimation of the derived parameters. For most optical combinations of μ_s' and μ_a overestimations of the derived optical properties occur while minor underestimations occasionally are observed when the absorption is low.

When comparing Fig. 1 and 2, one should take into consideration that the effective fitting ranges of the two are different, despite both of them using an 80/20 fit range. Regardless, they exhibit similar behaviour. This indicate that the performance of EBC-diffusion based evaluation is not heavily affected by the presence of a reasonably short, non-ideal IRF (as long as the IRF is recorded accurately).

3.2. Experimental results

The experimental results for λ =786 nm are presented in Fig. 3, and includes evaluations based on both WMC (a), and EBC diffusion modeling (b). The three runs, 1, 2, and 3, are presented as

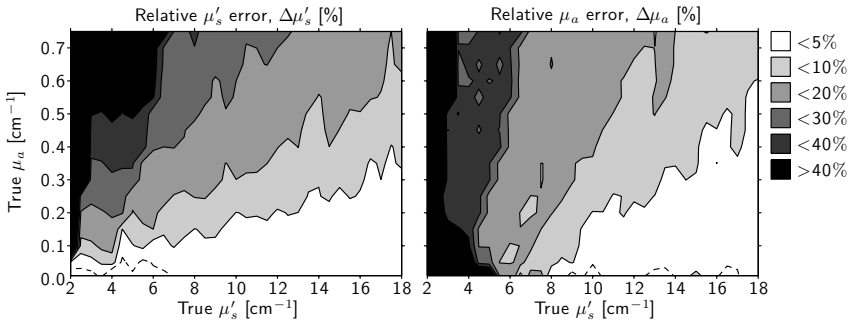

Fig. 2. Relative errors due to EBC diffusion modeling when using a 80/20 fit range for the impulse response. The dashed line indicates the zero relative error and hence the border between overestimation and underestimation of the derived parameters. As in Fig. 1, overestimations of the derived optical properties dominate. The apparent instability in derived μ_a for high absorption and low scattering media is most likely related to the few number of data points eligible for evaluation resulting from the short pulses exhibited by such media.

circles, diamonds and squares respectively, illustrating the high reproducibility of our measurements. Note that a single outlier is present (A7, run 2), presumably related to an experimental error. The mean scattering and absorption of all the constant-level series, as obtained from

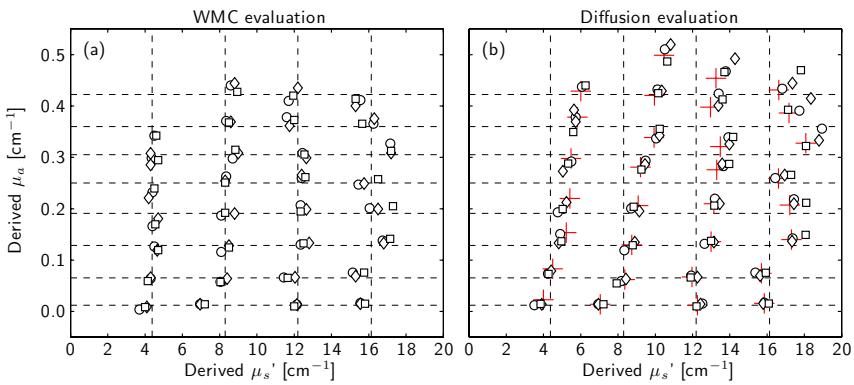

Fig. 3. A so called *accuracy plot* (see Ref. [19]) showing derived μ_s' and μ_a at 786 nm for run 1 (circles), run 2 (diamonds) and run 3 (squares), using (a) WMC evaluation, and (b) diffusion evaluation. From the design of the phantoms, points are expected to fall on a grid. The mean scattering and absorption values for the WMC measurements are shown as dashed lines in both figures. In addition, the mean WMC-derived optical properties with corrections according to the error-map (Fig. 1) are shown in (b) as red crosses.

WMC-based data evaluation, are presented as dashed lines (vertical lines for constant scattering series and horizontal lines for constant absorption series). For comparison, these lines are also presented in part (b) where the outcome of diffusion modeling is presented. It is apparent that the optical properties derived using the WMC approach exhibit linear behavior, while the linearity is disrupted by model-related errors when data evaluation is based on EBC diffusion modeling. This erroneous behavior was predicted in Sect. 3.1. All the WMC-derived data (for all four wavelengths) are explicitly given in Tab. 1 and 2 in order to allow other researchers to

directly compare their results to those presented here.

It is important to note that the overall pattern of derived optical properties deviates from the perfect grid-like pattern expected from the phantom design. An obvious example is the B1 phantom, exhibiting significantly lower scattering than other B-phantoms. In addition, the variations in scattering among the D-phantoms are surprisingly large. The good reproducibility shows that this deviation is related to phantom manufacturing rather than measurement uncertainty. This conclusion is further supported by noting that correlated systematic variations from phantom design have been reported by Pifferi *et al.* (their work is based on transmission measurements and diffusion modeling, resulting in patterns similar to that shown in Fig. 3(b)).

To verify the quantification of the diffusion related errors as presented in Fig. 1, the mean WMC-derived optical properties of each phantom were multiplied by the corresponding (interpolated) relative error. The resulting optical properties constitute a prediction of the outcome of diffusion modeling, and are presented in Fig. 3(b) as red crosses. The agreement appears very good, showing that the error map is highly relevant and applicable to actual measurements.

Linearity plots of the derived μ_a for the four constant scattering series (A-D) are shown in Fig. 4. The WMC-derived μ_a exhibits linear behavior, while the EBC-diffusion derived data

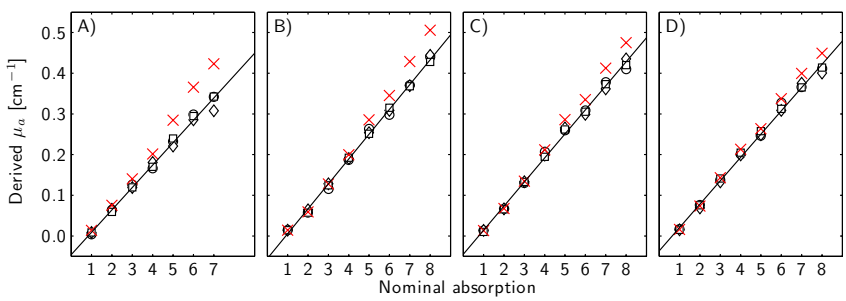

Fig. 4. Linearity plot of the derived μ_a (at 786 nm) for the four constant scattering series (A-D). All WMC-derived data are shown as well as the best linear fit to these points. The mean EBC-diffusion values are shown as red crosses.

features a non-linear increase. This is more evident in the lower scattering series (*e.g.* A phantoms) as the relative error decreases with increasing scattering (as previously shown in Sect. 3.1). Note that at higher scattering (*e.g.* D phantoms), the obtained μ_a pattern can easily be mistaken for a linear increase.

The corresponding linearity plots for the derived μ_s', for the constant absorption series (1-8), are shown in Fig. 5. As expected from the phantom design, both diffusion and WMC modeling results in a linear increase in derived μ_s'. However, in good agreement with previous results reported in Ref. [14], the parameters derived from the diffusion model exhibit an offset-like behavior that causes the extrapolated scattering at zero nominal scattering to significantly deviate from zero. The severity of this overestimation is directly related to the amount of absorber added to the phantom. Due to the imperfections in phantom manufacturing it is, however, difficult to analyze these linearity plots in more detail. An example of this issue is the non-zero offset resulting from the linear extrapolation of the μ_s' values of the 8-phantoms (highest absorption) even for WMC modeling (this offset is further discussed in Sect. 4).

3.3. Model stability with regards to fit range

The importance of the fit range was studied by evaluating experimental data using both EBC diffusion and WMC for different fit range settings. All data points beyond the trailing edge point corresponding to 20% of the peak maximum were always disregarded. The start of the

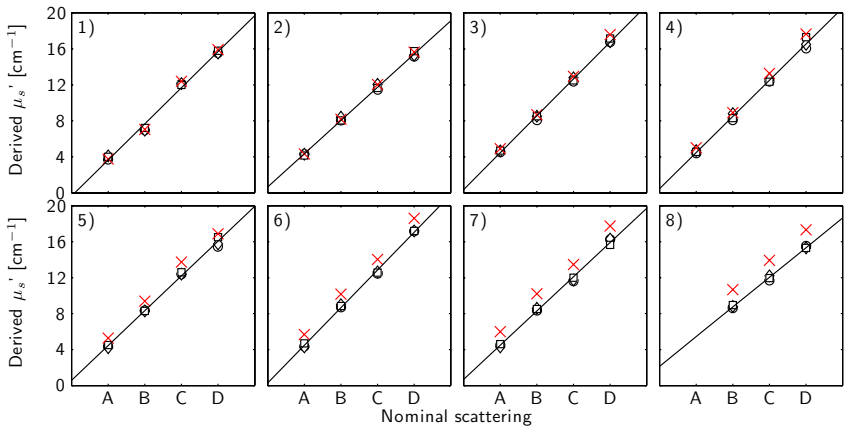

Fig. 5. Linearity plot of the derived μ_s' (at 786 nm) for the constant absorption series (1-8). All WMC-derived values (for all runs) are shown, as well as the best linear fit to these points. The mean values obtained from diffusion modeling are shown as red crosses.

fit range was varied between 1% on the leading edge to 50% on the trailing edge (of peak maximum). The results for the phantoms A1, A7 B4 and D4 (the 786 nm measurement, run 1) are shown in Fig. 6. For diffusion evaluation, the trend is that severe overestimations occur when early data are included. The overestimation decrease (or turn to underestimations) as fewer early data points are included in the fit. The magnitude of the overestimation decreases with increasing scattering and decreasing absorption, as seen also in Fig. 1, while the negative slope with respect to the early fit range limit remains. Using WMC data evaluation, both derived scattering and absorption exhibits insensitivity to the early fit range limit as long as the peak of the data is included. With a few exceptions, such as the D4-phantom (run 1) where a slight positive slope is present, this desirable behavior was seen in almost all measurement. Note that the occurrence of minor slopes appears to be measurement specific, rather than phantom or modeling specific. The phenomenon is observed mainly in highly attenuating phantoms, and may be attributed to *e.g.* light leakage into the collecting fibre, uncertainties in the recorded IRF or temporal drifts.

4. Discussion

Time-resolved measurements of diffuse reflectance (*i.e.* time-of-flight spectroscopy, TOFS) are frequently used for characterization of turbid materials. Although the diffusion approximation of light propagation is the current standard for data evaluation in TOFS, this work clearly shows that the accuracy can be significantly improved if refined models (*e.g.* WMC) are used.

Although the limited validity of diffusion models has been known for many years [9], little has been done to understand and overcome the corresponding errors in diffusion-based data evaluation. This is presumably related to the difficulty in finding alternatives suitable for practical use. The WMC approach proposed in the present paper is a competitive scheme for routine data evaluation, and is shown to avoid the errors of diffusion-based data evaluation. Since it is based on Monte Carlo simulation, being the gold standard for modeling of light propagation within the field of biomedical optics, it is difficult to identify obvious further improvements in terms of model correctness. It should, however, be noted that scalability requirement of the WMC limits its applicability to *e.g.* infinite or semi-infinite geometries. More complex geometries can be handled by a similar approach, involving multiple MC simulations at different μ_s'

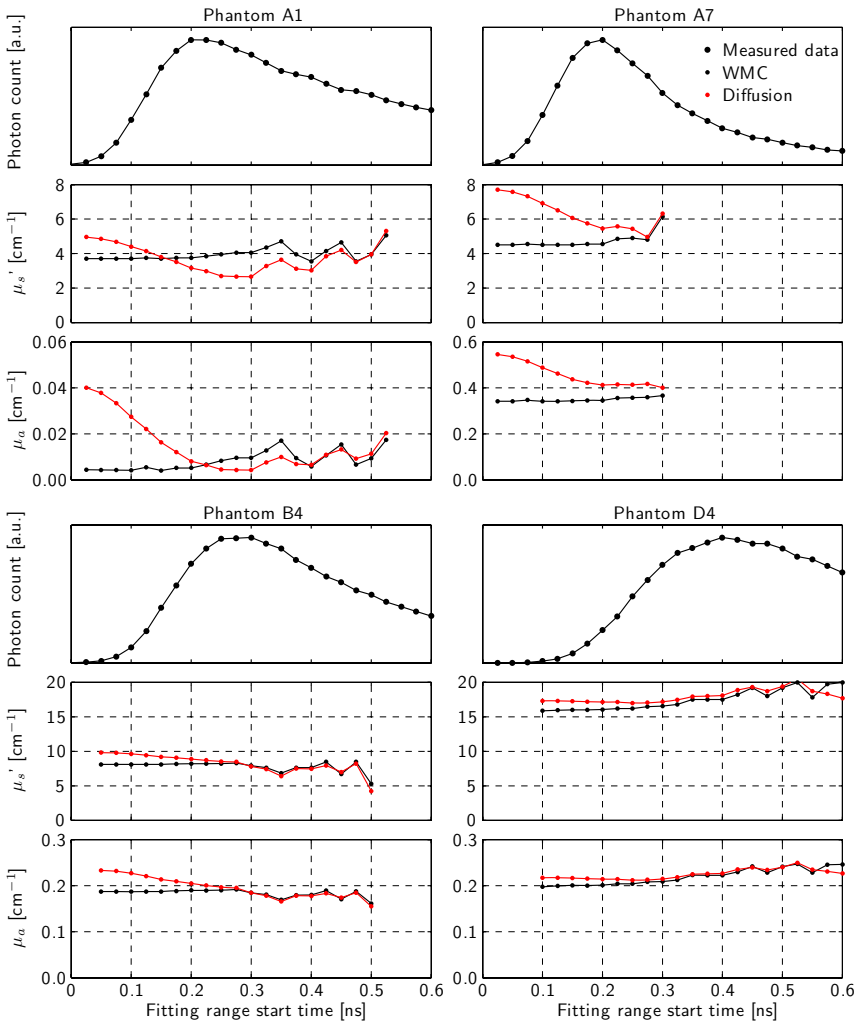

Fig. 6. Derived μ_s' and μ_a as a function of the early fit range limit for the Phantoms A1, A7, B4 and D4 (786 nm data from run 1). The small black and red dots indicate WMC and diffusion evaluation respectively. Each point illustrates the derived μ_s' and μ_a when excluding all earlier the data points during the nonlinear fitting procedure, *i.e.* the fitting range extend from that point (inclusive) to 20% of the peak maximum at the trailing edge. The corresponding TOF histograms are shown for reference. A1 and A7 illustrates the performance in low scattering A phantoms while B4 and D4 exemplifies behavior in the B, C and D phantoms.

[15, 17]. Higher order approximations of the radiative transport equation may in the future provide additional means for implementing refined data evaluation in TOFS.

The value of the WMC approach, and the deficiency of diffusion modeling, is highlighted in several ways. The three following paragraphs discuss important aspects of this important finding:

First, the diffusion model is compared numerically to Monte Carlo simulations in Sect. 3.1. There, error-maps are used to provide a quantitative measure of the errors induced by diffusion evaluation. In contrast to previous studies, where Monte Carlo and diffusion are compared at a single or at few combinations of μ_a and μ_s' [11, 13], these maps shows the errors in an entire range of optical properties. In addition, Fig. 3(b) shows how the error-maps can be used to predict the erroneous outcome of diffusion evaluation of experimental data. The error-maps can be considered to provide estimates of relative errors and a guidance to whether diffusion is applicable (their potential value as a tool for correction of diffusion-based data evaluation is not fully examined). It is also interesting to note that the error-maps for semi-infinite (reflectance) geometries, as presented in the present article, resemble those presented for infinite geometries in Ref. [14] (despite differences in refractive index, anisotropy factor and fit range). Hence, one can argue that the poor performance of diffusion theory in semi-infinite media should be assigned to the breakdown of the diffusion approximation itself, rather than to inappropriate account for boundary conditions. Hielscher *et al.* came to a similar conclusion when investigating different boundary conditions, as they all failed to predict Monte Carlo derived results [11]. Logically, if the diffusion approximation breaks down in a certain region of optical properties even in infinite media [14], one should not expect a performance improvement when investigating the more complex case of geometries with boundaries.

Second, the performance of WMC and diffusion evaluation are compared experimentally using the MEDPHOT set of tissue-simulating phantoms. Fig. 3. These phantoms were manufactured to produce four levels of reduced scattering, and eight levels of absorption (32 phantoms in total). In a so called accuracy plot shown in Fig. 3, derived values μ_s' and μ_a are expected to fall on a grid consisting of equidistant vertical and horizontal lines (different spacing between μ_a and μ_s' levels). As seen in Fig. 3(b), diffusion evaluation clearly fails to reproduce a grid-like pattern. The discrepancy between observed and expected pattern has been reported in several publications, and is often referred to as absorption-to-scattering coupling (or crosstalk) [19, 12, 20]. In contrast, WMC evaluation produces data points on a grid that is consistent with the nominal values of the phantoms. Hence, the above mentioned artifacts are related to the breakdown of the diffusion approximation, and can be completely eliminated by employing the WMC approach. The minor and irregular deviations from a perfect grid that remains even when WMC is employed is most likely related to imperfections in phantom manufacturing (*i.e.* the actual optical properties are not as intended). As discussed in Sect. 3.2, convincing evidence for this conclusion is (i) the good reproducibility as shown in Fig. 3(a), and (ii) that the observed deviations correlate to inter-phantom variations as reported by Pifferi *et al.* despite difference in measurement geometry, instrumentation and operators (see Fig. 6(c) in Ref. [20]). Note that this holds also for the surprisingly large variations in μ_s' for the D-phantoms. The apparent difficulty in the manufacturing of phantoms suggests that intra-phantom heterogeneity cannot be ruled out (and since heterogeneity would decrease reproducibility, this issue may deserve further attention). Futhermore, it is important to remember that phantom imperfections affect the linearity plots shown in Figs. 4 and 5. This is particularly obvious in part (8) in Fig. 5, where the scattering of B8 is slightly above the average B scattering level while the D8 phantom exhibits a scattering slightly lower than the average D phantom (see Fig. 3(a)), misleadingly suggesting a significant scattering offset (note that this plot also suffers from the lack of the A8 phantom). Nonetheless, the linearity plots clearly shows the deficiency of diffusion evaluation, while the outcome of WMC evaluation is highly satisfying. Note, however, that the outcome of diffusion evaluation unfortunately may be mistaken for a linear increase in derived μ_a or μ_s' together with a scattering offset.

Third, the two evaluation schemes are compared by investigating their robustness with respect to fit range. As clearly seen in Fig. 6, and as expected for a correct model, the WMC evaluation is largely independent of the selection of fit range (as long as the peak is included). In great contrast, diffusion evaluation is often highly sensitive to the selection of fit range start time. Since the influence of the fit range selection varies with the range of optical properties (and differs between μ_a and μ_s'), this figure also illustrates that finding an optimal fit range is not possible. In general, if diffusion is used for data evaluation, it appears wise to exclude a majority of the early data points while still keeping the peak data point. This is in agreement with the findings of Cubbedu *et al.* [12]. It is interesting to note that both WMC and diffusion evaluation becomes unstable when the fit range start time is selected so that the peak reflectance data point is excluded from data evaluation. Since most of the information on scattering is found in the early part of the TOF distribution, this may come as no surprise. However, Kienle *et al.* conducted a similar (but theoretical) study of diffusion stability with respect to fit range, showing that stable evaluation can be achieved even when excluding the peak [13]. The failure of both models to do so (in the present experimental study) might indicate a systematic error in the measurements, such as an inaccurate IRF recording procedure.

A question related to the fit range aspect discussed in the previous paragraph, is whether an investigation of fit range sensitivity can reveal measurement quality. If the fit range selection has a systematic influence on WMC-based evaluations, this may indicate systematic measurement problems such as temporal drifts or light leakage (assuming that the WMC model is valid, which can be questioned in, for example, heterogenous materials). In fact, a slight fit range dependence, such as that shown for phantom D4 in Fig. 6, was sometimes observed for the more highly attenuating phantoms. This problem may be assigned to light leakage, as this effect becomes increasingly important for phantoms with higher attenuation. In addition, this difficulty may influence the reproducibility (the highly attenuating D phantoms exhibit a slightly lower reproducibility than the other groups).

Finally it should be noted that the present work is concerned with time-of-flight spectroscopy and time-resolved diffusion theory. Frequency domain photon migration instrumentation, involving lower detection frequencies than TOFS, may be less sensitive to the breakdown of the diffusion approximation [31].

5. Conclusion

The present work presents experimental and theoretical evidence that the transition from diffusion models to WMC significantly improves the accuracy of time-resolved diffuse reflectance spectroscopy in ranges of optical properties of great interest to the biomedical optics community. Of particular importance is (i) that WMC evaluation eliminates the previously reported and familiar artifacts of TOFS known as absorption-to-scattering coupling or crosstalk, and (ii) that the evaluation outcome is largely independent of the fit range setting. In this work, the artifacts are identified as being due to the breakdown of the diffusion approximation. The use of error-maps allows accurate prediction of the errors related to diffusion evaluation, and is a valuable tool when determining the validity of diffusion theory. While the use of refined data evaluation is shown crucial in certain ranges of optical properties, it is also shown that diffusion model can be used successfully as long as scattering is sufficiently high. Since the breakdown is gradual, and depends on optical properties and measurement geometry, it is difficult to generalize when diffusion modeling should be avoided.

The present article also provides the first characterization of the MEDPHOT phantoms that is consistent with the nominal optical properties. The derived optical properties of these phantoms are therefore carefully stated for the wavelengths 660, 786, 830 and 916 nm. Also, we argue that the observed deviations from the phantom design are due to imperfections in phantom manufacturing. These imperfections must be considered when using these phantoms for performance assessment.

Acknowledgment

We are grateful to the biomedical optics group at Politecnico di Milano for generously letting us use the MEDPHOT phantoms. We gratefully acknowledge the financial support through the EC grant Nano-UB Sources.

Appendix

Table 1. Derived reduced scattering coefficients [cm^{-1}]. * Due to the limited time range where WMC is valid, these measurement had to be evaluated using a reduced fit range (20/40).

	660 nm			786nm			830 nm			916 nm		
	run1	run2	run3	run1	run2	run3	run1	run2	run3	run1	run2	run3
A1	4.75	5.00	5.00	3.70	4.10	4.00	3.35	3.70	3.65	3.00	3.25	3.20
A2	5.40	5.25	5.15	4.30	4.30	4.15	3.65	3.90	3.75	3.05	3.35	3.25
A3	5.55	5.85	5.85	4.50	4.65	4.70	3.95	4.20	4.10	3.50	3.65	3.50
A4	5.55	5.75	5.65	4.40	4.70	4.55	3.95	4.25	4.15	3.10	3.60	3.60
A5	5.15	5.30	5.25	4.40	4.20	4.50	3.90	3.80	3.90	3.20	3.20	3.55
A6	5.35	5.45	5.75	4.35	4.30	4.70	3.90	3.95	4.30	3.30	3.30	3.80
A7	5.70	5.40	5.55	4.50	4.30	4.60	3.95	3.90	4.00	3.40	3.00	3.40
B1	8.35	8.55	8.50	6.95	6.95	7.20	6.20	6.30	6.45	5.25	5.50	5.65
B2	10.35	10.35	10.30	8.05	8.40	8.05	7.10	7.60	7.40	6.50	6.65	6.60
B3	10.20	10.45	10.40	8.10	8.50	8.50	7.30	7.70	7.65	6.45	6.80	6.80
B4	10.05	10.85	10.00	8.10	8.80	8.30	7.40	8.10	7.55	6.45	7.05	6.55
B5	10.30	10.20	10.15	8.35	8.30	8.30	7.55	7.55	7.65	6.55	6.55	6.55
B6	10.65	11.20	10.65	8.70	9.00	8.85	7.90	8.00	8.00	6.70	7.10	7.00
B7	10.25	10.60	10.30	8.35	8.60	8.50	7.60	7.95	7.80	6.45	6.95	6.70
B8	10.50	10.75	11.35	8.60	8.80	8.95	7.85	7.90	8.15	6.45	6.85	7.25
C1	14.60	14.90	14.85	12.15	12.15	12.00	11.10	10.90	10.95	9.35	9.55	9.50
C2	14.15	14.95	14.40	11.45	12.05	11.65	10.30	11.00	10.40	9.00	9.60	9.25
C3	15.20	15.95	15.60	12.35	12.80	12.50	11.00	11.65	11.35	9.70	10.45	10.20
C4	15.30	15.65	15.40	12.35	12.65	12.35	11.25	11.55	11.15	9.85	10.25	9.90
C5	15.15	15.00	15.25	12.40	12.40	12.60	11.45	11.30	11.40	9.90	9.90	10.35
C6	15.55	15.85	15.70	12.45	12.65	12.55	11.25	11.75	11.60	9.75	10.35	10.20
C7	14.65	14.95	14.50	11.60	11.75	12.00	10.65	10.70	10.70	9.10	9.55	9.55
C8	14.35	15.35	14.95	11.70	12.20	11.95	10.80	11.20	11.15	9.20	9.55	9.70
D1	19.40*	19.25*	20.00*	15.55	15.55	15.80	14.00	14.05	14.20	12.30	12.40	12.50
D2	18.40	18.85	19.05	15.15	15.30	15.75	13.65	14.00	14.15	12.30	12.30	12.50
D3	20.95	20.95	20.70	16.75	16.80	17.15	15.20	15.30	15.40	13.50	13.40	13.85
D4	20.00	20.70	21.00	16.05	16.50	17.30	14.60	15.05	15.40	12.80	13.30	13.80
D5	19.60	19.65	20.55	15.45	15.75	16.50	14.25	14.75	14.75	12.20	12.95	13.25
D6	20.70	20.80	21.00	17.15	17.20	17.20	15.40	15.45	15.40	13.40	13.90	13.45
D7	19.70	19.70	19.65	16.25	16.30	15.65	14.25	14.50	14.45	12.55	12.90	12.35
D8	19.00	18.75	18.30	15.55	15.30	15.30	14.00	14.15	13.50	12.45	12.20	12.40

Table 2. Derived absorption coefficients [cm^{-1}]

	660 nm			786nm			830 nm			916 nm		
	run1	run2	run3	run1	run2	run3	run1	run2	run3	run1	run2	run3
A1	0.01	0.01	0.01	0.00	0.01	0.01	0.01	0.01	0.02	0.07	0.07	0.07
A2	0.08	0.07	0.07	0.06	0.07	0.06	0.06	0.07	0.07	0.11	0.12	0.12
A3	0.15	0.15	0.14	0.13	0.12	0.12	0.12	0.12	0.12	0.18	0.18	0.16
A4	0.20	0.21	0.20	0.17	0.18	0.17	0.17	0.19	0.18	0.19	0.23	0.22
A5	0.25	0.28	0.26	0.23	0.22	0.24	0.23	0.23	0.23	0.25	0.26	0.28
A6	0.34	0.35	0.34	0.30	0.29	0.29	0.29	0.30	0.30	0.32	0.33	0.34
A7	0.41	0.37	0.38	0.34	0.31	0.34	0.33	0.31	0.32	0.37	0.33	0.36
B1	0.01	0.01	0.01	0.01	0.01	0.01	0.02	0.02	0.02	0.07	0.08	0.08
B2	0.08	0.07	0.07	0.06	0.06	0.06	0.06	0.07	0.06	0.12	0.13	0.13
B3	0.14	0.14	0.14	0.12	0.13	0.12	0.12	0.13	0.12	0.18	0.19	0.19
B4	0.22	0.22	0.21	0.19	0.19	0.19	0.19	0.20	0.19	0.25	0.25	0.24
B5	0.30	0.30	0.28	0.26	0.25	0.25	0.26	0.26	0.26	0.32	0.31	0.31
B6	0.34	0.35	0.34	0.30	0.31	0.31	0.30	0.30	0.32	0.33	0.36	0.36
B7	0.42	0.43	0.42	0.37	0.37	0.37	0.37	0.38	0.38	0.40	0.42	0.41
B8	0.51	0.50	0.52	0.44	0.44	0.43	0.45	0.43	0.43	0.46	0.47	0.47
C1	0.01	0.01	0.01	0.01	0.01	0.01	0.02	0.01	0.01	0.07	0.07	0.07
C2	0.08	0.08	0.08	0.07	0.07	0.07	0.07	0.07	0.06	0.13	0.13	0.13
C3	0.15	0.15	0.15	0.13	0.13	0.13	0.13	0.14	0.13	0.19	0.21	0.20
C4	0.24	0.23	0.23	0.21	0.20	0.19	0.21	0.20	0.20	0.27	0.26	0.26
C5	0.30	0.30	0.29	0.26	0.27	0.26	0.27	0.27	0.26	0.31	0.32	0.33
C6	0.36	0.35	0.36	0.31	0.30	0.31	0.31	0.31	0.32	0.35	0.36	0.37
C7	0.46	0.45	0.42	0.38	0.36	0.37	0.38	0.36	0.37	0.42	0.42	0.42
C8	0.48	0.52	0.50	0.41	0.44	0.42	0.42	0.44	0.44	0.45	0.47	0.47
D1	0.02*	0.02*	0.02*	0.02	0.02	0.02	0.02	0.02	0.02	0.08	0.08	0.07
D2	0.08	0.08	0.08	0.08	0.07	0.08	0.07	0.07	0.07	0.14	0.13	0.14
D3	0.16	0.16	0.15	0.14	0.13	0.14	0.14	0.13	0.14	0.21	0.20	0.21
D4	0.24	0.24	0.23	0.20	0.20	0.20	0.20	0.20	0.20	0.26	0.26	0.26
D5	0.30	0.30	0.30	0.25	0.25	0.26	0.26	0.26	0.25	0.30	0.32	0.31
D6	0.37	0.36	0.36	0.33	0.31	0.31	0.32	0.30	0.30	0.37	0.37	0.36
D7	0.41	0.41	0.42	0.37	0.38	0.37	0.35	0.36	0.37	0.39	0.42	0.40
D8	0.47	0.47	0.46	0.41	0.40	0.41	0.40	0.42	0.40	0.46	0.45	0.48